

AD-A184 046

FATIGUE '87 VOLUME 2(U) VIRGINIA UNIV CHARLOTTESVILLE  
SCHOOL OF ENGINEERING AND APPLIED SCIENCE  
R O RITCHIE ET AL. JUN 87 N00014-87-G-0006

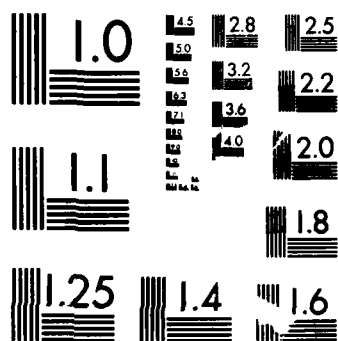
1/6

UNCLASSIFIED

F/G 20/11

NL

179



MICROCOPY RESOLUTION TEST CHART  
NATIONAL BUREAU OF STANDARDS-1963-A

DTIC FILE COPY

①

# FATIGUE '87

## VOLUME II

AD-A184 046

DTIC  
SELECTED  
SEP 03 1987  
S D

Approved for public  
Distribution Under E.O.

Papers present at the Third International Conference  
on Fatigue and Fatigue Thresholds  
held at the University of Virginia, Charlottesville, Virginia  
June 28 - July 3, 1987

87 3 1 204

UNCLASSIFIED 17-41840X6 MASTER COPY  
SECURITY CLASSIFICATION OF THIS PAGE

FOR REPRODUCTION PURPOSES

REPORT DOCUMENTATION PAGE				
1a. REPORT SECURITY CLASSIFICATION Unclassified			1b. RESTRICTIVE MARKINGS	
2a. SECURITY CLASSIFICATION AUTHORITY			3. DISTRIBUTION/AVAILABILITY OF REPORT Approved for public release; distribution unlimited.	
2b. DECLASSIFICATION/DOWNGRADING SCHEDULE				
4. PERFORMING ORGANIZATION REPORT NUMBER(S)			5. MONITORING ORGANIZATION REPORT NUMBER(S) ARO 24134.2-MS-CF	
6a. NAME OF PERFORMING ORGANIZATION Univ. of Virginia		6b. OFFICE SYMBOL (If applicable)	7a. NAME OF MONITORING ORGANIZATION U. S. Army Research Office	
6c. ADDRESS (City, State, and ZIP Code) Charlottesville, VA 22904			7b. ADDRESS (City, State, and ZIP Code) P. O. Box 12211 Research Triangle Park, NC 27709-2211	
8a. NAME OF FUNDING/SPONSORING ORGANIZATION U. S. Army Research Office		8b. OFFICE SYMBOL (If applicable)	9. PROCUREMENT INSTRUMENT IDENTIFICATION NUMBER DAAL03-87-G-0102	
8c. ADDRESS (City, State, and ZIP Code) P. O. Box 12211 Research Triangle Park, NC 27709-2211			10. SOURCE OF FUNDING NUMBERS PROGRAM ELEMENT NO. PROJECT NO. TASK NO. WORK UNIT ACCESSION NO.	
11. TITLE (Include Security Classification) Fatigue "87", Volume II				
12. PERSONAL AUTHOR(S) R. O. Richie, E. A. Starke, Jr. (Editors)				
13a. TYPE OF REPORT Final		13b. TIME COVERED FROM 6/1/87 TO 5/1/88	14. DATE OF REPORT (Year, Month, Day) August 1987	15. PAGE COUNT
16. SUPPLEMENTARY NOTATION The view, opinions and/or findings contained in this report are those of the author(s) and should not be construed as an official Department of the Army position, policy, or decision, unless so designated by other documentation.				
17. COSATI CODES FIELD GROUP SUB-GROUP			18. SUBJECT TERMS (Continue on reverse if necessary and identify by block number) Fatigue, Cyclic Deformation, Crack Initiation, Crack Propagation, Crack Closure	
19. ABSTRACT (Continue on reverse if necessary and identify by block number) The current proceedings (3 volumes) of the third conference, "Fatigue 87" which was held at the University of Virginia, Charlottesville, covered a wide range of diverse views of the fundamental and applied aspects of fatigue. This includes questions of cyclic deformation, crack initiation and propagation, small cracks, crack closure, variable amplitude effects, and environmentally-influenced behavior. The proceedings should provide a comprehensive state-of-the-art review of the field, suitable for students, researchers and practising engineers alike. (Volume II)				
20. DISTRIBUTION/AVAILABILITY OF ABSTRACT <input type="checkbox"/> UNCLASSIFIED/UNLIMITED <input type="checkbox"/> SAME AS RPT. <input type="checkbox"/> DTIC USERS			21. ABSTRACT SECURITY CLASSIFICATION Unclassified	
22a. NAME OF RESPONSIBLE INDIVIDUAL			22b. TELEPHONE (Include Area Code)	22c. OFFICE SYMBOL

FORM 1473, 84 MAR

83 APR edition may be used until exhausted.  
All other editions are obsolete.

SECURITY CLASSIFICATION OF THIS PAGE  
UNCLASSIFIED

# FATIGUE '87

## VOLUME II

### EDITORS:

R.O. Ritchie and E.A. Starke, Jr.

Papers presented at the  
Third International Conference on Fatigue and Fatigue Thresholds  
held at the University of Virginia, Charlottesville, Virginia.  
June 28 – July 3, 1987

### EDITORIAL PANEL

R.P. Gangloff, R.O. Ritchie, E.A. Starke, Jr., and J.A. Wert.

### ORGANIZING COMMITTEE

E.A. Starke, Jr., C.J. Beevers, R.P. Gangloff, R.O. Ritchie,  
and J.A. Wert

### RE: Distribution Statement

Approved for Public Release. Distribution  
Unlimited.

Per Dr. Ralph Judy, Office of Naval Research,  
Code 1131

For  
RA&I ☒  
B ☐  
ced ☐  
in

*per call*

### Availability Codes

Dist	Avail and/or Special
A-1	

**EMAS** ENGINEERING MATERIALS  
ADVISORY SERVICES LTD.  
339, Halesowen Road, Cradley Heath,  
Warley, West Midlands, B64 6PH, U.K.



## PREFACE

Fracture by the progressive growth of incipient flaws under cyclically varying loads, i.e., by fatigue, must now be considered as the principal cause of in-service failures of engineering structures and components, whether associated with mechanical sliding and friction (fretting fatigue), rolling contact, aggressive environments (corrosion fatigue), or elevated temperatures (creep-fatigue). Of particular importance are the early stages of fatigue damage, involving the initial extension of microcracks and their subsequent growth at very low velocities, as these processes tend to dominate overall lifetime. This has been reflected by trends in fatigue research over the past five years, which have focused largely on so-called "small cracks," of dimensions comparable with the scale of microstructure or local plasticity, and on crack growth in the near-threshold regime, i.e., at stress intensities approaching the fatigue threshold below which cracks are presumed dormant. In addition, associated mechanistic studies have highlighted the critical role of crack tip shielding in fatigue, which arises predominantly from crack closure and deflection, and this has proved to be important in modeling aspects of environmentally-assisted cracking and behavior under variable amplitude loads, and in rationalizing the classical stress/strain-life and defect-tolerant design approaches.

The series of international conferences on Fatigue and Fatigue Thresholds, although devoted to all aspects of fatigue, has emphasized these topics of small cracks and near-threshold behavior, and consequently, has become an international forum for the exchange of information in this field. The series, which has been run under the auspices of a steering and international committee with representatives from Australia, Austria, Canada, China, Czechoslovakia, France, Holland, Japan, Norway, Sweden, U.K., W. Germany and the U.S.A., began in Stockholm, Sweden, in 1981, and continued at the University of Birmingham in England in 1984.

The current proceedings of the third conference, "Fatigue '87," which was held at the University of Virginia, Charlottesville, covered a wide range of diverse views of the fundamental and applied aspects of fatigue. This includes questions of cyclic deformation, crack initiation and propagation, small cracks, crack closure, variable amplitude effects, and environmentally-influenced behavior. The proceedings should provide a comprehensive state-of-the-art review of the field, suitable for students, researchers and practising engineers alike.

The Editors would like to thank the Editorial Committee, particularly Professors R.P. Gangloff and J.A. Wert, the International Committee and the University of Virginia for their help over the past couple of years. We express our sincere thanks to Dr. A.H. Rosenstein of the Air Forces Office of Scientific Research, Dr. G. Mayer of the Army Research Office, Dr. B.A. MacDonald of the Office of Naval Research, and Dr. G. Hartley of the National Science Foundation for their financial support, and to Ms. Tana B. Herndon for her sterling efforts as the conference secretary.

R.O. Ritchie  
E.A. Starke, Jr.  
June 1987.

①

# FATIGUE 87

## RECOMMENDED SYMBOLS

$a$	Crack-Length - One-Half the Total Length of an Internal Crack or Depth of a Surface Crack
$\Delta a$	Crack Growth Increment
a.c.	Alternating Current
$B$	Test Piece Thickness
$C$	Compliance
$C_1 - C_5$ & $D$	Constants
$da/dN$	Rate of Fatigue Crack Propagation
$\Delta \frac{da}{dN}$	Additional Growth Rate due to Environment
$\left[ \frac{da}{dN} \right]_{CTB}$	Growth Rate Retarded by Crack Tip Blunting
$\left[ \frac{da}{dN} \right]_{LHE}$	Growth Rate Enhanced by Localised Hydrogen Embrittlement
$\left[ \frac{da}{dN} \right]_{TCF}$	Overall Growth Rate for 'True Corrosion Fatigue'
$\left[ \frac{da}{dN} \right]_{SCF}$	Stress Corrosion Fatigue Crack Growth Rate
$\left[ \frac{da}{dt} \right]_p$	Stress Corrosion Plateau Growth Rate Per Second
$da/dt$	Crack Extension Rate
d.c.	Direct Current
$\delta$	Value of Crack Opening Displacement (see British Standard BS5762)
$\delta_c$	Critical Crack Opening Displacement, being One of the Following: <ol style="list-style-type: none"> <li>(1) Crack Opening Displacement at Fracture</li> <li>(2) Crack Opening Displacement at First Instability or Discontinuity</li> <li>(3) Crack Opening Displacement at which</li> </ol>

## FATIGUE 87

an Amount of Crack Growth Commences

$\delta_m$	Crack Opening Displacement at First Attainment of Maximum Force
$D_H$	Diffusion Coefficient for Hydrogen in Iron
$E$	Young's Modulus of Elasticity
$\exp$	Exponential Base of Natural Logarithms
$\epsilon$	Creep Strain
$\dot{\epsilon}_S$	Secondary Creep Rate
$\epsilon_T$	Transient Creep Strain
$F$	Cyclic Frequency
$G$	Strain Energy Release Rate
$G_I G_{II} G_{III}$	Crack Extension Forces for Various Modes of Crack Opening
$I$	Current
$i_a$	Anodic Current Density
$K$	Stress Intensity Factor - a Measure of the Stress-Field Intensity Near the Tip of a Perfect Crack in a Linear-Elastic Solid
$K_C$	Fracture Toughness - The Largest Value of the Stress-Intensity Factor that exists Prior to the Onset of Rapid Fracture
$K_{cl}$	$K$ in Fatigue Cycle Below which Crack is Closed
$K_I$	Opening Mode Stress Intensity Factor
$K_{IC}$	Plane-Strain Fracture Toughness as Defined by ASTM Standard Designation E 399-74 or British Standard BS 5447
$K_{Ii}$	Elastic Stress-Intensity Factor at the Start of a Sustained-Load Flaw-Growth Test
$K_{ISCC}$	Plane-Strain $K_I$ Threshold Above which Sustained Load Flaw-Growth Occurs

# FATIGUE 87

$K_{IH_2S}$	Value of $K_{ISCC}$ in Dry $H_2S$ Gas
$K_Q$	Provisional Fracture Toughness Value Corresponding to a 5% Deviation of the Load/Displacement Relationship from Linearity
$K_{max}$	Maximum Stress-Intensity Factor
$K_{min}$	Minimum Stress-Intensity Factor
$\Delta K$	Stress Intensity Range
$\Delta K_{th}$	Threshold Stress Intensity Factor Below which Fatigue Crack Growth will not occur
$\Delta K_i^o$	$\Delta K_i$ to just cause Fatigue Initiation
$\Delta K_n$	Next Value of $\Delta K$
$\Delta K_{th}^o$	Value of $\Delta K_{th}$ at $R = 0$
$\Delta K_o$	Constant Value of $\Delta K_{th}$
$d\Delta K$	Notional Extra Stress Intensity due to Environment
$k_T, k_N$	Stress Concentration Factor, Neuber Correction Factor
$\ln$	Natural Logarithm
$\log$	Common Logarithm
$m$	Power Exponent in Paris-Erdogen Expression $\frac{da}{dN} = A \Delta K^m$
$N$	Cycles
$N_i$	Cycles to Initiate
$N_F$	Cycles to Failure
$\Delta N$	Cycles Increment
$n$	Strain Hardening Exponent
$\Delta P$	Load Range
$\nu$	Poisson's Ratio

# FATIGUE 87

$Q$	Flaw Shape Parameter
$\sigma$	Stress
$\Delta\sigma$	Stress Range
$\sigma_{\max}$	Maximum Stress
$\sigma_{ps}$	Proof Stress
$\sigma_{\min}$	Minimum Stress
$\sigma_u$	Ultimate Tensile Strength
$\sigma_y$	Yield Stress under Uniaxial Tension
$\Delta\sigma_{\text{net}}$	Stress Range on Net Section
$R$	Minimum Load/Maximum Load
$R_{cl}$	R below which Crack Closure Occurs
$r_p$	Plastic Zone Size
$\rho$	Crack Tip Radius
$\rho_o$	Notional Minimum Value of $\rho$
$T$	Temperature
$t$	Time
$t_h$	Hold Time in Load Cycle
$t_r$	Rise Time in Load Cycle
$t_r^o, t_r^{\max}$	Values of $t_r$ at Minimum and Maximum Environmental Enhancement
$V$	Potential Difference
$V_o$	Reference Potential Difference
$V(a)$	Potential Difference at Crack Length, $a$
$W$	Test Piece Width
$\phi$	Electric Potential
$x, y$	Cartesian Co-ordinates

## FATIGUE 87

Y Compliance Function

$\Omega$  Ohms

### RECOMMENDED ABBREVIATIONS

BFS Back Face Strain

BRF Blunting Retardation Factor

CCP Centre Cracked Plate

COD Crack Opening Displacement

CT Compact Tension

CTB Crack Tip Blunting

DCPD Direct Current Potential Drop

EEF Environmental Enhancement Factor

LHE Localised Hydrogen Embrittlement

PD Potential Drop

SENB Single Edge Notched Bend

SENT Single Edge Notched Tension

SCC Stress Corrosion Cracking

SCF Stress Corrosion Fatigue

TCF True Corrosion Fatigue

T-Type WOL T-Type Wedge Open Loading

UTS Ultimate Tensile Strength

FATIGUE 87

# CONTENTS

## VOLUME II

### FATIGUE OF METALS

Fatigue Damage Maps - DARRELL F. SOCIE	599
An Investigation of Fatigue Crack Growth in a Ductile Material at High Growth Rates - K.J. NIX, N. KNEE, T.C. LINDLEY AND G.G. CHELL	617
Cyclic Deformation Behaviour of Cast Irons with Various Graphite Shapes in the Temperature Range $20\text{ C} \leq T \leq 500\text{ C}$ - K.H. LANG, D. EIFLER AND E. MACHERAUCH	627
Fatigue Crack Growth and Fracture of Copper- Bismuth Bicrystals - S. CHIKWEMBANI AND J. WEERTMAN	637
Life Prediction of Steel Cords - A. PRAKASH, G.A. COSTELLO, R.M. SHEMENSKI AND D.K. KIM	645
Effect of Hold Time on Fatigue of Lead Rich PbSn Solder - S. VAYNMAN, M.E. FINE AND D.A. JEANNOTTE	655
On Cleavage in Fatigue for Rail Steels - ZHU DONG, CAI QIGONG and YAO HENG	667
Influence of Cleavage on Fatigue Propagation Rates in a Low Carbon Steel - Y. BLANCHETTE, J.I. DICKSON AND J.P. BAILON	677
Effect of Metal Surface Properties on the Fatigue Crack Growth Behavior - A.V. PROKOPENKO AND V.N. TORGOV	687

## FATIGUE 87

Fatigue Crack Growth Behavior in Hydrogen Gas Environment - S. YOSHIOKA, M. KUMASAWA, M. DEMIZU AND A. INOUE	697
Application of Fatigue Analysis on Railroads in China - LIU SHU-ZHEN AND WANG JIA- DEE	707

## FATIGUE THRESHOLDS

Near-Threshold Fatigue - PETR LUKAS	719
Notch-Geometry Effect on Propagation Threshold of Short Fatigue Cracks in Notched Components - K. TANAKA AND Y. AKINIWA	739
Influence of Crack Closure on Fatigue Crack Propagation and Threshold - A. DIAS, A. BIGNONNET AND H.P. LIEURADE	749
An Explanation of the Fractography of Near- Threshold Fatigue in FCC Metals - J.I. DICKSON, LI SHIQIONG AND J.-P. BAILON	759
The Relationship Between Microstructural Size and Fatigue Threshold in Iron and Steel - GU HAICHENG AND LIU XIAO DU	769
Threshold Behaviour of Semi-Elliptic Hydrogen-Induced and Fatigue-Induced Cracks - M.N. JAMES	779
Effect of Compressive Portion of Loading Cycles on the Near Threshold Fatigue Closure Behavior - HEINRICH KEMPER, BRIGITTE WEISS AND ROLAND STICKLER	789
Absolute Fatigue Thresholds in Metallic Materials - J.A. LEWIS	801
Thermometrical Investigations on the Near Threshold Fatigue Crack Propagation Behavior - K. MULLER AND H. HARIG	809
A Reevaluation of Fatigue Threshold Test Methods - W.A. HERMAN, R.W. HERTZBERG, C.H. NEWTON AND R. JACCARD	819

## FATIGUE 87

The Factors which govern the Acceleration of Corrosion Fatigue Crack Growth Rate of a Ferritic Stainless Steel - Y. KIMURA, T. YAGASAKI AND T. KUNIO	829
Fatigue Thresholds of C-Mn Steels in Saline Environments - P.R.G. ANDERSON, R. BROOK AND C.E. NICHOLSON	839
A Model for Ultra-Low Fatigue Crack Growth - J.C. RADON AND L. GUERRA-ROSA	851
Influence of Stress Ratio R on Fatigue Threshold Delta $K_{th}$ for 40Cr Steel - LI NIAN AND DU BAI-PING	861
The Effects of Loading History on Fatigue Crack Growth Threshold - T. OGAWA, K. TOKAJI, S. OCHI AND H. KOBAYASHI	869
Threshold Stress Intensity for Stable Crack Growth in High Strength Steel at Ambient Temperature and Below - L. WEBER	879
The Effect of Shear Lips on Fatigue Crack Growth in Al2024 Sheet Material - J. ZUIDEMA AND H.S. BLAAUW	889
Near-Threshold Fatigue Crack Growth Behavior at Cryogenic Temperature - P.K. LIAW AND W.A. LOGSDON	899
The Effect of Nonmetallic Inclusions on Fatigue and Fatigue Thresholds of 25Mn-5Cr-1Ni Steel - I. MAEKAWA, J.H. LEE AND S. NISHIDA	911
Role of Interstitials and Precipitates in Initiation and Propagation of L.C.F. Cracks in Austenitic Stainless Steels - S. DEGALLAIX AND J. FOCT	921

## RESIDUAL STRESS

Threshold and Crack-Growth Tests on Pre-Cracked Specimens Produced in Cyclic Compression - R. PIPPAN	933
--	-----

## FATIGUE 87

Micromechanics of Fatigue Crack Initiation under Axial and Torsional Loadings - T.H. LIN, S.R. LIN AND W.U. COOLEY	941
Study of the Characteristic Curve of Hardening and Softening During Low- Cycle Fatigue Process - CHEN XINZENG, FEN ZHONGXIN, ZHANG JIANZHONG AND CHAI HUIFEN	951
The Effect of Prestraining on Fatigue Crack Growth in Nickel-Base Alloys - J.M. KENDALL, M.A. HICKS AND J.E. KING	959
Mixed Mode Fatigue Crack Growth Using the Brazilian Disc - M. LOUAH, G. PLUVINAGE AND A. BIA	969
Crack Closure Phenomena in Modes I and II Interactions - H. NAYEB-HASHEMI, S.S. HWANG AND P.G. POLES	979
Multiaxial Fatigue Failure Criterion: A New Approach - K. DANG VAN AND Y.V. PAPADOPOULOS	997
Profiles of Self Stress and of Load Stress at Notches - H.O. FUCHS AND S.B. LEE	1009

## HIGH TEMPERATURE FATIGUE

Fatigue Oxidation Interaction in Low Cycle Fatigue - M. LEBIENVENU, Z. AZARI AND G. PLUVINAGE	1021
Effect of Temperature Exposure on Fatigue Crack Propagation - K.K. BRAHMA, B. DATTAGURU AND R. SUNDER	1027
High Temperature Low Cycle Fatigue of Oxide Dispersion Strengthened and Single Crystal Nickel Base Superalloys - M. MARCHIONNI, V. CATENA AND D. RANUCCI	1037
Orientation Effects in Copper Single Crystals Fatigued at Elevated Temperatures - L.L. LISIECKI, F. BOEHME AND J.R. WEERTMAN	1047

# FATIGUE 87

Elevated Temperature Fatigue Crack Propagation - D.J. MICHEL AND A.W. THOMPSON	1057
High Temperature Low Cycle Fatigue Behavior and Creep-Fatigue Interaction of MA 6000 ODS Alloy - M. NAZMY, W. EBELING AND M. STAUBLI	1067
Creep-Fatigue Cracking in High Temperature Turbine Rotors - A.T. STEWART, D.A. MILLER, D.C. MARTIN AND G. WIGMORE	1077
The Effect of Temperature on Fatigue Crack Initiation from Aluminosilicate Inclusions - P. WOOLLIN AND J.F. KNOTT	1087
Dependence of Strain Range Partitioned Fatigue Life at Elevated Temperature on Monotonic Stress-Strain Properties - A. BERKOVITS AND S. NADIV	1101
Thermal Mechanical Low Cycle Fatigue of 25CDV4-10 Steel - J. GILGERT, M. LEBIENVENU AND G. PLUVINAGE	1113
Axial Creep-Fatigue Damage Assessment in Type 316 SS Material - S.Y. ZAMRIK AND D.C. DAVIS	1123
An Analysis of Temperature Effect on LCF Crack Growth Rates in Superalloy GH36 - XIE JIZHOU AND LIU SHAOLUN	1133
Thermomechanical Fatigue of Lead-Base Low Tin Solder - L.R. LAWSON, M.E. FINE AND D.A. JEANNOTTE	1143

FATIGUE 87

FATIGUE 87

## FATIGUE OF METALS

FATIGUE 87

FATIGUE DAMAGE MAPS

Darrell F. Socie\*

SYNOPSIS

Observations of fatigue crack nucleation and early growth are presented. The state of stress/strain has been shown to play a significant role in this process. Early crack growth occurs on planes experiencing the largest range of shear strain (Mode II) or normal strain (Mode I) depending on stress state, strain amplitude and microstructure. These observations have been summarized in a fatigue damage map for each material. Extension of the fatigue damage maps to complex loading is presented.

INTRODUCTION

Fatigue damage is a process resulting in failure under cyclic loads. A universal definition of fatigue damage is unlikely because there are many mechanisms involved in the fatigue process. Each mechanism is dominant over a limited range of materials, strain amplitudes, stress states and environments. In this paper, fatigue damage is defined and quantified as the nucleation and growth of cracks in metals. Fatigue mechanisms describe the manner in which the microstructural features of the material interact with the applied loads to produce fatigue damage.

Much if not most of our knowledge of the fatigue process comes from constant amplitude uniaxial tension tests at room temperature. Ewing and Humfrey (1) were among the earliest investigators to systematically examine and document surface crack formation of a cyclically loaded specimen. Crack nucleation is a result of reversed plastic slip on crystallographic slip planes within single grains that are favorably oriented with the maximum

\*Department of Mechanical and Industrial Engineering, University of Illinois at Urbana-Champaign, 1206 West Green Street, Urbana, IL 61801

applied shear stress. Reversed slip during cyclic loading results in the development of discrete regions called slip bands. During the fatigue process, these regions coarsen and material is displaced resulting in the formation of intrusions and extrusions. At some point in this process decohesion occurs, and these regions become crack-like. Failure then results from the growth of this crack to a critical size.

Forsyth (2) suggested a two-stage model for crack growth. Stage I has been defined as a period of crystallographically oriented growth that usually includes some initiation. Crack dimensions are typically small and microstructural features can influence the crack behavior. Both shear stress/strain and normal stress/strain on the crack surface are important during Stage I growth. Normal stresses tend to reduce the amount of Stage I growth. Cracks will sometimes change direction from Stage I planes and grow in a Stage II orientation. Stage II is a period of continuum crack growth occurring macroscopically on a plane perpendicular to the maximum principal stress range. These observations have been coupled with appropriate mechanics models to form the basis of both the local stress/strain and fracture mechanics approaches to fatigue damage analysis. Observations of multiaxial fatigue damage are presented in this paper. Attention is focused on the regime where crack nucleation and early growth dominate the behavior of the material.

#### CRACK OBSERVATIONS

Detailed crack observations have been made on three materials, 304 stainless steel, Inconel 718, and SAE 1045 steel during tensile and torsion fatigue testing. Each of these materials exhibits different regions of cracking behavior. Experimental data can be found in earlier papers: Hua and Socie, (3); Socie, Kurath and Koch, (4); Bannantine and Socie [5]. The type of behavior observed is summarized in Fig. 1 for 304 stainless steel. The vertical scale is presented in terms of life fraction and the horizontal scale in terms of fatigue life. The solid line represents the first observation of a surface crack 100  $\mu\text{m}$  long and serves as a demarcation between crack nucleation and growth. It could be argued that nucleation occurs much earlier at, say, 10  $\mu\text{m}$ . This would simply shift the line down without changing the qualitative phenomena represented by the nature of the plots. The dashed lines represent the demarcation between crack growth on planes of maximum shear strain amplitude and crack growth on planes of maximum principal strain amplitude. The diagrams have been divided into three regions depending on the type of failure that was observed. Region A in Fig. 1a for 304 stainless steel loaded in torsion denotes a failure mode that is dominated by shear crack growth. Cracks initiated in slip bands and at grain boundaries. Once initiated, the cracks become more distinct but showed no significant increase in length. At failure, a large

density of small, coarse cracks dominated the surface of the specimen. A small amount of branching onto tensile planes (Stage II planes) was observed. Failure cracks can grow on either Stage I or Stage II planes by a slow linking of previously initiated shear cracks. Region B is characterized by shear crack nucleation followed by crack growth on planes of maximum principal strain amplitude. Shear crack growth consumes a small fraction of the fatigue life. Region B behavior was observed at the longest lives in torsion. The fraction of life spent growing the crack on shear planes was reduced, as was the crack density. A small number of cracks initiated on shear planes but quickly branched to Stage II planes. Growth on these planes occurred by the propagation of the main crack rather than by a linking process.

Surface replicas and scanning electron examination of fracture surfaces of AISI 304 stainless steel specimens tested in tension showed no perceptible evidence of Stage I growth. As a result, no region A behavior is shown in Fig. 1b. The fracture surfaces appeared to be almost entirely dominated by Stage II growth. Plumbridge (6) also reported that at low strain amplitudes, up to 90 percent of life may be taken up in initiation and Stage I growth while at high strain amplitudes a similar fraction may be spent in Stage II crack growth.

The behavior of Inconel 718 is summarized in Fig. 2. Unlike the stainless steel which displayed mixed behavior, results of the Inconel 718 torsion tests showed that cracks initiated and remained on maximum shear planes, Region A behavior, at all values of shear strain investigated. Even at the lowest strain amplitude, in which the normal stress-strain response was essentially elastic, cracks initiated and remained on shear planes throughout the life. Crack density decreases with increasing fatigue life as it did in 304 stainless steel but no branching onto tensile planes was observed.

Under tensile loading, cracks remained on shear planes for the majority of fatigue life and a large zone of Region A behavior is observed. Final failure in all tension tests was in a macroscopic tensile direction comprised of large portions of microscopic shear growth. Large amounts of shear growth are observed at failure for short and intermediate fatigue lives. Growth on Stage II planes occurred only late in life.

Damage accumulation in Inconel appears to be shear dominated. This is attributed to localized shear deformation bands developed during cyclic loading. Reversed movement of dislocations progressively shears precipitates in these bands. Crack propagation then occurs along the bands with extensive shear crack growth exhibited throughout the fatigue life.

Two types of cracking systems have been observed in SAE 1045. A large density of microcracks was reported at high strain amplitudes, with the final failure occurring by a very rapid linking of these cracks. This type of damage has been termed the R system by Marco and Starkey (7). Alternatively, the S system, which dominated crack behavior at low strain amplitudes, exhibited one dominant crack which grew until failure.

In torsion, at high amplitudes, the R system crack behavior was characteristic of Region A in Fig. 3b. Two common features were observed. First, the number of microcracks increased with the number of loading cycles. Second, the surface length of microcracks which appeared in the early stages remained almost unchanged during the fatigue life. Darkness and clarity of the microcracks substantially increased with progress of fatigue cycles. These observations indicate that the crack opening and hence crack depth have increased. Cracks initiate on the surface and propagate into the surface, while the surface crack length remains nearly constant. Also, crack orientations were developed equally on both planes of maximum shear. These multi-microcracks are almost uniformly distributed over the entire gage length. The failure was similar to that observed in the stainless steels at high amplitudes except that the linking of microcracks and final failure in 1045 occurred over a very few cycles, while the growth of the Region A failure crack in stainless steels occurred progressively throughout the life. At lower amplitudes, progressive growth of a single crack occurred by a linking process on the shear plane.

Region B behavior was observed only at long lives. At the lowest strain amplitude, 0.26 percent, the crack branched and growth occurred on the tensile plane by a linking of previously initiated shear cracks. After a period of tensile growth, the crack linked with a large shear crack which had been developing simultaneously. Final failure occurred by a mixture of Regions A and B behavior.

In tension, Fig. 3a, failure occurred in both the R and S systems on Stage II planes. Microcracks initiated on shear planes at high amplitudes, in a manner representative of the R crack system. A very rapid linking of these microcracks occurred immediately prior to failure such that the failure crack was on tensile (Stage II) planes. At low amplitudes, cracks initiated on shear planes but progressive growth occurred on Stage II planes.

In Region C, crack nucleation plays the dominant role. This region has been extensively studied by others. Nisitani (8) and Nisitani and Kawano (9,10) made extensive observations of long life fatigue failures in low carbon steels. He concluded that at the fatigue limit, cracks formed within single grains but were unable to propagate into neighboring grains because of the

differences in crystallographic orientation. This long life region should be controlled by cyclic shear stress. Tensile crack growth consumes a small portion of the total fatigue life. For low ductility materials containing flaws, non-propagating cracks should be considered and maximum principal strain amplitude is the controlling parameter.

#### FATIGUE DAMAGE MAPS

The preceding discussion has shown that the type of fatigue damage is dependent on strain amplitude stress state and material. Physical damage phenomena presented in Figs. 1 through 3 are quantified in Fig. 4 in a fatigue damage map. The vertical axis is plotted in terms of hydrostatic stress normalized by the maximum principal stress. This format allows representation of all the stress states from torsion to biaxial tension on a single diagram. Little test data now exists for biaxial tension tests and the demarcation between regions are shown as dashed lines. These maps are analogous to the fracture maps of Ashby (11).

As expected, all of the materials show a decrease in the shear dominated portion of the fatigue life as the cyclic hydrostatic stress is increased. Contrary to conventional wisdom, the material with the highest ductility, 304 stainless steel ( $\epsilon_f = 1.6$ ), has the smallest region of shear dominated failure. Incoel 718 with a lower ductility ( $\epsilon_f = 0.3$ ) has the largest region of shear dominated failure. These fatigue damage maps can then be used to estimate the type of failure to be expected for any state of stress.

Once the failure mode has been identified, the appropriate life estimation model can be selected. Each region requires a separate damage model that is based on the observed failure mode. The following damage models are proposed for each region:

Region A:

$$\hat{\gamma} + \hat{\epsilon}_n + \hat{\sigma}_{no}/E = \tau_f'(2N)^c + \tau_f'/G (2N)^d. \quad (1)$$

This model was proposed by Kandil, Brown and Miller [12] and modified by Socie, Kurath, and Koch [4] to include mean stress effects.

Region B:

$$\sigma_1^{\max} \epsilon_1 = \sigma_f' \epsilon_f' (2N)^{b+c} + \sigma_f'^2/E (2N)^{2b}. \quad (2)$$

This model was originally proposed by Smith, Watson and Topper (13) for mean stress effects during uniaxial loading. It has subsequently been successfully used for multiaxial loading by Socie (14).

Region C:

$$\hat{\tau} + \hat{\sigma}_n = \sigma_f'(2N)^b. \quad (3)$$

This model was proposed by Findley [15] for long life fatigue and has extensive experimental verification for multiaxial fatigue.

#### DISCUSSION

A common feature of all of these damage models is that they are evaluated on a critical plane for crack nucleation and growth. They can easily be extended to complex non-proportional loading by evaluating the damage parameter on all planes to determine the plane experiencing the greatest fatigue damage and shortest expected fatigue life.

One such example is the common nonproportional loading path consisting of tension and torsion loading with a 90° phase difference. Material constants given in Eqs. (1) and (2) were determined from torsion and tension tests respectively with the results given in Table 1. The fatigue strength and ductility exponents are nearly the same in both tension and torsion and no demarcation between them is needed. These properties were then used to estimate the lives of out-of-phase tests. The damage maps indicate that shear failures are expected in Inconel 718 and tensile failures are expected in 304 stainless steel. Table 2 gives the predicted results from Eqs. (1) and (2) with the experimental data. Both models overestimate the observed fatigue lives. Failure cracks for the Inconel 718 specimens were found to be on the predicted planes of maximum shear strain amplitude. Failure cracks for the 304 stainless steel tests were found on the planes experiencing the largest range of principal strain. It is not surprising that the shear model gives a better estimate of the Inconel 718 test results and the tensile model gives a better estimate of the 304 stainless steel tests. It is unlikely that a single model could ever correlate all of the available test data because the failure modes are in fact different.

A second area of interest is the effect of mean stress. Both models have a mean stress term. In the shear model, only the mean stresses normal to the maximum shear strain amplitude planes contribute to fatigue damage. Likewise, only the mean stresses normal to the maximum principal strain plane contribute to the fatigue damage. Two loading cases that result in the same shear damage parameter are shown in Fig. 5. On the top left, consider a standard uniaxial test with a strain ratio  $R = 0$ . This test results in some axial mean stress of  $\sigma_o$ . Now consider a second test, B, of the same strain range only now applied with a strain ratio  $R = -1$ . No mean axial stress results. Instead, a mean stress equivalent to the mean stress measured in Test A is applied in the hoop direction of a pressurized tube. Both tests result in the same shear damage parameter even though in one case the mean

stress and cyclic stress are in the same direction and in the other case the mean stress is oriented  $90^\circ$  from the cyclic stress. The tensile damage parameters for these two tests are not identical. The mean stress is fully effective in Test A and has no effect in Test B if the tensile damage parameter is applied. Test results on Inconel 718 for these two test conditions are given in Table 3 with the results of  $R_e = -1$  tests.

Results in Table 3 show mixed behavior. At high strains, mean stresses applied in the hoop direction are just as damaging as mean stresses applied in the axial direction. This is consistent with the shear damage model. At lower strains the mean hoop stress has a small effect and fatigue lives are much more like the completely reversed test data. This behavior is predicted from the fatigue damage map in Fig. 4. A transition from shear dominated behavior to tensile dominated behavior occurs at about  $10^5$  cycles. Therefore mean hoop stress assessed by the tensile damage model should not be damaging for fatigue lives longer than  $10^5$  cycles.

In the present form, the fatigue damage maps provide no information about variable amplitude loading. Block loading tests were conducted on 1045 steel specimens in combined tension and torsion (16). Figure 6 shows the low-high step loading results. The arrows provide a common reference point in all of the photos. The test was cycled for half of the fatigue life, 56,000 cycles, at a low strain level before changing to a high strain level and then cycling until failure occurred. A Type-S crack, region B in the damage map, was developed during the low strain level. The length of the crack formed during the first 10 percent of life was about  $20\text{ }\mu\text{m}$  and grew to 0.1 mm. After changing to the high strain level after 56,000 cycles, this single dominant crack grew continuously until a Type-S failure occurred. The results indicate that if, upon the application of the initial cycles, a crack length greater than the initiation phase crack size occurs, and the damage is established, then this crack will grow continuously to failure even if a high strain level is applied and no change to a Type-R crack system will occur. It is therefore important to note that the knife edge of an extensometer can sometimes cause a small notch during the initiation phase and the specimen always fails with a Type-S crack. Conversely, a Type-R crack system of region A in the damage map continuously develops until final failure with the high-low loading sequence and is shown in Fig. 7. These tests show that once a damage state is established it will propagate to failure faster than a new damage state can nucleate.

SUMMARY

The concept of a fatigue damage map analogous to the fracture maps of Ashby has been introduced. These maps give the material and stress state dependence of the fatigue damage mechanisms and allow the selection of the most appropriate damage model for life estimation. Results from out-of-phase loading and mean stress tests have been interpreted in the context of the fatigue damage map.

NOMENCLATURE

$\hat{\gamma}$	= maximum shear strain amplitude
$\hat{\epsilon}_n$	= normal strain amplitude on $\hat{\gamma}$ plane
$\hat{\sigma}_{no}$	= mean stress on $\hat{\gamma}$ plane
$\sigma_1^{\max}$	= maximum principal stress on $\epsilon_1$ plane
$\epsilon_1$	= maximum principal strain amplitude
$\hat{\tau}$	= maximum shear stress amplitude
$\hat{\sigma}_n$	= maximum stress on $\hat{\tau}$ plane
$\sigma_f'$	= tensile fatigue strength coefficient
$\tau_f'$	= torsion fatigue strength coefficient
$\epsilon_f'$	= tensile fatigue ductility coefficient
$\gamma_f'$	= torsion fatigue ductility coefficient
$b$	= fatigue strength exponent
$c$	= fatigue ductility exponent
$E$	= elastic modulus
$G$	= shear modulus
$2N$	= reversals to failure
$R_\epsilon$	= strain ratio $\epsilon_{\min}/\epsilon_{\max}$

## REFERENCES

- (1) Ewing, J. A., and Humfrey, J. C. "Fracture of Metals Under Repeated Alterations of Stress," Philosophical Trans., of the Royal Soc. of London, Vol. 200, (1903), Series A, pp. 241-253.
- (2) Forsyth, P. J. E. "A Two Stage Process of Fatigue Crack Growth," Proc., Symp. Crack Propagation, Cranfield, England, (1961), pp. 76-94.
- (3) Hua, C. T., and Socie, D. F. "Fatigue Damage in 1045 Steel Under Variable Amplitude Biaxial Loading," Fatigue of Engineering Materials and Structures, Vol. 8, No. 2, (1985), pp. 101-114.
- (4) Socie, D. F., Kurath, P., and Koch, J. L. "A Multiaxial LCF Parameter," Second International Symposium on Biaxial Multiaxial Fatigue, (1985).
- (5) Bannantine, J. A., and Socie, D. F. "Observation of Cracking Behavior in Tension and Torsion Low Cycle Fatigue," accepted for publication ASTM STP XXX Low Cycle Fatigue: Direction for JC Fracture, (1987).
- (6) Plumbridge, W. J. Review: Fatigue Crack Propagation in Metallic and Polymore Materials," J. Materials Science, Vol. 7, (1982), "pp. 939-962.
- (7) Marco, S. M., and Starkey, W. L. "A Concept of Fatigue Damage," Trans. ASME, Vol. 76, No. 4, (1954), pp. 627-632.
- (8) Nisitani, H. Japan Society of Mechanical Engineers Bulletin, Vol. 11, No. 48, (1968), pp. 947-957.
- (9) Nisitani, H., and Kawano, K. Japan Society of Mechanical Engineers Bulletin, Vol. 15, No. 82, (1972), pp. 433-438.
- (10) Nisitani, H., and Kawano, K. in Proc., 11th Japan Congress on Materials Research (Metallic Materials), (1968), pp. 49-51.
- (11) Ashby, M. F., Embury, J. D., Coohsley, S. H., and Teirlinck, D. "Fracture Usages with Pressure as a Variable," Scripta Metallurgical, Vol. 19, (1985), pp. 385-390.
- (12) Kandil, F. A., Brown, M. W., and Miller, K. J. "Biaxial Low-Cycle Fatigue Fracture of 316 Stainless Steel at Elevated Temperatures," Book 280, The Metals Society, London, (1982), pp. 203-210.

FATIGUE 87

- (13) Smith, R. N. Watson, P., and Topper, T. H. "A Stress-Strain Function for the Fatigue of Metals," Journal of Materials, JMLSA, Vol. 5, No. 4, (1970), pp. 767-778.
- (14) Socie, D. F. "Multiaxial Fatigue Damage Models," submitted to Journal of Engineering Materials and Technology, (1986).
- (15) Findley, W. N. Journal of Engineering for Industry, Transactions, American Society of Mechanical Engineers, Series B, Vol. 81, (1959), pp. 301-306.
- (16) Hua, C. T., and Socie, D. F. "Fatigue Damage in 1045 Steel Under Variable Amplitude Biaxial Loading," Fatigue and Fracture of Engineering Materials and Structures, Vol. 8, No. 2, (1985), pp. 101-114.

# FATIGUE 87

TABLE-1 Material properties

	Inconel 718	304 Stainless	1045 Steel
$\sigma_f'$	2936 MPa	984 MPa	998 MPa
$\epsilon_f'$	14.3 0.15	0.30	
$\tau_f'$	2035 MPa	535 MPa	471 MPa
$\gamma_f'$	26.3 0.41	0.41	
b	-0.145	-0.11	-0.095
c	-0.99 -0.37	-0.45	
G	77.8 GPa	78.9 GPa	78.9 GPa
E	208 GPa	205 GPa	205 GPa

TABLE-2 90° Out-of-phase loading

	$\Delta\epsilon$	Shear Model	Fatigue Life, Cycles Tensile Model	Experimental
Inconel 718	0.007	1491	3639	560, 565
	0.0035	6095	39736	5810, 5150
304 Stainless	0.0035	24322	8012	3560, 3730
	0.002	155611	95890	45000, 50000

TABLE-3 Mean stress tests

$\Delta\epsilon/2$	$\sigma_0$ MPa	Fatigue Life, Cycles $R_e = 0$	$R_e = -1 + \sigma_0$	$R_e = -1$
0.005	270	4,245 9,768	6,735 7,221	14,420 17,430
0.0025	517	37,530 65,960	142,100 165,100	187,791 237,702

# FATIGUE 87

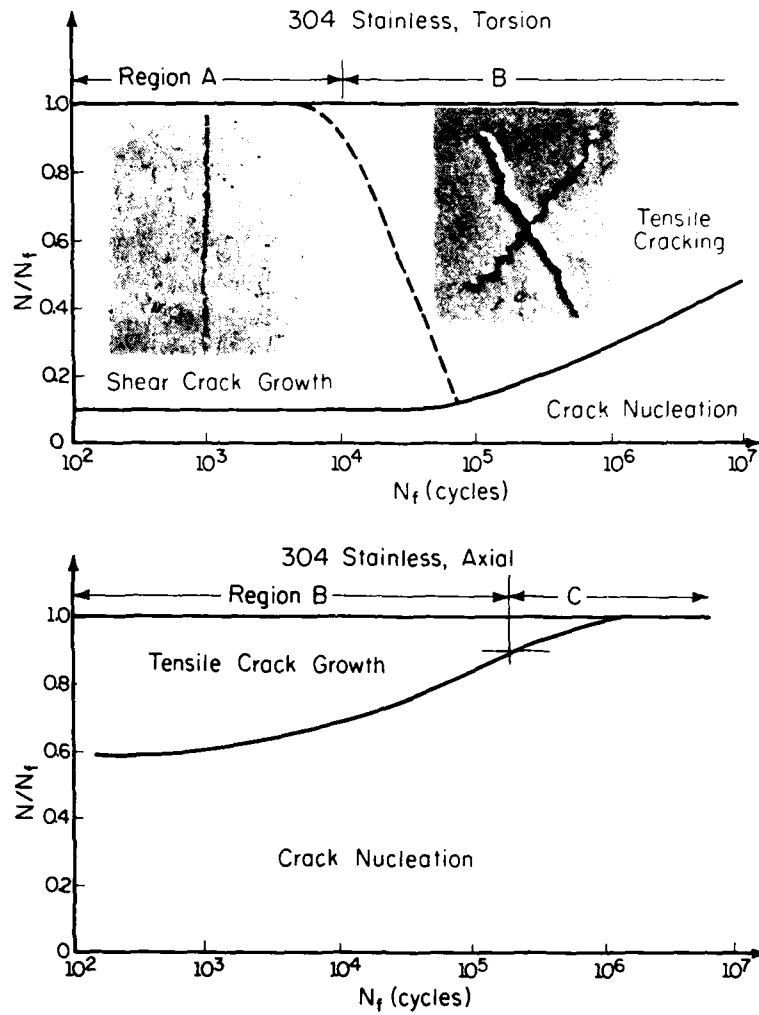


Figure 1 Cracking behavior of 304 stainless steel (a) torsion (b) tension

# FATIGUE 87

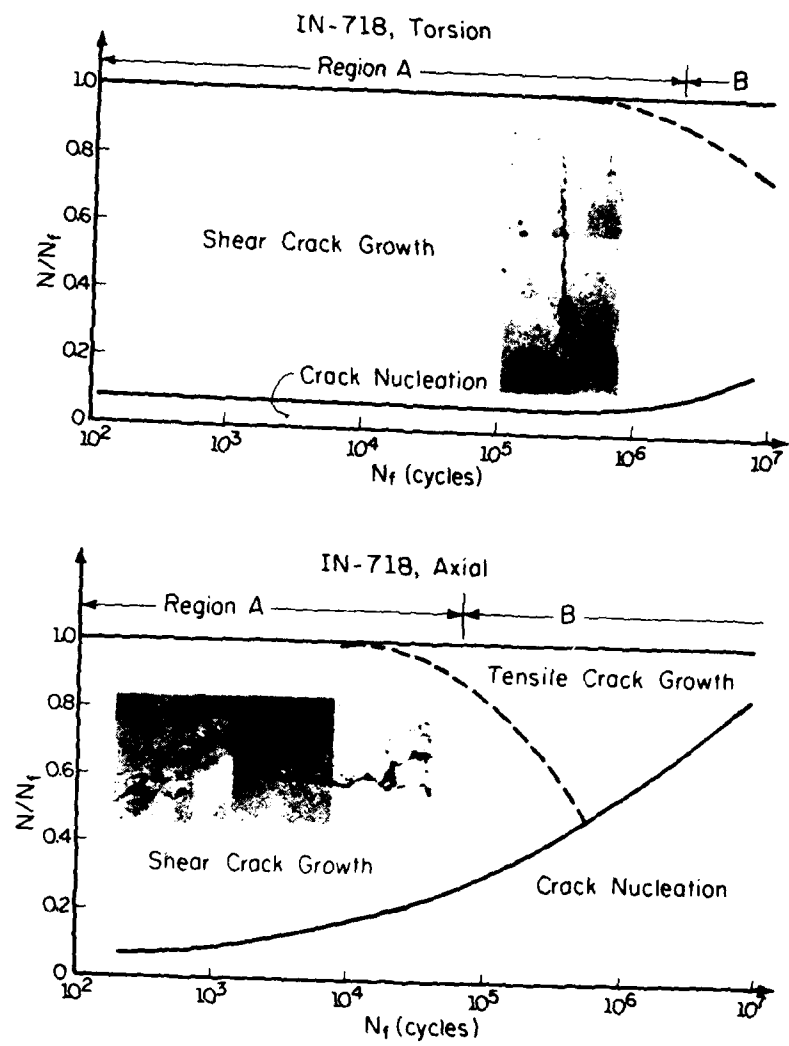


Figure 2 Cracking behavior of Inconel 718 (a) torsion (b) tension

# FATIGUE 87

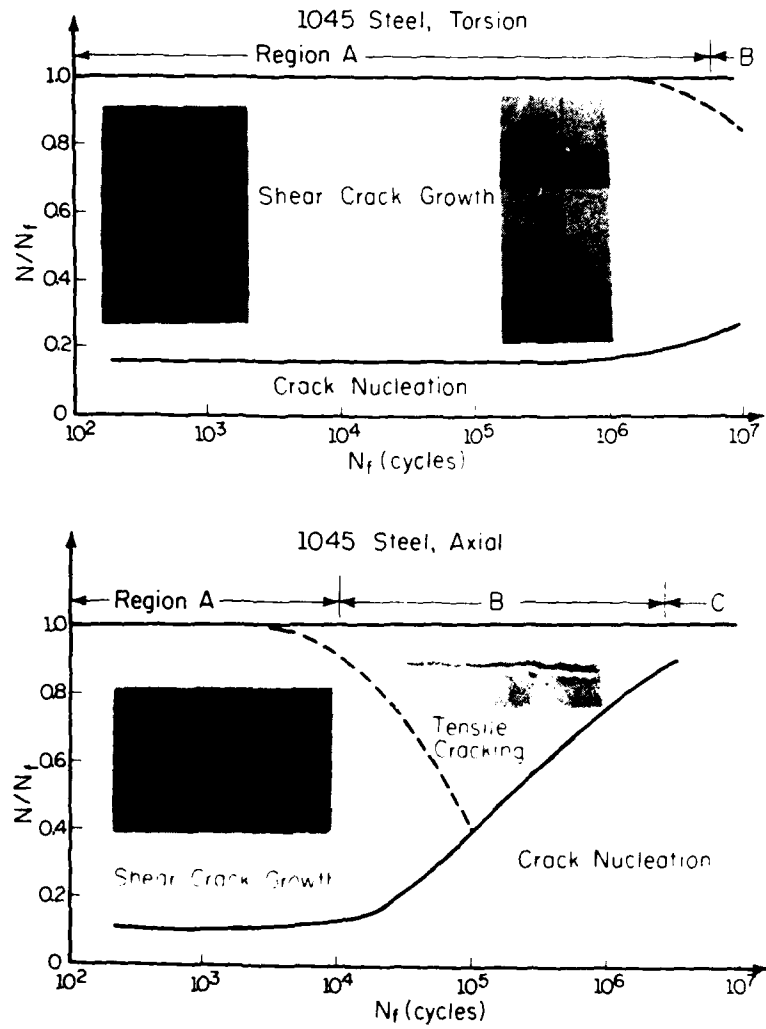


Figure 3 Cracking behavior of 1045 steel (a) torsion (b) tension

# FATIGUE 87

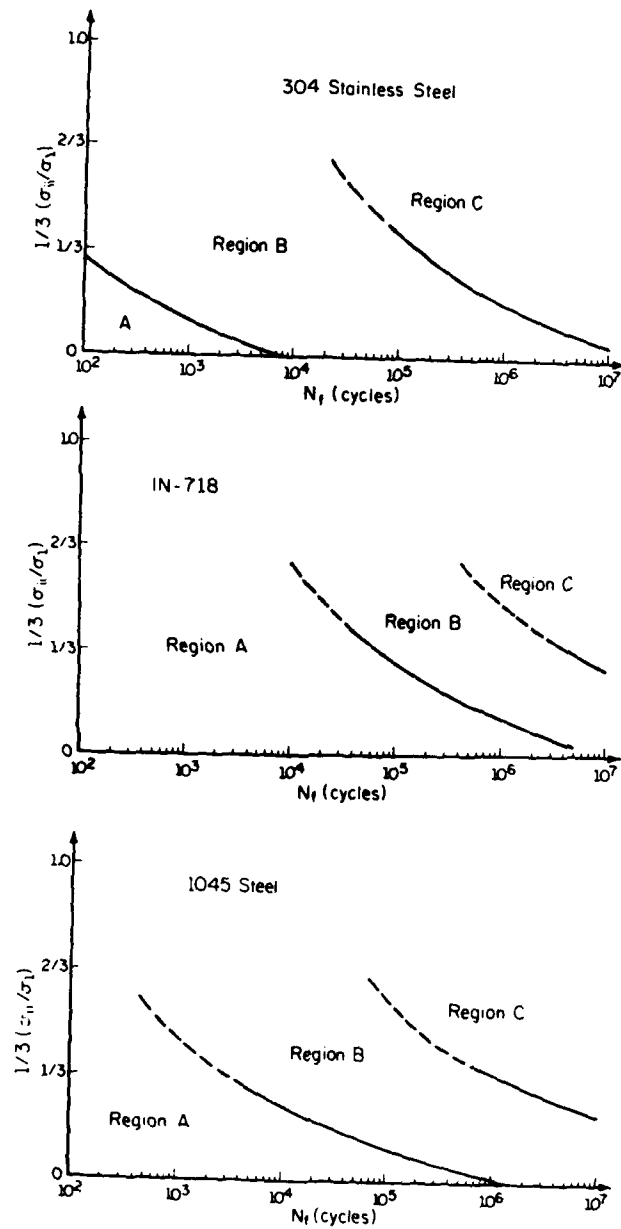


Figure 4 Fatigue damage map (a) 304 stainless steel; (b) Inconel 718; (c) 1045 steel

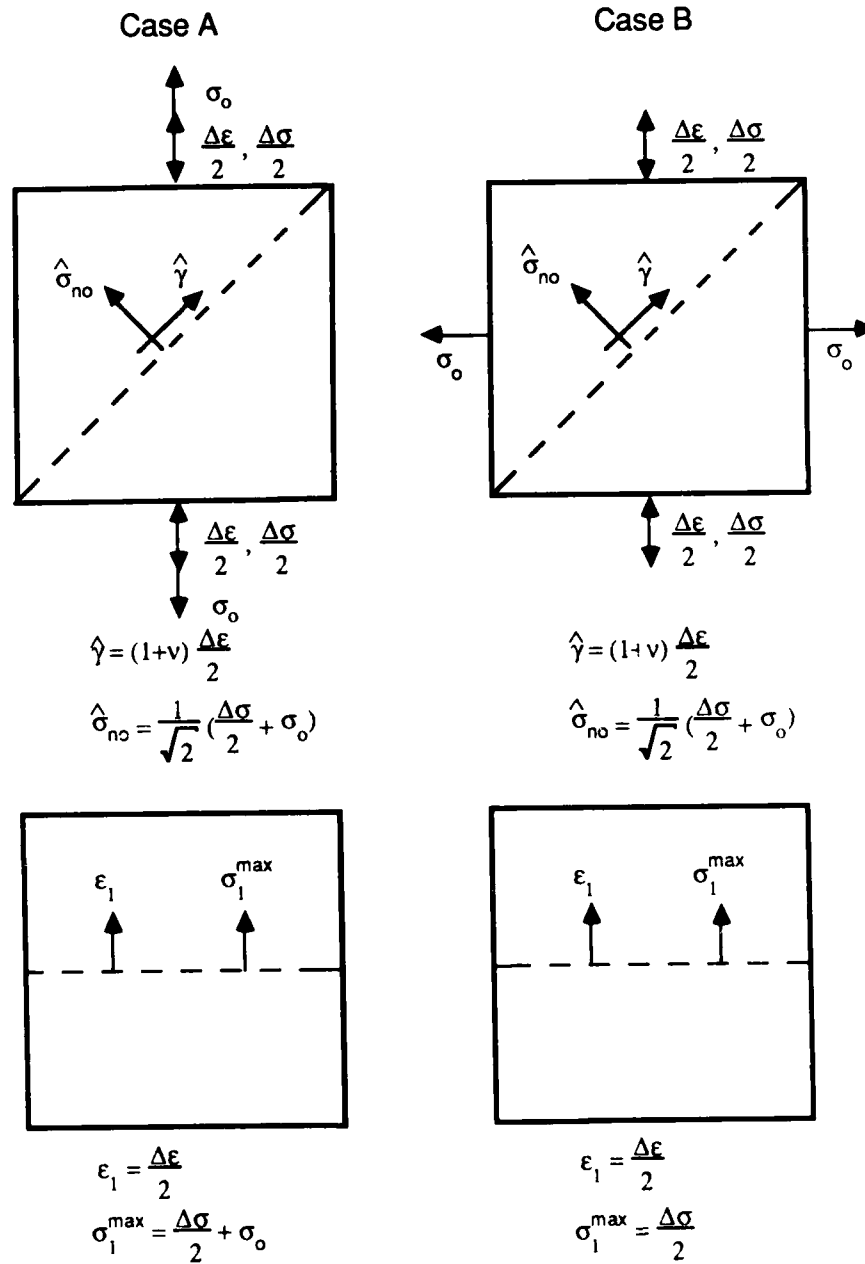


Figure 5 Mean stress test illustration

# FATIGUE 87

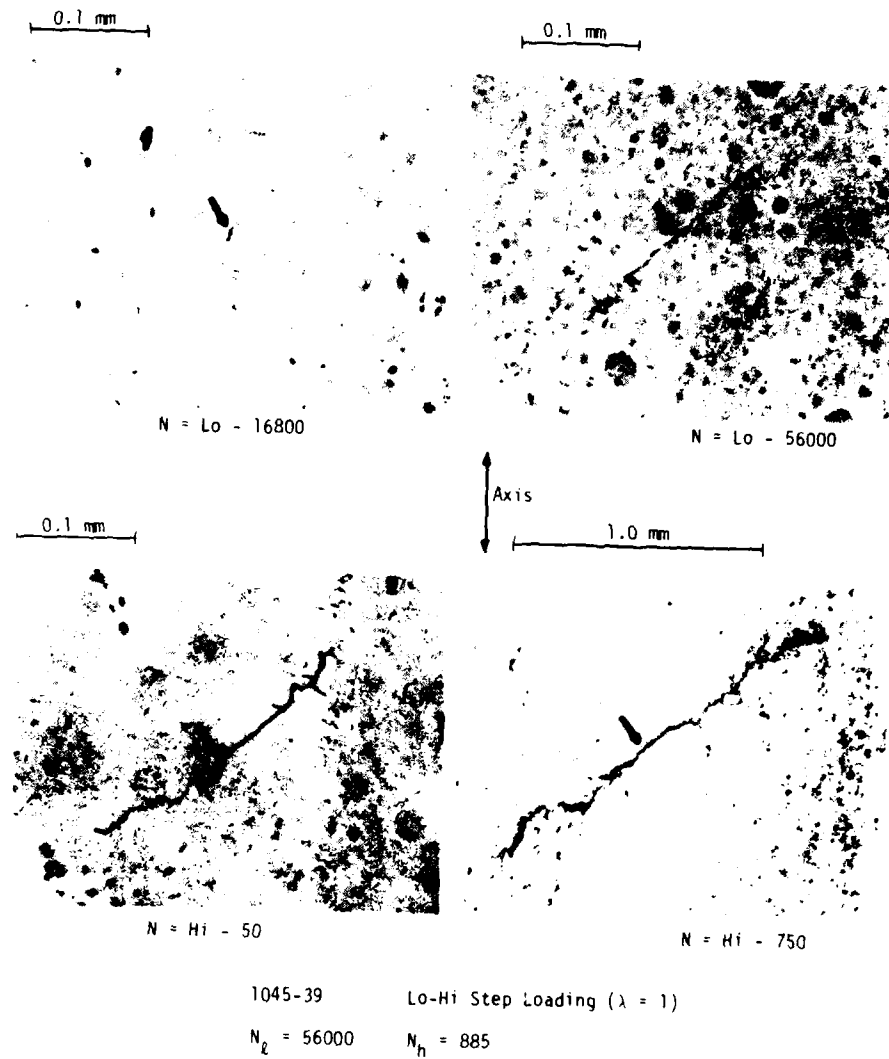
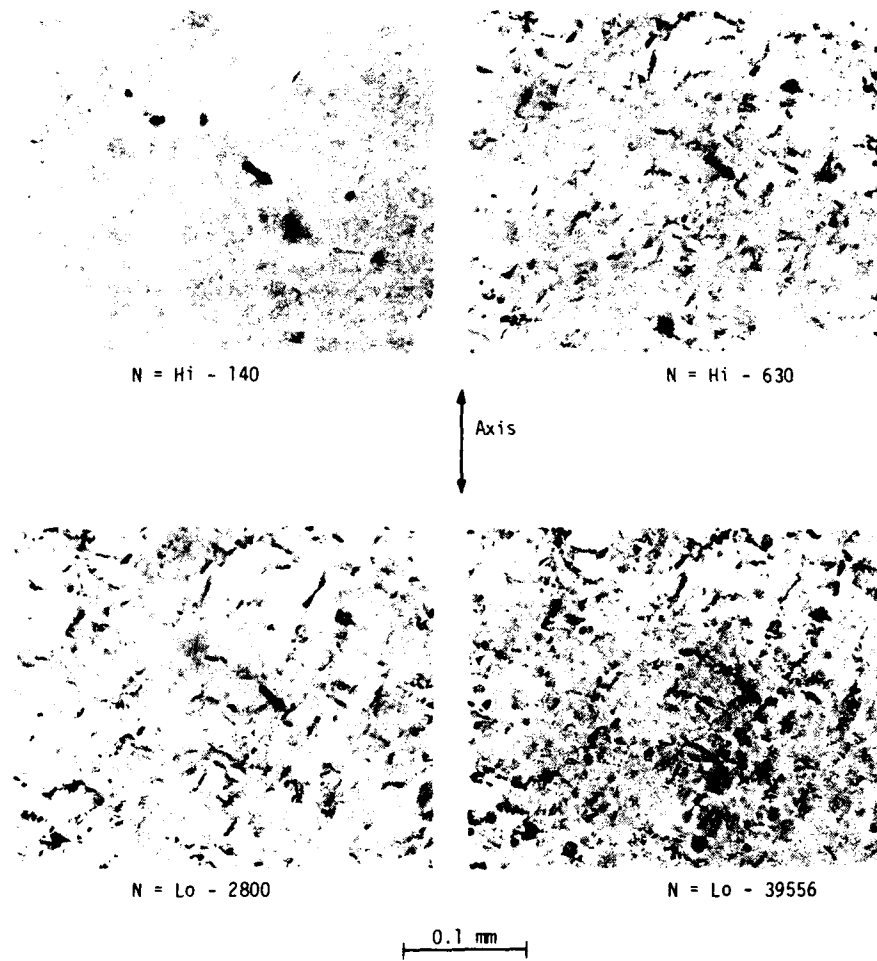


Figure 6 Crack growth under low-high step loading ( $\lambda = 1$ )  
 (a) after 16,800 cycles at low strain; (b) after 56,000 cycles  
 at low strain; (c) after 50 cycles at high strain; (d) after 759  
 cycles at high strain

# FATIGUE 87



1045-38 Hi-Lo Step Loading ( $\lambda = 1$ )  
 $N_h = 700$   $N_L = 39690$

Figure 7 Crack growth under high-low step loading ( $\lambda = 1$ )  
 (a) after 140 cycles at high strain; (b) after 630 cycles at high strain; (c) after 2,800 cycles at low strain; (d) after 339,556 cycles at low strain

## FATIGUE 87

### AN INVESTIGATION OF FATIGUE CRACK GROWTH IN A DUCTILE MATERIAL AT HIGH GROWTH RATES

K.J. Nix\*, N. Knee\*, T.C. Lindley\* and G.G. Chell\*

An investigation has been made of fatigue crack growth in a ductile steel in the high growth rate regime where ductile tearing can contribute to crack growth. A computerized testing system for a servo-hydraulic testing machine has been developed to enable controlled fatigue testing in this regime. Results for three point bend specimens of mild steel indicate that a crack growth model in which the fatigue and ductile fracture contributions are considered additive and non-interactive provides a satisfactory method for predicting crack growth rates.

#### INTRODUCTION

It is well established that the fatigue crack growth rate  $da/dN$  for a component subject to fatigue loading in the intermediate range can be described by the Paris law (Paris and Erdogan (1))

$$da/dN = A \Delta K^m \quad \dots (1)$$

If the maximum loading is increased then crack growth rates can exceed those predicted by (1) due to the onset of static fracture modes such as cleavage or ductile fracture. In relatively low toughness materials a relationship such as that proposed by Forman et al. (2) can be used to predict crack growth rates in this regime:

$$\frac{da}{dN} = \frac{A' \Delta K^{m'}}{(1-R)K_c - \Delta K} \quad \dots (2)$$

\*Technology Planning and Research Division, Central Electricity Generating Board, Central Electricity Research Laboratories, Kelvin Avenue, Leatherhead, Surrey KT22 7SE, England

## FATIGUE 87

In tough materials which exhibit stable ductile tearing, equations such as (2) are inadequate since the static mode fracture contribution cannot be quantified simply by an initiation fracture toughness  $K_{IC}$ . Models have been developed for this 'tearing fatigue' regime (Kaiser (3), Cheil (4)) which postulate that the individual contributions to crack growth in each cycle due to fatigue and to ductile tearing can be considered as non-interactive and additive. The pure fatigue component of growth,  $(da/dN)_f$  is given by the Paris law (1) with  $\Delta K$  calculated using linear elastic fracture mechanics (LEFM) from the load range  $\Delta P$ . The incremental component of growth due to ductile tearing  $(da/dN)_t$  is given by:

$$\left(\frac{da}{dN}\right)_t = \left(\frac{dJ_{max}}{dN}\right) / \left(\frac{dJ_R}{d(\Delta a_t)}\right) \quad \dots (3)$$

where  $J_{max}$  is the maximum value of the J integral and  $dJ_{max}/dN$  is the change in  $J_{max}$  from one cycle to the next.  $\Delta a_t$  is the total crack growth due to ductile tearing and  $dJ_R/d(\Delta a_t)$  is the slope of the monotonic  $J_R$ - $\Delta a$  ductile crack growth resistance curve evaluated at  $J_R = J_{max}$ . The total crack growth rate is then given by:

$$\frac{da}{dN} = \left(\frac{da}{dN}\right)_f + \left(\frac{da}{dN}\right)_t \quad \dots (4)$$

In order to test this growth summation model it is necessary to carry out fatigue tests where the rate of increase of  $J_{max}$  is controlled (analogous to constant or reducing  $\Delta K$  control in the LEFM regime). Testing at a constant load or displacement range is not sufficient since it does not enable this control.

### FATIGUE TESTING

A schematic load (P) - load line displacement ( $\Delta$ ) curve for a fatigue specimen subject to loading in the tearing fatigue regime is shown in Figure 1. Plastic deformation results in the total displacement increasing with each cycle (ratchetting). In order to carry out a tearing fatigue test a computerized control system for a servo-hydraulic testing system has been developed. This enables control over one of three parameters: [1] the total cyclic displacement in each cycle,  $\Delta t$  in Figure 1, [2] the total plastic displacement in each cycle,  $\Delta p$  in Figure 1, and [3] the total energy input during each cycle calculated by integrating beneath the load displacement curve,  $\Delta U$  in Figure 1. In addition to controlling the test machine, the computer system carries out on-line measurement of load, load line displacement, the area beneath the load-load line displacement curve and crack mouth opening. Crack length is determined using the equation due to Garwood and Briggs (5) from the linear relationship between crack mouth opening and load during unloading. After the test, a further correction is made to crack length to account for

## FATIGUE 87

specimen rotation due to ratchetting and  $da/dN$  is then calculated for sets of crack length data, the size of each data set being determined by crack length resolution.

With reference to equations (1) and (3), the parameters predicting the crack growth rate under tearing fatigue conditions are  $\Delta K$ ,  $J_{\max}$  and  $dJ_{\max}/dN$ .  $J_{\max}$  and hence  $dJ_{\max}/dN$  are calculated from the total plastic energy input to the specimen given by the area under the load displacement curve,  $U_p$  in Figure 1. The method of  $J$  calculation is that described by Garwood et al. (6). The method enables the near field value of  $J_{\max}$ , suitably corrected for crack growth, to be calculated.

### RESULTS AND DISCUSSION

A series of tearing fatigue tests have been carried out on mild steel three point bend specimens,  $B = 70$  mm,  $W = 140$  mm. Chemical composition and mechanical properties of the material are given in Table 1. The initial value of  $a/W$  was  $<0.4$  in order to achieve high values of  $K$  and a stress ratio of  $R \approx 0$  was applied. The test environment was laboratory air at room temperature. Monotonic  $J_R$ - $\Delta a$  data have been measured using the single specimen unloading compliance technique, Clarke et al. (7), on side grooved,  $B = 50$  mm, compact tension specimens cut from the ends of the bend test bars.

Results for both fatigue in the elastic regime and tearing fatigue are plotted as  $da/dN$  v  $\Delta K$  in Figure 2. The best fit straight line to the elastic data gives the Paris law coefficients as:

$$\left(\frac{da}{dN}\right)_f = 10^{-7.6} \Delta K^{2.65} \quad \text{mm/cycle} \quad \dots (5)$$

In the tearing fatigue regime crack growth rates up to 0.1 mm/cycle were measured, exceeding the rate predicted by

TABLE 1 - Chemical Composition and Mechanical Properties of Mild Steel Specimens.

Element	C	Mn	Si	S	P	Cu	Cr	Ni	Mo
Wt%	0.13	0.59	0.24	0.027	0.017	0.08	0.08	0.05	0.02

0.2% Proof Stress	255 MPa
UTS	397 MPa
Elongation	48%
Reduction in Area	74.5%

## FATIGUE 87

equation (5) by a factor of 10, clearly demonstrating the acceleration due to the onset of ductile tearing.

In order to apply equations (3) and (4) to predict tearing fatigue crack growth rates it is convenient to fit an equation to the monotonic  $J_R - \Delta a$  data, Figure 3. A straight line fit to all the test data which satisfy J validity conditions according to Neale et al. (8) (which corresponds to all data for  $0.2 < \Delta a < 2.6$  mm in this case) is of the form:

$$J = 142 + 352 \Delta a \text{ kN/m} \quad \dots (6)$$

where  $\Delta a$  is measured in mm.

The accuracy of any crack growth predictions can be determined by plotting predicted versus measured rates: in Figure 4 such a plot is given for predictions made using the Paris law only, equation (5), taking no account of the ductile tearing contribution. As expected, this results in a considerable underestimate of growth rates. The incorporation of ductile tearing into the predictions using the growth summation model, equation (4), gives a much better agreement between predicted and measured growth rates, Figure 5;  $(da/dN)_f$  is given by equation (5) and  $(da/dN)_t$  by equation (6). Linear regression analysis on all the results gives a ratio of growth rates, predicted/measured, equal to 0.94, close to the ideal value of unity.

A second method of presenting the tearing fatigue results is to construct a 'fatigue' J resistance curve by subtracting the predicted total growth by fatigue  $\Delta a_f$ , as derived using equation (5), from the total crack growth in each test.  $J_R - \Delta a$  results, obtained in this manner, are plotted in Figure 6 where they are compared to the monotonic data. The two show good agreement, demonstrating that fatigue loading has an insignificant effect on the ductile fracture resistance of the material.

In another series of tests the loading conditions were varied in order to change the relative contributions of ductile tearing and fatigue whilst maintaining the fatigue contribution approximately constant. A typical P- $\Delta$  curve for such a test is shown in Figure 7: in the first part of the test the control mode was constant  $\Delta p$  (see Figure 1) giving an approximately constant value of  $dJ_{max}/dN$ . The control mode was then changed to constant  $\Delta U$  and the cyclic energy input reduced slightly to give a value of  $dJ_{max}/dN \approx 0$  whilst reducing the maximum load and hence  $\Delta K$  by only about 2%. The plot of crack length versus cycles, Figure 8, demonstrates a large and immediate reduction in growth rate. Although the reduction in growth rate is much larger than could be predicted by the 2% reduction in  $\Delta K$ , it is predicted by the growth summation model: after the mode change  $dJ_{max}/dN \approx 0$  and hence from equation (3) the ductile tearing contribution is zero and the crack growth rate is predicted to

## FATIGUE 87

revert to that described by the Paris law. Quantitatively the crack growth rates before and after the mode change are predicted to be 107 and 11.5  $\mu\text{m}/\text{cycle}$  respectively which compare well with the measured values of 103 and 16  $\mu\text{m}/\text{cycle}$ , Figure 8.

In the scanning electron microscope, the fracture surfaces produced in the tearing fatigue regime show evidence of both striation and void coalescence mechanisms, Figure 9. At lower growth rates, a major contribution to crack growth is from the fatigue mechanism and striations are clearly visible in many areas, Figure 9(a). At higher growth rates however,  $>50 \mu\text{m}/\text{cycle}$ , the fracture surface consists largely of void coalescence, Figure 9(b), demonstrating the increasing contribution of ductile tearing consistent with the growth summation model.

### ACKNOWLEDGEMENTS

This work was carried out at the Central Electricity Research Laboratories and is published by permission of the Central Electricity Generating Board. The authors would like to thank Dr N. Trigwell of Testwell Ltd., Daventry for his work in developing the testing system.

### ADDITIONAL SYMBOLS USED

$(da/dN)_f$ , $(da/dN)_t$	= contributions to total crack growth rate from fatigue and from tearing
J	= J integral
$J_{\max}$	= maximum value of the J integral
$J_p$	= plastic component of J
$J_R$	= ductile crack growth resistance value of J
$U_p$	= plastic component of total energy input to the specimen
$\Delta a_f$ , $\Delta a_t$	= total crack growth increment due to fatigue and to tearing
$\Delta p$	= plastic displacement range in each cycle
$\Delta t$	= total displacement range in each cycle
$\Delta U$	= cyclic change in energy input to the specimen
$\Delta$	= load line displacement.

### REFERENCES

- (1) Paris, P.C. and Erdogan, F., J. Basic Engng., 85D, 1963, p. 528
- (2) Forman, R.G., Kearney, V.E. and Engle, R.M., J. Basic Engng., 89D, 1967, p. 459
- (3) Kaiser, S., Fat. Engng. Mater. Struct., Vol. 6, 1983, pp. 33-49

# FATIGUE 87

- (4) Chell, G.G., Fat. Engng. Mater. Struct., Vol. 7, 1984, pp. 237-250
- (5) Garwood, S.J. and Briggs, E.K., Welding Inst. Research Bull., 24, Welding Institute, Cambridge, 1983, pp. 226-232
- (6) Garwood, S.J., Robinson, J.N. and Turner, C.E., Int. J. Fract., Vol. 11, 1975, p. 528
- (7) Clarke, G.A., Andrews, W.R., Paris, P.C. and Schmidt, D.W., ASTM STP. 590, ASTM, Philadelphia, PA, 1976, pp. 27-42
- (8) Neale, B.K., Curry, D.A., Green, G., Haigh, J.R. and Akhurst, K.N., Int. J. Pres. Ves. and Piping, Vol. 20, 1985, pp. 155-179 (see also Akhurst et al., *ibid*, pp. 181-205)

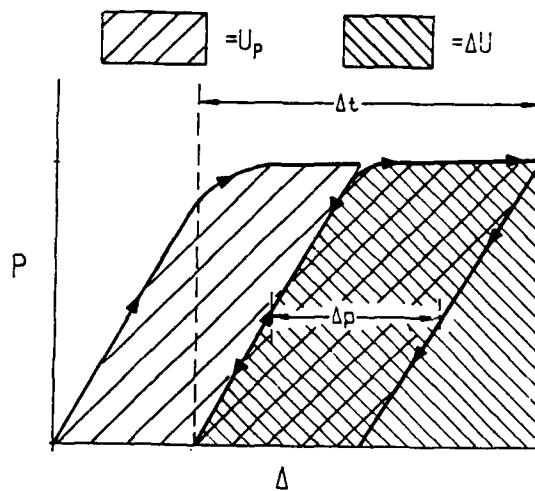


Figure 1 Schematic load v load line displacement curve showing test machine control modes

# FATIGUE 87

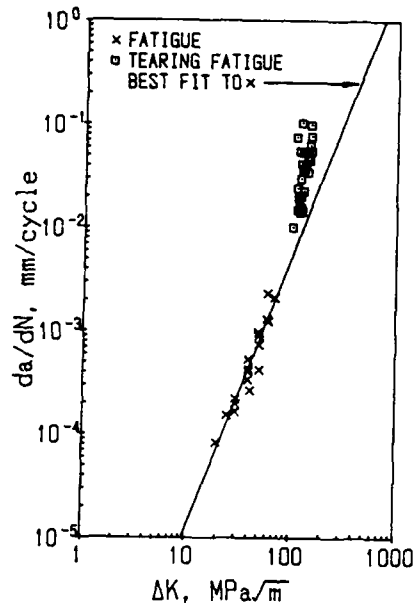


Figure 2 Measured crack growth rates plotted v  $\Delta K$

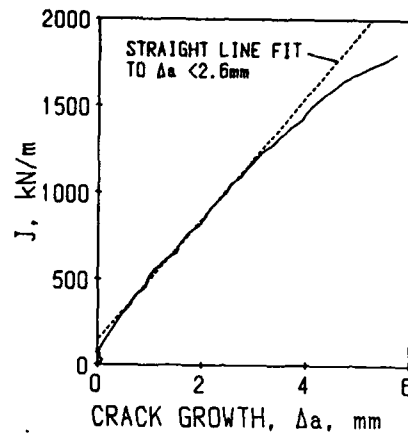


Figure 3 Monotonic ductile fracture crack growth resistance curve

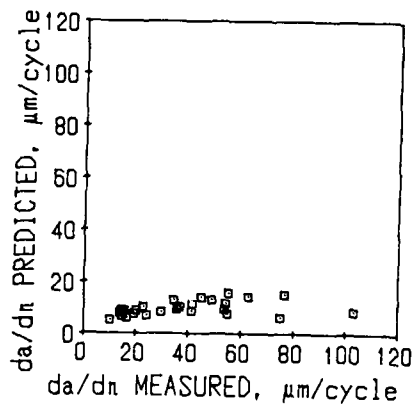


Figure 4 Crack growth rate predictions using  $\Delta K$

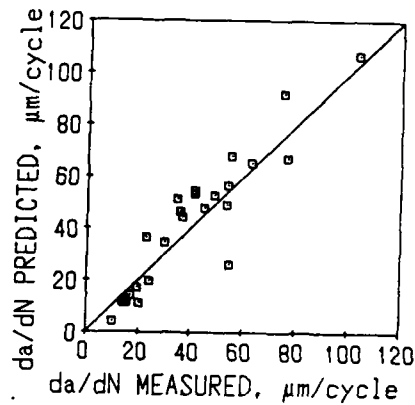


Figure 5 Crack growth rate predictions incorporating ductile tearing

# FATIGUE 87

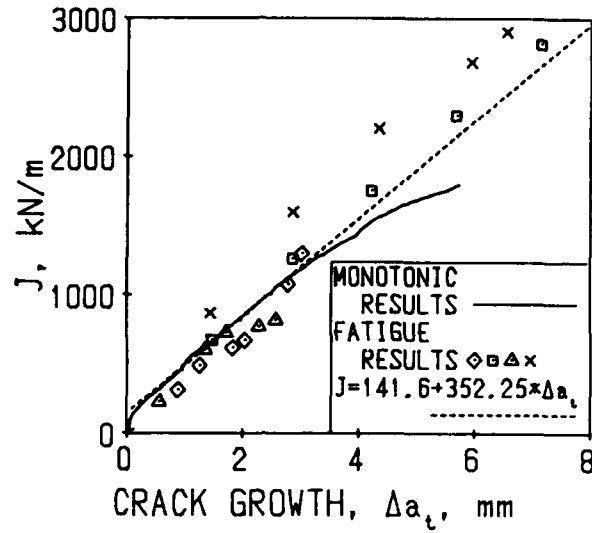


Figure 6 Crack growth resistance curve for tearing fatigue results

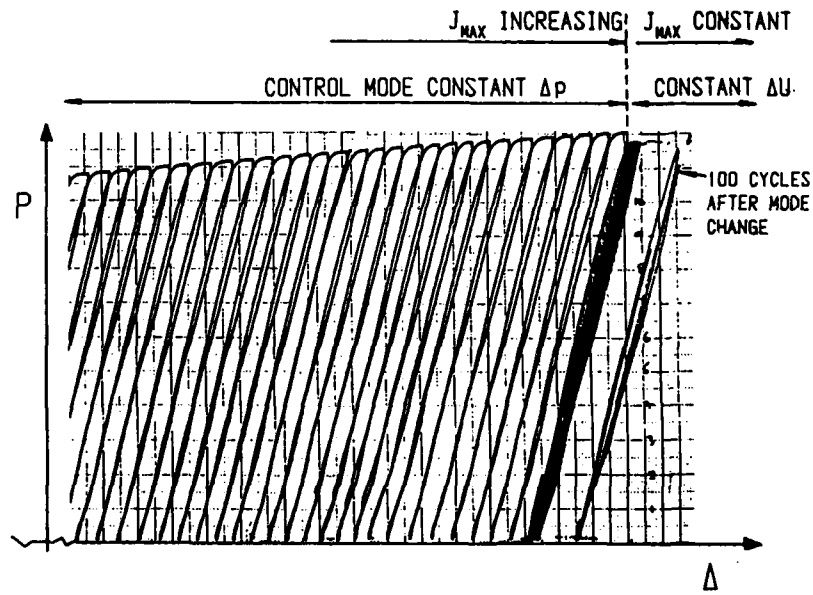


Figure 7 Load v load line displacement record for test including control mode change

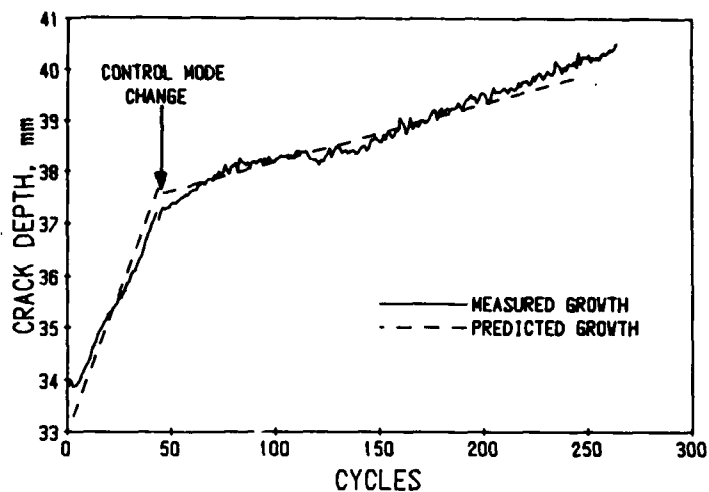


Figure 8 Plot of measured and predicted crack growth for period near control mode change

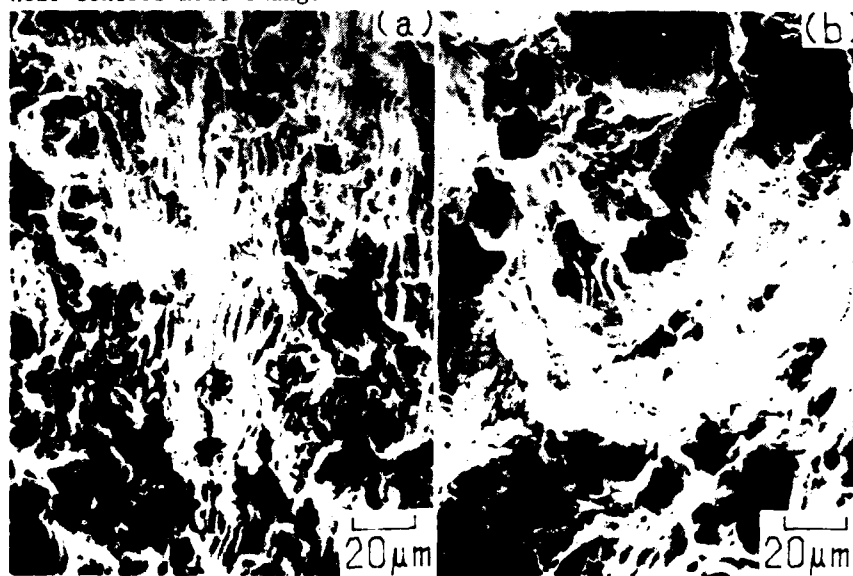


Figure 9 Scanning electron micrographs of tearing fatigue surfaces: (a)  $da/dN=15 \mu\text{m}/\text{cycle}$ , (b)  $da/dN=50 \mu\text{m}/\text{cycle}$

FATIGUE 87

CYCLIC DEFORMATION BEHAVIOUR OF CAST IRONS WITH VARIOUS GRAPHITE SHAPES IN THE TEMPERATURE RANGE  $20^{\circ}\text{C} < T < 500^{\circ}\text{C}$

K. H. Lang\*, D. Eifler\*, E. Macherauch\*

Stress and strain controlled push-pull tests were performed in a fully computerized servohydraulic test system between  $20^{\circ}\text{C}$  and  $500^{\circ}\text{C}$  with smooth specimens of nodular graphite cast iron, vermicular graphite cast iron and flake graphite cast iron. The appertaining plastic strain amplitudes were measured and recorded with an on-line computer system. The material behaviour was described by cyclic deformation curves. Supplementary transmission electron microscope (TEM) investigations were carried out. Characteristic experimental results are presented and discussed.

INTRODUCTION

Cast irons with different graphite shapes are frequently used materials for components which are both mechanically and thermally highly stressed. Consequently, the understanding of their cyclic deformation behaviour in dependence on test temperature and loading conditions is of great importance. However, the state of knowledge of the fatigue behaviour of cast irons is mainly based on SN-curves including the information about the influence of shape, size and distribution of the graphite and of the loading conditions (Blackmore and Morton (1), Socie and Fash (2) and Starkey and Irving (3)). In all cases, SN-curves with a distinct fatigue strength were observed. Only few investigations are known concerning the cyclic deformation behaviour of these materials in the macrocrack free stage of fatigue life. In the case of ferritic nodular cast iron (GGG-40) cyclic hardening effects were reported (Grubisic and Neugebau-

\* Universität Karlsruhe, Institut für Werkstoffkunde I, Postfach 6980, D-7500 Karlsruhe 1, FRG

er (4) and Starkey and Irving (5). However, cyclic hardening effects are less pronounced and not measurable for nodular cast irons with a perlite matrix structure (Testin (6)). On the other hand, the cyclic deformation behaviour of flake graphite cast iron seems to be characterized by cyclic softening effects due to early crack initiation and broken graphite lamella (Fash and Socie (7)). Almost no investigations are known concerning the influence of loading conditions including test temperature on the cyclic deformation behaviour of cast irons. The aim of this paper is to investigate quantitatively the development of plastic deformation during the fatigue life of typical cast irons in stress- and total strain controlled experiments at different temperatures up to 500°C.

#### MATERIALS AND TEST CONDITIONS

Nodular graphite cast iron (GGG-40) and vermicular graphite cast iron (GGV-30) both with ferritic matrix and flake graphite cast iron (GG-30) with perlite matrix were investigated. Characteristic quantities of these materials determined in monotonic tensile tests with a strain rate  $\dot{\epsilon} = 2,4 \times 10^{-4} \text{ s}^{-1}$  are given in Table 1.

TABLE 1 - Monotonic tensile properties

		GG-30	GGG-40	GGG-60
$E_0$	(KN/mm <sup>2</sup> )	121	165	171
$R_{p0.2}$	(N/mm <sup>2</sup> )	223	323	473
$R_m$	(KN/mm <sup>2</sup> )	283	470	769
$A_g$	(%)	0,9	17,3	8,6

Shape and dimensions of the specimens used in the cyclic deformation tests are shown in Figure 1. Push-pull single step tests with  $R = -1$  and triangular loading waves were performed under stress and total strain control with a 63 kN Schenck servohydraulic testing machine. The test frequency was 5 Hz. A resistometric heating system enabled constant test temperatures in the range  $20^\circ\text{C} < T < 500^\circ\text{C}$ . This equipment and the ca-

capacitive extensometer used for the strain measurements are described elsewhere (8). During cyclic loading, hysteresis loops were recorded at preselected cycles with an on-line computer system. A typical stabilized hysteresis loop with characteristic quantities such as stress amplitude  $\sigma_a$ , total strain amplitude  $\epsilon_{a,t}$  and plastic strain amplitude  $\epsilon_{a,p}$  is shown in Figure 2. From the measured data the relation between plastic strain amplitude and the logarithm of the number of cycles was evaluated in form of cyclic deformation curves. After mechanical testing, structural features of characteristic parts of the material were studied by TEM-observations.

### EXPERIMENTAL RESULTS

Distinct changes of the mechanical properties during cyclic loading are characteristic of the cyclic deformation behaviour of the cast irons investigated. Typical results of stress and total strain controlled room temperature tests for GGG-40 are shown in Figure 3 and 4. Typical of both experimental procedures and the loading amplitudes chosen is the occurrence of plastic strain amplitudes already in the first loading cycle. The initial plastic strain amplitudes are the higher the higher the loading amplitudes applied are. During cycling the materials harden and the plastic strain amplitudes decrease up to the number of cycles where macrocrack initiation is observed. The cyclic hardening effects are more pronounced in stress controlled tests. Experiments with  $\sigma_a = 400 \text{ N/mm}^2$  and  $\epsilon_{a,t} = 3.79 \text{ }^\circ/\text{oo}$  reveal initial plastic strain amplitudes of about  $2.5 \text{ }^\circ/\text{oo}$ . However, at crack initiation in the stress controlled test, just  $\epsilon_{a,p} = 0.4 \text{ }^\circ/\text{oo}$  is measured, whereas in the total strain controlled test a value of  $1 \text{ }^\circ/\text{oo}$  is observed.

A comparison between the cyclic and the monotonic deformation behaviour of GGG-40 is presented in Figure 5. The cyclic stress strain curves determined under constant stress and total strain conditions at  $N = N_f/2$  result in one common curve proving the cyclic hardening behaviour of the cast iron investigated.

The development of plastic deformation during cyclic loading is strongly influenced by the loading temperatures. The dependence of the plastic strain amplitude from the number of cycles in the temperature range  $20^\circ\text{C} < T < 500^\circ\text{C}$  is exemplarily shown in a three-dimen-

sional plot in Figure 6 for GGG-40. Beginning from 20°C, the initial plastic strain amplitudes increase up to 200°C and the shape of the appertaining cyclic deformation curves are comparable to the room temperature curves measured at higher stress amplitudes (see Figure 3). At temperatures  $> 250^{\circ}\text{C}$ , very high plastic strain amplitudes are measured in the first cycle. Since the cyclic hardening effects start immediately, the plastic strain amplitudes decrease rapidly with increasing number of cycles. The cyclic hardening effects are most pronounced at 350°C, where a relative maximum in the fatigue life is observed. As can be seen from Figure 7, the tests with GGV-30 reveal similar results. Also in this case, cyclic hardening occurs. However, the plastic strain amplitudes at crack initiation are higher than in the case of GGG-40, although the initial  $\epsilon_{a,p}$ -values are comparable. The temperature dependence of the cyclic deformation behaviour of the flake graphite cast iron GG-30 looks quite different compared with that of GGG-40 and GGV-30. As shown in Figure 8 nearly no influence of temperature on the plastic strain amplitude was detectable in tests with  $\sigma_a = 150 \text{ N/mm}^2$ .

#### DISCUSSION

Under cyclic loading the cast irons investigated reveal cyclic hardening effects of different intensities. At loading amplitudes above the fatigue strength, plastic deformations occur in the first cycle. It is well accepted that magnitude and development of the plastic strain amplitudes depend on the number and the mean free path of glide dislocations (Macherauch and Mayr (9)). Consequently, dislocation density, graphite shape and matrix structure are of great importance for the specific cyclic deformation behaviour. The change of the plastic strain amplitude during cycling is a consequence of microstructural processes in the elastically-plastically deformed areas of the materials, predominantly in the ferrite, which lead to typical dislocation structures. These processes are different in the cast irons investigated and explain the different cyclic deformation capability. For example, the relative small ductility of GG-30 is caused by the existing microstructural features of lamella graphite and perlitic matrix. The differences observed in the cyclic deformation behaviour under stress and total strain control are a consequence of the feed-back of the decreasing plastic strain amplitudes on the external loading in the total strain controlled tests. According

## FATIGUE 87

to  $\epsilon_{a,t} = \epsilon_{a,e} + \epsilon_{a,p}$ , the elastic strain amplitude  $\epsilon_{a,e}$ , and thus  $\sigma_a$ , must increase, if  $\epsilon_{a,p}$  decreases during cyclic hardening.

There exist some consistencies between the temperature dependence of the cyclic deformation curves of the cast irons investigated and that of normalized plain carbon steels (Pohl et al. (10)). Both, the stress and total strain controlled tests, reveal a defined dependence of the number of cycles to failure on the temperature. As can be seen in Figure 9, GGV-30 and GGG-40 reveal a relative maximum in fatigue life around 350°C. This increase in fatigue life is caused by dynamic strain aging effects. In the temperature range mentioned, the diffusion rate of interstitially solved C-atoms just reaches a magnitude to reduce the mobility of glide dislocations considerably. TEM-investigations confirm the close relation between plastic strain amplitudes and microstructural changes in the ferrite of the cast irons in constant amplitude tests at different magnitudes. As an example, Figure 10 shows characteristic dislocation structures at  $N = N_f$  in the temperature range 20°C < T < 500°C after constant amplitude loading ( $\sigma_a = 270 \text{ N/mm}^2$ ) for GGG-40. At 20°C statistically distributed dislocations are observed, at 200°C wall- and cell-like structures are to be seen. At 350°C, in the temperature range of maximum dynamic strain aging, the dislocations form veins and bundle-like structures. Finally, at 500°C, large block-like cells are the predominant structural feature of the fatigued material states.

### SYMBOLS USED

$\dot{\epsilon}$	=	strain rate ( $\text{s}^{-1}$ )
$\sigma_a$	=	stress amplitude ( $\text{N/mm}^2$ )
$\epsilon_{a,p}$	=	plastic strain amplitude ( $\text{N/mm}^2$ )
$\epsilon_{a,t}$	=	total strain amplitude ( $\text{N/mm}^2$ )
$R_{p0.2}$	=	0.2 % - proof stress ( $\text{N/mm}^2$ )
$R_m$	=	tensile strength ( $\text{N/mm}^2$ )
$A_g$	=	percentage elongation before reduction (%)

### REFERENCES

- (1) Blackmore, P. A. and Morton, K., Int. J. Fatigue, July 1982, pp. 149 - 155.

# FATIGUE 87

- (2) Socie, D. F. and Fash, J., Gießerei-Praxis, No. 18, 1983, pp. 276 - 284.
- (3) Starkey, M. S. and Irving, P. E., Int. Journal Fatigue, Vol. 4, No. 3, 1982, pp. 129 - 136.
- (4) Grubisic, V. and Neugebauer, J., Gießerei-Forsch. 4, 1979, pp. 123 - 128.
- (5) Starkey, M. S. and Irving, P. E., DVM Proc. Int. Conf. on Low Cycle Fatigue, Stuttgart, 1979, pp. 261 - 272.
- (6) Testin, R. A., T. & A. M. Report No. 371, 1973, University of Illinois.
- (7) Fash, J. and Socie, D. F., Int. J. Fatigue, Vol. 4, No. 3, 1982, pp. 137 - 142.
- (8) Lang, K. H., Eifler, D. and Macherauch, E., Int. J. Fatigue, Vol. 8, No. 2, 1986, pp. 98 - 100.
- (9) Macherauch, E. and Mayr, P., Z. f. Werkstofftechn. 8, 1977, pp. 213 - 224.
- (10) Pohl, K., Mayr, P. and Macherauch, E., Int. J. Fracture, Vol. 17, 1981, pp. 221 - 233.

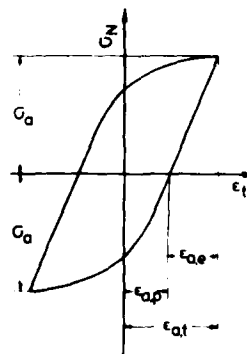
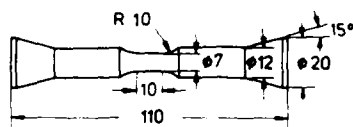


Figure 1 Shape and dimensions of the specimen

Figure 2 Hysteresis loop

# FATIGUE 87

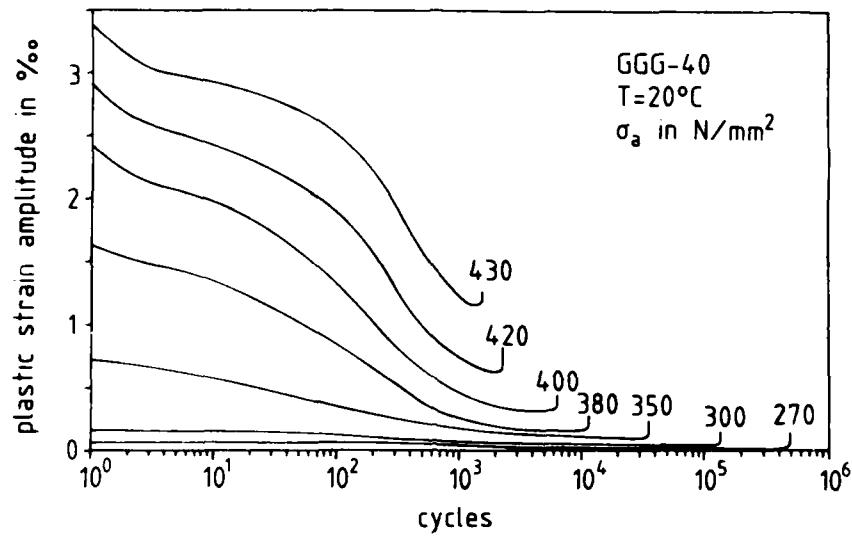


Figure 3 Cyclic deformation curves of ferritic nodular cast iron;  $\sigma_a = \text{const.}$

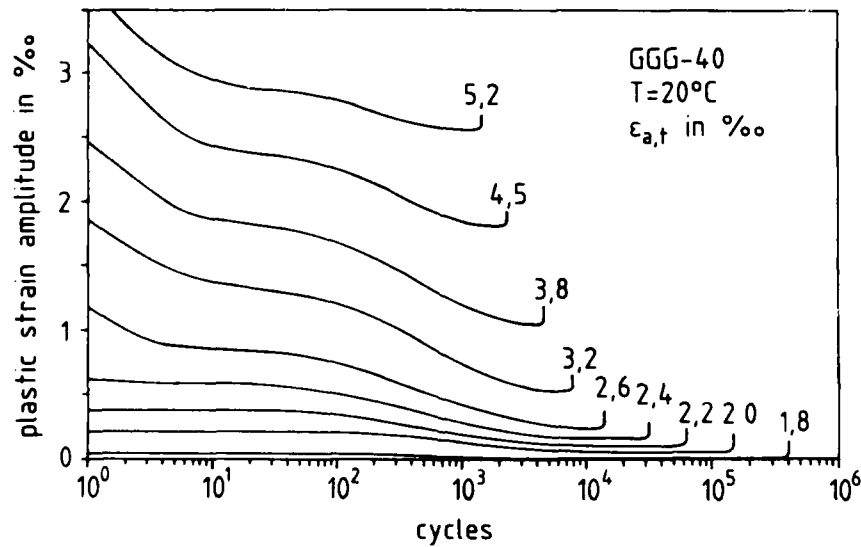


Figure 4 Cyclic deformation curves of ferritic nodular cast iron;  $\epsilon_{a,t} = \text{const.}$

# FATIGUE 87

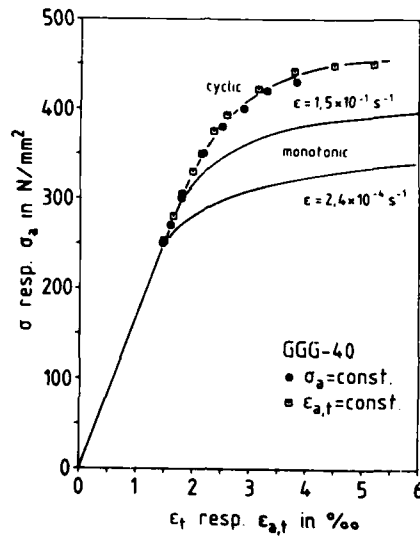


Figure 5 Cyclic and monotonic stress-strain curves

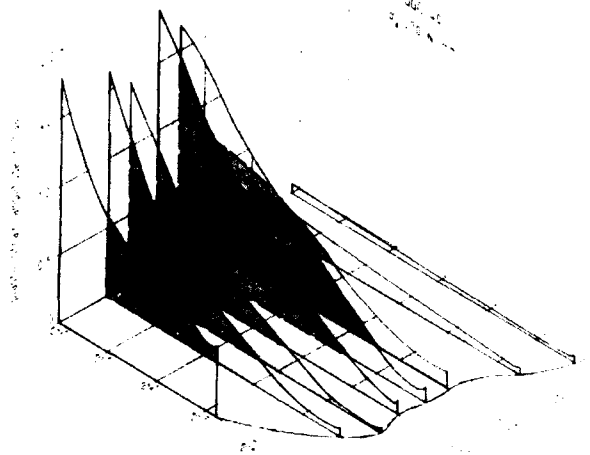


Figure 6 Cyclic deformation curves of ferritic nodular cast iron

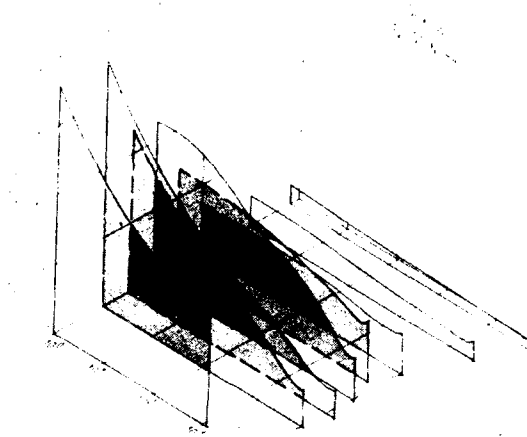


Figure 7 Cyclic deformation curves of ferritic vermicular graphite cast iron

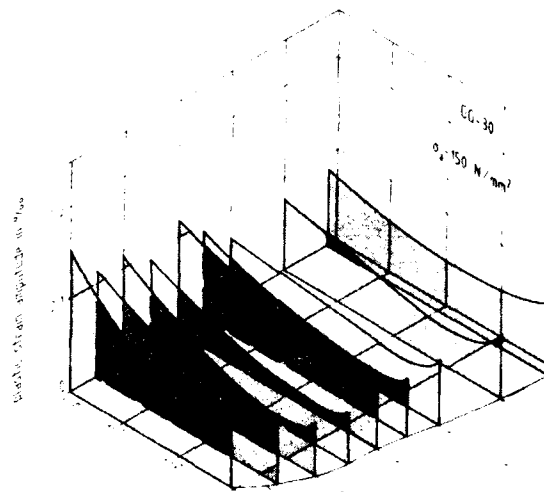


Figure 8 Cyclic deformation curves of perlitic flake graphite cast iron

# FATIGUE 87

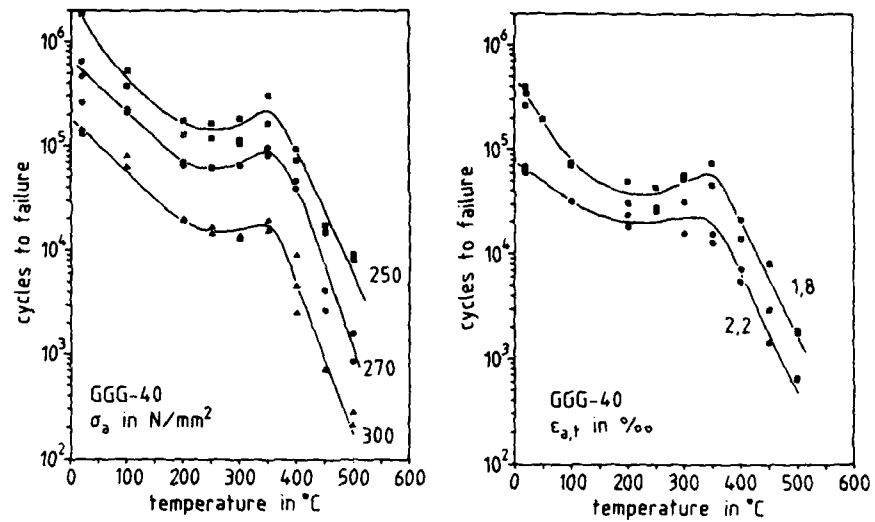


Figure 9 Influence of test temperature on the number of cycles to failure of ferritic nodular cast iron

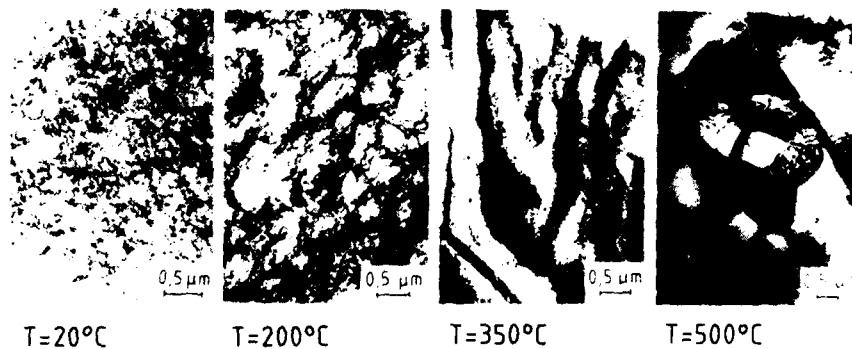


Figure 10 Typical dislocation structures at  $N = N_f$  after cyclic loading with  $\sigma_a = 270\ \text{N/mm}^2$

## FATIGUE CRACK GROWTH AND FRACTURE OF COPPER-BISMUTH BICRYSTALS

S. Chikwembani and J. Weertman\*

Copper doped with bismuth bicrystals show fatigue crack growth along the boundary for bulk bismuth contents higher than about 0.003 wt%. At a given  $\Delta K$ ,  $da/dN$  increases with increasing bismuth concentration (i.e.,  $da/dN$  increases with decreasing surface energy). Overload effects in the bicrystals are so prominent to the extent that they could, in some cases, easily swamp the effects of changes in bismuth concentration. The Paris equation power exponent  $m$  is found to increase with increasing bismuth concentration.

INTRODUCTION

Fatigue crack growth studies are very useful in providing information about a material's ability to withstand cyclic loading. In metals, for the most part, fatigue testing has been performed on polycrystalline samples. In cases where failure occurs along grain boundaries the crack path tends to be tortuous. This makes crack growth measurements rather difficult and inaccurate.

Hondros and McLean (1) found that multiple cracking occurs at grain boundaries of copper doped with bismuth monotonically loaded in tension. The copper grain boundaries are weakened by the segregation of bismuth to them. The surface energy of copper is reduced quite considerably by the addition of bismuth (1). Elastic enclave theories for fatigue crack growth predict that surface energy should play an important role in determining fatigue crack growth rate (Weertman (2-3)). Because the surface energy of copper decreases with increasing bismuth content (1) we expect that  $da/dN$ , at a given  $\Delta K$ , should increase with increasing bismuth concentration. Fatigue crack growth should occur in a brittle mode if the bismuth content is high enough in the copper-

\* Northwestern University, Department of Materials Science and Engineering, Technological Institute, Evanston, IL 60201

bismuth system. To avoid the problem of multiple cracking we chose to use bicrystals instead of polycrystals in our fatigue experiments.

#### EXPERIMENTAL PROCEDURE

Bicrystals were grown in a graphite mold using the Bridgeman technique. 99.999% copper shot and 99.9999% bismuth powder were melted together during the growth process. The bicrystals were grown of random orientations. However, these orientations could be reproduced by reusing the "seed parts" of the originally grown bicrystal. This is illustrated in figure 1. The position where the seeds started melting is clearly evident from the figure.

After growth the bicrystal was cut into parallelepipedic specimens using an electrode discharge machine. The specimens were then etched in 50%  $\text{HNO}_3$  as a way of cleaning them. An initial heat treatment was carried out at 850°C for 24 hours in order to homogenize the samples. This was followed by a 5 hour heat treatment at 530°C in order to allow segregation of bismuth to the grain boundaries to occur. In the initial stages of this work the bismuth segregation heat treatment was carried out at 550°C for 24 hours (Chikwembani and Weertman (4)). We changed to the shorter heat treatment after reading the paper of Johnson, et al., (5). They conclude that a heat treatment of 70 minutes at 530°C is sufficient to attain equilibrium surface concentration in the segregation of bismuth to copper grain boundaries. We have not noticed any change in the behavior of the bicrystals that could be attributed to our having changed the final heat treatment procedure.

Laue back reflection pictures were taken to determine the crystallographic orientation of the bicrystals. The tensile axis orientations of those bicrystals that are of interest in this paper are shown in figure 2. A single edge notch was introduced on the boundary of each fatigue specimen using an electrode discharge machine. The specimens were mechanically polished before fatiguing them. The fatigue tests were carried out in mode I with the plane of the boundary (and crack plane) perpendicular to the tensile load axis. Tests were performed in load control with an R ratio of 0.1 and a cycling frequency of 10 Hz. Crack growth measurements were made using a traveling microscope.

Fracture and external surfaces of fatigued specimens were examined using both optical and electron microscopes. X-ray analysis was performed in the SEM in order to find out if any regions of localized bismuth concentration were present on the fracture surfaces. Specially prepared specimens were also fractured under high vacuum in an Auger chamber in order to determine the bismuth coverage at the grain boundary.

## FATIGUE 87

The bulk bismuth concentrations of the bicrystals were measured by Chicago Spectro Laboratory and Charles C. Kawin Company both from Illinois.

### RESULTS

The lower limit in bulk bismuth concentration required to sufficiently weaken the boundary so as to get grain boundary crack growth has been found to vary from orientation to orientation. From all the orientations studied so far, it has been found that at bulk bismuth contents lower than about 0.003 wt% the bicrystals are too ductile to give crack propagation. A profusion of slip lines is formed on all faces of the bicrystal with no associated crack growth.

In those cases where crack grows relatively easily, crack growth is preceded by slip line formation ahead of the crack tip. When crack is growing at a fast enough speed so that its motion is easy to follow in the microscope, we have seen that the crack appears to stop briefly while a set of slip lines is forming directly ahead of the crack tip. The crack tip then advances and breaks through this region before stopping to wait for another turn of slip line formation. This sequence of events repeats itself while the crack grows.

Figure 3 shows plots of  $da/dN$  versus  $\Delta K$  for bicrystal specimens of different concentrations. The bulk bismuth content, the maximum stress at which the specimen was fatigued and specimen orientations (see figure 2) are shown on each graph. It is clear from figure 3 that, for a given  $\Delta K$ ,  $da/dN$  increases with increasing bismuth content. A straight line is drawn through those points believed to make up the Paris region. It is seen that the power exponent  $m$  appears to increase with bismuth concentration.

Reducing the stress range at which a specimen is fatigued reduces the crack growth rate because  $\Delta K$  is also reduced. However, as the crack grows longer  $\Delta K$  rises and eventually reaches and surpasses the highest  $\Delta K$  value attained prior to the stress range reduction. We have found (see figure 4) that when we compare crack growth rates at a given  $\Delta K$  for the two stress ranges, the high stress range  $da/dN$  values are higher than the low stress range  $da/dN$  values. So it would appear that the bicrystals show an overload effect in their fatigue behavior. The exponent  $m$  also appears to decrease somewhat as a result of the stress range reduction.

For those bicrystals that failed to give crack growth even when the bulk bismuth content was quite high, rolling was found to be an effective way of making crack growth possible. The bicrystals were rolled to a 15% thickness reduction in a direction parallel to the tensile axis. Both concentration

## FATIGUE 87

(figure 5) and overload (figure 6) effects show the same trends as was observed in the unrolled specimens. Below about 0.002 wt% Bi, however, even rolling could not effect crack growth along the boundary. In such cases the crack started off from the notch tip at some point in one of the crystals and crack growth took place in the matrix of that crystal. The crack growth behavior in these cases was much the same as is observed in ordinary single crystals.

In bicrystal specimens with more than about 0.03 wt% Bi the crack tended to propagate to total failure in a catastrophic manner at very low stress levels. In some cases the crack would grow all of a sudden over a distance of say about 1 mm and stop. Continued cycling would then not give any new growth. But a very small increase in load would make the crack grow suddenly again. This behavior would continue until at some stress level total failure would occur. These specimens tended to fail at stress levels below about 10 MPa. In extreme cases of embrittlement the grain boundary was so weak that the bicrystal specimens could easily be broken by hand. The fracture surfaces of these weak bicrystals looked very smooth when viewed by the unaided eye. However, at high magnifications in the SEM it was observed that slip steps were present on the fracture surface. Figure 7 gives an example of this for a specimen of orientation D and concentration 0.036 wt% Bi. Also note the presence of particles on the fracture surface. X-ray analysis in the SEM showed these particles to be rich in bismuth (typically between about 30 and 100 wt% Bi). Such particles have also been seen by Fraczkiewicz and Biscondi (6). The slip steps seen in Figure 7 presumably are produced on the fracture surfaces behind the advancing crack tip as pointed out in the work of Bursle and Pugh (7).

Auger analysis of specimens of orientation E gave us bismuth coverages of 0.6 monolayer for a bulk bismuth content of 0.013 wt% and 1.4 monolayers for a bulk bismuth content of 0.025 wt%. The thickness of the bismuth layer at the grain boundary was estimated as follows. Since bismuth is the only major impurity at the grain boundary, for a bismuth layer of thickness  $t$  on the fracture surface the intensity  $I_E^0$  of any copper peak at energy  $E$  is attenuated to

$$I_E = I_E^0 \exp(-t/\lambda_E \cos \theta) \quad (1)$$

$\lambda_E$  is the mean free path of electrons with energy  $E$ .  $\theta$  is angle from specimen surface normal at which Auger electrons are collected. By measuring the peak to peak heights of copper peaks at 61 eV and 918 eV from clean surface (i.e., bismuth layer sputtered off) and unsputtered surface  $t$  is calculated from

$$t = \ln \left[ \frac{I_{61} / I_{918}}{I_{61}^{\circ} / I_{918}^{\circ}} \right] / \left[ \left( \frac{1}{\lambda_{918}} - \frac{1}{\lambda_{61}} \right) \frac{1}{\cos \theta} \right] \quad (2)$$

We have to multiply this  $t$  by 2 because on average the bismuth is shared equally on the two fracture surfaces. A monolayer was taken to be 3 Å thick.  $\lambda_{61}$  and  $\lambda_{918}$  were estimated to be 4 Å and 13.5 Å respectively from the mean free path versus energy curve given by Ertl and Kuppers (8). And  $\theta = 42.3^{\circ}$  for the setup we used.

#### DISCUSSION AND CONCLUSIONS

Our  $da/dN$  versus  $\Delta K$  data show that  $da/dN$  increases with decreasing surface energy (or increasing bismuth content) as expected from elastic enclave theories for fatigue crack growth. However, the data bring out additional features which the theories do not address. First, the power exponent  $m$  is experimentally found to increase with decreasing surface energy,  $\gamma$ . Since in the theories  $da/dN$  is inversely proportional to  $\gamma^p$  ( $p$  being a positive power which is itself in part determined by  $m$ ) there is the possibility that a decreasing  $\gamma$  can give rise to a decreasing  $da/dN$  especially at low  $\Delta K$  values. Secondly,  $m$  has also been found to decrease somewhat with decreasing stress range,  $\Delta\sigma$ . Because in these tests  $R = 0.1$ ,  $\sigma_{\max} \approx \Delta\sigma$ . So it is possible that what is considered to be a  $\Delta\sigma$  effect may in fact be a  $\sigma_{\max}$  effect. Whether it is  $\Delta\sigma$  or  $\sigma_{\max}$  that determines this behavior is not so important. The more crucial point is the possibility that the effect of surface energy may be easily swamped by the stress effects. On comparing crack growth data of different specimens it is important to have a knowledge of the load history of each specimen.

The observation that crack tip stops advancing briefly as slip lines form directly ahead of it implies that work hardening of slip planes is necessary prior to crack growth. Another point which comes to light is that crack propagation is not a smoothly continuous process. It appears that it is necessary for the crack to remain stationary in some cycles while the region directly ahead of the tip is receiving some form of hardening and/or damage prior to further crack advance.

The presence of slip steps even on fracture surfaces of specimens that appear to have undergone brittle fracture on a macroscopic scale points to the fact that locally, at the crack tip, plastic deformation always accompanies crack growth. The bismuth rich particles found on grain boundary surfaces in specimens with more than about 0.03 wt% bismuth confirm the finding of others (1,6) regarding the limited solid solubility of bismuth in copper. It is possible that the presence of these

## FATIGUE 87

particles is in part responsible for the sudden crack growth characteristics of these bicrystals.

More work is required on Auger analysis before we can draw some definitive conclusions on the extent of surface coverage by bismuth at the copper grain boundaries. Suffice to point out that a surface coverage of the order of a monolayer has been found for one studied orientation with bismuth contents of 0.013 wt% and 0.025 wt%. This coverage implies an enrichment ratio (surface concentration/bulk concentration) of the order of  $10^4$ .

### ACKNOWLEDGMENT

This research was supported by the National Science Foundation under NSF Grant DMR-8304644. The authors would like to express their thanks to Professor Y. W. Chung of Northwestern University for his help with the Auger analysis.

### REFERENCES

- (1) Hondros, E.D, and McLean, D., Phil. Mag., Vol. 29, 1974, pp. 771-795.
- (2) Weertman, J., "Fatigue Crack Growth Theory for Ductile Material" in "Three Dimensional Constitutive Relations and Ductile Fracture", Edited by Z.A. Foroulis, The Metallurgical Society of AIME, New York, 1979.
- (3) Weertman, J., Acta Met., Vol. 32, 1984, pp. 575-584.
- (4) Chikwembani, S. and Weertman, J., Scripta Met., Vol. 19, 1985, pp. 1499-1502.
- (5) Johnson, W.C., Joshi, A. and Stein, F., Met. Trans., Vol. 74, 1976, pp. 949-951.
- (6) Fraczkiwicz, A. and Biscondi, M., J. de Physique, Colloque C4, Supplement au N<sup>o</sup>4, Tome 46, Avril 1985, pp. 497-503.
- (7) Bursle, A.J. and Pugh, E.N., "An Evaluation of Current Models for the Propagation of Stress-Corrosion Cracks" in "Environment-Sensitive Fracture of Engineering Materials, Edited by Z.A. Foroulis, The Metallurgical Society of AIME, New York, 1979.
- (8) Ertl, G. and Koppers, J., Low Energy Electrons and Surface Chemistry, Verlag Chemie, Weinheim, FRG, 1974.



Figure 1 Seeded bicrystal of copper doped with bismuth

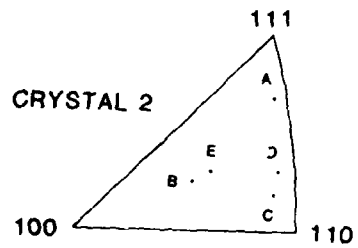
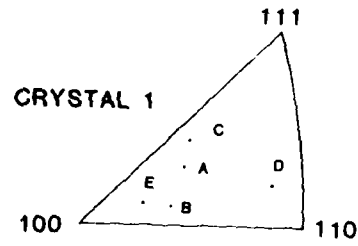


Figure 2 Tensile axis orientations for bicrystal specimens

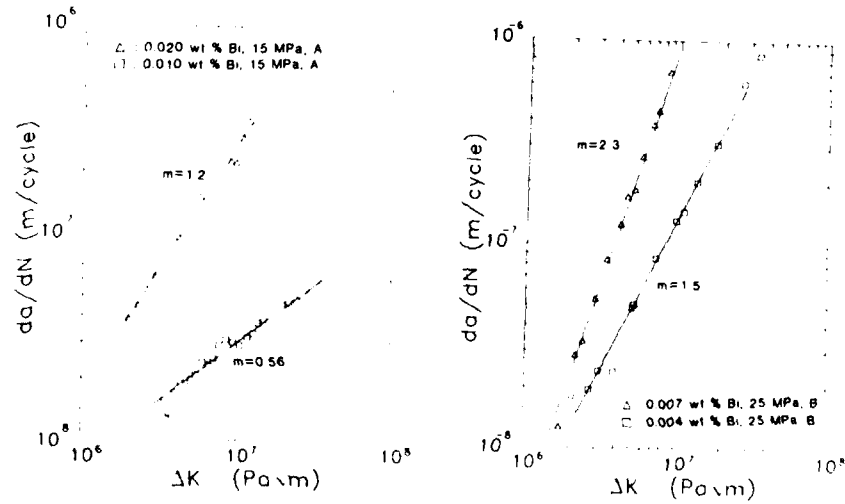


Figure 3  $da/dN$  versus  $\Delta K$  curves for bicrystal specimens of different bismuth contents and orientations.

# FATIGUE 87

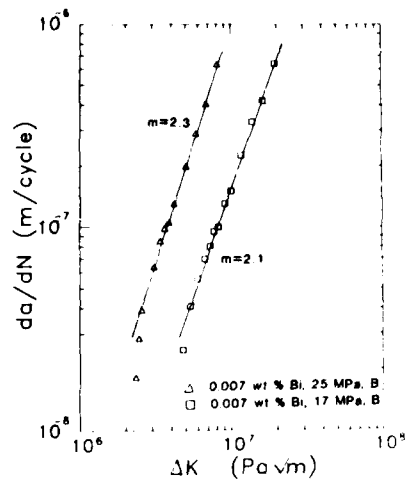


Figure 4  $da/dN$  versus  $\Delta K$  curves for different stresses

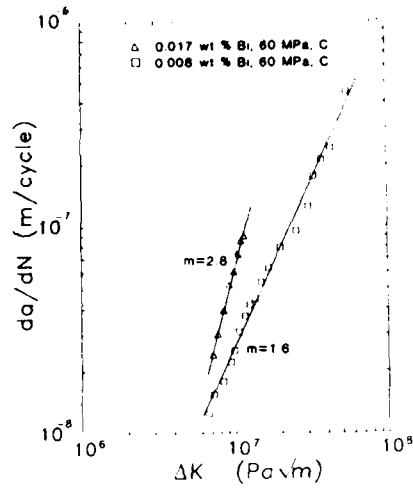


Figure 5  $da/dN$  versus  $\Delta K$  curves for rolled specimens

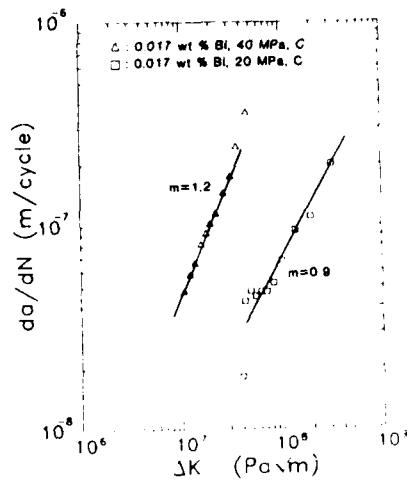


Figure 6  $da/dN$  versus  $\Delta K$  curves for rolled specimen



Figure 7 Fracture surface of a weak bicrystal specimen

LIFE PREDICTION OF STEEL CORDS

A. Prakash (1), G.A..Costello (2), R.M. Shemenski (1)  
and D.K. Kim (1)

Steel cables are used under cyclic tension and bending loading and failures usually have been attributed to fatigue accelerated by fretting and corrosion. Bending and axial stresses in a typical cable are presented. Low cycle fatigue (LCF) characterization have been carried out for cyclic bending loading over a fixed cord tension. Bending LCF behavior correlates with cable's bend hysteresis property.

INTRODUCTION

Steel wire cord (or rope or cable) provide a unique combination of strength, ductility, resistance to fatigue and cost. A typical cord is shown in Figure 1. Under bending and twisting, a multi-filament cord develops reduced stresses compared with an equal strength monofilament. This improves cyclic flexural properties. In such cases the metallurgical structure of the wire and the flexural behavior of the construction usually control low cycle fatigue (LCF) life of the cord. To characterize LCF behavior, applied stresses have to be first evaluated. Analytical work has shown that tension, bending, twisting and contact stresses in individual filaments of a cord are related to number and diameter of filaments, twist, surface and the physical properties of the wire (1-6). Analysis also shows that Hertz contact stress is a major factor,

- (1) Sr. Engineer, Manager, Research Assoc. respy., Steel Technology, Goodyear Research, Akron OH 44236
- (2) Professor, Fellow ASME, Dept of Theoretical and Applied Mechanics, Univ. of Illinois, Urbana, IL 61801

responsible for fretting and fatigue failures. Theoretical analyses, however, are usually based on an assumption that there is no interfilament frictional force.

AISI-SAE 1070 plain carbon steel wire of .15 to .38mm in dia with carbon content ranging from 0.65 to 0.75 weight percent has been used for this study. Strength is typically in the range of 2300 to 3000 MPa with 1.5 to 4% elongation. These wires are brass plated to facilitate final drawing. A cold drawn wire represents a highly anisotropic microstructure, probably with a high residual surface stress. Due to the complexities of loading and construction, analytical expressions alone can not completely characterize cord behavior. Optimization of cord construction for maximum cyclic life needs to be done by experiment. Laboratory fatigue studies, especially under reverse bending, have shown satisfactory correlation between material quality and performance.

#### STRESSES IN A CORD

Figure 1 shows a loaded strand or cable, which consists initially of a straight center wire of radius,  $R_1$ , surrounded by  $m_2$  (six wires are actually shown) helical wires of radius  $R_2$ . It is assumed that the center wire is of sufficient size to prevent the outer wires from touching each other. Therefore, the initial radius of the helix of the outside wires,  $r_2$ , is given by the expression

$$r_2 = R_1 + R_2 \quad (1)$$

The initial helix angle,  $\alpha_2$ , of the outside wires is given by

$$\tan \alpha_2 = \frac{p_2}{2\pi r_2} \quad (2)$$

where  $p_2$  is the original pitch of the outside wires.

Several of the equations listed in the forthcoming are derived in (1,2,3,4) and are listed here again for completeness. A linearization of the equation describing the undeformed and deformed configuration of the strand or cord yields

$$\xi_1 = \frac{\bar{h}-h}{h} = \xi_2 + \frac{\Delta\alpha_2}{\tan\alpha_2} \quad (3)$$

$$\beta_2 = r_2 \frac{(\bar{\theta}_2 - \theta_2)}{h} = \frac{\xi_2}{\tan\alpha_2} - \Delta\alpha_2 + \frac{\nu}{r_2} \frac{(R_1 \xi_1 + R_2 \xi_2)}{\tan\alpha_2} \quad (4)$$

where  $\xi_1$  is the axial strain in the center wire and also the cord;  $h$  is the original length of the cord;  $\bar{h}$  is the final length of the cord;  $\xi_2$  is the axial strain in an outer wire;  $\Delta\alpha_2 = \bar{\alpha}_2 - \alpha_2$  is the increase in the original helix angle,  $\alpha_2$ , of an outer wire;  $\bar{\alpha}_2$  is the final helix angle of an outer wire;  $\beta_2$  is the rotational strain of an outer wire and, of course, the cord; and  $\theta_2$  and  $\bar{\theta}_2$  are the original and final angles respectively that an outer wire sweeps out in a plane perpendicular to the axis of the cord. The angle of twist per unit length of the cord,  $\tau$ , is given by the expression

$$\tau = \frac{\bar{\theta}_2 - \theta_2}{h} \quad (5)$$

The change in curvature,  $\Delta\kappa_2$ , of an outer wire is given by

$$R_2 \Delta\kappa_2 = - \frac{2\sin\alpha_2 \cos\alpha_2}{r_2/R_2} \Delta\alpha_2 + \frac{\cos^2\alpha_2}{r_2/R_2} \frac{\nu}{r_2} (R_1 \xi_1 + R_2 \xi_2) \quad (6)$$

and the angle of twist per unit length,  $\Delta\tau_2$ , of an outer wire is expressed as

$$R_2 \Delta\tau_2 = \frac{(1-2\sin^2\alpha_2)}{r_2/R_2} \Delta\alpha_2 + \frac{\sin\alpha_2 \cos\alpha_2}{r_2/R_2} \frac{\nu}{R_2} (R_1 \xi_1 + R_2 \xi_2) \quad (7)$$

The following expressions can now be written down for the cord shown in Figure 1.

$$\frac{G_2}{ER_2^3} = \frac{\pi}{4} R_2 \Delta\kappa_2 \quad (8)$$

$$\frac{H_2}{ER_2^3} = \frac{\pi}{4(1+\nu)} R_2 \Delta\tau_2 \quad (9)$$

$$\frac{N_2}{ER_2^2} = \frac{H_2}{ER_2^3} \frac{\cos^2\alpha_2}{r_2/R_2} - \frac{G_2}{ER_2^3} \frac{\sin\alpha_2 \cos\alpha_2}{r_2/R_2} \quad (10)$$

$$\frac{T_2}{ER_2^2} = \pi \xi_2 \quad (11)$$

$$\frac{X_2}{ER_2^2} = \frac{N_2}{ER_2^2} \frac{\sin \alpha_2 \cos \alpha_2}{r_2/R_2} - \frac{T_2}{ER_2^2} \frac{\cos^2 \alpha_2}{r_2/R_2} \quad (12)$$

$$\frac{F_2}{ER_2^2} = m_2 \left[ \frac{T_2}{ER_2^2} \sin \alpha_2 + \frac{N_2}{ER_2^2} \cos \alpha_2 \right] \quad (13)$$

$$\begin{aligned} \frac{M_2}{ER_2^3} = m_2 & \left[ \frac{H_2}{ER_2^3} \sin \alpha_2 + \frac{G_2}{ER_2^3} \cos \alpha_2 \right. \\ & \left. + \frac{T_2}{ER_2^2} \cos \alpha_2 - \frac{N_2}{ER_2^2} \frac{r_2}{R_2} \sin \alpha_2 \right] \quad (14) \end{aligned}$$

where  $E$  is modulus of elasticity of the material;  $G_2$  is the bending moment in an outer wire;  $H_2$  is the axial twisting moment in an outer wire;  $N_2$  is the shearing force in an outer wire;  $T_2$  is the axial force in an outer wire;  $X_2$  is the resultant contact force per unit length acting on an outer wire;  $F_2$  is the total axial force acting on the outer wires and  $M_2$  is the total axial twisting moment acting on the outer wires. The axial force,  $F_1$ , and axial twisting moment,  $M_1$ , acting on the outer wire are

$$\frac{F_1}{ER_1^2} = \pi \xi_1 \quad (15)$$

and 
$$\frac{M_1}{ER_1^3} = \frac{\pi}{4(1+\nu)} R_1 \tau \quad (16)$$

The total axial force,  $F$ , acting on the cord is

$$F = F_1 + F_2 \quad (17)$$

and the total axial twisting moment,  $M_T$ , acting on the cord is

$$M_T = M_1 + M_2 \quad (18)$$

Let, for example,  $\xi_1 = \epsilon$  and  $\tau = 0$ . This means that the axial strain is known and the cord is not allowed to rotate. Equations (3), (4) and (5) can then be used to determine the values of  $\xi_2$  and  $\Delta\alpha_2$ . Equations (6) and (7) yield  $R_2\Delta\kappa_2$  and  $R_2\Delta\tau_2$  and Eqs. (8)-(16) determine  $G_2, H_2, N_2, T_2, X_2, F_2, M_2, F_1$ , and  $M_1$ . Once these values are known, the elementary strength of material formulae can be used to determine the stresses in the wires. Also, with  $X_2$  known, the values of the contact stresses can be determined.

If the strand or cord shown in Fig. 1 is bent into a curvature of radius,  $\rho$ , expressions can also be determined for the bending stresses. The bending stress in the center wire,  $\sigma_{B1}$ , is simply

$$\sigma_{B1} = \frac{ER_1}{\rho} \quad (19)$$

The bending stress in an outer wire,  $\sigma_{B2}$ , is

$$\sigma_{B2} = \frac{2\sin\alpha_2}{(2+\nu\cos^2\alpha)} \frac{ER_2}{\rho} \quad (20)$$

These stresses must be superimposed on the stress due to the axial loading.

#### BEHAVIOR OF CORD UNDER CYCLIC LOADING

The concept of 3-roll test was developed to study the LCF in a combination of bend and tensile loadings in wire ropes. This led to the use of Drucker's non-dimensional test parameter to predict fatigue life of wire rope from tests on single wire (7). A schematic of a Goodyear type 3-roll fatigue set up is shown in Figure 2. The specimen was made by curing the test cord in a rubber filled mold. This represented a cord in a tire. The 3-rollers assembly cycled at a rate of 150 to 300 per minute. A Wheatstone bridge type circuit was used to detect failure of filaments in the cord. This test represented a fully reversed (bending) strain controlled test with sinusoidal cycle with mean stress depending upon the pre-load on the specimen. Figure 3 shows 3-roll fatigue test results of cords of comparable construction but of various filament diameters and lay lengths with and without a wrap wire (8). Bare cords and single filaments have also been successfully tested in 3-roll machine by appropriately protecting the wire from the moving roller. This can be done by placing the wire in a plastic tubing. Fatigue lives of some typical constructions are given in Table-1.

# FATIGUE 87

TABLE 1 - Typical 3-Roll Fatigue Data; Roller Dia.  
2.54 cms; Cord Tension -10% of strength

CONSTRUCTION	STRENGTH N	TEST MPa	TEST CONDITION	FATIGUE LIFE CYCLES
.22mm wire	105	2760	A	4500
4 x .25mm	540	2755	B	5700
2+7x.22+1*	871	2545	B	23800
3+9x.22+1*	1225	2700	B	20000
3+9x.22+1*	1225	2700	C	12000
3+9+15x.22+1*	2733	2662	B	10000

(\*) +1 indicates a wrap wire (A) filament was tested in a plastic tube over 32 mm pulleys to compensate for the rubber thickness of other cord samples. (B) Cord embedded in rubber, (C) Bare cord in plastic tube

Steel cords always showed better fatigue life when tested in rubber, attributed to reduced fretting in individual filament due to rubber penetration. As discussed earlier, when a cord is subjected to bending loading, the individual filaments experience tensile, bending and contact stresses. The assumption of zero interfilament frictional force in computing stresses is not quite correct and depending upon the surface quality and construction, friction is expected. This poses a difficulty in comparing 3-roll fatigue lives of various constructions on the basis of stress calculations. However, it has generally been felt that for approximately identical constructions, the 3-roll data can be meaningfully compared. To get an appreciation of interfilament frictional force, two cords of identical construction, but from different manufacturers were tested in the 3-roll machine. Three-point bending hysteresis data were also obtained by cyclically flexing one bare cord placed on 2 pivots 5 cms apart. Load vs. displacement hysteresis of the cords in arbitrary scale along with the 3 roll data are shown in Figure 4. The cord which showed minimum hysteresis loss had the highest fatigue life. The hysteresis loss is attributed to the interfilament frictional force.

## SUMMARY AND CONCLUSION

In this paper an attempt has been made to identify factors expected to affect the life of a steel cord and the experimental techniques to evaluate them.

The stress analysis of stranded cords subjected to axial and bending forces have been presented. The study is based on a frictionless model. From the experimental study, it appears that there is a definite amount of friction between the filaments which is responsible for the fretting damage. In bending fatigue test, as theoretically predicted, fatigue life increased with decrease in filament diameter. Among the techniques used, the 3-roll reverse bend fatigue test appeared to provide the best data. The load vs bending hysteresis energy loss of cords correlated with 3-roll fatigue life. The energy loss is attributed to inter-filament friction. This observation is parallel to gross behavior of metals where stress-strain cyclic hysteresis loss is due to plastic strain and correlates with fatigue life. Cords showed higher bending fatigue life in rubber compared to bare cord. This has been attributed to reduced fretting damage due to rubber penetration.

#### REFERENCES

- (1) Costello, G.A. and Butson, G.J., "Simplified Bending Theory for Wire Rope," J of the Engineering Mechanics Division, ASCE Vol. 108, No. EM2, April, 1982, P. 219.
- (2) Costello, G.A., "Stresses in Multilayered Cables," ASME J of Energy Resources Technology, Vol. 105, 1983, p337
- (3) Velinsky, S.A., Anderson, G.L. and Costello, G.A., "Wire Rope with Complex Cross Sections," J of the Engineering Mechanics Division, ASCE, Vol. 110, 1984, p380
- (4) Phillips, J.W. and Costello, G.A., "Analysis of Wire Ropes with Internal-Wire-Rope-Cores," J of Applied Mechanics, Vol. 107, 1985, p 510.
- (5) Leissa, A.W., "Contact Stresses in Wire Ropes," Wire, March, 1959, p. 307
- (6) Starkey, W.L. and Cress, H.A., "An Analysis of Critical Stresses and Mode of Failure of a Wire Rope," J of Eng. for Industry, Trans. of ASME, November 1959, p. 307
- (7) Gambrell, S.C., Jr., "Predicting Fatigue Life of Wire Rope from Tests on Single Wire", Wire & Wire Products, November, 1970, p. 45
- (8) Tokusen Kogyo Co., Ltd., Japan; Technical Report, 1984.

# FATIGUE 87

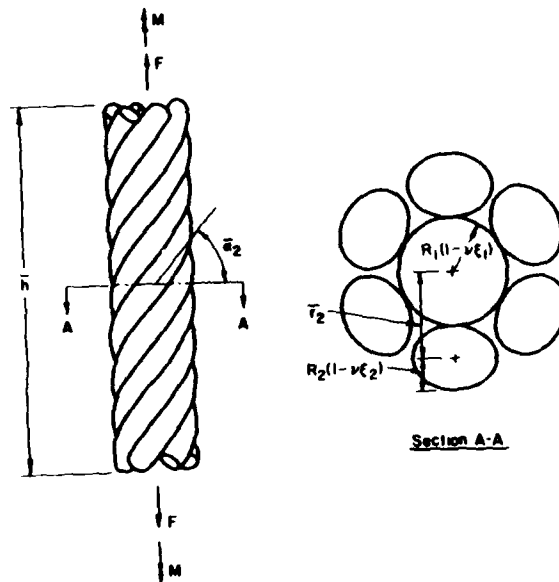


Figure 1 An axially loaded cord

## 3-ROLL FATIGUE TESTER

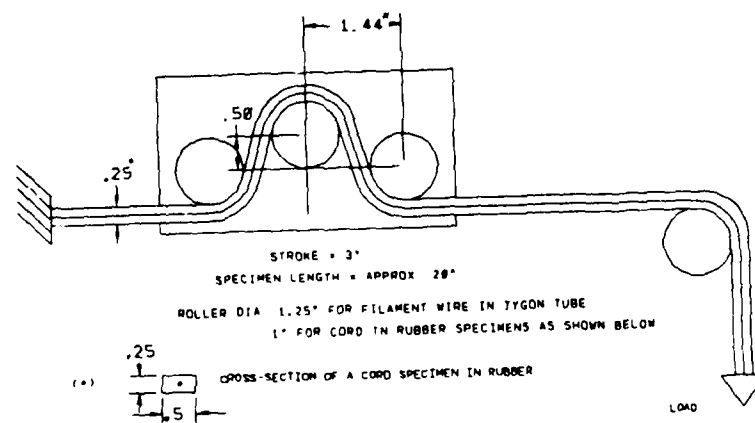


Figure 2 A three-roller band fatigue tester

# FATIGUE 87

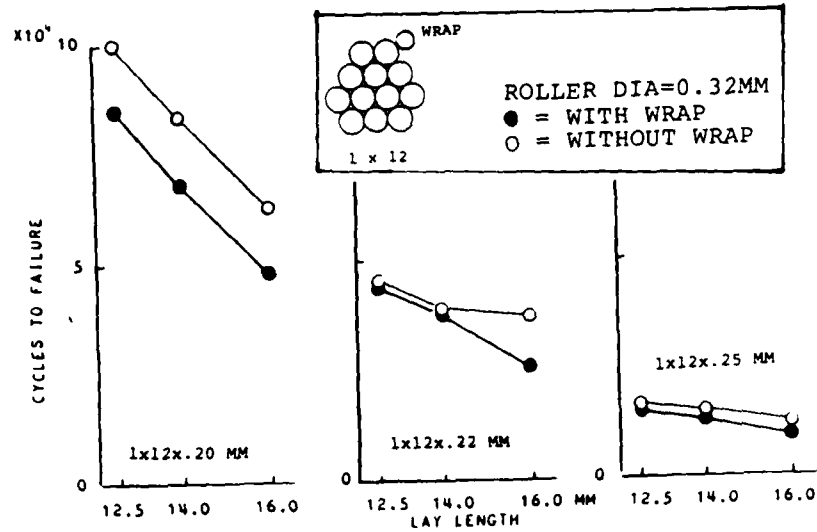


Figure 3 Effect of lay length, wire diameter and wrap on 3-roll fatigue life of similar constructions.

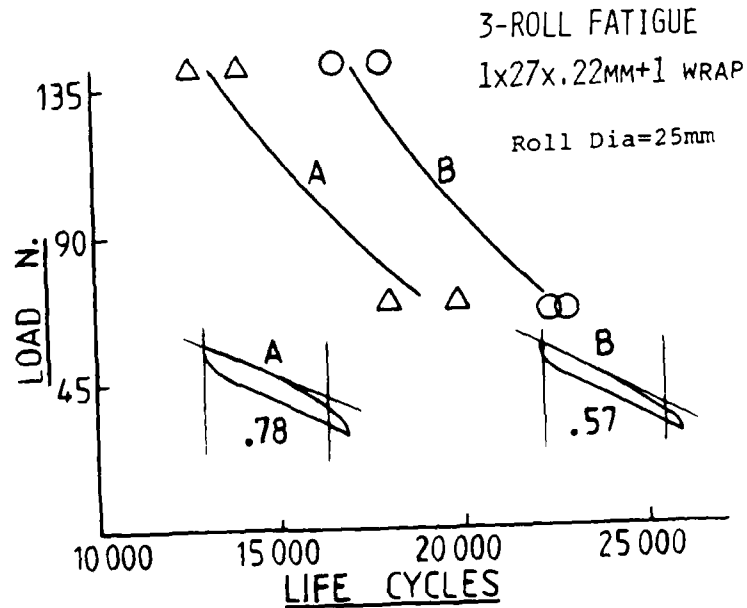


Figure 4 3-roll fatigue and load vs. bend hysteresis of two cords. Areas (.78 and .57) in arbitrary units.

FATIGUE 87

## FATIGUE 87

### EFFECT OF HOLD TIME ON FATIGUE OF LEAD RICH PbSn SOLDER

S. Vaynman\*, M.E. Fine\*, D.A. Jeannotte\*\*

Effect of tensile and compressive hold times on the fatigue life of lead rich PbSn solder was studied. Tensile and combined tensile and compressive hold times were found to reduce dramatically the number of cycles to failure. A simple mathematical relation between the isothermal fatigue life and tensile and compressive hold times was developed.

#### INTRODUCTION

Failure of solders due to thermal fatigue is a very serious problem in electronics and power industry (Lau(1), Burges(2)), however little experimental data is available on fatigue behavior and mechanisms of fatigue failure of solder for development of a model for fatigue life prediction.

Understanding of the isothermal behavior of solder at different temperatures is required to build a thermal fatigue life prediction model, therefore effect of such variables as hold time at maximum and minimum strains on the fatigue life of 96.5Pb-3.5Sn solder in the 25-80°C temperature range was undertaken.

---

\* Department of Materials Science and Engineering,  
Northwestern University, Evanston, IL 60201  
\*\*IBM Corporation, East Fishkill Facility, Hopewell  
Junction, NY 12533-0999

## FATIGUE 87

### EXPERIMENTAL PROCEDURE

This research was done with 96.5 wt.%Pb-3.5 wt.%Sn solder received from Semi-Alloys Inc. The impurities reported by Semi-Alloys Inc. totaled less than 0.1%.

Specimens were cast in a flat open aluminum mold. Each specimen was 6 mm thick and 12 mm wide in the gage section. Subsequent to casting, the specimens were machined flat and then homogenized at 175°C for 100 hours. A second anneal at 150°C for 2 hours was done approximately one week before testing to standardize testing conditions since age hardening was detected in 96.5Pb-3.5Sn solder. The specimens were mechanically polished down to 1 micrometer grit size prior to testing. Since specimens were prepared by casting, a coarse structure was produced with grain dimensions depending on the orientation of the solder in the mold during crystallization. The grains, elongated in the direction of the specimen width, varied widely from approximately 50 to 500 microns in the short dimension and their length was up to few millimeters. These large grains were divided into subgrains 25-100 micrometers long.

Fatigue tests were done in pull-pull, i.e. the strain was changed during testing from zero to a maximum value. While strain in tests was varied from zero to a maximum strain level, the values for peak tensile and compressive stresses were almost equal due to the very high plastic to elastic strain ratio in the solder. Heating or cooling of specimens was done through the grips of the testing machine by the aid of an apparatus developed at Northwestern University (Lawson(3)). Temperature variation along the gage section of the specimen during testing did not exceed 2°C. Testing was done in air of approximately 50% relative humidity.

Testing in the strain controlled mode generally causes cyclic hardening in annealed materials: the stress needed to enforce the strain limit increases with cycling. This continues until the saturation stress value is reached. Then due to micro-crack development there is gradual decrease in the value of maximum stress. 96.5Pb-3.5Sn solder exhibited such behavior during fatigue testing. The cycle number corresponding to the maximum value of tensile stress was defined as the number of cycles to failure in this research. Similar to ours, fatigue failure defined at maximum stress was used by Raynor(4) and Rao(5).

### RESULTS AND DISCUSSION

Figure 1 shows that hold time at maximum strain (tensile stress hold time) in tests with constant ramp time,  $t_r$ , equal to 2.5 seconds has a dramatic effect on the number of cycles to failure,  $N_f$ .

The decrease in  $N_f$  is most rapid for small hold times. It is evident that some limit,  $N_f'$ , with increasing tensile hold time exist. All specimens tested under given conditions (strain range, ramp time, temperature) are expected to survive at least  $N_f'$  cycles at any value of tensile hold time.

These experimental results are plotted as time to failure versus tensile hold time per cycle coordinates (Figure 2) and the following linear relation between time to failure,  $t_f$ , and tensile hold time,  $t_{ht}$ , was found to hold:

$$t_f = A + Bt_{ht} \dots \dots \dots (1)$$

where A and B are constants.

The number of cycles to failure is equal to time to failure divided by the time per cycle,  $t_c$ :

$$N_f = \frac{t_f}{t_c} \dots \dots \dots (2)$$

$$\text{where } t_c = 2t_r + t_{ht} \dots \dots \dots (3)$$

Substituting the time to failure from Eq.(1) and time per cycle from Eq.(3) into Eq.(2) we get:

$$N_f = \frac{A + Bt_{ht}}{2t_r + t_{ht}} \dots \dots \dots (4)$$

When hold time is much greater than twice the ramp time, ramp time may be neglected and Eq.(4) may be reduced to:

$$N_f = \frac{A + Bt_{ht}}{t_{ht}} = \frac{A}{t_{ht}} + B \dots \dots (5)$$

This Eq.(5) may be used for data extrapolation from small tensile hold times to longer tensile hold times.

The first term, A, in Eq.(5) is equal to the time to failure in tests with short ramp time and without hold time. A is of the order of a few hours for high strain ranges and 25-30 hours for low strain ranges at room temperature and even less than that at elevated temperature. Thus, when tensile hold time is large, the first term drops out and we are left with:

$$N_f = B = N_f' \dots \dots \dots (6)$$

Thus,  $N_f'$ , the minimum number of cycles the specimen will

## FATIGUE 87

survive under given conditions with any tensile hold time is determined by the slope of the line in time to failure versus tensile hold time coordinates (as in Fig. 2).

Figure 3 shows the effect of tensile hold time on the number of cycles to failure of 96.5Pb-3.5Sn solder at elevated temperature. As at room temperature, a linear relation between the time to failure and tensile hold time is also observed (Figure 4). It shows that Eqs.(1)-(5) remain valid at other temperatures also.

The data for another 95.5Pb-3Sn-1.5Sb solder was found also to approximately fit Eq.(1) (Figure 5).

A limited number of tests with hold time at zero strain, i.e. with compressive stress hold time, and ramp time of 2.5 seconds indicated no or almost no effect of such hold time on fatigue life of the 96.5Pb-3.5Sn solder. In a test with 30 seconds of compressive hold time the specimen survived more than 2500 cycles ( $N_f$  for tests without hold was equal to 2200-2900 cycles,  $N_f$  for test with 2.5 seconds ramp and 30 seconds tensile hold was equal to 450 cycles). In test with 120 seconds compressive hold time specimen buckled after 1000 cycles (in test with 120 seconds tensile hold specimen failed after 280 cycles).

However, the compressive hold time dramatically reduced the number of cycles to failure when it was combined with a tensile hold time. Figure 6 shows how variable compressive hold time affects the number of cycles to failure for solder in tests with constant ramp time of 2.5 seconds and with fixed tensile hold times of 120 and 360 seconds.

Line 1 in the Figure 6 corresponds to tests with only tensile hold time. By using Eq.(5) the limit,  $N_f'$ , for tensile hold tests with 2.5 seconds ramp time at 0.75 total strain range and at room temperature was found to be equal to approximately 200 cycles. However, compressive hold in addition to tensile hold reduced the number of cycles to failure below this value. It is evident that as in tests with just variable tensile hold time, reduction in the number of cycles to failure is most dramatic during the first few minutes of compressive hold application. Thus, addition of compressive hold into the cycle which already contains tensile hold time leads to a saturation in the number of cycles to failure when the total time spent in tensile and compressive holds is increased, i.e. it leads to another  $N_f''$ , where  $N_f''$  is the minimum number of cycles to failure all specimens made of 96.5Pb-3.5Sn solder will survive at any combination of tensile and compressive hold times under given conditions of strain range, temperature and ramp time of 2.5 seconds.

The time to failure for tests with combined tensile and

# FATIGUE 87

compressive hold times was plotted versus total time per cycle spent in tensile and compressive hold (Figure 7). While experimental results for tests with only tensile hold time in the cycle fall on the line 1, experimental results for tests with combined tensile and compressive hold time fall on the line 2 (with the exception of the short, 30 seconds, compressive hold test result).

It is evident from the Figure 7 that the following linear relation between the time to failure and combined hold time per cycle exist:

$$t_f = C + D(t_{ht} + t_{hc}) \dots \dots \dots (7)$$

where  $t_{hc}$  is compressive hold time.

The number of cycles to failure then may be found by dividing the time to failure on the time per cycle:

$$N_f = \frac{t_f}{t_c} = \frac{C + D(t_{ht} + t_{hc})}{2t_r + t_{ht} + t_{hc}} \dots \dots \dots (8)$$

When tensile and compressive hold time are long we may neglect C:

$$N_f = \frac{D(t_{ht} + t_{hc})}{2t_r + t_{ht} + t_{hc}} \dots \dots \dots (9)$$

Since a ramp time of 2.5 seconds is much smaller than the hold times, at long hold times Eq.(9) may be reduced to:

$$N_f = D = N_f'' \dots \dots \dots (10)$$

Thus,  $N_f''$ , the minimal number of cycles the solder will survive under given conditions of strain range, temperature and ramp time is determined by D, the slope of line 2 in Figure 7.

The small effect of compressive hold time alone in the cycle with short ramp time on the fatigue life of 96.5Pb-3.5Sn solder may possible be due to the expectation that no or almost no grain boundary cavitation may be formed during the fast ramp as well as during the compressive hold.

According to Wells(6) voids are assumed to nucleate during tensile hold and then grow by vacancy diffusion. When voids become large enough they are assumed to grow by plastic deformation and to propagate under cyclic loading along grain boundaries. In the case of tensile hold, voids were assumed to be rounded, while in compression, the voids were believed to

## FATIGUE 87

grow into elongated flat cracks. The work required to fracture a grain boundary is lower in the case of the elongated void because stress concentration of each void is higher and because the elongated voids cover a higher fraction of grain boundary than rounded voids. While this theory concerning the formation of voids in tension and propagation of voids in tension and compression appears to explain the effect of tensile and compressive hold times on the fatigue life of 96.5Pb-3.5Sn solder (formation of voids in this solder during creep was documented by Frost(7)), a higher rate of void propagation during compressive hold than during tensile hold seems to be not applicable to 96.5Pb-3.5Sn solder. At 0.75 total strain at room temperature the number of cycles to failure in test with 360 seconds of tensile hold and 120 seconds of compressive hold and in test with superimposed time, i.e. 120 seconds tensile hold and 360 seconds compressive hold was found to be practically the same (130 and 140 cycles respectively).

The saturation in fatigue life of 96.5Pb-3.5Sn solder with increasing tensile or combined tensile or compressive hold times per cycle may be attributed in part to the saturation in the relaxation strain per cycle as done for 304 and 316 stainless steels and for Incolloy 800 at elevated temperature by Wareing(8). He assumed, that surface cracks initiate and propagate during high rate fatigue plastic strain,  $\Delta \epsilon_p$ , and the initiation and propagation of grain boundary voids occurs during low rate tensile relaxation strain,  $\Delta \epsilon_{pr}$ .

Figure 8 shows how the relaxation strain per cycle defined as the difference between the width of the hysteresis loop for a test with a given hold time and the width of hysteresis loop for test without hold time, depends on tensile hold time in the test with 0.75% total strain at room temperature. The value of relaxation strain per cycle increases very rapidly during the first few minutes, later the increase is much slower and the relaxation strain tends toward a constant value. Effect of hold time on the relaxation strain per cycle and on the number of cycles to failure is similar, therefore the saturation in fatigue life may be related to the saturation in the relaxation strain per cycle. The strain rates associated with continuous cycling in present research varied from  $4 \times 10^{-6}$  to  $3 \times 10^{-2} \text{ sec}^{-1}$ , while the highest strain rate associated with the stress relaxation during tensile hold time was approximately equal to  $10^{-6} \text{ sec}^{-1}$ .

The relaxation strain per cycle as a function of variable compressive hold time when added to the cycle containing already 360 seconds of tensile hold time in test with 0.75 total strain at room temperature is depicted in Figure 9. It is evident, that compressive hold in addition to tensile hold time leads to another saturation in the relaxation strain per cycle (one satu-

## FATIGUE 87

ration was observed with only tensile hold time (Figure 8)). Thus, this saturation in the relaxation strain per cycle may be a reason for a saturation in fatigue life with increasing combined tensile and compressive hold times.

### SUMMARY

1. Tensile hold time and combined tensile and compressive hold times were found to reduce dramatically the number of cycles to failure.
2. The simple mathematical relation between the isothermal fatigue life of 96.5Pb-3.5Sn solder and tensile and compressive hold times was developed.

### SYMBOLS USED

- A = constant in fatigue life expression (seconds)  
B = constant in fatigue life expression (cycles)  
C = constant in fatigue life expression (seconds)  
D = constant in fatigue life expression (cycles)  
 $N_f$  = number of cycles to failure (cycles)  
 $N_f'$  = fatigue life limit in tests with tensile hold time (cycles)  
 $N_f''$  = fatigue life limit in tests with combined tensile and compressive hold time (cycles)  
 $t_f$  = time to failure (seconds)  
 $t_r$  = ramp time (seconds)  
 $t_{hc}$  = compressive hold time (seconds)  
 $t_{ht}$  = tensile hold time (seconds)  
 $\Delta\epsilon_p$  = plastic strain  
 $\Delta\epsilon_{pr}$  = relaxation strain

### REFERENCES

- (1) Lau, J.H. and Rice, D.W., Solid State Technology, Vol. 28, No. 10, 1985, pp. 91-104.

## FATIGUE 87

- (2) Burges, J.F. et al, IEEE CHMT-7, No. 4, 1984, pp. 405-410.
- (3) Lawson, L., "Thermomechanical Fatigue Testing of 97Pb-3Sn Solder", MS Thesis, Northwestern University, 1986.
- (4) Raynor, D. and Skelton, R.P., "The Onset of Cracking and Failure Criteria in High Temperature Fatigue Testing", Elsevier Applied Science Publishers, London and New York, 1985, pp. 143-146.
- (5) Rao, K.B.S. et al, Int. J. Fatigue, Vol.7, 1985, pp. 141-147.
- (6) Wells, C.H. and Sullivan, C.P., "Interaction Between Creep and Low-Cycle Fatigue in Udimet 700 at 1400°C", "Fatigue at High Temperature", ASTM STP 459, ASTM, 1969, pp. 59-74.
- (7) Frost, H.J. et al, "Flow and Fracture Mapping of Tin-Lead Alloys", Report to IBM Corp., 1985.
- (8) Wareing, J., Metall. Trans., Vol. 8A, 1977, pp. 711-721.

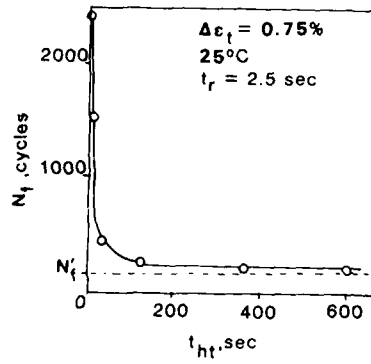


Figure 1 Effect of tensile hold time on  $N_f$

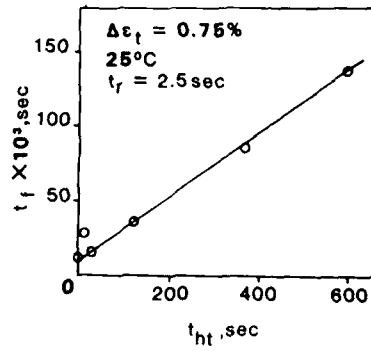


Figure 2 Effect of tensile hold time on  $t_f$

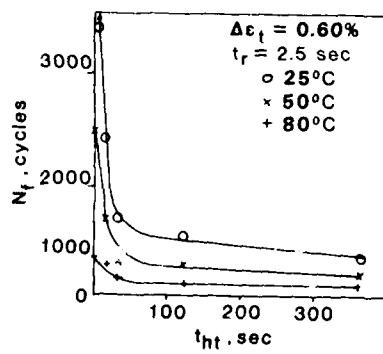


Figure 3 Effect of tensile hold time on  $N_f$

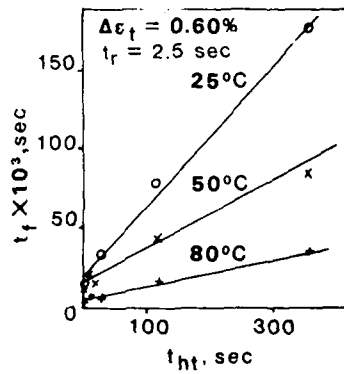


Figure 4 Effect of tensile hold time on  $t_f$

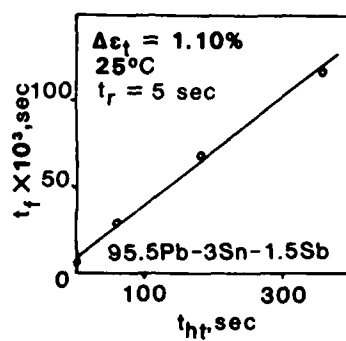


Figure 5 Effect of tensile hold time on  $t_f$

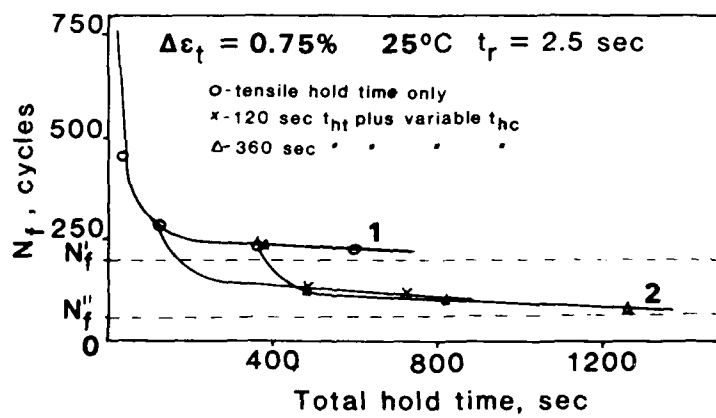


Figure 6 Effect of combined tensile and compressive hold time on  $N_f$

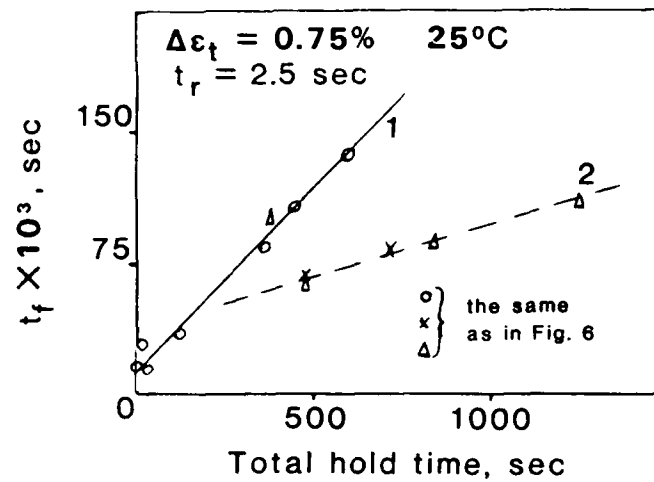


Figure 7 Effect of combined tensile and compressive hold time on  $t_f$

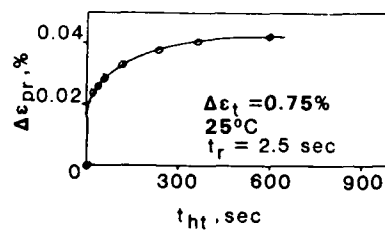


Figure 8 Effect of tensile hold time on relaxation strain per cycle

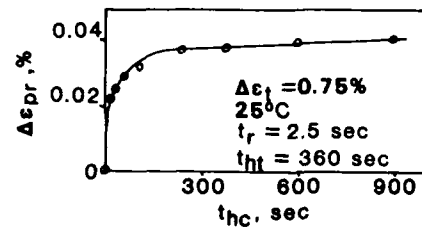


Figure 9 Effect of compressive hold time on relaxation strain per cycle

FATIGUE 87

## ON CLEAVAGE IN FATIGUE FOR RAIL STEELS

ZHU DONG, JAI JIGONG, YAO HENG \*

The cleavage during fatigue of rail steels has been studied. The effect of strain rate and microstructure on fatigue crack propagation rate has been examined. The cyclic cleavage occurred in pulsating waveform of load to increase  $da/dN$  by about an order of magnitude. Cleavage burst occurred frequently in the front of the notch. The cleavage in fatigue was an statistical occurrence, the probability increased with the strain rate and the radius of crack tip within certain range. To refine the microstructure made cleavage in fatigue occur hardly. The reasons were discussed according to fracture mechanics.

INTRODUCTION

It is well known that cleavage fracture occurs frequently in the experiment of fracture mechanics for fully pearlitic steels at ambient temperature (1). The microstructure influences not only the ordinary mechanical properties (2), but also the characteristic of fracture mechanics (3). The prior austenite grain size plays an important role in the failure of rail steels, it controls the toughness of these steels, so some processings to refine the austenite grain size, e.g. alloying and heat treatment, can be employed to improve the properties of fracture mechanics (4).

A lot of work has been done for fatigue of rail steels (5), considerable previous work showed that a

\* Department of Physical Metallurgy  
Central Iron and Steel Research Institute  
No. 76 Xue Yuan Nan Lu  
Maidian District  
BEIJING, P. R. CHINA

## FATIGUE 87

few of cleavage facets were surrounded in striations of fatigue (6).

Dickson (7) found that cleavage facets could be obtained within regions of ductile fatigue in the study of fatigue crack propagation in iron and steels at relatively low temperatures, but similar works were few for rail steels. For certain testing conditions, it has been observed (6) that the appearance of cleavage facets together with ductile striations does not necessarily result in a measurable acceleration of the macroscopic fatigue crack propagation rate. The phenomenon is called cleavage burst which results from the maximum stress intensity,  $K_{max}$ , approaching the fracture toughness,  $K_{Ic}$ .

The evidence presented by Heumann (8) for Fe - 3%Si Single crystal referred to cleavage bursts as fatigue crack propagation in quasi - brittle mode. In polycrystalline material the evidence is less clear.

The purpose of the present work is to study the effect of the waveform of load on cleavage in fatigue for rail steel, and the appearance of fatigue failure by using SEM to discuss the reason why cleavage bursts form.

### EXPERIMENTAL PROCEDURE

To study the effect of strain rate, heat treatment and microstructure on the cleavage in fatigue, the rail steel with 0.67 - 0.80%C; 0.70 - 1.00%Mn; 0.13 - 0.28%Si;  $\leq 0.04\%P$ ;  $\leq 0.05\%S$  was selected to nominate steel No. 1 as received. Steel No. 2 was normalized at 920°C to refine the microstructure. Three Point Bend specimens having thickness of 16 mm, width of 20 mm and length of 80 mm were employed and the fatigue tests were performed on a closed - loop servohydraulic MTS 880 machine in load control. A sinusoidal load was applied at an average frequency of 25 Hz, a pulsating load was done at 2 Hz. The strain rate was measured in term of stress intensity factor rate,  $dK/dt$ , for sinusoidal waveform it was 600  $KNm^{-3/2}/sec$ , and 6600  $KNm^{-3/2}/sec$  for pulsating one. The length of crack was measured by the compliance in an interval of 60 seconds during fatigue testing, the results were calculated by micro - computer. The fracture appearance produced were studied in a PHILIPS scanning electron microscope.

### RESULTS

Fatigue crack propagation rates for the steel No. 1 are presented in Fig. 1 as determined by sinusoidal waveform

of load and pulsating, one respectively. It was found that an average  $da/dN$  for pulsating waveform of load was about an order of magnitude greater than that for sinusoidal one at the same value of  $\Delta K$ . On macroscopic appearance of fracture surface, there were a great number of cleavage bursts concentrated in the centre of the cross section where was considered as plain strain region. These cleavage bursts were formed on pulsating waveform of load, and the fatigue crack propagated in the form of cyclic cleavage.

On the sinusoidal waveform of load, the propagation of fatigue crack was basically stable for both steels. The appearance of the surface formed in fatigue consisted of randomly oriented regions of hills and valleys with respect to the overall propagation as shown in the right of Fig. 2. This appearance would be referred to as the striae although they bore only a slight resemblance to the classical fatigue striations in ductile alloys. The general fracture appearance and random orientations of these striae suggested that their orientation was the same as the ferrite/cementite lamellae orientation in each pearlite colony, so the striae did not necessarily indicate the direction of crack propagation (6).

There was no difference macroscopically between the morphology of cyclic cleavage surface formed in the pulsating waveform and cleavage fracture in the monotonic load. It was observed by using SEM that the fracture surface of the cyclic cleavage formed in fatigue consisted of a great number of striae and some cleavage facets as shown in Fig. 3. In fact, during the fatigue at any waveform of load, the crack propagated stably for most cycles to form striae, even on the pulsating waveform of load. However,  $da/dN$  for cyclic cleavage was so fast that the length of crack locally increased by 50 - 200  $\mu m$  for only one cycle, by comparison,  $da/dN$  for striae was only 0.01 - 0.1  $\mu m$ /cycle, because the size of cleavage facet was much larger than the distance between the striae as shown in Fig. 3. This was one of the reasons why data for the pulsating waveform of load in Fig. 1 were so scattered, and these data were the average values contributed by both striae and cleavage facets although the average data were about an order of magnitude greater than that for sinusoidal waveform. It has been known that the cyclic cleavage consists of many cleavage bursts in plain strain region, it made crack propagation rate in the core of a sample much faster than that near surfaces, so the front of the crack formed was a curve, the length of the crack was only measured in average value. In fact, cyclic cleavage was a random

## FATIGUE 87

occurrence, the higher the strain rate, the higher the probability of forming the cleavage burst.

At the beginning of the fatigue, cleavage burst was initiated from the notch of a sample on very low amplitude of SIF as shown in Fig. 2. It indicated that the cleavage burst was not only related to the strain rate, and also to the radius of crack tip.

In steel No. 2, few cleavage facets were observed on the surface of fatigue fracture formed in both waveforms. On the sinusoidal waveform of load, the curve of  $da/dN$  vs  $\Delta K$  for steel No. 2 is close to the one for No. 1 as shown in Fig. 4, it explains the microstructure of fully pearlitic steel has important effect on the cleavage in fatigue, but not on stable propagation of fatigue crack.

### DISCUSSION

The previous work (6) has concluded that cleavage in fatigue results from the maximum value of SIF approaching  $K_{Ic}$ , but it can't explain some phenomena appeared in the present work. In Fig. 1, cleavage burst occurred in  $\Delta K$  of 14 - 25  $\text{MN/m}^{3/2}$ , and  $K_{max}$  was between 17 - 31  $\text{MN/m}^{3/2}$  ( $R = 0.2$ ), the  $K_{Ic}$  for rail steel was not less than 40  $\text{MN/m}^{3/2}$  (53  $\text{MN/m}^{3/2}$  measured). It has been well known that a sample break up once SIF is over  $K_{Ic}$  if the load is held. In the present work, cleavage burst increased the SIF with the length of crack because the test was done in load control, it indicated that the crack growth in the form of cleavage burst could be arrested in higher SIF. Additionally, cleavage burst initiated from the notch could also not be explained by SIF approaching  $K_{Ic}$ .

It has been well known that according to KKK criterion of cleavage fracture, cleavage failure occurs once the maximum stress is equal to or over the cleavage stress  $\sigma_f$  within the effective distance in the front of crack tip. With increasing in the strain rate, the yield stress increased, but both plastic zone size in the front of crack tip and volume of higher stress were decreased, so cleavage fracture could happen at lower SIF.

By comparison to the sinusoidal waveform, the pulsating waveform had higher strain rate, the cleavage occurred at some locations in the front of crack tip because the maximum stress exceeded the cleavage stress, which made crack propagate for a long distance. The crack would arrest on some boundaries where the cleavage

stress had higher value, additionally cyclic cleavage resulted in the closure of crack that arrested the propagation in the form of cleavage for next cycle. The crack had to exceed the region in the form of striae, so the appearance of the fracture surface for pulsating waveform of load consisted of the mixture of cleavage facets and striae. In fact, the cyclic cleavage was only a random occurrence, the probability of forming the cleavage in fatigue increased with the strain rate.

The other reason which the cyclic cleavage did not extend through a whole sample was considered as the period of the load holding in higher level was too short, the crack did not have enough time to extend.

On the sinusoidal waveform of load, cleavage facets could be observed on the appearance of fracture surface but their number were much less than for pulsating waveform of load because the lower strain rate reduced the probability of forming cleavage in fatigue. However, some cleavage facets were found on the front of the notch of a sample where both  $K_{max}$  and  $\Delta K$  were very low by comparison to ones after some cycles were applied, although the sinusoidal waveform of load was used here. During the propagation of fatigue crack after the initiation from the notch, few cleavage facets could be observed on sinusoidal waveform of load. These explained that the radius of crack tip effected on the cleavage in fatigue.

Generally, the larger the radius of crack tip, the more difficult the cleavage fracture, but in some "quasi-brittle" materials like the rail steel, the cleavage fracture could not be affected by the radius of crack tip which was not too large (9). Additionally, along the direction of the propagation of fatigue crack, the microstructure of rail steel was not isotropic. The relationship between the orientation of the ferrite/cementite lamellae in the pearlitic colony and the direction of the propagation of cleavage crack has been described in reference (10). During the fatigue for rail steel, the larger the radius of crack tip, the larger the volume of the zone affected by higher stress although the maximum stress was not very high by comparison to sharper crack, so it was possible that small cleavage facet initiated from the notch was not just in the direction of crack axis. It could be explained that cleavage was formed from the notch more easily than from the sharper crack, because the larger volume of higher stress included the more orientations of pearlite colony satisfied for the condition of cleavage fracture

## FATIGUE 87

to increase the probability of cleavage in lower SIF. It has been well known that the cleavage stress  $\sigma_f$  is a statistical parameter, so this phenomenon could be described as the larger the radius of crack tip, the lower the cleavage stress,  $\sigma_f$ .

refining the microstructure of rail steel increased its  $\sigma_f$  although little change in  $K_{IC}$  was made, so cleavage occurred hardly on lower SIF, but it was less clear which parameter of microstructure affected it.

Both the reason why cleavage in fatigue was formed on lower SIF and the effect on cleavage in fatigue were less clear, the more work must be done in the future.

### CONCLUSION

1. During fatigue of rail steel, strain rate influenced on cleavage. Cyclic cleavage can be formed on load of pulsating waveform.
2. Cyclic cleavage increased fatigue crack propagation rate,  $da/dN$  for pulsating waveform was about one order of magnitude higher than  $da/dN$  for sinusoidal one at same  $\Delta K$ .
3. The appearance of fracture surface for cyclic cleavage consisted of the mixture of cleavage facets and striae in the observation by using SEM.
4. The shape of crack tip effected on cleavage in fatigue, some cleavage facets observed in the front of notch which formed at very low SIF.
5. The effect of microstructure on cleavage in fatigue has been examined in present work.
6. The maximum stress in the front of crack tip being over cleavage stress was considered as one of reasons to form cleavage in fatigue.
7. The reason of cleavage bursts initiated easily from the notch was considered as the larger volume affected by higher stress increased the probability of forming cleavage.

## FATIGUE 87

### REFERENCES

- (1) Park, Yong - Jin and Bernstein, "Mechanism of Cleavage Fracture in Fully Pearlitic 1080 Rail steel" Rail Steels - Developments, Processing and Use, ASTM STP644, D. H. Stone and G. G. Knupp, Eds., ASTM 1978, P237
- (2) Lowandowski, J. J. and Thompson, A. W., Metall. Trans. A, Vol.17, 1986, P461
- (3) Alexander, D. J. and Bernstein, I. M., Metall. Trans. A, Vol.13, 1982, P1865
- (4) Bouse, G. K., Bernstein, I. M. and Stone, D. H., "Role of Alloying and Microstructure on the Strength and Toughness of Experimental Rail Steels", Rail Steels - Developments, Processing and Use, ASTM STP 644, D. H. Stone and G. G. Knupps, Eds., ASTM 1978, P145
- (5) Johnson, D. H. and Johnson, A. A., Fatigue Fracture Engng. Mater. Structure, Vol.3, 1985, P287
- (6) Fowler, G. J. and Tetelman, A. S., "Effect of Grain Boundary Ferrite on Fatigue Crack Propagation in Pearlitic Rail Steels", Rail Steels - Development, Processing and Use, ASTM STP 644, D. H. Stone and G. J. Knupps, Eds., ASTM 1978, P363
- (7) Dickson, J. I., et al, Mater. Sci. Eng. Vol.6C, 1983, P231
- (8) Neumann, P., et al, Fatigue Mechanisms, ASTM STP 675, J. T. Pong, Eds., ASTM 1979, P371
- (9) Yao Heng, No published work
- (10) Miller and Smith, J. Iron Steel Inst. Vol.203, 1970, P998

# FATIGUE 87

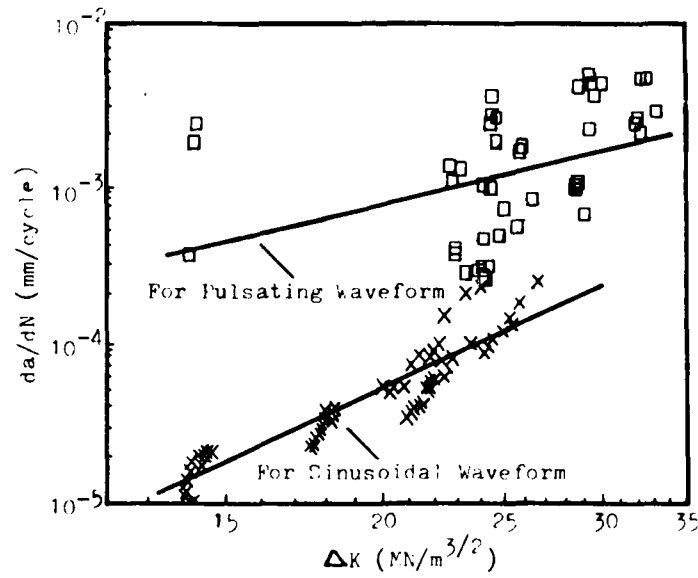


Fig. 1 Fatigue crack propagation rate of Steel No. 1, X for sinusoidal waveform of load,  $\square$  for pulsating one

The direction of the propagation  
for fatigue crack

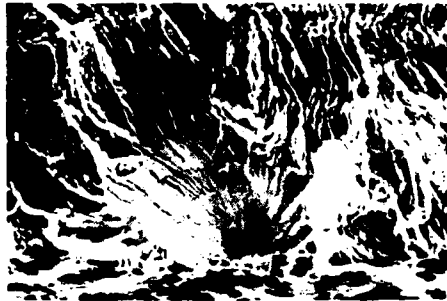


Fig. 2 The appearance of fatigue crack near the notch in Steel No. 1. 500X, SEM

# FATIGUE 87

The direction of the propagation for fatigue crack



Fig. 3 The appearance of fatigue crack for pulsating waveform of load in Steel No. 1. 250X, SEM

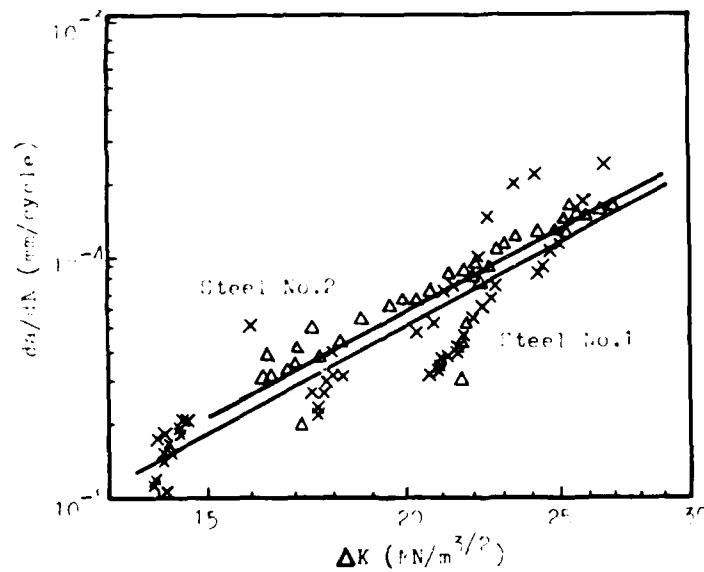


Fig. 4 On the sinusoidal waveform of load fatigue crack propagation rate, X for Steel No. 1, Δ for Steel No. 2

FATIGUE 87

AD-A184 046

FATIGUE '87 VOLUME 2(4) VIRGINIA UNIV CHARLOTTESVILLE  
SCHOOL OF ENGINEERING AND APPLIED SCIENCE  
R O RITCHIE ET AL JUN 87 N00014-87-G-0006

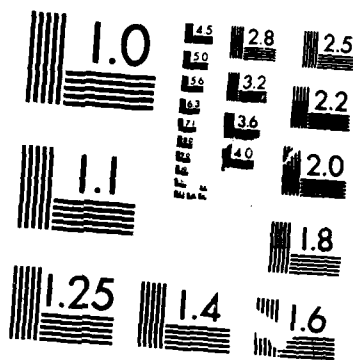
2/6

UNCLASSIFIED

F/G 20/11

NL





MICROCOPY RESOLUTION TEST CHART  
NATIONAL BUREAU OF STANDARDS-1963-A

INFLUENCE OF CLEAVAGE ON FATIGUE PROPAGATION  
RATES IN A LOW CARBON STEEL

Y. Blanchette\*, J.I. Dickson\* and J.P. Bailon\*

A study of fatigue crack propagation in an SAE-AISI 1005 steel showed that at 233 and 173 K patches of cleavage occurred during fatigue propagation, with the amount of cleavage determined largely by  $\Delta K$  and by the cyclic crack tip plasticity. Sufficient cleavage occurred at 173 K to result, near  $\Delta K = 20 \text{ MPa}\sqrt{\text{m}}$ , in a change in the exponent  $m$  of the Paris-Erdogan relationship. This enhanced crack propagation was explained by stress transfer to the uncracked ligaments in the neighborhood of the cleaved patches and was modelled by the presence of a semi-cohesive zone and by its influence on the crack tip opening displacement.

INTRODUCTION

The fatigue crack propagation behaviour of metals at low temperatures can differ from that obtained at room temperature, especially in the case of metals whose tensile properties are temperature and strain rate sensitive. Of particular practical importance is the influence of a decreasing temperature,  $T$ , on the fatigue crack growth properties of steels. The usually observed effect (Ritchie and Knott (1), Moody and Gerberich (2), Tobler and Reed (3), Burck and Weertmann (4)) is that initially the crack growth rate decreases as  $T$  decreases, but that eventually a tendency appears for the occurrence of some brittle cleavage or intergranular cracking. The occurrence of such brittle cracking modes has generally been associated with an increase in the exponent,  $m$ , of the empirical Paris-Erdogan (5) relationship, expressing the crack growth rate as a function of the cyclic stress intensity factor,  $\Delta K$ ,

$$da/dN = C\Delta K^m \quad (1)$$

\* Département de génie métallurgique, École Polytechnique, C.P. 6079, Succ. "A", Montréal, Québec, Canada, H3C 3A7.

## FATIGUE 87

Values of  $m$  of 5-20 have been reported (1-4), to result from the occurrence of cleavage in the third stage of the  $\log da/dN$  vs  $\log \Delta K$  crack growth curve near  $K_C$ , which critical value for unstable crack propagation generally decreases for steels as the temperature decreases. These results have been analyzed by the authors previously cited, based on evaluating the contribution of the static or brittle crack propagation mode. This contribution can be expected to be strongly influenced by the mean value of  $K$  during cycling, generally expressed through the  $R$ -ratio,  $K_{min}/K_{max}$ . For these high values of  $m$ , it remains unclear whether one should consider the influence of fatigue on a crack which has initiated under an essentially static mode or the influence of locally occurring brittle cracking zones on a more generally occurring ductile fatigue cracking mechanism.

The present study carried out on a low carbon steel will show that the occurrence of a local brittle crack propagation mode by cleavage does not always result in a high value of  $m$ . The objectives of this study were to evaluate the influence of  $\Delta K$  and of  $K_{max}$  on the occurrence of cleavage during fatigue crack propagation as well as to model the influence of this cleavage on the macroscopic value of  $da/dN$ .

### EXPERIMENTAL

The tests were carried out on a normalized AISI-SAE 1005 steel with equiaxed grains of 30  $\mu m$  approximate size. Compact tension specimens ( $B = 12.5$  mm,  $W = 50$  mm), oriented for crack propagation in the long transverse direction and machined from 12.7 mm thick plate, were employed. Tests were carried out at room temperature ( $\approx 295$  K) and at 233 K and 173 K, with the tests at the latter two temperatures carried out in an environmental chamber whose temperature was controlled within  $\pm 2$  K of the desired temperature by controlling the injection of liquid nitrogen into this chamber. The tests were performed at 10 Hz with a sinusoidal waveform employing an Instron model 1330 servohydraulic machine, interfaced to a desk-top computer for test control and data acquisition. The crack lengths were determined using the compliance calibration proposed by Newman (6) and crack growth rates were calculated using a central, incremental, second order polynomial regression to seven ( $a, N$ ) couples.

### RESULTS

#### Crack Growth Rate Curves

The results at a given temperature showed practically no influence of the  $R$ -ratio on the  $\log da/dN$  vs  $\log \Delta K$  curve above  $da/dN \approx 2 \times 10^{-6}$  mm/cycle. As well, above this crack growth rate, no closure effects were detected from the analysis of the load-crack mouth opening displacement hysteresis loops. Figure 1 pre-

## FATIGUE 87

sents the  $\log da/dN$  vs  $\log \Delta K$  and vs  $\log \Delta K_{eff}$  curves obtained at the three test temperatures for an R-ratio of 0.1. Decreasing the test temperature reduces the fatigue crack growth rate for a given value of  $\Delta K$ . At 173 K, the typical fatigue crack growth rate is for most of the  $\log da/dN$  vs  $\log \Delta K$  curve approximately twice lower than at 295 K. At 173 K, as  $\Delta K$  becomes sufficiently high, the slope of the  $\log da/dN$  vs  $\log \Delta K$  curve is seen to increase, with the  $da/dN$  values approaching those obtained at room temperature. A similar change in slope corresponding to an increase in the Paris-law exponent  $m$  was also obtained at this same temperature for  $R = 0.3$ . For both R-ratios, this noticeable increase in  $m$  corresponded to a  $K_{max}$  value approximately equal to 60% of the plane strain fracture toughness,  $K_{IC}$  (40 MPa $\sqrt{m}$  at 173 K). In all tests, unstable crack growth was achieved when  $K_{max}$  became equal to  $K_C$ , within the experimental scatter expected in toughness values. At 173 K for  $R = 0.5$ , this condition was attained while the amount of cleavage being produced during fatigue only corresponded to 8% of the fracture surface. As a consequence, this cleavage had not yet produced a noticeable increase in the Paris-Erdogan exponent  $m$ .

For  $\Delta K < 20 \text{ MPa}\sqrt{m}$ , the  $m$  values obtained for the three R-ratios were between 3.17-3.39 at room temperature, between 3.30-3.40 at 233 K and between 3.60-3.70 at 173 K. The overall scatter in these values is only approximately 10% from the mean value at 173 K. For  $\Delta K \geq 20 \text{ MPa}\sqrt{m}$ ,  $m$  values of 4.70 and 5.30 were obtained for  $R = 0.1$  and 0.3, respectively.

### Fractographic Observations

For tests at 233 K and 173 K, fractographic observations revealed an increasing occurrence of islands or patches of cleaved grains as  $\Delta K$  increased. At 233 K, the fraction of fracture surface corresponding to cleavage only reached 5%, with no effect noticed on the macroscopic crack growth rates measured. A greater amount of cleavage occurred at 173 K, reported in Figure 2 as the fraction of cleaved surface vs  $\Delta K$ , with a resulting clearly resolvable effect on the macroscopic crack growth rate (Figure 1). The experimental points of Figure 2 represent the average of five measurements across the thickness, each on an area of 1.5 mm<sup>2</sup>. These results show that the amount of cleavage increases with increasing  $\Delta K$  and is only slightly influenced by the R-ratio. The same results are replotted in Figure 3 as a function of  $K_{max}$  and, on this basis, the fraction of cleaved fracture surface clearly decreases with increasing R-ratio. These results indicate that the initiation of this cleavage during fatigue for values of  $K_{max}$  below  $K_{IC}$  is essentially controlled by  $\Delta K$  rather than by  $K_{max}$ . This demonstrates that the occurrence of such cleavage during fatigue is strain-controlled and not stress-controlled. The small effect of R-ratio suggested by Figure 2 may simply reflect the high experimental dispersion in the individual measurements for

## FATIGUE 87

the amount of cleavage; however, this also could reflect the influence of  $K_{max}$  to favour cleavage propagation and, thus, to tend to increase the average number of cleaved grains per island of cleavage, which aspect will be verified. These results also demonstrate that it is this cleavage initiated by the cyclic strain which is responsible for the increase in the slope of the Paris-Erdogan law, observed in the upper portion of the  $\log da/dN$  vs  $\log \Delta K$  curve for the tests at 173 K and  $R = 0.1$  and  $0.3$ . Since the amount of such cleavage depends more on  $\Delta K$  than on  $K_{max}$ , only 8% of the fracture surface was cleaved at  $R = 0.5$  before unstable crack growth occurred, which amount of cleavage was too small to result in a clear increase in the  $m$  value.

### DISCUSSION

Previous studies (1-3) have pointed out the strong correlation between the occurrence of cleavage and sharp increases in the value of  $m$ ; however, quantitative data on the amount of cleavage occurring has generally not been presented. In cases, such as in the present study, in which patches of cleavage are contained within a matrix in which ductile fatigue occurs, the values of  $m$  attainable should tend to be limited. The occurrence of such islands of cleavage should only effect the redistribution of the stresses and thus of the cyclic strains on the yet uncracked ligaments in the vicinity of these patches of cleavage. In the present study, almost the same Paris-Erdogan law exponent ( $m = 3.65$ ) was obtained at 173 K for the major portion of the crack growth curve as that obtained at 233 K and 298 K ( $m = 3.35$  and  $3.31$ , respectively). It is only for the upper portion of this curve at 173 K that a clear increase in  $m$  is seen. Moreover, this increase is only seen for  $R = 0.1$  and  $0.3$ , since  $K_{IC}$  was attained at  $R = 0.5$  before such an increase could occur.

It will now be shown how the increase in  $m$  observed for these conditions can be related to the fraction of fracture surface corresponding to cleaved islands. The influence of these cleaved patches can be interpreted as resulting in a loss of cohesive strength (Gerberich (7)) within the crack tip plastic zone (Figure 4), which can then be included relatively easily in the elastoplastic analysis of the Dugdale strip yielding model as applied to the specimen geometry employed. The plastic zone of size  $r_p$  ahead of the macroscopic crack front is separated into two portions, a portion  $\lambda \cdot r_p$  of partial cohesion which contains the cleaved islands and a portion  $(1-\lambda) \cdot r_p$  which does not contain such islands. All, none or only some of the patches of cleavage may extend to the macroscopic crack front. The cohesive stress in the region between the origin located at the macroscopic crack front and  $\lambda \cdot r_p$  is assumed to be reduced proportionately to the fraction,  $\gamma$ , of eventual fracture surface covered by cleaved grains, in order to account simply for the effective reduction of the section of cohesive material. The full cohesive strength  $\sigma_{p1}$  is applied

# FATIGUE 87

to the remainder of the plastic zone which is free of cleaved patches.

Assuming linearly elastic - perfectly plastic behaviour, this simple model permits the evaluation of the influence of the amount of cleavage in the semi-cohesive zone on the crack tip opening displacement,  $\delta$ , under conditions of constant remote loading. These calculations were performed for plane strain conditions by a collocation technique (Newman (8)) employing the complex stress function developed by Muskhelishvili (9). Figure 5 shows the influence on  $\delta$  of a semi-cohesive zone in which 20% of the grains are cleaved,  $\gamma = 0.2$ , and in which the semi-cohesive zone is 25% of the plastic zone,  $\lambda = 0.25$ , in comparison to the case in which patches of cleavage are absent,  $\gamma = 0$  and  $\lambda = 0$ . The results are expressed, for different crack lengths  $a/W$ , as the crack tip opening compliance as a function of the normalized ratio of the remote load over the stress in the plastic zone. The calculated curves show the expected linear relationship for small scale yielding, with the deviation from linearity increasing as  $r_p/(W-a)$ , the size of the plastic zone with respect to the uncracked ligament, increases. Also as expected,  $\delta$  is seen to be increased by the presence of the cleaved patches within the semi-cohesive zone, indicating that such cleavage should result in enhanced fatigue crack propagation when this propagation occurs as a result of the cyclic plasticity at the crack tip.

TABLE 1 - Calculated Percentage Increases in  $\delta$  for Different Values of  $\gamma, \lambda$  and Normalized Load,  $a/W = 0.5$ .

		P/(W.B. $\sigma_{pl}$ )											
		0.01				0.02				0.05			
$\gamma$ $\lambda$		0.8	0.6	0.4	0.2	0.8	0.6	0.4	0.2	0.8	0.6	0.4	0.2
0.1		20.1	14.8	9.7	4.7	21.1	15.4	10.0	4.9	26.9	19.1	12.0	5.6
0.2		36.8	26.5	17.0	8.2	36.4	26.1	17.6	8.5	54.1	38.7	22.2	10.0
0.3		53.6	37.6	23.5	11.1	56.4	40.5	25.1	11.6	66.5	55.6	32.2	14.1
0.4		71.4	48.8	28.7	13.7	78.4	53.3	32.0	14.5	126	77.2	42.6	17.9
0.5		91.3	60.3	35.7	16.1	104	67.0	36.9	17.1	186	103	53.7	21.6

# FATIGUE 87

The calculated increase in  $\delta$  for different loads and values of  $\lambda$  and  $\gamma$  are presented in Table 1 for  $a/W = 0.5$ . Since the fractographic results presented in Figures 2 and 3 indicate that the amount of cleavage occurring during fatigue propagation is largely controlled by the cyclic plasticity, it appears reasonable to assume that this occurrence of cleavage should be primarily limited to the cyclic plastic zone. The size of this is generally taken as one quarter of that of the monotonic zone. For the corresponding value of  $\lambda = 0.25$ , it can be seen that, for small-scale yielding, the increase in  $\delta$  lies between 9%-32% for cleavage fractions,  $\gamma$ , of 0.2 and 0.6, while the increase in  $\delta$  can be up to 41% under more pronounced plasticity. Thus an increase in crack tip opening displacement with an increase in the fraction of cleaved grains,  $\gamma$ , and in the length of the semi-cohesive zone  $\lambda \cdot r_p$  is clearly indicated. The resulting enhancement of the macroscopic crack growth rate can then be calculated.

The range or cyclic value of the crack tip opening displacement,  $\Delta\delta$ , can be expressed as:

$$\Delta\delta = \frac{\alpha \Delta K^2}{E \sigma_y} \quad (2)$$

where  $E$  and  $\sigma_y$  are Young's modulus and the yield stress, respectively, and, for small scale yielding,  $\alpha$  is a geometrical constant. The value of  $\Delta\delta$  in the presence of cleaved patches can be expressed as:

$$\Delta\delta_{\gamma,\lambda} = \frac{\alpha}{\sigma_y E} (\beta_{\gamma,\lambda} \Delta K)^2 \quad (3)$$

where  $\beta$  is a function of the amount of cleavage,  $\gamma$ , and of the relative size of the semi-decohesive zone  $\lambda$  and, for small-scale plasticity, is nearly independent of the loading conditions. In the absence of crack closure effects, the parameter  $(\beta_{\gamma,\lambda} \Delta K)$  can be interpreted as an effective cyclic stress intensity factor which takes into account the global interaction of microcracks in the semicohesive zone with the main crack, with the value of  $\Delta K$  being that measured for remote loading conditions. Substitution of equation 3 into equation 2 yields the value of  $\beta_{\gamma,\lambda}$  for a given  $\Delta K$ ,

$$\beta_{\gamma,\lambda} = [\Delta\delta_{\gamma,\lambda} / \Delta\delta_{0,0}]^{1/2} \quad (4)$$

where the subscripts 0,0 denote the absence of cleavage.

Thus in the presence of cleaved grains, whose presence is assumed limited to the cyclic plastic zone, i.e.,  $\lambda = 0.25$ , the Paris relationship can be expressed as:

$$\left. \frac{da}{dN} \right|_{\gamma, 0.25} = C (B_{\gamma, 0.25} \Delta K)^m \quad (5)$$

or

$$\left. \frac{da}{dN} \right|_{\gamma, 0.25} = \left. \frac{da}{dN} \right|_{0,0} \cdot (B_{\gamma, 0.25})^m \quad (6)$$

Figure 6 shows the influence, thus calculated of different values of  $\gamma$  or loss of cohesive strength within the cyclic plastic zone on the Paris-Erdogan relationship. This figure also compares these calculated curves, each for a constant value of  $\gamma$ , with the experimentally obtained curve at 173 K and  $R = 0.1$ . It is seen that the calculated curves are essentially parallel to that for  $\gamma = 0$  and that the increase in  $m$  value observed experimentally can be related to an increase with  $\Delta K$  in the amount of cleavage occurring during fatigue propagation, approximately of the type observed (Figure 2). The loss of cohesive strength corresponding to the intersections of the experimental curves at 173 K and  $R = 0.1$  and  $0.3$  with the calculated curves are plotted in Figure 7 as a function of the amount of cleavage experimentally observed for the same values of  $\Delta K$ . It is seen that for  $\gamma > 15\%$  the values of loss of cohesive strength become significantly higher than the measured values of cleavage fracture. Part of this discrepancy can be attributed to the values of  $(da/dN)_{0,0}$  employed in equation 6. These value were taken as corresponding to the experimentally determined curve at 173 K for  $\Delta K < 20 \text{ MPa}\sqrt{\text{m}}$ ; however, some cleavage was produced at these low  $\Delta K$  values. This discrepancy, nevertheless, suggests that as  $\Delta K$  increases and  $K_{IC}$  is approached, the islands of cleavage are no longer restricted to the cyclic plastic zone and thus that  $\lambda$  becomes greater than  $0.25$ , resulting in a stronger than calculated increase in  $\Delta\delta$  and in  $da/dN$ . Such an effect would be consistent with the fact that Figure 2 suggests that there is some tendency for an increasing  $R$ -ratio to increase the amount of cleavage obtained at a given value of  $\Delta K$ . The amount of cleavage experimentally determined and the calculated curves for  $\lambda = 0.25$ , nevertheless, still permit to explain somewhat more than half of the crack growth enhancement observed at 173 K for the highest values of  $\Delta K$  attained, where the discrepancy between the observed amounts of cleavage and the required values of  $\gamma$  was greatest.

### CONCLUSIONS

From the present study, it can be concluded that, for the material and test conditions studied, the occurrence of islands of cleavage during fatigue propagation was essentially controlled by  $\Delta K$  and by the cyclic plastic strain. The increase in  $da/dN$  and in the Paris-Erdogan exponent  $m$  associated with the occurrence of these patches of cleavage can be explained by the stress transfer which occurs from the cleaved zones to the neighboring uncracked ligaments. This enhancement in  $da/dN$  can be modelled by treating this cleavage as occurring within a semi-cohesive zone, whose presence increases the crack tip opening displacement.

## FATIGUE 87

### ACKNOWLEDGMENTS

Financial assistance from the FCAR (Quebec) and NSERC (Canada) research support programs is gratefully acknowledged. The authors are grateful to Nicole Roy for typing the manuscript.

### REFERENCES

1. Ritchie, R.O. and Knott, J.F., Acta Metal., Vol. 21, 1973, pp. 639-648.
2. Moody, N.R. and Gerberich, W.W., Mater. Sci. Eng., Vol. 41, 1978, pp. 271-280.
3. Tobler, R.L. and Reed, R.P., Advances in Cryogenic Engineering, Vol. 22, 1977, pp. 35-46.
4. Burck, L.H. and Weertmann, J., Scripta Metal., Vol. 12, 1978, pp. 417-420.
5. Paris, P.C. and Erdogan, F., J. Basic Eng., Trans. ASME, Series D, Vol. 85, 1963, pp. 528-534.
6. Newman, J.C., Intern. J. Fracture, Vol. 17, 1981, pp. 567-578.
7. Gerberich, W.W., Intern. J. Fracture, Vol. 13, 1977, pp. 535-542.
8. Newman, J.C., NASA report TN D-6376, 1971.
9. Muskhelishvili, N.E., "Some Basic Problems of Mathematical Theory of Elasticity", Third edition, Noordhoff Ltd., 1953.
10. Kachanov, M., Intern. J. Fracture, Vol. 30, 1986, pp. R65-R72.

# FATIGUE 87

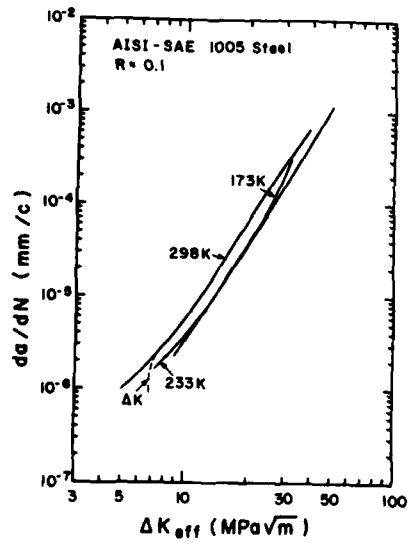


Figure 1 Crack propagation curves,  $R=0.1$

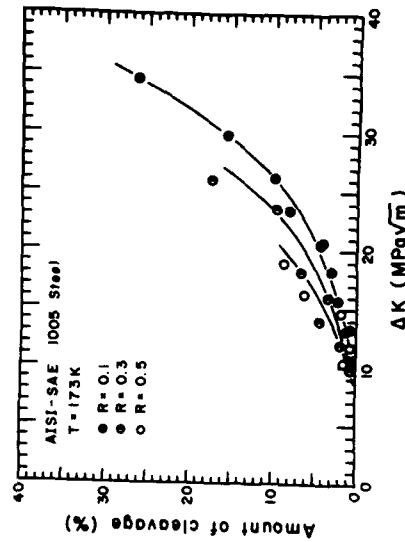


Figure 2 Cleavage observed at 173 K vs  $\Delta K$

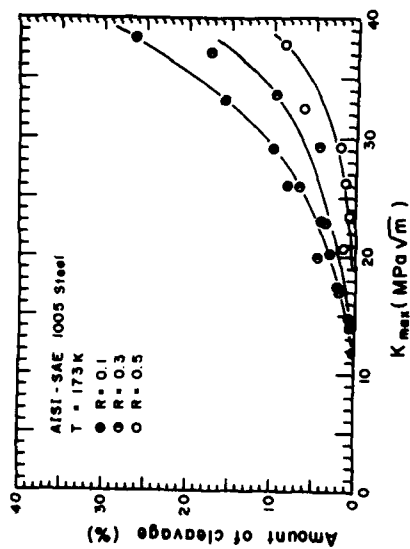


Figure 3 Cleavage observed at 173 K vs  $K_{max}$

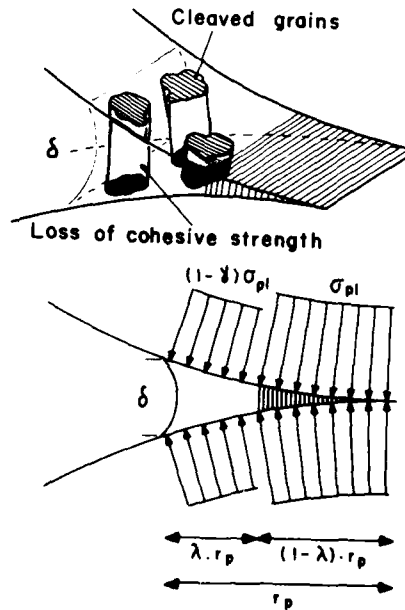


Figure 4 Schematic drawing of assumed crack tip plastic zone

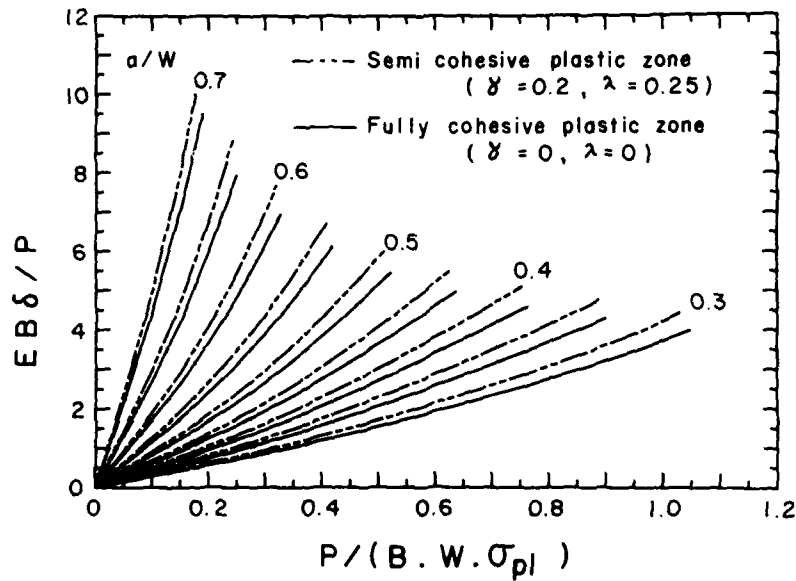


Figure 5 Influence of the presence of a semi-cohesive zone ( $\gamma=0.2, \lambda=0.25$ ) on crack tip compliance

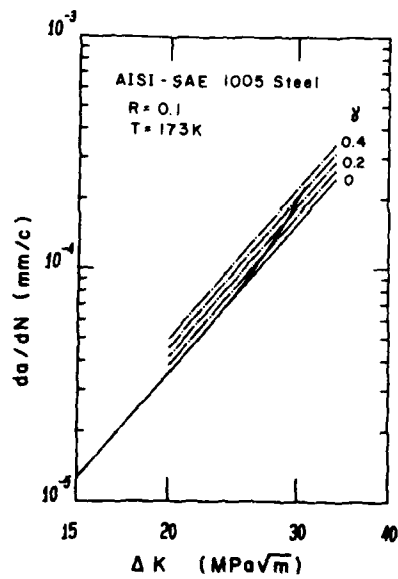


Figure 6 Calculated crack growth curves for  $\lambda=0.25$  and  $R=0.1$  at 173 K

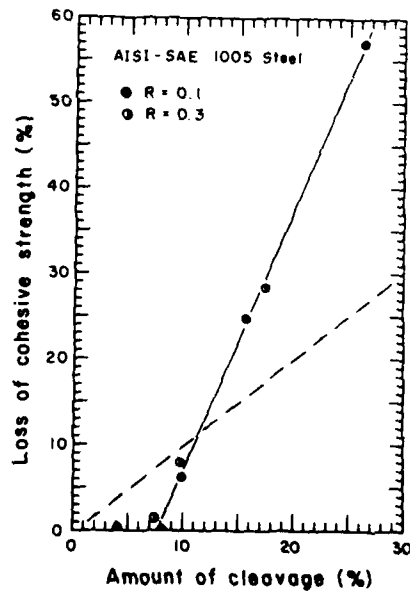


Figure 7 Loss of cohesive strength from Figure 6 compared to measured cleavage

# EFFECT OF METAL SURFACE PROPERTIES ON THE FATIGUE CRACK GROWTH BEHAVIOR

A.V. Prokopenko\* and V.N.Torgov\*

The authors formulated and verified experimentally a model of metals fatigue fracture behavior for a lower local yield stress on the surface as compared to the macroscopic yield stress. The model makes it possible to calculate fatigue limit basing on the critical size of a nonpropagating crack in cyclic bending, tension-compression at different stress ratios in a cycle, for notched and unnotched elements taking into account residual stresses. The model is used for the analysis of short crack growth.

## INTRODUCTION

Yield stress is a characteristic associated with the fatigue fracture resistance. Plastic deformation of a metal occurs both in the stage of crack initiation and its propagation. A lower resistance of surface layers to plastic deformation was found for different materials (1), (2).

The present paper deals with the anomaly of the yield stress near the surface of the metal. The measured values have been used for the calculation of the fatigue limit on the basis of the critical crack length and for the analysis of short crack growth.

## EXPERIMENTAL RESULTS

Indentation of spheres of different diameter  $D$  with force  $P$  makes it possible to calculate the metal

\* Institute for Problems of Strength Ukr.SSR Academy of Sciences. USSR 252014 Kiev, Timiryazevskaya str.,2

yield stress  $G_Y$  at different distances from the surface  $H$  of the material, the stress-strain curve for which is close to an ideal elasto-plastic one, using the following equation from ref.(3)

$$G_Y = 2P/SA\pi\sqrt{Dh - h^2}. \quad (1)$$

The values of  $A$  and  $H$  can be obtained using the depth of the indentation from the following equations:

$$H/D/2 = 2.04(h/D/2) + 0.071, \quad (2)$$

$$A = 1 + 7.375(h/D/2) - 2.813(h/D/2)^2. \quad (3)$$

The indentation diameter to the sphere diameter ratio should be taken within the range of 0.5...0.8 (2). Coefficient  $S$  is close to unity and is obtained by comparing the macrovalue of  $G_Y$  and  $G_Y$  calculated by Eq.(1) for a large diameter of the sphere ( $D \geq 2\text{mm}$ ).

The results of  $G_Y$  measurements are presented in Fig.1 and in Table 1. The minimum values of  $G_Y$  in the subsurface zone  $H'$  are limited by the straight line

$$G_Y^H = G_Y' + (dG_Y/dH)H, \text{ where } dG_Y/dH = (G_Y - G_Y')/H. \quad (4)$$

The values of the yield stress on the surface  $G_Y'$  and other mechanical properties are listed in Table 1. Cyclic preloading did not affect the relationship  $G_Y(H)$ . Static stress-strain curves for the metals studied are close to an ideal elasto-plastic stress-strain curve.

#### FATIGUE FRACTURE MODEL

Let us enunciate the main thesis of the fatigue fracture model which takes into account the lower strength of the surface layer. A crack in the surface layer does not grow in the absence of the nominal plastic deformation and in the case when the stress intensity factor is lower than the threshold stress intensity factor determined for a large crack. Here the following assumptions are made: stress-strain curves for all the layers of the material are close to the ideal elasto-plastic stress-strain curve; cyclic loading does not affect the stress-strain curve. Basing on the  $G_Y(H)$  value and the magnitude of the threshold stress intensity factor one can calculate the fatigue limit for a component. With the stress amplitude above  $G_Y'$  and the depth of plastic deformation below the crack length corresponding to  $\Delta K_{th}$ , a nonpropagating fatigue crack exists.

### FATIGUE LIMIT CALCULATION

When the contribution of the yield zones into the total deformation of the specimen of the thickness  $B$  is small, the nominal stress  $\sigma_{nom} = M/W_r$  (where  $M$  is the bending moment,  $W_r$  is the moment of resistance) is related to the stress on the yield zone boundary with the account taken of Eq. (4) by the expression

$$\sigma_y' + (d\sigma_y/dH)H = \sigma_{nom} y/B/2, \quad y = B/2 - H. \quad (5)$$

On the other hand, when fatigue limit is reached the condition of the crack growth resistance must be met (stress ratio  $R = -1$ )

$$\sigma_a = \sigma_{nom} = \Delta K_{th}^{R=-1} / Y(H) \sqrt{H}. \quad (6)$$

Solving the system of equations (5) and (6), we shall obtain the fatigue limit  $\sigma_{-1} = \sigma_{nom}$  and the size of a nonpropagating fatigue crack which is equal to the depth of the layer  $H$  where plastic deformation is absent. The geometric factor  $Y(H)$  is assumed for a through edge crack since the ratio of semi-axes  $a/c$  for a semi-elliptical crack can be small and  $Y$  is approximately equal to its magnitude for a through crack. The results of calculations for 3-mm thick specimens and for compressor blades of the same thickness, as well as experimental values of the fatigue limit (the frequency is 400 Hz, test basis is  $10^7$  cycles) are listed in Table 2. The experimental and calculated data correlate well for the tests conducted in air and worse for tests in a 3% NaCl solution. For titanium compressor blades residual tensile stresses in surface layers are of importance.

### SIZE EFFECT

Equation (5) includes the thickness of a specimen which makes it possible to evaluate its effect upon fatigue limit in bending. It was shown in (2) that for steel 08Cr17Ni6Ti both calculated and experimental fatigue limits increased from 430 MPa for  $t = 3$  mm to 480 MPa for  $t = 0.5 \dots 1$  mm. Since the system of equations (4), (6) for tension-compression does not include the specimen thickness, the fatigue limit with this mode of loading does not depend on the specimen thickness which is observed in experimental works (4). We should note that the properties of the surface layer affect the fatigue limit in bending if the thickness of specimens is comparable to that of the anomalous surface layer.

TABLE 1 - Integral and Surface Mechanical Properties of Steels (1-3) and Titanium Alloy (4) in air (a) and in a 3%NaCl (s).

No	Material	$\sigma_Y$ MPa	$\sigma_u$ MPa	$\epsilon$ %	S	Environ- ment	$\sigma_Y'$ MPa	H' mm	$d\sigma_Y/dH$ GPa/mm
1.	20Cr13	655	755	23.6	1.0	a	250	0.125	3.24
						s	120	0.135	3.96
2.	15Cr12Ni2VMoW	885	1075	16.2	1.18	a	360	0.15	3.5
						s	300	0.17	3.44
3.	08Cr17Ni16Ti	840	895	17.3	1.18	a	320	0.22	2.36
						s	220	0.22	2.82
4.	BT3 - 1	1069	1101	16.8	1.14	a,s	400	0.21	3.19

TABLE 2 - Fatigue limits for specimens (s) and compressor blades (b) in cyclic bending.

Material	Environment	$\sigma_{-1}^{exp}$ (s)	MPa (b)	$\sigma_{-1}^{calc}$ MPa	H mm	$R=-1$ $K_{th} \sqrt{m}$ MPa
20Cr13	a*	420	405	412	0.0462	5.47
	s*	250	225	315	0.0462	4.20
	p*	-	325	390	0.0641	6.28
15Cr12Ni2VMoW	a	-	503	510	0.039	6.16
	s	-	258	385	0.024	3.64
08Cr17Ni6Ti	a	430	464	434	0.0423	5.54
	s	330	295	342	0.0420	4.23
	p	-	360	395	0.0592	5.97
BT3 - 1	a	520	260	515	0.0315	5.63
	s	380	180	445	0.0126	3.08

a\* air, s\* solution, p\* magnesium protector

a\* air, s\* solution, p\* magnesium protector

#### STRESS CONCENTRATION

The endurance limit for a specimen with an edge notch of depth  $D_p$  and radius  $\rho$  in tension-compression can be calculated by solving a system of equations

$$\{\sigma_p = \Delta K_{th}^{R=-1} / 1.12 \sqrt{\pi} (H+e), \quad (7)$$

$$\{\sigma_p = [\sigma_y' + (d\sigma_y'/dH)H] \sqrt{H/(H+e)}, \quad (8)$$

where  $e = (K_t^2 - 1) H \sqrt{D_p \rho} / \rho$  when  $H / \sqrt{D_p \rho} \leq 1 / (K_t^2 - 1)$ ,

$e = D_p$  when  $H / \sqrt{D_p \rho} \geq 1 / (K_t^2 - 1)$ .

Here a method of the stress intensity factor calculation for cracks in the notch root from (5) is used involving the theoretical stress concentration factor  $K_t$ . In (2) equations (7) and (8) are also modified for bending. This approach allows one to evaluate the danger of service defects (pitting, dents) of different depth. The calculated and experimental data for 3 mm thick specimens with semicircular notches are in good agreement (Table 3).

#### RESIDUAL STRESSES

The hatched zone in Fig.2 represents the distribution of residual stresses induced in the specimen after single overloading with the stress  $\sigma_1$  exceeding the yield stress on the surface  $\sigma_y'$ . Under fully reversed

TABLE 3 - Fatigue limits for notched specimens in bending.

Material	$\rho$ , mm	Environ- ment	$\sigma_{-1}^{\text{calc}}$ MPa	$\sigma_{-1}^{\text{exp}}$ MPa
BT3-1	0.1	air	266	250
		3% NaCl	175	170
	0.3	air	213	210
		3% NaCl	174	170
20Cr13	0.1	air	252	240
		3% NaCl	191	190
	0.3	air	179	180
		3% NaCl	169	150

loading with the amplitude of  $\sigma_a$  the extreme stresses  $\sigma_{\text{max}}$  and  $\sigma_{\text{min}}$ , which do not induce plastic cyclic deformation, are limited by the lines  $OA_2$ ,  $OB_2$ . Let us define the condition of fatigue crack growth resistance. As is shown in (6) for a crack in the field of residual stresses the stress intensity factor can be determined by superposition of applied and residual stresses. With this in mind, we shall obtain the fatigue limit by solving a system of equation (4) and the following one

$$\sigma_a = \begin{cases} \Delta K_{th}^R / 2Y(H)\sqrt{H}, & R \geq 0, \\ \Delta K_{th}^R / Y(H)\sqrt{H} - \sigma_m, & R \leq 0, \end{cases} \quad (9)$$

$$\text{where } R = \sigma_{\text{min}} / \sigma_{\text{max}}, \quad \sigma_m = \sigma_{\text{max}} - \sigma_a. \quad (10)$$

The tests conducted with 08Cr17Ni6Ti steel specimens after tension with  $\sigma_1 = 700$  MPa revealed an increase in the fatigue limit from 430 MPa to 480 MPa which is in good agreement with the calculated value of 488 MPa for the residual compressive stresses similar to those shown in Fig. 2. Variation of  $\Delta K_{th}$  with the stress ratio in a cycle was taken into account using the following experimental relationship

$$\Delta K_{th}^R = (0.585 - 0.415 R) \Delta K_{th}^{R=-1}. \quad (11)$$

Similar calculations and experiments were carried out for 20Cr13 steel with  $\sigma_1 = 0, 400, 600$  MPa;  $\sigma_{-1}^{\text{calc}} = 412, 434, 454$  MPa;  $\sigma_{-1}^{\text{exp}} = 420, 440, 460$  MPa. With the account taken of the residual tensile stresses distribution in BT3-1 alloy compressor blades, the endurance limits calculated in such a way are 242 and 178 MPa in air and in a 3% NaCl solution (2) which correlates well with the

experimental data listed in Table 2.

### ASYMMETRIC CYCLIC LOADING

In an asymmetric load cycle residual stresses induced during the first half-cycle increase the fatigue limit. Figure 3 presents the results of calculations made with the residual stress relaxation absent (I), complete (II) and partial (III) and experimental results (dots) for 20Cr13 steel. For ambient temperatures variants (I) and (III) of the calculation yield data which correlate well with experimental data for steels 10Cr13, 1Cr16Ni9Ti and 08Cr17Ni6Ti (2). For higher temperatures the curves of type (II) are more typical.

### INITIATION AND GROWTH OF SHORT CRACKS

The initiation of cracks of  $2c=0.02\dots0.05$  mm was observed on perfectly polished specimens (Fig. 4). The fraction of the number of cycles to crack initiation was small (5...14%). The processing of the "initiation" data in the  $dc/dN$  vs  $\Delta\epsilon_p$  coordinates yielded the following equations:

$$dc/dN = 3.15(\Delta\epsilon_p - 5.7 \cdot 10^{-4})^{2.04} \quad (\text{in air}), \quad (12)$$

$$dc/dN = 0.0272(\Delta\epsilon_p - 4.4 \cdot 10^{-4})^{4.47} \quad (\text{in } 3\% \text{NaCl}) \quad (13)$$

The  $dc/dN$  value was obtained dividing the half-length of the detected crack by the number of load cycles to its initiation, and the plastic deformation range was obtained from the formula

$$\Delta\epsilon_p = (\sigma_a - \sigma_y')/E. \quad (14)$$

The analysis of specimens fracture surfaces showed that the ratio of the crack depth to its half-length  $a/c$  was close to unity. The stress intensity factor for such a crack is calculated by the formula from (7). Taking into account a correction for the ratio of nominal plastic deformation  $\Delta\epsilon_p$  to elastic one  $\Delta\epsilon_e$ , which was introduced by the authors of (8), the equivalent stress intensity factor was defined

$$K_{Ip} = K_I (1 + \Delta\epsilon_p/\Delta\epsilon_e), \quad (15)$$

$$\Delta\epsilon_p = [\sigma_a - \sigma_y' - 0.25(d\sigma_y'/dH)c]/E, \quad (16)$$

$$(\Delta\epsilon_p/\Delta\epsilon_e) = \{\sigma_a/[\sigma_y' + 0.25(d\sigma_y'/dH)c]\} - 1. \quad (17)$$

The resulting crack growth rate was expressed as the sum of two components obtained from Eqs. (12), (13), (16) and (15), (17). Figure 5 shows results of the calculations of individual components and the total crack

growth rate which is in good agreement with that observed in tests with short cracks. Here a line is also shown which was calculated with the account taken of El Haddad correction factor determined from the equations

$$K_1 = 1.21(2/\sqrt{\pi}) G \sqrt{\pi} (C + C_0), \quad (18)$$

$$C_0 = [\Delta K_{th}^{R=-1} / 1.21(2/\sqrt{\pi}) G \sqrt{\pi}]^2. \quad (19)$$

The above correction factor does not account for the physical reasons of the accelerated short crack growth but it is simple and easy in practical use. Close agreement of the crack growth rate calculated with the use of this correction factor and of the experimental data confirms the possibility of its successful practical application.

#### REFERENCES

- (1) Alekhin, V.P., "The Physics of Strength and Plasticity of the Surface Layers of Materials" Nauka, Moskva, USSR, 1983.
- (2) Prokopenko, A.V. and Torgov, V.N., Problemy Prochnosti, 1986, No.4, pp.28-34, No.6, pp.44-51, No.10, pp.18-26.
- (3) Timoshenko, V.A., Ermilov, V.V. and Brukhis, M.M., Trenije i iznos, Vol.3, No.5, 1982, pp.813-820.
- (4) Troshchenko, V.T., "Fatigue and Inelasticity of Metals", Naukova Dumka, Kiev, Ukr.SSR, 1972.
- (5) Smith, R.A. and Miller, K.J., Int. J. Mech. Sci., No.1, 1977, pp.11-22.
- (6) Liu, A.F. "Behaviour of Crack at Hole", Proceedings Second Int. Conf. on Mechanical Behaviour of Materials, Boston, U.S.A., 1978.
- (7) Smith, F.W., Emery, A.F. and Kabayashi, A.S., Trans. ASME, Ser. E, Vol.4, 1967, pp.232-239.
- (8) Leis, B.N., J. Pressure Vessels and Piping, Vol.10, No.2, 1982, pp.141-158.

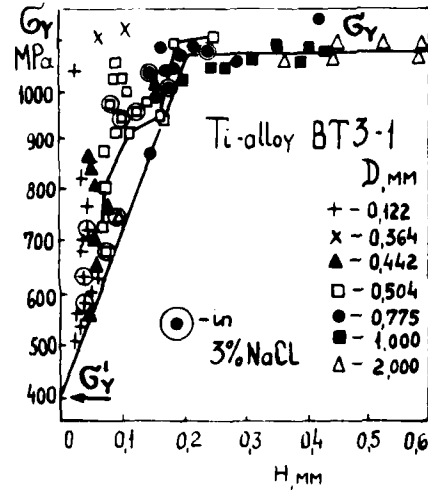


Fig. 1. Yield stress vs layer depth

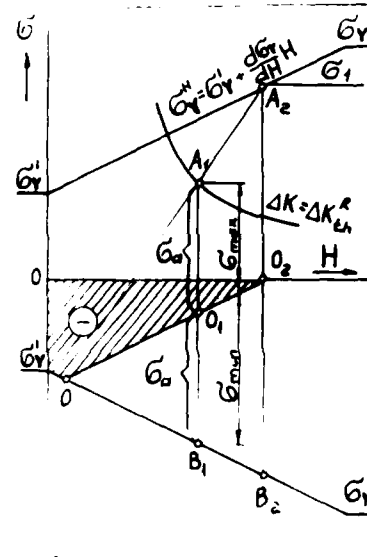


Fig. 2. Fatigue limit calculation involving residual stresses.

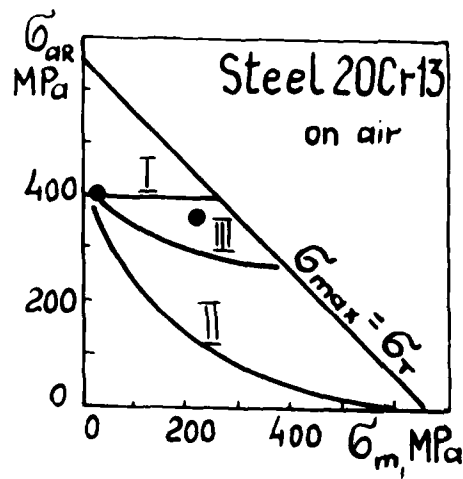


Fig. 3. Fatigue limit vs mean stress.

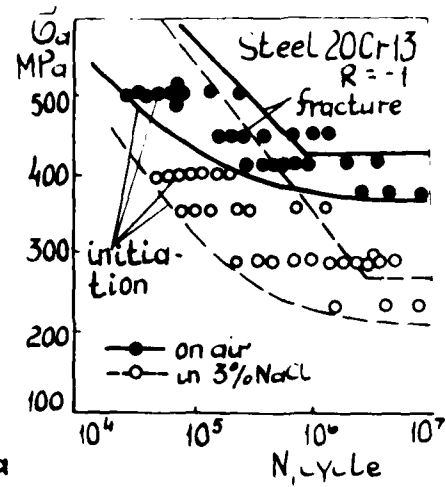


Fig. 4. Fatigue curves.

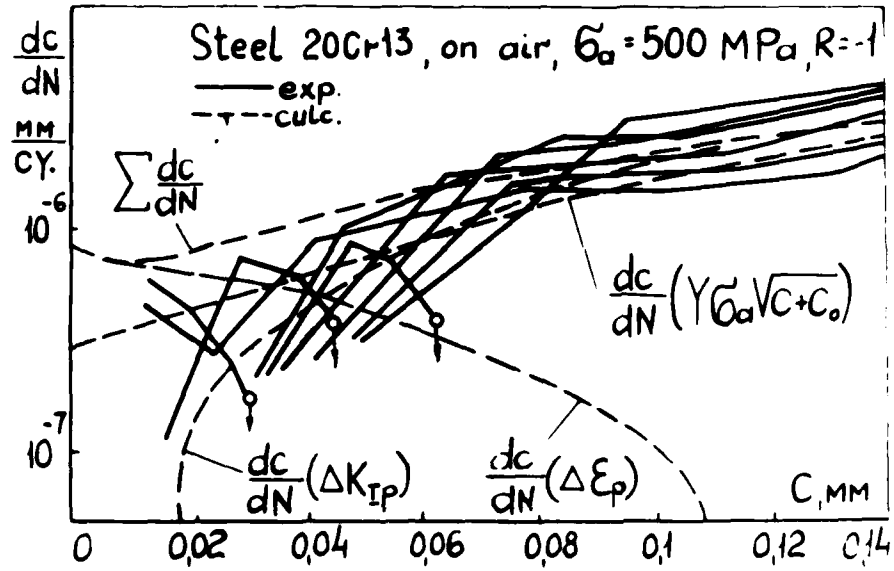


Fig. 5. Crack growth rate vs crack length (arrows-crack arrest).

## FATIGUE 87

### FATIGUE CRACK GROWTH BEHAVIOR IN HYDROGEN GAS ENVIRONMENT

S. Yoshioka\*, M. Kumasawa\*, M. Demizu\*\*, A. Inoue\*

Fatigue crack growth behavior in hydrogen gas environment was examined using compact tension specimens of five kinds of materials, i.e., low alloy steel (Ni-Mo-V, Ni-Cr-Mo-V), austenitic alloy steels (18Mn-5Cr, SUH660) and a copper alloy (Be-Cu). Fatigue crack growth rates in laboratory air and in hydrogen gas were obtained and the relation between fatigue crack growth rate and fracture morphology was discussed based on fractographical observations.

#### INTRODUCTION

It is popularly regarded important to evaluate strength of materials absorbing hydrogen and a number of studies have been reported. However, we seldom come across strength evaluation of materials absorbing no hydrogen in hydrogen gas environment. As for the study of influence of hydrogen gas environment over fatigue crack growth rate ( $da/dN$ ), in particular, only a few examples are known to medium and high strength steels (Wei and Landes (1), Mukherjee (2), Yoshioka et al. (3), Suresh and Ritchie (4), and Liaw et al. (5)) and Ti-alloy (Pittinato (6)). Using five kinds of materials of different strength, structure, and components, therefore, we have studied fatigue crack growth in hydrogen gas environment.

Reported in this paper are the result of measurement of  $da/dN$  characteristic of each material in hydrogen gas environment and the results of some study on the relationship between the  $da/dN$  characteristic and the fracture morphology.

- \* Central Research Laboratory, Mitsubishi Electric Corp., Amagasaki, Japan.
- \*\* Material Engineering Laboratory, Mitsubishi Electric Corp., Amagasaki, Japan.

# FATIGUE 87

## SPECIMEN AND EXPERIMENTAL PROCEDURE

As the specimens, five kinds of materials were used; low alloy steels of hardened and tempered structure (Ni-Mo-V, Ni-Cr-Mo-V), austenitic alloy steels (18Mn-5Cr, SUH660), and a copper alloy (Be-Cu). The chemical compositions and the mechanical properties of the specimens are shown in Table 1 and Table 2.

As for Ni-Mo-V steel and 18Mn-5Cr steel, three kinds of materials of somewhat different strength were used respectively. Except for 10 mm thick ( $W = 30$  mm) specimens of SUH660, compact tension specimens of 25 mm thick ( $W = 50$  mm) were used. The specimens of Ni-Mo-V were cut from a shaft, those of Ni-Cr-Mo-V and 18Mn-5Cr from a ring, and those of SUH660 and Be-Cu were cut from a flat square rod.

Table 1 Chemical composition (wt.%)

Material		C	Si	Mn	P	S	Ni	Cr	Mo	V
Ni-Mo-V	A	0.23	0.05	0.39	0.005	0.004	3.58	0.36	0.39	0.10
	B	0.32	0.35	0.55	0.021	0.022	2.78	0.22	0.41	0.06
	C	0.26	0.28	0.46	0.009	0.001	3.64	0.32	0.44	0.12
Ni-Cr-Mo-V		0.38	0.16	0.65	0.008	0.012	2.62	1.46	0.38	0.09
18Mn-5Cr	A	0.49	0.44	17.90	0.023	0.005	0.18	4.72	0.05	0.02
	B	0.47	0.50	17.70	0.018	0.003	0.23	4.70	0.05	0.03
	C	0.48	0.52	17.35	0.024	0.006	0.21	4.65	0.10	0.02
SUH660		0.03	0.84	1.06	0.010	0.010	25.68	13.84	2.49	-
Be-Cu		Co: 2.56 , Be: 0.53 , Cu: bal.								

Table 2 Mechanical properties

Material		Yield strength (MPa)	Tensile strength (MPa)	Elongation (%)	Reduction of area (%)	$K_{IC}$ (MPa·m <sup>1/2</sup> )
Ni-Mo-V	A	596	709	25	65	217 *
	B	539	696	23	51	58.9*
	C	749	869	18	43	71.3
Ni-Cr-Mo-V		1128	1236	18	44	93.0*
18Mn-5Cr	A	909	1107	37	45	223 *
	B	1021	1181	32	50	217 *
	C	1043	1213	28	48	205 *
SUH660		967	1079	24	50	143 *
Be-Cu		744	875	17	23	65.1*

\*  $K_{IC}$  calculated from  $J_{IC}$

## FATIGUE 87

Table 3 shows the test conditions. Besides the  $da/dN$  characteristic of each material in air and in hydrogen gas environment (briefly shown in  $H_2$  in the following text) at room temperature, influence of stress ratio (R), frequency (f), and hydrogen gas pressure (P) was also found for some materials. For the test in  $H_2$ , pure hydrogen gas for industrial use ( $H_2 = 99.98\%$ , standard pressure  $P = 588$  KPa, dew point =  $-55^\circ C$ ) was sealed in a vacuum chamber. As the test procedure, ASTM E647-81 was applied.

Table 3 Test conditions

Material	P (KPa)	R	f (Hz)
Ni-Mo-V	294, 588, 1078	0, 0.5	0.5, 5, 5 ~ 20
Ni-Cr-Mo-V	588	0	0.5, 5
18Mn-5Cr	588	0	2 ~ 20
SUH660	588	0	5
Be-Cu	588	0	20

### EXPERIMENTAL RESULTS AND DISCUSSION

#### Measurement of Fatigue Crack Growth Rate

Figure 1 to Fig. 5 show the results of measurement of  $da/dN$  characteristic of five kinds of materials in air and in  $H_2$  within the range of stress intensity factor from about  $9 \sim 620 \text{ MPa} \cdot \text{m}^{1/2}$ .

Ni-Mo-V-steel. Fig. 1 shows the relationship between  $da/dN$  and  $\Delta K$  of Ni-Mo-V steel. The relationship in  $H_2$  is expressed by an S-letter as shown in Fig. 1 (a) and is divided into three regions; region I where  $da/dN$  in air remains unchanged, region III where  $da/dN$  becomes faster than that in air, and region II as the transition between region I and region III. Like in air, influence of the difference in frequency, holding time, and strength is not noted in particular even in  $H_2$  (3). Influence of stress ratio is rather outstanding in  $H_2$  than in air as shown in Fig. 1 (b). Influence of  $H_2$  gas pressure is also noted, and  $da/dN$  tends to be faster at higher pressure as shown in Fig. 1 (c). As the feature of the influence of the factor accelerating  $da/dN$ , the regions II and III in which  $da/dN$  becomes faster are moved to the lower side of  $\Delta K$ .

Ni-Cr-Mo-V steel. Fig. 2 shows the relationship between  $da/dN$  and  $\Delta K$  of Ni-Cr-Mo-V steel. In the whole range of

## FATIGUE 87

experiment,  $da/dN$  in  $H_2$  is faster than in air and the characteristic differs greatly from that of Ni-Mo-V steel in that the growth rate is dependent on frequency. The dependency on frequency in  $H_2$  tends to be more outstanding at higher  $\Delta K$  side.

18Mn-5Cr steel, SUH660 steel. Fig. 3 shows the relationship between  $da/dN$  and  $\Delta K$  of 18Mn-5Cr steel. No particular difference is noted in  $da/dN$  characteristic in air and in  $H_2$ , and among the specimens of three different kinds. Fig. 4 shows the relationship between  $da/dN$  and  $\Delta K$  of SUH660 steel, and  $da/dN$  characteristic of this material in  $H_2$  remains unchanged from that in air. For the austenitic alloy steels of these two kinds, therefore, influence of  $H_2$  gas environment over  $da/dN$  characteristic may be disregarded.

Be-Cu alloy. Fig. 5 shows the relationship between  $da/dN$  and  $\Delta K$  of Be-Cu alloy. With this material,  $da/dN$  tends to be lower in  $H_2$  than in air, and the tendency is a little more outstanding at low  $\Delta K$  side.

### Fractographical Observation

Figure 6 to Fig. 7 show the results of observation of fracture surface of the specimens. TEM was primarily applied to observation of striation and SEM was also used in addition to find fracture mode.

Fig. 6 shows fractographical observation of Ni-Mo-V steel in  $H_2$ . In region I of low  $\Delta K$ , intergranular fracture is seen together with transgranular fracture of ductile striations as shown in Fig. 6 (a). In region III of high  $\Delta K$ , brittle striations are observed on cleavage fracture as shown in Fig. 6 (b). In this manner, fracture morphology in  $H_2$  is quite different from that in air (transgranular fracture with clear ductile striations) (5).

Fig. 7 (a) shows a typical example of observation of Ni-Cr-Mo-V steel in  $H_2$ . The fracture in  $H_2$  includes both transgranular fracture containing rather a large number of quasi-cleavages and intergranular fracture, and more number of intergranular fractures are seen than in air. In any region, almost no clear striation is seen either in air nor in  $H_2$ .

Fig. 7 (b) and Fig. 7 (c) show typical results of observation of 18Mn-5Cr steel and SUH660 steel in  $H_2$ . In either case, clear striation is seen in the transgranular fracture and no effect of  $H_2$  gas environment is noted in particular.

Fig. 7 (d) shows a typical result of observation of Be-Cu alloy in  $H_2$ . No difference is noted in particular on the fracture in air and in  $H_2$ , and striations are observed in significant regions on the transgranular fracture.

### Discussion

Relationship between  $da/dN$  and striation spacing. Fig. 8 shows the relationship between  $da/dN$  and striation spacing in air and in  $H_2$  to four kinds of materials excluding Ni-Cr-Mo-V steel to which almost no clear striation was seen. Except in the region where  $da/dN$  is lower than about  $5 \times 10^{-5}$  mm/cycle,  $da/dN$  and striation spacing of each material are in the relation of approximately 1 : 1 both in air and in  $H_2$ , and this relation remains unchanged to brittle striation as well. With the range of the experiment of this time, therefore, macroscopic fatigue crack growth rate of these material in air and in  $H_2$  is supposed to be primarily dependent on the mechanism of striation formation except for the region of low  $\Delta K$ .

Change in fracture morphology. To Ni-Mo-V steel and Ni-Cr-Mo-V steel in which  $da/dN$  is accelerated in  $H_2$ , the change in fracture morphology was subjected to quantitative analysis.

Fig. 9 shows the relationship between  $da/dN$  and fracture mode for Ni-Mo-V steel in  $H_2$ . Fracture mode was classified into four types; intergranular fracture, transgranular fracture with ductile striation, transgranular fracture with brittle striation on the cleavage fracture, and other transgranular fractures of no clear feature. The relationship between fracture mode and  $\Delta K$  differs under each one of four test condition. However the relationship between fracture mode and  $da/dN$  is not affected by the test conditions and is approximately constant as shown in Fig. 9 (which indicates close relation between  $da/dN$  and fracture morphology). It is noted, in particular, that region III in which acceleration of  $da/dN$  is outstanding ( $da/dN \geq 10^{-4}$  to  $10^{-3}$  mm/cycle) is characterized by cleavage fracture.

Fig. 10 shows the relationship between intergranular fracture area and  $\Delta K$  region which is sensitive to structure (Kobayashi et al. (7)), and in  $H_2$ , increase in intergranular fracture area and transfer of intergranular fracture region to high  $\Delta K$  side are noted. Although no quantitative measurement was made, increase of the pattern of quasi-cleavage was also noted in  $H_2$ , which indicates the influence over acceleration in addition to

the effect on intergranular fracture.

Influence of H<sub>2</sub> gas environment over fatigue crack growth rate. Among five kinds of specimens, low alloy steels of hardened and tempered structure (Ni-Mo-V, Ni-Cr-Mo-V) showed outstanding acceleration of  $da/dN$  in H<sub>2</sub> under the test conditions of this time (room temperature,  $P = 588$  KPa). The austenitic alloy steels (18Mn-5Cr, SUH660) and the copper alloy (Be-Cu) showed no acceleration of  $da/dN$  in H<sub>2</sub>. With Be-Cu alloy, in particular, deceleration of  $da/dN$  was noted, which is probably due to moisture and oxygen contained in air and in H<sub>2</sub> (6). Effect of H<sub>2</sub> gas environment over  $da/dN$  characteristic differs depending on the kind of material but acceleration of  $da/dN$  in H<sub>2</sub> is also reported with 2-1/4Cr-1Mo steel (4), and  $da/dN$  characteristic of low alloy steels of medium and high strength seems susceptible to H<sub>2</sub> gas environment.

Acceleration of  $da/dN$  of high strength steels absorbing hydrogen is probably related to K<sub>ISCC</sub> growth (Hirano et al. (8)), but K<sub>ISCC</sub> in H<sub>2</sub> gas of these low alloy steels with which acceleration of  $da/dN$  starts at 9.3 to 21.7 MPa·m<sup>1/2</sup> is over 62 to 92 MPa·m<sup>1/2</sup> ((3), (4), Kumasawa et al. (9)). Accordingly, the relation with K<sub>ISCC</sub> does not explain the acceleration. Acceleration of  $da/dN$  of these low alloy steels, therefore, is considered to be one of the phenomena relation to cyclic stress corrosion cracking in H<sub>2</sub> (Endo et al. (10)). Like in the case of 2-1/4Cr-1Mo steel, Ni-Cr-Mo-V steel shows dependency on frequency (4), but Ni-Mo-V steel shows no dependency on frequency. The difference seems to be related to the characteristic cleavage fracture of Ni-Mo-V in H<sub>2</sub> but this is a subject to be studied further in detail in future.

#### CONCLUSION

As the result of an experiment to find the effect of H<sub>2</sub> gas environment on  $da/dN$  characteristic and fracture morphology using five kinds of materials, we have reached the following conclusions.

- (1) Influence of H<sub>2</sub> gas environment over  $da/dN$  characteristic can be classified into the following four groups.
  - (a) No influence (18Mn-5Cr and SUH660 steels)
  - (b) Slightly decelerated (Be-Cu alloy)
  - (c) Accelerated but no dependency on frequency (Ni-Mo-V steel)
  - (d) Accelerated and dependent on frequency (Ni-Cr-Mo-V steel)

## FATIGUE 87

- (2) The materials classified into (a) and (b) groups show no difference in the fracture morphology either in air or in  $H_2$ . Those materials classified in group (c) and (d) show characteristic changes such as cleavage fracture in  $H_2$  and increase of intergranular fracture area.
- (3) Except for Ni-Cr-Mo-V, striation spacing coincides well with  $da/dN$  both in air and in  $H_2$ .

### SYMBOLS USED

$da/dN$  = fatigue crack growth rate  
 $f$  = cyclic frequency  
 $P$  = hydrogen gas pressure (absolute)  
 $R$  = stress ratio  
 $K_{IC}$  = plane-strain fracture toughness  
 $K_{ISCC}$  = threshold value of stress corrosion cracking  
 $\Delta K$  = stress intensity factor range  
 $W$  = test specimen width

### REFERENCES

- (1) Wei, R.P., and Landes, J.D., Materials Research & Standards, Vol. 9, 1969, pp.25-46.
- (2) Mukherjee, B., ASTM STP 642, 1978, pp.264-285.
- (3) Yoshioka, S., Demizu, M., Kumasawa, M. and Hijikata, A., J. Soc. Materials Science, Japan, Vol. 29, 1980, pp.628-633.
- (4) Suresh, S., and Ritchie, R.O., Proc. 5th Int. Conf. on Fracture, Vol. 4, 1981, pp.1873-1880.
- (5) Liaw, Peter K., Hudak, S.J., and Donald, J. Keith, Metallurgical Trans. A, Vol. 13A, 1982, pp.1633-1645.
- (6) Pittinato, G.F., Metallurgical Trans., Vol. 3, 1972, pp.235-243.
- (7) Kobayashi, H., Fujita, K., Komine, A. and Nakazawa, H., J. Soc. Materials Science, Japan, Vol. 29, 1980, pp.580-584.
- (8) Hirano, K., Kobayashi, Y., Kobayashi, H. and Nakazawa, H., Proc. JSME, No. 790-13, 1979, pp.247-249.
- (9) Kumasawa, M., Yoshioka, Y. and Demizu, M., Proc. Soc. Materials Science, Japan, 1982, pp.119-121.
- (10) Endo, K., Komai, K., Fujimoto, T., Matsuda, Y., Trans. JSME, Ser. A, Vol. 45, 1979, pp.1152-1159.

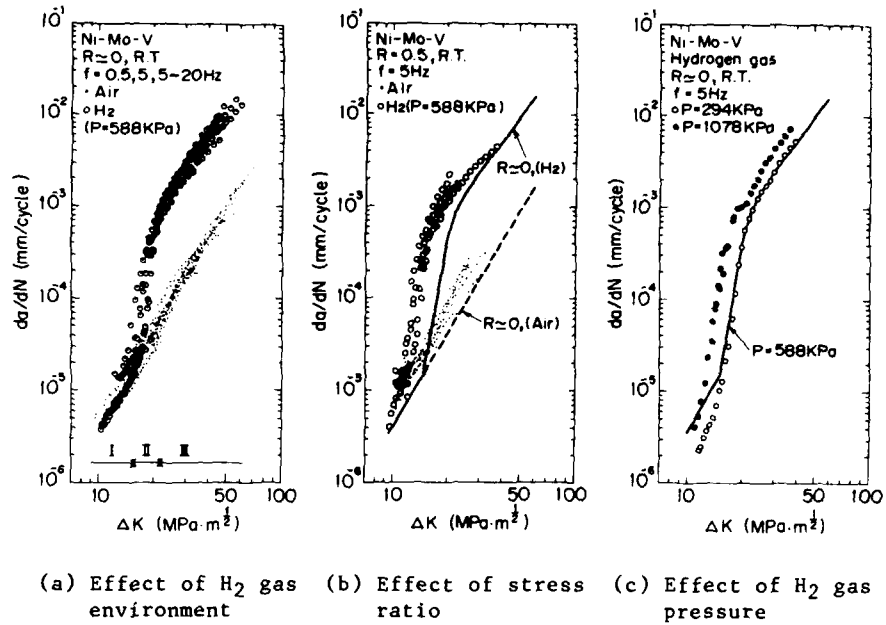
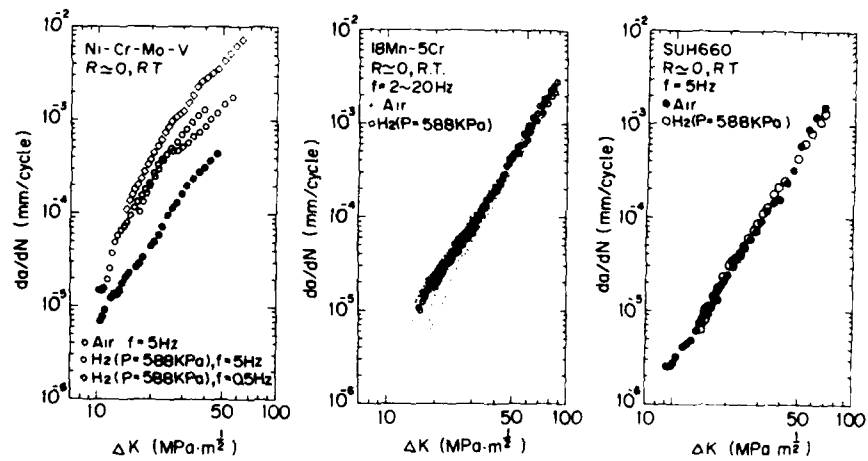


Fig. 1  $da/dN$  v.s.  $\Delta K$  for Ni-Mo-V steel in air and  $H_2$  gas



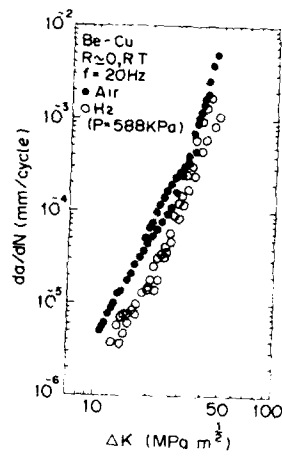


Fig. 5 da/dN v.s. ΔK for Be-Cu alloy

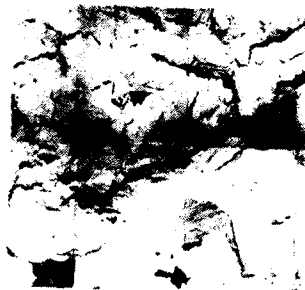


(a) Region I (Intergranular fracture)



(b) Region III (Brittle striation)

Fig. 6 Fractographs of Ni-Mo-V steel in H<sub>2</sub> gas (R=0, P=588KPa)



(a) Ni-Cr-Mo-V steel



(b) 18Mn-5Cr-steel



(c) SUH660 steel



(d) Be-Cu alloy

Fig. 7 Fractographs in H<sub>2</sub> gas (R=0, P=588KPa)

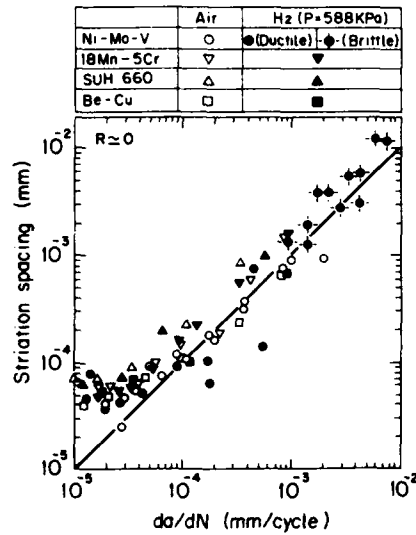


Fig. 8 Striation spacing v.s.  $da/dN$  in air and H<sub>2</sub> gas

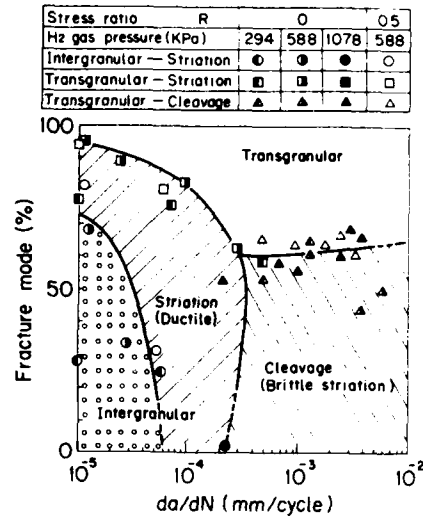


Fig. 9 Fracture mode v.s.  $da/dN$  for Ni-Mo-V steel in H<sub>2</sub> gas

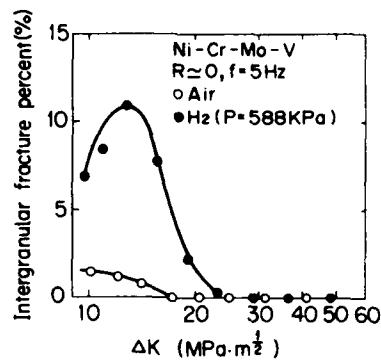


Fig. 10 Area percentage of intergranular fracture v.s.  $\Delta K$  for Ni-Cr-Mo-V steel in air and H<sub>2</sub> gas

APPLICATION OF FATIGUE ANALYSIS ON RAILROADS IN CHINA

LIU SHU-ZHEN\* WANG JIA-DEE\*

A brief introduction to application of fatigue analysis on Chinese railroads, particularly in the field of operation of locomotives and cars, is presented. A new test method for rapidly determining the threshold with the help of cold compression technique is proposed.

A HISTORICAL PERSPECTIVE

Safety of transportation is considered as the first thing on Chinese railroads. In particular, a great attention has been paid to the fatigue problems. This is because rails and most of the mechanical elements of locomotives and cars are subjected to variable or alternative loads. Many components and parts of vehicles and equipment operated on railroads and designed for infinite life time have been operated for decades. Fatigue of key elements or structures of vehicles usually caused disasters. Even the newly designed and manufactured elements can hardly avoid existing of initial flaws and cracks. Owing to the widely-used non-destructive testing the accidents caused by fracture of being worked for a long time elements decrease, but the detected cracks in these elements noticeably increase. Therefore, safety evaluation on defects of components has become an urgent problem needed to be solved. For these reasons the project of research on fatigue crack propagation at near-threshold has been encouraged and supported by the Ministry of Railroad of China.

Since 1982 over ten universities, research institutes and locomotive factories have jointly carried out a project of researching the fatigue crack propagation at near-threshold for commonly used steels on railroads. The stress ratio  $R$ , relative crack length  $a/w$ , specimen geometry and the patterns of loading were studied. The threshold values  $\Delta K_{th}$  of commonly used materials for engineering design were measured. A draft of test method for determining threshold of fatigue crack propagation of commonly used metallic materials on railroads was worked out. Three point bend specimens are recommended to be used for test by the draft, because it makes the perform of test easier and it corresponds with the actual

\* Department of Engineering Mechanics. Southwestern Jiaotong University. Emei, Sichuan, 614202, P.R.C

situation of Chinese railroads. It has been proved by a sequence of comparative tests that the threshold values  $\Delta K_{th}$  obtained by the proposed method which is to be introduced later in this paper under the specified test condition are fairly stable and can be used for engineering practice.

It was in early 1976 that the concept of threshold and fatigue crack growth at near-threshold was accepted by the engineers on Chinese railroads to evaluate the defects of crank-shafts of locomotive diesel engines and estimate their residual service life. In China spheroidal cast iron has been used as the material of crank-shafts for locomotive diesel engines. In addition to the ability of wear resistance and vibration reduction spheroidal cast iron is characterized by its lower cost (it's only 1/8~1/9 of that of steel) and higher threshold value  $\Delta K_{th}$  than that of steel. Furthermore  $\Delta K_{th}$  may be increased by 33% after nitriding. This kind of crankshafts have been used on Chinese railroads at least for twelve years and over thousand diesel locomotives have been equipped with them. There has been no one accident caused by the fracture of crank-shafts ever since (1).

The joint action of mechanical forces and thermal stress on 10L207 diesel engine pistons of locomotives which were operated in a mountain area usually resulted in cracks at the fillets of inside of pistons. 152 pistons were observed and statistically analysed (2). It was found that when locomotives ran about  $2.9 \times 10^4$  km, surface cracks which in average were 1.52 mm deep and 37.6 mm long of average circumference were found at the fillets of about 80% of all the pistons. The fracture analysis of pistons shew that although the cast alloy iron was used as piston material, whose threshold value was higher than that of common steel, the cracks still occurred in the early time of piston operation. This is because the variable stress at the fillets of piston exceeded the fatigue limit of the material. Based on the threshold of material the rate of fatigue crack propagation, the measurement of thermal stress field and calculation by finite element method an evaluated service life of piston for  $(62.7 \sim 69.2) \times 10^4$  km was recommended. This life time was fairly close to the value of  $71.5 \times 10^4$  km estimated by the technicians operating locomotives.

Fracture of cam-shafts of locomotive diesel engines occurred occasionally. The origin of crack was located at the sharp corner of key groove where stress concentration existed. The measured value of dynamic shear stress  $\tau_{max} = 82$  MPa, material used was 18Cr2Ni4WA(HRC 44). The fractured cam-shafts were investigated. The tests for determining the mechanical properties of two kinds of materials treated by different technological processes were made. The test results are shown in Table 1. Owing to reducing the stress concentration through modifying construction and using 12CrNi3A(HRC 30) steel as the cam-shaft material instead which has a high threshold value the phenomenon of cam-shaft fracture has

## FATIGUE 87

been much improved.

TABLE 1 - Mechanical Properties of Cam-Shaft Materials

Material	Heat Treat- ment Schedule	$\sigma_u$ (MPa)	$\sigma_y$ (MPa)	$K_{IC}$ (MPa $\sqrt{m}$ )	$\Delta K_{th}$ (MPa $\sqrt{m}$ )
18Cr2Ni4WA (HRC 44)	860°C, OQ 180°C, T	1450		121	2.8
18Cr2Ni4WA (HRC 30)	860°C, OQ 650°C, T	921	843	129	7.0
12CrNi3A (HRC 30)	860°C, OQ 480°C, T	936	921	142	8.0

Wheel axles are the components of large quantity on railroads. A project for research of evaluation on axle defects had been carried on for several years, that led to establishment and publication of regulations for allowable crack size of tender axles in 1980.

Fatigue crack propagation at near-threshold of base metal, welded seams and heat-affected zone for butt welds of 15MnVN steel used to construct bridges of big span length was studied. It was found that the service life of welded members is chiefly determined by threshold at heat-affected zone. Application of exponential curve described by the following equation

$$\lg(\Delta K) = C_1 + A \exp [ \lg (da/dN) ] \quad \dots(1)$$

to fit the test points of  $(da/dN) > 10^{-7}$  mm/cycle can give a very good prediction of low speed propagation of fatigue cracks and threshold value.

Based on the value of  $\Delta K_{th}$  tested under the condition of different overload ratio  $\beta$  and taking the crack closure effect into account a semi-empirical formula expressing the effect of overload ratio  $\beta$  on threshold value  $\Delta K_{th}$  in the reducing load method has been proposed as follows:

$$\Delta K_{th} = \frac{(\Delta K_{th})_b}{(1-C_2\beta^2)} \quad \dots(2)$$

where both  $(\Delta K_{th})_b$  and  $C_2$  are obtained through experiment. The test data and some conclusions are very useful to the designers for constructing long span bridges.

The railroad construction department of Ministry urged research on cracks in vicinity of holes and plane elliptical cracks in rails to be included in current project of research on fatigue crack

propagation at near-threshold for the purpose of establishing criteria of defect evaluation and survival prediction of rails.

#### A PROPOSED TEST METHOD FOR DETERMINING $\Delta K_{th}$

The conventional method for determining the threshold value  $\Delta K_{th}$  is based on application of gradually reducing load to precrack a specimen. In order to simulate an acute crack on engineering element and eliminate the influence of loading history much time and effort have to be spent on preparing fatigue cracks. Not a few efforts have been directed to seek a rapid test method of threshold so far. In this paper a new method for rapidly determining  $\Delta K_{th}$  with the help of cold compression in liquid nitrogen - method of multi-specimen with cold precompression-tension cracks (hereinafter CPTC for short) is proposed. According to the proposed method an acute precrack can be produced in about 1 minute, then through one-time fatigue loading test a data point of threshold will be obtained.

#### Method for Precracking A Specimen by Cold Compression

Put a four point bend specimen with "V" notch in a tank filled with liquid nitrogen (Fig. 1<a>). After the heat exchange between the specimen and liquid nitrogen is finished, a load P is applied to the specimen that results in considerable plastic compression deformation around the notch tip of specimen. During unloading the residual tensile stress is produced at the notch tip due to the effect of the broad elastic zone. The magnitude of load P is great enough to lead the residual tensile stress to initiate notch tip precracking. Plastic deformation does not appear at the crack tip but at its tail (Fig.2). In order to entirely eliminate residual tensile stress and extend the crack the specimen is to be turned over and a load P' ( $P' \approx 0.1P$ ) is applied to it. In this case the notch tip is subjected to tension and the crack length increases(4). The crack length chiefly depends on the magnitude of applied load P which can be evaluated by the formula:

$$P = C_3 \sigma_y B(w-a)^2 / (3b) \quad \dots\dots(3)$$

were B, (w-a) and b are shown in Fig. 1<b>.

#### Validity Test of CPTC

It was examined that specimen with CPTC could be used for fracture toughness test at low temperature(4). In order to verify the validity of CPTC used to determine threshold we conducted J<sub>g</sub> resistance curve test at room temperature with two sets of specimens, half of which were with CPTC and the rest - with fatigue precracks. Tests were performed according to the provisions

# FATIGUE 87

specified in GB 2038-80 (5). The material used was 16Mn steel. Dimension of the three point bend specimen was 20×24×96 mm. The test results are given in Table 2. As shown in this Table,  $K_R$  obtained from specimens with CPTC is about 5% higher than that from specimens with fatigue precracks.

TABLE 2 -  $J_R$  Comparative Test Results of 16Mn Steel

Type of Pretcrack	Equation of Regression	Regr. Points	Coeff. of Corelation	$J_i$ (KN/m)	$\Delta J$	$K_R = \sqrt{E' J_i}$ (MPa $\sqrt{m}$ )
CPTC	$J_R = 9.09 + 45.8\lambda a$	6	0.912	133	18.6	171
Fatigue	$J_R = 9.63 + 31.2\lambda a$	6	0.965	122	7.8	164

The yield limit of material immersed in liquid nitrogen (77K) noticeably increases, but ductility decreases. Specimens, in general, can meet the requirements of plane strain. A preliminary cracking sound like "POP-in" was heard during unloading stage of cold compression and application of load  $P'$  to the overturned specimen. The fracture surface of specimen with CPTC was examined with the help of scanning electron microscope (Fig.3). There were a lot of secondary cracks on cleavage terraces. The front edge of crack on fracture surface was likely straight. All of these said that the CPTC tip was sufficiently acute.

The micro-hardness of the region near crack tip was measured by micro-hardmeter Microment II. It was observed that there was no change in hardness near the fracture crack tip but decrease of hardness by about 10 was detected near the CPTC tip (Table 3).

TABLE 3 - Hardness of CPTC (50CrMoA Steel)

Distance from Crack-tip	5 ( $\mu m$ )	10 ( $\mu m$ )	15 ( $\mu m$ )	20 ( $\mu m$ )	25 ( $\mu m$ )
Hardness (HB)	259	251 243	275 279 292	265 262	280

The residual stress components at crack tip were measured by MSF-2M X-ray residual stress meter. It was shown that the residual stress components at the crack tip for both types of cracks were compressive ones of great value and almost equal to each other. As the temperature of specimen with CPTC rose to room temperature, the yield limit of material decreased and ductility increased, that resulted in residual tensile stress relaxation. So the residual tensile stress gives no effect on test. In order to examine whether the specimen immersed in liquid nitrogen for a short time (less

## FATIGUE 87

than 5 minutes) underwent cold treatment and changed its mechanical properties we conducted a sequence of comparative tests. Half of specimens used for tension and Charpy impact tests were immersed and kept in liquid nitrogen for 10 minutes. After the temperature of these specimens had risen to room temperature, they were tested on tension and impact together with those not immersed. F Test and t Test were carried out to the results at the level of significance  $\alpha = 0.05$ . It was shown that there was no significant difference between them.

### Method of Multi-Specimen with CPTC for Rapidly Determining $\Delta k_{th}$

From the crack propagating stage at low speed ( $da/dN < 10^{-7}$  mm/cycle) a threshold value  $\Delta k_{th}$  corresponding to  $da/dN=0$  may be evaluated. It must be pointed out that  $\Delta k_{th}$  cannot be obtained directly from test. It is only an estimated value. For the purpose of engineering needs it is necessary to establish a commonly accepted value which should provide engineering practice and experiment work with convenience. For example, if  $\Delta k$  corresponding to  $da/dN=10^{-7}$  mm/cycle is supposed to be  $\Delta k_{th}$  and test error = 5% the quantity of crack propagation must not be less than 0.2 mm as the cycles  $N=2 \cdot 10^7$ . Under this condition a high frequency vibrophore machine whose frequency usually ranges from 100 to 200 HZ has to run continuously for 43 hrs (at  $F=130$  HZ) in order to obtain one datum. Such situation causes much expenditure of time and some difficulty in experiment. At present  $\Delta k$  corresponding to  $da/dN=10^{-7}$  mm/cycle has been most accepted as  $\Delta k_{th}$  and method of gradually reducing load is used for test.

From the view point of physics the crack propagation rate  $da/dN = 10^{-7}$  mm/cycle implies that the crack propagates 1 Å as stress passes through one cycle. As we know the value 1 Å is so small (it's about 1/2 - 1/5 of the length of metal crystal edge and approximately equal to the radius of atom) that crack propagation has already exceeded the macro concept. Experimental research on  $\Delta k_{th}$  of three kinds of low alloy steels subjected to different heat treatments shows that  $\Delta k_{th}$  has neither definite relations to the strength, ductility and toughness, nor to the cyclic hardening-softening in case of low cycle fatigue (6). It has been determined that micro structure is the important factor affecting  $\Delta k_{th}$  which decreases in order of Tempering Sorbite  $\rightarrow$  Ferrite + granular Bainite  $\rightarrow$  granular Bainite + tempering Troostite  $\rightarrow$  low carbon Martensite. It is also observed that crack usually extends along the least resistance phase and interphase and the path of crack propagation is not a straight line that shows discontinuity of crack propagation. Therefore threshold is not correlated strictly to the concept of speed rate. It represents ability of material to resist cyclic loading and is characterized by whether the macro crack propagates. Coming to an agreement we may set a number of cycles, for example  $N_j = 10^7 \sim 10^8$ . The threshold  $\Delta k_{th}$  may be defined as amplitude of the maximum stress intensity factor under the condition of  $N=N_j$  and no crack

## FATIGUE 87

propagation occurs. The quantity of crack propagation  $\Delta a$  can be directly measured from fracture surface. For the observed value of  $\Delta a$  due to the system and random errors of test no crack propagation does not mean that  $\Delta a$  must be zero. Based on the experience of experimental research on Chinese railroads it has been recommended that  $\Delta a < 0.05$  mm may be accepted as a criterion of no crack propagation.

Method of multi-specimen with CPTC suggests the procedure of determining  $\Delta K_{th}$  as follows:

Set one of the specimens with CPTC on fatigue test under an evaluated load with a pre-chosen load ratio  $R$ . As soon as  $N=N_i$  or  $\Delta a=0.5$  mm, break down the tested specimen and measure the crack length  $a$  and  $\Delta a$  carefully. Based on  $\Delta a/\Delta N$  and the precrack length of the specimen which is to be tested next infer the required load for next testing. A test datum of  $\Delta K_{th}$  will be obtained for each specimen. Among the sifted data the magnitude of maximum amplitude of stress intensity factor  $\Delta K_{max}$  which meets the requirement  $\Delta a=0$  is accepted as threshold, that is  $\Delta K_{max}=\Delta K_{th}$ .

In order to check the validity of the proposed method a sequence of comparative tests were conducted of both the proposed and conventional test methods at room temperature. Material used: 20CrMnTi. Dimension of three point bend specimens:  $10 \times 40 \times 160$  mm. Load ratio  $R=0.1$ .  $N_i=3.5 \times 10^6$  cycles. A high frequency machine with  $F=130 \sim 170$  HZ was used. The threshold values obtained from specimens with CPTC and with fatigue precracks were  $6.82 \text{ MPa}\sqrt{\text{m}}$  ( $a/w=0.17$ ) and  $8.06 \text{ MPa}\sqrt{\text{m}}$  ( $a/w=0.25$ ) respectively. The former is less than the latter by 15%. The chief reasons of the difference may be stated as follows:

- 1)  $\Delta K_{th}$  from specimens with CPTC was obtained at  $N=3.5 \times 10^6$  cycles and  $\Delta a=0$ .  $\Delta K_{th}$  from those with fatigue precracks was nothing else but the amplitude of stress intensity factor corresponding to  $da/dN=10^{-7}$  mm/cycle.
- 2) There was no effect of loading history on specimens with CPTC. Our experiment on 15MnVN steel shew that  $\Delta K_{th}$  might increase by 5.5% due to the effect of loading history ( $R=0.1$  and load was reducing with gradient of  $10^\circ$ ).
- 3) Both types of specimens had different  $a/w$ . It is known that  $\Delta K_{th}$  will decrease slightly as  $a/w \leq 0.2$ .
- 4) Nitriding effect is worth further studying.

## CONCLUSIONS

- 1) Research on fatigue crack propagation rate and threshold

## FATIGUE 87

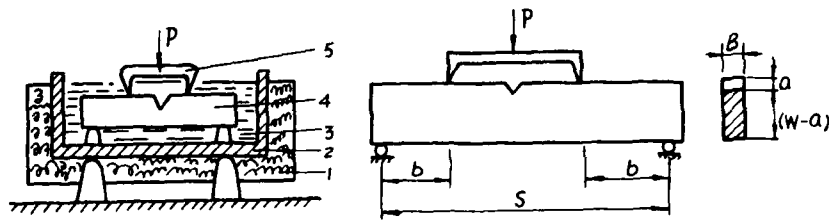
has been encouraged and supported on Chinese railroads and a preliminary success had been achieved. A project for further study in this field is scheduled to meet the needs of railroads.

- 2) It has been shown that method of CPTC is feasible for threshold test. Its test data coincide nearly with those from conventional method.
- 3) Proposed method does not need continuously running of test machine for a long time and provides a possibility of direct measuring  $\Delta a$  that will benefit the data collection and test accuracy.
- 4) Liquid nitrogen supply is necessary for proposed method. The front edge of crack on fracture surface of specimen with CPTC is not so smooth as that of fatigue precracking specimen. Application of proposed method for fracture toughness testing may cause dispersity of data.

## REFERENCES

- (1) Railway Research Ins., J. of Diesel Locomotives, No.3, 1977, pp. 1—22 (Beijing).
- (2) Feng Yu-fu. et al, J. of The China Railway Society, Vol.9, No.3, 1986, pp. 73-85 (Beijing).
- (3) Wu Yen-chuan, J. of Diesel Locomotives, No.4, 1980, pp. 48—52 (Beijing).
- (4) Sakano, K., Welding Research Abroad, Vol.XXIV, No.9, 1978.
- (5) P. R. C. STANDARD, GB 2038-80.
- (6) Zhang Yi, J. of Mechanical Strength. Vol.8, No.1, 1986, pp. 12-17 (Beijing).

# FATIGUE 87



1-Heat preservation layer

2-Low temperature tank

3-Liquid nitrogen

4-Specimen

5-Attached beam

a) Equipment for cold compression

b) Four point bend specimen under loading

Fig.1 Cold precompression tension cracking



Fig.2 CPTC on specimen



Fig.3 Fracture mechanism (SEM) 1000x

FATIGUE 87

FATIGUE 87

## FATIGUE THRESHOLDS

FATIGUE 87

NEAR-THRESHOLD FATIGUE

P. Lukáš<sup>x</sup>

The mechanisms of the near-threshold, high cycle fatigue and the nature of the fatigue limit are discussed on the basis of experimental data concerning the effect of grain size and temperature on the cyclic stress-strain response, fatigue life, fatigue crack growth and dislocation structures in copper. The interpretation of the fatigue limit as a short crack propagation threshold made it possible to derive simple engineering formulas for the calculation of the size and sharpness of non-damaging notches and for the description of the effect of small notches on fatigue strength.

INTRODUCTION

Generally, we can call fatigue threshold any critical value of stress, strain, stress intensity factor etc, which marks the beginning of a fatigue process. From that point of view, the oldest fatigue threshold is the fatigue limit on the S/N curve. Nevertheless, the term threshold has been most frequently used for the critical value of the stress intensity factor, below which the cracks do not propagate. Under the term near threshold fatigue we can then equally well understand the slow fatigue crack growth at low stress intensities and the high cycle fatigue in originally crack-free bodies at low stresses and strains.

Fatigue damage is caused by the cyclic plastic deformation, which is homogeneous at the beginning of cycling and highly localized in the later stages, namely in the persistent slip bands (PSBs) in the stage of

<sup>x</sup> Institute of Physical Metallurgy, Czechoslovak Academy of Sciences, Brno.

microcrack nucleation and in the plastic zone surrounding crack tip in the stage of crack propagation. This cyclic plastic deformation and its critical values determine also all kinds of the fatigue threshold. At present, we are on the level of the basic qualitative understanding; the quantitative description of these processes and thresholds in terms of cyclic plasticity is at the beginning of its development.

The aim of this paper is to further elucidate the role of the localized cyclic plastic deformation in the near-threshold fatigue process, to bring further evidence that the stress-fatigue limit can be understood as a short crack propagation threshold and to present a model (and its experimental verification) describing non-damaging notches in fatigue.

#### EFFECT OF GRAIN SIZE AND TEMPERATURE

In this part we shall deal with the high cycle behaviour (cyclic stress-strain response, fatigue life, crack growth and dislocation structures) in copper mainly in terms of the cyclic plastic strain.

Copper of 99.98% purity was used. The cylindrical specimens (gauge diameter, 4 mm ; gauge length, 20 mm) were heat treated to obtain two groups of substantially different grain sizes  $D$ , namely 0.07 mm and 1.2 mm. The specimens were cycled on the modified Amsler machine enabling continuous recording of the hysteresis loops at a frequency of about 100 Hz. The tests were run under total strain control. The full amplitude was built up slowly over about 1000 cycles. A large number of specimens (total, 180) were run either until complete fracture or at least 107 cycles (for amplitudes below the fatigue limit). The cyclic stress-strain curves (CSSC) were constructed from the values of the stress amplitude and the plastic strain amplitude with the number of cycles equal to 50% of the total number of cycles.

Fig.1 shows the results for fine-grained specimens, and Fig.2 the results for coarse-grained specimens at room temperature. For fine-grained copper the best fit curve is a straight line (on the log-log plot) given by the power law relationship

$$\sigma_a = k_1 \epsilon_{ap}^n \quad \dots (1)$$

The leastsquares analysis yields  $k_1 = 562$  MPa and  $n = 0.205$ . The best fit curve for coarse-grained mate-

rial is certainly not a straight line. However, there is no plateau in the sense that the constant stress amplitude extends over a certain range of plastic strain amplitudes, but there is a clear bulge in the stress range corresponding to the single-crystal plateau stress converted by different orientation factors. The results for both grain sizes are displayed together (without the experimental points) in Fig.3. It can be seen that in the range of the bulge the smaller-grained material gives a lower saturation stress.

A higher stress for coarser grains contradicts the generally accepted understanding of the grain size effect. For monotonic loading the flow stress always increases with decreasing grain size according to the well-known Hall-Petch equation. The untypical grain size effect in the saturation stress of cyclically loaded copper was noted for the first time by Horibe et al (1). Our results together with the data from literature (only the data from tests run until complete fracture are taken into account), are displayed in Fig.4. It can be seen that the saturation stress decreases here roughly linearly as  $D^{-1/2}$ . There are two other sets of data on the grain size dependence of the saturation stress. One is the above-quoted paper by Horibe et al (1) (polycrystalline Al-4%Cu alloy containing  $\theta''$  precipitates) and the other paper by Boutin et al (2) (polycrystalline Cu-30%Zn alloy). While in Al-4%Cu alloy the grain size dependence is of the same type as in pure copper (i.e. the smaller-grained material gives a lower saturation stress), the grain size dependence for Cu-30%Zn alloy is just the opposite (i.e. the smaller-grained material gives a higher saturation stress). Thus we have copper and Al-4%Cu alloy on the one hand and Cu-30%Zn alloy on the other hand. What is the difference between these two extremes? Copper and Al-4%Cu do exhibit localization of the cyclic slip in PSBs. The structure of these slip bands may be different for copper (a ladder-like dislocation structure) and for Al-4%Cu (zones of disordered and/or dissolved precipitates, see Gerold et al (8)), but in both the cases they are clearly defined zones of higher slip activity. The "reversed" grain size effect in copper occurs within the range of plastic strain amplitudes from about  $2 \times 10^{-5}$  to  $4 \times 10^{-4}$  (Fig.3). This corresponds very well to the range in which the dislocation structure is of a two-phase nature(3), i.e. it consists of veins (matrix structure) and ladder-like PSBs. Below  $2 \times 10^{-5}$  there is only a vein structure and above  $4 \times 10^{-4}$  there is only a cell structure, i.e. in both cases a one-phase structure.

In the case of Cu-30%Zn planar slip alloy there is either no slip localization at all (the cyclic slip and consequently the dislocation structure is more or less homogeneous (9)) or only a limited one. Laird and Buchinger (10) found recently strain localization in another planar slip alloy, in Cu-16at%Al, occurring in association with the plateau in CSSC of single crystals and with the formation of so called persistent Lüder's bands (PLBs). For our discussion it is important that the volume fraction of these PLBs is much lower (at least by a factor of 5) than the volume fraction of the PSBs in copper. Thus our conclusion relating the reversed grain size effect with two-phase structure remains intact, it is perhaps necessary to add the restriction that a sufficient amount of the second phase is needed for this effect to occur.

Horibe et al (1) explained the effect of grain size on CSSCs in copper by applying different orientation factors for different grain sizes. In principle, their explanation is also applicable to Cu-30%Zn (which exhibits the opposite effect). Thus the proposal of Horibe et al cannot be considered to be of general validity. The question of the "reversed" grain size effect remains open.

Fig.5 shows the effect of lower temperature on the CSSC of fine-grained material. It can be seen that the reduction of temperature leads to a shift of the curve to higher stress amplitudes. Here again a straight line is the best-fit curve and thus Eq.1 can be applied with the constants  $k_1 = 675 \text{ MPa}$  and  $n = 0.196$ . The exponent  $n$  is practically temperature independent (i.e. the straight lines in Fig.5 are parallel). This temperature effect is relatively easy to explain. Cyclic flow stress is composed of two components, the effective stress (short range stress fields) and the internal stress (long range stress fields). In f.c.c. metals it is mainly the athermal internal stress component which is responsible for the temperature dependence. This component is in turn related to the characteristic size of the dislocation structure. Pratt (11) showed for polycrystalline copper fatigued at low cycle region that the cell size (for a constant strain amplitude) decreased with the reduction of temperature. In the case of copper single crystals cycled in the plateau region the wall spacing in the PSBs was found to decrease with decreasing temperature (Basinski et al (12)). The decrease of the characteristic sizes of the dislocation structure (i.e. the intervein spacing in the matrix and the interwall spacing in the PSBs) is most probably the reason for the effect shown in Fig.5.

Coffin-Manson plots are presented in Figs.6 and 7. For fine-grained copper a straight line (on the log-log plot) represents a very good fit to the experimental points. The Coffin-Manson law of the type

$$\epsilon_{ap} = k_2 N_f^c \quad \dots (2)$$

is therefore obeyed. The least-squares analysis yields  $k_2 = 0.125$  and  $c = -0.500$ . The Coffin-Manson law is not obeyed for coarse-grained copper; the curve certainly cannot be described in this case, by the power law relationship. For all the amplitudes the fatigue life is shorter than in fine-grained material (see also Fig.11). The plastic-strain-fatigue limit strongly depends on the grain size. While it is  $4 \times 10^{-5}$  for fine-grained material, the value for coarse-grained material ( $2.3 \times 10^{-5}$ ) is lower by a factor of almost 2.

Fig.8 presents the results for fine-grained copper at both temperatures. It can be seen that there is no difference in the resulting curves, i.e. the Coffin-Manson plot is temperature independent.

The room temperature S/N curves for different grain sizes are shown in Fig.9 (without the experimental points). The coarse-grained material exhibits a slightly lower fatigue life. Nevertheless, the stress-fatigue limit is, within the scatter, the same in both cases, namely 67 MPa. The diagram also contains the stress-controlled results obtained by Thompson and Backofen (13). Qualitatively, our results are in full agreement with theirs. The grain size affects the fatigue life more at shorter lives and the fatigue limit is grain size independent. Quantitatively, small differences can be found which may be attributed to different purities and to different regimes of cycling.

The effect of temperature on the S/N curves for fine-grained material can be seen in Fig.10. The shift of the curve towards higher stress amplitudes with the reduction of temperature is analogous to the shift of the CSSC in Fig.5.

Let us first discuss the effect of temperature. The most important conclusion is that the Coffin-Manson curve is temperature independent, while the S/N curve is strongly temperature dependent. It is, in fact, an analogy to our earlier finding (Lukáš et al (14)) that the plot of the fatigue crack propagation rate on the local crack tip plastic strain amplitude is almost temperature independent, while the fatigue crack propaga-

tion rate expressed in terms of the stress intensity factor depends strongly on temperature. It means that in both cases it is the plastic strain amplitude which is the controlling parameter, the change in temperature only shifts the stress response. The whole fatigue process consists of the relatively short period of homogeneous deformation, then crack nucleation at the surface and eventually crack propagation follow. In the Coffin-Manson plot the average bulk value of the strain amplitude is used. As for the processes of nucleation and propagation, it is the local value of the plastic strain amplitude which must be taken into account. The presented results then mean that the ratio of the local plastic strain values (at the nucleation sites and at the crack tip) to the average value is also temperature independent.

The effect of grain size is more difficult to rationalize. Fig.11 summarizes our results together with the results of Wang (4), whose paper is the only other research presenting Coffin-Manson curves for two grain sizes. The curve for single crystals from the paper by Cheng and Laird (7) is also given; the shear strain amplitude was converted using a Sachs factor 2.24 ; an application of a Taylor factor 3.06 would not substantially change the position of the curve with respect to the polycrystalline data. The polycrystals exhibit a shorter fatigue life than the single crystals, the coarser-grained material gives a shorter life than the finer-grained material. This indicates the decisive role that the grain boundaries play in crack nucleation. The data on near-threshold macrocrack propagation in materials identical with those studied in this paper (14) show that the coarse-grained copper exhibits a lower crack growth rate than the fine-grained copper for the same value of the local plastic strain amplitude at the crack tip. This means that the stage of high cycle, near-threshold macrocrack propagation (expressed in terms of the plastic strain) is longer for coarse-grained material, in spite of the fact that the total fatigue life for this coarse-grained material is shorter. There is only one possibility for explaining this effect: The nucleation of microcracks takes a much lower number of cycles in coarse-grained copper than in fine-grained copper.

The effect of grain size on the slope of the Coffin-Manson plots in Fig.11 simply means that the grain size affects the low cycle region to a smaller extent. This can be again correlated with the dislocation structures; in the low cycle region there is only a one-phase

structure, namely the cell structure. It is interesting that our curve for coarse-grained material has in its middle part almost the same slope as the curve for single crystals.

The discussion concerning the effect of temperature and grain size can be summarized as follows. Temperature affects primarily the stress-strain response. This holds both for the average values (experimentally determined CSSC) and for the stress and strain values in the zones of localized slip, i.e. in the PSBs. Temperature most probably does not affect the spatial distribution of the plastic strain. On the other hand, grain size affects primarily just this spatial distribution of the plastic strain. This is due to the inherent dependence of the length of the PSBs on grain size. The PSBs determine both the nucleation and early crack growth (these processes take place within them) and the near-threshold growth of macrocracks (via the length of the PSBs outside the "fracture-mechanical" plastic zone ahead of the crack tip).

#### NATURE OF FATIGUE LIMIT

The results presented can also contribute to the current discussion on the nature of the fatigue limit. The plastic-strain-fatigue limit depends strongly on the grain size, being smaller for the coarser-grained material (Fig.11). It has been well proved that PSBs may even form at lower plastic strain amplitudes provided that there is sufficient cycling (Müllner et al (15)). The critical event is therefore not the nucleation of PSBs. However, we can exclude the threshold for macrocrack propagation as the critical parameters. Apart from other arguments, the local plastic strain amplitude at the crack tip ( $5.6 \times 10^{-5}$  for fine-grained material and  $1.5 \times 10^{-4}$  for coarse-grained material (14)) of dormant cracks are too high and exhibit an opposite grain size dependence. Thus the remaining possibility is the threshold for the propagation of nucleated short cracks which were many times observed at and even below the fatigue limit.

The stress-fatigue limit is then the threshold stress for short cracks which nucleated (at the stress-fatigue limit), grew up to a critical size  $a_0$  and then stopped to grow. Kitagawa-type diagram presented schematically in Fig.12 shows the dependence of the threshold stress amplitude on the crack size. Up to the critical crack size  $a_0$  the threshold stress is identical with the stress-fatigue limit. From this

Kitagawa-type diagram we can easily derive the dependence of the threshold stress intensity factor for short cracks,  $K_{ath}$ , on the crack size. In such a diagram the short crack threshold stress intensity factor increases with the crack size in the range of short cracks and reaches the crack-size independent value  $K_{ath}$  for macrocracks. It is very important that the discussed plot does not depend on the geometry of specimens. This point was proved by James and Smith (16), who found that this plot was (within experimental scatter) the same for plain specimens and for notched specimens. This is, in fact, the justification for the description of the thresholds for short cracks in terms of the stress intensity factor (which - contrary to the threshold for macrocracks - is crack size dependent).

The non-propagating cracks at the stress-fatigue limit  $\sigma_c$  are semi-elliptical short cracks of the depth  $a_0$ . Thus we can write

$$K'_{ath} \sim \sigma_c \sqrt{\pi a_0} \Rightarrow \sigma_c \sim K'_{ath} / \sqrt{\pi a_0} \quad \dots (3)$$

The grain size dependence of the stress-fatigue limit is now given by the grain size dependence of the threshold stress intensity factor for short cracks of the size  $a_0$  and by the grain size dependence of this critical crack size  $a_0$ . The threshold for macrocracks increases with the grain size as

$$K_{ath} = a + b \sqrt{D} \quad \dots (4)$$

This is, in fact, also a "reversed" grain size effect. Assuming that the grain size dependence of threshold K-factor for short cracks is of the same type (given by Eq.4) and assuming that  $a_0$  increases linearly with  $D$ , we get from Eq.3 the grain size dependence of the stress-fatigue limit of the Hall-Petch type. But if we assume that both the short crack threshold K-factor and the critical size  $a_0$  increase with  $D$  in such a way that their ratio remains constant, we get from Eq.3 a grain size independent stress-fatigue limit. Thus the reason why in some materials the stress-fatigue limit is strongly grain size dependent (e.g. low carbon steels), while in another materials it is grain size independent (e.g. copper) is to be sought in the grain size dependences of these two short crack quantities.

NON-DAMAGING NOTCHES

The presented interpretation of the stress-fatigue limit makes it possible to derive the relation for the size and sharpness of non-damaging notches (i.e. notches having no effect on the fatigue limit) and to describe the effect of small notches on the fatigue limit. For this some simplifying assumptions are required about the cracks nucleated at the fatigue limit:

- (i) these short cracks are Mode I semi-elliptical cracks,
- (ii) the driving force for their propagation can be expressed by the stress intensity factor,
- (iii) their depth on the surface of smooth specimens and their depth at the notch root is the same at the respective fatigue limits.

For un-notched bodies, the K-factor for the deepest point of a small surface semi-elliptical crack is

$$K_{\text{plain}} = Q \sigma \sqrt{\pi a} \quad , \quad \dots (5)$$

where  $Q$  is the shape factor depending exclusively on the aspect ratio. For notched bodies, the K-factor for cracks starting at the notch root were found numerically for several notch/crack configurations. These numerical solutions can be for the deepest point of a small semi-elliptical crack starting from the notch root approximatively expressed by (Lukáš (17))

$$K_{\text{notch}} = \frac{Q k_T}{\sqrt{1 + 4.5(a/\rho)}} \sigma \sqrt{\pi a} \quad , \quad \dots (6)$$

where  $k_T$  is the stress concentration factor and  $\rho$  is the notch radius.  $Q$  is identical with the corresponding value in Eq.5. Let us now consider the assumption (iii) for the cracks of the depth  $a_0$ . The border between propagation and non-propagation is given by

$$K'_{\text{ath}} = Q \sigma_c \sqrt{\pi a_0} \quad \dots (7)$$

for un-notched specimens ( $\sigma_c$  is the plain fatigue limit), and

$$K'_{\text{ath}} = \frac{Q k_T}{\sqrt{1 + 4.5(a_0/\rho)}} \sigma_{cn} \sqrt{\pi a_0} \quad \dots (8)$$

for notched specimens ( $\sigma_{cn}$  is the notched fatigue limit).

The condition for a notch to be non-damaging with respect to the fatigue limit is

$$K_{\text{notch}} \leq K_{\text{plain}} \quad \dots (9)$$

for the same stress level (i.e. for  $\sigma = \sigma_c = \sigma_{cn}$ ) and for the same crack depth  $a_0$ . Inserting Eqs. 7 and 8 into relation 9 we get

$$(k_T^2 - 1) \varphi \leq 4.5 a_0 \quad \dots (10)$$

The fatigue limit of notched specimens can be obtained by combination of Eqs. 7 and 8 in the form

$$\sigma_{cn} = \frac{\sigma_c}{k_T} \sqrt{1 + 4.5(a_0/\varphi)} \quad \dots (11)$$

This equation gives for large notch radii  $\sigma_{cn} = \sigma_c/k_T$ . From that it follows that Eq. 11 is important for the range of small notches. The condition for a notch to be non-damaging presented by relation 10 can be derived also from Eq. 11 by applying the assumption that the notched fatigue limit cannot exceed the plain fatigue limit.

On the basis of the just derived relations, the notch size effect can be - at least formally - presented in a similar diagram as the Kitagawa plot, i.e. in the plot relating the fatigue limit with the notch size. Fig. 13 shows schematically such a representation. For a constant value of  $k_T$  (for example, for a hole of varying radius in an infinite plate) the notch has no effect up to the radius  $\varphi_0$  given by

$$(k_T^2 - 1) \varphi_0 = 4.5 a_0 \quad \dots (12)$$

This equation represents the boundary case of the more general relation 10. Typical small notches as holes, cavities and scratches have the  $k_T$  factor in the range from 2 to 3. Thus the critical notch radius  $\varphi_0$  is comparable with the critical crack size  $a_0$ . For radii exceeding the value of  $\varphi_0$  the fatigue limit decreases with increasing radius according to Eq. 11; for the range of small notches in Fig. 13 is the notch effect highly size dependent. For large notch radii the size effect weakens and the notch fatigue limit approaches the value  $\sigma_c/k_T$ .

Experimental verification of the presented relations will be shown for the pressure vessel steel 2.25Cr/1Mo

(yield stress 380 MPa, tensile strength 530 MPa). Specimens with a cylindrical gauge section of 5 mm diameter were used for the determination of both the un-notched and notched S/N curves. Circumferential semi-circular notches with radii ranging from 10 to 800  $\mu\text{m}$  were machined in the middle of the gauge length. The range of the stress concentration factors, taken from charts by Peterson (18), correspond to values between 3.04 and 1.83. After machining all specimens were subjected to a stress relief heat treatment. Cycling was performed under symmetrical loading conditions (push-pull,  $R = -1$ ) at a frequency of about 140 Hz.

The effect of notches on the fatigue limit is presented in Fig.14. The data points correspond to the fatigue limits of specimens with notches of various radii. It can be seen that the smallest notches (having the highest  $k_T$  values) do not reduce the value of the fatigue limit. This is in agreement with relation 10. The curve shown in Fig.14 represents Eq.11 for  $a_0 = 100 \mu\text{m}$ . This value gives the best fit of Eq.11 with the experimental points. Inserting this value of  $a_0$  into Eq.12 (and respecting the fact that in our case the  $k_T$  - factor depends on the notch radius) we get the critical notch radius  $\rho_0 = 60 \mu\text{m}$  below which the circumferential notch can be considered as non-damaging. Preliminary results of the direct measurement of the size of non-damaging cracks (in the Kitagawa plot) are in a reasonable agreement with the value  $a_0 = 100 \mu\text{m}$  obtained in the above described way.

From the point of view of engineering applications of the relations for non-damaging and small notches, the critical point is determination of the material parameter  $a_0$ . The determination of  $a_0$  as performed in this paper, i.e. by the measurement of the notch size effect (see Fig.14), is hardly acceptable for the engineering use. At present, it seems that the best possibility is the measurement of the initial part of the Kitagawa diagram, i.e. direct measurement of the size of non-damaging cracks at the fatigue limit. Measurement of this type is unfortunately also time taking. Therefore it has a sense to work out approximate methods. There are two possible ways.

The first possibility is based on the assumption that the ratio of the short crack threshold for crack size  $a_0$ ,  $K_{ath}$ , to the macrocrack threshold,  $K_{ath}$ , i.e. the ratio  $K_{ath}/K_{ath}$ , is constant for all the steels. Inserting the relevant values for our steel ( $\sigma_c = 220\text{MPa}$ ,  $a_0 = 100 \mu\text{m}$ ) into Eq.7 for assumed semi-circular crack shape ( $Q = 0.65$ ) we get the short crack

threshold  $K_{ath} = 2.53 \text{ MPa}\sqrt{\text{m}}$ . The macrocrack threshold for our steel is  $K_{ath} = 6.0 \text{ MPa}\sqrt{\text{m}}$ . The ratio of the thresholds is 0.42. If we proved that this holds approximatively for all the steels, it would be possible to calculate the value of  $a_0$  from Eq.7 simply by inserting the mentioned fraction of the macrocrack threshold for  $K_{ath}$  and the plain fatigue limit  $\sigma_c$ . The second possibility is to seek the relations between the effective threshold for macrocracks and the short crack threshold. This possibility is based on the indications that the crack size dependence of the short crack threshold lies mainly in closure effects. Thus the macrocrack effective threshold data could serve directly as the short crack threshold. Both the possibilities require experimental verification.

### CONCLUSIONS

- 1) High cycle fatigue behaviour of copper polycrystals is determined primarily by the cyclic plastic deformation both homogeneous and localized. Specifically it was found:
  - (i) There is no plateau in CSSCs of polycrystals. The saturation stress shows a reversed grain size effect: the coarser the grain, the higher the stress.
  - (ii) Coffin-Manson plot depends strongly on grain size: the coarser the grain, the shorter is the fatigue life. On the other hand, Coffin-Manson plot is temperature independent.
  - (iii) The growth rate of fatigue macrocracks expressed in terms of the local crack tip plastic strain depends also strongly on grain size, but very weakly on temperature.
 All these findings were related to the processes in the PSBs.
- 2) The plastic-strain-fatigue limit and the threshold value of the local crack tip plastic strain depend on grain size, but they are temperature independent. On the other hand, the stress-fatigue limit is strongly temperature dependent and practically grain size independent. This together with other findings leads to the conclusion that the fatigue limit can be interpreted in terms of stress and plastic strain requirements for the propagation of short cracks. The stress-fatigue limit is then the threshold stress for short cracks which nucleated, grew up to the critical crack size  $a_0$  and became dormant.

## FATIGUE 87

- 3) The interpretation of the stress-fatigue limit as a short crack threshold made it possible to describe the non-damaging and small notches. The condition for a notch (characterized by the stress concentration factor  $k_T$  and the notch radius  $\rho$ ) to be non-damaging in a metallic material (characterized by the critical short crack size  $a_0$ ) was found to be

$$(k_T^2 - 1)\rho \leq 4.5 a_0 .$$

The notched fatigue limit is given by

$$\sigma_{cn} = \frac{\sigma_c}{k_T} \sqrt{1 + 4.5(a_0/\rho)} .$$

The critical short crack size  $a_0$  is related to the short crack stress intensity threshold and to the plain fatigue limit. These relations were experimentally verified on pressure vessel steel 2.25Cr/1Mo.

### SYMBOLS USED

- $D$  = grain size  
 $\sigma_a$  = stress amplitude  
 $\epsilon_{ap}$  = plastic strain amplitude  
 $\sigma_c$  = plain fatigue limit  
 $\sigma_{cn}$  = notch fatigue limit  
 $K_a$  = stress intensity factor amplitude

### REFERENCES

- (1) Horibe, S., Lee, J.K. and Laird, C., Fatigue Eng. Mater. Struct., Vol.7, 1984, pp.145-154.  
(2) Boutin, J., Marchand, N., Bailon, J.P. and Dickson, J.I., Mater.Sci.Eng., Vol.67, 1984, pp. L23-L27.  
(3) Lukáš, P. and Klesnil, M., Mater.Sci.Eng., Vol.11, 1973, pp.345-356.  
(4) Wang, R., Doctorate Thesis, Stuttgart University, 1982.  
(5) Polák, J. and Klesnil, M., Mater.Sci.Eng., Vol.63, 1984, pp.189-196.

- (6) Kuokkala, V.T. and Kettunen, P., *Fatigue Fract. Eng. Mater. Struct.*, Vol.8, 1985, pp.277-285.
- (7) Cheng, A.S. and Laird, C., *Mater. Sci. Eng.*, Vol. 51, 1981, pp.55-60.
- (8) Gerold, V., Lerch, B.A. and Steiner, D., *Z. Metallkd.*, Vol.75, 1984, pp.546-553.
- (9) Lukáš, P. and Klesnil, M., "Fatigue damage and resultant dislocation structures", *Proc. 2nd Int. Conf. on Corrosion Fatigue*, Edited by A.J. McEvily et al, NACE, Houston, TX, 1972, pp.118-132.
- (10) Laird, C. and Buchinger, L., *Metall. Trans. A*, Vol.16A, 1985, pp.2201-2214.
- (11) Pratt, J.E., *Acta Metall.*, Vol.15, 1967, pp. 319-327.
- (12) Basinski, Z.S., Korbelt, A.S. and Basinski, S.J., *Acta Metall.*, Vol.28, 1980, pp.191-207.
- (13) Thompson, A.W. and Backofen, W.A., *Acta Metall.*, Vol.19, 1971, 597-606.
- (14) Lukáš, P., "Models for  $K_{th}$  and near-threshold fatigue crack growth", *Fatigue 84, Proc. 2nd Int. Conf. on Fatigue and Fatigue Thresholds*, Edited by C.J. Beevers, EMAS, Warley, 1984, Vol.1, pp.479-496.
- (15) Müllner, H., Weiss, B., Stickler, R., Lukáš, P. and Kurz, L., "The effect of grain size and test frequency on the fatigue behaviour of polycrystalline copper", *Fatigue 84, Proc. 2nd Int. Conf. on Fatigue and Fatigue Thresholds*, Edited by C.J. Beevers, EMAS, Warley, 1984, Vol.1, pp.423-434.
- (16) James, M.N. and Smith, G.C., *Res. Mechanics*, Vol.9, 1983, pp.129-136.
- (17) Lukáš, P., *Eng. Fract. Mech.*, 1986, in print.
- (18) Peterson, R.E., "Stress Concentration Factors", John Wiley and Sons, New York, 1969.

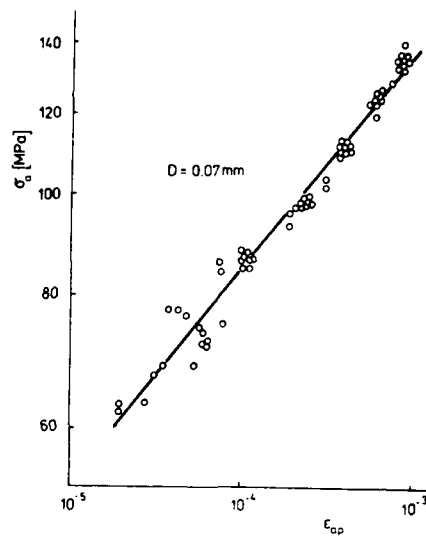


Figure 1 CSSC of fine-grained specimens

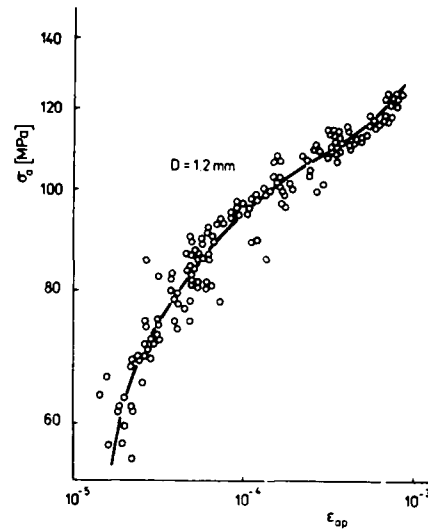


Figure 2 CSSC of coarse-grained specimens

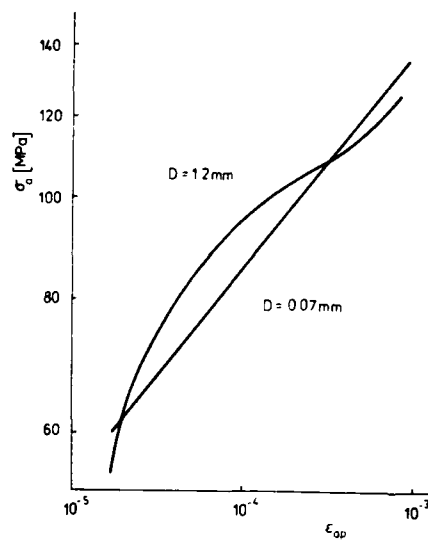


Figure 3 CSSCs for both grain sizes

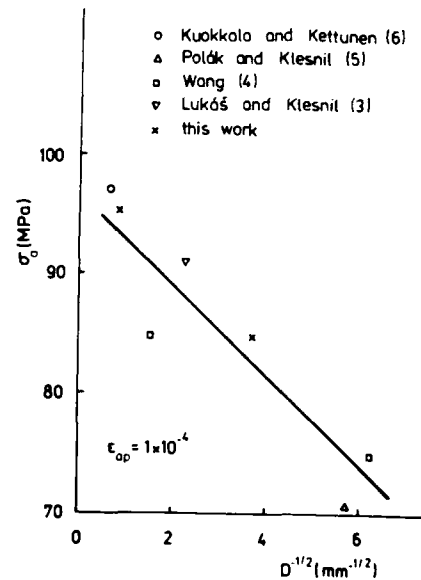


Figure 4 Saturation stress vs. grain size

# FATIGUE 87

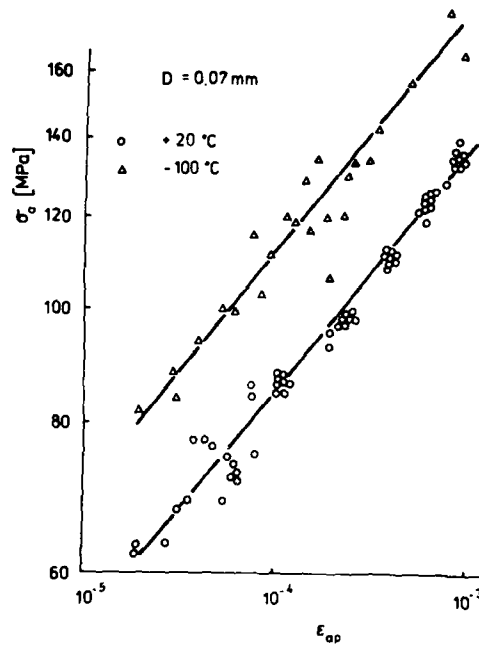


Figure 5 Effect of temperature on CSSCs

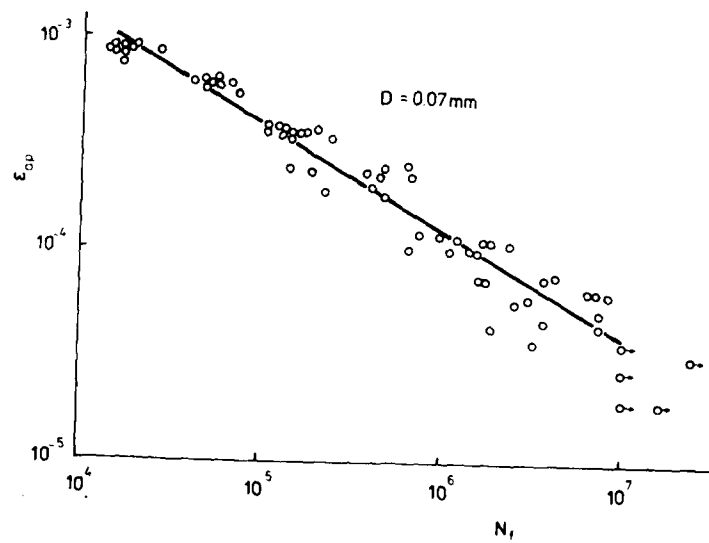


Figure 6 Coffin-Manson plot for fine-grained specimens

# FATIGUE 87

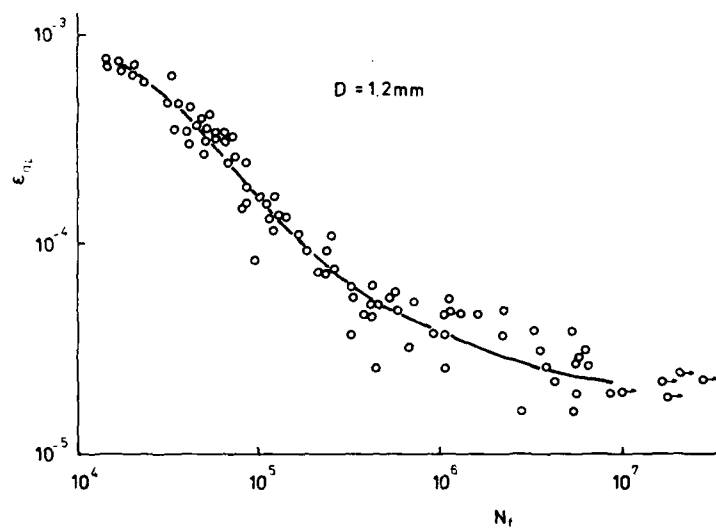


Figure 7 Coffin-Manson plot for coarse-grained specimens

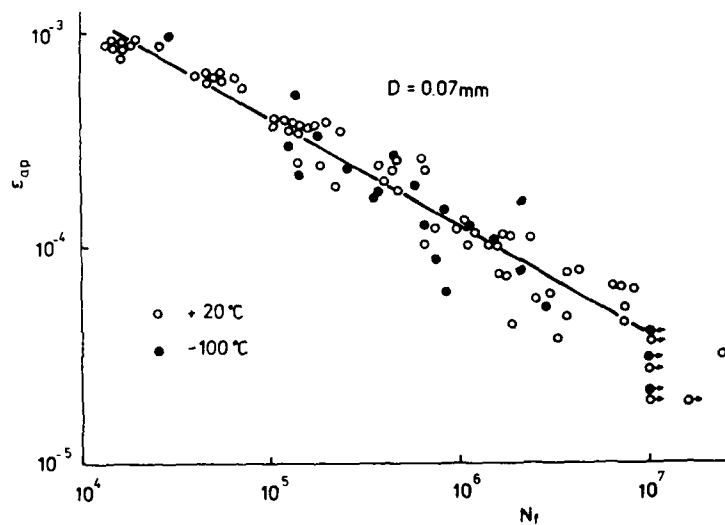


Figure 8 Effect of temperature on Coffin-Manson plot

# FATIGUE 87

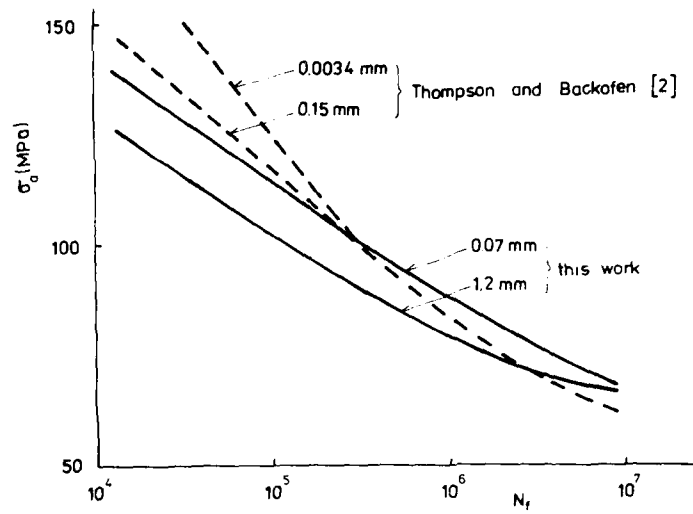


Figure 9 S/N curves for different grain sizes

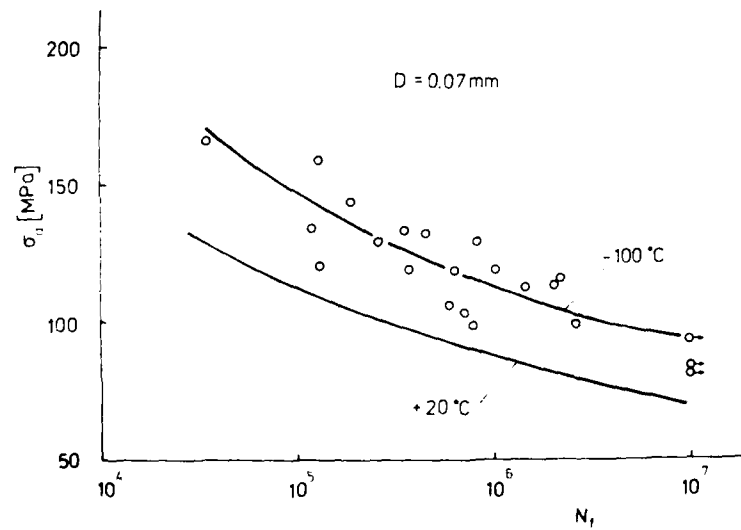


Figure 10 Effect of temperature on S/N curves

# FATIGUE 87

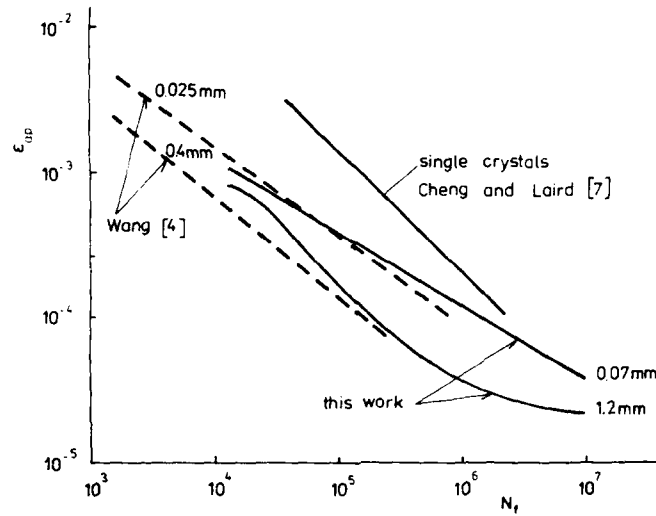


Figure 11 Coffin-Manson plots for single crystals and for polycrystals

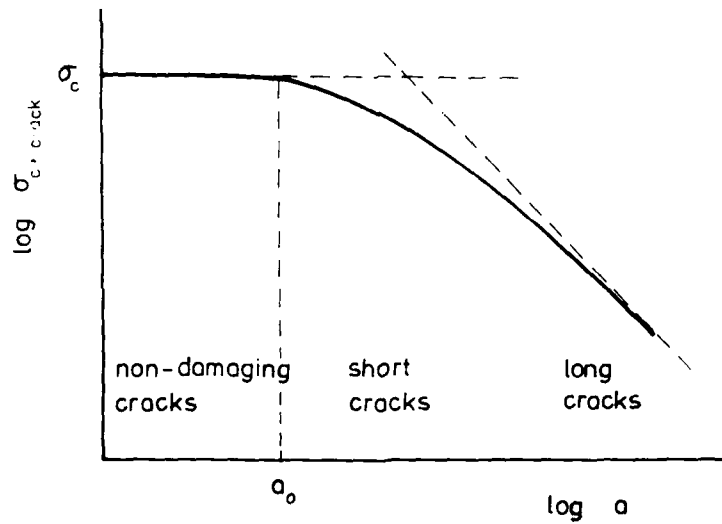


Figure 12 Dependence of fatigue limit on crack size (Kitagawa plot)

# FATIGUE 87

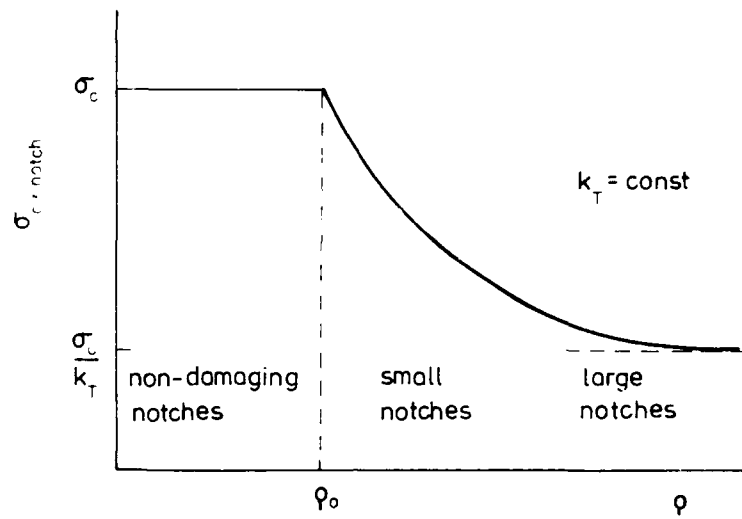


Figure 13 Dependence of fatigue limit on notch size

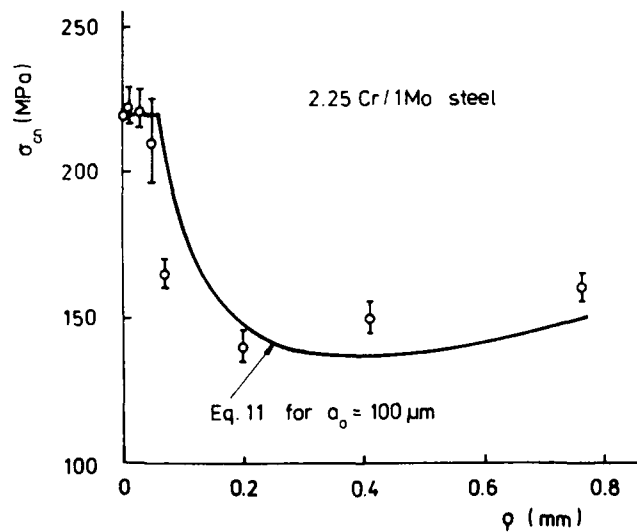


Figure 14 Experimentally determined dependence of fatigue limit on notch radius

NOTCH-GEOMETRY EFFECT ON PROPAGATION THRESHOLD OF SHORT FATIGUE  
CRACKS IN NOTCHED COMPONENTS

K. Tanaka\* and Y. Akiniwa\*

A consistent method was proposed to predict the fatigue threshold of notched components by combining crack closure with the micromechanical criterion for crack growth. The predictions of the effects of notch-tip radius and notch depth on the propagation threshold of short fatigue cracks were compared with the experimental results obtained with notched specimens of low-carbon steels. Good agreement was found between predictions and experiments.

INTRODUCTION

The reduction of fatigue strength due to notches is a classical problem for fatigue engineers. The growth rate of a small fatigue crack nucleated at the tip of a sharp notch first decreases as the crack propagates. The crack then becomes non-propagating under low stresses, while it begins to accelerate after reaching a minimum growth rate under high stresses. Since the stress intensity factor (SIF) is an increasing function of the crack length,  $\Delta K$ -based conventional fracture mechanics fails to predict a dip in the growth rate of a crack at notches. An increasing body of experimental data showed that the effective stress intensity range  $\Delta K_{eff}$  decreased with crack growth because of the increase of crack closure, and that the growth rate was uniquely related to  $\Delta K_{eff}$  irrespective of crack length or stress amplitude (Tanaka (1), Nishikawa (2), Akiniwa (3,4)).

In the present paper, the development of crack closure for a short crack emanating from the notch root was modeled, and a consistent method was proposed to predict the fatigue threshold of

\* Department of Engineering Science, Kyoto University,  
Kyoto 606, Japan

notched components by combining crack closure with the micro-mechanical criterion for crack growth. The predictions of the effects of notch-tip radius and notch depth on the propagation threshold of short fatigue cracks were compared with the experimental results obtained with notched specimens of low-carbon steels.

#### MODEL FOR PREDICTING NOTCH FATIGUE THRESHOLD

A consistent model for predicting the fatigue threshold of notched components, which was first proposed by Tanaka and Nakai (5,6) and was later modified by Tanaka and Akiniwa (7), requires three experimental data of materials: the fatigue limit of smooth specimens,  $\Delta\sigma_{w0}$ , the threshold stress intensity range for a long crack,  $\Delta K_{th\infty}$ , and the effective stress intensity range at the threshold for a long crack,  $\Delta K_{effth\infty}$ . A brief description of the model is given below for the case of the stress ratio  $R=-1$ .

The total range of the stress intensity factor (SIF),  $\Delta K$ , for a crack of length  $c$  formed at the notch tip can be expressed as

$$\Delta K = \Delta\sigma\sqrt{\pi c} F(c) \quad (1)$$

where  $\Delta\sigma = \sigma_{\max} - \sigma_{\min} = 2\sigma_{\max}$  ( $\sigma_{\max}$ =the applied maximum nominal stress,  $\sigma_{\min}$ =the applied minimum nominal stress), and  $F(c)$  is the geometrical correction factor. The effective stress intensity range  $\Delta K_{eff}$  is defined by

$$\Delta K_{eff} = K_{\max} - K_{op} \quad (2)$$

where  $K_{\max}$  is the maximum SIF value and  $K_{op}$  is the SIF value at crack opening. The effective fraction is given by

$$U = \Delta K_{eff} / \Delta K \quad (3)$$

Figure 1(a) illustrates a non-propagating crack of length  $c_{np}$  formed at a notch. When  $c_{np}$  diminishes to zero, we have the model for the threshold for crack initiation as shown in Fig.1(b). The length of an intrinsic crack  $c_o'$  is determined from the condition that the fatigue limit of smooth specimens is to be derived from the non-propagating criterion for an edge crack of length  $c_o'$  in a semi-infinite plate:

$$c_o' = (\Delta K_{effth\infty} / 1.122 \sigma_{w0})^2 / \pi \quad (4)$$

where  $\sigma_{w0} = \Delta\sigma_{w0} / 2$ . The crack propagation condition is given by the SIF range at the tip of a fictitious crack of length  $c_{np}$  plus  $c_o'$  equal to  $\Delta K_{effth\infty}$  as follows:

$$\Delta K_{effth\infty} = \Delta\sigma_{effth} [\pi (c_{np} + c_o')]^{1/2} F(c_{np} + c_o') \quad (5)$$

## FATIGUE 87

where  $\Delta\sigma_{\text{effth}}$  is the effective threshold stress range. The value of  $\Delta K_{\text{effth}}$  for small cracks at the notch root is calculated from  $\Delta\sigma_{\text{effth}}$  and  $c_{\text{np}}$  as  $\Delta K_{\text{effth}} = \Delta\sigma_{\text{effth}}(\pi c_{\text{np}})^{1/2} F(c_{\text{np}})$ . Then, we have

$$\frac{\Delta K_{\text{effth}}}{\Delta K_{\text{effth}\infty}} = \left( \frac{c_{\text{np}}}{c_{\text{np}} + c_o'} \right)^{1/2} \frac{F(c_{\text{np}})}{F(c_{\text{np}} + c_o')} \quad (6)$$

Tanaka and Akiniwa (7) assumed the following equation of the effective fraction for a short crack near the notch root at the threshold:

$$U_{\text{th}}/U_{\text{th}\infty} = [(c_{\text{np}} + c_o)/(c_{\text{np}} + c_o')]^{1/2} \quad (7)$$

where  $c_o$  is determined by

$$c_o = [(\Delta K_{\text{th}\infty}/2)/1.122 \sigma_{w0}]^2/\pi \quad (8)$$

and  $U_{\text{th}\infty} = \Delta K_{\text{effth}\infty}/\Delta K_{\text{th}\infty} = (1/2)(c_o'/c_o)^{1/2}$ .  $U_{\text{th}}$  is half at  $c_{\text{np}}=0$ , and decreases down to  $U_{\text{th}\infty}$  with increasing crack length.

The threshold stress intensity range,  $\Delta K_{\text{th}}$ , is given from eqs.(6) and (7) as

$$\frac{\Delta K_{\text{th}}}{\Delta K_{\text{th}\infty}} = \left( \frac{\Delta K_{\text{effth}}}{\Delta K_{\text{effth}\infty}} \right) / \left( \frac{U_{\text{th}}}{U_{\text{th}\infty}} \right) = \left\{ \frac{c_{\text{np}}}{c_{\text{np}} + c_o} \right\}^{1/2} \frac{F(c_{\text{np}})}{F(c_{\text{np}} + c_o')} \quad (9)$$

The corresponding stress range  $\Delta\sigma_{\text{th}}$  is calculated from  $\Delta K_{\text{th}}$  through

$$\begin{aligned} \Delta\sigma_{\text{th}} &= \Delta K_{\text{th}} / [(\pi c_{\text{np}})^{1/2} F(c_{\text{np}})] \\ &= \Delta K_{\text{th}\infty} / [\sqrt{\pi}(c_{\text{np}} + c_o)^{1/2} F(c_{\text{np}} + c_o')] \end{aligned} \quad (10)$$

The stress amplitude at the crack initiation threshold,  $\sigma_{w1}$ , is obtained by substituting  $c_{\text{np}}=0$  and  $\Delta\sigma_{\text{effth}}=\sigma_{w1}$  into eq.(5):

$$\begin{aligned} \sigma_{w1} &= \Delta K_{\text{effth}\infty} / [(\pi c_o')^{1/2} F(c_o')] \\ &= 1.122 \sigma_{w0} / F(c_o') \end{aligned} \quad (11)$$

where eq.(4) is used. The above equation can be derived by substituting  $c_{\text{np}}=0$  and  $\Delta\sigma_{\text{th}}=2\sigma_{w1}$  into eq.(10).

### EXPERIMENTAL PROCEDURE

The material is a structural low-carbon steel (JIS SM41B) with the following chemical compositions in weight %: 0.17C, 0.19Si, 0.79Mn, 0.016P and 0.020S. The specimens were fully annealed after machined. The ferrite grain size was 64 $\mu\text{m}$ . The yield strength was 194MPa and the breaking strength was 423MPa. The fatigue properties of this material was determined in our previous studies (Akiniwa (3)). Under  $R=-1$ , the values of  $\sigma_{w0}$ ,  $\Delta K_{\text{th}\infty}$ , and  $\Delta K_{\text{effth}\infty}$  were

## FATIGUE 87

163MPa,  $12.36\text{MPa}\sqrt{\text{m}}$ , and  $2.78\text{MPa}\sqrt{\text{m}}$ , respectively. From eqs.(4) and (8), the lengths  $c_0'$  and  $c_0$  are calculated as  $c_0'=74\mu\text{m}$  and  $c_0=364\mu\text{m}$ .

The shape and dimensions of test specimens are shown in Fig.2. The radius of the notch root is varied in center-notched plate (CNP) specimen, while the notch depth is varied in single-edge-notched (SEN) specimens. Center-notched plate specimens were fatigued under axial tension-compression; edge-notched specimens under in-plane bending. The elastic stress concentration factor  $K_t$  for CNP specimens given in Fig.2 was calculated from Ishida(8)'s formula, and that for SEN specimens was determined by the finite element method (Akiniwa (4)). All the specimens were fatigued at the constant load amplitude with zero mean stress.

The length of non-propagating cracks was measured with a scanning electron microscope by observing the fracture surface of the fatigued specimen broken at liquid nitrogen temperature. The measured length of a through-thickness crack was the average of nine measurements over the specimen thickness, while that for a part-through crack is an equivalent length of a through-thickness crack converted by using SIF-equality equation. The SIF value for a notch-tip crack in CNP specimens was calculated by using Lukas (9) equation combined with the equation for a center-cracked plate (Akiniwa (3)). The finite element method was used to obtain SIF for a crack in SEN specimens (Akiniwa (4)). For a part-through crack at the notch root, a modified Murakami(10)'s method was used for SIF calculation. The crack opening point was identified as an inflection point in stress-strain curves after subtracting the linear elastic part. The strain signal was the output of the strain gage glued on the notch as shown in Fig.2.

### CRACK CLOSURE AND THRESHOLD CONDITION OF SHORT CRACKS AT NOTCHES

A non-propagating fatigue crack which showed Stage II growth characteristics was formed in CNP specimens having the notch-tip radius  $\rho$  smaller than 0.83mm. In the case of  $\rho=3.0\text{mm}$ , only a small Stage I crack lying on the slip plane became non-propagating. Non-propagating cracks were detected in all types of SEN specimens. The length of non-propagating cracks varied depending on the notch size and the applied stress amplitude. For each non-propagating Stage II crack, the crack opening point was measured, and the threshold values of the SIF range,  $\Delta K_{th}$ , and the effective SIF range,  $\Delta K_{effth}$ , were determined.

Figure 3 shows the effects of notch-tip radius (in CNP specimens) and notch depth (in SEN specimens) on the changes in  $\Delta K_{th}$  and  $\Delta K_{effth}$  with crack length  $c_{np}$ . The curves drawn in the figures indicates the model prediction derived by using eqs.(6) and (9). With increasing crack length,  $\Delta K_{th}$  becomes larger, approaching to

$\Delta K_{th\infty}$ . The calculated value of  $\Delta K_{effth}$  is almost constant, equal to  $\Delta K_{effth\infty}$ , when the crack length is longer than 0.1mm. Differences of the calculated values of  $\Delta K_{th}$  and  $\Delta K_{effth}$  due to different radii appear only in very short-crack regime. The influences of the notch depth and the loading mode (axial loading *vis-a-vis* in-plane bending) on these values is relatively small. The experimental data were obtained only for non-propagating Stage II cracks longer than about 0.1mm. The data lie close to the predicted curves. The measured values of  $\Delta K_{th}$  and  $\Delta K_{effth}$  are almost identical for various notches as predicted theoretically. The  $\Delta K_{effth}$  values measured were nearly constant for all the cases tested.

In Fig.4, the effective fraction at the threshold  $U_{th}$  is plotted against  $c_{np}$ , where the solid line indicates eq.(7). The  $U_{th}$  values measured for SEN specimens are slightly larger than those for CNP specimens. The data roughly follow the theoretical prediction. Strictly speaking, the measured value at shorter crack lengths is larger than the prediction both for CNP and SEN specimens. This increase of  $U_{th}$ , or the decrease of the crack opening stress, is caused by the tensile residual stress due to notch plasticity (Tanaka (11)). The notch plasticity effect on crack closure should be included in the model for refinement.

#### FATIGUE THRESHOLD OF NOTCHED COMPONENTS

The relation between the threshold stress amplitude  $\sigma_{th}$  and the crack length  $c_{np}$  calculated by using eq.(10) for CNP specimens are shown with the solid lines in Fig.5(a). The relations obtained under the condition of  $\Delta K_{th} = \Delta K_{th\infty}$  for the case of  $\rho=0$  and  $t=3\text{mm}$  and for the case of  $\rho=0$  and  $t=0\text{mm}$  are also drawn with the dash-dotted line and the dashed line, respectively. For the cases of notch-tip radii smaller than 0.83mm,  $\sigma_{th}$  increases with increasing crack length, and then decreases after taking the maximum value. The  $\sigma_{th}$  value corresponding to zero crack length is the fatigue limit for crack initiation  $\sigma_{w1}$  and its maximum value is the fatigue limit for fracture  $\sigma_{w2}$ . Larger  $\rho$  values give higher  $\sigma_{w1}$  value, while  $\sigma_{w2}$  is constant. The notch-tip radius at which  $\sigma_{w1}$  becomes equal to  $\sigma_{w2}$  is calculated to be 1.63mm. When the applied stress amplitude  $\sigma_a$  is between  $\sigma_{w1}$  and  $\sigma_{w2}$ , a fatigue crack nucleates at the notch root and grows up to the non-propagating crack length given by the solid line. For the case of  $\rho=3\text{mm}$ ,  $\sigma_{w1}$  is larger than  $\sigma_{w2}$ , that is, any crack does not stop once initiated.

The experimental data of non-propagating crack lengths are plotted in Fig.5(a), where the open mark indicates a through-thickness crack, the open mark with a bar means a part-through Stage II crack, and the solid mark corresponds to a part-through Stage I crack. Agreement of the non-propagating crack lengths between prediction and experiment is good. The changes in  $\sigma_{w1}$  and  $\sigma_{w2}$  with the stress concentration factor  $K_t$  is given in Fig.5(b). The predicted

## FATIGUE 87

$\sigma_{w1}$  value agrees with the experimental result of the threshold stress for the nucleation of a Stage II crack. The prediction of  $\sigma_{w2}$  gives a conservative estimate for the experimental value. As seen in Fig.5(a), the prediction based on  $\Delta K_{th} = \Delta K_{th\infty}$  and  $\rho=0$  is dangerous, giving higher threshold stress amplitude.

Figure 6 shows the  $\sigma_{th}-\sigma_{np}$  relation for SEN specimens including the case of unnotched specimens ( $t=0, \rho=0\text{mm}$ ). In unnotched specimens, the present model becomes identical to the fictitious crack model proposed by Haddad et al.(12). The relation is given by

$$\sigma_{th} = \sigma_{w0} [1 + \sigma_{np}/\sigma_o]^{-1/2} \quad (12)$$

and is shown with the dash-dotted line in Fig.6. The  $\sigma_{th}$  value is close to  $\sigma_{w0}$  at short cracks, and decreases with crack length, approaching to the value given by the condition of  $\Delta K_{th} = \Delta K_{th\infty}$ . Equation (12) was confirmed to be a good estimate for a cracked specimen without a notch (Tanaka (13)). When  $t$  is not zero,  $\sigma_{w1}$  is lower than  $\sigma_{w2}$ . A non-propagating crack is formed when the applied stress amplitude is above  $\sigma_{w1}$  and below  $\sigma_{w2}$ . The non-propagating crack at  $\sigma_{w2}$  is smaller for the shallower notch. The experimental data plotted in the figure show that the predicted  $\sigma_{w1}$  is close to the experimental result and that an estimate of  $\sigma_{w2}$  is slightly conservative.

Figures 5 and 6 can be regarded as the fatigue failure diagram, with which we can judge the propagation, non-propagation or arrest of short fatigue cracks made at the notch root. The effects of the mean stress and load history on these failure diagrams are being studied in Kyoto University.

### CONCLUSIONS

(1) The measured value of the threshold SIF range,  $\Delta K_{th}$ , of short cracks at the notch root increased with increasing crack length, approaching to the  $\Delta K_{th\infty}$  value for a long crack. The threshold value of the effective SIF range  $\Delta K_{effth}$  was nearly constant for notch-tip cracks longer than about 0.1mm. The effective fraction,  $U_{th}$  ( $=\Delta K_{effth}/\Delta K_{th}$ ), decreased with increasing crack length. The changes in  $\Delta K_{th}$ ,  $\Delta K_{effth}$ , and  $U_{th}$  with crack length agreed fairly well with Tanaka-Nakai-Akiniwa's model.

(2) Both in the model and experiments, the length of the non-propagating crack and the  $\Delta K_{th}$  value at the fatigue limit for fracture were independent of the notch tip radius and increased with increasing notch depth. The predicted value of the fatigue limit for crack nucleation at the notch root agreed with the experimental value of the threshold stress for the nucleation of a Stage II crack. The prediction of the fatigue limit for fracture gave a conservative estimate for the experimental result.

## FATIGUE 87

### REFERENCES

- (1) Tanaka, K. and Nakai, Y., *Fatigue Eng. Mater. Struct.*, Vol.6, 1983, pp.315-327.
- (2) Nishikawa, I., Konishi, M., Miyoshi, Y. and Ogura, K., *J. Soci. Mater. Sci. Jpn*, Vol.35, 1986, pp.904-910.
- (3) Akiniwa, Y. and Tanaka, K., *Trans. JSME*, Paper No.86-0719A, 1986.
- (4) Akiniwa, Y. and Tanaka, K., *Trans. JSME*, Paper No.86-1247A, 1986.
- (5) Tanaka, K. and Nakai, Y., *Trans. ASME, J. Eng. Mater. Tech.*, Vol.106, 1984, pp.192-199.
- (6) Tanaka, K. and Nakai, Y., "Fatigue Crack Growth Threshold" Edited by D.L. Davidson and S. Suresh, *AIME*, 1984, pp.497-516.
- (7) Tanaka, K. and Akiniwa, Y., *Trans. JSME*, Paper No.86-0718A, 1986.
- (8) Ishida, M., *Trans. JSME*, Vol.21, 1955, pp.507-513.
- (9) Lukas, P. and Klesnil, M., *Mater. Sci. Eng.*, Vol.34, 1978, pp.61-66.
- (10) Murakami, Y., Tsuru, H. and Sakamoto, K., *J. Soci. Mater. Sci. Jpn*, Vol.35, 1986, pp.998-1003.
- (11) Tanaka, K. and Akiniwa, Y., *Trans. JSME*, Vol.52A, 1986, pp.1741-1748.
- (12) Haddad, M.H.El, Topper, T.H. and Smith, K.N., *Eng. Fract. Mech.*, Vol.11, 1979, pp.573-584.
- (13) Tanaka, K., Nakai, Y. and Yamashita, M., *Int. J. Fract.*, Vol.17, 1981, pp.519-533.

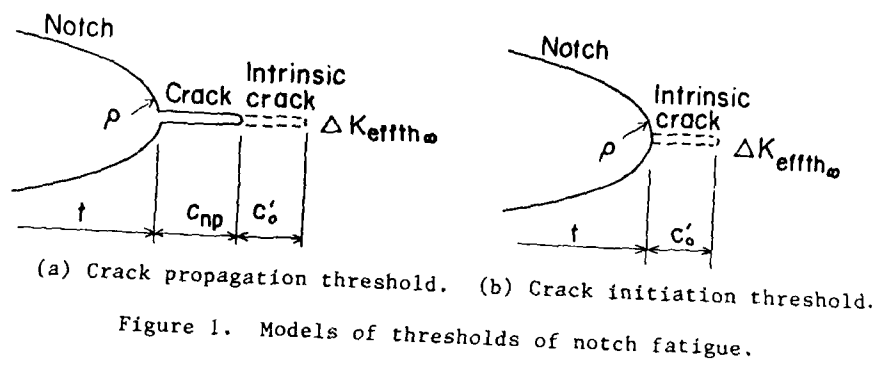


Figure 1. Models of thresholds of notch fatigue.

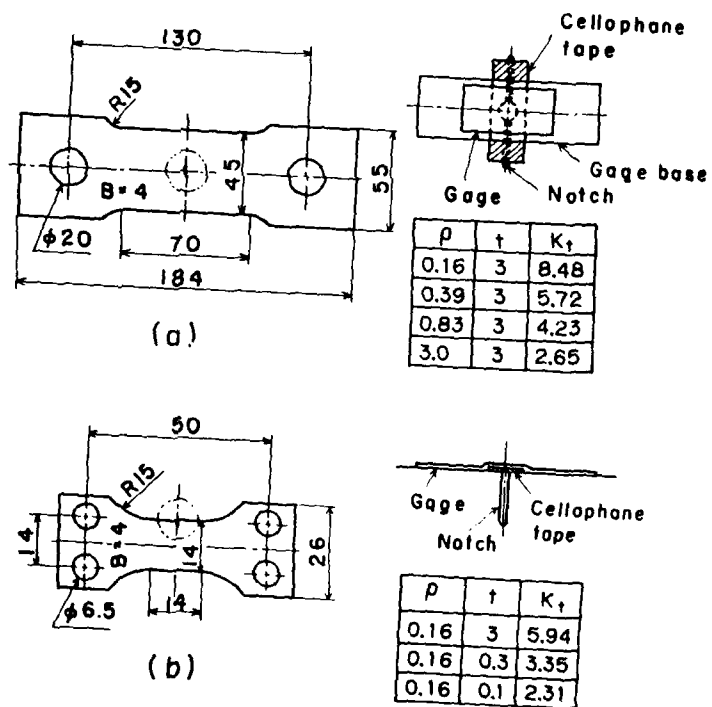
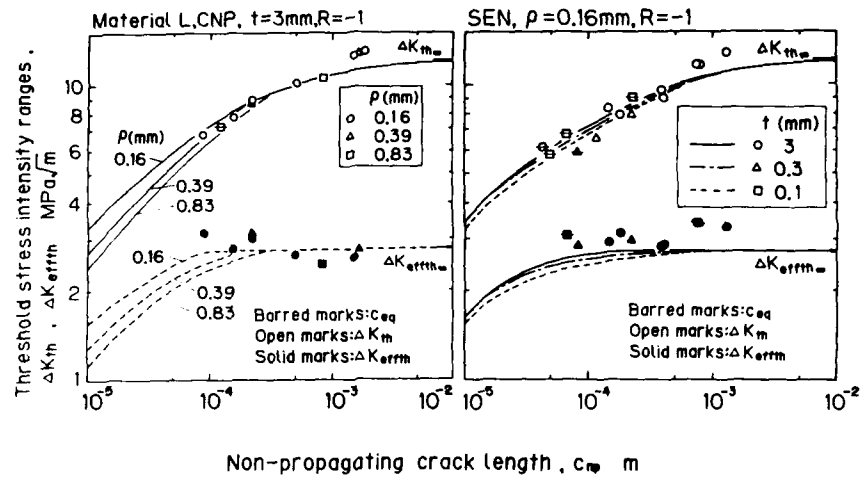


Figure 2. Test specimens. (a) Center-notched plate. (b) Single-edge-notched plate.



(a) Notch-tip-radius effect. (b) Notch-depth effect.  
Figure 3. Effect of notch geometry on the changes in  $\Delta K_{th}$  and  $\Delta K_{effth}$  with non-propagating crack length.

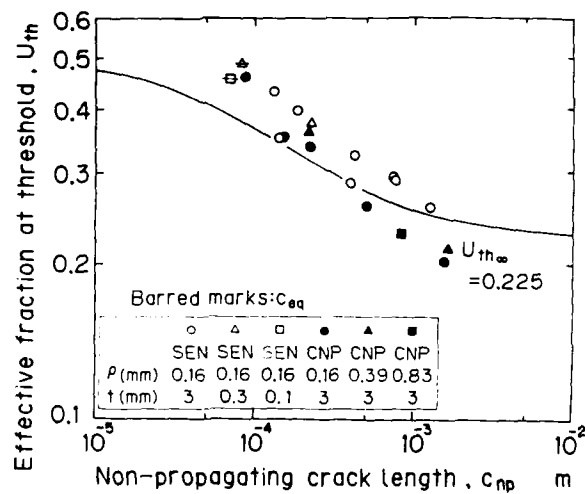


Figure 4. Relation between effective fraction and crack length at the threshold.

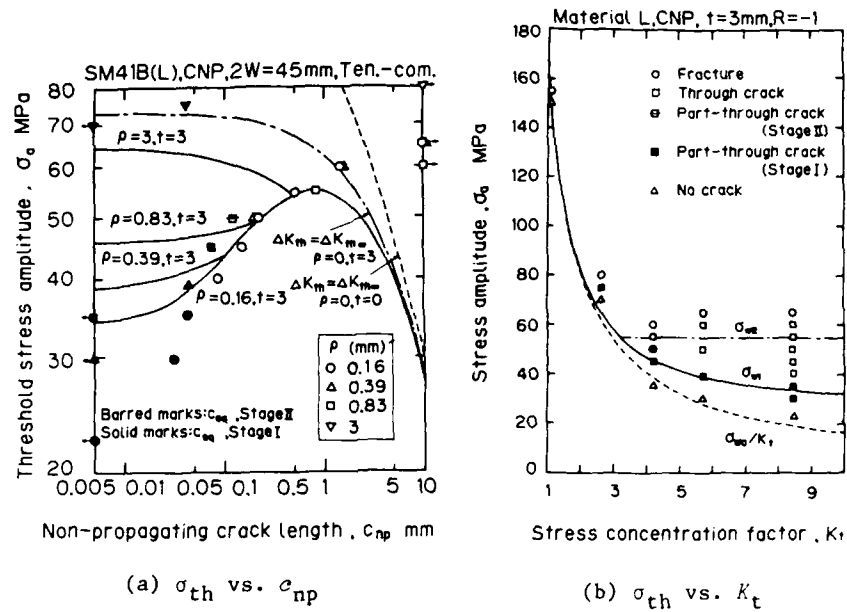


Figure 5. Effect of notch tip radius on threshold stress amplitude.

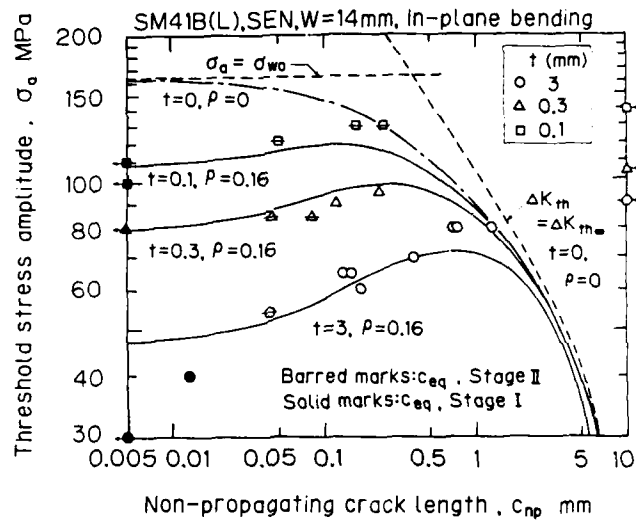


Figure 6. Effect of notch depth on the relation between the threshold stress amplitude and crack length.

## FATIGUE 87

### INFLUENCE OF CRACK CLOSURE ON FATIGUE CRACK PROPAGATION AND THRESHOLD

A. DIAS\*, A. BIGNONNET\*\* and H.P. LIEURADE\*\*

The effects of load ratio,  $R$  and test frequency upon closure response have been investigated for a wide range of materials.

The crack opening stress intensity factor,  $K_{op}$ , was evaluated as a function of  $\Delta K$ ,  $R$  and test frequency. It was found that at intermediate growth rate regime of the Paris plot,  $K_{op}$  is independent of  $\Delta K$ ,  $R$  and test frequency.

A conservative estimation of the threshold values from the crack opening stress intensity level :  
 $\Delta K_{th} = (1-R).K_{op}$  is possible.

### INTRODUCTION

Upon the crack closure mechanisms three main sources are usually considered : the plastic strains left in the wake of the crack, the fracture surface roughness and the oxidation or corrosion products left on the fracture surfaces. For materials which microstructure leads to a very rough crack path (large carbides or inclusions...) the fatigue growth occurs with a mixed mode (I + II) which enhances closure.

In this paper we analyse experimental closure data obtained with a large range of metallic materials in tests performed at  $R = 0$ . The influence of negative  $R$  ratio and environment were also investigated for 80C4 steel. The crack opening load was detected for all tests using the elastic compliance method. The crack closure effect was evaluated as a function of  $\Delta K$ ,  $R$  and test frequency.

Furthermore, attempts were made to correlate the threshold value ( $K_{max(th)}$ ) with  $K_{op}$  measurements in the linear regime of the Paris plot.

\* Université de Coimbra, Engenharia Mecânica. 3000 Coimbra (PORTUGAL)

\*\* IRSID Saint-Germain-en-Laye (FRANCE)

## FATIGUE 87

### MATERIALS

A wide range of steels, one Al-alloy, one  $\alpha$ -brass and one white cast iron have been investigated. Chemical composition and mechanical properties are listed in Table 1.

TABLE 1 - Chemical analysis, heat treatment and mechanical properties of the materials at ambient temperature

Material	Heat Treatment	Chemical composition (weight %)						Mechanical properties		
		C	Mn	Si	Ni	Cr	Mo	$\sigma_{ys}$ (MPa)	UTS (MPa)	%
<u>Steels</u>										
E 36 Z	Annealed	0.145	1.40	0.29	0.42	0.075	0.031	380	555	33
E 550	Quench-and Temp. 625°	0.145	1.41	0.36				640	720	20
Rail gr. 70		0.481	1.10	0.26	0.044	0.028		406	766	20
Rail gr. 90		0.622	1.39	0.33	0.043	0.021		489	928	14.4
35NCD16 (A)		0.36	0.23	0.34	3.98	2.05	0.43	630	1040	13.6
35NCD16 (B)	Q + T. 200	-	-	-	-	-	-	1515	1915	9
35CD4	Q + T. 500	0.35	0.67	0.21		0.91	0.21	1180	1270	12.9
80C4	Q + T. 500	0.80	0.8	0.4	0.7	1.0	0.3	860	1200	14
160C4	Annealed	1.6	1.3	0.4	0.7	1.2	0.3	470	500	1
White cast Iron	Q + T.	2.9	0.8	0.6	0.64	19.6	1.5	480	480	0
<u>Iron</u>										
		Cu	Mg	Mn	Fe					
<u>Al-Alloy</u>										
Al-Cu 2024	T 351	4.81	1.51	0.7	0.014			319	458	21.9
<u>Brass</u>										
		Zn	Pb	Mn	Fe					
<u>Brass</u>										
$\alpha$ -brass 70-30	Annealed 450°	28.88	0.007	0.006				103	330	66

### EXPERIMENTAL PROCEDURES

Crack growth tests were conducted in laboratory air and vacuum using constant amplitude loading, with different R values and frequencies ( $R = -1$  to  $0.7$  and  $f = 5-65$  Hz). Three point bending and CT specimens were used.

Crack opening measurements were performed using a crack mouth displacement gauge or back face strain gauges. The load-displacement (or load-back face strain) signals were recorded either conventionally by reducing the test frequency to  $f = 0.1$  Hz, or at the test frequency by using a digital storage oscilloscope with a 16 K word (16 bit), buffer memory. To ensure high accuracy a light clip-on gauge (operating frequency up to 200 Hz) or 350 back face

# FATIGUE 87

strain gauges in a full bridge were used. To get an accurate detection of the opening load, an offset system was used.

The determination of the  $\Delta K$  threshold was made in this study by the decreasing  $\Delta K$  technique.  $\Delta K$  was reduced slowly so that  $dK/da \approx 1 \text{ MPa}\sqrt{\text{m/mm}}$  and  $(1/\Delta K)$ .  $(dK/da) \approx 0.1 \text{ mm}$  until a growth rate less than  $10^{-10} \text{ m/c}$  was reached.  $\Delta K_{th}$  was taken, as the value of  $\Delta K$  at which  $da/dN = 10^{-10} \text{ m/c}$ .

## RESULTS AND DISCUSSION

### Crack closure in linear regime of Paris plot

Experimental data are presented in figure 1 for three different materials : 35 NCD16, 2024 T351 and 160 C4. This figure shows the variation of  $K_{op}$  with  $\Delta K$  :  $K_{op}$  is roughly independent of both  $\Delta K$  and  $R$ . All the materials studied have shown similar behaviour and a detailed list of  $K_{op}$  values is given in Table 2. These results point out the influence of the environment on crack closure. For the 80C4 steel, crack closure is enhanced under vacuum. This is in agreement with other works on the influence of the environment on crack closure and on the plastic zone size (1, 2). Figure 2 shows the variation of the effective stress intensity range ratio,  $U = \Delta K_{eff} / \Delta K$ , as a function of  $\Delta K$  for different  $R$  ratios.

TABLE 2 - Crack opening stress intensity factor value in air for various materials in different experimental conditions

Material	Test frequency (Hz)	$K_{op} \text{ (MPa}\sqrt{\text{m}})$				$\bar{K}_{op}$ (MPa $\sqrt{\text{m}}$ )
		R=0.1	R=0.2	R=0.3	R=0.5	
E 36 Z	40	$4.6^{+0.6}$				$4.6^{+0.6}$
E 550	65	$4.1^{+0.3}$				$4.1^{+0.1}$
35 NCD 16 (A)	40	$6.9^{+0.6}$	$6.9^{+0.5}$	$7.4^{+0.3}$	$7.3^{+0.3}$	$7.2^{+0.5}$
35 NCD 16 (B)	40	$2.9^{+0.6}$	$2.9^{+0.2}$	2.9		$2.9^{+0.6}$
35 CD4	40	$3.4^{+0.6}$	$3^{+0.5}$			$3.2^{+0.8}$
Rail gr. 70	40	$6.3^{+0.8}$				$6.3^{+0.8}$
Rail gr. 90	40	$6.1^{+0.7}$				$6.1^{+0.7}$
	30	$3.6^{+0.6}$				$3.6^{+0.6}$
80 C4	5	$3.5^{+0.5}$				
	30	$11.2^{+1}$			$10.7^{+0.5}$	$11^{+1}$
160 C4	5	$11^{+0.7}$				
2024 T 351	30	$3.8^{+0.2}$		$4^{+0.2}$		$3.9^{+0.3}$
$\alpha$ -brass 70-30	30	$4.1^{+0.3}$		$4^{+0.2}$		$4.1^{+0.3}$
White cast iron	30	$6.2^{+0.8}$				$6.2^{+0.8}$

The experimental results fit a simple relationship :

$$U = \frac{\Delta K_{eff}}{\Delta K} = \frac{K_{max} - K_{op}}{\Delta K} = \left[ \frac{\Delta K}{1-R} - K_{op} \right] \cdot \frac{1}{\Delta K}$$

i.e.  $U = \frac{1}{1-R} - \frac{K_{op}}{\Delta K}$  with  $K_{op} = \text{constant [1]}$

The curves calculated from equation [1] are plotted in figure 2. It should be pointed out that the variation of  $U$  predicted by equation [1] reflects rather well the fact that usually no closure is detected for high  $R$  ratio or high  $\Delta K$ . For high  $R$  ratios, closure can exist only for very low  $\Delta K$ .

#### Crack closure at low fatigue crack growth rate

Two steels, 80 C4 and 160 C4, of composition and properties listed in Table 1, with very different fracture surface morphology (see table 3) were chosen in order to investigate the relative influence of the two closure mechanisms. The results obtained are shown in figures 3 and 1-C where opening stress intensity factors,  $K_{op}$ , are plotted versus stress intensity range,  $\Delta K$ .

For steel 80 C4 tested in air, figure 3,  $K_{op}$  remains roughly constant for high  $\Delta K$  values and the two different test frequencies (0.2 Hz and 30 Hz). Below a  $\Delta K$  of 12 MPa $\sqrt{m}$  the closure behaviour depends on test frequency : at low frequency test (5 Hz)  $K_{op}$  follows the results obtained at high  $\Delta K$  level ; for higher frequency (30 Hz)  $K_{op}$  does not follow this trend but begins to increase for  $\Delta K$  values smaller than 12 MPa $\sqrt{m}$ . This latter behaviour is in close agreement with the oxide induced closure (14, 15) model and the test frequency dependent fracture surface oxide thickening observed by Bignonnet and al. (3). Figure 4 shows the difference of oxidation on the fracture surface in areas corresponding to tests at  $f = 30$  Hz and those at  $f = 5$  Hz. Fractographic observations on the fracture surfaces of the specimens tested in air suggest that the difference of crack closure between the threshold region and the Paris law region are related to the wedge effect by oxide debris but also to the increase of the surface roughness associated with an intergranular fracture mode (6). From table 1 and 2 it can be observed that materials with the rougher fracture surface have the higher levels of closure and threshold. For steel 80 C4, in air at  $R = 0.5$ , the crack is fully open for stress intensity ranges above 5 MPa $\sqrt{m}$ . Below this value, which is near to the threshold, crack closure occurs with a  $K_{op}$  level higher than the characteristic one, found in the Paris region at  $R = 0.1$  (see figure 3). This increase in closure level is induced by fretting oxides build up when  $K_{min}$  became lower than the characteristic  $K_{op}$ . In vacuum  $K_{op}$  remains constant but with a greater value : as shown figure 3, although no oxide was observed on the fracture surface.

As a consequence of the variation of the crack closure behaviour, fatigue threshold values change in the same way as  $K_{op}$ .

# FATIGUE 87

Table 3 shows the values of  $K_{op}$ ,  $K_{op(th)}$ ,  $K_{max(th)}$  and fracture surface roughness for the different test conditions. The  $K_{op(th)}$  values are very close to the  $K_{max(th)}$  values and differences between these values and  $K_{op}$ , measured in the linear region of Paris plot, are due to wedge effect of corrosion deposit as discussed above.

For steel 160 C4, a high value of  $K_{op}$  was found independent of R, K and test frequency, even for near threshold level (figure 1-C).  $K_{op}$ ,  $K_{op(th)}$ ,  $K_{max(th)}$  and the fracture surface roughness are listed in table 3. The values of  $K_{op}$ ,  $K_{op(th)}$  and  $K_{max}$  are very close for all test conditions. This behaviour can be related to the marked roughness of the fracture surface which dominates the crack closure. In this case, the influence of oxide-induced closure is negligible in comparison with roughness-induced closure, although oxide debris also exist on the fracture surface.

From these considerations,  $K_{op}$  at low fatigue crack growth rate depends on the fracture surface roughness of the material and the test frequency, as well as test environment and load ratio. According, the fatigue threshold value also depends on the same parameters (16).

TABLE 3 - Comparaision between  $K_{op}$ ,  $K_{op\ th}$  and  $K_{max\ th}$ .

Material	Freq. (Hz)	Env.	R	$K_{op}$ (MPa/m)	$K_{op(th)}$ (MPa/m)	$K_{max(th)}$ (MPa/m)	$\Delta K_{effth}$ (MPa/m)	Ra ( $\mu m$ )
Rail gr.70	40	air	0,1	$6.3^{+0.8}$		8		
Rail gr.90	40	air	0,1	$6.1^{+0.7}$		8		
80 C4	30	Vacuum	0,1	$7.2^{+0.5}$		10		1.9
80 C4	30	air	0,1	$3.6^{+0.6}$	$6^{+1}$	8.4	$2.4^{+1}$	5
80 C4	5	air	0,1	$3.6^{+0.6}$	$3.5^{+0.5}$	5.7	$2.2^{+0.5}$	2.5
80 C4	30	air	0,5		$6^{+0.5}$	8	$2^{+0.5}$	4.5
160 C4	30	air	0,1	$11^{+1}$	$11.2^{+1}$	12.2	$1^{+1}$	25
160 C4	5	air	0,1	$11^{+1}$	$11^{+0.7}$	12.2	$1.2^{+0.7}$	25
160 C4	30	air	0,5	$10.7^{+0.5}$		12.4	$1.7^{+0.5}$	25
2024 T351	30	air	0,1	$3.8^{+0.2}$		4.4		
brass70-30	30	air	0,1	$4.1^{+0.3}$		4.7		

In summary :

- $K_{op}$  and  $K_{max(th)}$  are remarkably sensitive to environment and test frequency when closure is oxide-induced ;
- $K_{op}$  and  $K_{max(th)}$  do not depend on R ratio or test frequency when closure is roughness-induced.

## FATIGUE 87

It is evident that in the case of oxide-induced closure the increase of  $K_{op}$  created by oxide deposits invalidates equation [1] (see figure 5).

The good agreement between  $K_{op}$  at threshold and  $K_{max(th)}$  confirm earlier results from Mc Evily and Minakawa (4) who suggest that the two concepts are very closed, and that the threshold dependence on R ratio results from closure. Similar observations were made Blom (5) for 2024 aluminium alloy and 17-4 stainless steel.

The different behavior at threshold between 80 C4 and 160 C4 has to be pointed out. With 160 C4 steel a very sharp knee is observed around  $da/dN \approx 10^{-9} m/c$  in the crack growth curve. So far the threshold is well defined. Whilst  $\Delta K_{th}$  is at rather high level ( $\approx 11 MPa\sqrt{m}$ ) the strong closure due to the roughness gives a very low  $\Delta K_{eff th}$  (0-1  $MPa\sqrt{m}$ ). For 80 C4 steel there is a progressive change of slope in the crack growth curve due to a gradual increase of the closure level caused by fretting oxidation on the fracture surfaces. Therefore threshold is not well defined and is influenced, by several parameters such as environment, frequency (cf table 3). Nevertheless this is more or less taken into account by closure and  $\Delta K_{eff(th)} \approx 2 MPa\sqrt{m}$  appear to be roughly independent of testing conditions (R, environment, frequency).

### USE OF $K_{op}$ AS A LOWER BOUND OF THE THRESHOLD VALUE

The fatigue crack growth threshold may be interpreted in terms of fatigue crack closure. The idea of the to interpret of fatigue threshold by a crack closure concept was first suggested by Schmidt and Paris (7). This model suggests that the stress intensity for crack closure,  $K_{op}$ , is constant and  $\Delta K$  must exceed a limiting value above  $K_{op}$ , insensitive to stress ratio variation, to cause crack growth. Afterwards, several studies were made in order to evaluate the effective stress intensity range at the threshold,  $\Delta K_{eff(th)}$  (3, 8, 9, 10).

In summary, it is generally accepted that in the near-threshold region the crack remains closed over most of the load cycle, but an objective understanding of  $\Delta K_{eff(th)}$  is not yet available.

In spite of the uncertainties about  $\Delta K_{eff(th)}$ , it seems reasonable to consider that  $\Delta K_{eff}$  approaches zero at threshold. In such an analysis, we can use equation [1]:

$$U = \frac{\Delta K_{eff}}{\Delta K} = \frac{1}{1-R} - \frac{K_{op}}{\Delta K} = 0 \quad \text{at} \quad \Delta K = \Delta K_{th}$$

i.e.  $\Delta K_{th} = (1-R) \cdot K_{op} \quad \text{or} \quad K_{max(th)} = K_{op}$

As shown above,  $K_{op}$  (measured in the linear region of the Paris plot) is constant and independent of R. Figure 6 illustrates this hypothesis and shows why  $K_{op}$  can be taken as an estimate of  $K_{max(th)}$ .

## FATIGUE 87

Table 3 gives a comparison between  $K_{op}$  measured in the linear regime of the Paris plot and  $K_{max(th)}$  for some of the materials studied. As discussed above, when oxide-induced closure is significant, the effect of an oxide deposit build up at low fatigue crack growth rates cannot be estimated from  $K_{op}$  data measured for growth rates well above threshold. Figure 7 shows the expected behaviour of  $K_{op}$  for oxide-induced closure. In this case, the threshold  $\Delta K_{th}$  estimate from equation [2] must then be interpreted as a lower bound.

The crack closure behavior proposed, allows to justify empirical relationships taking into account the influence of R ratio, for instance the Klesnil and Lukas relation (11)  $\Delta K_{th} = (1-R)Y \cdot \Delta K_o$ .  $\Delta K_o$  being the threshold value at  $R = 0$  and  $\gamma = 1$ .

Equation [2],  $\Delta K_{th} = (1-R) \cdot K_{op}$  can be compared with the other relation proposed by Masounave and Bailon (12)  $\Delta K_{th} = (1-R) \cdot K_{max(th)}$  where  $K_{max(th)}$  is an intrinsic characteristic of the material, independant of R.

Equation [2] also agrees with results of other authors (7, 13) who have shown that for a given material the maximum threshold stress intensity factor ( $K_{max(th)}$ ), under constant amplitude loading, is nearly constant over a large range of R ratio.

In case of significant influence of oxide induced closure, threshold would be estimated by  $\Delta K_{th} = \beta \cdot K_{op} (1-R)$  with  $\beta$  being the parameter which takes into account the oxide induced closure at threshold and depends on environment and frequency,  $K_{op}$  is the constant value of crack opening measured in the Paris region.

### CONCLUSION

Fatigue crack propagation in wide range of alloys has been studied in a moist air environment for different R ratio and test frequencies. Crack closure was monitored in all tests using the elastic compliance method, from which the following conclusions may be drawn :

- in the linear region of the Paris plot

- .  $K_{op}$  is roughly constant, independent of  $\Delta K$ , R and test frequency ;

- . the variation of  $U = \frac{\Delta K_{eff}}{\Delta K}$  can be described by the equation:

$$U = \frac{1}{1-R} - \frac{K_{op}}{\Delta K} \text{ with } K_{op} = \text{constant}$$

This equation accounts well for the influence of R and  $\Delta K$  on crack closure.

## FATIGUE 87

- at low fatigue crack growth rate
  - .  $K_{op}$  data are found consistent with either oxide-induced closure or roughness-induced closure, depending on the material ;
  - .  $\Delta K_{th}$  and  $K_{op}$  are sensitive to test frequency when oxide-induced closure dominates ;
  - . if roughness-induced closure dominates,  $K_{op}$  and  $\Delta K_{th}$  are independent of R and test frequency.
- a comparison between fatigue crack growth threshold and crack closure data has allowed a conservative estimate of  $\Delta K_{th}$  :

$$\Delta K_{th} \approx (1-R) \cdot K_{op} \text{ with } K_{op} = \text{constant}$$

where  $K_{op}$  is the crack opening stress intensity factor measured in the Paris regime.

Acknowledgments. The authors thank Dr. J. Petit who had performed fatigue test under vacuum .

### REFERENCES

- (1) D.L. Davidson, J. Lankford. ICF4, Waterloo, 1977.
- (2) M.C. Lafarie-Frenoit, J. Petit, C. Gasc. Fatigue of Eng. Mat. and Struct (1979), Vol. 1, pp. 432-438.
- (3) A. Bignonnet, D. Loison, R. Namdar, B. Bouchet, J.H. Kwon, J. Petit, "Fatigue crack growth Threshold concepts, Ed. Suresh, Davidson, AIME, 1984, pp. 99-113.
- (4) A.J. Mc Evily, K. Minkawa, Ibid, p. 517-530.
- (5) A.F. Blom, Ibid, pp. 263-279.
- (6) A. Morao, Dias, Thesis Dr. es Sciences Phys. Un. Paris-Sud 1985.
- (7) R.A. Schmidt, P.C. Paris, ASTM STP 536, 1973, p. 79-94.
- (8) M. Kikuwa, M. Jono, K. Tanaka. ICM2, Boston (1976).
- (9) K. Minakawa, A.J. Mc Evily. Fatigue Threshold (1982), Ed. Backlund, Blom, Beevers, EMAS, pp. 373-390.
- (10) G. M. Lin and M.E. Fine. Scripta Met. (1982), 16, pp. 1249-1254.
- (11) M. Klesnil, L. Lukas. Mat. Sc. Eng. (1972), 9, p. 231.
- (12) J. Masounave, J.P. Bailon. Scripta met (1975), 9, p. 723-730.
- (13) R.J. Cooke, C.J. Beevers, Mat. Sc. Eng. (1974), 13, p. 201-210
- (14) D.Benoit, R. Namdar-Irani, R. Tixier. Mat. Sc. Eng. (1980), 45, p. 1-7.
- (15) S. Suresh, G.F. Zamiski, R.O. Ritchie. Met. Trans. 12A (1981), p. 1435-1443.
- (16) A. Bignonnet, A. Dias, H.-P. Lieurade. ICF 6 (1984), p. 1861-1868.

# FATIGUE 87

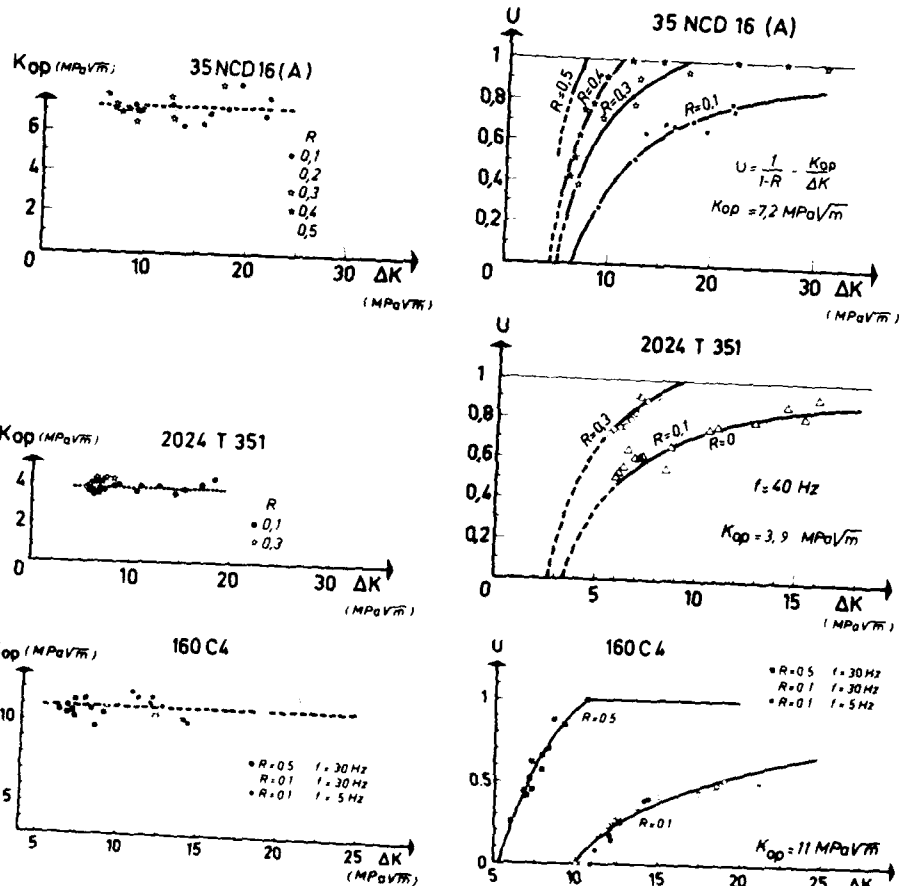


Fig 1 - Crack opening stress intensity factor versus stress intensity range for different materials

Fig 2 - Comparison of effective stress intensity range obtained from experimental measurements and calculated from eq. [1].

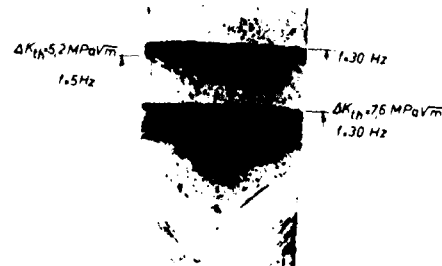
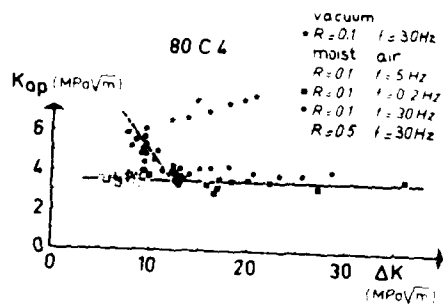


Fig 3 - Opening stress intensity factor versus stress intensity range for steel 80 C 4

Fig 4 - fracture surface of steel 80 C 4 produced by fatigue in moist air environment at 30 Hz, then at 5 Hz, finally at 30 Hz

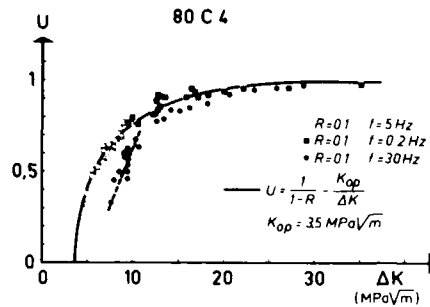


Fig 5 - Stress intensity ratio for 80 C 4 steel as function of  $\Delta K$ , influence of test frequency in moist air

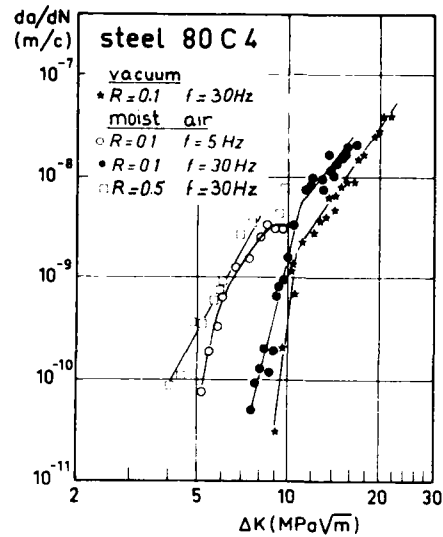


Fig 6 - Variation of crack growth rate with amplitude of stress intensity factor for steel 80 C 4 in moist air and in vacuum

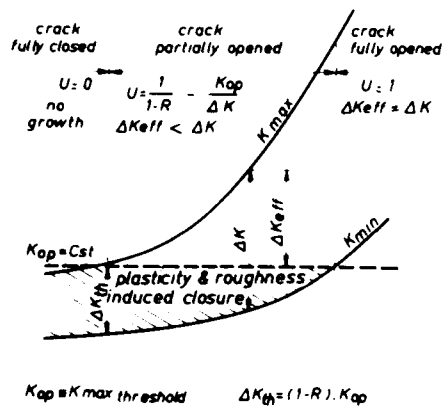


Fig 7 - Significance of crack opening stress intensity

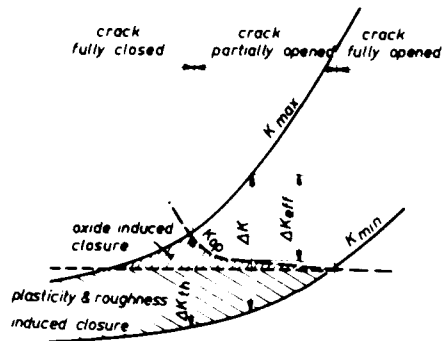


Fig 8 - Influence of oxide-induced closure at low  $\Delta K$  level

**AN EXPLANATION OF THE FRACTOGRAPHY  
OF NEAR-THRESHOLD FATIGUE IN FCC METALS**

**J.I. Dickson<sup>\*</sup>, Li Shiqiong<sup>\*\*</sup> and J.P. Bailon<sup>\*</sup>**

Fractographic features associated with fatigue cracking at low  $da/dN$  values in f.c.c. metals can be explained by fine-scale decohesion on {111} slip planes, with the crystallographic and fractographic details determined essentially by the number of slip planes on which decohesion occurs, their relative orientations with respect to the average orientation of the local fracture plane and by the relative amount of decohesion on each slip plane.

**INTRODUCTION**

The fractographic features produced at very low crack growth rates in the region of the fatigue threshold are very crystallographic and can vary from large, almost featureless facets to complex sets of fine facets. These fracture facets have been referred to by such terms as quasicleavage and slip plane decohesion, although the more complicated facets are difficult to reconcile with a cleavage-mechanism and the facet orientations usually identified do not correspond to slip planes. A number of studies (e.g., Bailon et al (1)) have shown that the influence of the R-ratio on the fatigue threshold is essentially a crack closure effect, thus indicating that the near-threshold fatigue propagation mechanism should be strain and not stress-controlled. In an earlier study, Bailon et al (2) concluded that the near-threshold cracking crystallography often appeared consistent with that which would result from fine-scale decohesion on two alternating slip planes.

The objective of the present study was to further analyze the detailed fractography associated with near-threshold fatigue

<sup>\*</sup> Département de génie métallurgique, Ecole Polytechnique, P.O. 6079, Sta. A, Montréal, Québec, Canada, H3C 3A7

<sup>\*\*</sup> On leave from Beijing University of Iron and Steel Technology

## FATIGUE 87

cracking of f.c.c. metals in order to better identify the associated propagation mechanism. The study focussed primarily on metals of low stacking fault energy, namely 316 austenitic stainless steel (s.s.) and 70 Cu-30 Zn ( $\alpha$ -brass), based on the assumption that reducing the stacking-fault energy should increase the size of the basic decohesion steps if these occur on alternating slip planes. Some observations were also carried out on copper and on 2024-T351 Al alloy. Etch-pitting techniques (Mukai et al (3), Meakin and Wilsdorf (4), Young (5), Pelloux (6)) were employed with varying success in an attempt to identify the cracking crystallography. Extensive use was made of stereofractography. The fatigue tests were performed (El Boujdaini (7), Marchand (8)) at different R-ratios generally 0.1 or 0.5 and in different environments including dry and wet argon, silicone oil and lab air; however, these differences in R-ratio and test environment did not influence the basic fractographic features, although they influenced the cleanliness of the fracture surfaces as well as the amount of closure-induced flattening of fracture surface asperities.

### OBSERVATIONS

**316 Stainless Steel.** The low stacking fault energy metal for which clear etch pits were produced most readily was 316 s.s., with the etch pits bounded by {111} planes. For this steel, large flat facets were found to have {100} orientations (region A of Figure 1), and to be favoured by a {100} plane almost perpendicular to the stress axis or less often by such a plane permitting to fracture an uncracked ligament between two existing fracture facets. Such {100} facets perpendicular to the stress axis tended to be almost featureless, while facets inclined to the tensile axis more clearly presented  $\langle 110 \rangle$  striation-like markings. These markings will be referred to as striations, although the inter-striation spacings are much larger than the average values of  $da/dN$ . River lines or tear ridges tended to lie along the  $\langle 110 \rangle$  direction perpendicular to the striations and along one or both  $\langle 100 \rangle$  directions. Many of the secondary facets along river lines were quite flat and perpendicular to the primary {100} facets and thus corresponded to {110} and {100} orientations. Other river lines presented large serrations, which also corresponded to {100} and {110} facets (Figure 2), although smaller serrations on river lines tended to correspond to {111} facets. The primary {100} facets were seen often to change orientation by rotating about the  $\langle 110 \rangle$  striation direction. In a few cases, deviations approaching  $90^\circ$  were observed to result in a strongly striated facet of near-{110} orientation.

Also observed in a number of grains were series of small tetrahedra-like facets (region B of Figure 1), consisting of three fracture facets, the orientations of which were identified as {100}, {110} or {111}, with at least two different families of

planes involved with any such set of facets studied.

An example of a complex type of near-threshold fractographic feature commonly observed is shown in Figure 3. Such sets of facets occurred for cases in which no  $\{100\}$  plane was well oriented for cracking with respect to the stress axis or occasionally with the requirement to fracture a ligament between a pair of neighboring fracture facets leading the macroscopic crack front. The main aspect of this fractography is the presence of a number of wedge-shaped facets having an edge along a  $\langle 100 \rangle$  direction, a relatively flat side (indicated as A) corresponding to a  $\{100\}$  orientation and a side (B) making an angle of approximately  $45^\circ$  with the former and having an average orientation near  $\{110\}$  but clearly made up of two finer sets of  $\{111\}$  facets, with one set generally longer than the other. The flat  $\{100\}$  side could generally be seen at high magnification to present fine  $\langle 110 \rangle$  striations. A few larger  $\{111\}$  facets (C) were often also present, possibly corresponding to one side of another set of wedge shaped-facets having an edge along a  $\langle 110 \rangle$  direction. The  $\{111\}$  plane corresponding to these larger facets also was parallel to one of the finer sets of facets making up the near- $\{110\}$  side of the main set of wedge-shaped facets, with the trace of this same  $\{111\}$  also parallel to the  $\langle 110 \rangle$  striations observed on the  $\{100\}$  side of these facets.

**70 Cu-30 Zn.** Only rare success was achieved in producing reasonably clear etch pits on the near-threshold fracture facets of 70 Cu-30 Zn. The details of some of the main fractographic features, however, could be recognized from their similarity with those identified in detail in the 316 s.s. and from their relative orientations with respect to interfaces of  $\{111\}$  annealing twins. The flattest facets also appeared to have  $\{100\}$  average orientations and were generally very clearly striated along  $\langle 110 \rangle$ , with the river lines generally present along the perpendicular  $\langle 110 \rangle$  direction but with some river lines present along  $\langle 100 \rangle$  directions at  $45^\circ$  to these  $\langle 110 \rangle$ . Generally such facets could be seen to consist clearly of two sets of finer facets. The orientations of these fine facets appeared to be  $\{111\}$  from the manner in which they were tilted with respect to the average facet orientation, which was assumed to be  $\{100\}$ . Examples are shown in Figures 4-6, in the first two of which an annealing twin interface is seen parallel to the striation-like markings. A few small etch pits in Figure 4 confirm the cracking crystallography assumed. In Figure 6, one region within a grain presents one set of striations along which two sets of fine facets meet and another region presents a perpendicular set of striations along which two different sets of facets meet, with roughly the same average facet orientation observed for both regions, although this orientation depends on the relative size and number of each orientation of fine facets. This aspect is fully consistent with two sets of  $\langle 110 \rangle$  striations contained in an average  $\{100\}$  fracture plane, with the four sets

## FATIGUE 87

of fine facets corresponding to the four  $\{111\}$  planes. In the region separating these strongly striated regions, the fractographic features are more complex but still often present fine striations parallel to one or the other of the sets of more marked striations. As well, some of the river lines in this intermediate region can be seen to be serrated parallel to the striations in the other two regions.

**Copper.** The individual facets observed in the threshold region of copper were often very fine and complex complicating their study. Again little success was obtained in forming clear etch-pits on these facets, although clear etch-pits were produced on the fracture surfaces corresponding to higher  $da/dN$  values and presenting ductile striations. Some facets formed at very low  $da/dN$  values were seen, however, to present features similar to the striated  $\{100\}$  facets observed on 316 s.s. and on  $\alpha$ -brass. Examples are shown in Figures 7 and 8. The fracture facets are seen to be finely striated and clearly to be made up of two sets of fine facets, which meet along the striations and both of which are inclined with respect to the average facet plane. Except for the presence of the numerous river lines perpendicular to the striation-like markings, this micrograph could be easily mistaken for crystallographic ductile fatigue striations which form on the average  $\{100\}$  fracture plane as a result of decohesion along the two sets of  $\{111\}$  slip planes which share the common  $\langle 110 \rangle$  striation direction ((6), Neumann (9)).

**2024-T351 Al alloy.** Some aspects of the near-threshold fractography of 2024-T351 have been previously described (1,2). The crack plane is  $\{100\}$  and river lines most often are parallel to  $\langle 100 \rangle$  although these  $\langle 100 \rangle$  river lines can be made up of serrations parallel to the two  $\langle 110 \rangle$  directions. There is also a lesser tendency for  $\langle 110 \rangle$  river lines, with such lines being predominant in a few grains. Figure 9 shows the presence of  $\langle 100 \rangle$  river lines presenting serrations along the two  $\langle 110 \rangle$  directions contained in a  $\{100\}$  fracture plane. In stereofractographs, the facets corresponding to the very large serrations are seen to correspond to  $\{111\}$  facets, and some of the small serrations along the fine river lines can also be seen to correspond to the same pair of  $\{111\}$  facets. A few very fine  $\langle 110 \rangle$  striations are also present ahead of the arrow indicated.

## DISCUSSION

The relatively flat fracture facets observed in 316 s.s. can be explained by fine-scale microscopic decohesion on two  $\{111\}$  slip planes which meet along the  $\langle 110 \rangle$  striations. In regions in which these  $\{100\}$  facets are perpendicular to the stress axis, equal amounts of decohesion along the two slip planes meeting along the  $\langle 110 \rangle$  crack front should result. That this condition particularly favours flat facets indicates that the individual decohesion steps

should be very small, which suggests that this condition also favours emission of dislocations at or near the crack tip along sets of very closely spaced slip planes. As the  $\{100\}$  facet deviates away from exactly perpendicular to the stress axis, slip on one plane in the crack tip region should become more important than on the other. This should result in larger decohesion steps on the favoured plane, helping to explain the more marked striations observed on inclined  $\{100\}$  facets. This type of striated facets was also observed to be able to deviate away or back towards  $\{100\}$  by rotations occurring at  $\langle 110 \rangle$  striations. Such rotations of less than  $90^\circ$  away from  $\{100\}$  can be explained as caused by the amount of decohesion becoming greater on one set of slip planes than on the other and were generally found to result in the striations becoming more pronounced. A rotation of  $90^\circ$  to a  $\{110\}$  orientation would again result in equal amounts of decohesion occurring on the two sets of slip planes. While a few rotations to near- $\{110\}$  orientations were observed and quite large secondary  $\{110\}$  facets along large river lines were found frequently, large primary  $\{110\}$  facets were not observed. Average  $\{110\}$  crack planes are also not found at higher  $da/dN$  values for the formation of ductile crystallographic  $\langle 110 \rangle$  striations by decohesion along two slip planes (6.9). Their absence has been explained by the  $\{110\}$  containing only a single  $\langle 110 \rangle$  direction, thus preventing the crack front from curving.

In 70 Cu-30 Zn, the regions of fracture facets presenting striations often have a stepped aspect, with the individual steps corresponding to fine facets along a pair of apparently  $\{111\}$  planes. This aspect of  $\{111\}$  or near- $\{111\}$  steps resulting in a  $\{100\}$  or near- $\{100\}$  average orientation of the fracture plane provides particularly strong evidence that fatigue propagation in the threshold region occurs by decohesion along slip planes, in a manner related to that by which slip in the crack tip region causes ductile crystallographic striations (6.9) at higher  $da/dN$ . The amount of decohesion per decohesion event and/or the frequency of these events must, however, differ at high  $da/dN$  from that in the threshold region.

One example of more complex near-threshold fractography can be found in the center of Figure 6. The average crack plane is near  $\{100\}$  and the river lines are parallel to  $\langle 100 \rangle$  and often finely serrated along the two  $\langle 110 \rangle$  directions. This region of complex fractography is situated between two regions which, in the same grain, present  $\langle 110 \rangle$  striations, along which two sets of fine  $\{111\}$  facets meet, with the striations of one region perpendicular to those of the other. It can then be concluded that slip and decohesion on all four sets of slip planes must have occurred in the intermediate region, and that it is the occurrence of this multiple slip which has produced these more complex fractographic features. Moreover, it can be noted that, although the roughness of the fracture facets can vary, these features resemble closely

those often observed on 2024-T351 Al alloy ((1,2) and Figure 9) which present  $\{100\}$  facets usually with  $\langle 100 \rangle$  river lines. These river lines are also often finely serrated along two  $\langle 110 \rangle$  directions. The explanation for the preferred occurrence of these  $\langle 100 \rangle$  river lines at low  $da/dN$  values for this Al alloy should then be that this cracking crystallography results when slip and decohesion on four  $\{111\}$  slip planes occurs in the crack tip region. Figure 9 shows an example for 2024-T351, in which the two orientations of facets which form the serrations along both large and small  $\langle 100 \rangle$  river lines correspond to  $\{111\}$  planes and each should result from decohesion occurring along an individual slip band. A few fine  $\langle 110 \rangle$  striations can also be discerned in this figure, indicating that zones of these  $\{100\}$  fracture facets are also produced by fine-scale decohesion on alternating  $\{111\}$  planes. Such  $\langle 110 \rangle$  near-threshold striations were more frequently observed by Koterazawa and Shimo (10) on 2017-T4 Al alloy, although their fractographs also present evidence for  $\{100\}$   $\langle 100 \rangle$  cracking similar to that observed for 2024-T351.

Figure 3 presents another example of complex near-threshold fractography which is commonly observed in 316 stainless steel and can be explained as resulting from slip and decohesion occurring on three  $\{111\}$  slip planes, but with the slip plane parallel to the large  $\{111\}$  facets being particularly important, since decohesion on this plane explains these large  $\{111\}$  facets and also contributes to the formation of each side of the wedge-shaped facets which meet along a  $\langle 100 \rangle$  edge.

Lastly, it can be noted that the fractographic details identified in the present study are consistent with the Lynch model (11) of environmentally-assisted transgranular cracking. The very strong similarity (2) between the transgranular fractographic features of near-threshold fatigue cracking and stress-corrosion cracking suggests that fine-scale decohesion on slip planes is also involved in the latter cracking mechanism.

#### CONCLUSIONS

From the present study, it can be concluded that fine-scale decohesion along  $\{111\}$  slip planes permits to explain well most of the fractographic features and crystallographic aspects associated with near-threshold fatigue propagation in f.c.c. metals, with the detailed microfractography being determined by the number of slip planes on which decohesion has occurred, by their relative orientations with respect to that of the local fracture plane, and by the amount of decohesion on the individual slip planes.

#### ACKNOWLEDGMENTS

Financial support from the NSERC (Canada) and FCAR (Quebec) research-support programs is gratefully acknowledged. The authors

are grateful to Nicole Roy for typing the manuscript.

# REFERENCES

- (1) Bailon, J.P., El Boujdaini, M. and Dickson, J.I., "Environmental Effects on Threshold Stress Intensity Factor in 70-30 Alpha Brass and 2024-T351 Aluminum Alloy", in "Fatigue Crack Growth Threshold Concepts", D.L. Davidson, S. Suresh, editors, TMS-AIME, 1984, pp. 63-82.
- (2) Bailon, J.P., Chappuis, P., Masounave, J. and Dickson, J.I., "Fractographic Aspects near the Threshold in Several Alloys", in "Fatigue Threshold", J. Backlund, A.F. Blom and C.J. Beevers, editors, EMAS Ltd., Vol. 1, 1982, pp. 277-291.
- (3) Mukai, Y., Watanabe, M. and Murata, M., "Fractographic Observation of Stress-Corrosion Cracking of AISI 304 Stainless Steel in Boiling 42% Magnesium Chloride Solution", in "Fractography in Failure Analysis", ASTM-STP 645, B.M. Strauss and W.H. Cullen, Jr., editors, ASTM, Philadelphia, 1978, pp. 164-175.
- (4) Meakin, J.D. and Wilsdorf, H.G.F., Trans. TMS-AIME, Vol. 218, 1960, pp. 737-745.
- (5) Young, F.W., Jr., J. Appl. Phys., Vol. 32, 1961, pp. 192-201.
- (6) Pelloux, R.M.N., Trans. ASM, Vol. 62, 1969, pp. 281-285.
- (7) Marchand, N., M.A.Sc. thesis, Ecole Polytechnique de Montreal, 1983.
- (8) El Boujdaini, M., M.A.Sc. thesis, Ecole Polytechnique de Montreal, 1985.
- (9) Neumann, P., Acta Met., Vol. 22, 1974, pp. 1155-1165.
- (10) Koterazawa, R. and Shimo, D., "Materials" (in Japanese), Vol. 25, 1976, pp. 35-41.
- (11) Lynch, S.P., Metal Sci., Vol. 15, 1981, pp. 463-467.

FATIGUE 87



Figure 1 Typical near-threshold facet: 316 s.s. tested in air

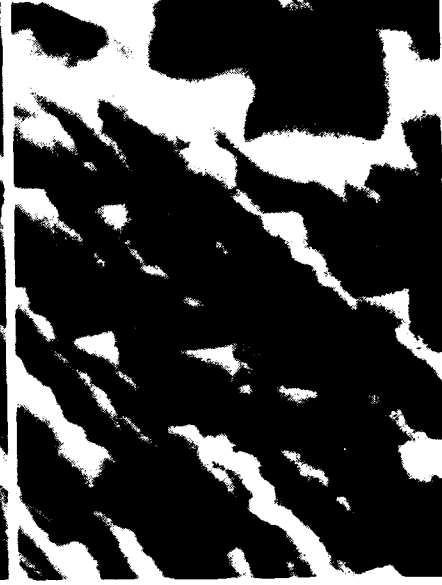


Figure 2 Serrated river lines: 316 s.s. tested in dry argon



Figure 3 Complex near-threshold facets: 316 s.s. tested in air (stereographic pair)



Figure 4 Striated near-threshold facet, 70-30  $\alpha$ -brass in air. Arrows indicate small etch pits



Figure 5 Near-threshold facet, striations parallel to twin interface;  $\alpha$ -brass in dry argon



Figure 6 Near-threshold facet for 70-30  $\alpha$ -brass in air, with two regions of striations separated by more complex region



Figure 7 Striated threshold facet for copper tested in air



Figure 8 Striated near-threshold facet for copper tested in air

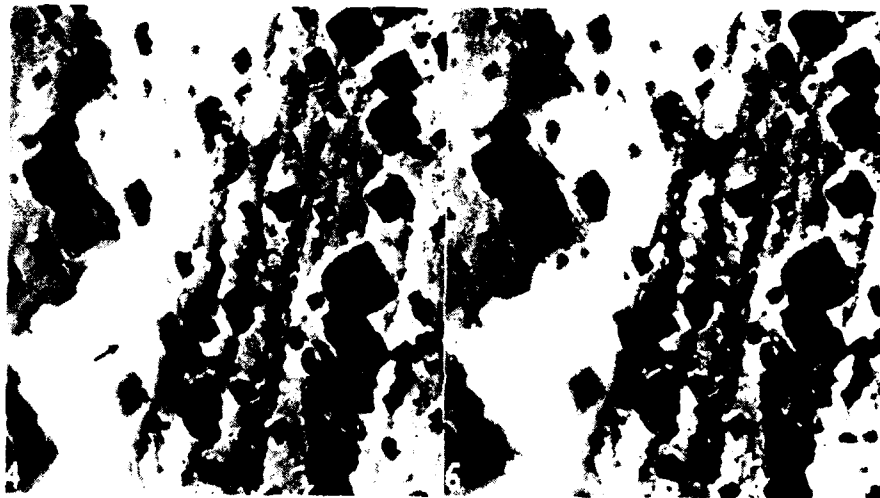


Figure 9 Primary {100} near-threshold facets, with secondary {111} facets corresponding to serrated river lines; 2024-T351 in air

## FATIGUE 87

### THE RELATIONSHIP BETWEEN MICROSTRUCTURAL SIZE AND FATIGUE THRESHOLD IN IRON AND STEEL

Gu Haicheng\* and Liu Xiao Du\*

Fatigue crack growth at near-threshold region has been studied in pure iron, medium carbon and high carbon steels, and austenitic steel. The front profile of crack tip, the height of asperities on fatigue fracture surface, and the crack closure have been found to be influenced by microstructure. The results are explained in terms of mechanical component  $\sigma_y$  incorporated with microstructural size  $d$  with concept of reversed plastic zone. This criterion is unique for steels with different microstructures: ferrite, pearlite, austenite, martensite and bainite.

### INTRODUCTION

It is generally accepted that at near-threshold region there is a strong influence of microstructure and load ratio on the fatigue crack growth rate. The values of fatigue threshold  $\Delta K_{th}$  are also sensitive to microstructure and mean stress. An excellent survey was contributed by Ritchie(1) on current research status of fatigue threshold. Ritchie concluded that the mechanical and microstructural factors which can influence  $\Delta K_{th}$  are effective via extrinsic mechanisms, such as crack closure and crack deflection. Some of the factors influence  $\Delta K_{th}$  was also highlighted by Beevers(2): The measured  $\Delta K_{th}$  consists of two components,  $\Delta K_{th}^c$  the extrinsic closure component which results from asperities on the fatigue fracture surface, and  $\Delta K_{th}^i$ , the intrinsic component, which has to be exceeded to overcome the intrinsic resistance of material to crack extension. Another micromechanistic model by use of a synergetic parameter  $\sigma_y \sqrt{d}$  was established by Yoder et al (3), and the influence of stress ratio

\*Research Institute for Strength of Metals, Xi'an Jiaotong University, The People's Republic of China

## FATIGUE 87

on  $\Delta K_{th}$  was considered as a problem of environmental effect. Many other researchers( Radhakrishnan(4) and Romaniv(5) have also made contribution to this subject. From viewpoints of both academic research and engineering application, it is of great importance to clarify the interaction between intrinsic component and extrinsic component contributing to fatigue threshold.

### MATERIALS AND EXPERIMENTAL PROCEDURE

Pure iron and steels, a host of different microstructural types( ferritic, pearlitic and austenitic), were used in this work. The chemical compositions of the materials are shown in Table1. Heat treatments and corresponding mechanical properties are given in Table2.

TABLE1-Chemical Compositions of Materials

Material	Element Content (%wt)				
	C	Si	Mn	P	S
pure iron	0.020	0.14	0.15	0.0075	0.0048
35	0.380	0.32	0.69	0.011	0.0048
T8	0.950	0.30	0.40	0.015	0.0059
18-8	0.080	0.58	1.08	Cr 17.73	Ni 9.09 Ti 0.64

TABLE2-Heat Treatment and Monotonic Mechanical Behavior

Material	Heat treatment	$\sigma_y$ (MPa)	$\sigma_u$ (MPa)	RA (%)	Elon. (%)
pure iron	1100°C 1h, FC	192	279	78.5	48.1
35	880° 1h, 680° 3h, FC	398	536	54.8	32.9
T8-L	900° 2h, 690° 1h, FC	471	765	18.3	14.7
T8-S	780° 1h, 690° 3h, FC	457	634	59.4	32.1
18-8	1100° 1h, WC	331	564	78.0	60.6

## FATIGUE 87

In order to compare the results with our previous work, SENB type specimens were used for the study of crack propagation. A Vibrophore fatigue testing machine operating at a frequency of 100Hz was used to establish the fatigue threshold. An optical travelling microscopy (120X) was used to measure the crack length with the accuracy of 0.01mm. Threshold levels were approached using a load-shedding technique involving a procedure of successive load reduction followed by a period of crack growth extending over the previous plastic zone, and the requirements suggested under the jurisdiction of ASTM Committee E-24 was satisfied, including

$$C = (1/K) \cdot (dK/da) \leq -0.08\text{mm}^{-1} \quad (1)$$

The  $\Delta K$  increasing test procedure was also used to check the validation of  $\Delta K_{th}$  values. Three specimens were used for each microstructural type of materials, and the repeatability of the results is quite well.

After fatigue threshold testing had performed, some of specimens were cooled to liquid nitrogen temperature and then broken by impact load, so that the front profile of the crack tip just at threshold condition could be examined with scanning electron microscopy JSM 35c. The height of asperities on the fatigue fracture surface at near-threshold region was measured by use of Zeiss Jena 'light knife' microscopy. To minimize the effect of crack closure, a load ratio  $R=0.33$  was chosen, and the actual crack closures on the specimens were measured for each kind of materials.

## RESULTS

Fig.1 shows the  $da/dn-\Delta K$  curves of pure iron and austenitic stainless steel. It is obvious that ferrite exhibits higher  $\Delta K_{th}$  than austenite does. Fig.2 shows the results of medium carbon steel and high carbon steel with lamellar pearlite or spheroidized structure. The crack growth behavior of medium carbon steel with ferrite plus pearlite is very close to that of pure iron; lamellae and spheroidized structure show no difference in  $\Delta K_{th}$  values, while lamellae show higher  $da/dn$  at high  $\Delta K$  range.

Fig.3 is an example of load/displacement trace of pure iron specimen to check crack closure. It was estimated that the fatigue crack is open for more than 90% of the load cycle.

The morphology of fracture surface of pure iron specimen examined with SEM shows that some intergranular facets and transgranular cyclic cleavage patterns appear near-threshold region(Fig.1). It is also demonstrated that the trace of cyclic cleavage are different each other in neighbouring grains. The boundary between fatigue threshold region and impact fracture region exhibits meandering profile alongside different ferrite grains(Fig.6). It is the evidence which shows that ferrite grains in different orientation fatigued in different ways. In eutectoid steel specimens with lamellae structure, the fractography also reveals the morphology of pearlite colonies. Some photos were taken just at the boundary between fatigue threshold zone and impact fracture zone(Fig.7). The parallel ridges in fatigued zone are coincident with the lamellae plates in impact fracture zone. It is interesting to note that fatigue crack can stop at a position within a pearlite colony. The fractography of medium carbon steel shows the feature of combining characteristic of pure iron and fully pearlite steel(Fig.8,a). Besides the presence of asperities and irregularities on the fatigue fracture surface, some of debris were also observed, and one example is demonstrated in Fig.8.b.

The mean grain sizes ( or colony size in pearlitic steel) calculated by secant method and confirmed with Image Analyser are shown in Table3. The average sizes of the reversed plastic zone at  $\Delta K_{th}$  calculated by following equation,

$$r_y^c = \frac{1}{3\pi} \left( \frac{\Delta K_{th}}{2\sigma_y} \right)^2 \quad (2)$$

are also included in Table3. Attached are the maximum height of asperities on the fatigued surface, measured with 'light knife' microscopy, as well as the results of the maximum and minimum opening at crack tip calculated by following equations,

$$(CTOD)_{max} = \frac{0.5}{E\sigma_y} \cdot \frac{\Delta K_{th}^2}{(1-R)^2} \quad (3)$$

$$(CTOD)_{min} = \frac{0.5}{E\sigma_y} \left[ \frac{\Delta K_{th}^2}{(1-R)^2} - \frac{\Delta K_{th}^2}{2} \right] \quad (4)$$

#### DISCUSSION

In the situation of  $R=0.33$ , it was found in our previous work that the crack closure is negligible for high strength steels( quenched and tempered, or austempered). But for low strength steels, as shown in this work,

AD-A184 046

FATIGUE '87 VOLUME 2(0) VIRGINIA UNIV CHARLOTTESVILLE  
SCHOOL OF ENGINEERING AND APPLIED SCIENCE  
R O RITCHIE ET AL JUN 87 N00014-87-G-0006

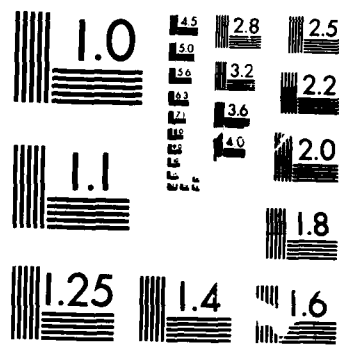
3/6

UNCLASSIFIED

F/G 20/11

NL





MICROCOPY RESOLUTION TEST CHART  
NATIONAL BUREAU OF STANDARDS-1963-A

# FATIGUE 87

TABLE3-Parameters of Materials with Equilibrium Micro-structure

Material	Mean grain or colony size ( $\mu\text{m}$ )	Reversed plastic zone( $\mu\text{m}$ )	Height of asperities ( $\mu\text{m}$ )	CTOD max ( $\mu\text{m}$ )	CTOD min ( $\mu\text{m}$ )
pure iron	61.4	65	65	2.7	2.0
35	11.8	14	33	1.2	0.9
T8-L	15.3	8	20	0.8	0.6
18-8	17.6	9	22	0.6	0.5

TABLE4-Data of Steels with Unequilibrium Microstructure

Steel	Heat treatment	$\sigma_y$ (MPa)	$\Delta K_{th}$ ( $\text{MPa}\sqrt{\text{m}}$ )	Reversed plastic zone( $\mu\text{m}$ )
45Cr	quench & temper at 200°	1700	4.9	0.22
	" "	300° 1600	4.9	0.25
	" "	400° 1450	6.1	0.47
	" "	500° 1200	5.0	0.46
	" "	600° 850	4.6	0.77
45Cr	850°, austemper at	280° 1662	8.9	0.76
	" "	350° 1282	6.9	0.77
	" "	400° 1065	6.4	0.96
	" "	450° 802	7.8	2.51
	" "	500° 708	8.1	3.47
	950° "	350° 1287	8.5	1.16
Si-Mn cast steel	890° "	280° 1243	12.3	2.60
	" "	360° 943	12.0	4.40

## FATIGUE 87

there is still certain amount of crack closure (in general less than 10%) during load cycle. This may be the reason that the load ratio has minor influence on  $\Delta K_{th}$  values in high strength steels to that of low strength steels.

It has been well documented that the change from continuum mode of crack growth to structure-sensitive mode occurs when the cyclic plastic zone size attains the mean grain size. It is also confirmed that the transition point closely approximates to  $\Delta K_{th}$ .

Based on the experimental results, a micromechanistic model of crack growth at near-threshold region could be suggested, as depicted in Fig. 4. The crack front is moving in a discontinuous manner; each grain behaves as a unit, either in cyclic cleavage or in intergranular cracking. Although the crack front is meandering, from viewpoint of statistic, the concept of reversed plastic zone is still useful. Within the reversed plastic zone, the global stress is equal to yield stress, but for some of grains, the local stress is not high enough to accumulate damage, so the crack will stop therein.

The results presented in Table 3 led us to believe that: In basically ferritic steels or austenitic steels grain size is the appropriate structural parameter; in eutectoid steels, the parameter seems to be the pearlite colony size, since  $\alpha$ -phase in a colony exhibits same orientation regardless of the lamellar or spheroidised carbides embedded in it. When cracks transmit across  $\alpha$ -phase, the second phase carbides will intervene the local crack path, so that the divergence between pearlite colony size and reversed plastic zone size may be greater than that in homogeneous alloys. In medium carbon steel with ferrite plus pearlite, ferrite is weaker, so the grain size of ferrite is the dominant parameter.

For the sake of completeness, some results from our own previous work on low alloy medium carbon steels with unequilibrium microstructures are included in Table 4 (Gu et al(7)).

To measure the size of martensite lath or bainite plate is rather difficult and time-consuming, and only a few data have reported. At present the above results led us to assume that: In 45Cr steel quenched and tempered at 200° or 300°C, the microstructural size parameter may be the width of martensite laths; while

tempered at 400° or 500° C, the martensite laths are replaced by more equi-axed fine ferrite grains; and the grains are growing further when tempered at 600° C. For same steel austempered, the microstructural parameter presumably is the size of lower bainite plate or packet of upper bainite laths. For cast steel or steel austenitized at higher temperature, the size of austenite is coarser, consequently the size of bainite unit is also coarser, so the higher values of  $\Delta K_{th}$  could be achieved in these conditions.

Some work involving studies of synergetic parameter  $\sigma_y/\sqrt{a}$  in prediction of  $\Delta K_{th}$  values is quite successful (Yoder et al(3)). A good approximation to  $\Delta K_{th}$  could be evaluated by following equation:

$$\Delta K_{th} = 5.5 \sigma_y \sqrt{a} \quad (5)$$

According to our opinion, this equation is true for only intrinsic material resistance. For high strength steels, the extrinsic component, i.e. crack closure, could be neglected, so the applicability of this equation is virtually reasonable. While for low strength steels, the crack closure will play an important role at low stress ratio. Based on our results, the crack closure may occupy 40% load cycle at  $R=0$ . In order to exclude the effect of extrinsic component, it would be better to make some modification. On the other hand, by use of cyclic yield stress  $\sigma_y'$  instead of monotonic yield stress, then the cyclic hardening or cyclic softening should be taken into account, but the point requires further investigation.

#### CONCLUSIONS

(1) The crack front profile at near-threshold, the crack closure, and the height of sperities on the fatiged surface are all influenced by microstructure, especially in low strength materials.

(2) In the situation of stress ratio  $R=0.33$ , the crack closure only occupy 10% of load cycle in low strength steels, while in high strength steels, it may be negligible.

(3) Based on the results of a host of steels, heat treated to a wide range of microstructure and strength, a micromechanistic model could be used to explain the intrinsic fatigue threshold. Both mechanical and microstructural components are incorporated in the model.

## FATIGUE 87

(4) The synergetic criterion  $\sigma_y \sqrt{a}$  will be a better parameter to elucidate the essence of fatigue threshold than either yield stress or grain size alone. When it is applied to low load ratio (  $R$  is less than 0.3), the criterion should be modified to take into consideration of crack closure.

### ACKNOWLEDGEMENTS

Thanks are due to Professor A.J.McEvily and Professor Zhou Huijiu for most helpful discussions. The authors also express their appreciation to National Natural Science Foundation for financial support.

### REFERENCES

- (1) Ritchie, R.O., "Thresholds for Fatigue Crack Propagation: Questions and Anomalies", Proceedings of ICF 6. Edited by Valluri, Pergamon Press, 1985, PP. 235-259.
- (2) Beevers, C.J., " Factors Influencing the Rate of Fatigue Crack Growth at Low Stress Intensities", Proceedings of the Conference on "Fracture Prevention in Energy and Transport Systems". Edited by Lain Le May, EMAS, Warley, England, 1984, PP. 665-674.
- (3) Yoder, G.R., Cooley, L.A., and Crooker, T.W., " A Critical Analysis of Grain-size and Yield-Strength Dependence of Near-Threshold Fatigue Crack Growth in Steels", ASTM STP 791, Edited by J.C.Lewis and G.Sines, 1983, PP. I-348- I-365.
- (4) Mutoh, Y., and Radhakrishnan, V.M., Trans. ASME, J. Eng. Mat. Tech. Vol. 108, April, 1986, PP. 174-178.
- (5) Romaniv, O.N., Physical-Chemical Mechanics of Materials, 1986, NO.1, PP. 106-116. (in Russian)
- (6) Bucci, R.J., "Development of a Proposed ASTM Standard Test Method for Near-Threshold Fatigue Crack Growth Rate Measurement", ASTM STP 738, Edited by S. J. Hudak, Jr., and R.J.Bucci, 1981, PP. 5-28.
- (7) Gu Haicheng, Zeng Jian, and Zhou Huijiu, "near-Threshold Fatigue Crack Propagation in Isothermally Transformed steels", Fatigue '84, Edited by C.J. Beevers, EMAS, Warley, England, PP. 211-220.

# FATIGUE 87

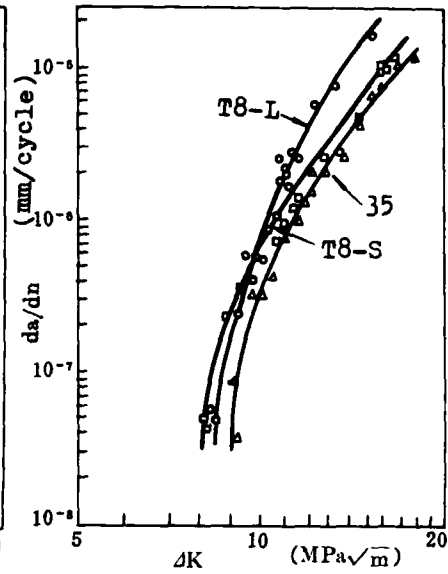
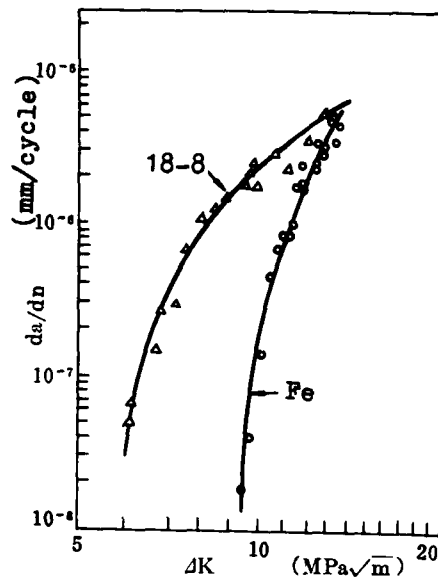


Figure 1  $da/dn$  vs.  $\Delta K$  for pure iron & austenitic steel medium & high carbon steels

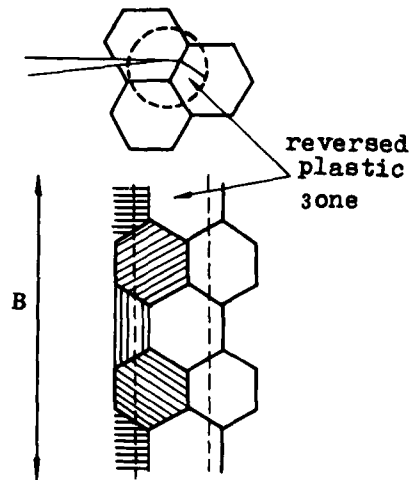
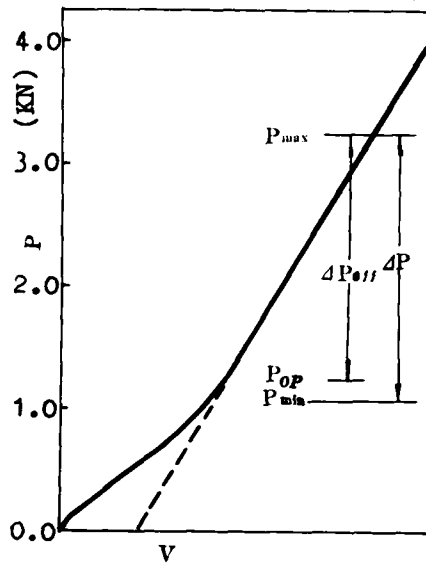


Figure 3 Plot of load vs. displacement for pure iron fatigue threshold

FATIGUE 87

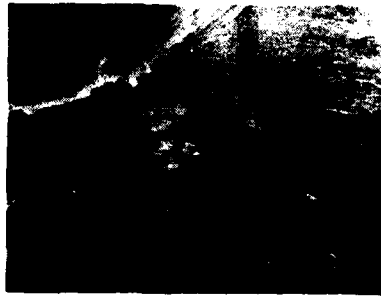


Figure 5 Fractographs at  $\Delta K_{th}$  in pure iron

Figure 6 Crack tip profile at  $\Delta K_{th}$  in pure iron

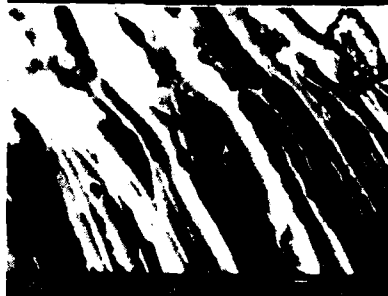
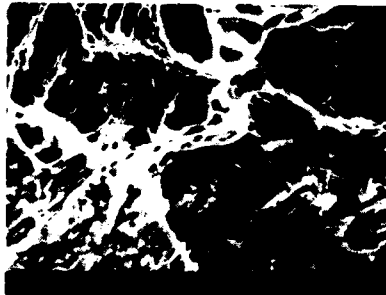


Figure 7 Crack tip profile at  $\Delta K_{th}$  in lamellae

Figure 8 a Fractograph of 35 steel b Debris on fatigue fracture surface

## FATIGUE 87

### THRESHOLD BEHAVIOUR OF SEMI-ELLIPTIC HYDROGEN-INDUCED AND FATIGUE-INDUCED CRACKS

M.N. James\*

This paper compares threshold data for small semi-elliptic fatigue cracks initiated in a region of bulk plasticity and then stress relieved, for hydrogen-induced cracks (no bulk plasticity, but blunter than fatigue cracks and with a different fracture surface morphology) and for fatigue cracks initiated and grown in a nominally elastic field.

#### INTRODUCTION

Considerable attention has been focused on the growth of small cracks in recent years, primarily with the ultimate engineering aim of understanding the fatigue behaviour of such cracks sufficiently well to enable the defect tolerant design approach to be extended to components in which the initial defect population has very small sizes.

During the course of research into the behaviour of small fatigue cracks, however, it has become apparent that the functional relationships established for long cracks between crack growth rate ( $da/dN$ ), the range of applied stress intensity ( $\Delta K$ ) and the stress ratio ( $R$ ) do not hold for very small cracks (e.g. 1-4). This situation is the most general definition of the "short crack" problem, which is usually most important in the near-threshold regime and is characterised by growth at values of  $\Delta K$  that are lower than the long crack threshold  $\Delta K_{th}$ .

\* Department of Metallurgy and Materials Engineering  
University of the Witwatersrand  
WITS, Johannesburg, 2050, South Africa.

The significance of this behaviour is that, over a range of crack sizes from perhaps the order of some microstructural dimension (e.g. the grain size) to the order of 0.1 - 1.0 mm, both the S-N approach and the defect tolerant approach (based on long crack growth rate data) are nonconservative.

However, considerable insight into the causes of short crack behaviour has now been gained (5) and, in certain cases, the differences in behaviour between long and "physically short" cracks are sufficiently well understood to allow a simple life prediction philosophy to be proposed (6). It has also become clear that the observed behaviour may be influenced by the type of crack considered (i.e. through-crack or part-through-crack) and by the method used to generate small cracks (7).

#### Effect of Geometry and Crack Generation Scheme

Where short crack data have been obtained from specimens that initially contain long through-thickness cracks generated (usually) by load shedding techniques, and which are then machined away to leave a short through-crack, the extent of the short crack regime may be of the order of 1-2 mm (8,9). When, however, small part-through (semi-elliptic) cracks are considered the extent of the short crack problem is usually much less, often being confined to cracks smaller than about 0.1 - 0.3 mm (10-12). This difference has been explained in terms of the different distributions of wake closure engendered by the generation techniques peculiar to each type of crack (7).

In essence, machining away a long through-crack to leave a short through-crack has the same effect on the magnitude of closure as does removing the wake of a long crack by electrodischarge machining (EDM) or sawing (Fig. 1). The distribution of closure in the remaining wake still reflects the details of the load shedding process, and it might then be expected that the subsequent crack increment to develop a closure level representative of 'long' cracks would not reflect the behaviour of part-through cracks, which are the class of defects more commonly found in engineering hardware.

Part-through cracks may be initiated in a variety of ways (5) and the factors which require consideration in interpreting the threshold and growth rate data include the resulting distribution of wake closure and the stress level (relative to the yield strength) at which cracks were initiated. Considering smooth bar specimens, which are widely used in short crack studies, at positive values of stress ratio the maximum value of the cyclic stress necessary to initiate cracks may approach, or even exceed, the macroscopic yield strength of the material. Even when the applied stress is below the yield stress, the individual grains

within which fatigue cracks initiate are locally yielded. Thus the early growth of part-through cracks often occurs within a plastic field. Such situations may accurately model the early behaviour of cracks in a piece of engineering hardware, which may well be the aim of the research.

If, however, the objective is to simulate the behaviour of pre-existing small defects in a nominally elastic material (such as might be the case for hydrogen-induced cracks in a welded and stress relieved structure) either a more representative crack initiation technique can be used or the specimen may be heat treated to anneal the plastically deformed material around the crack. Local bulk plasticity presumably influences the closure behaviour of small cracks and it is therefore pertinent to consider the effectiveness of typical stress relief heat treatments in annealing out these influences.

The above paragraph encompasses the thrusts of the present paper, whose approach is to consider the differences in threshold behaviour of small semi-elliptic cracks in a quenched and tempered low alloy steel, initiated in bending either at a low ratio of applied stress to yield stress by cathodic hydrogen charging of the specimen or from nonmetallic inclusions at stresses greater than yield. In both cases specimens were stress relieved prior to threshold testing. The initial hydrogen-induced cracks were subsequently extended by fatigue, stress relieved again and subjected to a second threshold test. Thus comparative data were obtained for (i) fatigue cracks initiated in a region of bulk plasticity and then stress relieved, (ii) hydrogen-induced cracks (no bulk plasticity, but blunter than fatigue cracks and with a different fracture surface morphology) and (iii) fatigue cracks grown in a nominally elastic field.

#### EXPERIMENTAL DETAILS

A low alloy steel (Q1N) with a composition closely similar to HY80, i.e. 2.5 Ni 1.5 Cr 0.5 Mo with  $< 0.2$  C, was used in this work. Smooth bar specimens were tested at room temperature in air using four-point bend on a 20 kN Amsler Vibrophore at frequencies of 150-170 Hz and a stress ratio of 0.2. The specimens used were 75 mm long and either 10 mm wide by 10 mm thick (inclusion initiation tests) or 12 mm wide by 12 mm thick (hydrogen-induced crack tests). The reason for this difference is simply that the specimens were all supplied with a 12x12 mm section, but the testing machine did not have the load capacity to initiate cracks in specimens of this size at  $R = 0.2$ .

Specimens were pre-cracked by one of two methods. The first method involved initiation at small ( $< 10 \mu\text{m}$ ) alumina inclusions at, or near, the surface in electropolished specimens in the as-

received (AR) quenched and tempered condition (UTS 743 MPa, yield strength 653 MPa, Vickers hardness 266). The stresses required for this exceeded the yield strength and therefore these specimens were subsequently stress relieved in vacuum at 650°C for 1.5 hours prior to threshold testing. The second method utilised hydrogen charging of specimens that had been water quenched after heating at 900°C for 1 hour (Vickers hardness 458). These testpieces were electropolished, placed in a simple bending frame and loaded to a surface stress of around 0.5-0.6 of the yield strength, estimated from microhardness data. The purposes of applying this stress were to ensure that the hydrogen-induced cracks would be perpendicular to the longitudinal axis of the specimen and to assist in rapid cracking. Except for a small area on the surface of the testpiece in the desired cracking location, both the loading frame and the specimen were covered with the proprietary lacquer 'Fortolac' to prevent hydrogen ingress.

The complete assembly was then immersed in a 4% solution of  $H_2SO_4$  poisoned with 20 mg/l of  $As_2O_3$  and galvanostatically charged at current densities in the range 50-200 mA/cm<sup>2</sup>. Cracks developed within a few minutes and their surface length was limited (at least initially) by the Fortolac lacquer. Their depths depended on the current density and the time of charging; aspect ratios (surface length 2c/depth a) between 2 and 10 could be obtained by varying these parameters. The data reported in this paper relate to aspect ratios in the range 2-4. Light fractographs showing typical crack shapes are given in Fig. 2. Once a crack of the desired surface length had been developed, the specimen was removed from the bending frame and tempered in vacuum at 650°C for 1.5 hours. This served the dual purpose of reducing the hardness to the same level as that of the AR condition and baking out the dissolved hydrogen.

Threshold testing of all specimens was performed using a load increasing technique which involved starting a test at a lower load than the expected threshold value and progressively increasing the load after intervals of 200 000 cycles. Surface crack lengths were monitored via replication and the threshold was taken to correspond to the onset of sustained growth, provided that growth rates lay in the range  $1-3 \times 10^{-7}$  mm/cycle. For the case of the hydrogen-cracked specimens, once a threshold had been found the load was increased and the crack grown by fatigue to a significantly larger size. A further stress relief treatment at 650°C was then employed prior to a second threshold determination.

RESULTS AND DISCUSSIONFractography

Fractography indicated that the sequence of events in developing the hydrogen-induced cracks in these smooth bar specimens was the following:

- i) A small "flake" of quasicleavage would be initiated at a suitable hydrogen trap (often alumina inclusions) usually situated about 0.16 mm below the surface of the specimen (Fig. 3), which presumably corresponds to the depth at which there is the greatest tensile hydrostatic stress.
- ii) This initial transgranular crack appears to develop an oval shape by intergranular separation, extending both towards the surface and into the specimen (Fig. 4). The depth that this oval crack attains presumably depends on the current density and time of charging required to initiate the crack (i.e. a function of the depth of hydrogen diffusion into the specimen).
- iii) Once the crack breaks the surface of the specimen the development of a semi-elliptic shape is presumably favoured.

Subsequent fatigue crack growth is by a ductile transgranular mechanism (Fig. 5), which is identical to that observed for the fatigue cracks initiated at inclusions.

Threshold Data

The results of the threshold testing programme are presented in Fig. 6, plotted as threshold stress intensity range,  $\Delta K_{th}$  against crack depth  $a$  (the semi-minor axis of the elliptical crack shape). It should be noted that LEFM is applicable to all the crack sizes in Fig. 6, as the average grain size in this material is about 10  $\mu\text{m}$  and the threshold plastic zone sizes are around 2 - 3  $\mu\text{m}$  (plane strain). Stress intensity values were all calculated using the results of Shah and Kobayashi given in Rooke and Cartwright (13). The data in this figure have been screened from a larger number of tests, as it was often found that growth of the hydrogen-induced cracks would not commence until quite high  $\Delta K$  values (around 6-7  $\text{MPa}/\text{m}$ ) were applied. Initial growth rates were then correspondingly higher than threshold values (up to  $10^{-6}$  mm/cycle).

Considering first the threshold for the hydrogen-induced (HI) cracks, it might be expected that closure values would be higher than for fatigue cracks grown under the same conditions, due to the intergranular fracture surfaces. Hence the threshold values should also be higher, as measured threshold values in this material reflect a constant closure-free component plus a closure-

based component (7). The data in Fig. 6 relating to hydrogen cracks extended by fatigue (H+F) appear to support this, with a difference of about 0.4 MPa/m apparent between the lines indicating the mean values of the two sets of data. Those data obtained from performing both threshold tests on the same specimen (marked with the superscripts 1 and 2) are particularly revealing in this respect. There may also be more scatter associated with the threshold data for the HI cracks, which would be consistent with varying crack blunting affecting closure values. It should be noted, however, that no closure measurements were made and crack tip blunting could, in itself, raise the threshold values slightly.

Threshold values for the fatigue cracks initiated at inclusions at high stress levels (IC-bending) show the most scatter and are also generally the highest in Fig. 6. The presence of plasticity usually raises growth rates, which implies a lowered threshold, and hence the elevation of threshold observed here is believed to be a closure effect rather than a direct effect of plasticity in the crack tip process zone. It is therefore surmised that closure values are the highest for the IC-bending cracks, presumably as a result of incomplete removal of plastic strains in the wake during the stress relief treatment.

As a check that the threshold values measured for the H+F cracks are indeed a lower bound representing fatigue cracks initiated at low stresses, tension specimens with a minimum cross-section of 2.5 x 5.0 mm were machined from the bend bars. A single tension threshold test has been conducted to date, with the following procedure. A crack was initiated at  $R = -1$  at a peak stress of 400 MPa (62% of yield), and the stress ratio changed to  $R = 0.2$  once the crack was established. The crack was grown at this stress ratio to a size comparable with the H+F cracks, stress relieved under the same conditions and a threshold test performed. It is clear that the result of this test agrees rather well with the lower bound data for the H+F cracks. This confirms that the lower threshold values observed for the HI and H+F cracks, relative to the IC cracks initiated at high stress, are not a result of incomplete baking out of dissolved hydrogen.

It is worth noting that the different threshold levels associated with the various crack generation schemes used in this study probably imply slightly different upper bounds on anomalous short crack behaviour, and this needs to be clarified in future work.

#### CONCLUSIONS

- 1) In Q1N quenched and tempered low alloy steel, small fatigue cracks initiated in bending in a region of bulk plasticity,

and subsequently stress relieved in vacuum at 650°C for 1.5 hours, have higher threshold values than fatigue cracks initiated and grown under conditions of bulk elasticity. The difference is about 0.75 MPa/m in the case considered here and this is attributed to increased plasticity-induced closure. Hence conventional stress relief treatments do not appear to anneal out all the effects of plasticity on fatigue crack growth in steels.

- 2) For cracks initiated and grown under nominally elastic conditions, the crack tip bluntness and intergranular fracture surface morphology of hydrogen-induced cracks raise measured threshold values in this steel by an average of some 0.4 MPa/m relative to transgranular fatigue cracks.
- 3) Fatigue life predictions for the small crack regime that are based on growth rate data acquired from cracks initiated in a region of bulk plasticity and subsequently stress relieved at temperatures up to 650°C may be nonconservative when applied to cracks initiated and grown under nominally elastic conditions.

#### ACKNOWLEDGEMENTS

Thanks are due to Professor R P King for the provision of laboratory facilities and to the University of Witwatersrand for the support of a Postdoctoral Research Fellowship.

#### REFERENCES

- (1) Pearson, S., Engng Fract. Mech., Vol.7, 1975, pp.235-247.
- (2) Tanaka, K. Nakai, Y. and Yamashita, M., Int. J. Fract., Vol.17, 1981, pp.519-533.
- (3) Taylor, D. and Knott, J.F., Metall. Technol., Vol.9, 1982, pp.221-228.
- (4) Lankford, J., Fatigue Engng Mater. Struct., Vol.5, 1982, pp.233-248.
- (5) Ritchie, R.O. and Suresh, S., Int. Metals Rev., Vol.29, 1984, pp.445-476.
- (6) Kendall, J.M., James, M.N. and Knott, J.F., The Behaviour of Physically Short Fatigue Cracks in Steels, 2nd Symposium on the Behaviour of Short Fatigue Cracks, Sheffield, England, to be published by Mechanical Engineering Publications, Bury St. Edmunds, 1986.

# FATIGUE 87

- (7) James, M.N. and Knott, J.F., *Fatigue Fract. Engng Mater. Struct.*, Vol.8, 1985, pp.177-191.
- (8) Breat, J.L., Mudry, F. and Pineau, A., *Fatigue Engng Mater. Struct.*, Vol.6, 1983, pp.349-358.
- (9) Bu, R. and Stephens, R.I., *Fatigue Fract. Engng Mater. Struct.*, Vol.9, 1986, pp.35-48.
- (10) Brown, C.W., King, J.E. and Hicks, M.A., *Metal Sci.*, Vol.18, 1984, pp.374-380.
- (11) James, M.N. and Smith, G.C., *Int. J. Fatigue*, Vol.5, 1983, pp.75-78.
- (12) De Los Rios, E.R., Tang, Z. and Miller, K.J., *Fatigue Engng Mater. Struct.*, Vol.7, 1984, pp.97-108.
- (13) Rooke, D.P. and Cartwright, D.J., *Compendium of Stress Intensity Factors*, HMSO, London, 1976.

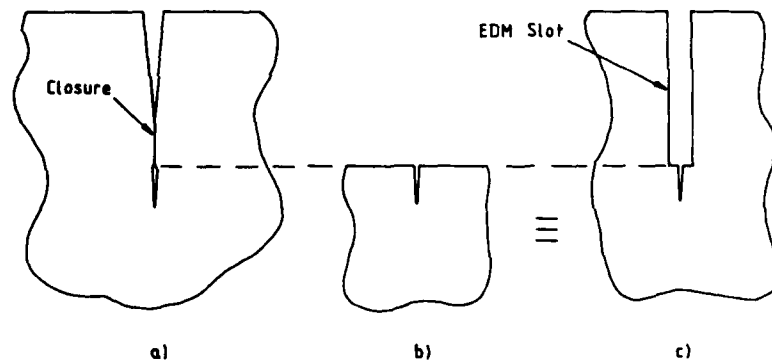


Fig. 1 Preparation of short through-thickness cracks.  
 a) Initial crack with closure contributions arising well behind the crack tip.  
 b) Machining away of wake reduces the closure value.  
 c) The equivalent situation can be obtained with a long crack.

FATIGUE 87



Fig. 2 Light fractographs showing typical hydrogen-induced cracks (arrowed) and subsequent fatigue growth.

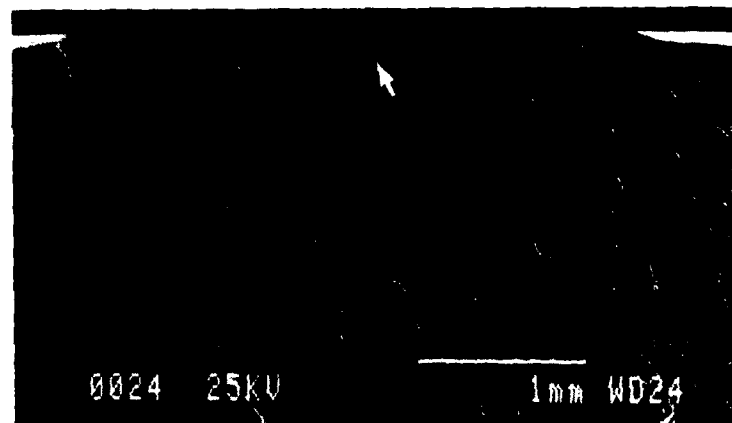


Fig. 3 SEM fractograph showing the typical initial "flake" of hydrogen-induced cracking, with a centre about 0.16 mm below the surface of the specimen.

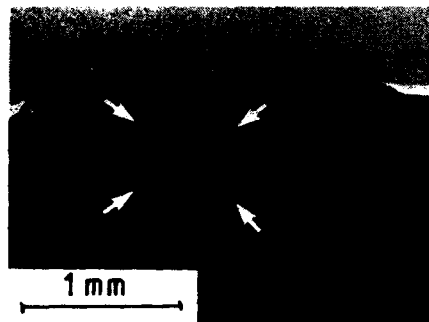


Fig. 4 Development of oval H - induced crack from initial "flake".

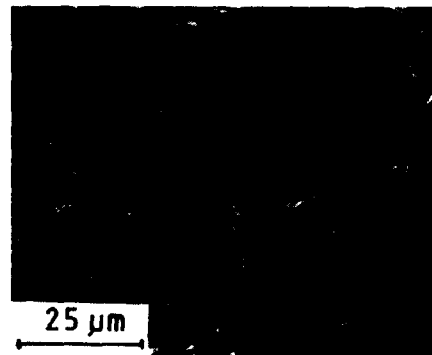


Fig. 5 Interface between H-crack and fatigue.

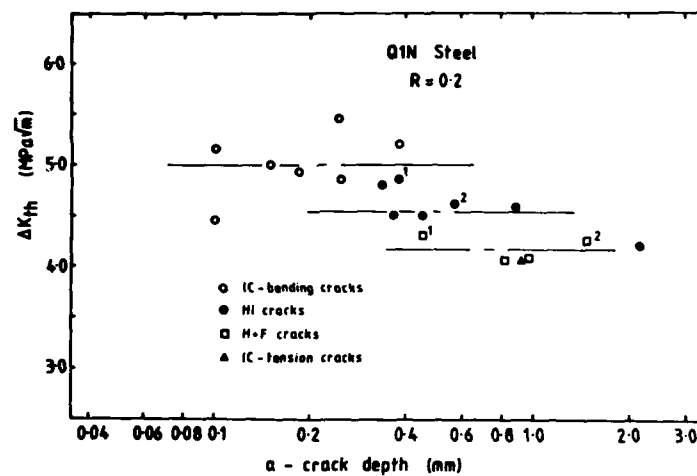


Fig. 6 Threshold data for cracks initiated by the various schemes. HI : hydrogen-induced cracks; H+F : such cracks grown by fatigue; IC-bending : inclusion initiation at high stresses; IC-tension : inclusion initiation at low stresses.

## FATIGUE 87

### EFFECT OF COMPRESSIVE PORTION OF LOADING CYCLES ON THE NEAR THRESHOLD FATIGUE CLOSURE BEHAVIOR

Heinrich Kemper, Brigitte Weiss, and Roland Stickler\*)

The influence of the compressive portion of loading cycles on the near-threshold fatigue crack growth and closure behavior was investigated for pure Cu, conventionally processed Al 2024-T3 and the mechanically-alloyed Al-Mg-Li alloy IN-905XL. Measurements were carried out for stress ratios between  $-2 < R < 0.6$  at 50 Hz and room temperature. The interrelationship between  $K_{max}$ ,  $K_{op}$  and R-ratio indicates for each material the existence of a characteristic critical compressive stress only below which closure effects become negligible, i.e.  $\Delta K_{th,eff}$  equals  $K_{max}$ .

### INTRODUCTION

The study of the effects of positive stress ratios ( $R > 0$ ) on the fatigue crack growth (FCG) and threshold behavior was subject of numerous investigations summarized in an extensive literature (1-4). The decrease of the threshold stress intensity range ( $\Delta K_{th}$ ) with increasing positive R-values was attributed mainly to a decrease in the contribution of crack closure (4). Relatively little attention has been paid, however, to the effects of compressive loading in spite of the fact that many engineering components experience compressive peak stresses under service conditions. In most measurements dealing with negative R-ratios the negative portion of the loading cycle was ignored under the assumption that a crack would be closed under compressive loading (e.g. see the pertinent ASTM recommendation, (10)). Only recently results of an investigation were published by Suresh (5) who studied the FCG behavior in specimens subjected to fully compressive far-field loading. Topper et al (6, 7) investigated the effects of compressive peak stresses on FCG in various steels and Al-alloys.

\*) University of Vienna, A-1090 Vienna, Austria

## FATIGUE 87

Their results indicate increased crack propagation rates with increasing compressive peak stresses, associated with a linear decrease of  $\Delta K_{th}$  and  $K_{op}$  values.

The objective of our investigation was to reveal further details of the effects of the compressive portion of the loading cycle on FCG and closure behavior in the range of  $-2 < R < 0.6$  for materials with differing microstructures, deformation behavior and mechanical properties. For this study recrystallized pure Cu, a conventionally processed precipitation hardened Al-alloy and an ultra-fine grained dispersion-strengthened Al-Mg-Li alloy were chosen.

### SPECIMEN MATERIALS AND EXPERIMENTAL TECHNIQUES

For this investigation bars of commercial oxygen-free Cu, plates of wrought and heat treated Al 2024-T3, and a billet of mechanically-alloyed IN-905XL in the as-extruded condition were selected as specimen materials. Composition, heat treatment and microstructure of these materials are listed in Table 1, data on tensile properties and the dynamic Young's modulus are summarized in Table 2.

TABLE 1 - Composition, heat treatment and microstructure of specimen materials

Cu:	Commercial oxygen-free P-deoxidized; Heat treatment: 2h/650°C/ Vacuum $5 \times 10^{-3}$ Pa; Grain size: 50 $\mu\text{m}$ ;
Al 2024:	4.5 Cu, 1.5 Mg, 0.6 Mn; Heat Treatment: T-3; Grain size: 120 $\mu\text{m}$ <L>, 65 $\mu\text{m}$ <T>, 25 $\mu\text{m}$ <ST>; Coarse and fine precipitates (8)
IN-905XL:	4 Mg, 1.5 Li, 1.1 C, 0.8 O <sub>2</sub> ; As-extruded; Grain size: $\sim 2 \mu\text{m}$ ; Fine oxide and carbide dispersoids

TABLE 2 - Mechanical properties of as-received specimen materials

Material	$R_{p0.2\%}$ , MPa	$R_m$ , MPa	$E_{dyn}$ , GPa
Cu	60	220	129
Al 2024-T3 (in <L>)	345	450	72.5
IN-905XL	430	500	81.3

The fatigue tests were carried out with a 20 kN servohydraulic testing machine operated at a frequency of 50 Hz at room temperature in laboratory air over a

## FATIGUE 87

range of R-values between -2 and 0.6, ( $R = S_{min}/S_{max}$  or  $K_{min}/K_{max}$ ).

For these investigations bar-shaped specimens were machined with a cross section in the gauge length of 20mm x 5mm or 30mm x 5mm for Cu and 16mm x 6mm for the Al-alloys. After metallographically polishing the mid-section of each specimen a lancet-shaped center surface notch (2mm length, 1mm depth, in accordance with ASTM (9)) was introduced by EDM, giving rise to semi-elliptical fatigue crack growth. For comparison, center through notched specimens were prepared by drilling a central hole of 1.5mm diam. and introducing two opposing side cuts of 0.5mm length by EDM.

Fatigue crack growth data were obtained for both types of specimens according to ASTM recommendations (10). Crack nucleation and FCG were observed under stroboscopic illumination by means of a travelling light microscope with a resolution of approx. 50  $\mu\text{m}$ .

Threshold values were measured by a load shedding technique in which the cyclic load was reduced from an initiating stress level (approximately 20% above the expected threshold) by 5% after each  $10^6$  loading cycles. The threshold was taken as that stress amplitude for which no FCG could be observed after  $10^7$  loading cycles, corresponding to a FCG-rate of less than  $5 \times 10^{-12} \text{m/cycle}$ .

To facilitate the microscopic observations of FCG and local deformation a grid with a mesh-size of 200  $\mu\text{m}$  was vapor-deposited onto the mid-section of the specimen. Crack closure effects were determined by a strain gauge method (11, 14), i.e. a miniature strain gauge with an active area of 0.6mm x 0.6mm was centered on the surface area of the unloaded specimen containing the tip of the fatigue crack. Penetration of adhesive was prevented by protecting the crack region with a narrow strip of vapor deposited carbon. Monotonic load-displacement curves were recorded after threshold measurements in tension ( $S_{open}$ ) as well as in compression ( $S_{closed}$ ) to obtain information on the total stress range between the completely closed and completely opened crack, as shown in Fig. 1. The stress intensity values for semi-elliptical surface cracks were calculated according to Raju and Newman (12) and verified by FEM-analyses of Blom (13) for our specific specimen geometry. To determine the required shape factor of the semi-elliptical surface cracks ( $2c/a$ ,  $2c$ ..length of crack on the specimen surface,  $a$ ..depth of crack) all specimens were ruptured after the threshold measurement. All  $\Delta K$  values listed refer to the deepest point, "a", of the fatigue crack. The calculations for center through cracks were performed according to literature (14).

The effective threshold range was calculated as

$\Delta K_{th,eff} = K_{max} - K_{op}$ , as recommended for the case of  $K_{op} > K_{min}$  (11). A comparison of the  $\Delta K_{th}$  and  $\Delta K_{th,eff}$  values obtained from specimens containing a surface notch or a through notch showed similar results for both types of specimens. In view of the ease of measurements most experiments described in this paper were carried out with surface-notched specimens. Calculations of the monotonic and cyclic plastic zone sizes for the near- $\Delta K_{th}$  loading conditions according to Lankford (15) indicate the validity of LEFM considerations with a possible exception for the stress levels applied to Cu at  $R > 0.5$ , for which cyclic creep may play a role (16).

The variation in the roughness of the fracture surface topography was determined with the aid of a light microscope by a focusing method. Values of the fine-focus control (calibrated in  $\mu m$  steps) between focus on the highest elevations and the adjacent deepest valleys were recorded. Considerable scatter in the measured values was encountered. The roughness values listed in the following were calculated as the mean of at least 10 difference-readings in the near- $\Delta K_{th}$  fracture region.

#### EXPERIMENTAL RESULTS AND DISCUSSION

The effect of mean stress on  $\Delta K_{th}$  can be deduced for the various materials from the diagrams in Figs. 2a-c. According to ASTM (10) only the positive part of the loading cycle is taken into account for  $R < 0$ . For Cu all experimental data points are plotted to indicate the typical scatter, the points for the other materials represent mean values of at least two independent measurements. The measured  $K_{op}$  and the calculated  $\Delta K_{th,eff}$  values plotted in the Figs. 2a-c show significant differences between the various materials.

##### Recrystallized Cu

For Cu the  $K_{op}$  values decrease steadily with  $R$  from 0 to -1.5, approaching negligible values. As a consequence  $\Delta K_{th}$  approaches  $\Delta K_{th,eff}$  for values of  $R < -1.5$ . The levelling-off of  $K_{op}$  for  $R > 0.3$  may be attributed to the effects of cyclic creep which may be deduced from the observation of considerably parted crack faces in the unloaded specimen after testing at  $R = 0.6$ . The LEFM evaluation of such a crack may be questionable. The results in the region of  $R > 0$  are similar to data listed by Liaw et al (17).

The low  $K_{op}$  values at  $R < -1.5$  can be explained by fractographic observations. Over the total  $R$ -range investigated a predominantly transcrystalline fracture mode with a small fraction of intercrystalline failure

could be observed. The latter is considerably decreased at  $R = -2$ , Fig. 3. The roughness of the fracture surface, Fig. 4, shows considerable flattening for  $R = -2$  (see the corresponding SEM-micrographs in Fig. 3). Our observations indicate that the closure is mostly related to roughness and plasticity, since exploratory tests in Ar-atmosphere resulted only in slightly lower values of  $K_{op}$  while  $\Delta K_{th,eff}$  remained essentially the same. In the evaluation of the test results of recrystallized Cu the cyclic hardening of the metal in the remaining cross-section should not be neglected.

#### Al 2024-T3

Measurements for Al 2024-T3 were only performed in the region of  $R < 0$ , data for  $R > 0$  were taken from a publication by Blom (14) for the same material, Fig. 2b. While  $\Delta K_{th}$  was found to decrease with increasing  $R > 0$ , the  $K_{op}$  values appear not to change between  $0 < R < 0.5$ . A steep rise in  $K_{op}$  is noticed only for larger  $R$ -values. These observations for  $R > 0$  are in agreement with data reported by McEvily et al (18) for Al 7090-T6, who explained the variation of  $\Delta K_{th,eff}$  by contributions of Mode II crack growth increasing with  $R$  from 0 to 0.5. Our fractographic evaluation shows that with increasing  $R$  the fracture surfaces exhibit increasing amounts of Mode II fracture. For  $R > 0.5$  a small fraction of ductile rupture can be recognized. It is of interest that at  $R = 0.7$  the  $\Delta K_{th,eff}$  is of the same magnitude as at negative  $R$ -values.

With  $R$  decreasing below zero  $\Delta K_{th}$  decreases until an almost constant value was found for  $R < -1$ , associated with constant  $K_{op}$ -values. The resulting  $\Delta K_{th,eff}$  appears to remain at a constant level between  $-2 < R < -0.3$ . If we attempt to extrapolate our data to lower negative  $R$ -values by using data published by Topper et al (7) we may speculate that  $K_{op}$  will approach zero at  $R$ -values between -4 to -8. The linear equation proposed by Topper for the relationship between  $\Delta K_{th}$  and the compressive portion of the stress cycle appears to be valid only within a limited range.

The roughness of the fracture surfaces of Al 2024-T3 decreases with decreasing  $R$  as shown in Fig. 4. Corresponding SEM-micrographs of representative regions of the fracture surfaces, Fig. 3, indicate also an effect of  $R$  on surface topography. The fracture surface of Al 2024-T3 appears covered with fretting debris and oxide particles most noticeable for  $R = 0$  which is an indication of contributions by oxide-induced closure. The apparent flattening of the fracture surfaces with decreasing  $R$  corresponds to the increase in compressive loading.

Extruded IN-905XL

For the ultra-fine grained IN-905XL a constant value of  $\Delta K_{th}$  was found over the whole range of  $-2 < R < 0.6$ . Since no  $K_{op}$  could be measured, the  $\Delta K_{th,eff}$  may be considered as constant and equal to  $\Delta K_{th}$ . Similar observations were reported for  $R > 0$  by McEvilly for the mechanically alloyed IN-9021-T4 (18) and of Ruch&Starke (19) for a mechanically alloyed Al-Mg-Li alloy. For IN-905XL the roughness of the fracture surface falls below the resolution of the experimental technique, Fig. 4. It is interesting to note in SEM-micrographs that the fracture surfaces of this material still show an influence of compressive loading, albeit to a much lesser degree than observed for the other materials. The absence of a closure effect and the resulting constant  $\Delta K_{th}$  can also be deduced from the near-threshold FCG curves, which overlap for a wide R-range, Fig. 5. Equivalent curves for Cu and Al 2024 (14) show a pronounced R-effect.

Effect of mean stress on threshold behavior

As an alternative to the R-dependence the threshold behavior may be presented as a function of the mean stress, e.g. in the form of  $K_{mean}/(K_{max}, K_{min})$  diagrams similar to Smith diagrams used for presenting mean stress effects of fatigue data. Such diagrams are shown for the tested materials in Figs. 6a-c. In addition, the measured values of  $K_{op}$  are included. For Cu also the measured values of  $K_{closed}$  are indicated. The  $\Delta K_{th,eff}$  can be deduced from the range  $(K_{max} - K_{op})$  or  $(K_{max} - K_{min})$ , the latter for the case  $K_{op} < K_{min}$ . The relationships expressed in these diagrams reveal marked differences between the three materials.

For Cu, a linear relationship of  $K_{max}$  and  $K_{min}$  with  $K_{mean}$  is apparent over a wide range, limited at high values of  $K_{mean}$  by the onset of cyclic creep and at low  $K_{mean}$  values at which  $K_{op}$  becomes zero. It is interesting to note that at this negative mean stress also the  $K_{closed}$  value approaches zero which indicates that from there on the fatigue crack is essentially closed. Further observations of this effect will be published.

For IN-905XL a similar linear relationship between  $K_{mean}$ ,  $K_{max}$  and  $K_{min}$  as for Cu can be observed over a larger  $K_{mean}$  range. Due to the absence of a closure contribution a constant  $\Delta K_{th,eff}$  occurs for  $K_{mean}$  values below which  $K_{min}$  is equal to zero. A similar behavior in Al 2024 is only apparent for high  $K_{mean}$  values. Due to the observed change in fracture mode a gradual transition takes place within a  $K_{mean}$  range where  $K_{max}$  arrives at a constant value. However, in the negative  $K_{mean}$  range evaluated in present study the  $K_{op}$  does not

## FATIGUE 87

decrease to negligible values. From these observations we may infer a  $K_{mean}$  limit for Cu and IN-905XL below which the ASTM recommendation of taking only the tensile portion of the loading cycle is justified. This appears not to be the case for Al 2024, which even at the lowest  $K_{mean}$  value investigated (equivalent to  $R = -2$ ) shows a marked closure contribution, that is,  $K_{max}$  remains larger than  $\Delta K_{th,eff}$ .

### CONCLUSIONS AND SUMMARY

1. FCG studies with center surface-notched specimens yield comparable results as obtained for conventional CN-specimens. In view of experimental simplifications and the ease of specimen preparation the use of the former specimens is of advantage as long as the applied maximum stresses (in particular during cyclic loading for crack initiation) remain sufficiently below the cyclic yield stress.
2. The experimental values of  $\Delta K_{th}$  plotted as function of  $R$  reveal a maximum at  $R=0$  for Cu and Al 2024, related to changes in closure contribution (mainly roughness-induced). The ultra-fine grained IN-905XL exhibits no measureable closure and hence a constant  $\Delta K_{th}$  value over the range of  $-2 < R < 0.6$ .
3. The compressive portion of the loading cycles for  $R < 0$  results in a gradual reduction of  $\Delta K_{th}$  and  $K_{op}$  because of a progressive flattening of the fatigue fracture surface.
4. The variations in the  $\Delta K_{th,eff}$  values with  $R$ , in particular noticeable for Al 2024, may be attributed to changes in material properties (e.g. due to cyclic creep) or failure modes (e.g. increasing contributions of Mode II cracking).
5. The presentation of  $\Delta K_{th}$  as function of  $K_{mean}$  (modified Smith diagram) appears of advantage for a separate consideration of tension and compression effects. In particular, the range of an influence of the compressive load on  $\Delta K_{th,eff}$  can be visualized. Such diagrams show that simple mathematical relations are only meaningful as long as no significant changes in failure mode or material properties take place.
6. The results indicate the existence of a critical compressive stress below which  $K_{op}$  approaches zero, i.e.  $\Delta K_{th} = \Delta K_{th,eff}$  equals  $K_{max}$ . It is only in this range that the ASTM recommendation to use only the tensile portion of the loading cycle for  $R < 0$  may be applied correctly.
7. The results of measurements of the  $\Delta K$ -values associated with a completely open or completely closed

## FATIGUE 87

fatigue crack appear interesting and may yield information on the critical compressive load which has to be applied to reduce crack closure to negligible values, hence, for which  $\Delta K_{th} = \Delta K_{th,eff} = K_{max}$  becomes valid.

### ACKNOWLEDGEMENTS

The authors acknowledge the support by the Fonds zur Förderung der Wissenschaftlichen Forschung and the Bundesministerium für Wissenschaft und Forschung, Vienna (part of COST Action 503). The Al 2024 was supplied by Dr. A.F.Blom. Ms E.Schulz prepared the typescript.

### LITERATURE

1. Proc.1st Internat.Conf. "Fatigue Threshold", Stockholm, EMAS Ltd, UK, 1982
2. Proc.Symp."Fatigue Crack Growth Threshold Concepts" Philadelphia, TMS-AIME, USA, 1984
3. Fatigue 84, Proc.2nd Internat.Conf.on Fat.and Fat. Thresholds, Birmingham, EMAS Ltd, UK, 1985
4. "Fatigue Crack Closure", ASTM-STP, 1986
5. Suresh S., Eng.Fract.Mech. 21, 1985, p. 453
6. Yu M.T., Topper T.H., DuQuesnay D.L. and Levin M.S., Internat.J.Fatigue 8, 1986, pp. 9-15
7. Yu M.T., Topper T.H. and Au P., Ref.3 Vol.I, p.179
8. Hatch J.H., "Aluminum", ASM-Metals Park, USA, 1984
9. ASTM Standard E 740-80
10. ASTM Standard E 647-81
11. Schmidt R.A. and Paris P.C., ASTM-STP 536, 1973, pp. 79-90
12. Raju I.S. and Newman J.C., Eng.Fract.Mech.11,1979, pp. 817-829
13. Blom A.F., Gustavson A.I., Hadrboletz A. and Weiss B., Proc.Int.Conf.Fat.Eng.Mat.&Struct., Sheffield, 1986, in print
14. Blom A.F., Hadrboletz A. and Weiss B., Proc. ICM-4 Stockholm, 1984, pp. 755-762
15. Lankford J., Davidson D.L. and Cook T.S., ASTM-STP 637, Philadelphia, 1977, pp. 36-53
16. Lorenzo F. and Laird C., Mat.Sci.Eng.62, 1984, pp. 205-210
17. Liaw P.K., Leax T.R., Williams R.S. and Peck M.G., Met.Trans. 13A, 1982, p. 1607-1618
18. Minakawa K., Levan G. and McEvily A.J., Met.Trans. 17A, 1986, pp. 1787-1795
19. Ruch W. and Starke E.A., Proc.Internat.Conf. "Al-Li Alloys III", Oxford, Inst.Metals, London 1986, pp. 121-130

# FATIGUE 87

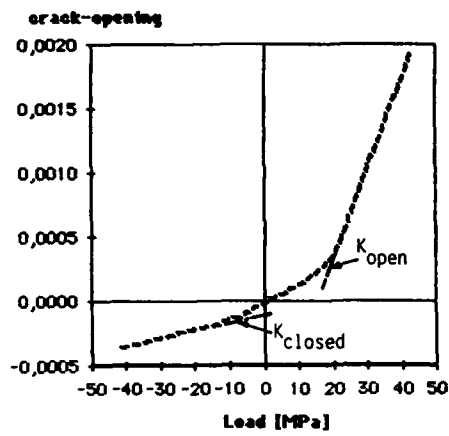


Fig. 1: Crack-opening-load curve,  
Cu,  $\Delta K_{th} = 4,2 \text{ MPa}\cdot\text{m}^{1/2}$   
at  $R = -1$

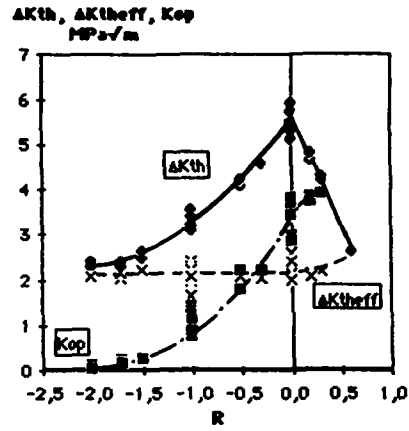


Fig. 2a: Cu

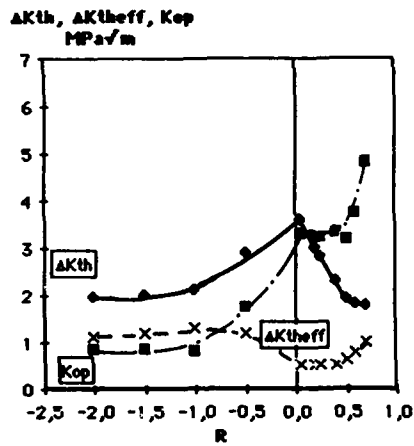


Fig. 2b: Al 2024-T3

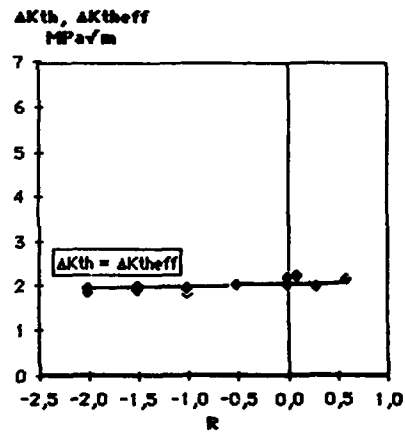
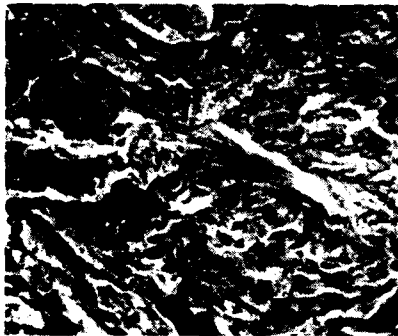


Fig. 2c: IN-905 XL

Fig. 2: Effect of R on  $\Delta K_{th}$  and  $\Delta K_{th_{eff}}$

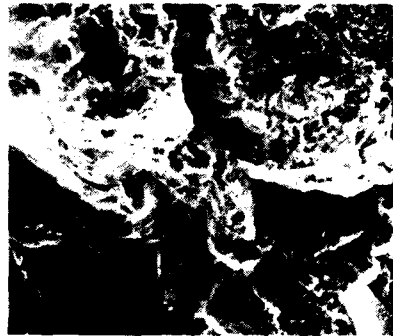
# FATIGUE 87



$R=-2$   $K_{Op} \approx 0$

10 $\mu$ m

Cu



$R=0,3$ ;  $K_{Op} = 3,9 \text{ MPa} \cdot \text{m}^{1/2}$

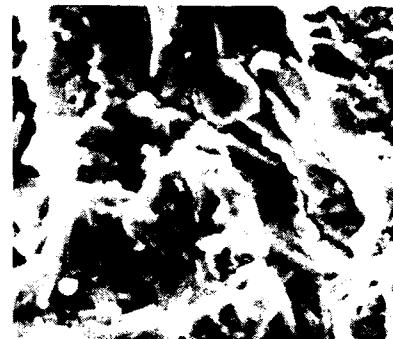


$R=-2$ ;  $K_{Op}=0,84 \text{ MPa} \cdot \text{m}^{1/2}$

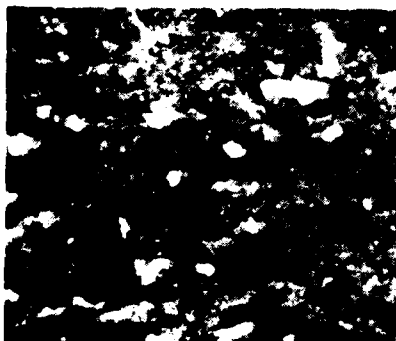
Al

2024-T3

10 $\mu$ m

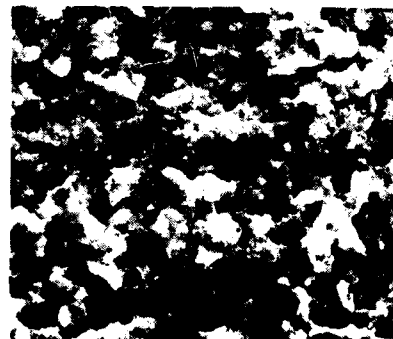


$R=0,7$ ;  $K_{Op}=4,8 \text{ MPa} \cdot \text{m}^{1/2}$



$R=-1$ ;  $K_{Op} \approx 0$

IN 905 XL



$R=0,3$ ;  $K_{Op} \approx 0$

10 $\mu$ m

Fig. 3: SEM-micrographs of fatigue fracture surfaces

# FATIGUE 87

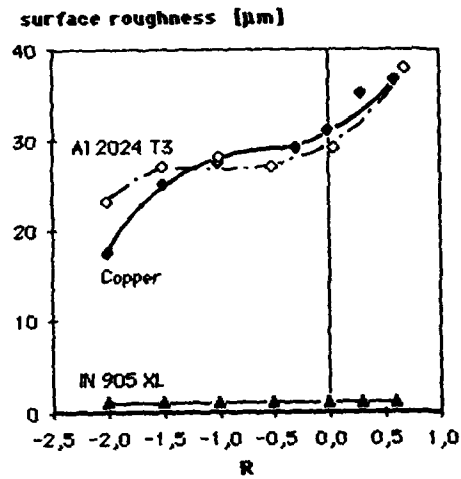


Fig. 4: Effect of R on the roughness of fatigue fracture surfaces

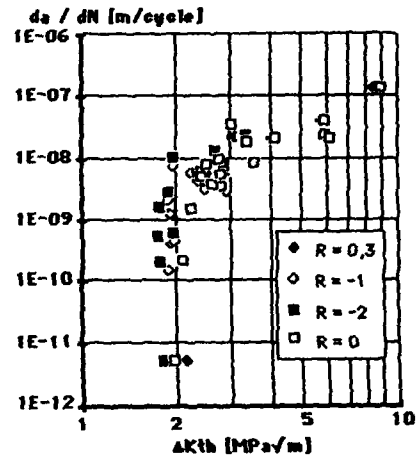


Fig. 5: Fatigue crack growth for  $-2 < R < 0.3$  in IN 905 XL

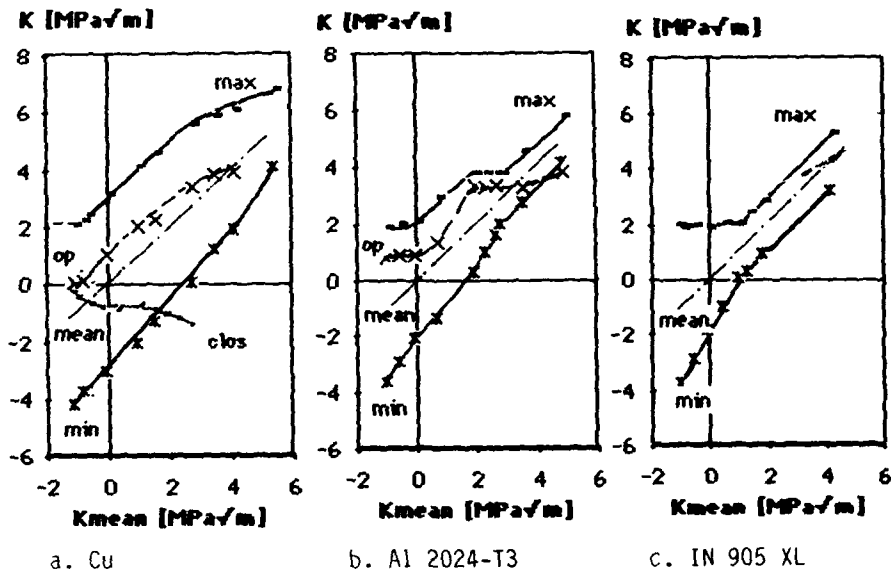


Fig. 6: Effect of mean-stress on fatigue threshold data ("Smith-diagram")

FATIGUE 87

800

ABSOLUTE FATIGUE THRESHOLDS IN METALLIC MATERIALS

J.A. LEWIS\*

Fatigue studies in the near threshold region on a range of materials show the existence of an absolute fatigue crack propagation threshold and an upper-bound fatigue crack propagation rate. These are observed when the fatigue testing conditions are such that transient effects associated with plasticity-induced crack closure are removed.

Under these conditions, multilinear  $da/dN-\Delta K$  curves were observed in Ti-8Al-1Mo-1V alloy, and type 303 stainless steel as well as aluminium alloys 7005-T591 and 5083-H321. Coincidental relationships were noted between the transition points and specific growth rates in these three material types.

INTRODUCTION

It is now well accepted in metal fatigue studies that the fatigue crack propagation rate is some function of the stress intensity factor range. Early studies were aimed at eliciting the exact functional relationship, or "crack growth law", and a common starting point has been the Paris-Erdogan equation (1). The discovery by Elber of the crack closure phenomenon (2), which helped explain the effect of the fatigue ratio,  $R$ , on crack growth rates, has extended our knowledge of some of the complexities of the fatigue crack propagation process.

Fatigue thresholds have been the subject of considerable attention in recent years, particularly as regards the supposedly anomalous behaviour of short cracks. The influences of microstructural features, such as grain size, of crack closure and fatigue ratio have been well documented. Similarly, the significance of the cyclic plastic zone size in respect of the fatigue threshold has long been recognised. Recent evidence, Yoder et al. (3) suggests that the cyclic plastic zone size and its relation to certain microstructural features gives rise to the transition points

\*Department of Mechanical Engineering, The University of Newcastle N.S.W. 2308, Australia.

## FATIGUE 87

observed in the multilinear  $da/dN$  curves. Multiple transition points are commonly observed in some aluminium alloys.

In order to obtain a better understanding of the threshold condition and the transition point phenomenon it is considered that fatigue testing should be carried out under conditions such that plasticity-induced crack closure effects are removed.

This paper presents the results of such studies in progress on a range of steels, aluminium alloys, and a titanium alloy, in a laboratory air environment.

### MATERIALS AND EXPERIMENTAL PROCEDURE

Some of the materials discussed in this paper have been described elsewhere by the author (4). Further fatigue studies have been carried out on the aluminium alloys, 7005-T591 and 5083-H321. In addition, duplex annealed Ti-8Al-1Mo-1V has been studied, and work on type 303 stainless steel is in progress. The titanium alloy sample was from material previously studied by Wanhill and Döker (5). Details of these materials are tabulated below.

Fatigue testing was carried out on an MTS closed loop electro-hydraulic testing facility of 300 kN static capacity. Cycling was mostly carried out with the minimum fatigue load maintained above the crack closure load. Compact tension specimens were used in thicknesses ranging from about 11 mm to 25 mm.

TABLE 1 - Materials studied

Material	Nominal Composition	Nominal Yield Stress
Al 5083-H321	4.5Mg, 0.7Mn	240 $\text{MNm}^{-2}$
Al 7005-T591	4.5Zn, 1.5Mg	350 "
Ti-8Al-1Mo-1V	7.7Al, 1.0Mo, 1.0V	845 "
Type 303 Stainless	0.1C, 1.8Mn, 0.3S, 9.0Ni, 18.0Cr	280 "

### RESULTS

#### Crack Propagation Data

The fatigue crack propagation rate versus stress intensity factor range behaviour of the materials are shown in Figs. 1 and 2. These results have also been normalised with respect to the respective Young's moduli, and plotted as  $da/dN - \Delta K/E$  curves in Fig. 3.

## FATIGUE 87

Typical multilinear  $da/dN$  curves were obtained for the two aluminium alloys, the type 303 stainless steel, and the Ti-8Al-1Mo-1V alloy. Surprisingly, one of the transition points was common to all three materials, when viewed in terms of crack growth rates. Two other transition points were shared by the aluminium alloys and either the titanium alloy or stainless steel. Fatigue cycling of the stainless steel was not carried through to growth rates above  $3 \times 10^{-9}$  m/cycle.

### Fractography

Macroscopic examination of the fatigue fracture surfaces of the three materials revealed bright and dull bands associated with the growth rates lower or higher than the transition point at  $2.5 \times 10^{-9}$  m/cycle common to all materials. In general, growth rates less than  $2.5 \times 10^{-9}$  m/cycle gave rise to much rougher surface topographies, while growth rates above this transition point resulted in smoother surfaces. The bright/dull appearance was dependent on the orientation of the sample with respect to viewing light.

Scanning electron microscope studies of the fracture surfaces of the titanium alloy showed large areas of smooth fracture and areas of cleavage facets associated with longitudinal texturing, throughout the whole growth range. At low growth rates, near the fatigue threshold, the fracture surface consisted of cleavage facets linked by ductile shear. Between  $T_1$  and  $T_2$ , the fracture surface consisted of cleavage facets linked by structure-insensitive crack growth. Above  $T_2$  the fracture surface consisted of structure-insensitive crack growth, with some cyclic crack growth markings and secondary cracking.

### DISCUSSION

The fatigue crack growth curves obtained on the aluminium alloys, the titanium alloy, and the type 303 stainless steel support the previously proposed concept of absolute fatigue thresholds and upper bound fatigue crack growth rates when plasticity-induced crack closure effects are removed. Normalising the data by plotting  $da/dN - \Delta K/E$  curves gives added support to this concept.

It has been suggested that the transition from a structure-sensitive to structure-insensitive mode of fatigue crack growth takes place when the plane strain cyclic plastic zone size exceeds a length parameter based on microstructural barriers to slip-band transmission (3). In the case of steels and some titanium alloys grain boundaries are considered to be the predominant barriers, hence the grain size is the limiting parameter. Published data generally show a bilinear form of  $da/dN - \Delta K$  curve, provided region III is excluded.

For aluminium alloys, a trilinear form of  $da/dN - \Delta K$  curve is

## FATIGUE 87

often observed, once again with region III excluded. In these instances, the transition points are considered to be associated with the plane strain cyclic plastic zone size exceeding the dispersoid spacing at the first transition, the sub-grain size at the second, and the grain size at the third. The structure-sensitive to structure-insensitive transition takes place at the second transition point, Stofanek et al. (6).

The present studies confirmed the trilinear form of  $da/dN - \Delta K$  curve for the aluminium alloys. Of interest was the fact that trilinear type curves were also obtained for the titanium alloy and the stainless steel. In each instance, it was apparent from macroscopic examination of the fracture surface that the structure-sensitive to structure-insensitive transition occurred at the second transition point. Coincidentally, this transition point was common for all three material, on a crack growth rate basis, i.e. it occurred at  $\sim 2.5 \times 10^{-9}$  m/cycle.

The fact that the stainless steel exhibited this type of behaviour is not unexpected, since it has the same FCC structure as the aluminium alloys. However, the behaviour of the titanium alloy was unexpected.

In the titanium alloy the  $\alpha$  phase was mainly Widmanstätten, with very variable packet size. The plane strain cyclic plastic zone size at the  $T_2$  transition point,  $1.95 \mu\text{m}$ , correlates well with the elongated  $\alpha$  minor dimensions,  $1-3 \mu\text{m}$ , reported for this sample (5).

The plane strain cyclic plastic zone sizes at each of the transition points for the aluminium alloys and titanium alloy were of the same orders of magnitude, as shown in Table 2.

TABLE 2 - Plane strain cyclic plastic zone size

	Al 7005-T591	Ti-8Al-1Mo-1V	Type 303 Stainless
$T_1$	$0.61 \times 10^{-6} \text{m}$	$0.47 \times 10^{-6} \text{m}$	$8.5 \times 10^{-6} \text{m}$
$T_2$	$1.68 \times 10^{-6} \text{m}$	$1.95 \times 10^{-6} \text{m}$	$20.0 \times 10^{-6} \text{m}$
$T_3$	$10.7 \times 10^{-6} \text{m}$	$10.4 \times 10^{-6} \text{m}$	-

An examination of results previously obtained on a range of steels (4), indicated that bilinear form  $da/dN - \Delta K$  curves were obtained with high strength quenched and tempered alloy steels, and medium strength pearlitic steels. Some of the lower carbon steels appeared to show a slight tendency towards a trilinear form of

## FATIGUE 87

$da/dN - \Delta K$  curve. These aspects are to be the subject of further investigation.

Values of the plane strain cyclic plastic zone size calculated at the single transition points for the range of steels examined did not correlate with the respective grain sizes. Hence it must be assumed that some other microstructural feature is acting as a barrier to slip-band transmission.

### CONCLUSIONS

The present results support the previously proposed concept of an absolute or real fatigue threshold required for fatigue crack propagation in steels, aluminium alloys and titanium alloy, and of relative or transient fatigue thresholds associated with plasticity-induced crack closure effects.

Multilinear  $da/dN$  curves were observed in the Ti-8Al-1Mo-1V alloy and type 303 stainless steel as well as the aluminium alloys 7005-T591 and 5083-H321. The former were unexpected. The change from structure-sensitive to structure-insensitive mode of fatigue crack propagation took place at the  $T_2$  transition point. In the case of the Ti-8Al-1Mo-1V alloy, the plane strain cyclic plastic zone size correlated well with the elongated  $\alpha$  minor dimensions reported on this alloy.

Values of the plane strain cyclic plastic zone size at the single transition point for the steels did not correlate with the respective grain sizes.

### REFERENCES

1. Paris, P.C. and Erdogan, F., J. Basic Engng., Vol. 85, 1963, pp. 528-534.
2. Elber, W., Engng. Fracture Mech., Vol. 2, 1970, pp. 37-45.
3. Yoder, G.R., Cooley, L.A. and Crooker, T.W., in "Fatigue 84", Proc. Intl. Conf. on Fatigue and Fatigue Thresholds, Edited by C.J. Beevers, EMAS Ltd., Warley, England, pp. 351-360.
4. Lewis, J.A., *ibid*, pp. 265-274.
5. Wanhill, R.J.H. and Döker, H., TMS-AIME Paper No. A78-35, The Metallurgical Society of AIME, New York.
6. Stofanak, R.J., Hertzberg, R.W., Leupp, J. and Jaccard, R., Engng. Fracture Mech., Vol. 17, 1983, pp. 541-554.

# FATIGUE 87

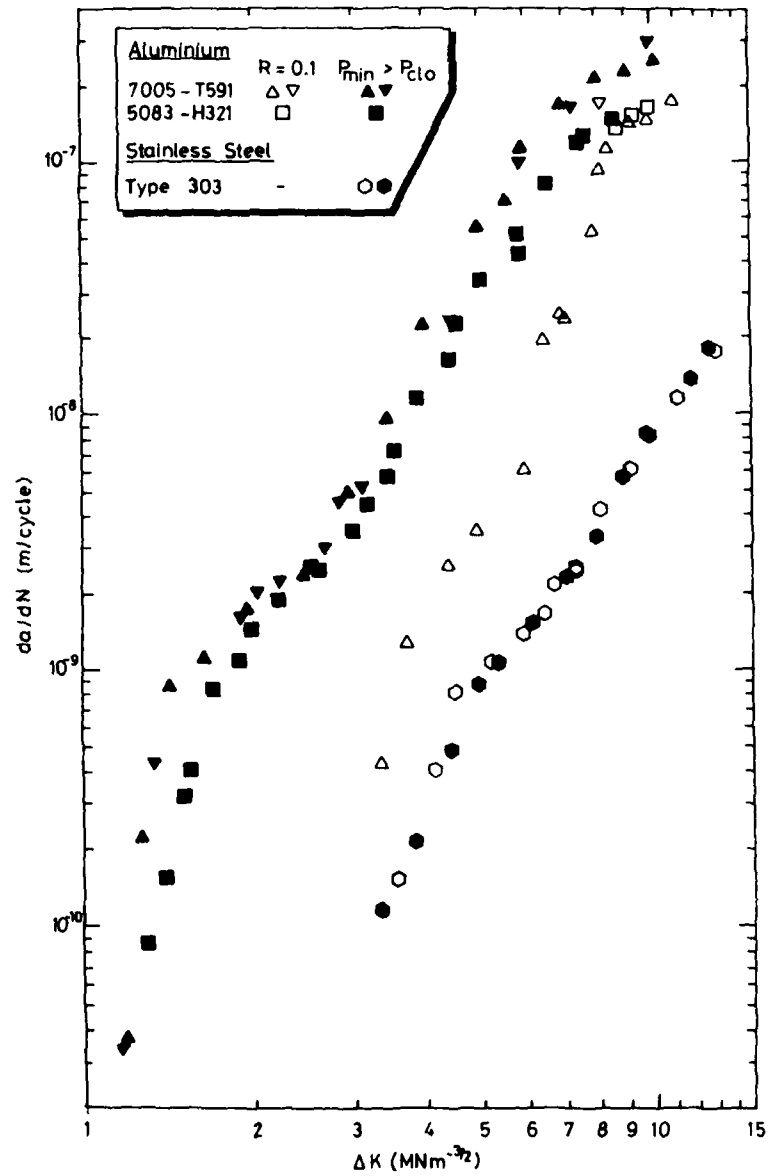


Figure 1 Fatigue crack growth curves -  $da/dN$ - $\Delta K$

# FATIGUE 87

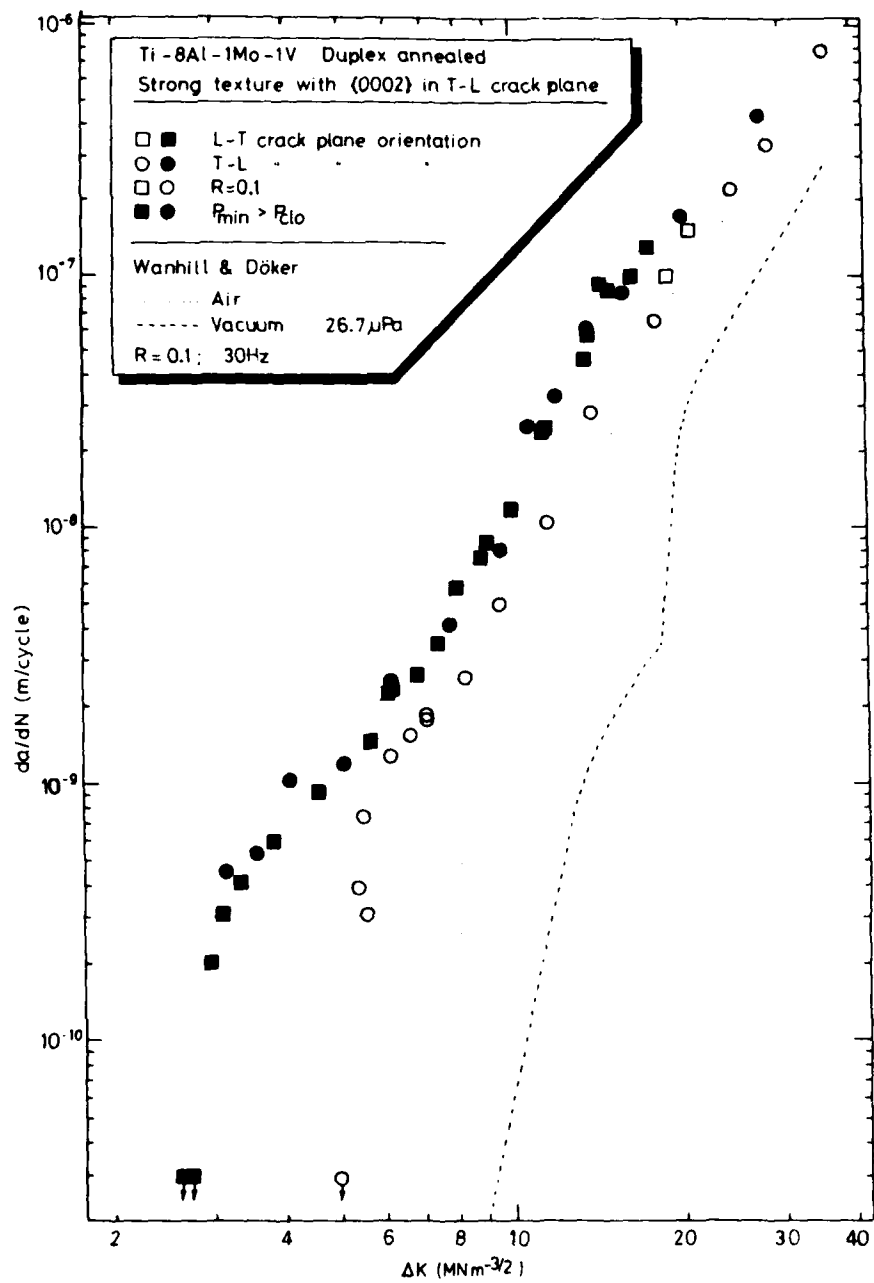


Figure 2 Fatigue crack growth curves -  $da/dN$ - $\Delta K$

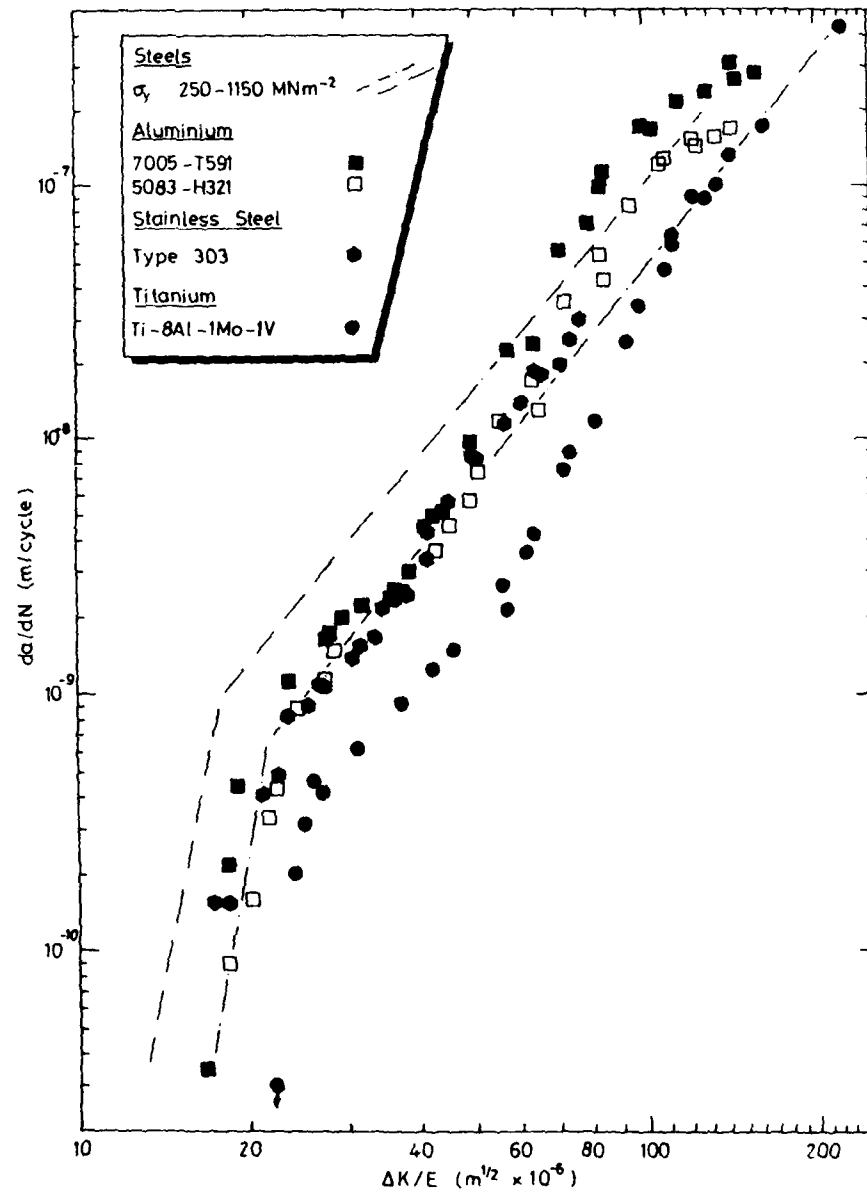


Figure 3 Fatigue crack growth curves -  $da/dN$ - $\Delta K/E$

## FATIGUE 87

### THERMOMETRICAL INVESTIGATIONS ON THE NEAR THRESHOLD FATIGUE CRACK PROPAGATION BEHAVIOR

K. Müller and H. Harig\*

Thermocouple measurements during monotonic and cyclic deformation were carried out. By means of the thermoelastic effect and the dissipation of work done during deformation, a thermometrical method is described which allows the separate registration of the elastic and the plastic deformation parts. By using this investigation method the crack opening load and the stress arrangement during crack growth near the threshold value can be determined.

### INTRODUCTION

Regarding periods of technical interest, in a metallic material fatigue crack propagation can be observed if the cyclic stress intensity exceeds a characteristic threshold value. Actually, elastic and small plastic deformations at the crack tip can be detected under loading histories, which do not induce measurable crack growth processes. According to the very small extension, the plastically deformed zones in front of the crack tips are very difficult to evaluate using conventional methods of deformation measurement. Recent investigations show the particular possibility to evaluate the behavior of a small volume unit during monotonic and cyclic deformation by using sensitive thermometrical methods (1-7, 13).

The determination of an effective threshold value requires the evaluation of the crack opening load. The thermoelastic effect can be used to determine the crack

\* Universität Essen, Werkstofftechnik,  
4300 Essen 1, FRG

## FATIGUE 87

opening load in a monotonic tension test with a stepwise load increase (3).

In this report, a thermometrical measuring system will be introduced, which can be used to evaluate a threshold value of crack propagation with a relatively small temporal expense. Furthermore, an effective threshold value can be estimated by using the thermometrically determined crack opening load. In addition, changes of active stress and changes of stress arrangements in front of a running crack can be reliably monitored due to the thermoelastic effect.

### CHANGES OF TEMPERATURE DURING ELASTIC AND PLASTIC DEFORMATION

Under pure elastic deformation the measurable changes of temperature are mainly based on reversible changes of volume (3, 7). The so called thermoelastic effect, which formulates this relation, has been derived thermodynamically by Thomson (8). The effect is also valid at multi-axial stress states. It can be assigned in the following way:

$$\Delta T_{ad} = - \frac{T_0 \cdot \alpha}{c \cdot \rho} (\Delta \sigma_{xx} + \Delta \sigma_{yy} + \Delta \sigma_{zz}).$$

The change of temperature  $\Delta T_{ad}$  is directly proportional to the applied stress  $\Delta \sigma$  under adiabatic conditions. Furthermore, the change of temperature is a function of the absolute temperature  $T_0$ , the linear coefficient of thermal expansion  $\alpha$ , the specific heat capacity  $c$  and the density of the material  $\rho$ . At a metallic material a positive change of stress induces a decrease of temperature and a negative change of stress induces an increase of temperature, respectively. This means physically that changes of temperature depend on direction of volume changes. At cracked as well as at unnotched flat samples the linear correlation between the change of temperature and the change of applied stress has been experimentally proofed by regarding the results of a tension test with a stepwise load increase (3).

On the other hand, any plastic deformation leads to heat production. By using a test procedure with a suitable load velocity, an increase of temperature due to the movement of dislocations can be reliably monitored.

## FATIGUE 87

During cyclic loading the changes of temperature per each cycle (as a result of elastic deformation) will be superposed by an increase of temperature (as a result of plastic deformation). The maximum value and the minimum value of temperature change per each cycle are shown in figure 1a, schematically. The mean value results from the dissipation of work. It is an essential criterion of the plastic deformation (figure 1b). The difference between both temperature curves represents the elastic part of deformation (figure 1c). Both, the change of the mean temperature and the amplitude of the oscillation of temperature are characteristic results of fatigue processes. Thus, it is possible to describe elastic-plastic deformation during cyclic loading not only for unnotched bars but also for small volume elements in front of a crack tip.

### EXPERIMENTAL PROCEDURE AND SET-UP

Unalloyed steels with a carbon content of 0,06% and 0,45 % were tested. Flat center cracked samples were used according to ASTM tentative test standard (9) (thickness  $B = 2$  mm, width  $W = 49$  mm and height  $H = 200$  mm). Cyclic tests with a stepwise load increase and with a constant amplitude loading were carried out on a servohydraulic testing machine. The test frequency was 5 Hz and the stress ratios were  $R=0$  and  $R=0,1$ . Load differences and corresponding changes of temperature were measured.

The changes of temperature resulting from external loading were measured directly at the surface of the sample by means of open thermocouples (iron-constantan). For managing a sensitive measurement, several constantan-wires with a diameter of 30  $\mu\text{m}$  were electrically welded on the surface in different distances from the crack tip. As a joint counterpart for all thermocouples an iron-wire with 0,2 mm diameter was used. The cold junction was fixed at the cooled mounting device. During the test period the measure of temperature variation at the mounting device was +0,1 K. Nearly any heat flux from the machine cylinder into the sample was prevented by the cooling system. Furthermore, thermal influences resulting from the ambient temperature were extensively reduced by means of an encapsulation of the sample. All measured thermoelectrical power signals were prepared in a constant voltage amplifier. The signals were transported to a peak-holder system. The covering and the processing of the signals were carried out in a

minicomputer. The Seebeck-coefficient, which was used to convert the thermoelectrical power signals into temperature values, was assumed as constant over the test regarded temperature range (0.053 mV/K).

The cyclic tests with a stepwise load increase were finished after the slope of the linear temperature-load-correlation had changed obviously. The transition point in the correlation of the temperature and the load was chosen as the starting level in the following test procedure to evaluate the crack growth velocity under cyclic loading. The number of cycles applied on each load level was  $5 \cdot 10^5$ . Then load amplitude was increased in steps of 0,25 kN. The investigation was finished when crack propagation velocities of about  $5 \cdot 10^{-6}$  mm/cycle were observed. Crack growth rates down to 0,015 mm could be identified reliably by light microscopy.

In order to evaluate changes in stress arrangements in front of a crack tip near the threshold value experiments for crack propagation in constant amplitude loading were carried out. The measurement devices in these tests were the same as in the above mentioned procedures.

#### EVALUATION OF THE CRACK OPENING LOAD AND THE EFFECTIVE THRESHOLD VALUE

Apart from the environment and the microstructure, the threshold value depends on the loading condition. It is well known, that the threshold value decreases with increasing stress ratio (10, 11). Partly it is caused by the increasing influence of mean stress. At cyclic deformation the crack is partly closed during loading time. Therefore it is ingenious to define an effective threshold value which leads to crack propagation (12). The effective stress intensity range can be calculated from the difference of the maximum load and the crack opening load.

In figure 2 the evaluation of the crack opening load from the monotonic tension test with a stepwise load increase is shown (3). The loading time used was 10 sec. The following temperature effects could be observed for a sample with a crack length of 3,85 mm. Directly at the crack tip, the cooling rate changed reaching a characteristic load. This effect can mainly be established by the good heat abstraction resulting from a changed crack formation (test

## FATIGUE 87

point 1). In larger distances from the crack tip, changes of temperature increase proportionally to increasing stress, which can be derived from the active notch effect (test point 2). The transition points in both temperature- stress- correlations mark the value of the crack opening load  $F_{op}$ . Changes of slopes indicate changes of local stress in relation to external loads. In this case the crack opening load was determined at 1,5 kN. Special notch effects can be assumed for being active only at loading standards significantly above this value. During cyclic loading at 3,0 kN no crack propagation was registered after  $6 \cdot 10^6$  cycles. First crack growth was observed at 3,5 kN.

In figure 3 the amount of temperature oscillation near the crack tip is plotted as a function of external load. The frequency used was 5 Hz. Due to the required experimental pre-loading a zero deviation can be stated. The transition point at 2,5 kN marks the crack opening load. Regardless of the distance of the test points from the crack tip, changes of slopes of the temperature- stress- correlation indicate an increase of the oscillation of temperature. Due to the relatively high deformation velocity, nearly adiabatic conditions will be reached during one cycle. As a result no heat conduction occurs and the oscillation of temperature gives quantitative information about the elastic deformation part and the active stress amplitudes directly at the test points. Crack propagation starts significantly above the crack opening load at 4,5 kN (figure 3). By regarding a crack length of 5,99 mm the crack opening load was determined at 6,0 kN. First crack growth rates were observed at 9,0 kN. The following effective threshold values were estimated:

$$a = 5,99 \text{ mm} : \Delta K_{th} = \Delta K_{eff} = 4,36 \text{ MNm}^{-3/2}$$

$$a = 10,99 \text{ mm} : \Delta K_{th} = \Delta K_{eff} = 4,34 \text{ MNm}^{-3/2}$$

The good agreement of the effective thresholds for the two cracks show that these values are physically ingenious. By regarding the stress ratio  $R=0$  crack propagation cannot be observed if cyclic stress intensity is smaller than the estimated effective threshold.

TEMPERATURE CHANGES AND CHANGES OF STRESS ARRANGEMENT  
DURING CRACK PROPAGATION

In figure 4 the arrangement of different test points in front of a crack tip are shown. Furthermore, the correlation between the oscillation of temperature and the number of cycles are plotted, schematically. If the test points were outside the plastically deformed zone, the greatest oscillation of temperature due to the elastic deformation was monitored near the crack tip. This result is in clear coincidence with the assumed initial stress distribution in front of a notch. Due to crack propagation a change of the stress arrangement in the remaining cross sectional area occurs. This effect leads to an increase of the oscillation of temperature beyond the plastically deformed zone. This increase becomes significantly smaller in a certain distance from the crack tip. If the cyclically plastified zone reaches the test point, cyclic softening occurs and the oscillation of temperature continuously decreases (13). Increase of the mean temperature due to the dissipation of work could also be registered.

In figure 5 and 6 typical results of the cyclic deformation behavior of a notched sample in the crack propagation stage are presented. After  $320 \cdot 10^3$  cycles a crack is detectable and changes of temperature occur as a result of the propagating crack. During the entire crack propagation stage a continuous increase of the mean temperature was measured also at a test point having a quite distance from the crack tip (figure 5). The temperature curve in figure 6 is characterized by a continuous increase of its slope. Small crack length indicates comparatively small changes in the stress arrangement per cycle; correspondingly long cracks lead to a greater addition in stress per cycle in front of a crack tip.

The evaluation of changes of stress arrangement in front of a crack tip using the thermoelastic effect during relatively small crack propagation velocities is shown in figure 7. It is to be seen that very small crack growth rates lead to clearly measurable changes of the stress arrangement near the crack tip. In a greater distance from the crack tip the changes of the oscillation of temperature become smaller. Crack growth rates down to 0,1 mm lead to clearly measurable changes of the oscillation of temperature in the vicinity of the crack tip so that the threshold value can be determined by using this thermometrical method in a relatively short time. No changes of the oscillation of

## FATIGUE 87

temperature can be seen if the crack does not propagate during cyclic loading. Then the cyclic elastic deformation part remains constant. Finally it can be stated, that the sensitivity of the presented thermometrical measuring system can be compared with that of the present conventional methods for crack growth measurements used so far apart from light microscopy.

### SUMMARY

A thermometrical investigation method is introduced, which allows the evaluation of a crack opening load. This value can be used for the determination of the effective threshold value of crack propagation. Furthermore, near the threshold value thermocouple measurements in the vicinity of the crack tip lead to the registration of the oscillation of temperature due to the thermoelastic effect (elastic deformation part) and the temperature development due to the dissipation of work done during cyclic loading (plastic deformation part). By using the thermoelastic effect quantitative statements become possible about the actual changes of stress directly at the test points. Very small crack growth velocities near the threshold value can be clearly identified by changes of the oscillation of temperature. Therefore it is possible to determine the threshold value by using this thermometrical method. Any plastic deformation near the crack tip leads to the production of heat, which can be measured sensitive and which leads to monotonic changes of temperature quite differing from those due to the thermoelastic effect. In extension to the results discussed so far, it is possible to determine the crack opening load and the threshold value with a relatively small temporal expense. From this an effective threshold value can be estimated.

### SYMBOLS USED

$F_{op}$	= crack opening load (kN)
$\Delta K_{eff}$	= effective stress intensity range ( $MNm^{-3/2}$ )
$\Delta T_a$	= oscillation of temperature (K)
$\Delta T_m$	= mean change of temperature (K)
$\Delta T_{max}$	= maximum change of temperature (K)
$\Delta T_{min}$	= minimum change of temperature (K)

REFERENCES

- (1) Harig, H. and Weber, M., "Estimation of Crack Initiation in Plain Carbon Steels by Thermometric Methods" in: Defects, Fracture and Fatigue. Edited by G.C. Sih, J.W. Provan, Martinus Nijhoff Pub., 1983.
- (2) Dengel, D. and Harig, H., Fat. Eng. Mat. Struc., Vol. 3, 1980, pp. 113-128.
- (3) Bach Quang, M. and Harig, H., Z. Werkstofftechn., Vol. 16, 1985, pp. 143-150.
- (4) Pippan, R. and Stüwe, H.P., "The temperature field surrounding the fatigue crack tip", Proc. of the "4th European Conference on Fracture", Leoben, Austria, 1982.
- (5) Kobayashi, A. and Suemasu, H., J. Mat. Science, Vol. 18, 1983, pp. 1645-1649.
- (6) Stanley, P. and Chan, W.K., "The determination of stress intensity factors and crack-tip velocities from thermoelastic infra-red emissions", Proc. Int. Conf. on "Fat. of Eng. Mat. and Struc.", Sheffield, England, 1986.
- (7) Jordan, E.H. and Sandor, B.I., J. Test. Eval., Vol. 6, 1978, pp. 325-331.
- (8) Thomson, W., The Quart. Journ. of pure and appl. Math., Vol. 1, 1857, pp. 57-77.
- (9) ASTM E 647-78T, Annual Book of ASTM Standards, Part 10, 1978.
- (10) Schijve, J., ASTM STP 415, 1967, pp. 415-459.
- (11) Smith, R.A., "Thirty Years of Fatigue Crack Growth- an Historical Review", in "Fatigue Crack Growth, 30 Years of Progress". Edited by R.A. Smith, Pergamon Press, 1986.
- (12) Elber, W., Materialprüfung, Vol. 12, 1970, pp. 189-193.
- (13) Harig, H. and Müller, K., Materialprüfung, Vol. 28, 1986, pp. 357-361.

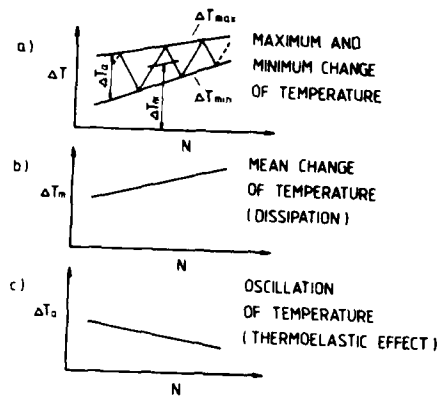


Figure 1 Temperature change during cyclic loading (schem.)

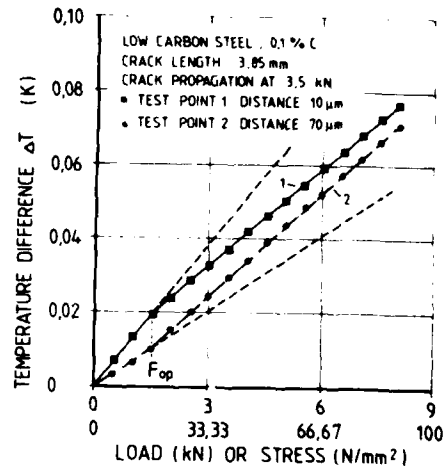


Figure 2 Temperature decrease near the crack tip, (monotonic)

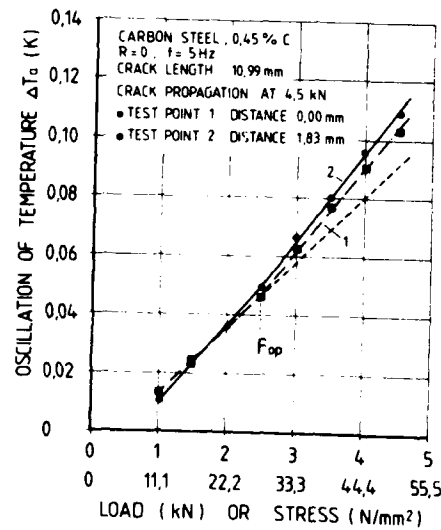


Figure 3 Increasing temperature oscillation, (cyclic)

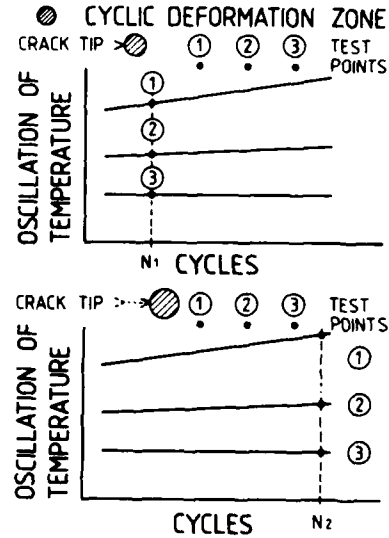


Figure 4 Temperature oscillation, (schem.)

# FATIGUE 87

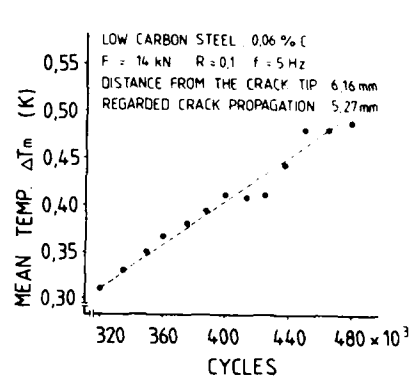


Figure 5 Temperature increase during cyclic loading

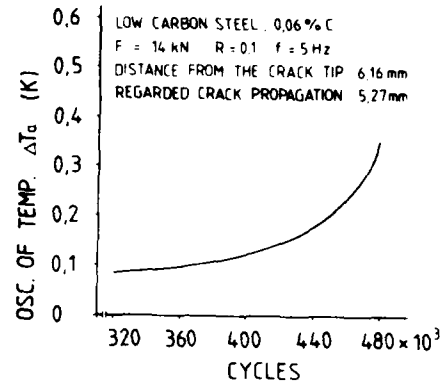


Figure 6 Temperature oscillation during cyclic loading

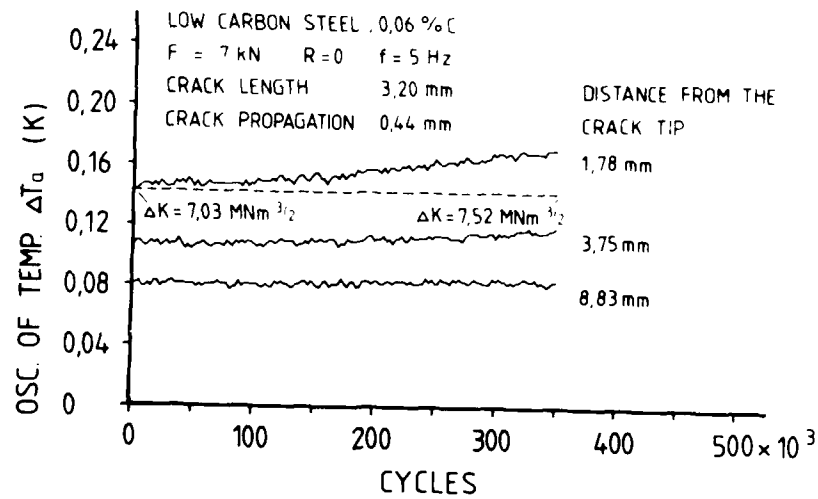


Figure 7 Temperature oscillation, different distances from the crack tip

## FATIGUE 87

### A Re-evaluation of Fatigue Threshold Test Methods

By: W.A. Herman\*, R.W. Hertzberg\*, C.H. Newton\*\* and  
R. Jaccard\*\*\*.

By varying the K-decreasing test procedure, threshold behavior was developed at significantly different stress intensity levels in both 2024-T3 aluminum and Astroloy nickel base alloy. The threshold level associated with low R-ratio  $\Delta K$ -decreasing test conditions is believed to represent a non-conservative measurement of the material's fatigue resistance at low K levels. It is recommended that high R ratio or constant  $K_{max}$  K-decreasing test methods be used to characterize fatigue threshold behavior. Implications regarding the comparison of short crack FCP rates with data determined from such test methods are discussed.

### INTRODUCTION

Currently accepted fatigue crack propagation (FCP) threshold test procedures, which utilize  $\Delta K$ -decreasing test methods at low R ratios, may generate nonconservative estimates of a material's intrinsic fatigue resistance (1). This arises from the fact that crack closure levels increase dramatically at low R ratios when the stress intensity factor range is reduced. Since the effective stress intensity level decreases in corresponding fashion, crack growth rates also decline (2). Clearly, such experimental conditions do not represent typical service situations for an engineering component. For example, the K level in an actual component would be expected to increase with increasing crack length and not decrease, as is the case in laboratory threshold testing.

\* - Department of Materials Science and Engineering  
Lehigh University, Bethlehem, PA 18015.

\*\* - Materials Science Corp, Spring House, PA 19477.

\*\*\* - Swiss Aluminum, Ltd., Zurich, Switzerland.

Furthermore, several factors pertaining to actual service conditions suggest that most laboratory threshold values obtained at low R ratios provide overly optimistic estimates of fatigue resistance. For example, the so-called "anomalous" growth behavior of physically short cracks may be attributed not only to the unique characteristics of short cracks, but also to the comparison of short crack data with FCP rates observed in long crack samples associated with a K-decreasing test procedure at a low R ratio. Crack growth rates may also be much higher in a structural component that experiences spectrum loading with compressive underloads than in a laboratory sample that experienced constant amplitude load excursions. Under such conditions, the negative load excursions serve to reduce the closure level and increase the effective stress intensity range, and thereby serve to increase the observed crack growth rates (3,4). Finally, if a component possesses a tensile residual stress, higher FCP rates would be expected because of the resulting higher R ratio service condition and associated low crack closure levels.

In each instance, low R ratio  $\Delta K$ -decreasing test data would provide an overestimation of available fatigue life for a given component or test sample. However, if K-decreasing threshold tests were conducted at high R ratios, closure levels would be decreased along with the threshold levels. The latter testing approach, therefore, should provide baseline data in closer agreement with actual components that contain physically short cracks, tensile residual stresses, and/or experience compressive underloads.

Conservative threshold data could also be generated by maintaining either a constant mean or constant maximum stress intensity level during the  $\Delta K$ -decreasing test procedure. In each case, the R ratio would increase with decreasing K level (Figure 1). Tests involving constant  $K_{max}$  are of particular interest in that the monotonic plastic zone dimension remains constant during the entire K-decreasing procedure. For this reason, the stress intensity reduction gradient could assume large values without introducing false threshold conditions (5,6).

The objectives of this paper are to explore the nonconservative nature of low R ratio threshold test procedures and to identify a more simple and convenient method to predict the FCP behavior of short cracks; the latter is of particular interest in view of the very tedious nature of short crack FCP data acquisition. To this end, experiments with 2024-T3 and Astroloy are described which obtain threshold stress intensity factor range values ( $\Delta K_{th}$ )

## FATIGUE 87

using K-decreasing procedures associated with constant R ratio or constant Kmax test conditions. These long crack data are then compared with existing long and short crack results (7-9). Also, constant R ratio and constant Kmax data are compared with crack growth results obtained in association with compressive underloads.

### EXPERIMENTAL PROCEDURES

The materials used in this study included low carbon Astroloy, a hot isostatically pressed Ni-base superalloy, 2024-T3 wrought aluminum and extruded 6005 aluminum alloys. The compositions of these alloys are given in Table 1.

TABLE 1  
Composition of HIP'd Astroloy (9)  
(wt %)

Co: 16.98; Cr: 14.80; Mo: 5.07; Al 3.99; Ti: 3.58;  
Fe: 0.21; Zr: 0.047; B: 0.026; C: 0.024; Si: 0.02;  
Mn: 0.01; Cu: 0.01; W: 0.01; P: 0.003; N: 0.002;  
S: 0.0011; Ni balance.

Composition of 2024-T3 Aluminum (10)  
(wt %)

Cu: 4.40; Mn: 0.60; Mg: 1.50; Al balance.

Composition of 6005-T3 Aluminum (3)  
(wt %)

Si: 0.63; Fe: 0.21; Cu: 0.17; Mn: 0.03; Mg: 0.54;  
Cr: 0.11; Zn: 0.08; Ti: 0.01; Al balance.

K-decreasing FCP experiments were conducted in the threshold regime at a constant stress ratio of  $R = 0.1$  and under test conditions of constant Kmax; the latter involves an increasing stress ratio during crack propagation (Figure 1). All tests were conducted at cyclic frequencies of 30 or 40 Hz.

All tests were conducted under computer control, using either a Digital Equipment Corporation (DEC) PDP 1103 or 1123 computer, interfaced with an Instron Corporation closed loop servo-hydraulic automated test system. A modified version of the Instron FCPRUN program was used in order to accommodate additional specimen geometries (DCT) and Kmax testing conditions. During variable K testing, the applied stress intensity range was controlled according to:

$$\Delta K_i = \Delta K_o \exp (C(a_i - a_o)) \quad (1)$$

## FATIGUE 87

where  $\Delta K_i$  is the instantaneous stress intensity factor range,  $\Delta K_0$  is the initial stress intensity factor range,  $C$  is the stress intensity factor gradient, and  $a_i$  and  $a_0$  are the current and initial crack lengths, respectively. Testing was conducted using a gradient of  $-.06 \text{ mm}^{-1}$ , and for tests run under  $K_{\max}$  control,  $K_{\max}$  values of 10 and 55  $\text{MPa}\sqrt{\text{m}}$  were used for the 2024-T3 and Astroloy samples, respectively.

Experiments to evaluate the role of compressive underloads (CUL) on 6005 aluminum alloy provided by Aluswiss, Ltd., were also performed and involved conducting a normal  $R = 0.1$   $\Delta K$ -decreasing test to the near threshold regime. At this point, 100% and 200% underloads were applied. Following the underload, the sample was load cycled under  $\Delta K$ -constant conditions in order to monitor any changes in crack growth rates due to the underload.

### RESULTS AND DISCUSSION

Vecchio and Hertzberg (4) recently reported FCP results for Astroloy nickel-based alloy, based on both long and short crack specimens. Their results indicate that for the same stress intensity factor range, FCP rates associated with short crack samples were considerably greater than growth rates generated with long crack samples. While there may be some intrinsic reasons to expect short and long crack data to differ, these differences were rationalized on the basis of the strain energy density range (Figure 2).

The current study demonstrates that long and short crack fatigue data may also be favorably (and more simply) compared as a function of  $\Delta K$  when long crack data are generated under constant  $K_{\max}$  testing conditions. To wit, Figure 3 compares the short crack results of Vecchio and Hertzberg (9) generated under  $R = 0.1$  test conditions with two sets of threshold data for long crack samples, corresponding to constant  $R = 0.1$  and constant  $K_{\max}$  (55  $\text{MPa}\sqrt{\text{m}}$ )  $K$ -decreasing test conditions, respectively. Clearly, the short crack data are in excellent agreement with the constant  $K_{\max}$  data base. Regarding the latter, crack closure levels were initially 35% but decreased quickly to zero as the  $R$ -ratio increased during the constant  $K_{\max}$ ,  $\Delta K$ -decreasing test procedure. By sharp contrast, crack closure levels corresponding to the  $R = 0.1$  data base increased from 30% to 80% as the test progressed toward threshold conditions. Since crack closure levels associated with short crack growth are generally low, if not negligible (11), short crack data should be in better agreement with any long crack data base associated with low closure levels (e.g., high  $R$  ratio test conditions). These findings confirm the concept of the effective stress intensity factor and its utility in correlating FCP data. In view of the excellent agreement between the short crack and constant  $K_{\max}$ ,

## FATIGUE 87

long crack results, the nonconservative nature of the low R-ratio threshold level ( $21 \text{ MPa}\sqrt{\text{m}}$ ) is contrasted with the value of  $7.7 \text{ MPa}\sqrt{\text{m}}$  corresponding to the constant  $K_{\text{max}}$  test result. Surely were one to have assigned  $\Delta K_{\text{th}}$  with a value of  $21 \text{ MPa}\sqrt{\text{m}}$ , an unrealistically long fatigue lifetime would have been computed for an Astroloy component that contain a short crack.

A similar comparison was made between long and short crack fatigue data for 2024-T3 aluminum alloy. At any  $\Delta K$  level, crack growth rates associated with constant  $K_{\text{max}}$  tests were consistently higher than FCP rates corresponding to low R ratio conditions (figure 4). It should also be noted that duplicate tests at different values of  $K_{\text{max}}$  (10 and  $20 \text{ MPa}\sqrt{\text{m}}$ ) produced identical crack growth behavior. Of particular note, the short crack data reported by Leis and Forte (7) are in good agreement with the  $K_{\text{max}}$  results (Figure 5). Furthermore, short crack results recently reported by Newman (8) also tend to coincide with the  $K_{\text{max}}$  results, although the amount of scatter associated with Newman's data makes the correlation less clear than in the case of the Leis and Forte (7) 2024-T3 results and the nickel-base alloy results shown in Figure 3. It should be noted that the crack closure levels quickly decreased to zero from an initial level of approximately 30% for all the 2024-T3 samples tested under  $K_{\text{max}}$  control. The nonconservative nature of the  $R = 0.1$  threshold value is again noted in that a crack arrest at  $3.5 \text{ MPa}\sqrt{\text{m}}$  was found for  $\Delta K$ -decreasing at  $R = 0.1$ , whereas a value of  $1.7 \text{ MPa}\sqrt{\text{m}}$  was determined under constant  $K_{\text{max}} = 10$  and  $20 \text{ MPa}\sqrt{\text{m}}$  test conditions.

Tests were also conducted on 6005 aluminum alloy to assess the effects of compressive underloads on fatigue crack growth in the threshold regime, where application of the underload causes a reduction in crack closure. It follows that an acceleration of crack growth is expected after an underload (3), resulting in reduced total fatigue life. Zaiken and Ritchie (4), have observed a temporary acceleration in crack growth, but reported no reduction of the threshold value, following the application of a compressive underload.

The current work examines the role of compressive underloads in the near-threshold regime. Since the application of the underload results in the compression of asperities and residual plastic strains on the two mating crack surfaces, lower values of  $K_{\text{op}}$  and higher crack growth rates should be expected. Furthermore, once the crack grows past the underload, growth rates should return to their previous (and lower) levels. In essence, the effect of an underload should be the reverse of a tensile overload (12).

## FATIGUE 87

Figure 6 reveals that crack growth rates accelerated by a factor of five times during constant  $K$  test conditions, following the application of a 100% underload. The influence of the underload on FCP behavior appears to be permanent as evidenced by the fact that the crack growth rate never returned to the pre-underload level. Furthermore, no further change in growth rate was noted when second and third underloads were applied. The permanently higher FCP rates following the underloads were related to a significant reduction of the high closure levels associated with the low  $R \Delta K$ -decreasing test procedure. Again, nonconservative life estimates would be expected.

A potentially significant ramification of this work is that it reveals a simple approach to the estimation of fatigue life in real components. For example, Jaccard (13) has suggested that a linear extrapolation of FCP data from the intermediate growth rate regime corresponding to Paris-power law behavior under constant  $R$  ratio conditions, could be used to accurately predict the fatigue life of structural components. Such an extrapolation would simulate progressively higher  $R$  ratio test results as  $\Delta K$  were reduced. Since this extrapolation closely resembles test results corresponding to constant  $K_{max}$   $\Delta K$ -decreasing test procedures, the latter test method offers considerable promise in accounting for short crack effects (Figures 3 and 5) and underloads (Figure 6) as well as the presence of tensile residual stress in a component.

### CONCLUSIONS

It is concluded that conventional threshold test procedures provide a nonconservative estimate of FCP behavior in engineering structures. As a result, computed fatigue lifetimes of engineering components may be incorrect and result in overestimations of total life.

It is further concluded that FCP data derived from constant  $K_{max}$ ,  $K$ -decreasing test methods provide a more realistic assessment of the fatigue response of engineering components that may contain short cracks, possess tensile residual stresses and/or experience compressive load excursions. That "short crack" data may be adequately predicted from long crack samples, represents a useful method by which the fatigue lifetimes of engineering components may be computed. The generation of "short crack" data with tedious experimental techniques might then be obviated.

### ACKNOWLEDGEMENTS

This research was sponsored by Swiss Aluminum Ltd and AFOSR under grant 83-0029.

## FATIGUE 87

### REFERENCES

- (1) ASTM Specification E647-86A, "Standard Test Method for Measurement of Fatigue Crack Growth Rates", 1986.
- (2) Elber, W., ASTM STP 486, 1971, pp. 230-242.
- (3) Newton, C. H., PhD Dissertation, Lehigh University, Bethlehem, PA, November 1984.
- (4) Zaiken, Z. and Ritchie, R.O., Engr. Frac. Mech., 22(1), 1985, pp. 35-48.
- (5) Doker, H., Bachman, V. and Marci, G., EMAS, Engineering Materials Advisory Service Ltd, 1982, pp. 45-57.
- (6) Doker, H. and Peters, M., Fatigue 84, 1984, pp. 275-285.
- (7) Leis, B.N. and Forte T.P., ASTM STP 743, 1981, pp. 100-124.
- (8) Newman, J.C., Swain, M.H., and Phillips, E.P., 2nd International Conference on Small Fatigue Cracks, Santa Barbara, CA, January, 1986.
- (9) Vecchio, R. S. and Hertberg, R.W., Engr. Frac. Mech., 22(6), 1985, pp. 1049-1060.
- (10) Hatch, J.E., ed., "Aluminum: Properties and Physical Metallurgy", ASM, Metals Park, OH, 1984, p. 354.
- (11) Ritchie, R.O. and Lankford, J., submitted to J. Mater. Sci. Eng., 1986.
- (12) Vecchio, R.S., Hertzberg, R.W., and Jaccard, R., Fat. Engr. Mat. Struc., 7(3), 1984, pp. 181-194.
- (13) Jaccard, R., 3rd Int'l Conference on Aluminum Weldments, Munich, FRG, April, 1985.

# FATIGUE 87

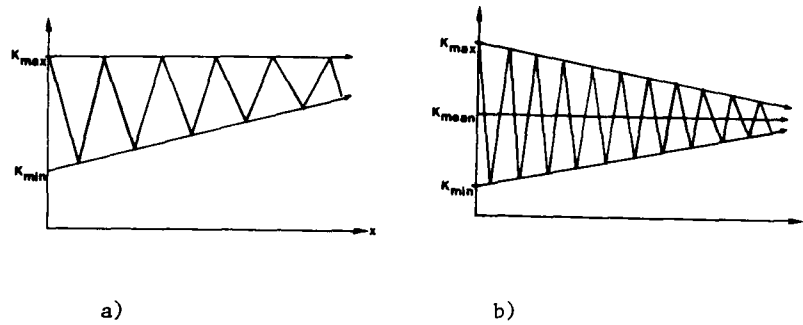


Figure 1 - Schema of alternative K-decreasing test methods.  
a) constant  $K_{max}$ ; b) constant  $K_{mean}$ .

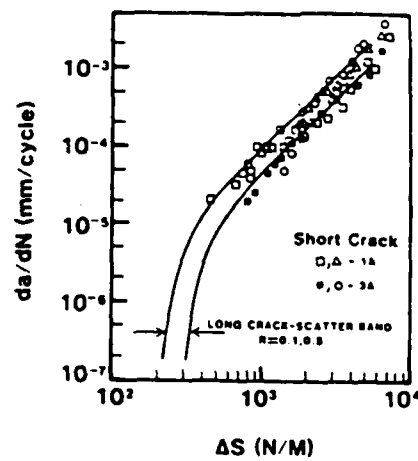


Figure 2 - Comparison of Long and Short Crack Data vs. Strain Energy Density (9).

# FATIGUE 87

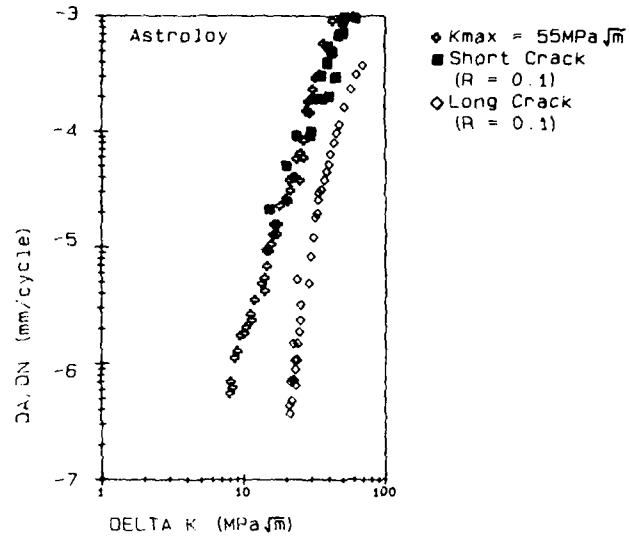


Figure 3 - Correlation of short crack data (9) with constant  $K_{max}$  long crack results in Astroloy nickel base alloy.

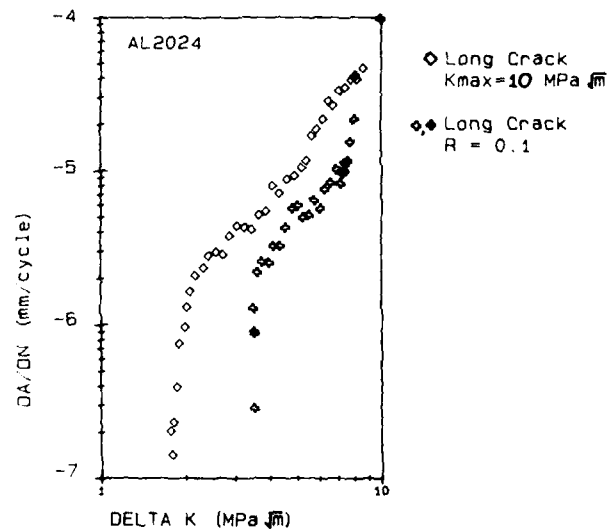


Figure 4 - Threshold data in 2024-T3 for constant  $R$  ratio (0.1) and constant  $K_{max}$  (10  $\text{MPa}\sqrt{\text{m}}$ ). Bold face data (7).

# FATIGUE 87

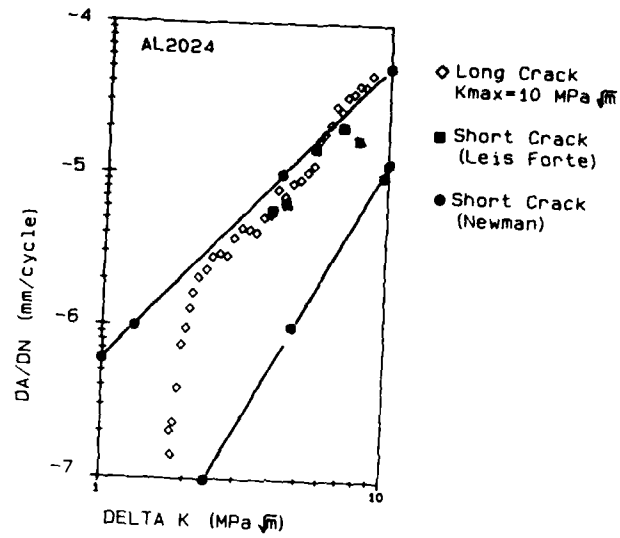


Figure 5 - Comparison of Long Crack under  $K_{max}$  Control with short crack data of (7) and (8).

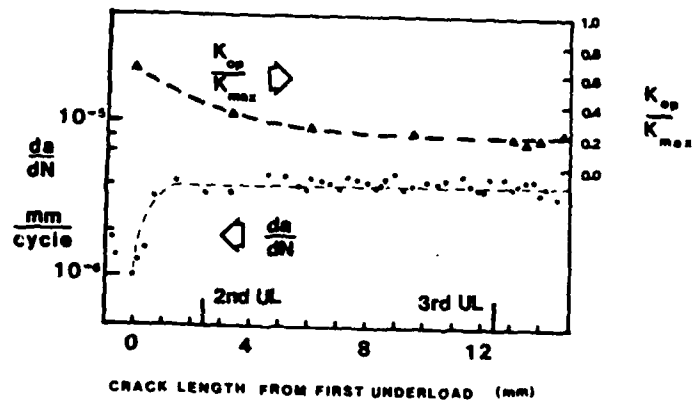


Figure 6 - Effect of compressive underloads applied following low R ratio K decreasing procedure - 6005 Aluminum.

THE FACTORS WHICH GOVERN THE ACCELERATION OF CORROSION  
FATIGUE CRACK GROWTH RATE OF A FERRITIC STAINLESS STEEL

Y. KIMURA\*, T. YAGASAKI\* AND T. KUNIO\*\*

Fatigue tests were mainly conducted in 0.03% and 3% NaCl aqueous solutions with WOL type specimen of a ferritic stainless steel AISI 405. The contribution of the anodic dissolution and the hydrogen embrittlement mechanisms toward the acceleration of fatigue crack growth rate in solution was discussed. As a result, the anodic dissolutive effect is dominant for the crack growth rate acceleration within lower  $\Delta K_{eff}$  value range. On the contrary, brittle mode fracture becomes important within higher  $\Delta K_{eff}$  value range. Furthermore, these factors have two different kinds of dependencies upon chloric ion concentration.

INTRODUCTION

Present authors have been investigated on the corrosion fatigue crack growth characteristics of a ferritic stainless steel AISI 405 in deionized water, 0.03% NaCl aqueous solution and also in laboratory air. As a result, remarkable acceleration of fatigue crack growth rate in solutions were recognized (1). The factor which governs the acceleration of fatigue crack growth rate, however, has not been clarified. This may have resulted from the situation that corrosive dissolutive effects and brittle mode fracture effects upon the fatigue crack growth rate acceleration have not yet been distinguished.

Therefore in this paper, fatigue tests were mainly conducted in 3% and 0.03% NaCl aqueous solution under the condition of  $R=0.1$  with WOL type specimens of the

\* Department of Chemical Engineering, Kogakuin University, Tokyo, Japan.

\*\* Faculty of Science and Engineering, Keio University, Yokohama, Japan.

## FATIGUE 87

same ferritic stainless steel AISI 405. The dependencies of fatigue crack growth rate upon chloric ion concentration were investigated through examining crack closure characteristics and morphologies of fractured surface. In this way, the contributions of the anodic dissolution and the hydrogen embrittlement mechanisms toward the acceleration of fatigue crack growth rate in solutions are examined.

### SPECIMEN AND EXPERIMENTAL PROCEDURES

A ferritic stainless steel AISI 405, whose chemical compositions are shown in Table 1, was used for the specimen of this experiment. Heat treatment of material and specimen preparation procedures are all the same as the previous paper (1). Fatigue tests were conducted with hydraulic fatigue testing machine using WOL type specimen at 5 Hz in 0.03% and 3% NaCl aqueous solutions. A triangular loading wave form was employed and 0.1 was selected as R ratio value. Solution temperature was held at  $T=303\pm0.5K$  during fatigue testing. Crack lengths were measured with a travelling microscope. Crack closure behavior was detected by a strain gauge attached to the back surface of the specimen. Examination of the fracture surface was conducted in detail using a scanning electron microscope.

TABLE 1-Chemical Composition of Test Specimen (wt%).

C	Si	Mn	P	S	Ni	Cr	Al
0.05	0.58	0.34	0.028	0.004	0.10	11.95	0.176

### EXPERIMENTAL RESULTS AND DISCUSSIONS

#### Dependency of Fatigue Crack Growth Rate upon NaCl Concentration of Solution

Under the condition of stress ratio  $R=0.1$ , fatigue tests were conducted in 0.03% and 3% NaCl aqueous solutions with WOL type specimen. Fatigue crack growth rate obtained from these experiments are represented by  $\Delta K$  as shown in Figure 1.

This figure shows that fatigue crack growth rate both in 0.03% and 3% NaCl aqueous solutions show almost the same dependencies upon  $\Delta K$  values. Fatigue crack

growth rate in 0.03% NaCl aqueous solution, however, was recognized to be accelerated to some extent within the larger  $\Delta K$  value range of  $\Delta K \geq 17 \text{ MPa}\sqrt{\text{m}}$ . And more remarkable acceleration of fatigue crack growth rate in 0.03% NaCl aqueous solution was indicated within the range of  $\Delta K \geq 28 \text{ MPa}\sqrt{\text{m}}$ . Threshold behavior of fatigue crack growth in above-mentioned solutions shows no remarkable differences as indicated in this figure when it was evaluated by  $\Delta K$  value.

#### Dependency of Crack Closure Characteristics upon chloric Ion Concentration

In order to evaluate true crack growth characteristics of a ferritic stainless steel AISI 405 in solutions, the closure effects of propagating crack have to be eliminated. And then, dependency of the crack growth rate upon chloric ion concentration can be examined. For this purpose, the opening and closure characteristics of fatigue crack in a corrosive environment was determined using the strain gauge attached to the back surface of specimen. Then, the crack opening ratio  $U = \Delta K_{\text{eff}} / \Delta K$  was determined using unloading elastic compliance method (2). In this way,  $U$  values were obtained and represented by  $K_{\text{max}}$  in Figure 2 for examining the dependency of this value upon chloric ion concentration. At the same time,  $U$  values obtained in deionized water within smaller  $K_{\text{max}}$  value range of  $K_{\text{max}} \leq 15 \text{ MPa}\sqrt{\text{m}}$  were plotted in this figure. Also in this figure,  $U$  value dependency of an austenitic stainless steel AISI 304 upon  $K_{\text{max}}$  value which was obtained in NaCl aqueous solutions (3) was shown by solid line.

This figure shows that there exists the differences in crack closure characteristics within relative smaller  $K_{\text{max}}$  value range of  $K_{\text{max}} \leq 15 \text{ MPa}\sqrt{\text{m}}$  between a ferritic stainless steel AISI 405 and an austenitic stainless steel AISI 304. That is,  $U$  values for AISI 405 steel become smaller than that for AISI 304 steel. And, the dependency of crack closure behavior upon chloric ion concentration was recognized within these  $K_{\text{max}}$  value range. The crack opening ratio  $U$  becomes smaller with the increase of chloric ion concentration. And, these differences in crack closure characteristics were more emphasized as the  $K_{\text{max}}$  value becomes smaller and smaller. However, in case when the data were obtained in deionized water  $U$  values almost correspond to those of an austenitic stainless steel AISI 304.

The reasons of these differences obtained in the crack opening ratio  $U$  are understood as the followings. As solution with NaCl concentration of 3% was more ag-

## FATIGUE 87

gressive environment, material at crack tip may more corroded than in solution with dilute chloric ion concentrations. Therefore much corrosion products may be generated at the crack tip and they may be accumulated on cracked surface. As a result, the contribution of corrosion products to crack closure behavior will become remarkable in case when the specimen was fatigue loaded in solutions with higher chloric ion concentration. In this case, the corrosion products attached on the fracture surface were easily detected by a scanning electron microscopic observations as shown in Figure 3(a)-(c). In these photographs, much corrosion products were recognized on fractured surface obtained in 3% NaCl aqueous solution. On the other hand, smaller amount of corrosion products were detected in case of 0.03% NaCl aqueous solution and deionized water. Therefore, the dependency of U value upon the chloric ion concentration was considered to be brought about by the difference in the dissolutive effects of solutions to a ferritic stainless steel AISI 405.

On the contrary, U values obtained in solutions with different chloric ion concentrations show almost equal values irrespective of  $\text{Cl}^-$  ion concentration and also almost correspond with that of a austenitic stainless steel AISI 304 within the larger  $K_{\text{max}}$  value range of  $K_{\text{max}} \geq 15 \text{ MPa}\sqrt{\text{m}}$ . Therefore in this case, the difference in the amount of corrosion products may not play an important role in crack closure behavior compared with the behaviors obtained within relatively smaller  $K_{\text{max}}$  value range. As a result, another closure mechanism such as plasticity induced crack closure behavior may play dominant role within these  $K_{\text{max}}$  regions.

In this way, two different kinds of U value dependencies upon chloric ion concentration were obtained.

### Factors Which Govern the Acceleration of Fatigue Crack Growth Rate in Solutions

In this section, with the aid of these U values obtained in the previous section, effective stress intensity factor range  $\Delta K_{\text{eff}}$  (4) was determined. The fatigue crack growth rate data shown in Figure 1 were re-plotted in Figure 4 using  $\Delta K_{\text{eff}}$ . Also in this figure, crack growth rate data obtained in deionized water within smaller stress intensity factor ranges were indicated by  $\Delta K_{\text{eff}}$  value. At first, the dependency of real crack growth rate represented by  $\Delta K_{\text{eff}}$  upon chloric ion concentration will be made clear. Then, the factors which govern the acceleration of fatigue crack growth rate in solutions were investigated through examining the mor-

## FATIGUE 87

phologies of fracture surface by a scanning electron microscope.

The crack growth rate represented by  $\Delta K_{eff}$  shows two different kinds of dependency upon chloric ion concentration as indicated in Figure 4. One is recognized within the lower  $\Delta K_{eff}$  value range. In this region, the crack growth rate becomes larger for the specimen tested in solution with higher chloric ion concentration. This may be caused by the difference in the extent of contribution of the anodic dissolutive effects to corrosion fatigue crack propagation. Also on the fracture surface, the difference in anodic dissolutive effects can be detected through conducting scanning electron microscopic observation as shown in Figure 5(a)-(c). In case when fatigue tests were conducted in 3% NaCl aqueous solution, much traces of anodic dissolution were recognized on fracture surface as shown in Figure 5(a). However, as the concentration of chloric ion becomes diluter, fracture surface morphology indicating anodic dissolution becomes less remarkable as shown in Figure 5(b) and (c).

Another difference in fatigue crack growth rate was recognized within the higher  $\Delta K_{eff}$  value range. In this region, crack growth rate was more accelerated in case fatigue tests were conducted in solution with lower chloric ion concentration. In case of 0.03% NaCl aqueous solution, some brittle mode fracture were recognized on fracture surface as shown in Figure 6(a). On the other hand, the fracture surface morphology of specimen fatigue tested in 3% NaCl aqueous solution shows a little different outlook. In this case, the brittle mode fracture was considered to be suppressed to some extent and more ductile mode fracture such as striation and so on was recognized on the fracture surface as shown in Figure 6(b). Therefore, chloric ion may have some suppressing effects on the hydrogen embrittlement mechanisms.

Concerning this point, fatigue tests under the condition of lower frequency such as 0.1 Hz were planned to do and further considerations will be made in near future, in order to investigate more clearly the effects of hydrogen embrittlement fracture upon the fatigue crack growth rate acceleration.

In this way, the contributions of the anodic dissolution and hydrogen embrittlement mechanisms toward the acceleration of fatigue crack growth rate of a ferritic stainless steel in NaCl aqueous solutions were clarified.

## FATIGUE 87

### CONCLUSIONS

Fatigue tests were conducted mainly in 3% and 0.03% NaCl aqueous solutions with WOL type specimen of a ferritic stainless steel AISI 405. Then, the contributions of the anodic dissolution and the hydrogen embrittlement mechanisms toward the acceleration of fatigue crack growth rate in solutions were examined.

Results obtained are summarized as follows;

- (1) Fatigue crack growth rate in 0.03% NaCl aqueous solution was recognized to be accelerated to some extent within the larger  $\Delta K$  value range. Threshold behavior of fatigue crack growth in above-mentioned solutions, however, shows no remarkable differences when it was evaluated by  $\Delta K$  value.
- (2) In order to evaluate true crack growth characteristics of a ferritic stainless steel, the opening and closure characteristics of fatigue crack in corrosive environments were determined employing the unloading elastic compliance method. In the evaluated  $U$  values, two different kinds of dependencies upon chloric ion concentration were detected. Within lower  $K_{max}$  value range,  $U$  values for AISI 405 steel become smaller than that for AISI 304 steel. The crack opening ratio  $U$  becomes smaller with the increase of chloric ion concentration and these characters were more emphasized as the  $K_{max}$  value decreases. On the contrary, obtained  $U$  values become almost equal irrespective of chloric ion concentration and they almost correspond with that of a austenitic stainless steel AISI 304 within higher  $K_{max}$  value range.
- (3) The crack growth rate represented by  $\Delta K_{eff}$  shows two different kinds of dependencies upon chloric ion concentration. Within lower  $\Delta K_{eff}$  value range, the crack growth rate in solution with higher chloric ion concentration shows larger values. This may be caused by the anodic dissolutive effects which can be detected through conducting scanning electron microscopic observation on fractured surface. Within the higher  $\Delta K_{eff}$  value region, crack growth rate was more accelerated in solution with diluter chloric ion concentrations. Therefore, it was recognized that the chloric ion may have some suppressing effects on the hydrogen embrittlement mechanisms. In this way, the contributions of the anodic dissolution and hydrogen embrittlement mechanisms toward the acceleration of fatigue crack growth rate of a ferritic stainless steel AISI 405 in NaCl aqueous solutions were clarified.

## FATIGUE 87

### REFERENCES

- (1) Kimura, Y., Yagasaki, T. and Kunio, T., Proceeding of the International Symposium on Microstructure and Mechanical Behavior of Materials, Oct. 21-24, Xi'an, China, 1985.
- (2) Kikukawa, M., Jono, M., Tanaka, K. and Takatani, M., J. of the Society of Materials Science, Japan, Vol.25, No.276, 1976, pp. 899-903.
- (3) Endo, K., Komai, K. and Murayama, S., Trans. of the Japan Society of Mechanical Engineers, Series A, Vol.48, No.436, 1982, pp. 1489-1495.
- (4) Elber, W., "Damage Tolerance in Aircraft Structures, ASTM STP 486", ASTM, 1971.

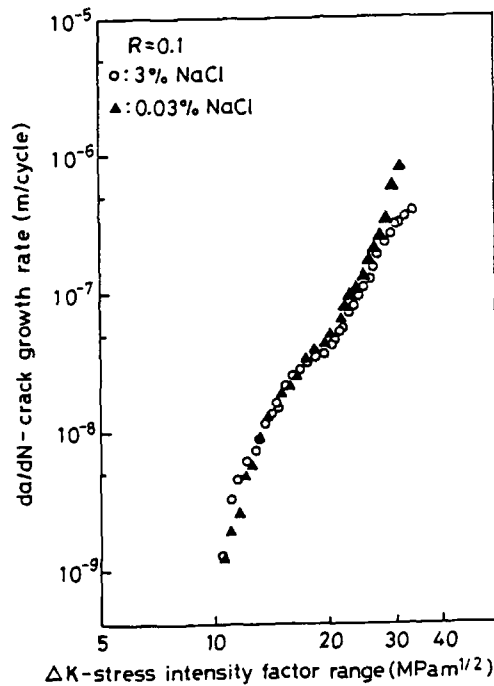


Figure 1  $da/dN$  vs.  $\Delta K$

# FATIGUE 87

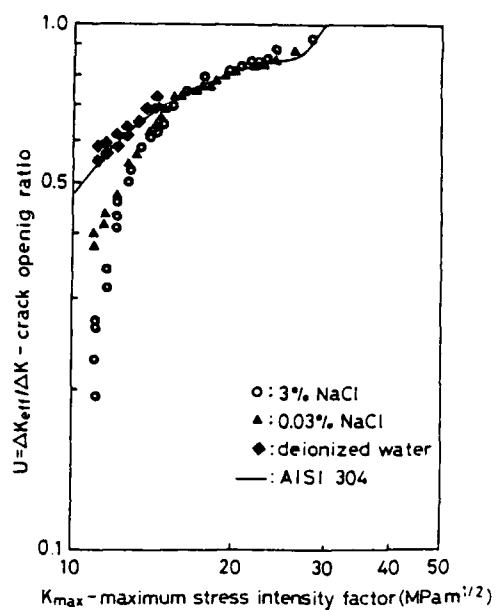


Figure 2 U vs.  $K_{max}$

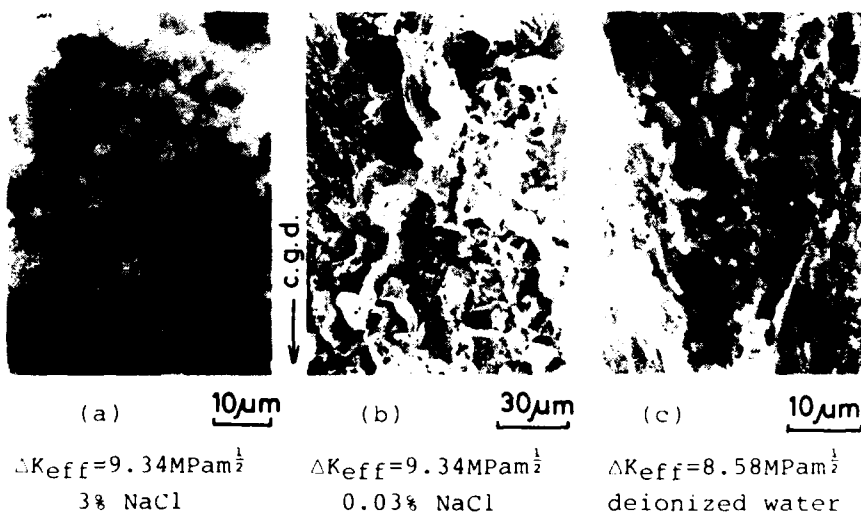


Figure 3 Difference in the amount of corrosion products

# FATIGUE 87

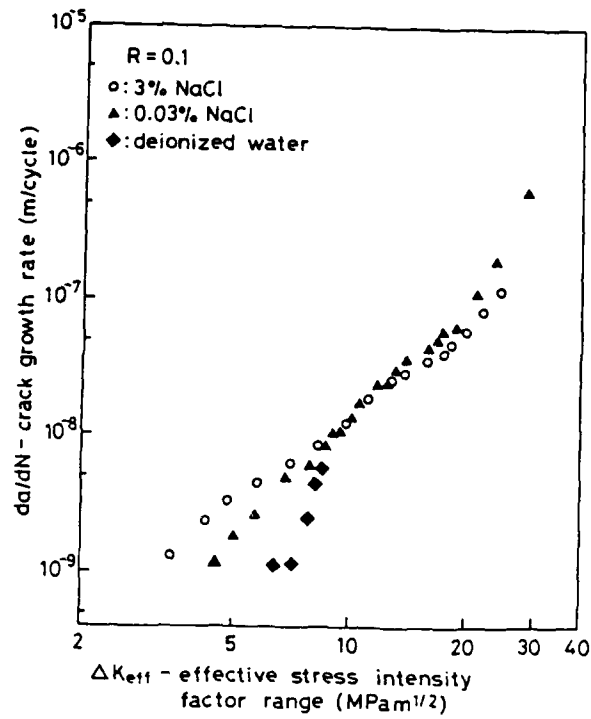


Figure 4  $da/dN$  vs.  $\Delta K_{eff}$

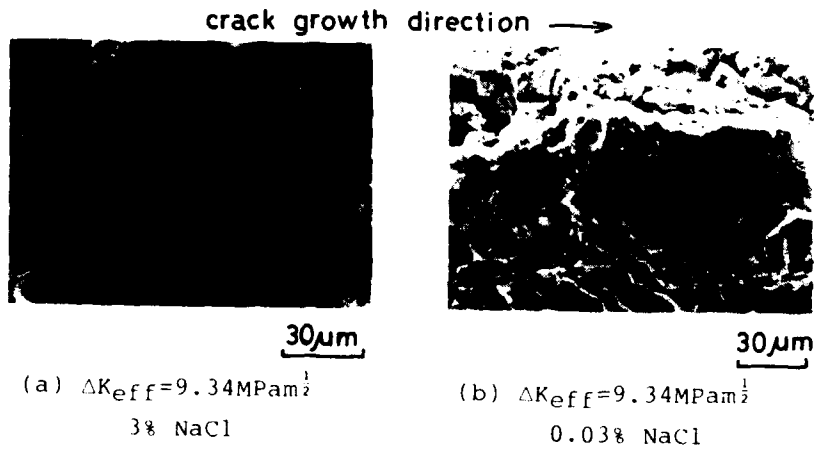
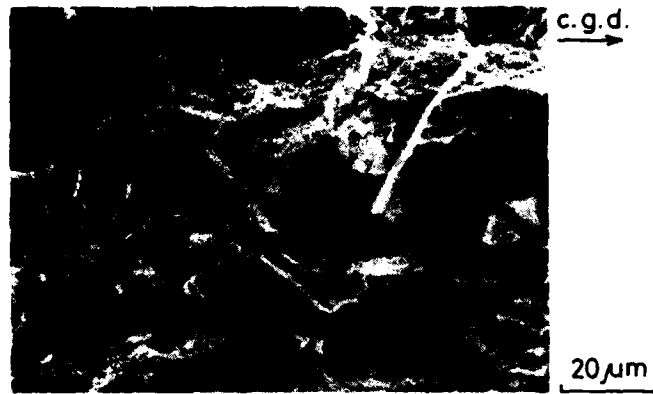


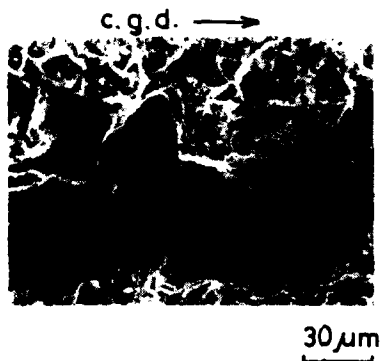
Figure 5 Morphologies of fracture surface

FATIGUE 87

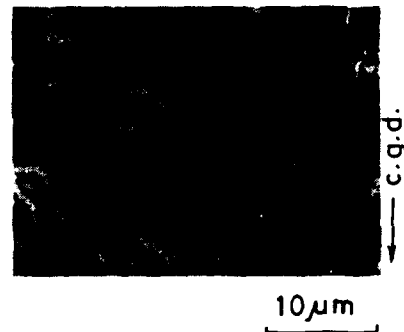


(c)  $\Delta K_{eff} = 8.44 \text{ MPam}^{\frac{1}{2}}$   
deionized water

Figure 5 Morphologies of fracture surface



(a)  $\Delta K_{eff} = 18.0 \text{ MPam}^{\frac{1}{2}}$   
0.03% NaCl



(b)  $\Delta K_{eff} = 18.0 \text{ MPam}^{\frac{1}{2}}$   
3% NaCl

Figure 6 Suppressing effect of chloric ion on hydrogen embrittlement fracture

## FATIGUE 87

### FATIGUE THRESHOLDS OF C.Mn STEELS IN SALINE ENVIRONMENTS

P.R.G. Anderson<sup>\*</sup>, R. Brook<sup>\*\*</sup> and C. E. Nicholson<sup>+</sup>

The fatigue threshold,  $\Delta K_{th}$ , and near threshold crack growth of a C.Mn. constructional steel (in two heat-treated conditions) have been determined in a series of aqueous saline solutions, one of which also contained hydrogen sulphide. Tests were made in three-point bending at  $\sim 100\text{Hz}$  and at R ratios of 0.15, 0.3 and 0.6 using a computer-controlled test facility. Compared with air, the saline environments slightly reduce  $\Delta K_{th}$  and the effect of R. The presence of  $\text{H}_2\text{S}$  apparently has no significant effect on  $\Delta K_{th}$  but increases crack growth rates at higher  $\Delta K$  values. Measurement of crack growth by dcpd becomes inaccurate near threshold due to the effect of conductive corrosion products in the crack.

### INTRODUCTION

In order to establish safety criteria for use of BS2772 15M12 C.Mn steel in UK coalmines, it has been necessary to determine fatigue thresholds in appropriate environments. Previous measurements (1, 2,3) of the threshold in air had also indicated that accuracy of measurement and control of test parameters are crucial to the consistency and reproducibility of threshold data. Thus, the aim of this research was to develop a computerised test facility based on an existing electromagnetic resonance fatigue machine, use this to establish the reproducibility of the threshold data measured in air and then determine the influence of solutions representative of aggressive conditions obtaining underground: a laboratory  $3\frac{1}{2}\%$  NaCl aqueous solution was also included for comparison.

The definition of threshold adopted at the outset was the stress intensity range at which the fatigue crack growth rate fell below  $10^{-8}\text{mm/cycle}$ , following the consensus of earlier opinion. Similarly, following usual practice the fatigue threshold was

\* Lucas Research Centre, Solihull, U.K.

\*\* University of Sheffield, U.K.

+ Health and Safety Executive, Sheffield, U.K.

## FATIGUE 87

measured under load-shedding conditions, taking into account the influence that the test routine used (2,4,5) may exert on the data obtained.

It has been shown previously that both yield strength and microstructure can affect threshold values: the effects, in general, appear to be inter-related (2,6,7). Differences in yield strength, coupled with microstructurally-limited crack closure effects, produced higher threshold values in as-rolled 150M12 steel than in the quenched and tempered condition.

By measuring thresholds at loads above those for closure, whilst holding either  $K_{min}$  or  $K_{max}$  constant, Lewis (8) was able to demonstrate that threshold data for steels in air is effectively unified, with only a slight yield strength dependence. The implication that microstructure interacts with the measured threshold values via geometrical closure follows the earlier rationale provided by Ritchie and Suresh (9).

No simple picture is to be found within the few studies on the effect of saline solutions on the fatigue thresholds of carbon-manganese constructional steels that have been made. For instance, Pook and Greenan (10) showed that for mild steel (at  $R = 0$ ) the threshold is reduced from  $6 \text{ MPa} \sqrt{\text{m}}$  in air to  $2 \text{ MPa} \sqrt{\text{m}}$  in brine. Radon (11), on the other hand, found that for a structural steel (at  $R = 0.08$ ) the threshold increased from  $5.5 \text{ MPa} \sqrt{\text{m}}$  in air to  $10 \text{ MPa} \sqrt{\text{m}}$  in brine. The position is not helped by the large number of complicating variables that may affect threshold. The literature indicates that there may be effects due to frequency, material composition, specimen orientation, oxygen content/pH of solution and/or temperature, for instance. A real need existed, therefore, to determine the effect of environments on the threshold of 150M12 steel under controlled conditions that were at the same time as realistic as possible.

### EXPERIMENTAL DETAILS

The chemical analysis of the steel studied is given in Table 1. The material was supplied in the form of plate 37 mm thick. Two different conditions of heat treatment were considered (a) as-rolled (A/R) having a yield strength  $\sigma_y = 350 \text{ MPa}$ , and (b) water quenched  $890^\circ\text{C}$ , tempered  $630^\circ\text{C}$  (Q/T) with  $\sigma_y = 450 \text{ MPa}$ . Three-point bend specimens, with an LT orientation and as specified in BS5447 (12) and 12.5 mm thick, were prepared.

Fatigue testing was carried out on a 20 kN Amsler Vibronhore at stress-ratios of 0.15, 0.3 and 0.6 and at  $\sim 100 \text{ Hz}$ . Crack length was monitored by the dcpd method and linked by computer to the load maintainer to provide a controlled  $\Delta K$ -reduction rate with crack growth towards threshold. This procedure followed the general procedure recommended elsewhere (4) except that a constant linear  $\Delta K$  reduction rate with respect to crack length of

## FATIGUE 87

$5 \text{ MPa} \sqrt{\text{m. mm}^{-1}}$ , rather than an exponential relation, was followed. The load-shedding was nominally continuous. A smoothly continuous load reduction was prevented by the fact that a single processor was used for both load shedding and data-logging, however the 'steps' introduced because of this become smaller as the crack growth rate decreased towards threshold.

The Hudak procedure (4) defines threshold as that  $\Delta K$  which corresponds to a fatigue crack growth rate of  $10^{-8}$  mm/cycle and therefore does not consider lower crack growth rates, nor does it specify a period over which this limiting growth rate should be monitored: a "false" threshold could result from a temporary retardation or arrest of the crack. In this work a threshold criterion dependent on the accuracy of crack length measurement rather than crack growth rate was preferred i.e. the crack growth which takes place in ten million cycles at constant  $\Delta K$  is less than is accurately measurable (in this instance, 0.1 mm). A more detailed discussion of threshold criteria will be given elsewhere (13).

Tests were made in

- (a) laboratory air,
- (b) a 3½% sodium chloride solution,
- (c) a saline solution from a deep shaft coal-mine, containing ~ 4.3% NaCl and traces of calcium, magnesium and potassium (Solution A),
- (d) as for (c) but with only about 0.9% NaCl and, additionally, containing ~ 100 ppm hydrogen sulphide (Solution B).

The liquid environments were maintained local to the crack during the fatigue test in three-point bending using a small cell made from a plastic 35 mm film canister. The medium was circulated by peristaltic pump from a 500 ml reservoir. A drip feed into the crack was used with all solutions except that containing hydrogen sulphide, where the crack was completely submerged and the system was air-tight. The specimen was the only metallic item with which the solution came into contact.

## RESULTS

The threshold data are summarised in Table 2. The values measured in air for both heat-treated and as-received material fall within the range determined earlier (1), confirming Cadman's data. By comparison with this data, the results of the tests in the saline solutions show a reduced sensitivity to stress ratio and the multiple tests indicate more scatter at a given R value in the solutions.

The data at  $R = 0.3$  from tests in the mine-solutions, either with or without hydrogen sulphide, are close to those in the

# FATIGUE 87

TABLE 1 - Chemical Composition of 150M12 Steel

C	Mn	Si	P	S	Ni	Cr	Mo	Al	Cu
0.15	1.43	0.31	0.006	0.007	0.15	0.1	0.06	0.043	0.05

TABLE 2 - Threshold Test Data

Env.	Mater- ial	$\Delta K_{th}$ (MPa $\sqrt{m}$ ) at R ratio of:			H <sub>2</sub> S Conc. (ppm)		Test Time (days)	pH	
		0.15	0.3	0.6	Start	Fin.		Start	Fin.
Air	A/R	7.2	7.0	4.4					
	Q/T	7.3	5.7	4.9					
3½% NaCl Sol.	A/R	4.2	5.2	3.9			2½	5.5	5.0
	"	5.9	5.6	5.3					
	"	3.6	5.0	4.4					
	Q/T	4.1	3.5	4.5					
	"	4.4	3.1	3.0					
	"	5.1	3.3	3.5					
Mine Sol. A	A/R		4.5						
	Q/T		3.9				2½	7.2	7.3
Mine Sol. B	A/R		4.3		163	107	4	7.4	8.0
	"		4.7		111	11	17½	7.4	7.8
	Q/T		4.2		108	68	6		
	"		5.4		160	111	2	7.3	7.5

laboratory 3½% NaCl solution. However the crack growth rate curves and the fractography reveal features specific to the presence of hydrogen sulphide. These results reveal (Fig. 1,2) that the crack growth rate above threshold is significantly faster in the presence of hydrogen sulphide. All growth plots show a discontinuity at  $\Delta K$  of about 12 MPa $\sqrt{m}$ , due to the need to change the air-gap on the Vibrophore at this point, a procedure which involves an interruption in the loading routine. Similarly, all growth plots show increased scatter as the growth rate decreases. This is a consequence of both the statistical nature of the fatigue process near threshold and electronic noise in the dc/d crack length measurement technique. Some early test data showed an extreme form of scatter, which we describe as striping, as threshold is approached (see Fig. 3). This originated in the original form of the computer program

## FATIGUE 87

when the system entered and left the threshold routine several times before the threshold criterion was achieved. The effect was eliminated by simply reducing the  $\Delta K$  decrement for crack growth in the threshold routine within the program. 'Striping' did not appear to affect the value of threshold measured.

The fractures were examined by light and by scanning electron microscopy. Fractures developed in aqueous environments were cleaned before examination in a solution of hydrochloric acid inhibited by 1% hexamine. Comparative tests with other fractures indicated that this treatment had no discernible effect on the surface, however not all the corrosion debris could be removed in this way.

All the fracture surfaces produced at high ( $\Delta K > 10 \text{ MPa}\sqrt{\text{m}}$ , say)  $\Delta K$  levels showed the irregular, transgranular fatigue fracture typical of this type of steel. Evidence of secondary cracking was found in the 3.5% NaCl solution and particularly in the solution containing hydrogen sulphide: in the latter instance there were also some areas containing up to 25 per cent of intergranular fracture. The occurrence of intergranular fracture and secondary cracking decreased with reduction in  $\Delta K$  and with fall in  $\text{H}_2\text{S}$  level as the test progressed (see Table 2). The tests in air produced comparable surfaces to those reported earlier for this material (3) with evidence of an oxide band present behind the crack tip at threshold due to closure effects.

### DISCUSSION

The results indicate (Table 2) that the threshold of quenched and tempered material is slightly more sensitive to the NaCl solution (as compared with air) than the as-rolled material. This is not unreasonable bearing in mind its higher yield strength and different microstructure (tempered martensite, as compared with ferrite/pearlite). No significant difference was found between the two materials in the presence of hydrogen sulphide (Solution B). In both instances the thresholds are indistinguishable from those for Solution A and it is clear that the effect of hydrogen sulphide in introducing areas of intergranular fracture, thereby increasing crack growth rates, has had no significant effect on threshold. However, it does seem that the effect of aqueous saline solutions on near-threshold fatigue crack growth is to increase the scatter in crack growth rates and thus measured data.

The thresholds measured are comparable with those made by other workers on similar materials in similar media, although such comparisons are limited by the paucity of data available (see Taylor (14)).

Radon (11) working on BS 4360-50D in both air and 3.5% sodium chloride shows data supporting that reported here for a slightly different material and a lower test frequency (30Hz cf. 100Hz).

## FATIGUE 87

Blom et al (15) and Guerra-Rosa et al (16) have also reported reduced thresholds but only a slight reduction in stress-ratio effect in brine: the test frequency in the latter instance was 25Hz.

Tests made at much lower frequencies on the other hand such as Booth et al (17) and Endo et al (18) show greater disagreement. Booth reports that at 1/16th Hz the threshold is reduced in BS4360 -50D steel in seawater compared with laboratory air (however, the threshold in seawater is restored to its air value when cathodic protection is introduced). Endo however has shown at 5Hz that the measured threshold is increased by brine. The variables involved prevent meaningful analysis of this limited data.

Further comment is necessary on the phenomenon of "striping" mentioned earlier (see Fig. 3). This was mainly attributable to the unmodified computer program but the fact that it was largely absent from tests in air (which used the same program version) indicates a change in material behaviour contributing to it. For it to occur at all requires that the crack remains dormant (or apparently, so) for considerable periods.

Two explanations are possible:

- (i) the crack approaches threshold via a series of arrests,
- (ii) the crack length measurement technique is confounded by corrosion products inside the crack.

There is evidence for both these phenomena dependent on the composition of the solution. If crack length at the end of the test, as measured optically on the fracture surface, agrees with that measured by dcpd and this value is approached monotonically, then situation (i) obtains. This is so in the saline solutions. A suspension of iron oxide developed during the test; this was probably hydrated ferric oxide resulting from oxygen dissolved in the solution.

However if the measurements at low  $\Delta K$  do not agree then situation (ii) may be operating and any threshold measurements made under these circumstances must be suspect. This would be the case if the particles of corrosion product in the crack were conductive. The behaviour of specimens measured in hydrogen sulphide containing solutions is certainly of this type.

Whereas a suspension of iron oxide developed in the  $H_2S$ -free saline environments the solutions containing  $H_2S$  developed large amounts of iron sulphide (as did also the fracture surface) during the test. The crack "arrests" were random and irregular (e.g. test durations varying from 12 million to 161 million cycles) at the same  $\Delta K$  reduction rate. The crack length did not vary mono-

## FATIGUE 87

tonically through the test and the final crack length measured by the two methods above did not correspond. In the longest test the final region, incidentally, showed evidence of ferric oxide, rather than sulphide, corresponding with the reduction in sulphide ion concentration with time (see Table 2).

To conclude, despite the results of these tests satisfying the threshold criterion adopted the nature of the data recorded, with instances of long intervals separating measurable crack growth increments, suggests that a finite fatigue threshold does not, in fact, exist. The apparent growth increment per cycle falls well below the interatomic spacing and the process may consequently be described as statistical and, given sufficient time and patience, crack growth may be measurable down to minute levels of stress intensity range under appropriate conditions of stress and environment.

### CONCLUSIONS

Threshold studies on BS2772 150M12 steel in saline environments show:

1. A 3.5% sodium chloride solution and a mine saline solution reduce slightly  $\Delta K_{th}$  threshold and also the effect of R compared with tests in air.
2. Crack measurement by dcpd becomes inaccurate at near-threshold rates in saline solutions containing sulphide ions.

The apparent crack length as measured by potential drop becomes progressively shorter than the true length, consistent with conductive corrosion products in the crack.

3. Despite the data satisfying an arbitrary 'standard' threshold criterion, evidence suggests that a finite fatigue threshold may not always exist.
4. Similar fatigue fracture mechanisms operate in air and in aqueous environments and do not change substantially as the crack approaches threshold.
5. Some secondary cracking occurs in aqueous environments, particularly in sulphide-ion containing solutions. The latter also introduces some intergranular fracture, giving an increased crack growth rate at high  $\Delta K$  values.

### ACKNOWLEDGEMENTS

The authors are grateful to Professor G. J. Davies for providing facilities for this research in the Department of Metallurgy at the University of Sheffield. Dr. P.R.G. Anderson acknowledges financial support from the Health and Safety Executive.

## FATIGUE 87

The authors would like to thank the Director of the Safety Engineering Laboratory, Health and Safety Executive for permission to publish this paper.

### REFERENCES

- (1) CADMAN, A.J., BROOK, R. and NICHOLSON, C.E. Proc. Conf. "Fatigue Thresholds", Stockholm, Vol. 1, pp. 59-75, EMAS Ltd., Warley, U.K., 1981.
- (2) CADMAN, A.J., BROOK, R. and NICHOLSON, C.E. Scripta Met., Vol. 17, 1983, pp. 1053-56.
- (3) CADMAN, A.J., NICHOLSON, C.E. and BROOK, R. Proc. Conf., "Fatigue Thresholds", Stockholm, Vol. 1, pp. 293-312, EMAS Ltd., Warley, U.K., 1981.
- (4) HUDAK, S.J., SAXEN, A. and BUCCI, R.J. ASTM Technical Report, AFML-TR-78-40, Appendix 1, 1978.
- (5) CADMAN, A.J., BROOK, R. and NICHOLSON, C.E. Proc. Conf., "Fatigue Crack Growth Concepts", Philadelphia, USA, pp. 281-298, Met. Soc., AIME, 1983.
- (6) RITCHIE, R.O., Int. Metals Rev., Vol. 20, 1979, pp. 205-30.
- (7) LINDLEY, T.C. and RICHARDS, C.E. Proc. Conf., "Fatigue Thresholds", Stockholm, pp. 1087-1113, EMAS Ltd., Warley, U.K., 1981.
- (8) LEWIS, J.A. Proc. Conf., "Fatigue '84", Birmingham, Vol. 1, pp. 307-314, EMAS Ltd., Warley, U.K., 1984.
- (9) RITCHIE, R.O. and SURESH, S. Met. Trans., v.13A, 1982, pp. 937-40.
- (10) POOK, L. and GREENAN, A.F. Proc. Conf., "Fatigue Testing and Design", Vol. 2, p. 80, Soc. Environ. Eng., London, U.K., 1976.
- (11) RADON, J.C. Proc. Conf., "Fatigue Thresholds", Stockholm, Vol. 1, pp. 113-32, EMAS Ltd., Warley, U.K., 1981.
- (12)  $K_{Ic}$  FRACTURE TOUGHNESS TESTING. BS.5447, London, 1979.
- (13) CADMAN, A.J., NICHOLSON, C.E. and BROOK, R. (To be published).
- (14) TAYLOR, D. "A Compendium of Fatigue Thresholds and Crack Growth Rates", EMAS Ltd., Warley, U.K., 1985.

## FATIGUE 87

- (15) BLOM, A.F., BACKLUND, J. and JILKEN, L. Proc. Conf., "Fatigue Thresholds", Stockholm, Vol. 1, pp. 133-52, EMAS Ltd., Warley, U.K., 1981.
- (16) GUERRA-ROSA, L., BRANCO, C.M. and RADON, C. Proc. Conf., "Fatigue '84", Birmingham, Vol. 1, pp. 231-9, EMAS Ltd., Warley, U.K., 1984.
- (17) BOOTH, E.S., WYLDE, J.G. and IWASAKI, T., Ibid., Vol. 3, pp. 1471-84.
- (18) ENDO, K., KONAI, K. and SHIKIDA, T. ASTM, STP 801, 1983, pp. 81-93.

# FATIGUE 87

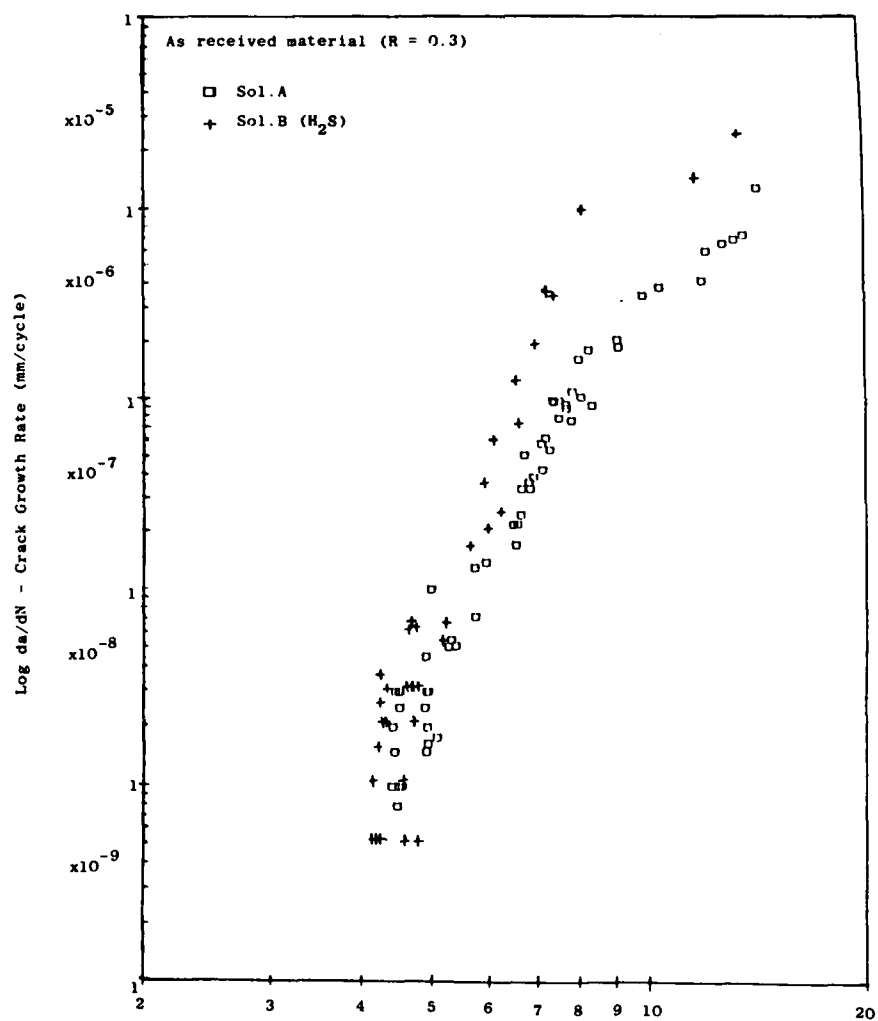


Fig. 1 Comparison of crack growth data for as-received material.

# FATIGUE 87

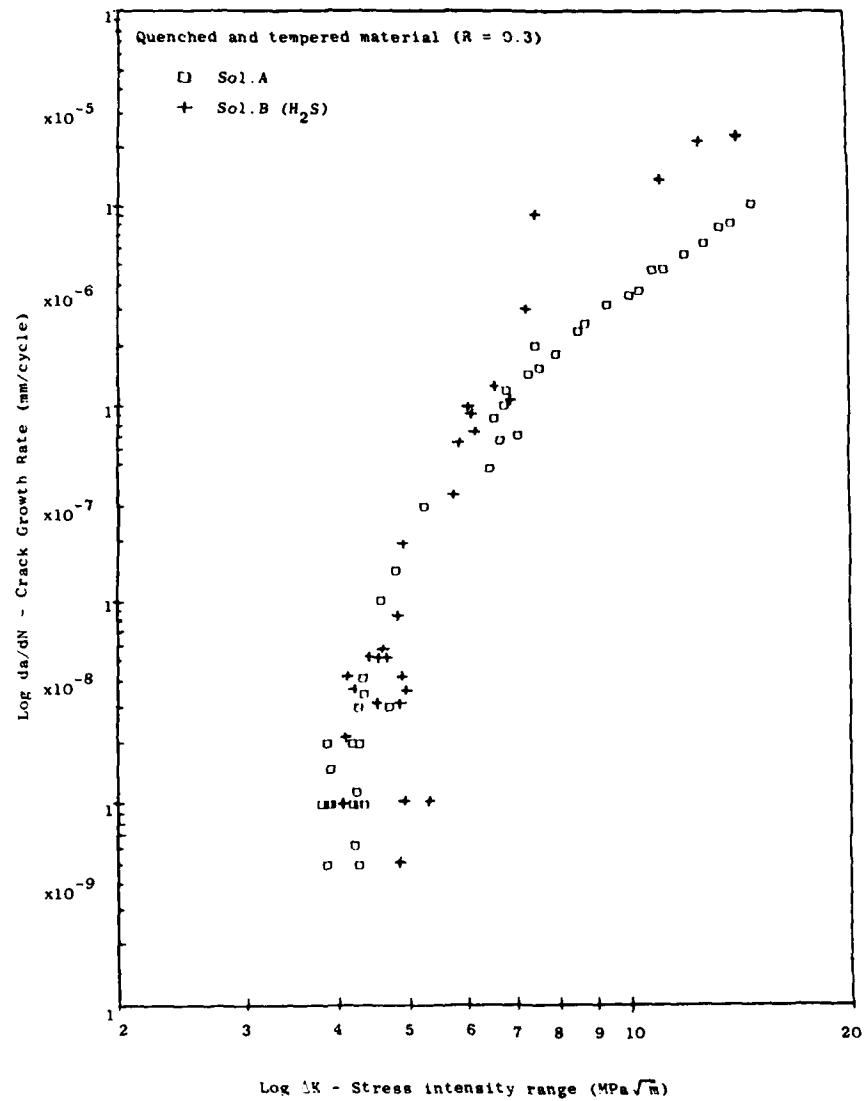


Fig. 2 Comparison of crack growth data for quenched and tempered material.

# FATIGUE 87

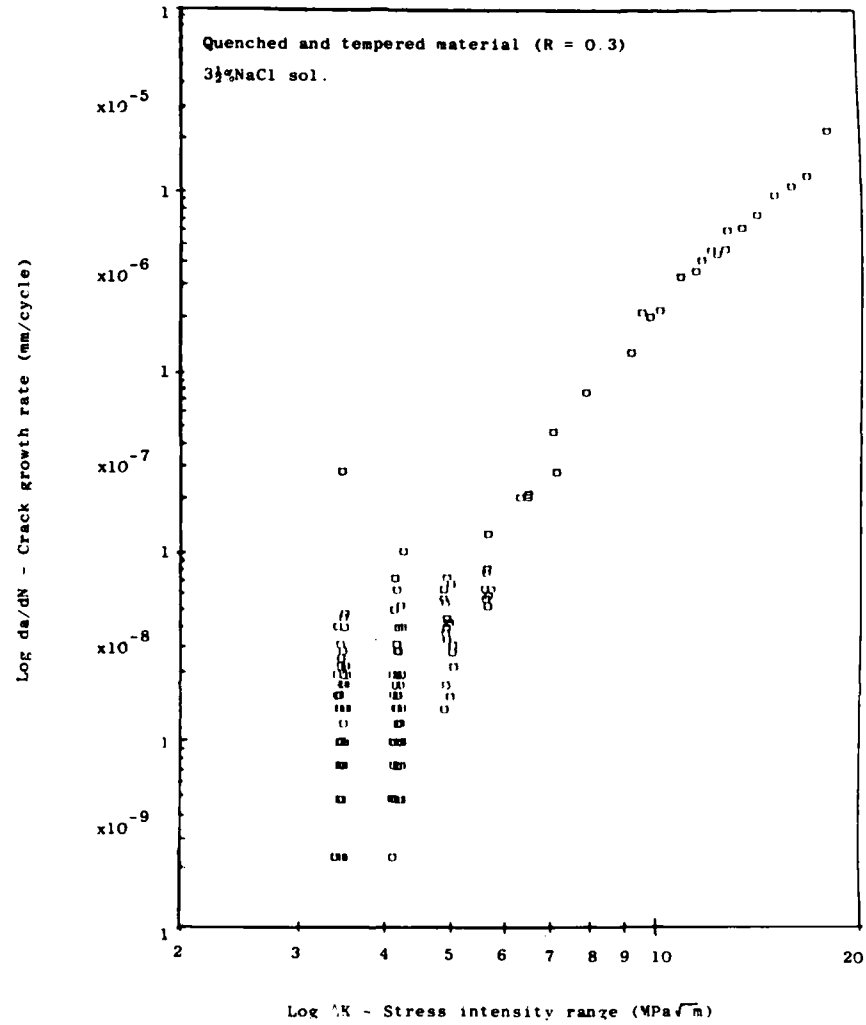


Fig. 3 Striping effect close to threshold.

A MODEL FOR ULTRA-LOW FATIGUE CRACK GROWTH

J.C. Radon\* and L. Guerra-Rosa<sup>+</sup>

A model was derived to predict the true threshold value for fatigue crack growth in the absence of crack closure. The model, based only on the tensile and cyclic properties of the material, was successfully verified against a set of experimental data on a typical structural steel. Good agreement with experimental results was obtained.

INTRODUCTION

In order to describe some deformation processes involved in the cyclic crack propagation, it is convenient to consider the conventional fatigue crack growth (FCG) as a sub-critical localised fracture process that occurs in a small element of a cyclic plastic zone positioned directly at the crack tip. Such cyclic growth is inevitably influenced by many factors, including the environment. However, if a fatigue crack growth takes place in the absence of environmental effects, causing statically-induced micro-cleavage, inter-granular embrittlement or other types of cracking due to corrosion, creep or radiation effects, one may describe the process as a pure fatigue crack growth. Here, the pure FCG will depend primarily on the cyclic mechanical deformation. Also, the response of the material to the cyclic loading will play a definite role.

The concept of a sub-critical growth, mentioned

\* Department of Mechanical Engineering, Imperial College College, London, England.

<sup>+</sup> Cemul, Instituto Superior Tecnico, Lisbon, Portugal.

above, requires some additional comments. As a sub-critical fracture process, pure FCG may occur in one single load cycle, not because  $K_{max}$  equals the fracture toughness of the material, but because the reversion of the load at the maximum and minimum points causes plastic work to be absorbed at the crack tip during the period of that cycle. In other words, in pure FCG processes, the damage is not induced by  $K_{max}$ , or any other static component, like mean stress or stress ratio,  $R$ , but only by the relevant  $\Delta K$ . The damage induced by  $\Delta K$  in one cycle will be added to the damage accumulated during the previous cycles and it is due to this accumulation of strain energies that FCG can occur. Since pure FCG originates exclusively in a reversed plastic flow mechanism, it may be concluded that an "ideal" fully elastic (fully brittle) material, without any plastic flow neither macroscopic nor microscopic, will never fail by pure FCG.

Finally, we have to define the concept of the pure FCG threshold,  $\Delta K_{c,th}$ , of a material. This concept was previously discussed in detail elsewhere (1,2,3) and called the "true" or "intrinsic" threshold. The true threshold is that critical or minimum value of  $\Delta K$  in pure FCG necessary for the normal development of plasticity at the tip of an "open" crack in the absence of perturbations or constraints. Most of these perturbations belong to the class of crack closure phenomena caused by crack surface roughness and are induced by abnormal residual stresses usually caused by load-history effects. Other residual stresses described here as "normal" residuals will always exist because of the mismatch between the plastic enclave (the monotonic and the cyclic plastic zones) and the surrounding elastic material. The influence of the residual stresses on the crack growth has been discussed by Welsch, et al. (4) and a convenient method of their evaluation in a structural steel investigated in the present work in (5). Experimental determination of  $\Delta K_{c,th}$  should be conducted at high stress ratios (usually  $R \geq 0.7$  for metals) because, in such cases, the crack tip closure is negligible and the applied stress intensity range is equal to the effective one.

#### THE BEHAVIOUR OF CYCLIC PLASTIC ZONES

In pure FCG processes of metallic materials, cyclic plasticity occurs only within the cyclic plastic zone. The deformation of an element in the material within this zone may be represented by a hysteresis loop (Fig. 1), such as is recorded in a low cycle fatigue (LCF)

test. There is some evidence available (6,7) that the plastic zone generally experiences strain cycles in the range  $10^{-3} < \Delta\epsilon_p < 10^{-1}$ . Here,  $\Delta\epsilon_p$  is the variation of the plastic strain range in the  $y$ -direction, i.e. perpendicularly to the macroscopic direction of crack growth. Also, it should be noted that the calculated number of cycles to fracture corresponds closely to that found in a typical LCF test. An estimate of the number of cycles necessary for the complete rupture of this cyclic plastic zone,  $N_f^*$ , can be made by dividing the length of the zone,  $r_c$ , by the corresponding macroscopic crack growth rate,  $\Delta a/\Delta N$ :

$$N_f^* = r_c / (\Delta a / \Delta N) \quad (1)$$

Apart from a cyclic plastic zone discussed above, a much smaller and highly deformed region located directly in front of the crack tip may now be considered. This is usually called the CTOD-affected zone or process zone, where plastic blunting, and subsequently the fracture process, occur. As reported (6,7), in the regime B of FCG in metallic materials, the process zone is subjected to strain cycles of the order of  $\Delta\epsilon_p > 10^{-1}$  and its length in the macroscopic direction of the crack propagation is about  $\Delta CTOD/2$ . The number of cycles to fracture of this process zone,  $N_f^{**}$ , can be estimated by a similar method to that used for the plastic zone, namely:

$$N_f^{**} = 0.5 \Delta CTOD / (\Delta a / \Delta N) \quad (2)$$

with  $\Delta CTOD$  calculated from the expression (7,8):

$$\Delta CTOD = \Delta K^2 / (4E \sigma_{yc}) \quad (3)$$

where  $\sigma_{yc}$  is cyclic yield stress at the appropriate strain rate.

Figures 2 and 3 show the estimated values of  $N_f^*$  and  $N_f^{**}$  for a structural steel BM45. The monotonic and cyclic mechanical properties of this steel may be found in (2,3). It will be noticed that both  $N_f^*$  and  $N_f^{**}$  depend on the dimensions, respectively, of the cyclic plastic zone and of the process zone. The length of both zones is also dependent on the value of  $\Delta K$  and on the appropriate cyclic yield stress,  $\sigma_{yc}$ . All the points plotted in Figs. 2 and 3 correspond to  $\Delta a/\Delta N$  and  $\Delta K$  values within regime B of FCG (Paris law region). It is noteworthy that different relationships, between number of cycles to fracture and size of the zone, are obtained for various microstructures. However, a straight extrapolation of these relationships to the thresh-

old region (regime A of FCG) is not possible because, although we can calculate the  $r_c$  and  $\Delta CTOD/2$  values at threshold, the respective macroscopic  $\Delta a/\Delta N$  values tend towards zero. Consequently, the  $N_f^*$  and  $N_f^{**}$  values at threshold,  $(N_f^*)_{th}$  and  $(N_f^{**})_{th}$ , will tend towards infinity.

#### KINETIC MODEL FOR THE PREDICTION OF $\Delta K_{c,th}$

This model is based on a kinetic approach, namely, on a known relationship between the applied stress and the corresponding displacement at the crack tip, and on the minimal possible crack advancing step on the atomic scale. It is assumed that the smallest step may be represented by one interatomic spacing,  $b_0$ , or the minimum length of a Burgers vector in a metallic crystalline structure. A simplified equation (equation (4)) was derived to predict the pure FCG threshold of a metallic material. This equation is valid for a work-hardening elastic-plastic material (Fig. 4), fatigue-loaded with the crack propagating in mode I. Full details of the derivation of equation (4) are given in (2,3). The value of the stress intensity threshold is:

$$\Delta K_{c,th} = \left[ \frac{3b_0 E^{1+n'} \sigma_{yc}^{1-n'} \epsilon_f^{1+n'}}{(1-2\nu)^2 / (4(1+n')\pi)} \right]^{1/2} \quad (4)$$

where  $b_0$  is the minimum length of a Burgers vector in a metallic crystalline structure,  $E$  is Young's modulus,  $\nu$  is Poisson's ratio,  $\sigma_{yc}$  is the cyclic yield stress,  $n'$  is the cyclic strain hardening exponent, and  $\epsilon_f$  is the true fracture strain (macroscopic value calculated from a tensile test). The values of  $\sigma_{yc}$ ,  $n'$  and  $\epsilon_f$  are obtained at the same test conditions and at relevant strain rate.

The model used for the derivation of equation (4) also takes account of the crack propagating in a field of local plasticity under plane strain (Pr) conditions. It has been shown in (6) that cyclic plastic zones in an FCG process are generated and developed under Pr conditions.

The term  $(1-2\nu)^2 / (4(1+n')\pi)$  in equation (4) is a non-dimensional parameter that quantifies the size of the cyclic plastic zone. Using the von Mises criterion, the length of a cyclic plastic zone ahead of a fatigue crack tip,  $r_c$ , is given by the following equation (5) derived in (8):

$$r_c = \frac{(1 - 2\nu)^2}{4(1 + n')\pi} \left( \frac{K_{max}}{\sigma_{yc}} \right)^2 \quad (5)$$

However, according to plastic zone studies recently carried out and described in (3), the average dimension of the cyclic plastic zone,  $r_c$ , can also be expressed by means of a more general relationship:

$$r_c = \alpha_c (K_{max}/\sigma_{yc})^2 \quad (6)$$

where  $\alpha_c$  is a non-dimensional parameter experimentally obtained and approximately equal to 0.012 for most metallic materials. Combining equations (5) and (6), it is possible to substitute the term  $(1 - 2\nu)^2 / \{4(1 + n')\pi\}$  in equation (4) with  $\alpha_c$ . Thus, the use of von Mises criterion for the prediction of the length of the cyclic plastic zone can be avoided and equation (4) rewritten as:

$$\Delta K_{c,th} = \left[ \frac{3b_0 E^{1+n'} \sigma_{yc}^{1-n'} \epsilon_f^{1+n'}}{\alpha_c} \right]^{\frac{1}{2}} \quad (7)$$

#### THE VALIDITY OF THE $\Delta K_{c,th}$ MODEL

The correct  $\Delta K_{c,th}$  prediction using equation (7) implies first of all a reliable determination of the cyclic mechanical parameters:  $\sigma_{yc}$  and  $n'$ . These two parameters have to be calculated from the cyclic stress-strain curve derived by any suitable method, such as described in (9). It is known that the cyclic mechanical properties of any material may differ considerably from the monotonic values (10). Also, the values of  $\epsilon_f$ ,  $E$ ,  $b_0$  and  $\alpha_c$  are necessary for the theoretical prediction of  $\Delta K_{c,th}$ . The values of  $\epsilon_f$  can be calculated from the relationship  $\epsilon_f = \ln 1/(1-\psi)$ , where  $\psi$  is the reduction of area of the material in a tensile test, again using appropriate strain rate and other testing conditions. The value of  $\alpha_c$  in the present calculations is 0.012.

In Table 1, the theoretically predicted value of  $\Delta K_{c,th}$  is compared with the experimental result for a structural steel BS4360-50D. Other necessary data were obtained from (11). Results on other materials are reported elsewhere (12).

#### WIDER APPLICATIONS AND CONCLUSIONS

In order to generalise the above approach for a wider range of materials in which the minimum Burgers vector

TABLE 1 - Theoretical and Experimental Values of  $\Delta K_{c,th}$ 

Material	E (GPa)	$\sigma_{yc}$ (MPa)	$n'$	$\epsilon_f$	$b_0$ ( $10^{-10}$ m)	$\Delta K_{c,th}$ (MN/m <sup>3/2</sup> )	
						Eqn.	Exp. ( $R > 0.7$ )
BS4360-50D steel	210	312	0.177	0.72	2.48	2.96	3.0

cannot easily be defined, it is suggested that the parameter  $b_0$  in equation (7) could be substituted by  $\rho^*$ , representing a minimum structurally-meaningful crack advancing step at the microscopic level. Furthermore, it can be assumed that, on attaining the true threshold, this parameter will be equal to the crack tip radius.

Then, using  $\rho^*$  instead of  $b_0$  and considering  $n' = 0$ , equation (7) takes the final form:

$$\Delta K_{c,th} = \sqrt{(3/\alpha_c)} \rho^* E \sigma_{yc} \epsilon_f \quad (8)$$

## REFERENCES

- (1) Guerra-Rosa, L. and Branco, C.M., "Influence of Plastic Zone Size on Fatigue Threshold in Steels", Proc. Conf. on "Fracture Prevention in Energy and Transport Systems", Rio de Janeiro, E.M.A.S., England (1984), pp. 24-33.
- (2) Guerra-Rosa, L., Branco, C.M. and Radon, J.C., Int. J. Fatigue, Vol. 7, No. 4 (1985), pp. 183-189.
- (3) Guerra-Rosa, L., "Fatigue of Carbon Steels", PhD Thesis, Technical University of Lisbon (1985) (in Portuguese).
- (4) Welsch, E., Eifler, D., Scholtes, B. and Macherauch, E., "Influence of a Residual Surface Stress Field near the Crack Tip on Crack Propagation", Proc. ECF6, E.M.A.S., Vol. II (1986), pp. 1303-1320.
- (5) Woodtli, J., Muster, W. and Radon, J.C., Eng. Fracture Mech., Vol. 24, No. 3 (1986), pp. 399-412.
- (6) Guerra-Rosa, L., Branco, C.M. and Radon, J.C., Int.

- J. Fatigue, Vol. 6, No. 1 (1984), pp. 17-24.
- (7) Hahn, G.T., Hoagland, R.G. and Rosenfield, A.R., Met. Trans., Vol. 3 (1972), pp. 1189-1202.
  - (8) Radon, J.C., Int. J. Fatigue, Vol. 4, No. 3 (1982), pp. 161-166.
  - (9) Landgraf, R.W., Morrow, J. and Emdo, T., Journal of Materials, JMLSA, Vol. 4, No. 1 (1969), pp. 176-188.
  - (10) Hertzberg, R.W., Deformation and Fracture Mechanics of Engineering Materials, J. Wiley & Sons (1976), p. 448.
  - (11) Glinka, G. and Radon, J.C., "Near-Threshold Fatigue Crack Growth Prediction", Proc. Fatigue 84, E.M.A.S. England, Vol. I (1984), pp. 529-541.
  - (12) Guerra-Rosa, L. and Radon, J.C., "On Some Applications of an Ultra-Low Fatigue Crack Growth Model", in print.

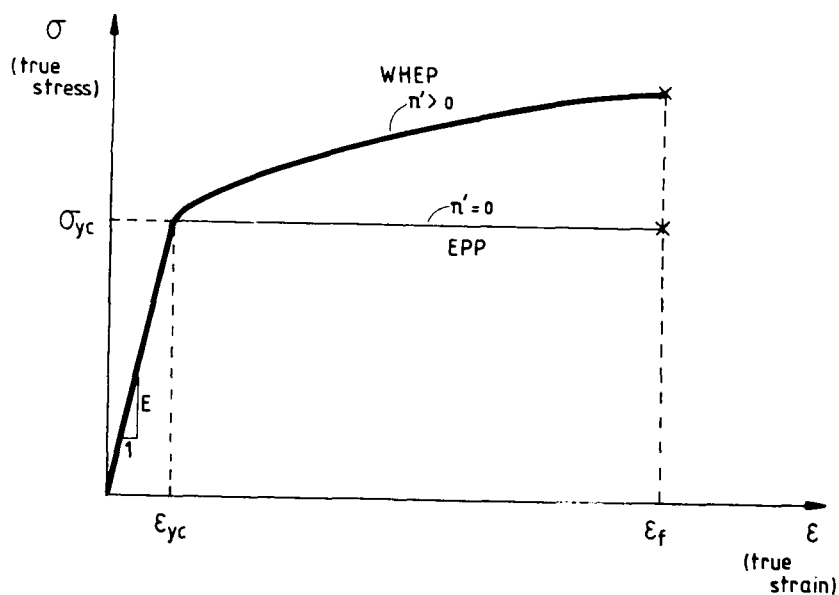


Figure 4. Stabilized cyclic stress-strain curve.

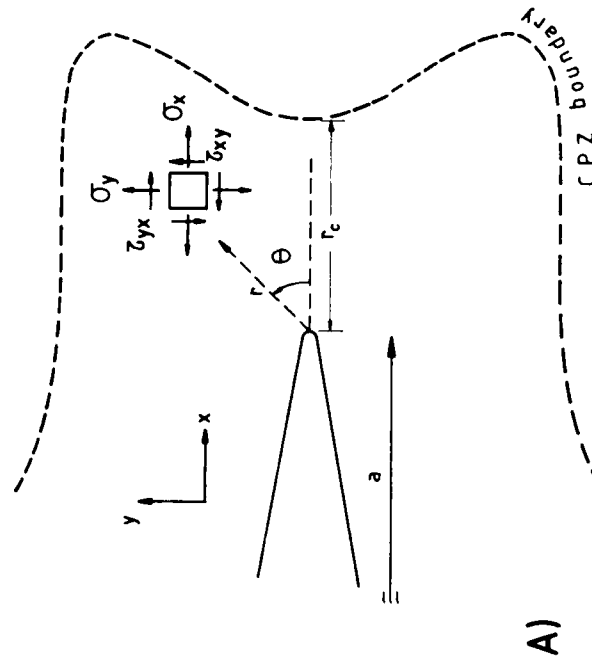


Figure 1a. Volume element is in a cyclic plastic zone near of a fatigue crack.

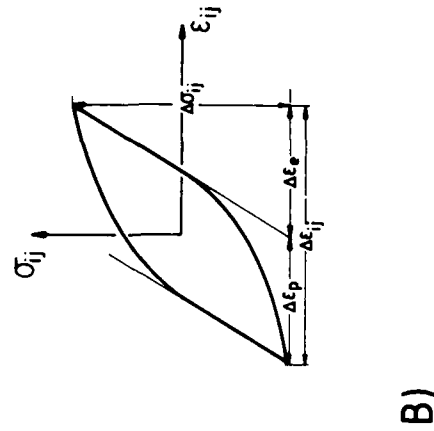


Figure 1b. Hysteresis loop of an element in C.P.Z.

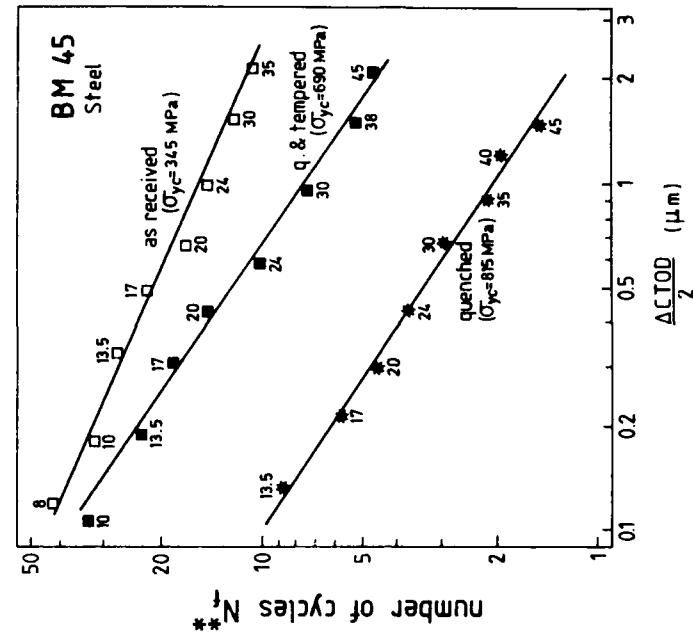


Figure 3. Estimated cycles  $N_f$  vs. stress  $\bar{\sigma}$ .

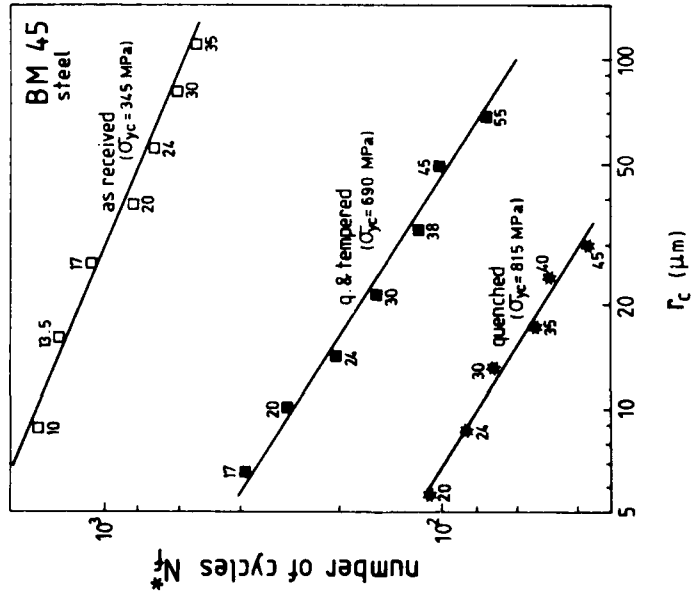


Figure 2. Estimated cycles  $N_f$  vs. the length of cyclic plastic zone  $r_c$ .

FATIGUE 87

860

INFLUENCE OF STRESS RATIO  $R$  ON FATIGUE THRESHOLD  $\Delta K_{th}$  FOR 40Cr  
STEEL

LI NIAN DU BAI-PING\*

Influence of stress ratio  $R$  on fatigue threshold  $\Delta K_{th}$  in 40Cr steel is studied. Results showed that the decrease in  $\Delta K_{th}$  with increasing  $R$  can not be entirely explained by crack closure effect, and there is influence of mean stress.

INTRODUCTION

It has been found that fatigue crack growth at near threshold region and the fatigue threshold stress intensity range  $\Delta K_{th}$  generally are extremely sensitive to stress ratio  $R$ . M.N. James et. al. demonstrate that  $\Delta K_{th}$  initially decreases with increasing  $R$  for long crack, and then remains constant at higher  $R$  (Figure 1). Such behaviour has been attributed to the effect of crack closure. In the closure-free condition, Figure 1 gives the threshold stress intensity range  $\Delta K_{eff. th}$  as an intrinsic parameter of the material, thus  $R$  has no influence on  $\Delta K_{eff. th}$  (1).

J. Byrne et. al. (2) demonstrate that in the nickel base alloy Nimonic 105, the decrease in  $\Delta K_{th}$  with increasing  $R$  can not be entirely explained by crack closure, even significant reduction in effective threshold  $\Delta K_{eff. th}$  occurs with increasing effective stress ratio  $R_{eff}$  ( $=K_c/K_{max}$ ) for closure-modified results. The  $R$  dependence of  $\Delta K_{th}$  is attributed to be a combined effect of crack closure and mean stress (Figure 2.)

\* Research Institute for strength of metals, Xi'an Jiaotong University, Xi'an, Shaanxi Province, People's Republic of China.

## FATIGUE 87

The objective of this paper is to study the influence of crack closure and stress ratio  $R$  on the fatigue threshold stress range  $\Delta K_{th}$ .

### EXPERIMENTAL PROCEDURES

The material studied is a medium-carbon steel, 40Cr, quenched and high-temperature tempered. Specimen is rectangular bar of 120x25x13mm. The stress ratio  $R$  used in three point bending fatigue are 0.1, 0.33, 0.5, 0.7. Testings were carried out in air at room temperature on an Amsler vibrophore at the frequency of 150 Hz. Threshold  $\Delta K_{th}$ , fatigue limit stress range  $\Delta \sigma_w$  and closure stress were determined.

### EXPERIMENTAL RESULTS AND DISCUSSIONS

#### Influence of closure on $\Delta K_{th}$ .

Influence of  $R$  on  $\Delta K_{th}$  is shown by curves A and B in Figure 3,  $\Delta K_{th}$  decreases with increasing  $R$ . By means of linear regression method:

for  $R < 0.5$

$$\Delta K_{th} = 8.9 - 9.6R \quad (\text{line A}) \dots \dots \dots (1)$$

$R \geq 0.5$

$$\Delta K_{th} = 5.3 - 2R \quad (\text{line B}) \dots \dots \dots (2)$$

When  $R < 0.5$  as  $K_{op} > K_{min}$ , influence of  $K_{op}$  on  $\Delta K_{th}$  is modified.

$$\Delta K_{eff. th} = K_{max. th} - K_{op} \quad \dots \dots \dots (3)$$

Where,  $\Delta K_{eff. th}$  is effective threshold stress intensity range at the crack tip. Influence of  $R$  on  $\Delta K_{eff. th}$  is shown by curve c, b in Figure 3.

for  $R < 0.5 \quad K_{op} > K_{min}$

$$\Delta K_{eff. th} = 6.5 - 4.4R \quad \dots \dots \dots (4)$$

for  $R \geq 0.5 \quad K_{op} < K_{min}$

$$\Delta K_{eff. th} = \Delta K_{th} = 5.3 - 2R \quad \dots \dots \dots (5)$$

However, for the relation of  $\Delta K_{eff. th}$  vs  $R$  (c -curve), influence of  $K_{op}$  on  $R$  has not been considered. If  $K_{op}$  is larger than  $K_{min. th}$ , and used for  $\Delta K_{min. th}$ , it is necessary to use  $R_{eff}$  rather than  $R$ , because stress ratio at the crack tip is not the nominal ratio  $R$ , but the  $R_{eff}$ .

$$R_{eff} = K_{op} / K_{max. th} \dots\dots\dots (6)$$

Here, we used  $K_{op}$  to replace  $K_c$ . As  $K > K_{op}$ , the crack is assumed to be fully open, and  $K < K_c$ , fully closed. When  $K > K_{op}$ , the influence of closure on  $\Delta K_{th}$  has no any effect at all.

The relationship of  $\Delta K_{eff. th}$  with  $R_{eff}$  is shown by curves d + b in Figure 3. However, even this approach is employed,  $\Delta K_{eff. th}$  data shows a decrease with increasing R.

$$\begin{aligned} R < 0.5 \quad K_{op} > K_{min} \\ \Delta K_{eff. th} = 8.6 - 8.7 R_{eff} \dots\dots\dots (7) \end{aligned}$$

$$\begin{aligned} R \geq 0.5 \quad K_{op} < K_{min} \\ \Delta K_{eff. th} = \Delta K_{th} = 5.3 - 2 R_{eff} \dots\dots\dots (8) \\ (\text{here, } R = R_{eff}) \end{aligned}$$

#### Influence of mean stress on $\Delta K_{eff. th}$

In the threshold region

$$\Delta K_{eff. th} = A \Delta \sigma_{eff. th} \sqrt{\pi a} \dots\dots\dots (9)$$

crack is not propagating. If we take the crack as a very sharp notch, then  $\Delta \sigma_{eff. th}$  can be considered as fatigue limit stress range. In the case of very sharp notch, it is known that fatigue limit stress range depends on mean stress, it is agree with Goodman's relationship. Fatigue limit stress range of smooth specimen were carried out in some R in 40Cr steel. Relationship of  $\Delta \sigma_w$  on mean stress  $\sigma_m$  is shown in Figure 4.

As R increases from 0.1 to 0.5, the mean stress increases, while  $\Delta \sigma_m$  significantly reduces. In the range of  $R > 0.5$ ,  $\Delta \sigma_w$  didn't significantly reduce with increasing R. In fact, fatigue limit stress range  $\Delta \sigma_{w.H}$  vs.  $\sigma_{m.H}$  curve is similar to  $\Delta \sigma_w$  vs  $\sigma_m$ .

Because of stress concentration, notch fatigue limit stress range  $\Delta \sigma_{w.H}$  is smaller than  $\Delta \sigma_w$ . If we can consider the crack as a sharp notch, then  $\Delta \sigma_{eff. th}$  vs. mean stress is similar to  $\Delta \sigma_w$  vs  $\sigma_w$ .

Consequently,  $\Delta \sigma_{eff. th}$  depends on mean stress in equation (9), so,  $\Delta K_{eff. th}$  in equation (9) depends on mean stress too. Figure 4 shows that  $\Delta K_{eff. th}$  vs  $K_m$  curve is similar to  $\Delta \sigma_w$  vs  $\sigma_m$ .

Therefore  $\Delta K_{eff. th}$  is not an intrinsic characteristic of the material, but dependent on mean stress.

## FATIGUE 87

The equations of calculated  $K_m$  are as follows.

$$\begin{aligned}
 R < 0.5 \quad K_{op} > K_{min. th} \\
 K_m &= 0.5(K_{max. th} + K_{op}) \quad \dots\dots\dots(10) \\
 R > 0.5 \quad K_{op} < K_{min. th} \\
 K_m &= 0.5(K_{max. th} + K_{min. th}) \quad \dots\dots\dots(11)
 \end{aligned}$$

### CONCLUSIONS

1. The decrease in the fatigue threshold stress intensity range  $\Delta K_{th}$  with increasing stress ratio  $R$  can not be entirely explained by crack closure effect.
2. When stress ratio  $R$  is less than 0.5, the closure effect exerts an influence on  $\Delta K_{th}$ . Once the effective stress ratio  $R_{eff}$  is employed to replace the nominal  $R$ ,  $\Delta K_{eff. th}$  still decreases with increasing  $R_{eff}$ . In the range of  $R > 0.5$ ,  $K_{min} > K_{op}$ ,  $\Delta K_{eff. th}$  is still related to  $R_{eff}$ .
3. The indicated dependence of  $\Delta K_{eff. th}$  on  $R_{eff}$  is due to the influence of mean stress.

### SYMBOLS USED

$R$	= stress ratio.
$R_{eff}$	= effective stress ratio.
$\Delta K_{th}$	= fatigue threshold stress intensity range. ( $MPa \sqrt{m}$ )
$\Delta K_{eff. th}$	= effective fatigue threshold stress intensity range ( $MPa \sqrt{m}$ )
$K_{op}$	= crack tip opening stress intensity in the threshold region. ( $MPa \sqrt{m}$ )
$K_{max. th}$	= minimum stress intensity in the threshold region ( $MPa \sqrt{m}$ )
$\Delta \sigma_{eff. th}$	= when crack determined, fatigue stress range, which is corresponding with $\Delta K_{eff. th}$ . (MPa)
$\Delta \sigma_w$	= fatigue limit stress range of smooth specimen. (MPa)
$\Delta \sigma_m$	= mean stress. (MPa)

ACKNOWLEDEMENTS

The authors gratefully thank the Science Fund of the Chinese Academy of Sciences for support for this programme.

REFERENCES

- (1) M.N. James and G. c. smith.  
International Journal of fatigue, Volume 5, No.2,  
April 1983, PP.75-78
- (2) J. Byrne, T.V. Duggan and C.J. Beevers, 7 ICSMA  
Proceeding. August 12-16, 1985, Volume 2, PP.1393-1398.

# FATIGUE 87

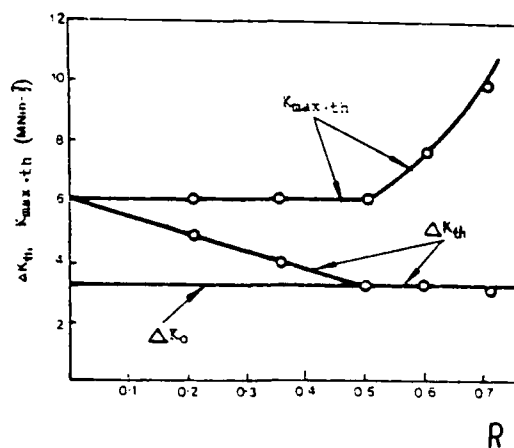


Fig. 1 Effect of stress ration,  $R$  on the threshold.

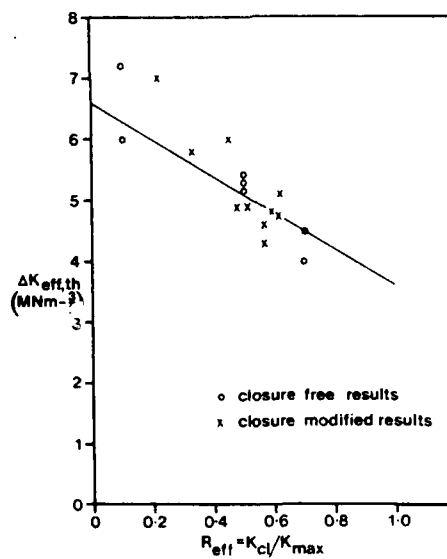


Fig. 2 Variation of  $\Delta K_{eff.th}$  with  $R_{eff}$ . where  $\Delta K_{eff} = K_{max} - K_{cl}$

# FATIGUE 87

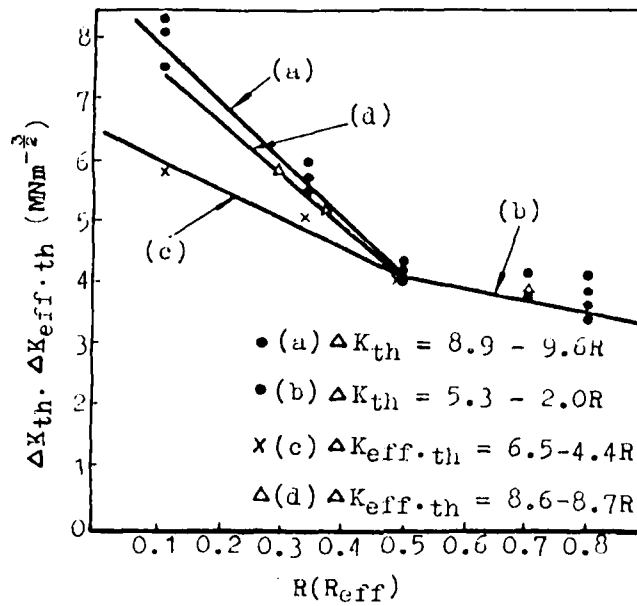


Fig. 3  $\Delta K_{th}$  ( $\Delta K_{eff,th}$ ) vs  $R$  ( $R_{eff}$ ) curve in 40Cr steel.

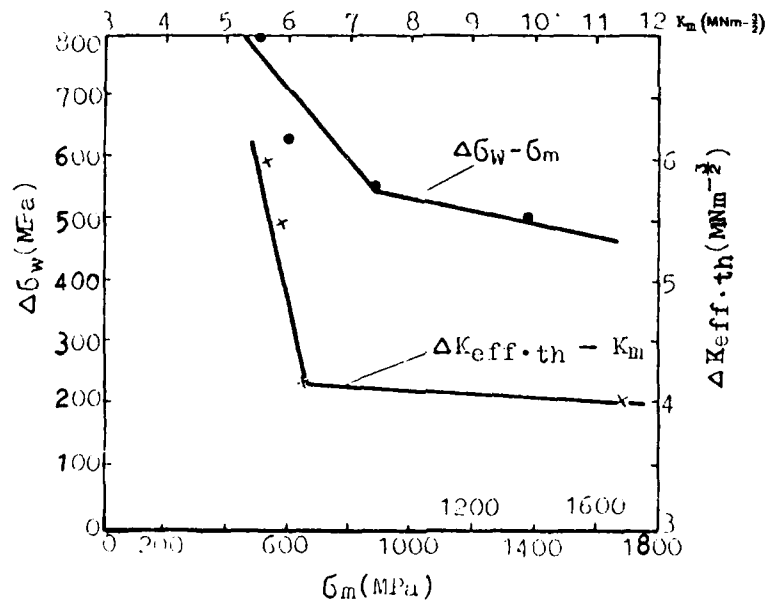


Fig. 4  $\Delta \sigma_w$  vs  $\Delta \sigma_m$ ,  $\Delta K_{eff,th}$  vs  $K_m$  curve in 40Cr steel.

FATIGUE 87

4D-A184 046

FATIGUE '87 VOLUME 2(U) VIRGINIA UNIV CHARLOTTESVILLE  
SCHOOL OF ENGINEERING AND APPLIED SCIENCE  
R O RITCHIE ET AL. JUN 87 N00014-87-G-0008

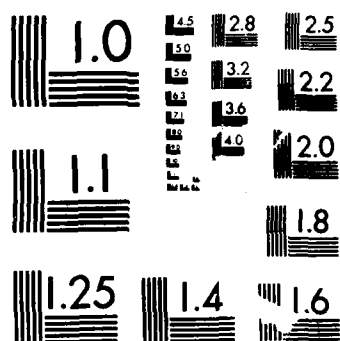
4/6

UNCLASSIFIED

F/G 20/11

NL

44  
44



MICROCOPY RESOLUTION TEST CHART  
NATIONAL BUREAU OF STANDARDS-1963-A

## FATIGUE 87

### THE EFFECTS OF LOADING HISTORY ON FATIGUE CRACK GROWTH THRESHOLD

T. Ogawa\*, K. Tokaji\*, S. Ochi\*\* and H. Kobayashi\*\*\*

The effects of loading histories on threshold stress intensity factor range ( $\Delta K_{th}$ ) were investigated in two steels. A single overloads and multiple overloads were chosen as loading history. The  $\Delta K_{th}$  values determined as a fatigue limit of preloaded specimens increased with increasing overload stress intensity factor ( $K_h$ ). For a given  $K_h$  value, it was found that multiple overloads produced much larger increase in  $\Delta K_{th}$  than a single overloads, and that threshold values expressed by maximum stress intensity factor ( $K_{max,th}$ ) were almost constant independent of load ratio. The results obtained are discussed in terms of crack closure behaviour, and a method is proposed to evaluate threshold value, based on plasticity-induced crack closure.

### INTRODUCTION

Threshold stress intensity factor range ( $\Delta K_{th}$ ) under constant amplitude loading is primarily controlled by oxide-induced crack closure (1)(2), which is sensitive to materials and environments. On the other hand, it is well known that fatigue crack growth rates ( $da/dN$ ) influenced by loading histories are due to plasticity-induced crack closure (3). Similarly, plasticity-induced crack closure is considered to be an important factor for the effects of loading history on  $\Delta K_{th}$ . However, the role of plasticity-induced crack closure has not been clarified. The contribution of plasticity-induced crack closure is insensitive to materials and environments (4). Therefore,  $\Delta K_{th}$  after loading history is expected to be evaluated independent of materials and environments.

In this study, the effects of loading histories on  $\Delta K_{th}$  were investigated in two steels having different strength levels. A

\*Department of Mechanical Engineering, Gifu University, Gifu, Japan.

\*\*Kubota, Ltd., Osaka, Japan.

\*\*\*Department of Physical Engineering, Tokyo Institute of Technology, Tokyo, Japan.

## FATIGUE 87

single overloads and multiple overloads were chosen as loading history. The results obtained are discussed in terms of crack closure behaviour, and a method is proposed to evaluate threshold value, based on plasticity-induced crack closure.

### EXPERIMENTAL PROCEDURES

The materials used were a low alloy steel SFVQ1A (a pressure vessel steel A508-3) and a low carbon steel S10C. The chemical compositions and mechanical properties are given in Tables 1 and 2, respectively. Fatigue crack propagation experiments were performed using compact specimens with a width ( $W$ ) = 50.8mm, which were machined in L-T orientation based upon ASTM standard (5). Specimen thicknesses ( $B$ ) are 12.5 and 4.0mm. Tests were conducted on 49 and 14.7kN electro servohydraulic testing machines for  $B=12.5$  and 4.0mm, respectively, operating at 30Hz under load control at room temperature in air. Crack closure was measured by back face strain gauge method in conjunction with a subtraction circuit.

The loading sequences are illustrated schematically in Fig.1.

#### A Single Overload Test (Fig.1(a))

Specimens used in this test were precracked to 3mm long from notch root, and then stress-relieved for 1hr at 620°C (SFVQ1A) and 650°C (S10C). A single cycle overloads ( $K_h$ ) were applied to specimens, followed by complete unloading. After this loading history, specimens were fatigue loaded at a certain initial stress intensity factor range ( $\Delta K_i$ ) at load ratios ( $R$ ) of 0.05 and 0.70. Crack growth and crack closure were measured under constant load range ( $\Delta P$ ). Tests were performed at various  $\Delta K_i$  values, and  $\Delta K_{th}$  was determined as the mean value of the lowest  $\Delta K_i$  value which causes crack growth and the highest  $\Delta K_i$  value which leads to crack arrest.

TABLE 1-Chemical Compositions (wt.%).

	C	Si	Mn	P	S	Cu	Ni	Cr	Mo	V	Al
SFVQ1A	0.18	0.22	1.46	0.003	0.005	0.05	0.69	0.15	0.57	<0.01	0.029
S10C	0.11	0.20	0.38	0.013	0.019						

TABLE 2-Mechanical Properties.

	Yield stress (MPa)	Tensile strength (MPa)	Elongation (%)	Reduction of area (%)
SFVQ1A	460	595	31	74
S10C	255	434	33	68

## FATIGUE 87

### Multiple Overload Test (Fig.1(b))

Multiple overloads were investigated in a limited number of tests. Specimens were stress-relieved, and fatigue precracks of 3mm long were grown from notch root by cyclic loading at a maximum stress intensity factor ( $K_{max}$ ) =  $K_h$  at  $R=0.05$ . The precracking is regarded as multiple overload history. Test procedures employed after this loading history were similar to those for a single overload tests.

The test conditions are listed in Table 3.

TABLE 3-Test Conditions.

Material	Thickness B (mm)	Loading history		Stress ratio R
		$K_h$ (MPa√m)	Overload	
SFVQ1A	12.5	20	Single	0.05
		30		
		45		
		60		
	4.0	30		
		45		
	12.5	30		0.70
				0.05
		0.70		
S10C	12.5	30	Single	0.05
		45		
		60		
		30		
	4.0	45		
		60		

## RESULTS

### Threshold after Overload Histories

Figure 2 shows the variations of  $da/dN$  and crack opening stress intensity factor ( $K_{op}$ ) with  $\Delta a (=a-a_0)$  at  $R=0.05$  for  $B=12.5$ mm in SFVQ1A; where  $a$  and  $a_0$  are crack length and precrack length, respectively. Overload plastic zone size  $r_p (=1/5.6\pi \cdot (K_h/\sigma_{ys})^2)$  is also represented in the figure; where  $\sigma_{ys}$  is the yield stress of the material. In a single overload tests, crack growth rates after overload history decrease progressively (delayed retardation), and cracks arrest after growing a certain distance; see Fig.2(a). This behaviour is not observed in multiple overload tests (Fig.2(b)). A similar crack growth behaviour was also observed at  $R=0.70$ .

The  $\Delta K_{th}$  values were determined as the mean value between the lowest  $\Delta K_i$  value which causes stable crack growth (solid symbols) and the highest  $\Delta K_i$  value which leads to crack arrest (open symbols). For the case of Fig.2(a), for example, the  $\Delta K_{th}$  value is obtained as the mean value of  $\Delta K_i=11.4$  and

# FATIGUE 87

10.0MPa $\sqrt{m}$ . The threshold results are listed in Table 4. Multiple overloads produce much larger increase in  $\Delta K_{th}$  than a single overload. The ratio of  $\Delta K_{th}$  values for both loading histories is given by the following equation independent of load ratio.

$$\frac{(\Delta K_{th})_{\text{single}}}{(\Delta K_{th})_{\text{multiple}}} = 0.7 \quad \dots\dots\dots (1)$$

Although the  $\Delta K_{th}$  values depend strongly on load ratio, the threshold values expressed by maximum stress intensity factor( $K_{max,th}$ ) are almost constant independent of load ratio. Similar results have been reported by Usami et al.(6) and Hopkins et al.(7).

In a single overload tests, the variations of  $K_{op}$  tend to correlate with crack growth behaviour at  $\Delta K_i > \Delta K_{th}$ . At  $\Delta K_i < \Delta K_{th}$ , the  $K_{op}$  values increase with crack growth until crack arrest occurs. However, the maximum values of  $K_{op}$  at  $\Delta K_i < \Delta K_{th}$  are much smaller than those at  $\Delta K_i > \Delta K_{th}$ . It is considered that the increase in  $K_{op}$  at  $\Delta K_i < \Delta K_{th}$  can not be detected because of the limited crack wake after overload. In multiple overload tests, the  $K_{op}$  value is almost constant. Crack surface contact during multiple overload history is detected in this case.

TABLE 4-Threshold Values.

SFVQ1A, B=12.5mm, $K_h=30\text{MPa}\sqrt{m}$					
Single overload			Multiple overloads		
R	$\Delta K_{th}$	$K_{max,th}$	R	$\Delta K_{th}$	$K_{max,th}$
0.05	10.7	11.3	0.05	15.0	15.8
0.70	3.8	12.8	0.70	5.2	17.3

(unit: MPa $\sqrt{m}$ )

## The Influence of Overload Magnitudes on Threshold

The  $\Delta K_{th}$  values at  $R=0.05$  after a single overload history are shown in Fig.3 as a function of  $K_h$ . The data plotted on the dashed line representing  $\Delta K_{th}(=K_{max,th})=K_h$  are obtained by  $\Delta K$ -decreasing tests according to ASTM tentative method (8), i.e. the data mean the basic  $\Delta K_{th}$  without loading history. For  $B=12.5\text{mm}$  in SFVQ1A, the  $\Delta K_{th}$  value at  $K_h=20\text{MPa}\sqrt{m}$  shows a slight increase (about 16%) compared with basic  $\Delta K_{th}$ . At  $K_h \geq 30\text{MPa}\sqrt{m}$ , however, the  $\Delta K_{th}$  values increase linearly with increasing  $K_h$ . Macroscopic fracture surfaces are presented in Fig.4. Fretting oxide deposits are seen more clearly at  $K_h=20\text{MPa}\sqrt{m}$  than at  $K_h=60\text{MPa}\sqrt{m}$ . This result suggests that the contribution of oxide-induced crack closure increases with

decreasing  $K_h$ , and thus the increase in  $\Delta K_{th}$  at low  $K_h$  levels are primarily dominated by oxide-induced crack closure. On the other hand, it is considered that the  $\Delta K_{th}$  values at  $K_h \geq 30 \text{ MPa}\sqrt{\text{m}}$  indicate the essential influence of loading history produced by plasticity-induced crack closure. The effect of specimen thickness on  $\Delta K_{th}$  is negligible in this material.

For  $B=12.5 \text{ mm}$  in S10C, the  $\Delta K_{th}$  values at  $K_h \leq 30 \text{ MPa}\sqrt{\text{m}}$  are larger than those in SFVQ1A. The increase in  $\Delta K_{th}$  in this material is due to the greater contribution of oxide-induced crack closure because of low strength level and rough fracture surface compared to those in SFVQ1A. In fact, considerable oxide deposits were seen on the fracture surfaces at low  $K_h$  levels. At  $K_h \geq 45 \text{ MPa}\sqrt{\text{m}}$ , however, the  $\Delta K_{th}$  values gradually approach those in SFVQ1A. For  $B=4.0 \text{ mm}$ , the  $\Delta K_{th}$  values at  $K_h=45$  and  $60 \text{ MPa}\sqrt{\text{m}}$  are much larger than those in SFVQ1A. As shown in Fig.5, the arrested crack fronts show a concave shape, which appears to be related to the difference of overload plastic zone size ( $r_p$ ) along the crack front due to stress state. Therefore, the ratio of  $r_p$  to specimen thickness ( $r_p/B$ ) is considered to be an important parameter for  $\Delta K_{th}$  after loading history.

## DISCUSSIONS

### Relation between Crack Closure and Threshold

Crack growth behaviour after a single overloads is understood as follows. As cracks grow into the plastic zone generated by a single overloads, plasticity-induced crack closure develops progressively and delayed retardation behaviour takes place. When effective stress intensity factor range ( $\Delta K_{eff} = K_{max} - K_{op}$ ) at the growth rate dip where  $K_{op}$  reaches a maximum value is larger than  $\Delta K_{eff}$  at threshold without loading history ( $\Delta K_{eff,th}$ ), cracks would continue to grow. On the other hand, crack arrests occur when  $\Delta K_{eff}$  value is smaller than  $\Delta K_{eff,th}$  value. At low  $K_h$  levels,  $K_{op}$  value is enhanced by oxide-induced crack closure, and thus in this case crack arrests occur at a higher  $\Delta K_i$  value, i.e.  $\Delta K_{th}$  is increased.

From the above argument,  $\Delta K_{eff,th}$  after a single overload history is considered to be expressed as

$$\Delta K_{eff,th} = K_{max,th} - (K_{op})_{max} \dots\dots\dots (2)$$

where  $(K_{op})_{max}$  is the maximum value of  $K_{op}$  in the post-overload crack growth. Assuming that the  $\Delta K_{eff,th}$  value is a material constant,  $K_{max,th}$  can be determined uniquely from  $(K_{op})_{max}$ . As demonstrated in Table 4,  $K_{max,th}$  is almost constant for a given  $K_h$  value independent of load ratio. Therefore,  $(K_{op})_{max}$  is expected to be a strong function of  $K_h$ .

## FATIGUE 87

The relationship between  $(K_{op})_{max}/K_h$  and  $r_p/B$  is shown in Fig.6; where the  $(K_{op})_{max}$  values were measured at  $\Delta K_i$  just above  $\Delta K_{th}$ , because the increase in  $K_{op}$  could not be detected at  $\Delta K_i < \Delta K_{th}$ . For  $r_p/B < 0.5$ ,  $(K_{op})_{max}/K_h$  are almost constant:

$$(K_{op})_{max}/K_h = 0.25 \sim 0.3 \quad \dots\dots\dots (3)$$

For  $r_p/B \geq 0.5$ , however,  $(K_{op})_{max}/K_h$  increases gradually as  $r_p/B$  increases. This behaviour may be attributed to a transition to plane stress from plane strain, but the detailed mechanism is obscure at present.

The relationship between  $K_{max,th}/K_h$  and  $r_p/B$  is presented in Fig.7, compared with the results of  $(K_{op})_{max}/K_h$  (Fig.6). The difference between  $K_{max,th}/K_h$  and  $(K_{op})_{max}/K_h$  decreases with an increase in  $r_p/B$ , i.e.  $K_h$ . This behaviour is considered to be due to the decreased contribution of oxide-induced crack closure with increasing  $K_h$ . Therefore, the small difference between  $K_{max,th}/K_h$  and  $(K_{op})_{max}/K_h$  means that the maximum values of  $K_{op}$  measured in the post-overload crack growth are well related to threshold values.

### Evaluation of Threshold after Overload Histories

The variations of  $K_{max,th}$  with  $K_h$  for a single overload history at  $R=0$  are shown in Fig.8; where the data in maraging steel and Ti-6Al-4V are quoted from the results obtained by Usami et al. (6) and Hopkins et al. (7), respectively. When  $r_p/B$  exceeds 0.5, Eq.(3) is not satisfied, then the data are excluded from the figure. Hatched area represents a prediction based on Eq.(2) and Eq.(3); where  $\Delta K_{eff,th}$  value is assumed to be  $\Delta K_{th}$  value at high load ratios ( $R \geq 0.7$ ), which is  $2\sim 3\text{MPa}\sqrt{\text{m}}$  for these materials. The prediction is in agreement with the results, and is appropriate for these materials having a wide range of strength level. As shown in Table 4,  $K_{max,th}$  is almost constant at  $R \geq 0$ . Therefore, it is concluded that the prediction based on Eq.(2) and Eq.(3) is valid for a single overload history at  $R \geq 0$  independent of materials.

For multiple overload history, the following equation is derived from Eq.(1), Eq.(2), Eq.(3) and Table 4.

$$(K_{op})_{max}/K_h = 0.4 \sim 0.45 \quad \dots\dots\dots (4)$$

In this case,  $(K_{op})_{max}$  is obtained immediately after multiple overloads. Thus the  $(K_{op})_{max}/K_h$  value is equivalent to  $K_{op}/K_{max}$  value in fatigue crack growth at  $K_{max}=K_h$  at  $R=0$ . The  $K_{op}/K_{max}$  values evaluated experimentally in various materials (4) and analytically (9) approximately agree with Eq.(4). Thus, it is considered that the prediction based on Eq.(2) and Eq.(4) is also valid independent of materials.

## FATIGUE 87

### CONCLUSIONS

Based on a study of the effects of loading history on fatigue crack growth threshold, the following conclusions can be made:

1. The  $\Delta K_{th}$  values increase linearly with increasing overload magnitude  $K_h$ . For a given  $K_h$  value, it is found that multiple overloads produce much larger increase in  $\Delta K_{th}$  than a single overloads, and that threshold value expressed by maximum stress intensity factor are almost constant independent of load ratio.

2. The effects of loading history on threshold are due to plasticity-induced crack closure. Threshold values after loading histories can be evaluated by the following equation independent of materials.

$$K_{max,th} = \alpha K_h + \Delta K_{eff,th}$$

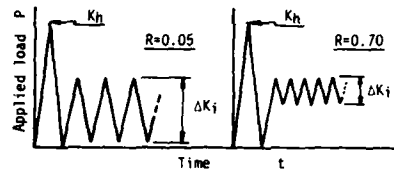
$$\alpha = \begin{cases} 0.25 \sim 0.3 & \text{for a single overload} \\ 0.4 \sim 0.45 & \text{for multiple overloads} \end{cases}$$

At low  $K_h$  levels, threshold values become larger than the above prediction in terms of the contribution of oxide-induced crack closure.

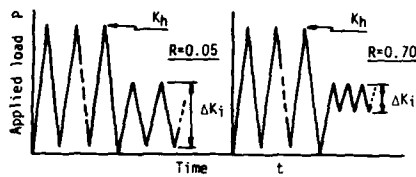
### REFERENCES

- (1) Stewart, A.T., Engng Fract. Mech., Vol.13, No.3, 1980, pp.463-478.
- (2) Suresh, S., Zamiski, G.F. and Ritchie, R.O., Metall. Trans., Vol.12A, No.8, 1981, pp.1435-1443.
- (3) Elber, W., ASTM STP486, 1971, pp.230-242.
- (4) Kobayashi, H., Trans. JSME, Vol.49A, No.443, 1983, pp.771-778(in Japanese).
- (5) Ann. Book ASTM Standards, E647-83, 1983, pp.472-485.
- (6) Usami, S. and Kitagawa, H., Proc. Fatigue '81, 1981, pp.472-485.
- (7) Hopkins, S.W., Rau, C.A., Leverant, G.R. and Yuen, A., ASTM STP595, 1976, pp.125-141.
- (8) ASTM Committee E-24, ASTM STP738, 1981, pp.340-356.
- (9) Budiansky, B. and Hutchinson, J.W., Trans. ASME, J. Applied Mechanics, Vol.45, No.2, 1978, pp.267-276.

# FATIGUE 87

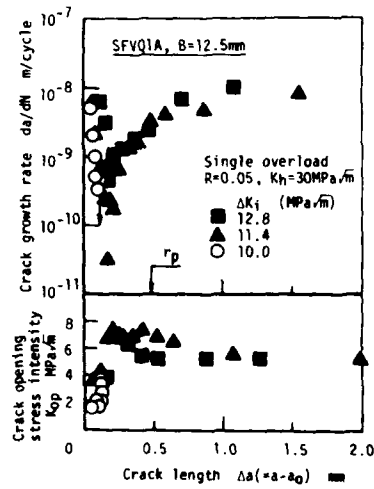


(a) A single overload

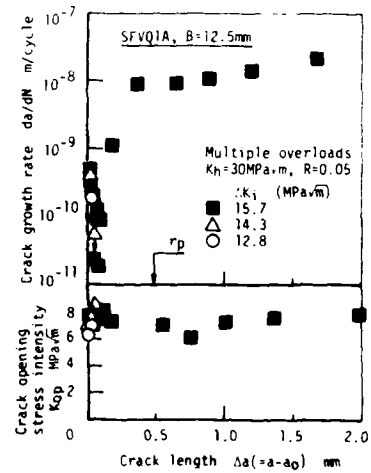


(b) Multiple overloads

Figure 1 Schematic illustrations of loading sequences.



(a) A single overload



(b) Multiple overloads

Figure 2 Crack growth and crack closure after loading history.

# FATIGUE 87

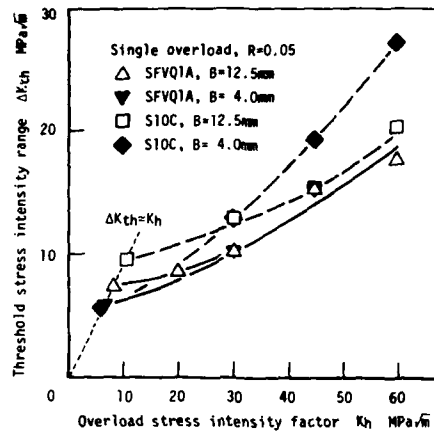


Figure 3 The influence of overload magnitudes on  $\Delta K_{th}$ .

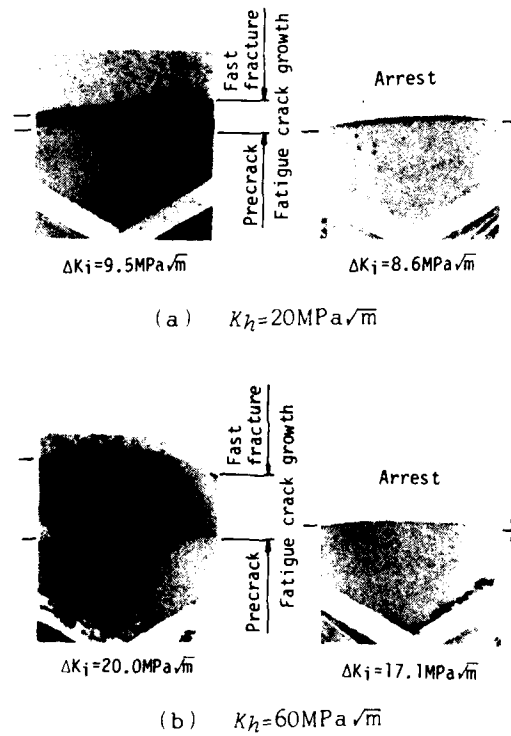


Figure 4 Macroscopic fracture surfaces (SFVQ1A).

# FATIGUE 87

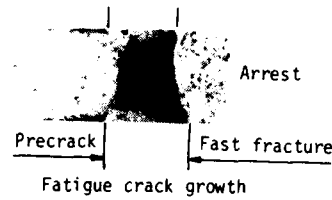


Figure 5 Macroscopic fracture surface showing arrested crack front shape (S10C,  $B=4.0\text{mm}$ ,  $K_h=60\text{MPa}\sqrt{\text{m}}$ ).

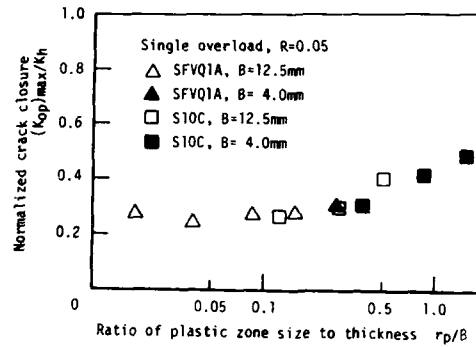


Figure 6 Relationship between  $(K_{op})_{max}/K_h$  and  $r_p/B$ .

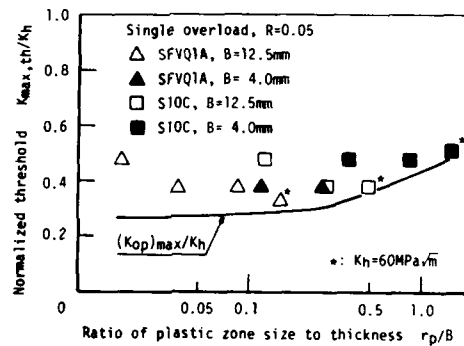


Figure 7 Relationship between  $K_{max,th}/K_h$  and  $r_p/B$ . Note that the maximum values of  $K_{op}$  are well related to threshold values.

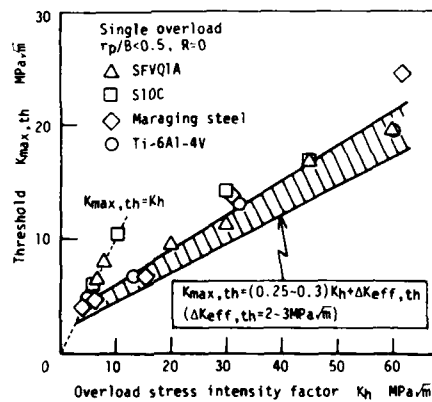


Figure 8 Comparison between prediction and experimental results in  $K_{max,th}$  after overload histories.

## FATIGUE 87

### THRESHOLD STRESS INTENSITY FOR STABLE CRACK GROWTH IN HIGH STRENGTH STEEL AT AMBIENT TEMPERATURE AND BELOW

L. Weber\*

Fatigue loading of unnotched surface treated specimens leads to crack initiation and subsequent crack growth until failure. Compressive residual stresses at the surface increase the time to crack initiation while they may stop a crack in subsurface layers due to a reduction of the stress intensity at the crack tip. Notched specimens without induced residual stresses show the influence of the UTS and the temperature on the threshold value of stable crack growth.

### INTRODUCTION

The topic of the investigations is to get information about the threshold stress intensity for the fatigue crack growth in the high strength steel 50 CrV 4. The tests are carried out on as rolled unmachined and then shot-peened unnotched 4-point-bending specimens and on notched CT-specimens

The testing parameters are the ultimate tensile strength (UTS) which ranges from 1200 to 1850 MPa and the testing temperature with values between ambient temperature and -70°C.

In the case of the unnotched specimens the main interest is to get information about crack initiation, crack growth and time to failure. The results are presented in Wöhler diagrams, such as the schematic graph

\*Institut für Werkstoffe, Lehrstuhl Werkstofftechnik,  
Ruhr-Universität Bochum, Postf. 102148, D-4630 Bochum

## FATIGUE 87

in figure 1. The characterization of crack growth in the notched specimens is done by  $\log da/dN-\Delta K$ -diagrams as shown schematically in figure 2.

For both types of specimens a special ultrasonic equipment is used which is able to detect cracks during fatigue and to follow their extension until failure.

### UNNOTCHED SPECIMENS

#### Testing set-up

A closed loop hydraulic testing machine is connected to a computer which controls all testing parameters like forces, strain and ultrasonic signals. The special ultrasonic testing set up is shown in figure 3. Five ultrasonic probes, attached at one end of the specimen, induce surface waves which cover the whole region of possible crack initiation and growth. As the testing is done under 4-point-bending several individual cracks may be induced. The ultrasonic supervision, which is carried out until failure of the specimen, provides not only information about the crack locations but also about their propagation. The detectable crack depth is found to be about 0.1 mm.

#### Surface treatment and materials state

Investigated is the high strength steel 50 CrV 4 with the following chemical composition:

C	Mn	Si	S	P	Cr	N
0.55	1.04	0.37	0.012	0.012	1.1	0.13 %

Hardening and tempering results in three UTS levels of 1200, 1500 and 1850 MPa. After heat treatment the specimens are surface treated by shot-peening with and without prestressing. After peening the surface roughness is measured to be about 65  $\mu\text{m}$ . Additional surface characterization is done by determining the residual stress distribution. Some results are presented in figure 4. Near the surface compressive residual stresses of about 550 to 750 MPa are found which increase at a depth of 0.2/0.4 mm below the surface to nearly 1000 MPa.

#### Crack initiation and growth

Figure 5 shows some testing results in a Wöhler diagram with the crack initiation time  $N_i$  and the time to failure

## FATIGUE 87

$N_f$ . With decreasing temperature  $N_i$  is shifted to greater values but at the same time the difference between  $N_f$  and  $N_i$  becomes smaller.

The effect of increasing  $N_i$  is greater than the decreasing of  $N_f - N_i$  so that the fatigue life will increase as it is shown in figure 6.

Figure 6 also shows the influence of the UTS which implies a greater fatigue life with growing UTS. Due to the ultrasonic testing device is possible to characterize the fatigue crack growth from  $N_i$  to  $N_f$ . Figure 7 shows some examples for different loading levels. After crack initiation at  $N_i$  with a crack length of 0.1 mm the crack grows for a while and then stops propagating. After a certain time - which depends on temperature, UTS and bending stress - the crack arrest is finished at  $N_g$  and stable crack growth until fracture sets in.

### Conclusions

The velocity of crack growth depends on the stress intensity  $K$  at the crack tip, which is a direct function of the internal and external stresses. It may be expressed as follows:

$$K = \sigma \sqrt{\pi a} Y \quad (1)$$

In the present case the bending stress acts like an external stress but at the same time there are compressive residual stresses in the surface layer which diminish the effective stress and therefore the stress intensity. Consequently equation 1 may be modified as follows:

$$K = (\sigma_{\text{bending}} + \sigma_{\text{residual}}) \sqrt{\pi a} Y \quad (2)$$

The factor  $Y$ , which defines the specimen's geometry, is found to be constant with a value of 0.34 for all crack lengths. In the case of the specimen which is loaded with a maximal bending stress of 1300 MPa (figure 7) the stress intensity is calculated to 3.4 MPa  $\sqrt{\text{m}}$  at a crack length of 0.1 mm. The growing crack runs into a field with increasing compressive residual stresses (figure 4) and therefore the stress intensity at the crack tip diminishes. Crack arrest sets in when the crack reaches the point where the compensation of the bending stress by the residual stresses is great enough to reduce the stress intensity below the threshold value. Crack stop is observed at crack lengths of 0.15 to 0.2 mm where the stress intensity is calculated to 2.7 MPa  $\sqrt{\text{m}}$ . This value is near the threshold value for stable crack growth, determined at notched specimens.

## FATIGUE 87

As the compressive stresses are not stable - a decrease is found by measurements after failure (figure 4) - the stress intensity raises with the testing time and the crack is able to restart propagating.

### NOTCHED SPECIMENS

#### Testing set-up

Figure 8 illustrates the testing set-up for the notched specimens. The significant difference to the unnotched specimens is that no surface but transmission waves are used. On the other hand only one ultrasonic probe calculates crack propagation for a certain crack extension region. When the crack leaves the receiving zone of the probe a next one will continue the measurement. By a lot of tests the ultrasonic signal is found to be linear to the crack length. By means of this testing device the investigations at low temperatures are enabled.

#### Material state

The material used is the same as the above mentioned. The heat treatment results in UTS levels of 1300, 1500 and 1800 MPa.

#### Crack growth

The specimens are tested under constant loading with crack velocities of  $10^{-6}$  mm/cycle and above. Some results are shown in figure 9. Raising the UTS results in increasing crack growth rates. The same tendency is to be observed when decreasing the temperature.

To get more information about the threshold stress intensity  $\Delta K_{th}$  at crack velocities beneath  $10^{-6}$  mm/cycle, additional tests are carried out using the load diminishing procedure. Starting the tests at the chosen  $\Delta K$  value of 10 MPa  $\sqrt{m}$  the crack growth is monitored by a program which uses the ultrasonic signal.

The program registers by the change of the ultrasonic signal if crack growth takes place and then reduces the applied stress.

The results (ambient temperature: UTS 1300 and 1800 MPa;  $-70^{\circ}\text{C}$ : UTS 1300 MPa) are presented in figure 10.

Independant of the UTS the threshold value for stable crack growth is found to be about 2.5 MPa  $\sqrt{m}$ . The low temperature of  $-70^{\circ}\text{C}$  results in an increasing threshold value of 4.5 MPa  $\sqrt{m}$ .

## FATIGUE 87

### Conclusions

The threshold value  $\Delta K_{th}$  is independant of the material strength but depends on the testing temperature. Raising the UTS means also an increase in the yield strength. The interaction between the size of the plastic zone (which depends on the yield strength) and crack growth is significant at high but negligible at extremely low crack velocities.

A change in the testing temperature influence the yield strength with a decrease at low temperatures and an increase at high temperatures. But this effect does not shift the  $\Delta K_{th}$  value to greater values at low temperatures so that the decisive material value which influence the threshold value is the elastic modulus which increase with descending temperatures.

### SUMMARY

The threshold value  $\Delta K_{th}$  is evaluated in a high strength steel for different strength levels in surface treated unnotched specimens and notched specimens. At testing temperatures from ambient temperature to  $-70^{\circ}\text{C}$  special ultrasonic testing devices enable the measurements of crack growth at low temperatures.

In the unnotched specimens crack initiation depends on the surface condition and fatigue crack growth on the effective stress distribution. Compressive residual stresses, induced by shot-peening, compensate the loading stress and lead to crack arrest if the threshold value is reached.

Notched specimens show that crack growth increase with increasing UTS and decreasing temperature. The threshold value is independant of the UTS but raises with decreasing temperature.

# FATIGUE 87

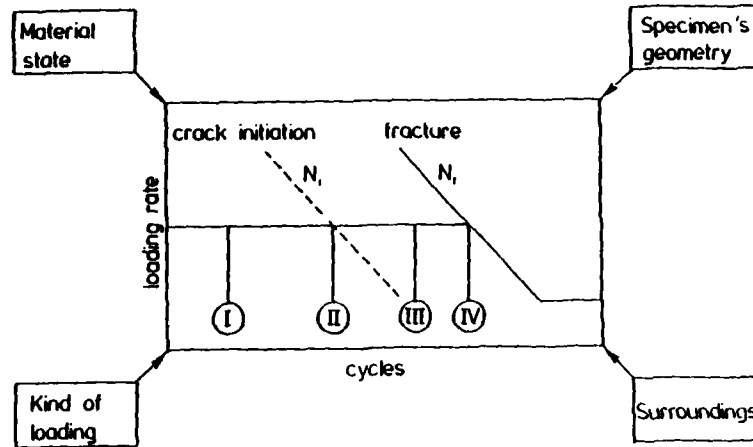


Figure 1 Schematic Wöhler diagram to represent the results of the unnotched specimens

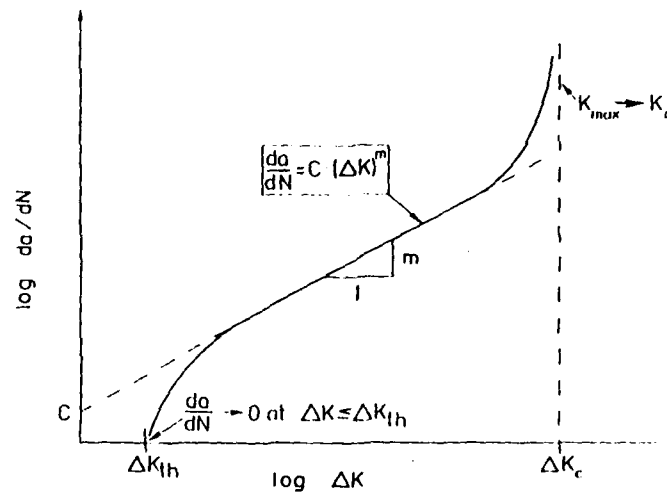


Figure 2 Log  $da/dN$ -log  $\Delta K$ -diagram to represent the results of the notched specimens

# FATIGUE 87

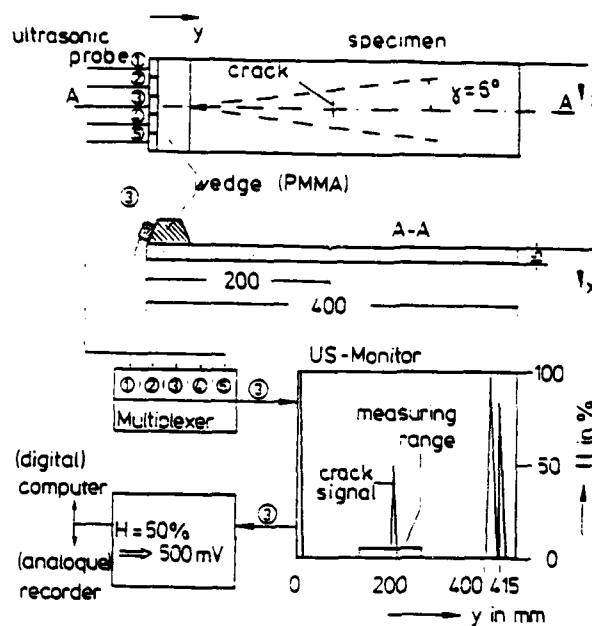


Figure 3  
Testing set-up for unnotched specimens to detect crack initiation and to follow crack growth

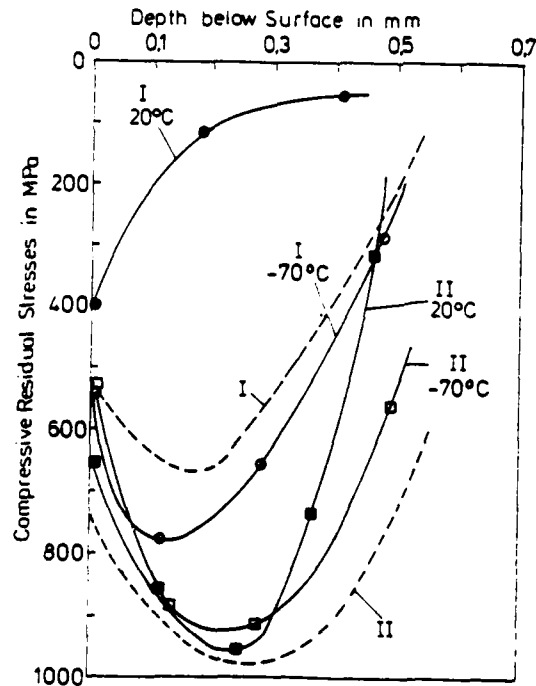


Figure 4  
Residual stress distribution before ----- and after ----- fatigue loading

# FATIGUE 87

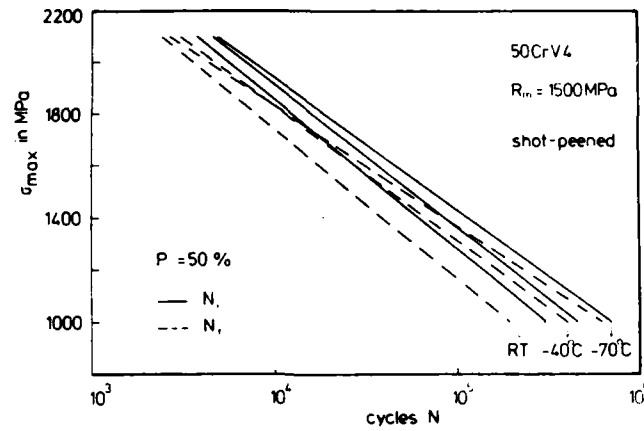


Figure 5 Influence of the temperature on  $N_i$  and  $N_f$

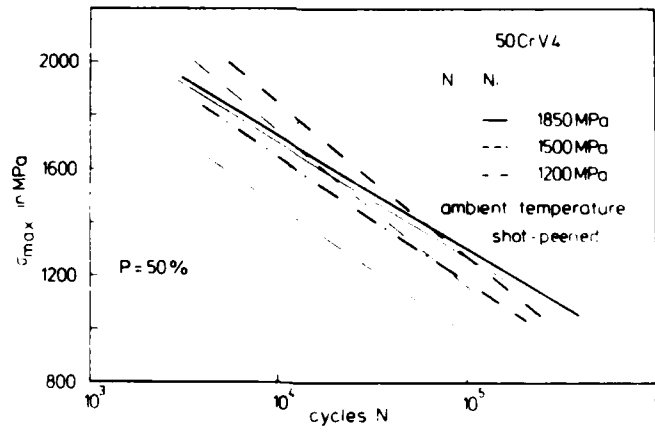


Figure 6 Influence of the UTS on  $N_i$  and  $N_f$

# FATIGUE 87

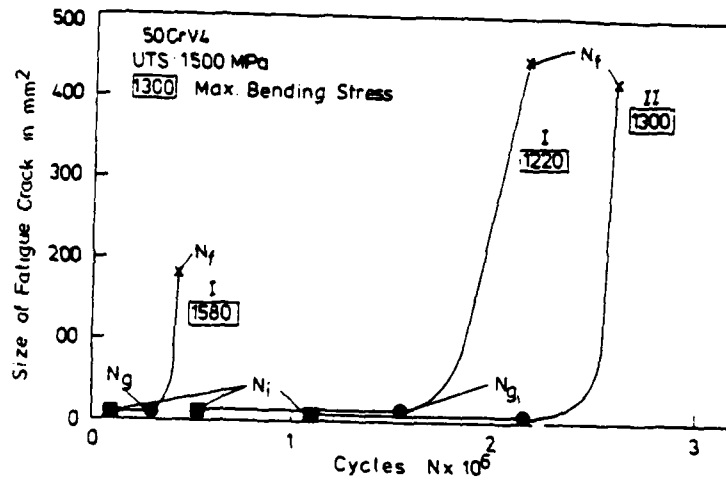


Figure 7 Fatigue crack growth in unnotched, surface treated specimens

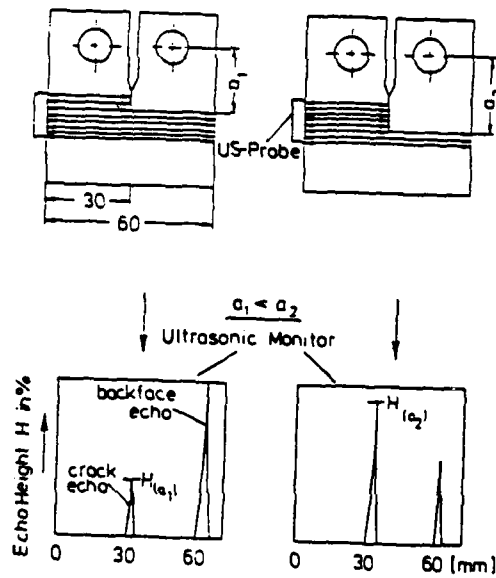


Figure 8 Ultrasonic testing set-up for notched specimens to follow crack growth

# FATIGUE 87

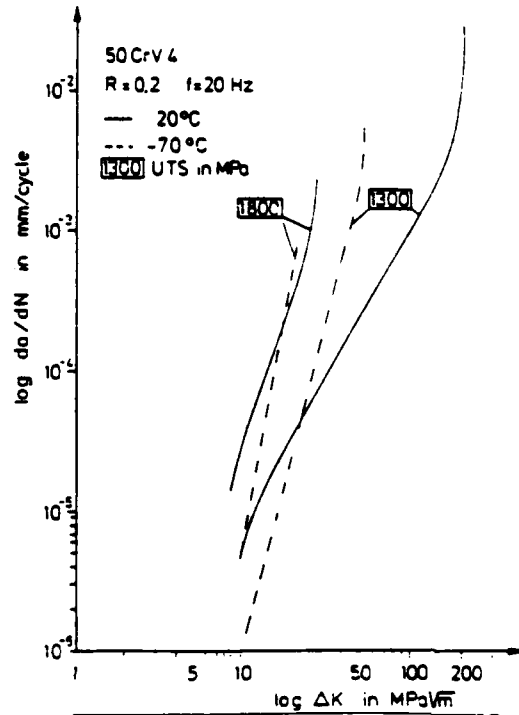


Figure 9

Influence of temperature and UTS on the fatigue crack growth

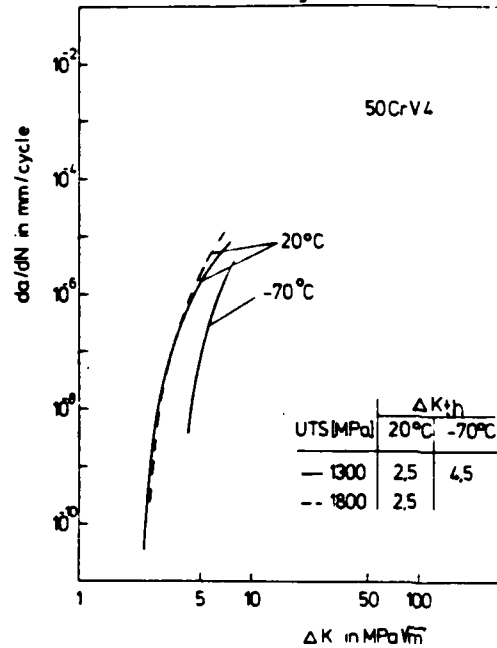


Figure 10

Influence of the temperature and the UTS on the threshold value  $\Delta K_{th}$

## FATIGUE 87

### THE EFFECT OF SHEAR LIPS ON FATIGUE CRACK GROWTH IN Al-2024 SHEET MATERIAL

J. Zuidema and H.S. Blaauw\*

Fatigue crack growth experiments have been performed on centre cracked specimens of Al-2024 T351. For two plate thicknesses experiments under constant stress intensity have been carried out. A very accurate technique was used to measure the shear lip width as a function of the crack length. It requires some length of growth before an equilibrium width of shear lips is reached. Both the steady and non steady state will be described. The results are used to explain the crack growth behaviour.

### INTRODUCTION

Aluminium plate specimens often show regions of fatigue fracture surfaces which are inclined at  $45^{\circ}$  to the plate surface (Hudson and Scardina (1), Voegelé and Schijve (2), Schijve (3), Edwards et al (4), Edwards and Zuidema (5)). An example of shear lip development under a constant stress amplitude ( $\Delta\sigma$ ) fatigue test is given in figure 1. As was shown earlier (4) shear lips can have an important effect on crack growth retardation when combined with load changes. To make quantitative predictions possible a more accurate technique was used in measuring the shear lip width than the photographic technique used before (4). Two thicknesses of Al2024 T351 plate (unclad) were chosen to give account of possible thickness effects. The tests were performed at constant  $\Delta K$  as this is the only possible manner to find the steady state behaviour of shear lips. The shear lip width  $t_s$  is defined as  $(B-tt)/2$  (1),  $B$  is the plate thickness and  $tt$  the width of the tensile part of the surface.

\* Department of Materials Science, Delft University of Technology, The Netherlands.

## FATIGUE 87

### EXPERIMENTAL DETAILS

Centre cracked plate specimens, 100 mm wide, were cut from 6 and 10.3 mm thick Al-2024 T351 plate material. Constant  $\Delta K$  tests were performed using a 350 kN, computer-controlled, servohydraulic fatigue machine. A d.c. potential drop method was used in measuring the crack length. The direction of the crack growth was perpendicular to the rolling direction. All tests were performed in air at a frequency of 10 Hz. In the table a survey is given of the tests performed. The shear lip width was determined by a grinding technique. One broken half of the specimen was destroyed by grinding every 0.5 mm in the crack length direction in critical areas where the shear lip width changes. On other places where a constant shear lip width was present 2 mm distance was used. Of the grinded surface under a microscope a magnified scetch was made. On it the tensile part was measured. Small deviations of the flat tensile part were ignored. Using (1) the shear part was determined. The crack length was found by measuring the length of the remaining part of the specimen by micrometer. This procedure was applied at both sides of the specimen with respect to the central hole. The data,  $t_s$  and  $a$ , were fed into a computer for further manipulation.

### THEORY AND RESULTS

Most cracks were grown at constant values of  $\Delta K$  and  $R$  over nearly the whole plate width in order to determine the width of shear lips for each value of  $\Delta K_{eff}$ . The value of  $\Delta K_{eff}$  is given by:

$$\Delta K_{eff} = U \Delta K \quad (2)$$

where  $U = 0.5 + 0.4 R$ ;  $-0.1 \leq R \leq 0.7$  (Elber (6)).  
For  $\Delta K$  the following formula was used:

$$\Delta K = (1-R)\sigma_{max}\sqrt{\pi a}/\sec(\frac{\pi a}{w}) \quad (3)$$

Two stages of shear lip development could be distinguished when the crack is started in tensile mode at a  $\Delta K_{eff}$  that is high enough for giving rise to (partially) shear mode. The first is a non steady state behaviour in which the shear lip width increases with the crack growth. At a certain crack length an equilibrium state of shear lip width is attained. This width tends to be the same for the rest of the crack growth. Trying to fit the shear lip width results in a mathematical formula, we suppose that the rate of increase of shear lip width,  $\frac{dts}{da}$ , is proportional to the difference in equilibrium shear lip width,  $t_{seq}$  and the actual shearlip width  $t_s$ . In formula:

$$\frac{dts}{da} = D(t_{seq} - t_s) \quad (4)$$

Integrating (4) leads to:

$$t_s = t_{seq}(1 - \exp(-D(a - a_s))) \quad (5)$$

## FATIGUE 87

A more general formula is found when the experiment is started at a level  $t_{s,start}$  of shear lip width:

$$(t_s - t_{s,start}) = (t_{seq} - t_{s,start})(1 - \exp(-D(a - a_s))) \quad (6)$$

In these formulae  $D$  is a constant and  $a_s$  is the start crack length. Most of our experiments had a  $t_{s,start} = 0$  which transforms (6) in (5). With equation (6) it is also possible to describe shear lip shrinkage when  $t_{s,start} > t_{seq}$ .

On the basis of equation (5) we made a computer fit program in which the two constants  $t_{seq}$  and  $D$  are determined. The best fit was assumed when the sum of the squares of the differences of the actual points and the values following from (5) was a minimum. An example of such a fit is given in figure 2. The results were as we expected for  $t_{seq}$  (ref. (4)). We found a straight line for  $t_{seq}$  as a function of  $\Delta K_{eff}$  (figure 3) given by the formula:

$$t_{seq} = 0.674 \Delta K_{eff} - 3.75 \text{ (mm)} \quad (7)$$

Before we found this formula we had to make an assumption, because a few points did not seem to fit very well. It appeared that these results came from experiments in which we had applied so high a  $\Delta K_{eff}$  that the resulting  $t_{seq}$  according (7) was bigger than half the plate thickness ( $B/2$ ). In these cases we omitted in the fitting procedure the points where  $t_s$  equals  $B/2$ . The procedure now gave results that were very nearly to that given by (7). An example of such a fit is given in figure 4. This was a surprising result, to assume that for high  $\Delta K_{eff}$  there was a tendency for shear lips to grow thicker than half the plate thickness. This shear lip width can actually only be obtained in a thicker specimen.

Equation (7) is based on 9 constant  $\Delta K$  experiments on 6 mm thick plates and 7 tests on 10.3 mm plates. The test data are given in the table.

It appeared that the constant  $D$  could best be given as a function of  $\Delta K_{eff}$ . The correlation coefficient was higher for  $\Delta K_{eff}$  than for  $K_{max}$ . Several mathematical formula were used. The best we found was:

$$D = 0.0167 \exp(22.1/\Delta K_{eff}) \quad (8)$$

There appeared to be no great difference between results from 6 and 10.3 mm plates. So all results have been used for the result of (8). A plot of this curve through the data points is given in figure 5. The fitting is less accurate than  $t_{seq}$  against  $\Delta K_{eff}$ .

Another phenomenon that we discovered was a slowly decreasing crack growth rate  $da/dN$  during the non steady state shear lip development. The crack growth rate seems to be not only a function of  $\Delta K_{eff}$  but also of the actual shear lip width. A higher  $t_s$  leads to a lower  $da/dN$ .

We made two assumptions. First we assumed that  $da/dN$  is an unique

## FATIGUE 87

function of  $\Delta K_{eff}$  and  $t_s$ . Secondly we assumed a linear decreasing of  $da/dN$  with  $t_s$ , at the same  $\Delta K_{eff}$ :

$$da/dN = \frac{(\frac{da}{dN})_{eq} - (\frac{da}{dN})_{start}}{t_{seq}} t_s + (\frac{da}{dN})_{start} \quad (9)$$

In this formula  $(\frac{da}{dN})_{eq}$  is the crack growth rate in the steady state period, i.e. when  $t_s = t_{seq}$ . Substituting (5) in (9) gives:

$$\frac{da}{dN} = ((\frac{da}{dN})_{eq} - (\frac{da}{dN})_{start})(1 - \exp(-D(a - a_s))) + (\frac{da}{dN})_{start} \quad (10)$$

By estimating  $(\frac{da}{dN})_{eq}$  and  $(\frac{da}{dN})_{start}$  and using  $D$  from (8) we plotted (10) through the actual crack velocity against crack length data points. The  $\Delta K_{eff}$  was 9.18 MPa $\sqrt{m}$ ; the plate thickness 6 mm. The plot is given in figure 6.

### DISCUSSION

Figure 6 shows that the crack growth rate in tensile mode (at 6 mm crack length) is nearly twice as high as in shear mode (above appr. 20 mm). The  $\Delta K_{eff}$  used was 9.18 MPa $\sqrt{m}$ . The  $t_{seq}$  that followed from the fitting procedure was 2.42 mm. An obvious reason why a crack should grow faster in tensile mode than in shear mode is the longer transverse crack front in shear mode. Nevertheless, this can not explain the whole difference. In the case of figure 6 the total transverse crack length in the (equilibrium) shear mode is about 8 mm when a shear lip angle of 45° is taken. Hereby we assumed to have almost the same surface roughness in both tensile mode and shear mode. When a linear dependence is assumed between crack growth rate and length of transverse crack front this could explain a velocity ratio of 8/6 = 1.3 instead of 2. Probably the asymmetric plastic zones, which develop in case of shear lips (Zuidema et al (7), will have an influence on the amount of crack closure or residual stresses before the tip.

### CONCLUSIONS

1. Steady state width of shear lips only depends on  $\Delta K_{eff}$ . The relation is:

$$t_{seq} = 0.674 \Delta K_{eff} - 3.75 \text{ (mm)} \quad (7)$$

2. The rate of growth of shear lips is proportional to the difference in  $t_{seq}$  and  $t_s$ . This leads to:

$$t_s = t_{seq}(1 - \exp(-D(a - a_s))) \quad (5)$$

3. The parameter  $D$  depends on  $\Delta K_{eff}$  too. It can be approximated by:

$$D = 0.0167 \exp(22.1/\Delta K_{eff}) \quad (8)$$

## FATIGUE 87

4. The steady state shear lip width can be higher than half the plate thickness for high values of  $\Delta K_{eff}$ .
5. The decrease in crack growth rate when the shear lip width increases depends on the initial crack growth rate and the crack growth rate in equilibrium. The formula is:

$$da/dN = ((\frac{da}{dN})_{eq} - (\frac{da}{dN})_{start})(1 - \exp(-D(a - a_s))) + (\frac{da}{dN})_{start} \quad (10)$$

### SYMBOLS USED

- $a_s$  = crack length where constant  $\Delta K$  test starts (mm)  
 $(\frac{da}{dN})_{eq}$  = crack growth rate when  $t_s = t_{seq}$  (mm/cycle)  
 $(\frac{da}{dN})_{start}$  = crack growth rate when  $a = a_s$  (mm/cycle)  
 $\Delta K_{eff}$  = effective trajectory of  $K$  (MPa $\sqrt{m}$ )  
 $s_{yy}$  = least sum of the squares of the differences of the actual  $t_s$  values and the corresponding values of the fitted curve (mm<sup>2</sup>)  
 $t_s$  = the shear lip width ( $t_s = (R - t_t)/2$ ) (mm)  
 $t_{seq}$  = the steady state shear lip width (mm)  
 $t_t$  = the tensile part of the thickness (mm)  
 $U$  =  $\Delta K_{eff}/\Delta K$

### ACKNOWLEDGEMENTS

The authors are grateful to Mrs. Anneke van Veen for her help in preparing the manuscript, to Chris van Beekum for performing a lot of grinding and to Bart Wiersma for his help in making plots of  $da/dN$  versus  $a$ .

### REFERENCES

- (1) Hudson, C.M. and Scardina, J.T., Eng. Fract. Mech., Vol. 1, 1969, pp. 429-446.
- (2) Vogelesang, L.B. and Schijve, J., Fat. Eng. Mat. Struct., Vol. 3, 1980, pp. 85-98.
- (3) Schijve, J., Eng. Fract. Mech., Vol. 14, 1981, pp. 789-800.

## FATIGUE 87

- (4) Edwards, R.A.H., De Jong, E.M. and Zuidema, J., "The Fracture Mode Transition and its Effect on Crack Growth Retardation", *Proceedings of Fatigue 84*, Edited by C.J. Beevers, University of Birmingham, England, 1984.
- (5) Edwards, R.A.H. and Zuidema, J., *Eng. Fract. Mech.*, Vol. 22, 1985, pp. 751-757.
- (6) Elber, W., "Fatigue Crack Closure under Cyclic Tension", ASTM STP 486, American Society for Testing and Materials, Philadelphia, USA, 1971.
- (7) Zuidema, J., Mense, P.J.M. and Edwards, R.A.H., "Environmental Dependence of Fatigue Crack Growth Retardation following a Single Overload in 2024-Al Alloy", accepted for publication in *Eng. Fract. Mech.*

# FATIGUE 87

TABLE 1 - Results of tests on 6 and 10.3 mm thick plates,  
syy is the least squares sum.

plate thickness (mm)	$\Delta K$ (MPa $\sqrt{m}$ )	R	$K_{max}$ (MPa $\sqrt{m}$ )	$\Delta K_{eff}$ (MPa $\sqrt{m}$ )	tseq (mm)	D (1/mm)	$s_{yy}$ (*10 <sup>-2</sup> ) (mm <sup>2</sup> )	number of data points
10.3	9.63	0.64	26.00	7.12	1.01	0.263	8.2	31
10.3	11.95	0.54	26.00	8.56	2.12	0.157	8.7	30
10.3	14.87	0.43	26.00	9.98	3.04	0.164	13	26
10.3	18.58	0.29	26.00	11.41	3.78	0.098	95	29
10.3	24.67	0.05	26.00	12.84	4.90	0.093	5.1	14
10.3	14.40	0.10	16.00	7.78	1.42	0.498	6.4	70
10.3	18.00	0.10	20.00	9.72	2.78	0.184	42	70
6	12.00	0.10	13.30	6.47	0.55	0.511	8.8	74
6	9.74	0.30	14.00	6.06	0.30	0.813	2.8	45
6	11.40	0.50	23.00	8.00	1.75	0.187	41	68
6	15.00	0.10	16.70	8.11	1.83	0.202	53	83
6	16.00	0.30	23.00	9.95	2.96	0.137	57	65
6	23.00	0.08	25.00	12.24	4.56	0.103	22	17
6	20.00	0.10	22.20	10.80	3.55	0.156	14	37
6	18.00	0.10	20.00	9.72	2.74	0.245	89	58
6	17.00	0.10	18.90	9.18	2.42	0.164	33	50

# FATIGUE 87

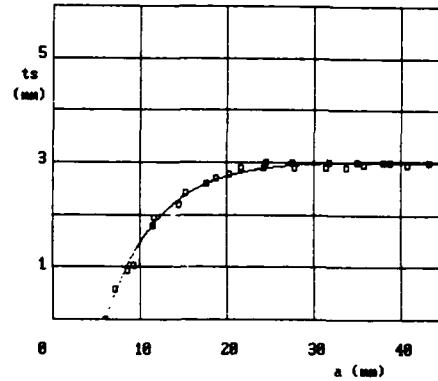
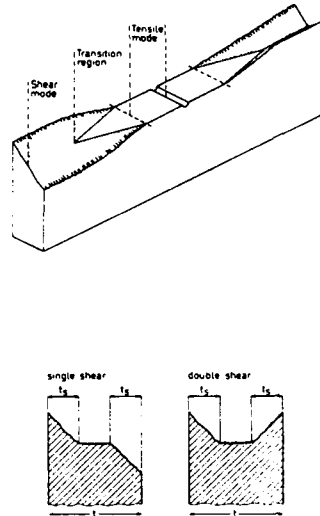


Figure 1 Tensile mode and shear mode fracture surface.

Figure 2 Fit with  $t_{seq} < B/2$ , 10,3 mm plate,  $\Delta K_{eff} = 9.98 \text{ MPa}/\text{m}$ .

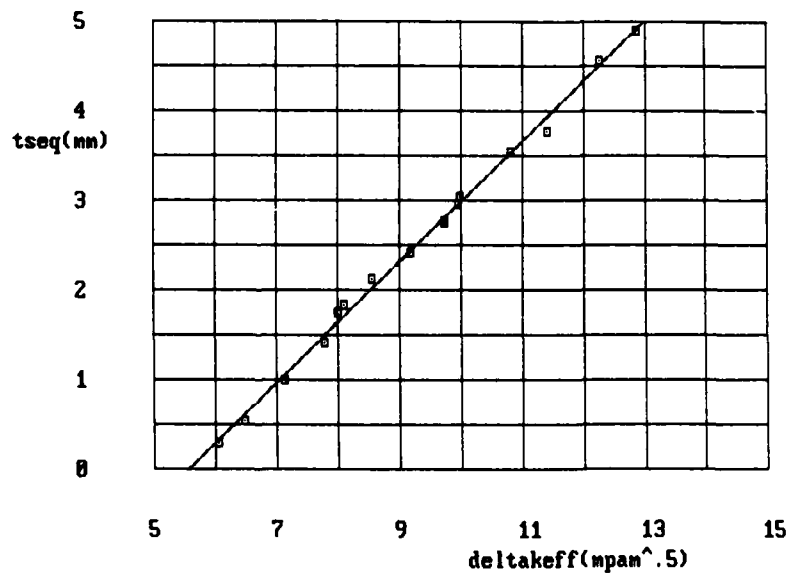


Figure 3 Fit of  $t_{seq}$  versus  $\Delta K_{eff}$ .  
Correlation coefficient = 0.9968053.

# FATIGUE 87

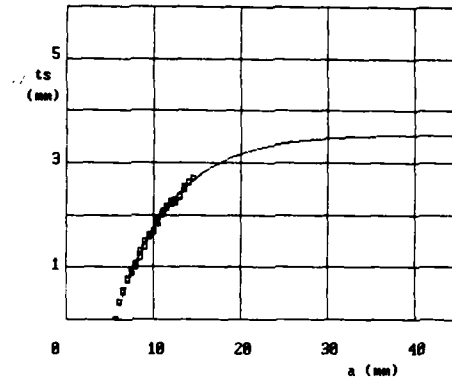


Figure 4 Fit with  $t_{seq} > B/2$ ,  
6 mm plate,  $\Delta K_{eff} = 10.8 \text{ MPa}\sqrt{\text{m}}$ .

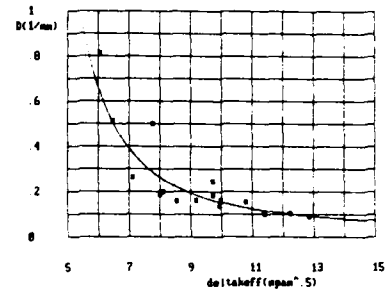


Figure 5 D as function of  $\Delta K_{eff}$ .  
Correlation coefficient = 0.8138071.

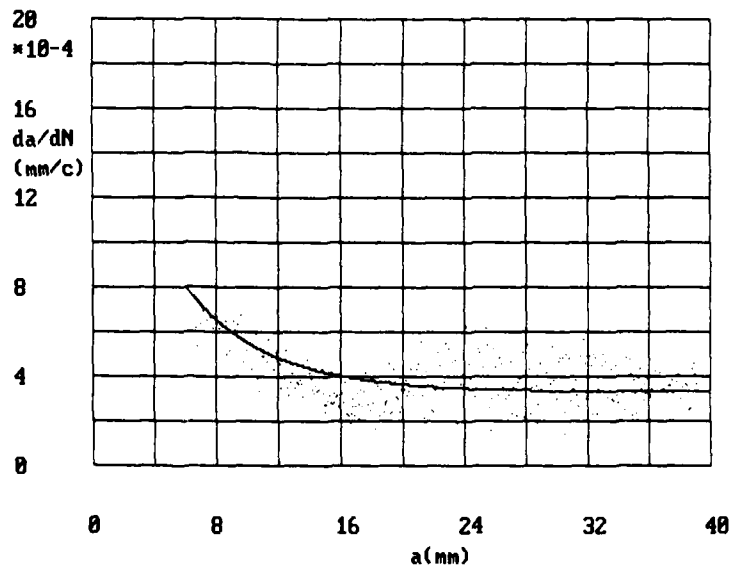


Figure 6 Predicted curve of  $da/dN$  versus  $a$  through the data points.

FATIGUE 87

## NEAR-THRESHOLD FATIGUE CRACK GROWTH BEHAVIOR AT CRYOGENIC TEMPERATURE

P. K. Liaw and W. A. Logsdon  
Materials Analysis Department  
Westinghouse R&D Center  
Pittsburgh, PA 15235

Near-threshold fatigue crack growth behavior of a nickel base alloy (Inconel 706) and a stainless steel (J8K-75) were developed at cryogenic temperature as low as liquid helium temperature (4.2K). Decreasing the temperature from 297 to 4.2K decreased the influence of R-ratio on the rates of near-threshold crack propagation in both materials. In particular, the R-ratio effect at 4.2K was marginal. The lack of oxide and roughness-induced crack closure at low temperatures was thought to be the reason for the decreased R-ratio effect.

Decreasing the temperature from 297 to 4.2K decreased the crack propagation rates in both materials. Crack closure cannot account for the effect of temperature on crack growth behavior. Dislocation dynamics has to be used to explain the temperature effect.

### 1. Introduction

Recently, a considerable amount of research has been conducted to examine near-threshold fatigue crack propagation behavior of structural materials. Most of near-threshold crack growth investigation was, however, performed at ambient temperature. Relatively little work has been done at cryogenic temperatures<sup>(1-8)</sup>. Some structural components, such as, superconducting generators<sup>(9)</sup> and magnets<sup>(10)</sup>, are designed to operate at extremely low temperatures, as low as liquid helium temperature (4.2K). In these machine components, the rates of cryogenic temperature crack propagation are essential for life prediction and structural reliability assessment. In this paper, low temperature near-threshold crack growth behavior was investigated on a nickel base alloy and a steel. Specifically, the effects of R-ratio ( $R = P_{min}/P_{max}$ , where  $P_{min}$  and  $P_{max}$  are the minimum and maximum applied loads, respectively) and temperature on crack propagation rate properties were emphasized.

## 2. Experimental Procedure

### 2.1 MATERIAL

Fatigue crack growth rate testing was conducted at liquid helium temperature (4.2K) and at room temperature (297K) for two materials; i.e., Inconel 706 and JBK-75 austenitic stainless steel. Inconel 706 was heat-treated at 1035K for 8 hrs, 922K for 5 hrs and then air-cooled to 297K. The stainless steel was solution-annealed at 1173K, cold-worked 15% and reaction-annealed at 973K for 30 hrs. The chemical compositions and mechanical properties of these two materials are presented in Tables 1 and 2, respectively.

In both materials, decreasing the temperature from 297 to 4.2K increases material strength and/or elongation. Note that some of crack growth rate results of JBK-75 stainless steel could be found in previous publications<sup>(3,6)</sup>.

### 2.2 CRYOSTAT AND TESTING TECHNIQUE

Liquid helium temperature fatigue crack propagation experiments were performed by using compact type (CT) specimens. The dimensions of CT specimens were 51 mm wide, 64 mm high, and 6.4 mm thick for Inconel 706, and 2.5 mm thick for JBK-75 stainless steel. The specimen was immersed in liquid helium gas which was contained in a specially designed cryostat. The cryostat was primarily made up of two layers of styrofoam chambers<sup>(8,11)</sup>. To maintain the desired temperature of 4.2K, liquid nitrogen was first filled up in the outer chamber to pre-cool the cryostat, and then liquid helium flew through the inner chamber in which the CT specimen was located. Thermocouples<sup>(12)</sup> were attached to the CT specimen in order to control the flow rate of liquid helium and to monitor test temperature. A detailed description of the chamber design for cryogenic temperature fatigue crack propagation testing can be found in Refs. 8 and 11.

Table 1  
CHEMICAL COMPOSITIONS (WEIGHT PERCENT)

Material	S	P	Mn	C	Cr	Mo	Ni	Si	Al	B	V	Co	Fe	Cu	Mg	Nb	Ti	O	N
Inconel 706	--	<0.01	0.16	0.04	15.7	0.14	41.4	0.17	0.25	0.004	--	0.08	Bal.	0.1	0.002	2.96	1.66	--	--
JBK-75 S.S.	0.001	0.008	0.02	0.014	13.91	1.24	29.33	0.08	0.29	0.0013	0.28	--	Bal.	--	--	--	2.11	0.0016	0.0019

## FATIGUE 87

Table 2  
MECHANICAL PROPERTIES

Material	Temperature (K)	0.2% Yield Strength (MPa)	Ultimate Tensile Strength (MPa)	Uniform Elongation (%)	Total Elongation (%)	Reduction in Area (%)
Inconel 706	297	959	1162	11.1	13.1	19.4
Inconel 706	4.2	1201	1529	22.1	23.7	22.9
JBK 75 S.S.	297	1031	1251	--	--	31.6
JBK 75 S.S.	4.2	1253	1585	18.4	21.4	34.3

The rates of near-threshold crack growth were developed by using an automated electrohydraulic fatigue machine which was interfaced with a PDP 11/34 computer for data acquisition and analysis. The details of this computerized crack propagation testing technique have been documented in Refs. 6 and 13. Briefly, the stress intensity range ( $\Delta K$ ) was decreased according to the following equation,

$$\Delta K = \Delta K_0 e^{c(a-a_0)} \quad (1)$$

where  $\Delta K_0$  is the initial stress intensity range,  $c$  is a negative value of  $-0.098$   $1/\text{mm}$ ,  $a$  is the crack length and  $a_0$  is the initial crack length. Note that the expression for determining  $\Delta K$  can be found in Ref. 14. A low temperature service MTS extensometer mounted on the front face of the CT specimen was used to measure crack opening displacements which were then converted into crack lengths by a compliance technique<sup>(14)</sup>. Fatigue crack growth testing was conducted at a frequency of 90 Hz and at two R-ratios of 0.1 and 0.8. Crack growth rates ( $da/dN$ ) were calculated by using a seven-point polynomial method<sup>(15)</sup>.

Room temperature fatigue crack propagation testing was conducted in laboratory air. The automated crack growth testing technique used at 4.2K was employed to develop 297K crack propagation rate properties. The specially designed cryostat was, however, not used for room temperature testing.

After fatigue crack growth experiments, fracture surfaces were carefully examined by using scanning electron microscopy (SEM).

### 3. Results and Discussion

Near-threshold fatigue crack growth rate results of Inconel 706 and JBK-75 stainless steel are presented in Figures 1 and 2, respectively. The values of threshold stress intensity ranges ( $\Delta K_{th}$ ) are shown in Table 3. The value of  $\Delta K_{th}$  is defined as the lowest  $\Delta K_{th}$  level experienced during each near-threshold crack propagation experiment.

# FATIGUE 87

Table 3  
THRESHOLD STRESS INTENSITY RANGES ( $\Delta K_{th}$ )

Material	Temperature (K)	R-Ratio	$\Delta K_{th}$ (MPa $\sqrt{m}$ )
Inconel 706	297	0.1	11.8
Inconel 706	297	0.8	6.3
Inconel 706	4.2	0.1	16.9
Inconel 706	4.2	0.8	13.9
JBK-75 S.S.	297	0.1	8.7
JBK-75 S.S.	297	0.8	5.6
JBK-75 S.S.	4.2	0.1	10.8
JBK-75 S.S.	4.2	0.8	9.6

## 3.1 R-RATIO EFFECT

In both materials at 297K, increasing the R-ratio from 0.1 to 0.8 significantly increases the rates of near-threshold crack growth (Figures 1 and 2), and thus greatly decreases  $\Delta K_{th}$  (Table 3). For example, at 297K,  $\Delta K_{th}$  at R = 0.1 is approximately two times greater than that at R = 0.8 for Inconel 706, and 1.6 times for JBK-75 stainless steel. Interestingly, at 4.2K the effect of R-ratio on crack propagation rates is much reduced, relative to that at 297K (Figures 1 and 2). Furthermore, at 4.2K the crack growth rate properties and the  $\Delta K_{th}$  values at R = 0.1 and 0.8 are nearly comparable. For instance, at 4.2K, the level of  $\Delta K_{th}$  at R = 0.1 is only 18% and 11% higher than that at R = 0.8 for Inconel 706 and JBK-75 stainless steel, respectively.

It has been reported that the influence of R-ratio on near-threshold crack growth behavior can be explained by the concept of oxide and/or roughness-induced crack closure<sup>(16-24)</sup>. In other words, the higher crack closure levels at lower R-ratios decreases the effective stress intensity range ( $\Delta K_{eff}$ ) [ $\Delta K_{eff} = K_{max} - K_{closure}$  where  $K_{max}$  and  $K_{closure}$  are the maximum and crack closure stress intensities, respectively], thereby resulting in slower crack growth rates with decreasing R-ratios. In both materials at 297K, little oxide deposit was observed on fracture surfaces at threshold levels. Moreover, the thicknesses of oxide debris at R = 0.1 were measured to be 40 and 140 Å for Inconel 706 and JBK-75 stainless steel, respectively<sup>(25)</sup>. These thin oxide deposits are not expected to introduce oxide-induced crack closure during near-threshold crack propagation<sup>(16,19,20)</sup>. Thus, roughness-induced crack closure is suggested to be the dominant crack closure mechanism which governs the effect of R-ratio on crack growth

rates for both materials. In Figures 3(a) and 4(a) at 297K, rough fracture surfaces of Inconel 706 and JBK-75 stainless steel were observed at threshold levels. In particular, large crystallographic facets were readily evident for Inconel 706. Slip lines were visible on some fracture facets [Figures 3(a) and 4(a)]. At 297K, these rough fracture surfaces at low R-ratios will introduce significant crack closure, which in turn yields a great influence of R-ratio on crack propagation rates.

The formation of oxide deposits at threshold levels has been attributed to fretting oxidation<sup>(16,19,20,26)</sup>. At the cryogenic temperature of 4.2K, oxide formation is expected to be difficult because of the lack of oxygen in liquid helium, and thus oxide-induced crack closure is minimal. In comparison with the fracture morphology at 297K [Figures 3(a) and 4(a)], fracture surfaces are much smoother at 4.2K for both materials [Figures 3(b) and 4(b)]. The smoother fracture surfaces at 4.2K than at 297K gives a decreased extent of crack closure at 4.2K, thereby resulting in a less influence of R-ratio on near-threshold crack propagation rate properties at the cryogenic temperature, as observed in Figures 1 and 2.

### 3.2 TEMPERATURE EFFECT

In both Inconel 706 and JBK-75 stainless steel at  $R = 0.1$ , the crack growth rates at 4.2K are slower than those at 297K (Figures 1 and 2). Consistently, at  $R = 0.1$ , the value of  $\Delta K_{th}$  at 4.2K is greater than that at 297K (Table 3). At  $R = 0.8$ , the same trend was observed. Moreover, the influence of temperature on crack propagation behavior at  $R = 0.8$  is much greater than that at  $R = 0.1$ . For instance, in Inconel 706, the ratio of  $\Delta K_{th}$  at 4.2K to that at 297K increases from 1.4 to 2.2 by increasing the R-ratio from 0.1 to 0.8, and the ratio changes from 1.2 to 1.7 for JBK-75 stainless steel.

It has been reported that in the higher temperature regime (above 297K), the effect of temperature on near-threshold crack growth rate properties can be rationalized by the oxide and/or roughness-induced crack closure concept.<sup>(17,27-30)</sup> If crack closure rationalized the temperature effect on crack propagation behavior, the rates of crack growth at 297 and 4.2K would be comparable at  $R = 0.8$  since crack closure was minimal at this high R-ratio. In contrast with the above trend, a significant difference in crack propagation rates at 297 and 4.2K was observed at  $R = 0.8$  (Figures 1 and 2). Thus, crack closure cannot account for the influence of temperature on near-threshold crack

growth rates. Dislocation dynamics must play a role in explaining the temperature effect<sup>(1,5,7)</sup>. It has been suggested that the improvement in near-threshold crack propagation resistance with decreasing temperature be related to a thermally activated process in light of a dislocation dynamics model<sup>(5)</sup>. In other words, in the vicinity of a crack tip, the thermally activated energy available to move the dislocations over the barriers decreases with decreasing temperature, which yields an increase in the fatigue crack growth resistance at lower temperatures. Similarly, other investigators<sup>(1,31)</sup> derived the following equation based on dislocation dynamics,

$$\Delta K_{th} \propto \sigma_s (2\pi s)^{1/2} \quad (2)$$

where  $\sigma_s$  is the stress required to activate a dislocation source located near the crack tip and at a distance  $s$  from it. They found that  $\sigma_s$  was associated with thermally activated processes, such as, dislocation cross-slip. Decreasing test temperature reduces the rates of thermally activated processes, thereby increasing  $\sigma_s$ , and thus  $\Delta K_{th}$ . Summarizing the above statements, the increase in fatigue crack growth resistance at cryogenic temperatures appears to be qualitatively explained by the concept of dislocation dynamics.

#### 4. Conclusions

Near-threshold fatigue crack growth behavior at 297 and 4.2K was investigated for Inconel 706 and JBK-75 stainless steel. At 297K, a significant influence of R-ratio on crack propagation rates was observed while at 4.2K, the R-ratio effect is minimal. Roughness-induced crack closure can be used to explain the effect of R-ratio on crack propagation behavior. The decreased R-ratio effect at 4.2K than at 297K correlates with the smoother surface roughness (or less roughness-induced crack closure) at 4.2K.

At two R-ratios of 0.1 and 0.8, the near-threshold crack growth rates at 4.2K are slower than those at 297K. Increasing the R-ratio from 0.1 to 0.8 increases the influence of temperature on crack propagation rates. Crack closure cannot account for the temperature effect on crack propagation behavior. Dislocation dynamics can be used to qualitatively explain the temperature effect.

## 5. Acknowledgments

The authors are grateful to E. J. Helm, R. R. Hovan, J. McPetridge, M. G. Peck and W. B. Pryle for conducting crack growth experiments, and A. Karanovich and D. Detar for characterizing fracture morphology. Financial support for the present research was provided by the Advanced Programs Department, Westinghouse Steam Turbine Generator Division.

## 6. References

1. J. McKittrick, P. K. Liaw, S. I. Kwun and M. E. Fine, Metall. Trans. 12A, 1535 (1981).
2. E. Tschegg and S. Stanzl, Acta Metall. 29, 33 (1981).
3. P. K. Liaw, W. A. Logsdon and M. H. Attar, Cryogenics, 23, 10 (1983).
4. D. H. Park and M. E. Fine, TMS-AIME Symposium on Fatigue Crack Growth Threshold Concepts, D. L. Davidson and S. Suresh, eds., p. 145 (1983).
5. W. Yu, K. Esaklul and W. W. Gerberich, Metall. Trans. 15A, 889 (1984).
6. P. K. Liaw, W. A. Logsdon and M. H. Attar, ASTM STP 857, R. I. Stephens, eds., p. 173-190 (1985).
7. P. K. Liaw and W. A. Logsdon, Engrg. Fract. Mech., 22, 585 (1985).
8. H. J. Choi and L. E. Schwartz, Metall. Trans. 14A, 1089 (1983).
9. J. C. White and W. R. McCown, Power Engrg., October, 72 (1981).
10. "Superconducting Magnet Coils for the Large Coil Program," Phase 2 Final Report to Union Carbide Corp., Oak Ridge, TN, by Westinghouse Electric Corp., Pittsburgh, PA, Contract 22X-31747C, March, 1980.
11. E. T. Wessel, Refrigeration Engineering, 65, 37 (1957).
12. T. M. Dauphine, D. K. C. MacDonald, and W. B. Pearson, J. of Scientific Instruments 30, 399 (1953).
13. R. S. Williams, P. K. Liaw, M. G. Peck and T. R. Leax, Engrg. Fract. Mech., 18, 953 (1983).
14. A. Saxena and S. J. Hudak, Jr., Intl. J. of Fract., 14, 453 (1978).
15. W. G. Clark, Jr. and S. J. Hudak, Jr., J. Test Eval., 3, 454 (1975).

# FATIGUE 87

16. S. Suresh, G. F. Zamiski and B. O. Ritchie, *Metall. Trans.* 12A, 1435 (1981).
17. P. K. Liaw, *Acta Metall.*, 8, 1489 (1985).
18. P. K. Liaw, T. R. Leax and W. A. Logsdon, *Acta Metall.* 31, 1581 (1983).
19. P. K. Liaw, T. R. Leax, R. S. Williams and M. G. Peck, *Metall. Trans.*, 13A, 1607 (1982).
20. P. K. Liaw, T. R. Leax, R. S. Williams and M. G. Peck, *Acta Metall.* 30, 2071 (1982).
21. K. Minakawa and A. J. McEvily, *Scripta Metall.* 15, 633 (1981).
22. N. Walker and C. J. Beevers, *Fat. Engrg. Mater. Struct.* 1, 135 (1979).
23. K. Endo, K. Komai and Y. Matsuda, *Mem. Frac. Engrg.*, 31, Kyoto University, 25 (1969).
24. A. T. Stewart, *Engrg. Fract. Mech.*, 13, 463 (1980).
25. P. K. Liaw and W. A. Logsdon, unpublished research, Westinghouse R&D Center, Pittsburgh, PA (1986).
26. D. Benoit, R. Nandar-Irani and B. Tixier, *Mater. Sci. Engrg.*, 45, 1 (1980).
27. P. K. Liaw, TMS-AIME Symposium on Synergism of Microstructure, Mechanisms and Mechanics in Fatigue, J. M. Wells and J. D. Landes, eds., p. 479 (1984).
28. P. K. Liaw, A. Saxena, V. P. Swaminathan and T. T. Shih, *Metall. Trans.*, 14A, 1631 (1983).
29. P. K. Liaw, A. Saxena, V. P. Swaminathan and T. T. Shih, *Proc. TMS-AIME Symposium on Concepts of Fatigue Crack Growth Threshold*, D. L. Davidson and S. Suresh, eds., p. 205 (1983).
30. J. L. Yuen, P. Roy and W. D. Nix, *Metall. Trans.* 15A, 1769 (1984).
31. M. E. Fine, *Bull. J. I. M.* 20, 668 (1981).

# FATIGUE 87

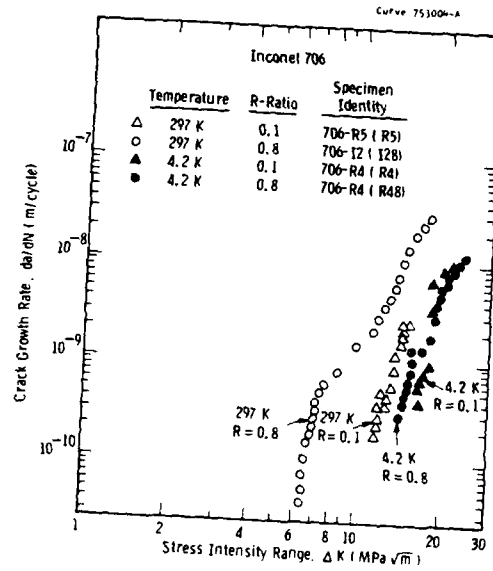


Fig. 1 - Fatigue crack growth rates of Inconel 706 at 297 and 4.2 K

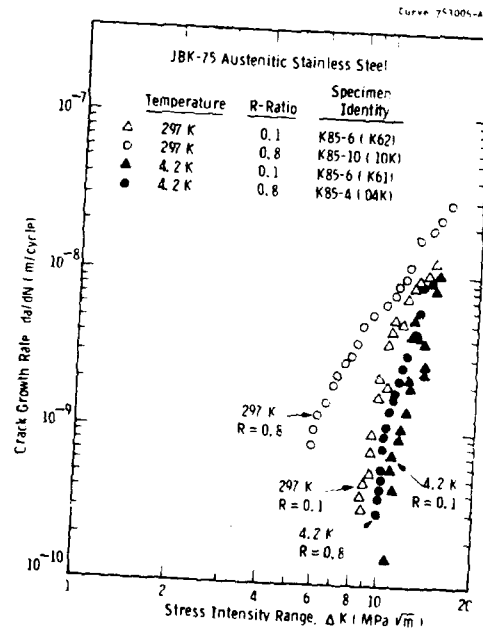


Fig. 2 - Fatigue crack growth rates of JBK-75 stainless steel at 297 and 4.2 K

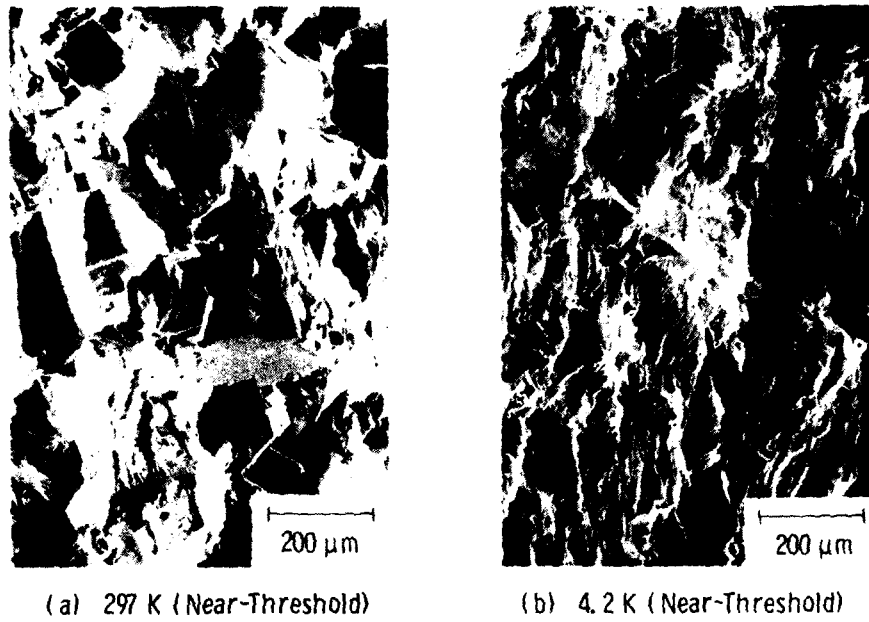


Fig. 3—Fracture morphology of Inconel 706 at 297 and 4.2 K ( $R=0.1$ )

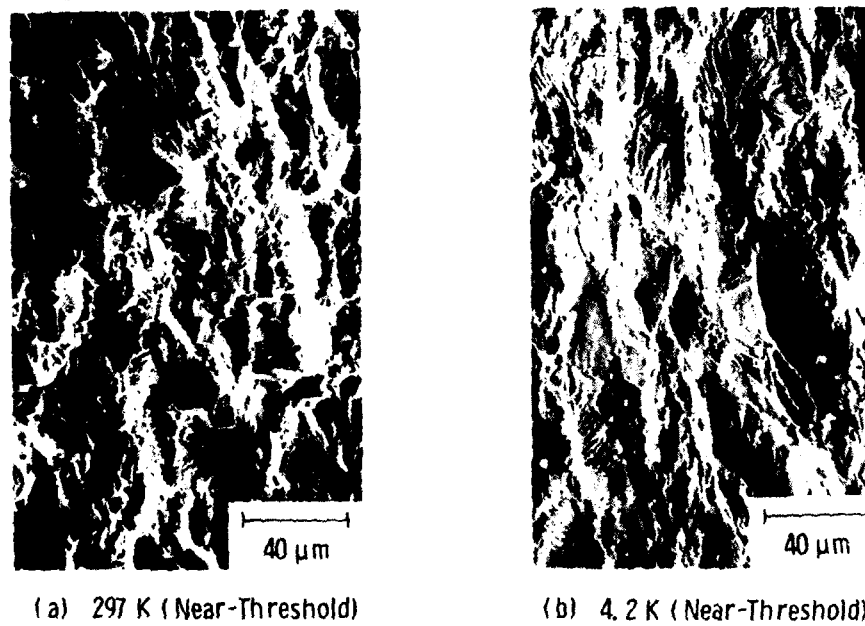


Fig. 4—Fracture morphology of JBK-75 stainless steel at 297 and 4.2 K ( $R=0.1$ )

FATIGUE 87

FATIGUE 87

THE EFFECT OF NON-METALLIC INCLUSIONS ON FATIGUE  
AND FATIGUE THRESHOLDS OF 25Mn-5Cr-1Ni STEEL

I. Maekawa\*, J.H. Lee\* and S. Nishida\*\*

Fatigue, tensile and Charpy experiments were performed using four series of high manganese steels which were specially prepared by changing the inclusion contents. Fatigue lives of these steels were found to increase at low temperatures and by increase of inclusion content. A staircase pattern was observed around an inclusion on a fracture surface and such a rugged surface seems to act as an arrester for crack propagation. Threshold stress intensity factor, crack growth rate, elastic-plastic fracture toughness and Charpy value were reduced by an increase of sulphide inclusion content.

INTRODUCTION

Many studies have been made concerning fatigue of steel, and it is well known that a fatigue life consists of crack initiation and propagation processes. For the onset of a crack growth, the mechanical condition is expressed by using the threshold stress intensity factor,  $\Delta K_{th}$ . In many cases, fatigue fractures were originated at a non-metallic inclusion. Then, the influence of inclusion on threshold stress intensity factor have also been studied (1), (2). But, their results were somewhat different with each other. And the influence of inclusion on the strength of high manganese steel has not ever been studied well.

Therefore, this paper intend to make clear the influence of inclusion on  $\Delta K_{th}$  and crack propagation behavior. Beside of this, the fracture toughness and Charpy absorbed energy were also evaluated for the sake of comparison with fatigue behaviors.

\* Department of Mechanical Engineering II, Tohoku University, Sendai, Japan.

\*\* Nippon Steel Corporation, Central R & D Bureau, Yawata R & D Laboratory, Kita-Kyushu, Japan.

MATERIALS AND EXPERIMENTAL PROCEDURESPreparations of material and specimen

The materials used were four series of 25Mn-5Cr-1Ni austenitic steel. The series A was the base steel. The series B, C and D were specially prepared by changing the sulphur and aluminum contents to see the influence of inclusion, which were MnS, FeS and  $Al_2O_3$ , on the fatigue behavior. Their chemical compositions are listed in Table 1.

They were hot rolled with a rolling ratio 4.5. And solution treatment, which consisted of heating at 1323K for 60 min and subsequent quenching in water, was carried out. The mechanical properties of this base steel are shown in Table 2. The number of non-metallic inclusion distributed in each steel were measured on the surface area of 14.2 mm<sup>2</sup> in conformity with the Japanese Industrial Standard (JIS G0555), and the numbers of inclusion per 1 mm<sup>2</sup>,  $N_A$ , are shown in Fig. 1 for all series.

Compact tension (CT) specimens with the thickness of 12.5 mm, and Charpy V-notched specimens were prepared in L-T direction with regard to the rolling direction, respectively.

TABLE 1 - Chemical Composition (Weight percent)

Series	C	Si	Mn	P	S	Cr	Ni	Al	Nb	N
A	0.22	0.86	25.6	0.024	0.001	4.67	0.97	0.009	0.043	0.04
B	0.18	0.15	24.0	0.02	0.008	4.50	1.0	0.017	0.04	0.02
	0.22	0.25	25.0	0.03	0.012	5.50	1.2	0.023	0.06	0.06
C	0.18	0.15	24.0	0.02	0.025	4.50	1.0	0.017	0.04	0.02
	0.22	0.25	25.0	0.03	0.035	5.50	1.2	0.023	0.06	0.06
D	0.18	0.15	24.0	0.02	0.008	4.50	1.0	—	0.04	0.02
	0.22	0.25	25.0	0.03	0.012	5.50	1.2	—	0.06	0.06

TABLE 2 - Mechanical Properties of Series A (Base steel)

Testing temp. (K)	$\sigma_y$ (MPa)	$\sigma_u$ (MPa)	Elongation $\psi$ (%) G.L.=35mm	$vE$ (J) L-T
288	270.7	710.5	63	235
77	571.5	1043.7	40	150

### Experimental procedure

Fatigue experiments were performed at 288, 198 and 113K under a repetition of triangular loading wave with the frequency of 10 Hz by using a servohydraulic testing machine in the similar way as the previous paper (3). The maximum load was 4.9KN and the load ratio was 0.1.

The threshold stress intensity factor was evaluated in terms of the  $\Delta K$  decreasing method (4), where  $\Delta K$  value was calculated by using the following formula (5).

$$\Delta K = \frac{\Delta P}{B\sqrt{W}} \frac{(2 + \alpha)}{(1 - \alpha)^{3/2}} \times (0.886 + 4.64\alpha - 13.32\alpha^2 + 14.72\alpha^3 - 5.60\alpha^4) \quad (1)$$

where  $\Delta P$  is the load range applied,  $\alpha = a/W$ ,  $a$  is the crack length and  $B$  is the specimen thickness.

Elastic-plastic fracture toughnesses were evaluated by using CT specimens at 288, 198 and 113K in terms of ultrasonic method (6). Charpy tests were performed at 77K.

### EXPERIMENTAL RESULTS AND DISCUSSION

#### Fatigue life

Figure 3 shows the crack growth behaviors. In this figure, fatigue life to fracture,  $N_F$ , increases with decreasing temperature for all series of steel used in this study and the fatigue life of the base steel is rather shorter than that of other series. These results are contrary to the usual temperature dependence of steel and to the expectation from the mechanical point of view by considering the stress concentration effect due to an inclusion.

According to Fig. 1, series C steel contains the greatest number of sulphide inclusion. It is about twenty times of series A. On the other hand, oxide inclusion content is comparable with each other for all series. Then it is considered that the effect of sulphide inclusion will appear predominantly. The relation between  $N_F$  and  $N_s$  is shown in Fig. 4. In this figure, it can be seen that fatigue life increases with increasing inclusion content at 288 and similarly at 113K.

In order to make clear the reason for the increase in fatigue life described above, fracture surfaces were observed by a SEM. A typical example is shown in Fig. 5. In this photograph, a clearance between an inclusion and the matrix steel and the staircase pattern

## FATIGUE 87

on the matrix around the inclusion can be seen, and the striation on the right hand side seems to be propagated to the staircase pattern. Another striation on the left hand side seems to be propagated to the staircase pattern on the another fracture surface.

Although any particular change in striation can not be seen in this photograph, the fracture surface is rugged near an inclusion. This rugged surface is correspond to the zigzag fracture on a side view of specimen as shown in Fig. 6. It is supposed that a crack needs much more surface energy to make such a rough surface compared with the case of flat fracture surface. Therefore, such a rugged crack propagation is supposed to cause the slow down in crack growth rate.

### Threshold stress intensity factor and crack growth rate

The relations between crack growth rate,  $da/dN$ , and stress intensity range,  $\Delta K$ , are shown in Figs. 7(a)-(d) for series A and C. From Figs. 7(a) and (c),  $\Delta K_{th}$  values can be obtained and shown in Fig. 8, and it can be seen that  $\Delta K_{th}$  value of series C is smaller than that of series A at 288 and 198K.

However, the  $da/dN$ - $\Delta K$  relations of series A and C are crossed each other and the growth rate of the series C is reduced compared with that of series A above the growth rate of  $10^{-8}$  mm/cycle in both Figs. 7(a) and (c). Thus, the increase of inclusion content reduces not only the  $\Delta K_{th}$  value but also  $da/dN$  value in the case of the L-T specimen in this study. That is, an inclusion exerts worse effect on the onset of fatigue crack growth but rather acts as an arrester for crack propagation. The growth rates of series A and C are reversed again at the later stage of fatigue life as shown in Figs. 7(b) and (d). Nevertheless, the fatigue lives of series C are more longer than those of series A as shown in Fig. 4. The similar results are obtained for series B and D, but they are not shown here owing to limited space. By applying the Paris expression

$$da/dN = A (\Delta K)^m \quad (2)$$

to those experimental results,  $m$  values are obtained as shown in Fig. 6. Since an inclusion is supposed to form microcracks around it due to the stress concentration effect under a repetition of loading, it is considered that an inclusion will promote the crack propagation. Therefore, the reduction in growth rate due to the increase of inclusion content seems to be contrary to the usual results. But, specimens are prepared to be in the L-T direction in this study and the stress concentration effect of an inclusion is not so considerable compared with the S-L or the S-T specimens(7). In addition to this, it is supposed that a crack needs many more repetition of loading to pass through an inclusion, because it makes a staircase pattern around an inclusion as shown in Fig. 5. This pattern is apt to appear in the case of the L-T specimen, and this

## FATIGUE 87

will be the reason of reduction in crack growth rate. This reduction may be explained simply by considering that a rough fracture surface probably needs much more surface energy to make it.

In Fig. 8,  $\Delta K_{th}$  values at 198K are more larger than that at 288K, and the reduction in  $\Delta K_{th}$  value due to the increase of inclusion content is reduced at 198K. The  $m$  values at 198K are smaller than at 238K.

### Elastic-plastic fracture toughness

This steel is very ductile even at low temperature, and so an elastic-plastic fracture toughness,  $J_{Ic}$ , is used to infer the mechanical condition for the crack growth under a monotonic loading, which corresponds to a very slow repetition of large stress amplitude in the case of fatigue. Then, it is expected to be able to see the effect of repetition of loading on crack growth by comparing  $J_{Ic}$  and  $\Delta K_{th}$ . Although the thickness of CT specimen is less than the half width,  $W/2$ , the  $J$  values evaluated satisfied the  $J_{Ic}$  condition in the case of the base steel, where  $W$  is the width of CT specimen (8). The  $J_{Ic}$  values are shown in Fig. 9. It reduces clearly with increasing inclusion content at first and gradually later. The reduction is more clear than the reduction in  $\Delta K_{th}$  value shown in Fig. 8. However,  $J_{Ic}$  value is obtained under a high stress state, and the crack growth rate of series C is again increased at the later stage in which stress should be increased even in the case of the fatigue as shown in Fig. 7(b) and (d). Therefore, the reduction in crack growth rate due to the increase of inclusion content is considered to appear under the repetition of comparatively lower loading in the case of the L-T specimen.

### Charpy value

The results of Charpy test are also shown in Fig. 9. And it can be seen that Charpy value,  $VE$ , reduces considerably with increasing inclusion content.

## CONCLUSIONS

The results of this study are summarized as follows. By increase of sulphide inclusion content in 25Mn-5Cr-1Ni austenitic steel, the threshold stress intensity factor, crack growth rate, elastic-plastic fracture toughness and the Charpy value are reduced. The worst effect of inclusion can be seen on Charpy value and considerable effect is seen on elastic-plastic fracture toughness.

At low temperatures, fatigue lives were increased for all series. The rugged crack propagation observed on a fracture surface is considered to reduce the crack growth rate under a repetition of comparatively lower amplitude of loading.

ACKNOWLEDGEMENTS

This work has been supported partially by the Grant-in-Aid for the Scientific Research from the Ministry of Education. The authors wish to express their hearty thanks to senior researcher Ken-ichiro Suemune, Nippon Steel Corporation, for supplying materials and for kind support.

SYMBOLS USED

- $vE$  = Charpy absorbed energy (J)  
 $J_{IC}$  = The value of J at the onset of initial crack growth (KJ/m<sup>2</sup>)  
 $N_A$  = Number of inclusion per unit area (number/mm<sup>2</sup>)  
 $N_s$  = Number of sulphide inclusion per unit area (number/mm<sup>2</sup>)

REFERENCES

- (1) Fowler, G.J., Mat.Sci.Engng, Vol.39, 1979, pp.121-126.
- (2) Mayes, I.C., and Baker, T.J., Fatigue Engng Mater.Struct., Vol.4, No.1, 1981, pp.79-86.
- (3) Yokobori, T., Maekawa, I., Tanabe, Y., Jin, Z., and Nishida, S., ASTM STP 857, 1985, pp.121-139.
- (4) ASTM Standard Designation, E647-78T, 1981.
- (5) Srawly, J.E., Int.J. of Fracture, Vol.12, 1976, pp.457-476.
- (6) Maekawa, I., Lee, J.H., Nishida, S., and Tanabe, Y., "Evaluation of  $J_{IC}$  of 25Mn-5Cr-1Ni austenitic steel at low temperatures", Proceeding of the conference on "Asian-pacific congress on strength evaluation", pp.513-518, Seoul, Korea, 1986.
- (7) Maekawa, I., Nishida, S., Tanabe, Y., and Lee, J.H., to be published.
- (8) ASTM Standard Designation, E813-81, 1981.

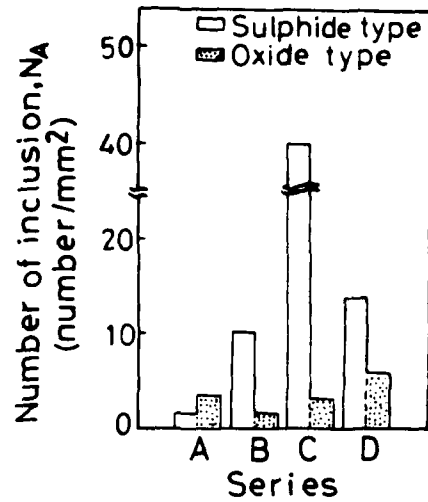


Figure 1 Number of inclusions per 1 mm²

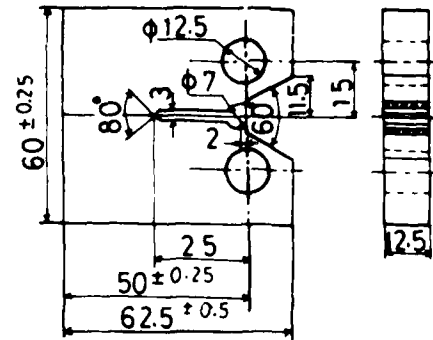


Figure 2 Dimension of CT specimen

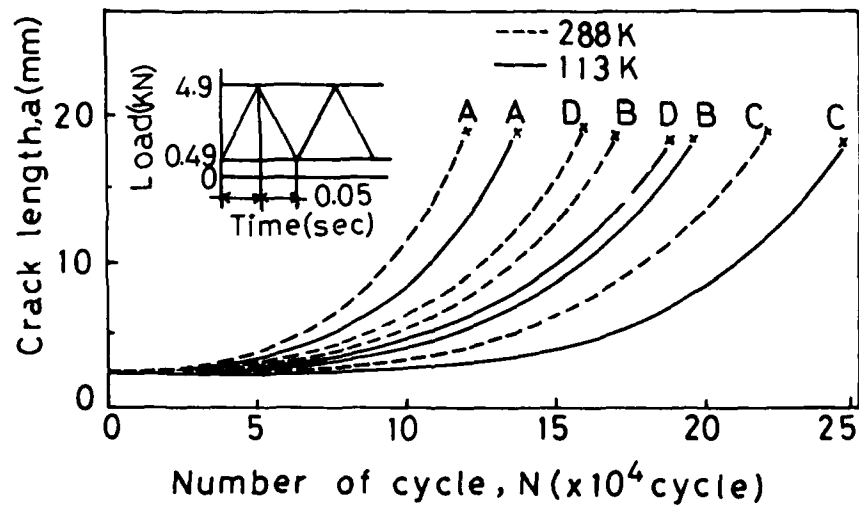


Figure 3 Fatigue crack growth behavior

# FATIGUE 87

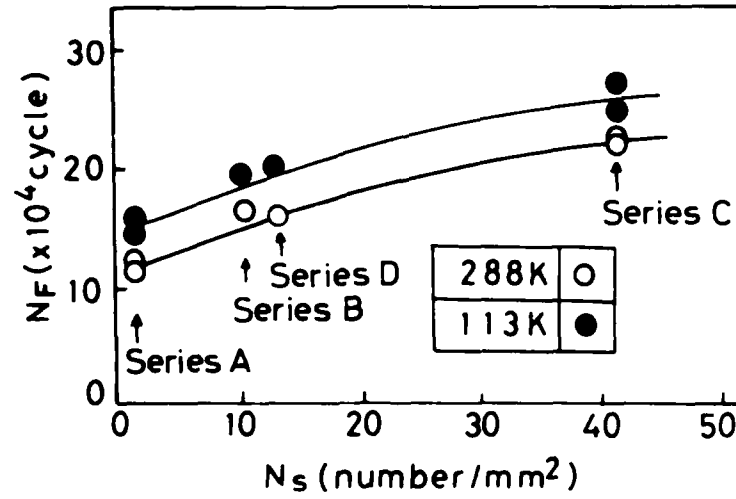


Figure 4 Effect of sulphide inclusion on fatigue lives

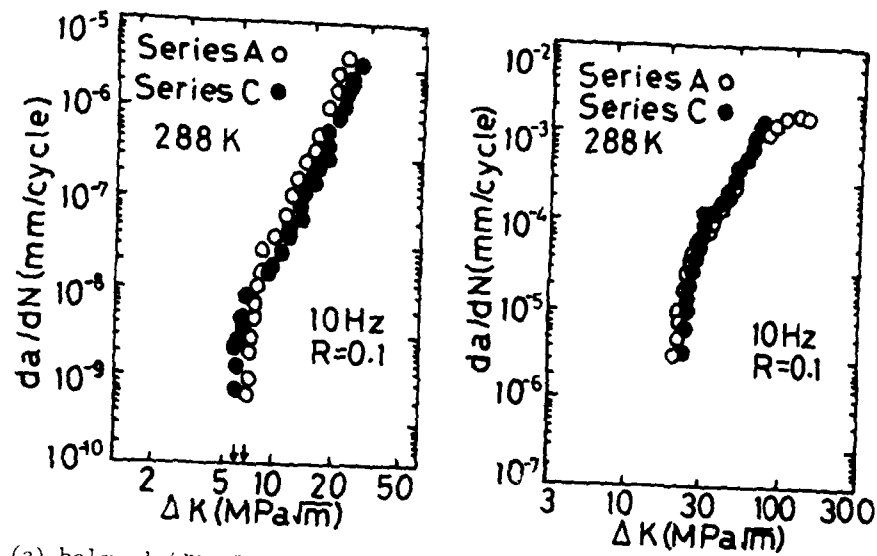


Figure 5 SEM fractograph near a sulphide inclusion



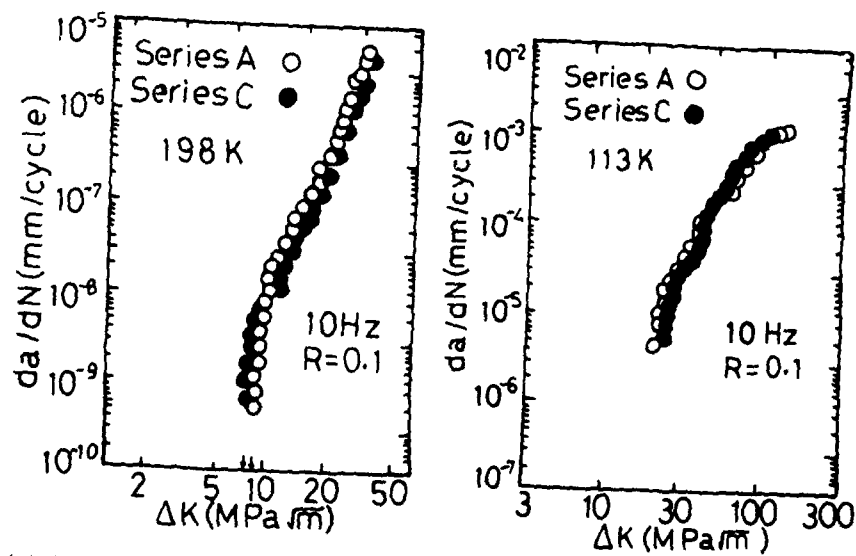
Figure 6 Side view of a fracture surface

FATIGUE 87



(a) below  $da/dN$  of  $5.5 \times 10^{-6}$  mm/cycle

(b) Above  $da/dN$  of  $5.5 \times 10^{-6}$  mm/cycle



(c) below  $da/dN$  of  $5.5 \times 10^{-6}$  mm/cycle

(d) Above  $da/dN$  of  $5.5 \times 10^{-6}$  mm/cycle

Figure 7 Crack growth rate vs. threshold stress intensity factor

# FATIGUE 87

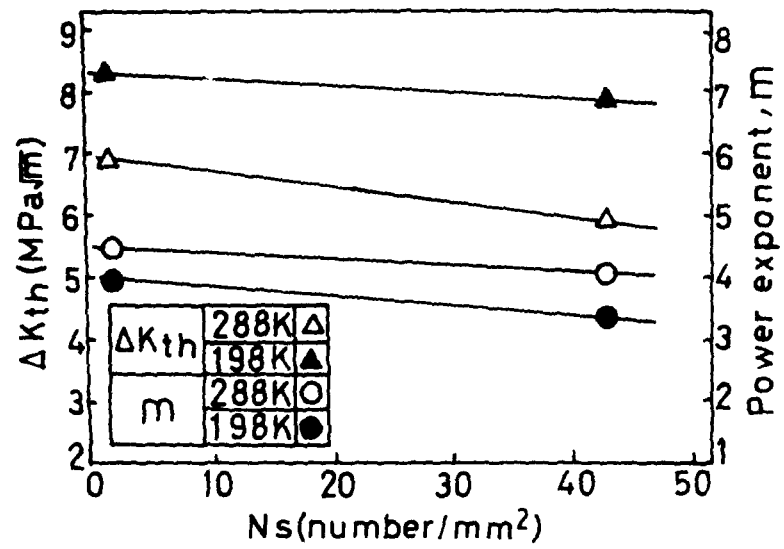


Figure 8 Effect of sulphide inclusion on threshold stress intensity factor and crack growth rate

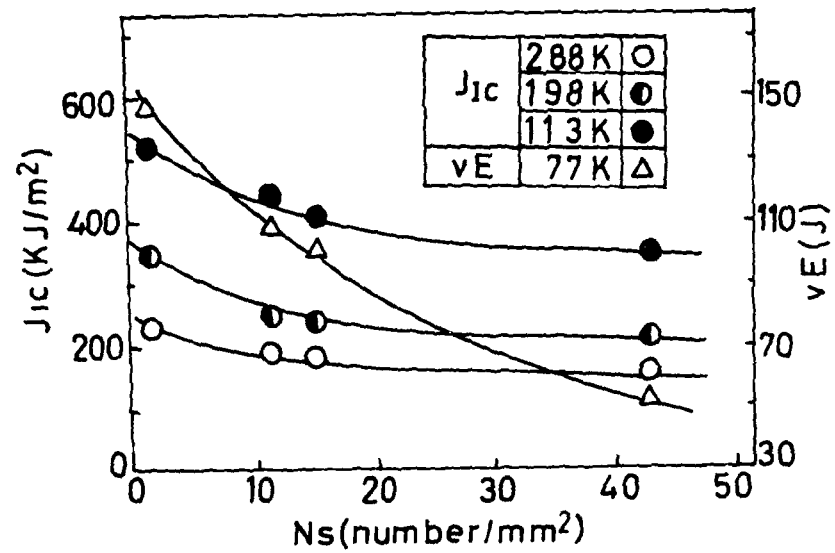


Figure 9 Effect of sulphide inclusion on elastic-plastic fracture toughness and Charpy value

## FATIGUE 87

### ROLE OF INTERSTITIALS AND PRECIPITATES IN INITIATION AND PROPAGATION OF L.C.F. CRACKS IN AUSTENITIC STAINLESS STEELS.

S. DEGALLAIX, J. FOCT\*

LCF tests were carried out at 20°C on two steels (316L and 316LN respectively) either water-quenched or previously aged at 600°C. Measurements of the striation spacing on the rupture surfaces lead to measurement of the crack growth rate  $da/dN$  as a function of crack depth "a". The influence of the nitrogen content and of the precipitation (either inter- or intragranular) due to previous aging is analysed concerning the various crack growth stages observed.

Previous studies have shown that the presence of interstitial nitrogen in austenitic stainless steels improves their low-cycle fatigue (LCF) resistance at room temperature (1,2,3) and at 600°C (4,5). The gain in fatigue life due to nitrogen is attributed to better reversibility of plastic deformation. In fact, nitrogen favours planar dislocation sliding (3,4,5), most probably by a decrease in stacking fault energy (6,7). Moreover we have demonstrated that previous aging at 600°C reduces the fatigue life of 316L steels in LCF at room temperature (8). This loss of strength is attributed to intergranular embrittlement(9). However the increase in fatigue life due to nitrogen presence is maintained(8).

In previous studies, the fatigue life was considered at the final fracture of the specimen, and composed both the initiation phase and propagation phase of a main crack.

By measuring the striations on the fracture surfaces of the LCF specimens, the rate at which cracks grow can be evaluated depending on their depth. By using this method, we propose a study of the influence of interstitial nitrogen and previous aging on, respectively, the initiation and propagation phases of 316L type steels in LCF at room temperature.

\* Laboratoire de Métallurgie Physique - Université de Lille  
I - Bâtiment C.6 - 59655 Villeneuve d'Ascq Cedex - France.

## FATIGUE 87

### Materials and Experimental Procedures

The compositions and grain sizes of the two steels used are defined in Table 1. These steels, referred to as I and II respectively, differ essentially in their nitrogen contents (0.08 and 0.25 wt % respectively).

The alloys were supplied in the form of 25 mm square sectioned bars. These bars were hot rolled and subsequently solution treated for 1 hour at 1100°C and then water quenched. Before machining, some specimens of each steel were aged in air at 600°C for 2000 hours and 10 000 hours. The three heat treatments will be called UA (unaged, i.e. water quenched), A (aged i.e. 2000 hrs aged) and LA (long aged, i.e. 10 000 hrs aged). The low-cycle fatigue samples are cylindrical and button-headed and have a 10 mm. minimum diameter and a 10 mm. gage length (8). Fully reversed low-cycle fatigue tests were performed in an axial push-pull mode using a MTS servohydraulic testing machine. The total axial strain was controlled by a strain gauge extensometer. The applied total strain ranges  $\Delta\epsilon_t$  were  $6 \cdot 10^{-3}$ ;  $10^{-2}$ ;  $1.6 \cdot 10^{-2}$ ;  $2.5 \cdot 10^{-2}$ . For each strain level, two fatigue tests were conducted to failure applying a triangular wave form signal at a nominal strain rate  $\dot{\epsilon}_t = 4 \cdot 10^{-3} \text{ s}^{-1}$ .

Some fracture surfaces were examined by a scanning electron microscope (SEM). Whatever the initial heat treatment, the area broken in fatigue shows, despite some intergranular areas (7) in the aged states, intragranular striations continuously distributed over the surface. The area broken in monotonic strain in the final quarter of the cycle develops from a ductile transgranular mode (UA steels I and II) to a mixed trans-intergranular mode (LA steel I) or to an intergranular mode (LA steel II) when aging time increases from 0 to  $10^4$  hours (9).

It has been recognized that, on the fatigue fracture surface, each well-defined striation corresponds to each strain cycle (10); then the striation spacing  $i$  coincides with the macroscopic crack growth rate  $da/dN$ . Striation spacing, as a function of their depth "a" with respect to initiation is measured on the fracture surfaces of specimens broken in fatigue at  $\Delta\epsilon_t = 1 \%$  and  $\Delta\epsilon_t = 2.5 \%$ , for each steel and each heat treatment studied.

TABLE 1 - Chemical composition (weight %) and grain sizes of studied steels

	C	Cr	Ni	Mo	Mn	N	d (μm)
Steel I	0.026	17.10	11.54	2.19	1.54	0.080	135
Steel II	0.024	17.01	12.98	2.62	1.59	0.250	100

## FATIGUE 87

### Experimental Results

LCF resistance. Table 2 provides the results of the LCF tests, in terms of the total, elastic and plastic strain ranges (noted on the hysteresis cycle, corresponding to 20 % of the fatigue life) and of the fatigue life  $N_R$  (defined at final rupture of the specimen).

Fatigue crack propagation. The tests which have previously been subjected to an analysis of crack surface by SEM have an asterisk in Table 2.

The results of crack growth rate  $da/dN$  as a function of crack depth "a" are shown in bilogarithmic diagrams in figures 1 and 2 for steels I and II respectively. The validity of the experimental results are confirmed by measurements on three pairs of specimens, which had undergone the same heat treatment and fatigue strain. These curves may be schematically represented by straight lines, (figure 1, I-A steel,  $\Delta\epsilon_t = 1\%$ ). The first stage, during which the crack growth rate is constant and equal to  $(da/dN)_0$ , is not always detected, owing to a certain matting effect. This stage has similarly been observed by C. Levailant (11) on a 316 L steel at 600°C (a steel very like steel I). During the second stage, the crack growth law can be applied  $da/dN = Da^\alpha$  (D and  $\alpha$  being constants) and during the third stage - when it exists - the law  $da/dN = D_1 a^{\alpha_1}$  can be applied (where  $D_1$  and  $\alpha_1$  are further constants). The constants D,  $\alpha$ ,  $D_1$  and  $\alpha_1$  - obtained by linear regression (least-squares method) - are defined in Table 3 and the resulting curves are given in figure 3.

The results of figure 3 indicate that, overall, the crack growth rates of the two steels do not differ fundamentally.

At  $\Delta\epsilon_t \approx 2.5\%$ , the propagation rates in steel II are always lower than those in steel I until a crack depth in the order of 2 mm. is obtained. Beyond this, the crack rates in steel II-UA are only slightly lower than those of steel I in all three states, but those of steel II-A are noticeably lower, as are the slopes of the lines obtained.

At  $\Delta\epsilon_t = 1\%$ , initial propagation rates are the same for both steels. Steel II-UA next shows higher rates, at least as far as a crack depth about 2 mm. Beyond this depth, steel I shows higher crack rates than steel II. The slopes of the lines are, in particular, higher than in steel I in the UA and in the LA steel II, but remain approximately the same in steels I-A and II-A.

### Discussion

Firstly our results show that the crack growth rates increase by an order of magnitude when the strain level  $\Delta\epsilon_t$  goes from 1 % to 2.5 %. Under the same conditions the slopes of lines tend to be reduced (from about 1.5 at  $\Delta\epsilon_t = 1\%$  to about 1 at  $\Delta\epsilon_t = 2.5\%$  for steel I). By using a mean exponent  $\alpha \approx 1.2$  for

## FATIGUE 87

steel I,  $\bar{\alpha} = 1$  for steel II, the crack laws can be expressed in the form :

$$\frac{da}{dN} = 0.82 (\Delta\epsilon_t)^{2.6} a^{1.2} \quad \text{for steel I}$$

and

$$\frac{da}{dN} = 1.10 (\Delta\epsilon_t)^{1.85} a^1 \quad \text{for steel II}$$

Yamaguchi's results (12) obtained at 20°C for a 316 steel cycled at  $\Delta\epsilon_t = 2\%$  and  $\dot{\epsilon}_t = 4 \cdot 10^{-3} \text{ s}^{-1}$  fit in very well with our results concerning steel I.

Figures 3a and 3b can be interpreted by reference to metallurgical factors likely to influence the various stages of crack propagation. These factors are summarized on figure 4 (13) by means of a diagram  $\log da/dN - \log \Delta K$ .

In these diagrams, the first linear portion of non-null slope corresponds to stage B of the cracking process, while the second linear area of non-null slope, when it exists, must be associated with the beginning of stage C. The initial linear portion of the null-slope can be associated with the so-called "short crack" propagation range.

In our steels, the following metallurgical factors can influence the various stages of propagation.

- the intragranular precipitation state, which should basically influence stages A and C, but possibly also stage B.
- the intergranular precipitation state, which should influence stage C
- the dislocation slip characteristics, which should basically influence stages A and B.

For steel I the experimental results seem to confirm that the precipitation state, - either intra - or intergranular, has little influence on crack propagation : below a crack depth of 2mm., the crack growth rates obtained in this steel are the same for the three heat treatments. On the other hand, for a crack depth greater than 2-3 mm., it is noted that, at  $\Delta\epsilon_t = 1\%$ , the rates are accelerated by the aging treatment, the more so as aging time is increased. It can be assumed that this acceleration represents an initiation of phase C - the rapid crack growth phase - in which the role of intergranular embrittlement is noticeable. This acceleration of the cracking process is not seen at  $\Delta\epsilon_t = 2.5\%$ , the striations being no longer visible beyond 2-3 mm.

Our results indicate that the relatively plane character of the strain has apparently little influence on stage B of the propagation, since the crack growth rates in steels I and II water quenched and fatigued at  $\Delta\epsilon_t = 2.5\%$  are virtually identical. In fact it is at this strain level that the nature of the slip differs the most between the two steels : the cross-slip - considerable in steel I - leads to a well-formed cellular structure, whilst the slip in steel II remains very plane (4).

## FATIGUE 87

On the other hand, at  $\Delta\epsilon_t = 1\%$ , the slip in steel I retains a largely plane character, thus hardly different from that observed in steel II. Other studies (13, 14, 15, 16) have however shown that a planar slip, caused for example by a decrease in the stacking fault energy, slows down the transgranular propagation of fatigue cracks.

The crack growth rates obtained for steel II at  $\Delta\epsilon_t = 2.5\%$  can be explained in the following way : the intragranular precipitation obtained after aging at  $600^\circ\text{C}$  leads during stage B, to a lower acceleration rate of the cracks than in the water quenched state; on the other hand it seems to have little effect on phase A, but intergranular precipitation has the opposite effect from stage A onwards. The crack growth rates increase by a constant factor of 1.5 between states A and LA. However it should be emphasized that the slowing down effect produced by the intragranular precipitation cannot be detected from the stage of the striations. It must therefore be interpreted as an effect on the dislocation slip mode and the sub-structures built at the bottom of the crack.

The crack rates obtained in steel II at  $\Delta\epsilon_t = 1\%$  are more difficult to explain. It appears that, contrary to the phenomenon observed at  $\Delta\epsilon_t = 2.5\%$ , the fatigue crack grows more rapidly in the water quenched state than in the aged states, at least when the crack depth is less than 2 mm. However the acceleration of the crack is less in the water quenched state. These curious and inexplicable results have nevertheless been confirmed by repeating tests and measurements.

Concerning crack initiation, our microscope observations enable no conclusions to be reached on the possible effect of nitrogen.

### Conclusion

An analysis of the propagation phase of fatigue cracks was carried out on the fracture surfaces of axisymmetric specimens in low-cycle fatigue. The study proved to be delicate in the initiation phase, but enabled the following essential points to be brought out :

- i) there is non fundamental difference between the crack growth rates for the two steels
- ii) previous aging at  $600^\circ\text{C}$  has little influence on the crack growth rates in steel I; it only accelerates the crack propagation at the end of phase B
- iii) the same aging at  $600^\circ\text{C}$  has a noticeable complex effect on propagation rates in steel II.

Based on the low-cycle fatigue tests the former analysis leads to a statement of the main tendencies concerning the effect of nitrogen and of aging; though this needs to be made clearer by crack growth measurements on notched specimens.

## FATIGUE 87

### References

- (1) Degallaix, S., Vogt, J.B., Foct, J., Mém. Et. Sci. Rev. Metall., Vol. 80, n° 12, 1983, pp. 619-633.
- (2) Vogt, J.B., Degallaix, S., Foct, J., Int. J. Fatigue, Vol. 6, N° 4, 1984, pp. 211-215.
- (3) Degallaix, S., Taillard, R., Foct, J., Conf. Proc. "Fatigue 84", Birmingham, sept. 84, pp. 49-59.
- (4) Nilsson, J.O., Fat. Eng. Mat. Str., Vol. 7, n° 1, 1984, pp. 55-64.
- (5) Namura, N., Kishimoto, Y., Shibata, K., Fujita, T., 102nd ISIJ Meeting, Nov. 1981, lecture n°S1274.
- (6) Schramm, R.E., Reed, R.P., Metall. Trans., Vol. 6A, 1975, pp. 1345-1351.
- (7) Stoltz, R.E., Vander Sande, J.B., Metall. Trans., Vol. 11A, 1980, pp. 1033-1037.
- (8) Taillard, R., Degallaix, S., Foct, J., Journ. Int. Print. SFM "Fatigue at high temperature", June 1986, pp.53-63.
- (9) Degallaix, S., Degallaix, G., Foct, J., ASTM STP 942, 1987.
- (10) Laird, C., Smith, G.C., Phil. Mag., Vol. 7, 1962, pp. 847-857.
- (11) Levaillant, C., Thèse de Doctorat d'Etat, June 1984, Paris.
- (12) Yamaguchi, K., Kanazawa, K., Metall. Trans., Vol. 10A, 1979, pp. 1445-1451.
- (13) Masounave, J., Bailon, J.P., Dickson, J.I., "La Fatigue des Matériaux et des Structures", C. Bathias, J.P. Bailon, 1980, pp. 210-236.
- (14) Mc Evily, A.J., Boettner, Jr. and R.C., Acta Metall., Vol. 11, Juli 1963, pp. 725-743.
- (15) Bathias, C., Pelloux, R.M., Metall. Trans., Vol. 4, May 1973, pp. 1265-1273.
- (16) Saxena, A., Antolovitch, S.D., Metall. Trans., Vol. 6A, sept. 1975, pp. 1809-1828.
- (17) Awatani, J., Katagiri, K., Koyanagi, K., Metall. Trans., Vol. 10A, April 1979, pp. 503-507.

# FATIGUE 87

TABLE 2 - LCF test results

Heat treatment	Steel I			Steel II		
	$\Delta\epsilon_t$ (%)	$\Delta\epsilon_p$ (%)	$N_R$	$\Delta\epsilon_t$ (%)	$\Delta\epsilon_p$ (%)	$N_R$
UA	2.440	1.940	540	2.440	1.880	1973
	2.460	1.960	899*	2.440	1.900	1097*
	0.980	0.712	8623	0.982	0.640	9970*
	0.986	0.708	9501*	0.988	0.656	12480
A	2.442	1.940	686	2.460	1.934	924
	2.460	1.950	878*	2.454	1.910	1051*
	0.980	0.702	7780	0.980	0.652	11500*
	0.979	0.674	8009*	0.974	0.638	13500
LA	2.440	1.970	606	2.450	1.910	827
	2.450	1.980	730*	2.440	1.905	954*
	0.972	0.652	8555*	0.976	0.648	10984
	0.974	0.674	9319	0.972	0.630	10129

TABLE 3 - Parameters of cracking laws with "a" in mm and da/dN in  $\mu\text{m}/\text{cycle}$

Steel	Heat Treatment	$\Delta\epsilon_t = 1 \%$				$\Delta\epsilon_t = 2.5 \%$	
		D	$\alpha$	$D_1$	$\alpha_1$	D	$\alpha$
I	UA	0.790	1.46	-	-	9.63	1.02
	A	0.850	1.46	0.383	2.25	8.37	0.92
	LA	0.815	1.30	0.273	3.54	8.77	0.99
II	UA	1.31	0.81	-	-	8.43	1.04
	A	0.85	1.42	-	-	3.62	0.676
	LA	0.90	1.02	-	-	5.70	0.703

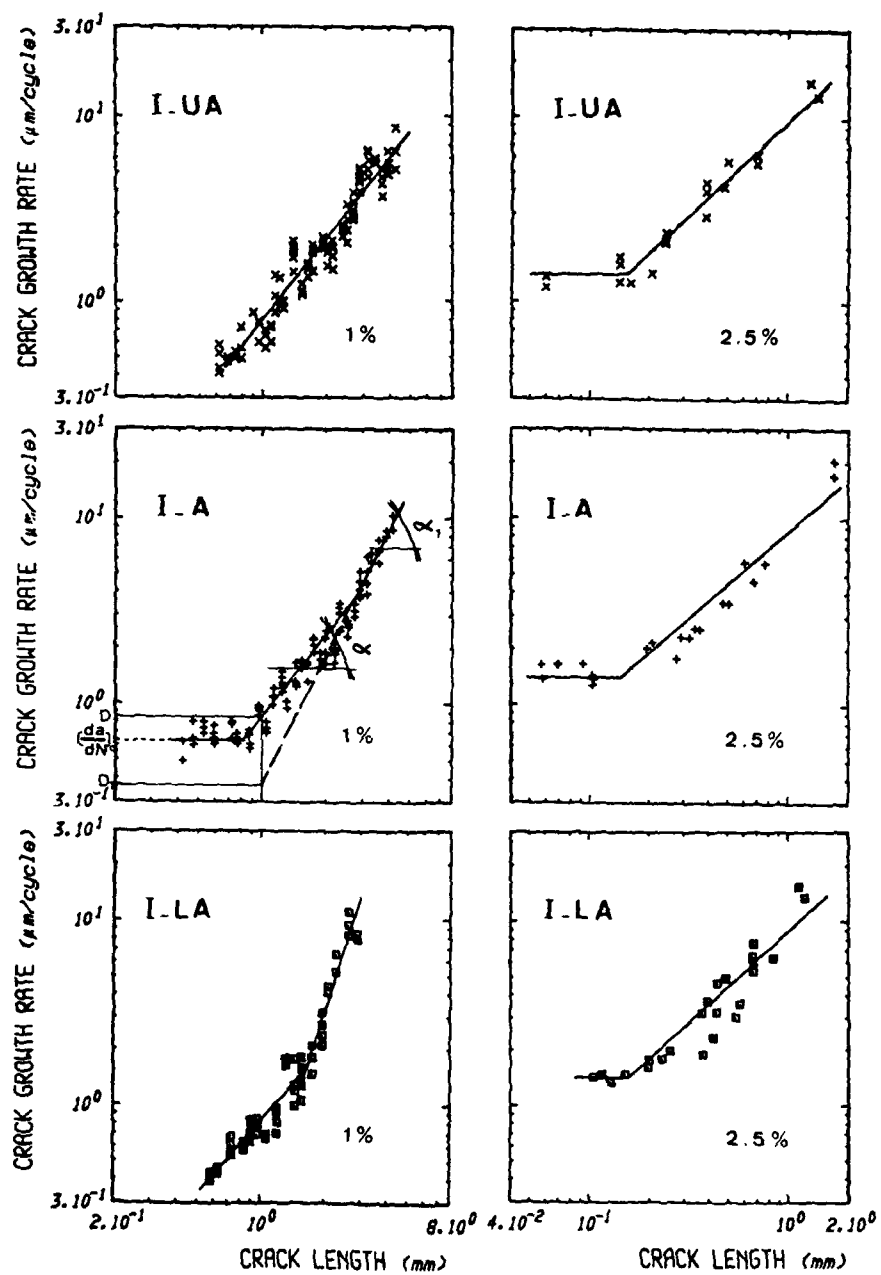


Figure 1 Crack growth rate measurement results in steel I

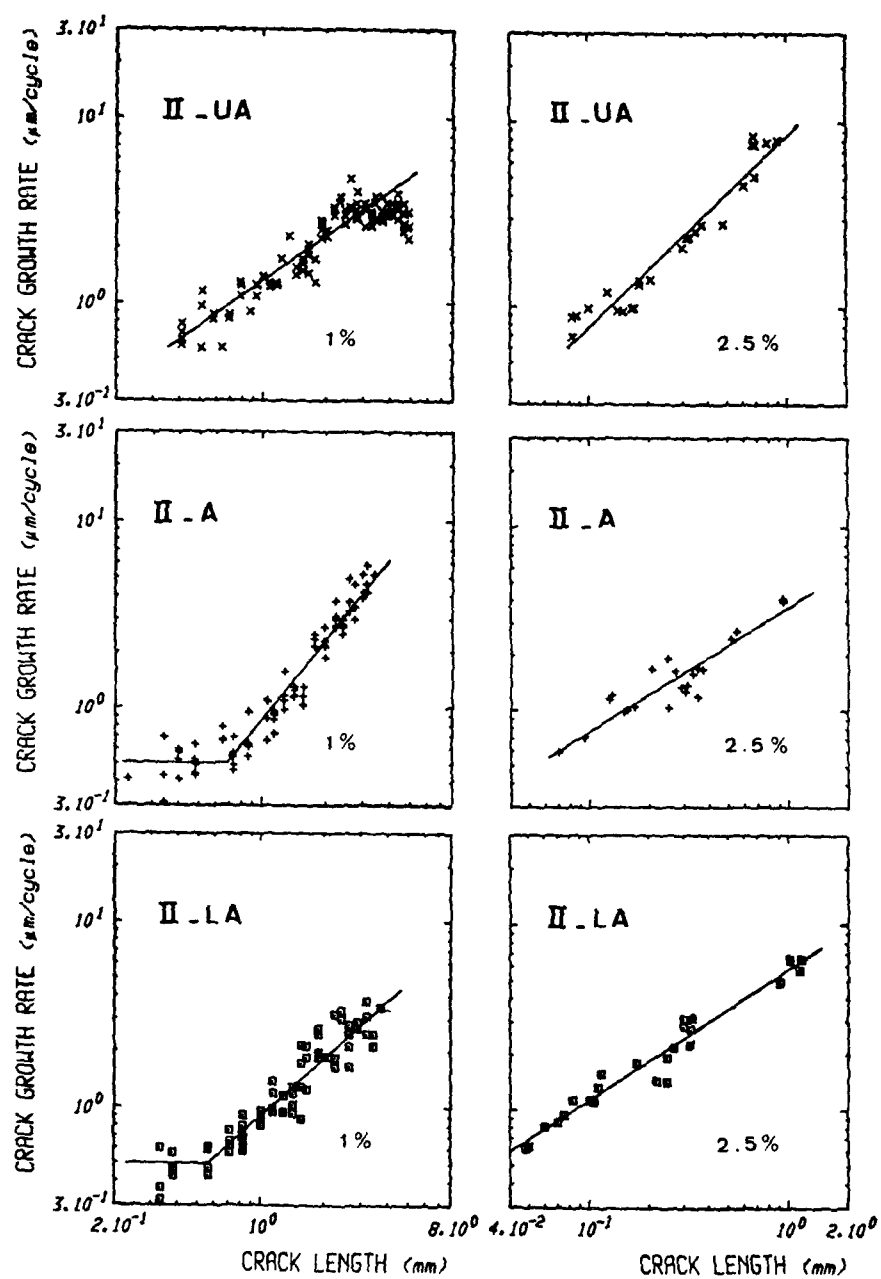


Figure 2 Crack growth rate measurement results in steel II

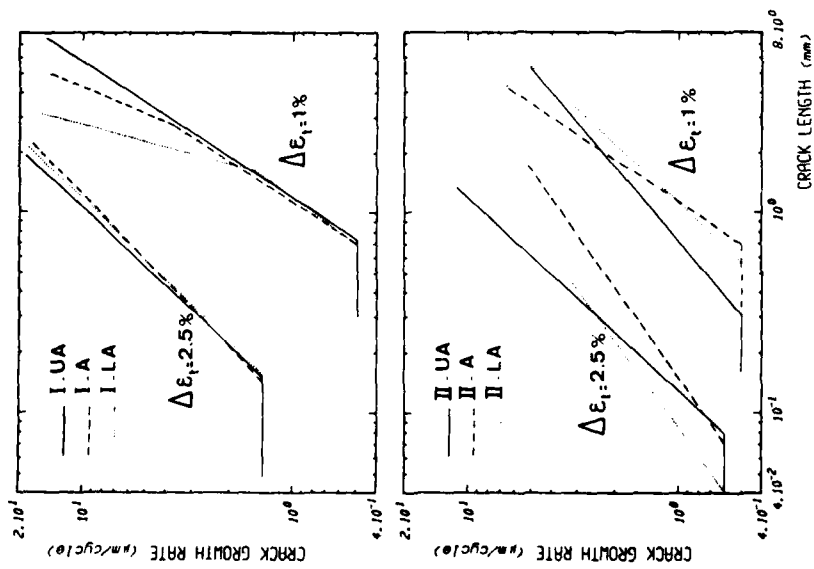


Figure 3 Schematic representation of results by straight lines

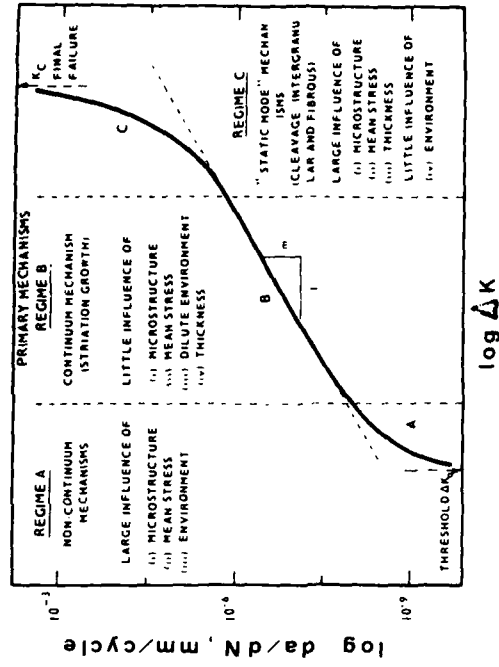


Figure 4 Summary diagram showing the primary fracture mechanisms associated with the crack growth results  $\log da/dN - \log K$  (13)

## RESIDUAL STRESS

FATIGUE 87

## FATIGUE 87

### THRESHOLD AND CRACK-GROWTH TESTS ON PRE-CRACKED SPECIMENS PRODUCED IN CYCLIC COMPRESSION

R. Pippan\*

The fatigue crack growth rate in tension-tension fatigue ( $R = 0.1$ ) was measured on specimens pre-cracked in cyclic compression. The material used was ARMCO iron. At the beginning the growth rate of a closure free crack was observed. With an increase of crack length the growth rate decreases. For  $\Delta K < \Delta K_{th}$  a crack arrest occurs. For  $\Delta K > \Delta K_{th}$  the growth rates (after a certain length) converge to the conventionally measured  $da/dN$  values. The distance over which crack closure develops can be estimated. By step-wise increases of the load amplitude on specimens pre-cracked in cyclic compression  $\Delta K_{eff\ th}$  and  $\Delta K_{th}$  were measured.

### INTRODUCTION

To know the threshold of the stress-intensity range,  $\Delta K_{th}$ , and the growth rate near  $\Delta K_{th}$  has become increasingly important in the last decade. But it is not clear how  $\Delta K_{th}$  should be measured exactly.

In most investigations  $\Delta K_{th}$  is measured by decreasing of  $\Delta K$ . In this case a crack is produced at a  $\Delta K$  value greater than  $\Delta K_{th}$ , then  $\Delta K$  is decreased in steps until crack arrest occurs.

It has been shown in some papers (Cadman et al.(1), and Döker et al.(2)) that the threshold measured with this method depends on the decreasing rate of  $\Delta K$ . The reason for this behavior is the strong dependence of the closure stress intensity,  $K_{cl}$ , on the loading history.

\* Erich-Schmid-Institut für Festkörperphysik, Österreichische Akademie der Wissenschaften, Leoben, Austria

## FATIGUE 87

A high level of  $K_{cl}$  caused by pre-loading gives the mistaken appearance of a too high  $\Delta K_{th}$ -value.

To avoid this effect another way to measure  $\Delta K_{th}$  was recently proposed by Suresh (3). He used pre-cracked specimens produced by cyclic compression for fatigue threshold ( $\Delta K_{th}$ ) tests.  $K_{cl}$  for such specimens is below zero at the start of the fatigue test in tension ( (3) and Pippan (4)). Up to now there are only few investigations (Christman et al. (5), (3)) made in tension-tension fatigue on specimens pre-cracked in cyclic compression. But from these papers it is not clear how  $K_{cl}$  increases and over which distance the crack closure occurs (in the case of long cracks).

The purpose of this paper is to investigate:

- how the fatigue crack growth rate behaves in the early stage of a tension-tension test on specimens pre-cracked in cyclic compression
- what can we learn from such tests over the location of crack closure
- what happens in a  $\Delta K_{th}$  test on specimens pre-cracked in cyclic compression, especially below  $\Delta K_{th}$ .

### EXPERIMENTAL PROCEDURE

#### A) Material

The material used was ARMCO iron (analysis in wt. %: C 0.007, Mn 0.08, P 0.015, S 0.015, the balance is iron). The experiments were performed on CT-specimens (width,  $W = 25$  mm, thickness  $B = 8$  mm, notch depth  $\sim 10$  mm, and notch angle  $60^\circ$ ). The specimens were machined in the LT-orientation from the cold-rolled sheet and were then annealed for one hour at  $1000^\circ\text{C}$  in a vacuum furnace. The average grain size was about  $70\text{ }\mu\text{m}$ . The 0.2%-offset yield stress was 150 MPa and the ultimate tensile strength was 280 MPa. The long-crack growth rate as a function of  $\Delta K$  measured with a conventional method (Pippan et al. (6)) is shown in fig. 1. The influence of the R-ratio is due to the crack closure effect. The investigation (6) shows that in a test with  $R = 0.8$  no closure occurs and therefore the  $da/dN - \Delta K$ -curve agrees with the  $da/dN - \Delta K_{eff}$ -curve.

## FATIGUE 87

### B) Crack initiation in cyclic compression

The pre-cracked specimens were produced with a constant load amplitude in full compression ( $R \approx 20$ ). In such an experiment a crack emanating from the notch, grows with a progressively decreasing rate, before it is arrested completely (Reid et al. (76), Chu et al. (8), Holm et al. (9), (3), (4)).

The used load amplitude corresponds to a  $\Delta K \sim 12 \text{ MPa}\cdot\text{m}$  which is in the same order of magnitude as used to initiate a crack in a tension-tension test.  $10^5$  cycles were used for the production of the pre-crack. The crack length measured from the notch root was about 0.4 mm and was uniform over the thickness of the specimen (this was controlled by fracturing of a pre-cracked specimen in liquid nitrogen).

### C) Tension-tension fatigue

Two different kinds of experiments were performed on the specimens pre-cracked in cyclic compression. The first group were made at different constant load amplitudes and the second group was a threshold test where the load amplitude was increased in steps. The ratio  $R$  was in both cases 0.1.

The tests were performed in air at room temperature and the load frequency was about 150 Hz. The crack length was measured with a travelling microscope, or in the case of very low extension of the crack, with a stationary optical microscope.

## RESULTS AND DISCUSSION

### Crack growth test at constant load amplitude

The crack growth rate was measured on three pre-cracked specimens at three different constant load amplitudes. At the beginning these load amplitudes correspond to a  $\Delta K = 2, 4$  and  $8 \text{ MPa}\cdot\text{m}$ . The growth rate as a function of  $\Delta K$  is shown in Fig. 2.

At the experiment with  $\Delta K = 2.0 \text{ MPa}\cdot\text{m}$  no extension of the crack was observed after  $2 \cdot 10^7$  cycles. (The detection limit for a crack extension in the optical microscope was between 1 and 2  $\mu\text{m}$ ). This result is in agreement with the suggested  $da/dN - \Delta K_{\text{eff}}$  - curve (6) since  $\Delta K$  is below the effective threshold stress intensity range,  $\Delta K_{\text{eff th}}$ .

## FATIGUE 87

In the experiment which start at  $\Delta K = 4.0 \text{ MPa}\sqrt{\text{m}}$  the crack grows in the first few micrometers ( $\sim 20 \text{ }\mu\text{m}$ ) with a relatively high growth rate ( $\sim 2 \cdot 10^{-7} \text{ mm/cycle}$ ), then the growth rate decreases and it is arrested after a crack extension of about  $70 \text{ }\mu\text{m}$ . The high growth rate at the beginning can be explained by the low  $K_{C1}$  value, since  $K_{C1}$  at the beginning of the tension-tension test is below zero. One can see that this growth rate agrees with the  $da/dN$  value at a  $\Delta K_{\text{eff}} = 4 \text{ MPa}\sqrt{\text{m}}$ . Therefore it is possible in such a test to measure the relation between  $da/dN$  and  $\Delta K_{\text{eff}}$  without measuring the closure level. With an increase of the crack length  $K_{C1}$  increases, and therefore  $da/dN$  decreases until  $\Delta K_{\text{eff}}$  is equal to  $\Delta K_{\text{eff th}}$ .

From such a test we can further estimate the distance over which the crack closure develops:

Since the crack produced in compression should not close in tension, the closure can only occur on the fracture surfaces produced in cyclic tension. The first significant decrease of the growth rate in a test at  $\Delta K = 4 \text{ MPa}\sqrt{\text{m}}$  was observed after an extension of  $20 \text{ }\mu\text{m}$ , and therefore the first closure should occur in this region behind the crack tip. (Such closure is not detectable with conventional closure measurement methods as compliance or back face strain technique). At the end of this test the closure which caused the arrest of the crack should happen in the region  $70 \text{ }\mu\text{m}$  behind the crack tip.

Such estimation, of the distance over which the crack closure develops, is correct for the plastic- and oxide-induced crack closure, but not for the roughness-induced crack closure (since the roughness at the crack, produced in cyclic compression, and a lateral shift during tension-tension cycling may cause a closure on the crack surface produced in cyclic compression).

The third experiment was performed with a load amplitude which corresponds to a  $\Delta K = 8 \text{ MPa}\sqrt{\text{m}}$  at the beginning, which is greater than the long-crack threshold value at this R-ratio. In this case the crack growth rate starts at a high level (which agrees also with the  $da/dN$ -value at a  $\Delta K_{\text{eff}} = 8 \text{ MPa}\sqrt{\text{m}}$ ), then it decreases and after a crack extension of about  $1.5 \text{ mm}$  it converges with a conventionally measured crack growth rate. This means that after a crack extension of  $1.5 \text{ mm}$  the crack closure levels in both tests are equal.

## FATIGUE 87

### Threshold test

This experiment was performed on one specimen by increasing the load amplitude in steps until no arrest of the crack occurred. The observed growth rates of this test are shown in fig. 3.

At the load amplitudes which correspond to  $\Delta K = 2$  and  $2.5 \text{ MPa}\sqrt{\text{m}}$  no increase ( $\Delta a < 2 \text{ }\mu\text{m}$ ) of the crack was observed after  $2 \cdot 10^7$  cycles. The first crack extension of about  $10 \text{ }\mu\text{m}$  was measured in a test at  $\Delta K = 3 \text{ MPa}\sqrt{\text{m}}$ . This is also in agreement with the suggested  $\Delta K_{\text{eff th}}$  (6) of this material. Since there is no closure at the beginning of the test,  $\Delta K_{\text{eff th}}$  should be between the last step where no extension of the crack is observed, and the first step where an increase of the crack occurs. We think that an estimate of  $\Delta K_{\text{eff th}}$  in such a test is easier than to a measuring  $K_{\text{cl}}$  at  $\Delta K_{\text{th}}$  in a conventional test. It certainly is easier to measure an extension of a crack of a few microns than to measure a closure over a distance of a few microns. In the following steps  $da/dN$  starts always at a relatively high level and after a certain distance the crack is arrested (Table 1). The last arrest of the crack was observed at a  $\Delta K = 6.5 \text{ MPa}\sqrt{\text{m}}$  where the extension of the crack (in tension)  $\Delta a$  was  $1780 \text{ }\mu\text{m}$ . At the following load amplitude (corresponding to  $\Delta K = 6.75 \text{ MPa}\sqrt{\text{m}}$  at the beginning) we obtained a typical  $da/dN - \Delta K$  - curve which was in good agreement with previous measurements (6).

TABLE 1 -  $\Delta a$  at different  $\Delta K$  values, where  $\Delta a$  is the difference between the length of the arrested crack and the length of the pre-crack produced in cyclic compression

$\Delta K \text{ [MPa}\sqrt{\text{m}}]$	2	2.5	3	3.5	4.0	4.6	5.5	5.8	6.25	6.5
$\Delta a \text{ [}\mu\text{m]}$	< 2	< 2	~10	~20	80	350	1510	1570	1740	1780

### CONCLUSIONS

In a tension-tension fatigue test on specimens pre-cracked in cyclic compression one can measure, at first, the growth rate of a closure-free crack. From the distance at which the growth rate decreases and from the crack length at which the crack is arrested one can estimate the distance over which crack closure develops.

## FATIGUE 87

When a step-wise increase of the load amplitude is applied on specimens pre-cracked in cyclic compression, the first extension of the crack occurs in the first step where  $\Delta K > \Delta K_{eff\ th}$ . The last arrest of the crack occurs during the last load amplitude where  $\Delta K < \Delta K_{th}$ .

### REFERENCES

- (1) Caldman, A.J., Brook, R. and Nicholson, C.E., Scripta Metallurgica, Vol.17, 1983, pp.1053-1056.
- (2) Döker, H., Bachmann, V. and Marci, G., A comparison of different methods of determination of the threshold for fatigue crack propagation, Proceedings, "Fatigue Thresholds", Stockholm, Sweden, Edited by J. Bäcklund et al., EMAS, Warley, U.K., 1981, pp.45-57.
- (3) Suresh, S., Engineering Fracture Mechanics, Vol.21, 1985, pp.453-463.
- (4) Pippan, R., The growth of short cracks under cyclic compression, Fatigue Fract.Eng.Mater.Struct., in press.
- (5) Christman, T. and Suresh, S., Engineering Fracture Mechanics, Vol.23, 1986, pp.953-964.
- (6) Pippan, R., Berger, M. and Stüwe, H.P., The influence of crack length on the propagation of fatigue cracks in deep sharp notches, Metallurgical Transactions A, in press.
- (7) Reid, C.H., Williams, K. and Hermann, R., Fatigue Engng.Mater.Struct., Vol.1, 1979, pp.67-270.
- (8) Chu, W.Y., Hsiao, C.M., Jin, L.J. and Liu, T.H., Scripta metall., Vol.17, 1983, pp.267-270.
- (9) Holm, D.K., Blom, A.F. and Suresh, S., Engineering Fracture Mechanics, Vol.23, 1986, pp.1097-1106.

# FATIGUE 87

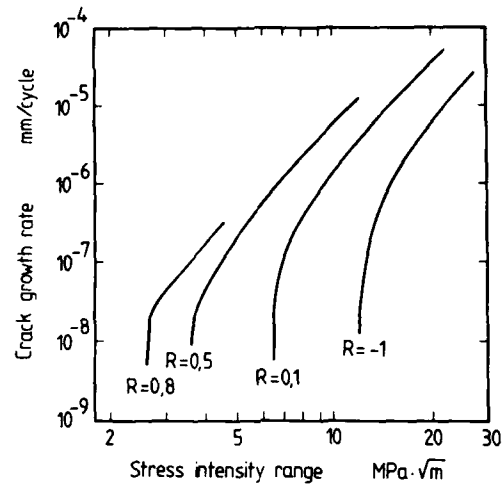


Figure 1 Long crack growth rate as a function of the stress intensity range for different R-ratios of ARMCO-iron (6)

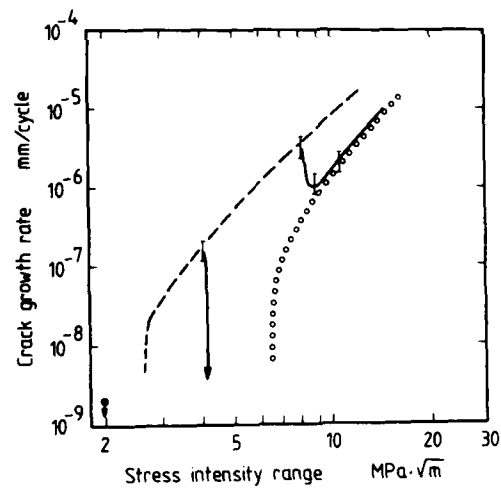


Figure 2 Crack growth rate as a function of  $\Delta K$  in experiments with constant load amplitude on specimens pre-cracked in cyclic compression (--- da/dN -  $\Delta K_{eff}$  and  $\circ\circ\circ$  da/dN -  $\Delta K$  for R = 0.1 (6))

# FATIGUE 87

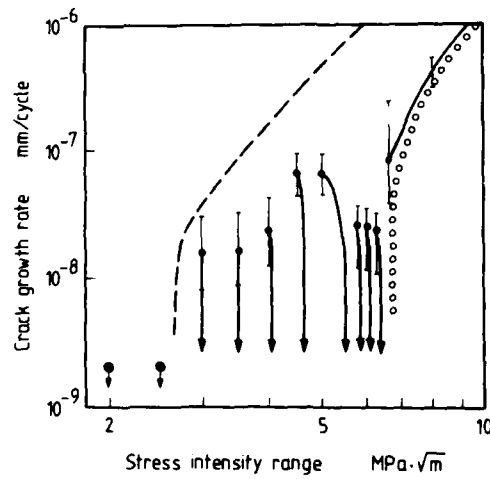


Figure 3 Crack growth rate as a function of  $\Delta K$ , caused by step-wise increase of the load amplitude on specimens pre-cracked in cyclic compression  
(---  $da/dn = \Delta K_{eff}$  and  $\circ\circ\circ da/dN = \Delta K$  for  $R = 0.1$  (6))

## FATIGUE 87

### MICROMECHANICS OF FATIGUE CRACK INITIATION UNDER AXIAL AND TORSIONAL LOADINGS

T.H. Lin\*, S.R. Lin\*\*, and W.U. Cooley\*\*\*

Micromechanic theory of fatigue crack initiation under axial loading (tension and compression) is reviewed. The same approach is applied to combined cyclic axial and torsional loadings. The component of intrusion depth normal to the free surface is taken as a measure of crack initiation. It is found that the rate of crack growth per cycle of loading varies more than linearly with the magnitude of alternate loading.

#### INTRODUCTION

Following the observations of extrusions and intrusions in fatigue bands, [1,2], different investigators have proposed different theories of fatigue crack initiation. For example, Mott, [3], proposed that a screw dislocation intersecting a free surface travels a complete circuit, the volume contained in the circuit moves parallel to the dislocation causing the metal to extrude. This mechanism does not explain why the dislocation does not oscillate back and forth along the same path rather than a closed circuit. Cottrell & Hull, [4], proposed that Frank Read sources exist in two intersecting slip planes and assumed the crystal to slide alternately on two of the four sliding planes of an f.c.c. crystal. A complete cycle of forward and reversed loading results in an extrusion and an intrusion. The mechanism does not explain why the sliding planes during forward and reversed loadings are not the same. This model would also predict the extrusion and intrusion to form in neighboring slip bands and to incline to each other, but they are shown to occur in the same slip band and to be parallel to each

\* Dept. of Civil Engr'g., UCLA, Los Angeles, CA 90024

\*\* The Aerospace Corporation, El Segundo, CA 90245-2691

\*\*\* Hughes Aircraft Corp., P.O. Box 902, El Segundo, CA 90245

other. Wood, [5], proposed a theory that unidirectional stressing causes layers of metal to slide in the same direction but forward and reverse stressing causes different amounts of net slip on different planes resulting in peaks and valleys. This theory does not explain why under an alternate loading, the slip continues to monotonically deepen the valley and raise the peaks as observed in experiments. Clearly there is some gating mechanism present to prevent the back and forth slip from occurring on the same planes. Lin and associates [6-8] have shown such a gating mechanism being supplied by the microstress fields generated by slip under cyclic loadings.

#### Method for Calculating Microstresses Caused by Slip

Referring to a set of orthogonal coordinates, the strain component  $e_{ij}$  is composed of the elastic part denoted by single prime and the inelastic part, by double prime.

$$e_{ij} = e'_{ij} + e''_{ij} \quad (1)$$

Inelastic strain includes thermal creep and plastic strains. Neglecting the anisotropy of elastic constants

$$\tau_{ij} = \delta_{ij}\lambda\theta' + 2\mu e'_{ij} = \delta_{ij}\lambda(\theta - \theta'') + 2\mu(e_{ij} - e''_{ij}) \quad (2)$$

where  $\lambda$  and  $\mu$  are Lamé's constants  $\theta$  is the dilatation. The condition of equilibrium within a body of volume  $V$  is expressed as

$$\tau_{ij,j} + F_i = 0 \text{ in } V. \quad (3)$$

where the subscript after comma denotes differentiation, the repetition of subscript denotes summation from one to three and  $F_i$  denotes the body force per unit volume along  $x_i$ -axis. Substituting (2) to (3), we have

$$\delta_{ij}\lambda\theta_{,j} + 2\mu e_{ij,j} + F_i + \bar{F}_i = 0 \quad (4)$$

where

$$\bar{F}_i = -(\delta_{ij}\lambda\theta'_{,j} + 2\mu e''_{ij,j}) \quad (5)$$

$\bar{F}_i$  is called the equivalent body force. This analogy was used to calculate microstress field caused by slip. This reduces to Duhammel's analogy of thermal stress analysis [11] when  $e''_{ij}$  is caused by thermal strain alone.

Strain crystal tests have shown that slip depends on the resolved shear stress and is independent of the normal stress on the sliding plane. This dependency under monotonic loadings has also been found to hold under cyclic loadings [9] and is used for present analysis.

#### Fatigue Crack Initiation Under Cyclic Tension and Compression

Imperfections exist in all metals and cause initial stress fields. For a slice of metal to extrude out of a surface, positive

shear deformation must occur on one side of the extrusion (denoted by P) and negative shear on the other side (denoted by Q) (Fig. 1). The initial resolved shear stress field near the free surface favorable for the initiation of an extrusion is one with positive shear stress above the slice and a negative one below. Based on Eshelby's method [10] of imaginary cutting, relaxing, restoring, welding, relieving in his famous paper on ellipsoidal inclusions, a linearly varying initial longitudinal strain [8] in the slice R will cause this set of plus and minus shear stresses. Under positive loading, the applied shear stress and the initial one have the same sign in P and different signs in Q. Hence P reaches the critical shear stress first and slides. Due to the continuity of stress field, this slip relieves the positive shear stress not only in P but also in the vicinity of P including Q. This relief of positive shear stress in Q is the same as the increase of negative stress in Q causing Q to be more ready to slide in the reversed loading. This explains why only P slides in the forward loading. Under the reversed loading, Q has the highest stress and slides. This relieves the negative shear stress not only in Q but also in the vicinity of Q including P. This increases the positive shear stress in P and causes it to be more ready to slide and hence slide under the next forward loading. This process is repeated and provides a gating mechanism to cause the monotonic raise of the peaks and deepening of the valleys.

Consider a polycrystal of pure aluminum. The grain size is small compared to the size of the aggregate. From the analogy described, the equivalent force caused by the plastic strain [11] may be considered to act in a semi-infinite elastic medium. The thickness of the slices P and Q is much less than the length of the slip lines seen on the surface. Hence this plastic strain and their equivalent forces are taken to be constant along the slip line direction, and this semi-infinite medium is taken to be under plane deformation. There are four slip planes in an f.c.c. crystal. In the present study, sliding in one plane only is considered. Referring to Fig. 1, the thickness of each (P, Q, R) was taken to be  $0.05\mu$ , the center distance between P and Q was  $0.10\mu$ , and the linear dimension of the crystal was taken to be  $50\mu$ . The initial resolved shear stresses in P and Q were assumed to be  $\pm 4.0\text{psi}$  respectively, and to approach zero elsewhere. The critical shear stress  $\tau^C$  is taken to be  $53.5\text{psi}$ . The strain hardening is assumed to be zero,  $\Delta\tau^C = 0$ . The elastic shear modulus G, is taken to be  $3.85 \times 10^6\text{psi}$  and the elastic Poisson's ratio to be 0.3. For numerical calculation, P, Q, each was divided into ten grids, each of which is  $0.5\mu \times 5\mu$ . Within each grid, the plastic strain was assumed to be uniform. From the plane strain solution of a semi-infinite medium, the stress field caused by a unit plastic strain  $e_{\alpha\beta}^P$  in one grid centered at  $X_r$ , i.e.  $(X_{1r}, X_{2r})$  was calculated, the relief of the resolved shear stress at X due to this  $e_{\alpha\beta}^P(X_r)$  is expressed as

$$\tau_{\alpha\beta}^R(X) = 2GC(X, \alpha\beta; X_r, \alpha\beta)e_{\alpha\beta}^P(X_r) \quad (6)$$

## FATIGUE 87

where  $C(X, \alpha\beta; X_r, \alpha\beta)$  is called the resolved shear stress influence coefficient. The resolved shear stress at  $X$  is the sum of the initial, applied and residual resolved shear stresses, i.e.

$$\tau_{\alpha\beta}^R(X) = \tau_{\alpha\beta}^I + \tau_{\alpha\beta}^A + 2G \sum_n C(X, \alpha\beta; X_n, \alpha\beta) e_{\alpha\beta_n}^P \quad (7)$$

where  $X_n$  denotes center point and  $e_{\alpha\beta_n}^P$  the plastic strain of the  $n$ th grid which slides. For a load increment  $\Delta\tau^A$

$$\Delta\tau_{\alpha\beta}(X) = \Delta\tau^A + 2G \sum_n C(X, \alpha\beta; X_n, \alpha\beta) \Delta e_{\alpha\beta_n}^P$$

In those grids, where  $\tau_{\alpha\beta}$  equals the critical shear stress  $\tau^C$ , incremental plastic strain generally occurs. For each such grid, there is one such equation by equating  $\Delta\tau_{\alpha\beta} = 0$ . Hence all the incremental plastic strain  $\Delta e_{\alpha\beta_n, s}$  can be readily determined.  $\tau_{\alpha\beta}(X) - \tau^C$  is called the excessive resolved shear stress. For an excessive resolved shear stress of 0.02psi, the distribution of plastic strain in P,Q after 200 cycles was calculated [8] as shown in Fig. 2. These plastic strains have been found to be approximately proportional to the number of cycles and proportional to the excessive resolved shear stress. The local plastic strain build-up at the free surface is much more than that at the interior. Hence, in general, fatigue cracks are initiated from the free surface.

### Fatigue Crack Initiation Under Cyclic Combined Torsion and Axial Loading

Single crystal tests have shown that extrusion occurs on the slip plane along the highest stressed slip directions but does not occur when the direction is parallel to the free surface [12]. In cyclic tension and compression, the highest stressed slip direction of the most favorably oriented crystal inclines  $45^\circ$  with the free surface. On a circular shaft under cyclic combined torsion and axial loading, the maximum shear stress occurs along a direction parallel to the free surface. Hence the extrusion or intrusion process will not occur in this maximum stress direction but may occur in some crystal with a slip direction making an angle  $\beta$  with the free surface. The effect of free surface on cyclic plastic deformation of a polycrystal was first pointed out by Brown and Miller in their very significant paper "A Theory for Fatigue Failure under Multiaxial Stress-Strain Conditions" [13]. The displacement normal to the free surface in P,Q is taken here as a measure of the amount of intrusion and crack nucleation.

Consider a circular shaft. Let  $\tau$  denote the shear stress due to torsion and  $\sigma$ , the axial stress. Under combined torsion and axial loading, the maximum shear stress

$$\tau_{\max} = \left[ \left( \frac{\sigma}{2} \right)^2 + \tau^2 \right]^{1/2} \quad (8)$$

This shear stress acts on a plane with normal denoted by "y" and along a direction denoted by "z". Consider a crystal with a slip direction on y-plane and making an angle  $\beta$  with z-axis (Fig. 3). Then

$$\tau_{y\beta} = \tau_{\max} \cos \beta \quad (9)$$

Referring to Fig. 4, the thin slices P,Q are taken to be 0.1 $\mu$ m apart. P is assumed to have a positive constant initial shear stress  $\tau_{y\beta}^I$  and Q a negative value. The process of cyclic deformation is similar to the case under cyclic tension and compression. Under a positive loading, the applied shear stress  $\tau_{y\beta}^A$  has the same sign as the initial stress in P. Hence, the resolved shear stress in P reaches the critical shear stress first and P starts to slide. Slip in P causes a residual shear stress field. Assuming strain-hardening to be zero as before, the resolved shear stress in P remains constant and equal to the critical shear stress during sliding. Due to the continuity of stress field and the closeness of Q to P, stress relief in Q is nearly the same as that of P. This keeps the positive shear stress in the neighboring region from reaching that of P during the forward loading. Hence, only P slides in the forward loading. The stress relief in Q is the same as increasing the negative shear stress. During the reversed loading, Q has the highest negative shear stress and hence slides. This slip causes the relief of negative shear stress not only in Q, but also in the neighboring region including P. This relief of negative shear stress is the same as increasing the positive shear stress thus causing P to be readier to slide in the next forward loading. During the next forward loading, P has the highest positive shear stress and slides. This process is repeated as the case of cyclic tension of compression. These stress fields give a natural gating mechanism causing alternate sliding in P,Q to give a monotonic increase in positive slip in P and negative slip in Q.

After sliding occurs in P,Q, residual stress  $\tau^R$  is produced. The total resolved shear stress in P,Q equals the sum of the initial shear stress  $\tau^I$ , the applied shear stress  $\tau^A$  and  $\tau^R$ . Slip occurs on the y-plane along  $\beta$ -direction causing  $e_{y\beta}''$ . This strain resolves into  $e_{yx}'' = e_{y\beta}'' \sin \beta$  and  $e_{yz}'' = e_{y\beta}'' \cos \beta$ . Noting  $e_{yz,z}'' = 0$ , the equivalent body forces are

$$\bar{F}_x = -2\mu e_{yx,y}''; \bar{F}_y = -2\mu e_{yx,y}''; \bar{F}_z = -2\mu e_{yz,y}''$$

For a unit line force  $F_z$  per unit length along z-direction, applied at  $x = x'$ ,  $y = y'$  in a semi-infinite medium, the stress given in polar coordinates shown by Cooley and Lin [14]

$$\tau_{zy} = g_{zyz} = -\frac{(y-y')}{2\pi} \left( \frac{1}{r_1^2} + \frac{1}{r_2^2} \right)$$

where  $r_1^2 = (x - x')^2 + (y - y')^2$ ;  $r_2^2 = (x + x')^2 + (y - y')^2$ . Thus  $g_{zyz}$  is the shear stress  $\tau_{zy}$  at  $(x,y)$  due to a unit line force applied at  $(x', y')$  along z-direction. Let  $g_{xyx}(x,y; x', y')$  be the shear stress  $\tau_{xy}$  at  $(x,y)$  due to unit line force applied at  $(x',y')$  along x-direction. These functions were derived by Cooley [14] using solutions given by Melan [15] and are given as

$$\begin{aligned}
g_{xyx}(x,y; x',y') &= \frac{-(y-y')}{4\pi(1-\nu)r_1^2} \left[ (1-2\nu) + \frac{2(x-x')^2}{r_1^2} \right] \\
&+ \frac{(y-y')}{4\pi(1-\nu)r_2^2} \left[ (1-2\nu) + \frac{2(x-x')^2}{r_2^2} \right] \\
&- \frac{x(y-y')}{\pi r_2^2} \left[ 2(x+x') + \frac{x'}{(1-\nu)r_2^2} 3(x+x')^2 - (y-y')^2 \right] \\
g_{xyy}(x,y; x',y') &= \frac{-(x-x')}{4\pi(1-\nu)r_1^2} \left[ (1-2\nu) + \frac{2(y-y')^2}{r_1^2} \right] \\
&+ \frac{(x+x')}{4\pi(1-\nu)r_2^2} \left[ (1-2\nu) + \frac{2(y-y')^2}{r_2^2} \right] \\
&- \frac{xx'(x+x')}{\pi(1-\nu)r_2^2} [(x+x')^2 - 3(y-y')^2] \\
&+ \frac{1}{\pi r_2^2} \left[ x + \frac{x'}{2(1-\nu)} \right] [(x+x') - (y-y')] - \frac{(x+x')}{\pi r_2^2}
\end{aligned} \quad (10)$$

The residual stresses are then

$$\begin{aligned}
\tau_{yx}^R(x,y) &= \int g_{xyx}(x,y; x',y') \bar{F}_x(x',y') dx' dy' \\
&+ \int g_{xyy}(x,y; x',y') \bar{F}_y(x',y') dx' dy' - 2\mu e_{yx}''(x,y) \\
\tau_{zy}^R(x,y) &= \int g_{zyz}(x,y; x',y') \bar{F}_z(x',y') dx' dy' - 2\mu e_{yz}''(x,y)
\end{aligned} \quad (11)$$

$$\tau_{y\beta}^R = -\tau_{yx}^R \sin \beta + \tau_{yz}^R \cos \beta \quad (12)$$

For numerical calculation P and Q each was divided into 10 thin rectangular grids. The plastic strain in each grid was assumed to be uniform. Dropping the subscripts y and z on the shear stress and plastic strain, the resolved shear stress in the mth grid due to plastic strain in all grids.

$$\tau_m^R = \sum_{n=1} G_{mn} e_n''; \Delta \tau_m^R = \sum_{n=1} G_{mn} \Delta e_n'' \quad (13)$$

Neglecting strain-hardening

$$\Delta \tau_m = \Delta \tau^A + \sum G_{mn} \Delta e_n'' = \Delta \tau^C = 0 \quad (14)$$

This gives one equation for each gliding grid. There are as many equations as the unknowns. This procedure was used to calculate the build-up of plastic strain in P,Q under cyclic loadings. The critical shear stress and the elastic constants were taken to be the same as those used for cyclic axial loadings. The initial shear stress  $\tau^I$  was taken to be 4psi in P and -4psi in Q. The applied shear stress was 53.5psi. The plastic strain distributions in P,Q were calculated at different numbers of cycles and are shown in Fig. 5. The build-up of plastic strain at the free surface varies linearly with the excessive resolved shear stress  $\tau^E = \tau^A + \tau^I + \tau^R - \tau^C$  and the angle  $\beta$ . The variation of this plastic

## FATIGUE 87

strain at the free surface with  $\beta$  for different values of excessive resolved shear stresses is shown in Fig. 6. The above derivations and calculations are for the surface crystal with a slip direction making an angle  $\beta$  with the surface. When  $\sigma = 0$ , these calculations reduce to the case of pure cyclic torsion [14].

The calculated result of surface plastic strain  $e''_{\alpha\beta}$  in a fatigue specimen under cyclic tension and compression [8] gives a value of 0.000016/cycle at an excessive shear stress  $\tau^E$  of 0.02psi. Since for this loading this plastic strain varies linearly with  $\tau^E$ , this gives a rate  $e''_{\alpha\beta}$  of 0.0032/cycle at a  $\tau^E$  of 4psi. The thickness of slices P,Q taken was .02 $\mu$ m. The displacement increment normal to the free surface per cycle is

$$\Delta u''_x = e''_{\alpha\beta} \times .02 \sin 45^\circ = .02 \times .707 \times .0032 = 4.525 \times 10^{-5} \mu\text{m/cycle}.$$

Under combined loadings with the same  $\tau^C$  and  $\tau^I$

$$\Delta u''_x = e''_{yx} \times .02 = .00061 \times .02 = 1.22 \times 10^{-5} \mu\text{m/cycle}.$$

$u''_x$  is a measure of intrusion or extrusion and hence of crack initiation. For this amount of  $\tau^E$ , it is seen that the rate of crack initiation is faster under cyclic tension and compression than that for combined loading and pure torsion.

The crystals on the surface of the polycrystal are of all possible orientations. The orientation  $\beta$  to give the maximum surface plastic strain varies with the magnitude of the excessive resolved shear stress  $\tau^E$ . From the curves taken from Fig. 6, we plot the rate of surface plastic strain growth vs.  $\tau^E$  for cyclic combined torsion and axial loading, shown in Fig. 7. In the same figure, we plot the same for cyclic tension and compression. It is seen that as  $\tau^E$  increases, the curve of the growth rate for cyclic combined loading and for pure torsion bends upward to approach that from cyclic tension and compression. This seems to agree with the recent test of Tanaka et al. [16].

In cyclic combined torsion and axial loading, we can have alternate slip in a crystal with a slip direction making an angle  $\beta$  with the free surface as described above and another crystal with a slip plane and a slip direction making  $45^\circ$  with the free surface. For the former crystal, the excessive shear stress  $\tau^E = \tau_{\max} - \tau^C$ . Using this  $\tau^E$ , we read from the lower curve of Fig. 7 to find the plastic strain rate. For the latter crystal, the excessive shear stress  $\tau^E = \frac{\sigma}{2} - \tau^C$ . Using this, we read from the upper line in Fig. 7 to obtain the plastic strain rate. Among these two rates, the higher one gives the rate of fatigue crack initiation of the polycrystal.

There is very little test data on fatigue crack initiation. For an aluminum alloy 14S-T4 under a cyclic loading of  $10^6$  cycles, [17], the maximum shear stress is higher for the cases of lying in the free surface than that making  $45^\circ$  to the free surface. This

## FATIGUE 87

seems to agree with the curves shown in Fig. 7.

Acknowledgement: The support of the Office of Naval Research through contract N00014-86-K-0153 and the interest of the scientific officer, Dr. Y. Rajapakse, are gratefully acknowledged.

### REFERENCES

1. Forsyth, P.J.E., *Nature*, Vol. 171, 1953, pp. 172-173.
2. Forsyth, P.J.E., *J. Inst. Met.*, Vol. 82, 1954, pp. 449-454.
3. Mott, N.F., 1958, *Acta Metallurgica*, Vol. 6, pp. 195-204.
4. Cottrell, A.H. and D. Hull, 1956, *Proc. Roy. Soc. London A.*, Vol. 242, pp. 211-213.
5. Wood, W.A., 1956, *Fatigue in Aircraft Structures*, Freudenthal, A.M., ed., Academic Press, New York, pp. 1-19.
6. Lin, T.H., 1977, *Reviews of the Deformation Behavior of Materials*, Felham, P., ed., Freund Publishing House, Tel-Aviv, Israel, pp. 262-316.
7. Lin, T.H. and Y.M. Ito, 1961, *J. Mech. Phys. Solids*, Vol. 17, pp. 511-523.
8. Lin, S.R. and T.H. Lin, 1983, *J. Appl. Mech.*, Vol. 50, pp. 367-372.
9. Parker, E.R., 1961, *Mechanical Behavior of Materials in Elevated temperatures*, Dorn, J.E., ed. McGraw-Hill, New York, pp. 129-148.
10. Eshelby, J.C., 1957, *Proc. Roy Soc. A.*, Vol. 241, pp. 376-396.
11. Lin, T.H., 1968, *Theory of Inelastic Structures*, John Wiley & Sons, New York, pp. 43-55.
12. Thompson, N. and N.J. Wadsworth, 1958, *Advances in Physics*, Vol. 7, pp. 72-170.
13. Brown, M.W. and K.J. Miller, 1973, *Proc. Institution Mech. Engrs.*, Vol. 18765/73, pp. 745-755.
14. Cooley, W.U. and T.H. Lin, 1986, *J. Appl. Mech.*, Vol. 53, pp. 550-554.
15. Melan, V.E., 1932, *Zeitsschift fur Angewandte Mathematik und Mechanik*, Vol. 12, pp. 343-346.
16. Tanaka, K., S. Matsuoka and M. Kimura, 1984, *Fatigue of Eng'g. Mater. and Structures*, Vol. 7, No. 3, pp. 195-211.
17. Bundy, R.W. and J. Marin, 1954, *Proc. Am. Soc. Testing Materials*, Vol. 54, p. 755.
18. Miller, K.J. and M.W. Brown, 1981, *Subcritical Crack Growth Due to Fatigue Stress, Corrosion and Creep*, edited by L.H. Larson, Elsevier Appl. Sc. Publisher, pp. 215-239.

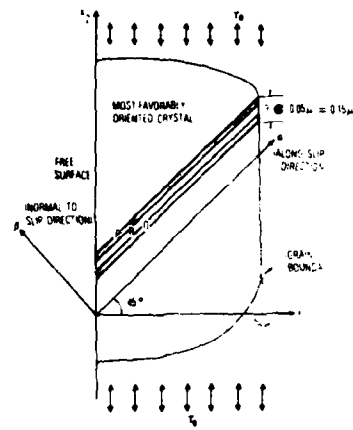


Fig. 1 Most favorably oriented crystal at free surface.

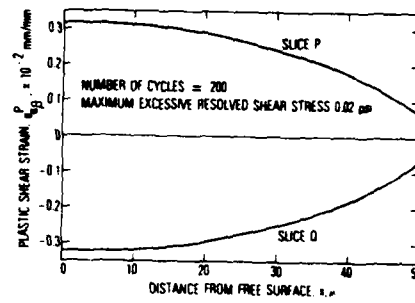


Fig. 2 Plastic shear strain distributions.

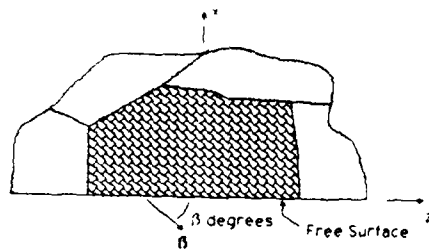


Fig. 3 Normal view of active glide plane. Slip direction,  $\beta$ , forms angle  $\beta$  with free surface.

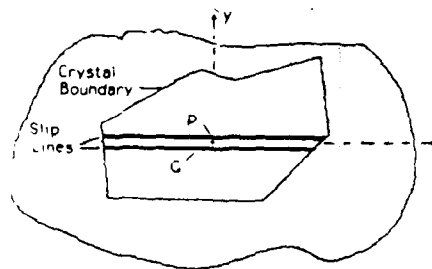


Fig. 4 Surface crystal with two slip lines, P and Q.

# FATIGUE 87

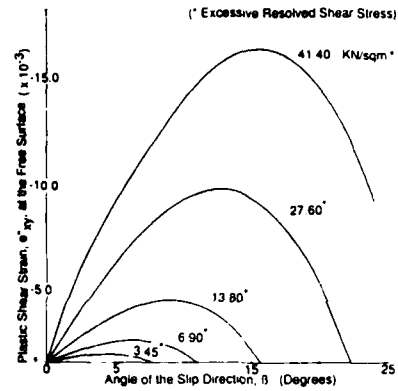
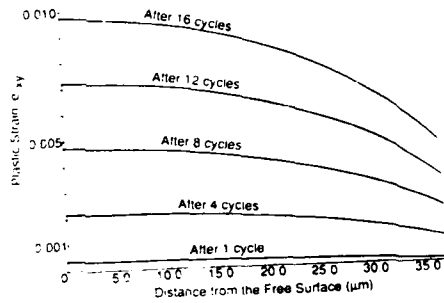


Fig. 5 Plastic shear strain dev.  $e''_{xy}$ , in lower slip line Q;  $\beta=12.75$  deg.

Fig. 6 Plastic shear strain in lower slip line Q, after 16 loading cycles.

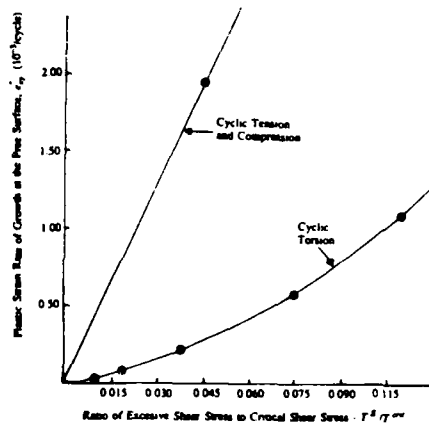


Fig. 7 Plastic strain rate of growth at free surface,  $e'''$ , vs. ratio of excessive shear stress to crit. shear stress

STUDY OF THE CHARACTERISTIC CURVE OF HARDENING AND SOFTENING  
DURING LOW-CYCLE FATIGUE PROCESS

Chen Xinzeng, Fen Zhongxin, Zhang Jianzhong, Chai Huifen.\*

The  $\epsilon$ a.p-N curve measured over the whole gauge length really represents rather the relative rate of the plastic strain spreading rate and the crack initiation rate than the hardening or softening behaviour of materials during fatigue. The hardening can appear in  $\epsilon$ a.p-N curve when the plastic strain spreads to the whole gauge length of specimen before the crack initiates. Otherwise, there will be no hardening. The factors, which favor the expansion of plastic strain and restraint of crack initiation, can promote the appearance of hardening. According to this idea, the first  $\epsilon$ a.p-N curve with hardening part for hardened and tempered steel is obtained finally.

INTRODUCTION

During fatigue process there always is the plastic strain in finite-life designed parts and at the root of sharp notch of infinite-life designed parts. The wide attention has been paid to the strain fatigue at home and abroad. The effect of change in structures and properties of materials during low-cycle fatigue process on the fatigue mechanism and the accurate estimate of fatigue life is of important significance.

So far the characteristics of hardening or softening of the materials under cyclic loading are generally described by fatigue hardening or softening curve, in which the stress amplitude (or strain amplitude) measured over the whole gauge length is expressed as a function of the number of cycles under strain control (or load control). If the stress amplitude is increased with the number of cycles under strain control, it has been simply considered that the hardening effect occurs. Otherwise, the softening effect occurs. (1-4)

\* The Research Institute for Strength of Metals of Xian Jiaotong University, Xian, P.R.C.

E. Macherauch and Eifler et al indicated that there only is softening part in  $\epsilon$ a.p-N curve for hardened and tempered 42CrMo4 steel no matter how the tempering temperature and time vary, as shown in Figures 1 and 2. Hence, according the point of view mentioned above, the hardened and tempered steel is considered as a cyclic softening material.(3,5)

It is worthwhile to discuss if there is no hardening effect at any stage of fatigue for hardened and tempered steel, and if the fatigue softening or hardening curve can represent the real softening or hardening effect of materials. The aim of the present study is to make better understanding of these questions.

#### EXPERIMENTAL PROCEDURES

##### Material

The steel used here is 42CrMo4 (German Specification). The chemical composition of the steel is 0.44%C, 0.32%Si, 0.73%Mn, 0.014%P, 0.028%S, 1.11%Cr, 0.22%Mo.

##### Heat Treatment

The heat treatment of the steel is as follows: austenized at 850 °C for 3 hours and quenched in oil, then tempered at 570 °C for 4 hours.

##### Testing

The testing was carried out on a Schenck electronic servohydraulic fatigue testing machine at 5Hz under load control.

#### RESULTS AND DISCUSSIONS

The results in the paper (6) have indicated the  $\epsilon$ a.p-N or  $\sigma$ -N, in which the strain was measured over the whole gauge length, could not really represent the hardening and softening behaviour of materials. The plastic strain amplitude of normalized state of 40Cr steel was increased at the beginning of cycling, reached its maximum and then decreased with increasing the number of cycles under the constant stress amplitude. However, it is well known that the dislocation density of normalized state is low and increases with increasing the number of cycles at the beginning of cyclic loading. So the hardening effect should occur at first instead of softening.

In order to explain the phenomenon the photoelastic film was pasted on the surface of specimens to observe directly the expansion of the plastic strain zones under the monotonic tension test and the fatigue test(6). As shown in Figures 3 and 4, experiment indicated that for both normalized and quench-tempered 40Cr steel the plastic deformation began at the local regions and then ex-

panded gradually along the gauge length at both loading modes. The similar results obtained by Lukas et al (7) were found in the annealed low carbon steel. The fatigue softening was explained in their paper in terms of the expansion of plastic zone, i.e. spread of Luders strain, which is associated with interaction between dislocations and interstitial atoms. Comparing the result in paper (6) with this result, it seems that, all the iron-carbon alloys will behave like annealed low-carbon steel.

The local macroscopic yielding always expands gradually along the gauge length from local regions, and the speed of expansion may greatly be different depending on the structure of materials. Therefore, the plastic zone either expands to the whole gauge length of specimen before the specimen fractures, or does not. In other words, the degree of plastic deformation may not be uniform in the gauge length. From above discussion it is clear that  $\epsilon_a.p-N$  curve measured over the whole gauge length of specimen does not necessarily represent actual softening or hardening behavior of materials. The softening part of  $\epsilon_a.p-N$  curve, in which the total plastic strain amplitude increases gradually, may be caused by spreading the plastic deformation to other area. Actually, the hardening effect already occurs in the plastic deformation zone. It is reasonable, that there is no hardening part in the  $\epsilon_a.p-N$  curve if the crack nucleates before the plastic strain spreads to the whole range of the specimen. Otherwise, the hardening part will occur after plastic strain expands to the whole range of the specimen.

During monotonic tension test the plastic strain starts from some areas and quickly spreads to the whole range of the specimen before the crack occurs for both normalized and quench-tempered steels, so the strain hardening always occurs in the stress-strain curve. The situation will be different in the fatigue test because of much slower strain spreading rate. There are several possibilities in the case of fatigue. If strain can spread to the whole range before the crack nucleation in the specimen, the hardening part will occur in  $\epsilon_a.p-N$  curve, such as normalized steel. But it is different for quench-tempered steel, in which the crack nucleates before the plastic strain spreads to the whole range of the specimen, no hardening part will occur in  $\epsilon_a.p-N$  curve. Hence, it means that the  $\sigma-N$  or  $\epsilon_a.p-N$  curves really represent rather the relative rate of the plastic strain spreading rate and the crack initiation rate under a specified condition than the hardening or softening behavior of materials under cyclic loading.

All factors, which favor expansion of plastic strain or restraint of crack initiation, will promote occurrence of hardening on the  $\epsilon_a.p-N$  curve. Otherwise, will not. So, it is possible that the different  $\epsilon_a.p-N$  curve can be obtained by change in internal and external factors.

The results in paper (8) showed that the fatigue crack initia-

tion can be delayed by increasing the compressive mean stress. In order to prove the idea that the delay of crack initiation will promote the occurrence of "hardening" effect, one set of test was designed. Figure 5 in which the result of this test was given, shows the  $\epsilon_{a.p}$ -N curves measured under different compressive mean stress for hardened and tempered 42CrMo4 steel. When the mean stress is zero ( $\sigma_m=0$ ), the curve goes up continuously with increasing the number of cycles. Then the curve deviates from original direction (dotted line) and flatten off with increasing compressive mean stress. At last, as expected, the curve drops down in the case of higher compressive mean stress ( $\sigma_m=-350$  N/mm<sup>2</sup>,  $\sigma_a=600$  N/mm<sup>2</sup>), i.e. the "hardening" part occurs in the curve. This result shows that once the crack initiation is restrained by compressive stress, the "hardening" part will occur in the  $\epsilon_{a.p}$ -N curve for hardened and tempered steel 42CrMo4. In addition, the  $\epsilon_{a.p}$ -N curves in Figures 7 and 8 can also be explained by the same view point. The prolongation of tempering time and the increase of tempering temperature benefit spreading of the plastic strain, so that ascending part of  $\epsilon_{a.p}$ -N curves may deviate from original direction.

#### CONCLUSIONS

(1) The  $\epsilon_{a.p}$ -N curve measured over the whole gauge length of the specimen really characterized rather the relative rate of the plastic strain spreading and the crack initiation than the hardening and softening behaviour of materials.

The "hardening" part can appear in  $\epsilon_{a.p}$ -N curve if the plastic strain spreads to the whole gauge length of the specimen before the crack initiates. Otherwise, there is no hardening.

(2) There is no absolute hardening or softening material, which may vary with the change of internal and external conditions.

The hardening part in  $\epsilon_{a.p}$ -N curve of hardened and tempered steel 42CrMo4, which do not appear in the case of symmetrical cyclic loading, can arise under a certain compressive mean stress.

#### SYMBOLS USED

P	= load (N)
$\Delta L$	= increment of length of specimen (mm)
$\sigma_a$	= stress amplitude (N/mm <sup>2</sup> )
$\sigma_m$	= mean stress (N/mm <sup>2</sup> )
$\epsilon_{a.p}$	= plastic strain amplitude (%)

## FATIGUE 87

- N = number of cycle (cycle)  
T = tempering temperature (°C)  
t = tempering time (hour)

### ACKNOWLEDGEMENT

The experiment were carried out mainly in the Laboratory of Research Institute of Materials of Karlsruhe University in Germany. The authors greatly appreciated their helps.

The authors gratefully thank the Science Fund of the Chinese Academy of Sciences for support for this programme.

### REFERENCES

- (1) The society of materials science of Japan, Fatigue of Metals, 1964. (in Japanese)
- (2) P.N Thielen, Acta Met. Vol. 24, 1976, PP.1-10.
- (3) D.Eifler, E.Macherauch, Arch Eisenhüttenwes, Vol.53, 1982, PP.355-360.
- (4) Group of compiling textbook, Mechanical Behaviour of Metals, 1983. (in Chinese)
- (5) D.Eifler, Dr. -Ing. Diss., Univ. Karlsruhe, 1981.
- (6) Chai Huifen, Chen Xinzeng, Liang Xin, Liu Jinghua, Journal of Xian Jiaotong Univ., Vol.20, No.4, 1986, PP.43-51.
- (7) M.Klesnil, P.Lukas, ISIJ. Vol.205, 1967, PP.746-749.
- (8) Wang Baijian, Selected papers of graduation theses, Xian Jiaotong Univ., 1985. PP.40-44. (in Chinese)

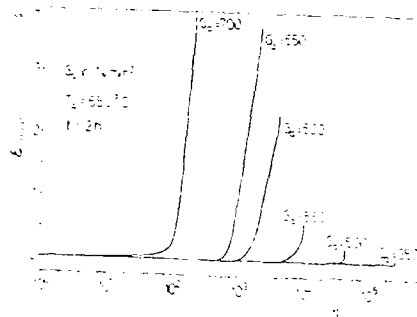


Figure 1 Cyclic strain curves for 42CrMo4.

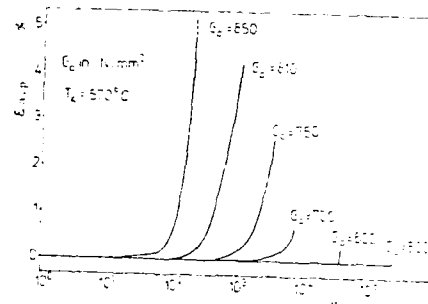


Figure 2 Cyclic strain curves for 42CrMo4.

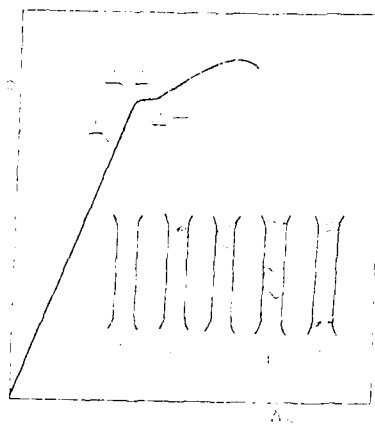
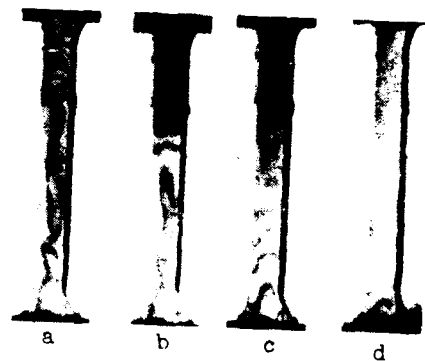


Figure 3 Stress-strain curve for 40Cr



- a. Isochromatic striations (upper) and elastic zone (under).
- b, c. Striations moving downwards.
- d. Striations disappearing.

Figure 4 Photos of plastic strain spreading for 40Cr

# FATIGUE 87

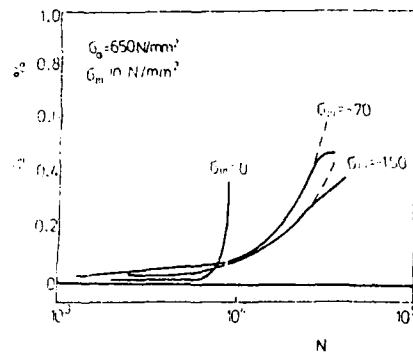


Figure 5 Cyclic strain curves under compressive mean stress.

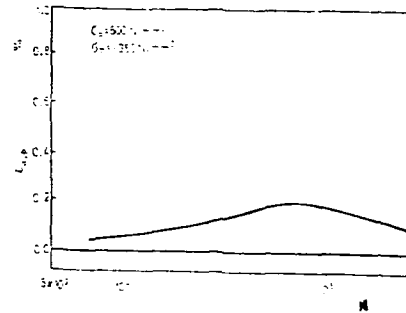


Figure 6 Cyclic strain curves under compressive mean stress.

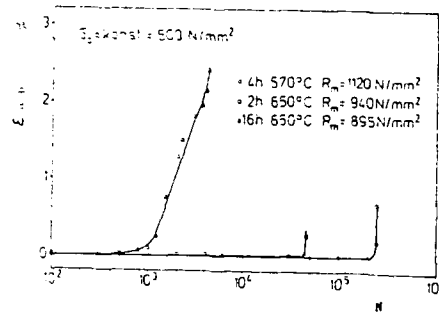


Figure 7 Cyclic strain curves for 42CrMo4

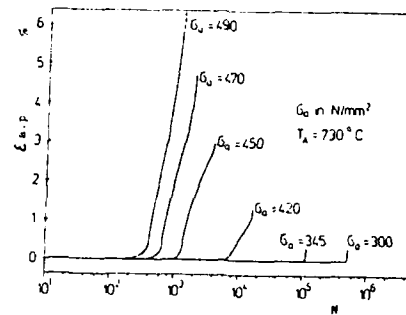


Figure 8 Cyclic strain curves for 42CrMo4

FATIGUE 87

## FATIGUE 87

### THE EFFECT OF PRETRAINING ON FATIGUE CRACK GROWTH IN NICKEL-BASE ALLOYS

J.M. Kendall\*, M.A. Hicks<sup>†</sup> and J.E. King\*

The effect of prestrain on near-threshold fatigue crack growth in the nickel-base alloy, N901, has been examined at 20°C and 600°C. Prestraining was carried out in tension at room temperature, producing planar dislocation arrays. Fatigue crack growth rates were slightly higher and threshold values lower in prestrained material than in as-received material, with most effect at 20°C and at low load ratios. Planar facets were observed on the fatigue fracture surfaces of prestrained material. The results are discussed in terms of the interaction of dislocations in the reversed plastic zone with the artificially introduced dislocation arrays, and the effect of prestraining on fatigue crack closure is considered.

### INTRODUCTION

In order to optimise the mechanical properties of critical aeroengine components such as compressor and turbine discs, it is essential to obtain good microstructural control of the forging route, such that fine and coarse grained structures can be established within particular regions of a disc (1). However, complex deformation structures are introduced into the material during forging, some of which are retained, in partially recrystallised grains, after forging and subsequent heat-treatment (2). These residual dislocation arrays, known as retained work structures, are now recognised as having an important influence on fatigue properties.

In the nickel-base alloy, N901, it has been shown that retained work in the form of planar dislocation arrays can adversely affect low cycle fatigue behaviour (2,3). This paper describes the results of a study to examine the effect of planar arrays on fatigue crack growth behaviour. An understanding of how these residual dislocation structures affect the growth of fatigue cracks

\*Dept. of Metallurgy & Materials Science, University of Nottingham.

<sup>†</sup>Rolls-Royce plc, Derby.

## FATIGUE 87

is important for microstructural optimisation and component life prediction.

### MATERIAL

The N901 alloy is a Ni-Cr-Fe alloy with a nominal composition of 42Ni, 37Fe, 12.5Cr, 3.0Ti, 5.7Mo, 0.25Al, 0.004C and 0.014B. The material was given a solution heat-treatment in the range 950 to 1050°C and quenched in oil. Two stage ageing was carried out at 700-750°C for 6 hours followed by 720°C for 2 hours. Finally the material was stress-relieved at 650°C for 12 hours and air cooled. The microstructure is shown in Figure 1. Groups of carbides were observed, associated with needles of the  $\eta$  phase. The 0.2% proof stress was measured as 960 MNm<sup>-2</sup>.

### EXPERIMENTAL TECHNIQUES

#### Specimens and Prestraining Method

Long crack threshold tests were carried out in the as-received condition and in prestrained material using single edge notched bend (SENB) specimens of the dimensions shown in Figure 2. Specimens to be tested in the as-received condition were machined directly from a disc forging after heat-treatment. Specimens to be prestrained were machined initially with gripping blocks at the ends and prestrained in tension as shown in Figure 3. Total prestrains of 5.5% and 7.0% were used, corresponding to maximum applied stresses of 1040 MNm<sup>-2</sup> and 1090 MNm<sup>-2</sup> respectively. SENB fatigue specimens were cut from the gauge length, with no further grinding.

#### Threshold Test Method

Threshold tests were carried out using a servohydraulic testing machine with a capacity of 50 kN. The specimens were tested in four point bend loading at a frequency of 50 Hz, and the crack length was measured continuously using the direct current potential drop (DCPD) technique. High temperature tests were carried out by positioning a furnace around the specimen, and the temperature was maintained to within  $\pm 2^\circ\text{C}$ .

Near-threshold crack growth rate data were obtained using a load-shedding procedure with load decrements of 5-10% until crack growth could not be detected in  $10^6$  cycles. The loads were then increased in increments of 10%, and it was found that there was good agreement between results obtained in the load-shedding and load-increasing parts of the test. Threshold tests were carried out at temperatures of 20°C and 600°C, at load ratios,  $R$ , of 0.1 and 0.8.

The fatigue fracture surfaces were examined by scanning electron microscopy, and nickel-plated sections of the surfaces

## FATIGUE 87

were examined by optical microscopy.

### RESULTS

#### Prestraining

The dislocation structures introduced by prestraining at room temperature were observed using transmission electron microscopy and found to consist of planar dislocation arrays, as shown in Figure 4 for a specimen subject to 7.0% total strain.

#### Threshold Tests

The results of the threshold tests are shown in Figure 5 and Figure 6. At 20°C near-threshold crack growth rates were higher in prestrained material than in as-received material, and the threshold was lower. The difference was most marked at a load ratio of 0.1. At 600°C near-threshold crack growth rates were higher and the threshold lower than at 20°C, for both material conditions, and the threshold was approached more suddenly at the higher temperature. There was a small difference in threshold values between the prestrained and as-received material.

On breaking open the test pieces it was found that the crack fronts were straight in all tests, indicating that uneven residual stresses were not produced by prestraining.

#### Fractography

It was found that the fracture surface appearance of the as-received material was similar to that reported in previous work (4). For material tested at 20°C at  $R = 0.1$  the surface at higher stress intensities was relatively flat with changes of direction at the grain boundaries, whilst near threshold the mode of fracture became more crystallographic with many sharp changes in crack plane. The fractographic appearance at  $R = 0.8$  was similar to that at  $R = 0.1$ .

At 600°C the fracture surface at higher stress intensities was similar to that at 20°C, but there was some oxidation of the surface. In contrast to the room temperature fractography, however, the fracture surface at threshold was not significantly different from that at higher stress intensities and there was no evidence of a crystallographic fracture mode. The near-threshold fractography in the as-received material tested at 20°C and 600°C is shown in Figures 7 and 8.

The fracture surface appearance of the prestrained material was characterised by the presence of planar facets, which were observed at near threshold and higher stress intensities at both load ratios and temperatures, although they were more distinct at 20°C. Some of the planar facets were isolated, but they were also found to

## FATIGUE 87

occur in groups, frequently at right angles or in the form of pyramidal peaks. Examples are shown in Figures 9-11 on near-threshold fatigue fracture surfaces at 20°C and 600°C.

The planar nature of the facets could be clearly seen when the fatigue fracture surfaces of the prestrained specimens were nickel-plated and sectioned. Figure 12 shows facets on the fatigue surface of a specimen prestrained 7.0% and tested at room temperature.

### DISCUSSION

The localisation of slip into dense planar arrays of dislocations on active slip planes within grains is characteristic of the deformation of many nickel-base alloys at room temperature, as discussed by Gell et al (5). The degree of cross-slip is low, due to the low stacking fault energy of the matrix and deformation processes involving the shearing of ordered coherent precipitates. Planar slip has been observed in both fatigue and monotonic deformation at room temperature (5).

It was found in the present study that the presence of planar dislocation arrays in prestrained material led to slightly higher fatigue crack growth rates and lower threshold values than in unstrained material. In places the artificially introduced dislocation arrays appeared to act as preferential paths for the fatigue crack to follow, producing large planar facets on the fracture surface. The effect was less marked at 600°C, when the mode of near-threshold fatigue crack growth was less crystallographic than at room temperature.

Previous studies have shown that prestraining can have different effects on fatigue behaviour in different materials. Similar effects to those observed here, that is, an elevation of fatigue crack growth rates and reduction in threshold values following prestrain, have been observed in low carbon steel (6) and aluminium alloys (7). Conversely, crack growth rates were reduced and threshold values increased by prestraining stainless and mild steels (8), dual-phase steel (9), copper (10) and 90/10  $\alpha$ -brass (10). In 70/30  $\alpha$ -brass, no effect of prestrain or prior cold work on crack growth rates was observed (10,11).

In order to rationalise these results it is necessary to consider a number of factors which may be influenced by the application of a tensile prestrain prior to fatigue testing, including any effect of prestrain on the mechanism of fatigue fracture, the interaction of the dislocation structures produced by prestraining with those in the reversed plastic zone and the degree of closure experienced at the crack tip.

It is generally found that the mechanism of fatigue failure is not significantly altered by prestraining (12). This was observed

## FATIGUE 87

in the present study, although additional planar facets were present on the fracture surface of the prestrained material. Attempts have been made to relate the results of monotonic tests to fatigue crack growth in prestrained materials (6), but the fracture mechanisms are significantly different. In particular, the tensile fracture of a specimen by work hardening of the whole gauge length followed by the growth and linkage of voids cannot be directly related to the mechanism of fatigue crack growth involving cyclically hardened material in the reversed plastic zone at the crack tip. The lack of consistency in the results of studies of the effect of prestrain on fatigue crack growth rates shows that a simple approach in terms of tensile parameters cannot be used to explain the results.

There is evidence that the nature of the dislocation structures introduced by prestraining, and their interaction with the dislocation structures in the reversed plastic zone, are significant factors determining the effect of prestrain on fatigue behaviour. Cellular dislocation arrays were produced when copper and 90/10  $\alpha$ -brass were prestrained or cold-worked, and it was found that crack growth rates were lower, and threshold values higher, than in unstrained material (10,12). In 70/30  $\alpha$ -brass, however, planar dislocation arrays were formed and there was no effect of prestrain on near-threshold behaviour (10,11). In the present study the introduction of planar dislocation arrays has been shown to lead to a slight elevation of crack growth rates. This suggests that for face centred cubic alloys, deforming by planar slip, pre-existing cellular dislocation arrays may hinder the development of intense slip bands and thus reduce the amount of crack extension per cycle, whereas prior localisation of slip into planar arrays provides a favourable path for fatigue crack growth and may lead to an elevation of crack growth rates. More work is needed to investigate the effect of different pre-existing dislocation substructures on fatigue crack growth in other materials.

A further factor to take into account is the effect of the tensile prestrain on the degree of closure experienced at the crack tip during subsequent growth of a crack through the material. Schijve (7) postulated that if the degree of plasticity-induced closure is directly proportional to the monotonic plastic zone size in the wake of the crack, then the effect of prestraining is to increase the monotonic yield stress, reduce the plastic zone size, and reduce the amount of closure. It was found, however, that although less closure was measured in prestrained aluminium alloy specimens than in unstrained specimens, the results of the closure measurements could not fully account for the significant elevation in crack growth rate in the prestrained material (7).

The results obtained in the present study also cannot be fully explained in terms of closure. It is possible that the amount of roughness-induced closure was in fact greater in the prestrained material than in the as-received material, due to the increase in

## FATIGUE 87

surface roughness associated with planar facets on the fracture surface after prestraining. It can be seen from Figure 5 that higher crack growth rates were measured in prestrained material than in as-received material at a load ratio of 0.8, when effects of closure on fatigue crack growth rates are minimal.

To summarise, it appears that the effect of prestrain on near-threshold fatigue crack growth behaviour is complex and cannot be explained simply in terms of monotonic tensile parameters or fatigue crack closure. It is considered that one of the most significant factors determining whether prestrain is beneficial or detrimental to fatigue properties is the nature of the dislocation substructure introduced by prestraining.

### CONCLUSIONS

1. For the nickel-base alloy, N901, a tensile prestrain at room temperature produces dense planar arrays of dislocations in the material.
2. At 20°C and 600°C fatigue crack growth rates in prestrained material were slightly higher and threshold values lower at both  $R = 0.1$  and  $R = 0.8$  when compared with unstrained material.
3. Fractographic evidence showed that the pre-existing planar dislocation arrays acted as favourable paths for the fatigue crack to follow.

### ACKNOWLEDGEMENTS

The authors are grateful to the SERC and Rolls-Royce plc for financial support for the project, and to Professor J.S.L. Leach for provision of laboratory facilities.

### REFERENCES

- (1) Postans, P.J. and Jeal, R.H., "Forging and Properties of Aerospace Materials", The Metals Society, 1978, pp. 300-307.
- (2) Meethan, G.W., Proceedings of the Conference on "High Temperature Alloys for Gas Turbines", Liege, Belgium, Applied Science Publishers, 1978, pp. 837-859.
- (3) Turner, F., "The Development of Gas Turbine Materials", Edited by G.W. Meethan, Applied Science Publishers, 1981, pp. 177-205.
- (4) Venables, R.A. and King, J.E., Proceedings of the Second International Conference on "Fatigue and Fatigue Thresholds", Birmingham, England, EMAS, Vol. 3, 1984, pp. 1371-1378.

AD-A184 046

FATIGUE '87 VOLUME 2(0) VIRGINIA UNIV CHARLOTTESVILLE  
SCHOOL OF ENGINEERING AND APPLIED SCIENCE  
R O RITCHIE ET AL JUN 87 N00014-87-G-0008

5/6

UNCLASSIFIED

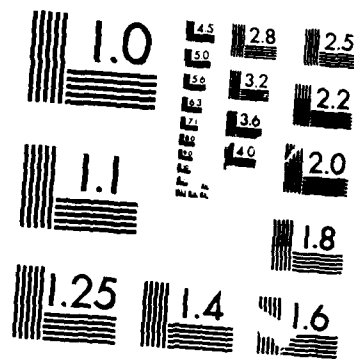
FAC 30/11 NL

5 30 3

5 30 3

5 30 3

5 30 3



MICROCOPY RESOLUTION TEST CHART  
NATIONAL BUREAU OF STANDARDS-1963-A

## FATIGUE 87

- (5) Gell, M., Leverant, G.R. and Wells, C.H., ASTM Special Technical Publication 467, "Achievement of High Fatigue Resistance in Metals and Alloys", 1970, pp. 113-153.
- (6) Blacktop, J., Nicholson, C.E., Brook, R. and Towers, R.T., Proceedings of the First International Conference on "Fatigue Thresholds", Stockholm, Sweden, EMAS, Vol. 2, 1982, pp. 629-637.
- (7) Schijve, J., Engng. Fract. Mech., Vol. 8, 1976, pp. 575-581.
- (8) Radhakrishnan, V.M. and Baburamani, P.S., Mats. Sci. and Engng., Vol. 17, 1975, pp. 283-288.
- (9) Wasen, J., Hamberg, K. and Karlsson, B., Scripta Met., Vol. 18, 1984, pp. 621-624.
- (10) Ishii, H. and Yukawa, K., Met. Trans., Vol. 10A, 1979, pp. 1881-1887.
- (11) McEvily, A.J., Boettner, R.C. and Bond, A.P., J. Inst. Metals, Vol. 93, 1965, pp. 481-482.
- (12) Mullner, H., Weiss, B. and Stickler, R., Proceedings of the First International Conference on "Fatigue Thresholds", Stockholm, Sweden, EMAS, Vol. 1, 1982, pp. 423-440.

# FATIGUE 87



Fig. 1. Microstructure of N901 alloy.

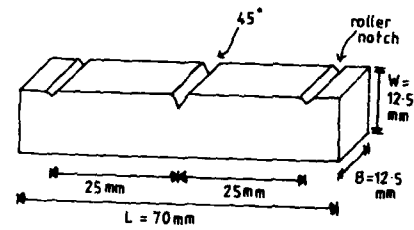


Fig. 2. Single edge notched bend specimen dimensions.

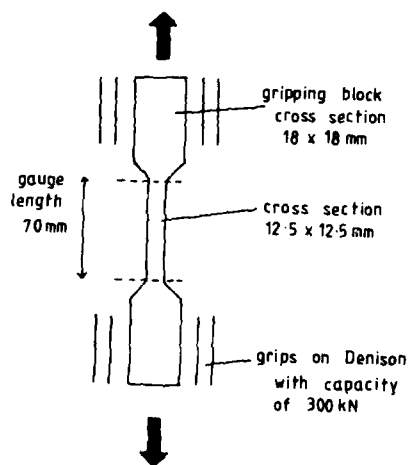


Fig. 3. Prestraining in tension. Fig. 4. Planar arrays of dislocations in specimen prestrained 7%.

# FATIGUE 87

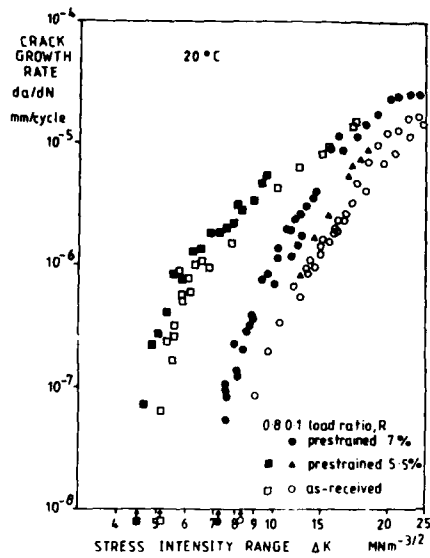


Fig. 5. Fatigue crack growth rate data at 20°C.

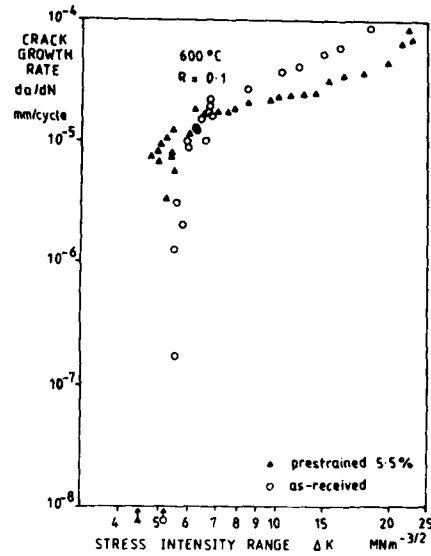


Fig. 6. Fatigue crack growth rate data at 600°C.



Fig. 7. Near-threshold, 20°C, R 0.1, as-received material.



Fig. 8. Near-threshold, 600°C, R=0.1, as-received material.



Fig. 9. Planar facets, near  $\Delta K_{th}$ , 20°C, R=0.1, prestrained 7%.

Fig. 10. Planar facets, high  $\Delta K$ , 20°C, R=0.1, prestrained 5.5%.



Fig. 11. Planar facets, near  $\Delta K_{th}$ , 600°C, R=0.1, prestrained 5.5%.

Fig. 12. Ni-plated section, 20°C, R=0.1, prestrained 7%.

## FATIGUE 87

### MIXED MODE FATIGUE CRACK GROWTH USING THE BRASILIAN DISC.

M. LOUAH\* G. PLUVINAGE\* and A. BIA.\*

Mixed mode fatigue crack growth has been studied using a Brazilian disc. This sample was chosen because of machining easiness and for the possibility of a continuous variation of the  $K_I/K_{II}$  ratio. It is necessary to define an equivalent straight crack which allows the computation of  $K_I, K_{II}$  according to the Atkinson formula. In this study, we have seen that the bifurcation angle follows the maximum circumferential stress criterion and to define fatigue crack growth, a new equivalent stress intensity factor range is necessary.

### INTRODUCTION

Mixed mode fatigue crack growth is a transient phenomenon which occurs during the period when a crack tends to initiate in a direction normal to the principal tensile stress. Such a situation occurs when a preexistent inclined crack is cyclically loaded or when there is a change in the loading directions. First, tests in mode I and mode II fatigue crack growth were conducted by IIDA and Kobayashi in 1969 on CCP samples. The same kind of sample was used later by Tanaka(2), Pustejowski(3), Bad Alliance(4), Barthelemy(5) and Chinadurai(6). In this kind of sample, the stress intensity factor of an inclined crack of  $2a$  length and inclined angle  $\beta_0$  is given by the following formula :

$$K_I = K_R \sin^2 \beta_0 ; K_{II} = K_R \cos \beta_0 \sin \beta_0 \quad (1)$$

$$K_R = \sigma \sqrt{\pi a} \cdot F(a/W) \quad (2)$$

where  $F(a/w)$  is a geometric correction factor.

The possibility of this kind of sample is limited to small thicknesses because a high load is generally required for fatigue cracking. Also the  $K_I/K_{II}$  ratio is relatively limited (less than 2).

\*Laboratoire de Fiabilité Mécanique de Metz France

Broek and Rice(7), Hua and al(8) preferred to use a four point bending sample with symmetrical loading. The values of the stress intensity factor of this sample were obtained by Wang and Pluvinage(9) using the weight function. Unfortunately these samples generally have a small ligament. Flavenot(10) used CT samples with two dissymmetric arms but the range of the ratio is very limited. High values are avoided because of the longest arm. Uniaxial compression fatigue crack growth was conducted by Smith(11) using a CCP sample with an inclined crack. Biaxial loading and mixed mode fatigue crack propagation were performed by Hourlier(12) and Truchon and al(13). These experiments require a biaxial fatigue testing machine, costly samples and also make for misalignment problems. Nevertheless out of phase solicitations are possible. At present, these are relatively rare. A good method of study, for in phase loading of mixed mode fatigue crack growth requires cheap and easily machined samples, a low capacity uniaxial fatigue machine. In addition, the sample can allow large continuous variations of the  $K_{II}/K_I$  ratio.

In the study of fatigue crack propagation in mixed mode there are two points of interest : the bifurcation angle and the loading parameter which governs the fatigue crack propagation. Prediction of the bifurcation angle is generally made using the same criteria as for mixed mode fracture. Although more than 33 criteria exist for this problem(14), many of these belong to the same family and give very close predictions. For mixed mode(1+2) fatigue crack growth, the criterion which is most often used and gives satisfactory results is the maximum tangential stress criteria which gives a bifurcation angle  $\Theta_0$  according to the following formula :

$$\tan(\Theta_0) = \frac{1}{4} \left( \frac{K_I}{K_{II}} \right) + \sqrt{\frac{K_I^2}{K_{II}^2} + 8} \quad (3)$$

It seems that the strain energy intensity criterion can be used only in a satisfactory manner for a limited range. The length is generally preferred due to the fact that the crack is curvilinear. Many authors have suggested that only the opening mode governs the fatigue crack propagation but experimental evidence of the influence of mode 2 led to the conclusion that an equivalent stress intensity factor range is needed. Several possibilities exist.

#### THE USE OF THE BRASILIAN DISC FOR MIXED MODE CRACK PROPAGATION.

The name of the "Brazilian disc" comes from the work of two Brazilian researchers(15) who have studied the failure path of big steel pipes filled with concrete and used for moving an old church. They found that the diametrical failure path was governed by a quasi-uniform tensile stress which characterises the state of stress of such a disc when a compression load is applied to it. This kind of sample slotted

or cracked is now often used to perform fracture mechanics tests on concrete, rock, ceramic and more seldom on metals. When the initial crack of  $2a$  length, is inclined with a  $\beta_0$  angle and punctually loaded in the X direction, a mixed mode of loading is present at the crack tip. Near this point, the state of stress can be described by superposing the  $K_1$ ,  $K_2$  parameters governing stress singularities. Several solutions to this problem can be found in publications /16/ 17/18/.

Atkinson has proposed a numerical resolution of the Fred Holm equation for this problem. The stress intensity factors  $K_1$  and  $K_2$  obey the following relation :

$$N_1 = \frac{K_2}{K_0} = \sum_{i=1}^5 T_i \left( \frac{a}{R} \right)^{2i-1} A_i(s); \quad N_2 = \frac{K_1}{K_0} = 2 \sin \beta \sum_{i=1}^5 S_i \left( \frac{a}{R} \right)^{2i-1} B_i(s) / 4$$

$$K_0 = \frac{P}{\sqrt{\pi a}} \sqrt{\frac{R}{B}}$$

with  $P$ =Load,  $R$ =radius of the disc,  $B$ =Thickness

Atkinson gives the value of  $T_i$ ,  $S_i$ ,  $A_i$ ,  $B_i$ , for  $i=1$  to 5. We have made experimental and numerical verifications and found that the Atkinson formula gives satisfactory values of  $K_1$  and  $K_2$ .

The use of the Brazilian disc offers the possibility of obtaining a large continuous range of  $K_1/K_2$  ratios. For  $\beta_0$  less than  $25^\circ$  ( $a/R=0,5$ ), this ratio is positive. For  $\beta_0 = 25^\circ$ , we obtain  $K_1/K_2 = 0$  and pure mode 2 and for  $\beta_0$  greater than this value, negative values of  $K_1/K_2$  give "non-pure" mode 2. All these values can be obtained simply by rotating the disc.

#### Experimental methods.

Tests have been performed on 2 materials : high strength steels 35NCD16 and stainless steel 316. Mechanical properties of these steels are listed in Table 1.

TABLE 1 - Mechanical properties of materials.

	MPa	MPa	MPa
35NCD16 (Heat treated)	1100	1500	46
35NCD16 (as received)	450	800	20
316	265	550	83

Crack is initiated in the disc by a compressive load of 7 tons at frequency 40 Hz with a stress ratio of 0,1.

After precracking, the disc is inclined and the crack propagates in a curvilinear manner in order to recover a crack propagation direction normal to the principal tensile stress.

Each increment of crack propagation is obtained by measuring the projection of crack propagation on to the X and Y axis and according the following formula :

$$ds = \sqrt{da_x^2 + da_y^2} \quad (5)$$

In the computation of the stress intensity factor, it is necessary to take into account the curvilinear shape of the crack path. Due to the complexity of such a problem, we preferred to use an equivalent straight-crack which is equal to segment OA. At each increment of crack propagation  $\Delta s_i$  a new bifurcation angle  $\theta_i$  and a new inclination angle  $\beta_i$  is defined:

$$\theta_i = \frac{\pi}{2} + \beta_{i-1} - \arctg\left(\frac{da_x}{da_y}\right)$$

$$\beta_i = \beta_{i-1} - \arctg\left(\left(\Delta s_{i-1}\right) \sin \theta_{i-1} / a_{eq,i-1} + \Delta s_i \cotg \theta_i\right)$$

$$a_{eq,i} = \left(a_{eq,i-1}^2 + 2a_{eq,i-1} \Delta s_i \cos \theta_i + \Delta s_i^2\right)^{1/2} \quad (6)$$

#### Results and discussion.

The crack trajectory is modified by the initial crack angle  $\beta_0$ . The crack curvature increases when we increase the amplitude of mode 2 by increasing  $\beta_0$ . For "non-pure" mode 2, the crack initiates, not at the precrack tip but on the free surface of the initial slot. For each value of  $\beta_0$  that we have tested ( $=0^\circ; 5^\circ; 9,5^\circ; 14,5^\circ; 25^\circ; 34^\circ; 45^\circ$ ), computed values of K1 increase and K2 values decrease during crack propagation. The crack bifurcation angle, which is maximum just after inclination of the disc decreases also when the crack propagates. The initial bifurcation angle increases with the  $\beta_0$  angle and reaches a constant value of  $70^\circ$  for  $\beta_0$  greater than  $25^\circ$ , as shown in figure 3. This initial bifurcation angle and current bifurcation angle obey the maximal circumferential stress criterion (current bifurcation angle predictions are calculated using equivalent straight crack). These results are in accord with those of other publications.

The total crack length for the same number of cycles decreases when the ratio  $K_{II}/K_I$  increases. For "non-pure" mode 2, a delay appears which can be explained by friction on crack surfaces. When the displacement of the slots measured, we can see that the linear part of the crack is under compression ( $V_a < 0$ ). After a certain amount of crack propagation, the compressive part of the crack disappears. Evidence of this compression can also be detected using a scanning electron microscope. It is important to notice that compression occurs only on the linear part of the crack and never on the curved branch.

An other phenomenon appears as well; for a  $\beta_0$  angle, greater than  $15^\circ$ , we obtained a forked crack; but one branch rapidly stops and the second tends to reach the direction of mode 1 propagation. The small branch is stopped because it propagates under

shearing stresses first, then 2 or 3 mm further under compressive stresses. As in the Paris' Law, it is interesting to express the crack growth rate  $da/dN$ , in terms of a parameter which expresses a stress gradient in a mixed mode of cyclic loading. The way to check the validity of such a parameter is to make sure all the data fit in a small scatter band in a log-log diagram.

Although the crack tends to recover the mode 1 and that many authors use the  $K_I$  parameter for solving this problem, we don't recommend its use because all our experimental results clearly show an influence of mode 2. For this reason it is necessary to use an equivalent stress intensity factor range which is a combination of  $K_I$  and  $K_{II}$ . After checking, many available criteria, we were disappointed by their poor measure of reliability. For this reason we proposed a new parameter for governing the fatigue crack growth in mixed mode of loading which is based on the following assumptions.

- Fatigue crack growth of the curved crack, loaded in mixed mode is governed by crack tip opening displacement.
- This crack tip opening displacement is a combination of the major equivalent straight crack displacements  $S_I^0$  and  $S_{II}^0$ .
- The crack opening displacement is the projection of two displacements of the equivalent straight crack in the bifurcation direction.

$$S_I = S_I^0 \cos \theta + S_{II}^0 \sin \theta$$

$$S_{II} = S_I^0 \sin \theta + S_{II}^0 \cos \theta \quad (7)$$

The total crack opening displacement is then given by :

$$S_T = S_I^0 (\cos \theta + \sin \theta) + S_{II}^0 (\cos \theta + \sin \theta) \quad (8)$$

Since  $S_I^0$  and  $S_{II}^0$  are respectively proportionnal to  $(\Delta K_I)^2$  and  $(\Delta K_{II})^2$ . The equivalent stress intensity factor range is given by the following relation :

$$\Delta K_{eq} = \sqrt{(\Delta K_I)^2 + (\Delta K_{II})^2} \cdot \sqrt{\cos \theta + \sin \theta} \quad (9)$$

To take into account the fact that the real crack is curved and our model is based on the equivalent straight crack, a geometrical correction is introduced :

$$\alpha_{i-1} = \frac{a_{eq,i-1} + \Delta a_i}{\Delta a_i} \quad (10)$$

The generalised equation is :

$$\Delta K_{eq,i} = \alpha_{i-1} \cdot \sqrt{\Delta K_{I,i-1}^2 + \Delta K_{II,i-1}^2} \cdot \sqrt{\cos \theta + \sin \theta} \quad (11)$$

The friction which occurs on the straight part of the crack for "non-pure mode 2 is taken into account by introducing a reduction factor  $\Phi$  into the equivalent stress intensity factor range. The effective stress intensity factor range is given by :

$$\Delta K_{eff} = \Delta K_{eq} (1 - \Phi) \quad (12)$$

## FATIGUE 87

The reduction factor  $\bar{\Phi}$  is equal to zero for an inclination angle  $\beta^*$ . Experimental measurements of  $V_H$  displacement (Figure 2) show that contact between crack surface appears for  $\beta^*$  greater than  $13^\circ$ .

A simple formula for  $\bar{\Phi}$  is proposed :

$$\bar{\Phi} = \left( \frac{\beta - \beta^*}{\beta^*} \right) \cdot f \quad (13)$$

Other experimental results "non-pure" mixed mode fatigue indicate that fatigue crack growth is stopped for  $\beta_0 = 45^\circ$ , and a new crack is initiated on the slot surface. These arrested condition gives  $\bar{\Phi} = 1$  and a friction coefficient value equal to which is a reasonable value for the friction between rough crack surfaces. All our experimental results are plotted in a diagram  $\log da/dN$  versus  $\Delta K_{eff}$  fit relatively well on a narrow scatter band (See figure 4).

A more sophisticated model can be used an equivalent straight kinked crack and the  $\Delta K_I^*$  and  $\Delta K_{II}^*$  stress intensity factor of the kinked crack. This model gives a more scattered representation of the phenomenon.

### CONCLUSION.

For the first time, a Brazilian disc was used to study mixed mode fatigue crack propagation. This sample has several advantages; easy machining and possibility of obtaining a continuous range (including negatives values) of  $K_I/K_{II}$  ratios. We have found that during crack propagation, the bifurcation angle follows the maximal circumferential stress. To represent fatigue crack growth in a similar way to the Paris Law, an equivalent effective stress intensity factor range which takes into account the friction on the straight part of the crack is required.

### BIBLIOGRAPHY.

- (1) IIDA, S. KOBAYASHI, A.S.J of basic Eng. ASME, 1969 pp 764 769.
- (2) TANAKA, K. Eng. Fract. Mech. Vol.6 , 1974 pp 493-507.
- (3) PUSTEJOVSKY M.A. Eng. Fract. Mech. Vol.11 , 1979 pp 9-31.
- (4) BADALIAN R. Greece Symp. on mixed mode crack propagation. Sitjhoff and Nordhoff Int. Pub Nederlands 1981.
- (5) SIH G., C. and Barthelemy, B.M. Eng. Fract. Mech. Vol. 13 1980 pp 657-666.
- (6) CHINADURAI, R. Pandey, R.,K. Joshi,B,K. Adv. in Fract. Res. I.C.F.G. New Dehli India Vol. 2 1984 pp 1703-1710.
- (7) BROEK, P. Rice R.C. Report FRA/ORD 81/30 Battele Columbus lab. 1981.

# FATIGUE 87

- (8) HUA, G. BROWN, M,W. MILLER, K,J. Fatigue of Engineering Mat and Structure, Vol. 5, 1980 pp 1-17.
- (9) WANG, PLUVINAGE G. Proceeding of ICSMA. G. Melbourne pp 995-1000.
- (10) FLAVENOT J.F., SERRES, D.GREGOIRE, R. ANTON, F. CEA rapport DSN N° 358 1980.
- (11) SMITH, M,C. Smith R.A., Wear, Vol. 76 1982 pp 105-128.
- (12) HOURLIER F. Thesis University of Compiègne 1982.
- (13) TRUCHON,M. AMESTOY,M.DANG VAN, K. Proc. of ICFS, Cannes, 1981 pp 1841-1850.
- (14) JODIN P., PLUVINAGE G.Cahiers du G.F.R., N°2,1979 pp 59-69.
- (15) CARNEIRO,F,L,L,B and Barcellos A. Report of Union of testing and research laboratories for materials and structures N°13. 1983.
- (16) KIM C.S KITAGAWA M. Fract. Mech. and Technology edited by SIH,G,C.Chow CL, Vol.2 1977 pp 1011-1019.
- (17) AWAJI, H. SATO,S. J of Eng. Mat Tech, Vol. 1100 1978 pp 175-182.
- (18) ATKINSON C. Int. J of Fract., Vol.8 N°4 1982 pp 279-291.

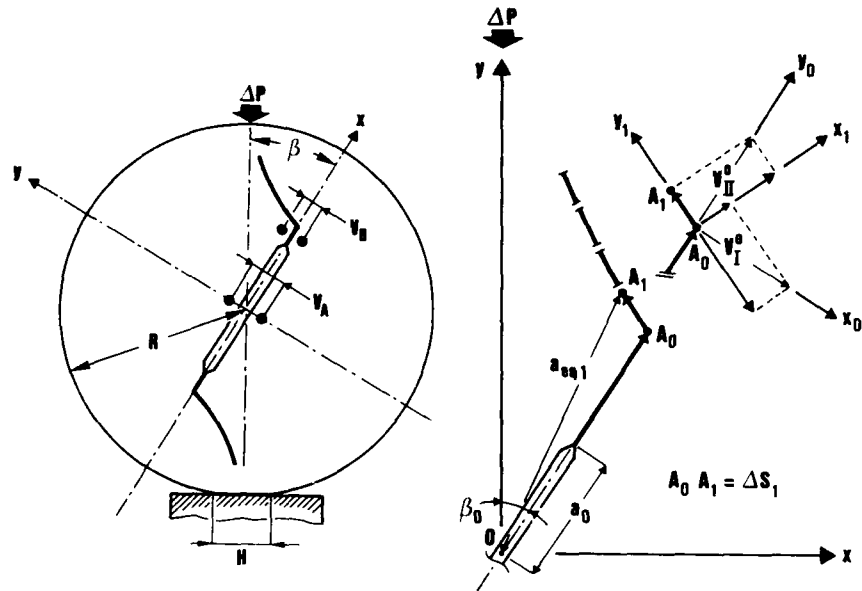


Figure 1 Geometry of the Brazilian disc. Figure 2 Definition of the equivalent crack length.

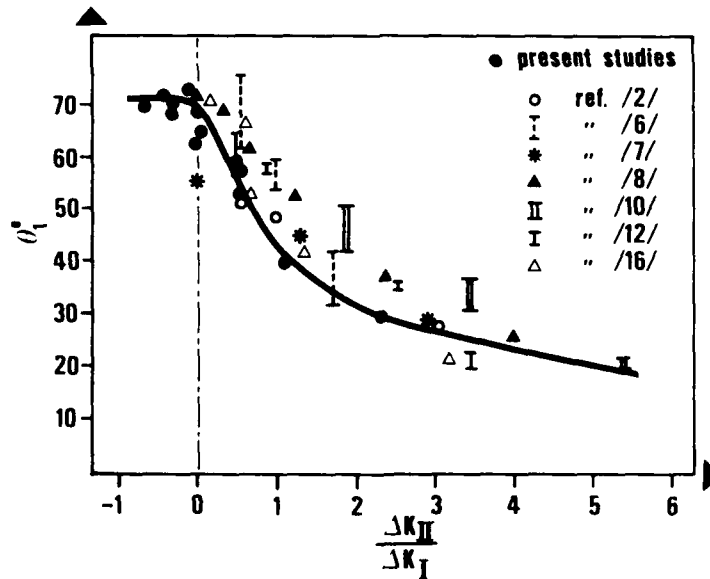


Figure 3 Initial bifurcation angle obtained on a Brazilian disc and comparison with past published results.

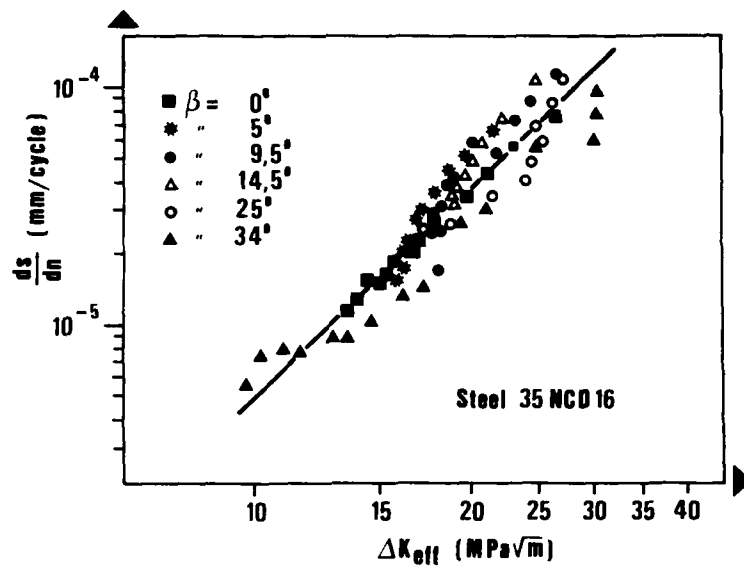


Figure 4 Representation of the fatigue crack growth versus effective stress intensity factor for mixed mode fatigue crack propagat.

FATIGUE 87

## CRACK CLOSURE PHENOMENA IN MODES I AND II INTERACTIONS

H. Nayeb-Hashemi<sup>\*</sup>, S.S. Hwang<sup>\*</sup>, P. G. Poles<sup>\*</sup>

Many mechanistic models for the effects of the load history on Mode I crack growth have been suggested. However the application and validity of these models in the case of other modes interactions ( Modes II, and III ) are not explored. In this paper, the effects of Mode I and II interactions have been studied and the validity of those models on subsequent Mode I crack growth have been investigated.

INTRODUCTION

It has long been recognized that an abrupt change in cyclic load amplitude, or a sudden single over-load, can significantly effect Mode I fatigue crack growth rate (1-4). Many mechanistic models for delay in the crack growth rates have been proposed. In a plane stress, the Elber's plasticity-induced crack closure concept (5-6), is generally accepted as the best explanation for the experimentally observed decrease in the rate of fatigue crack growth after an over-load. Plasticity-induced closure is considered to arise because of the plastic wake associated with the over-load. Because of the restraint of the surrounding elastic media, the crack flanks are compressed together. As a result of this, some of the applied loading in subsequent crack growth is used to open the crack faces, and thus the effective crack driving force  $\Delta k_{eff}$  is less than  $K_{max} - K_{min}$ . Such a closure also exists during steady state fatigue crack growth. There is now evidence that the crack flanks cause premature contact before the minimum applied load in the fatigue cycle is attained. Budiansky and Hutchinson (7) modeled the fatigue crack closure by considering the residual plastic stretch at the crack tip. As the crack grows, it leaves in its wake the plastically stretched material that remains

<sup>\*</sup> Northeastern University, Dept. of Mech. Eng. Boston, Ma. 02115.

appended to the upper and lower surfaces of the crack. In order for the crack to be open upon unloading, the total thickness of these stretched appendage just behind the crack tip must be equal to the plastic stretch ahead of the crack tip at  $k=k_{min}$ . It has been shown that this process does not take place because the crack opening is too small to accommodate the residual stretch. The stretched material attached to the crack surfaces will make contact before the unloaded state is reached. The results show the closure develops well behind the crack tip.

By closely examining the HRR fields (8-10) for plain strain fatigue crack growth, there seems to suggest that new mechanisms for explaining the load history dependence may be needed for the case where there is a lack of plastically deformed material directly ahead of the (plain strain) crack tip. Recently it has been recognized that other mechanisms could be more important than the Elber's plasticity induced closure model in explaining overload induced effects on the rate of fatigue crack growth. Micro-roughness (11) of the fatigue crack surface, blunting and branching of the crack after over-load (12-14), are among the models that seem to present good correlation with experimental results.

Despite this body of information on the effects of load history on Mode I fatigue crack growth, there has been little information on the interaction of transient cyclic Modes II and III on subsequent Mode I crack growth. Such transient Modes II and III are very common in turbo-generator and transmitting shafts, and rail road tracks. Under normal, operation these components are subjected to a steady state cyclic bending (Mode I).

Most studies on mixed-mode and Mode II crack growth to date, whether fracture or fatigue, have concerned themselves with predicting the crack growth angle. Interest in the crack growth rate has been secondary. Theories to explain the crack growth direction are: (a) Maximum tensile hoop stress at the crack tip (15) or at some specified distance from the crack tip (16-17). (b) Maximum opening mode stress intensity (18-20). (c) Minimum elastic energy density in the vicinity of the crack tip (21-22), (d) Contribution of Modes I and II stress intensities at the crack tip (23), (e) Maximum crack growth rate (24). The above theories may be applicable for certain materials but they can not be generalized.

The purpose of this investigation is to understand the effects of transient Mode II loading on subsequent Mode I crack growth. The specific parameters of interest are the effect of single and cyclic Mode II loading, micro structure, load ratio, and applicability of mechanistic models (Elber's plasticity induced crack closure, and crack blunting and branching on Mode II and Mode I interactions.

EXPERIMENTAL PROCEDUREMaterials

Studies were performed on hot rolled, and tempered martensite AISI 4340 steels (specimen were tempered at 200°C, 400°C, and 600°C). The details of the heat treatment are given (25). Chemical composition and ambient temperature mechanical properties are shown in Tables 1 and 2.

Four point bending and three point bending specimens were used for Mode I and II crack growth study. The specimen's dimensions is depicted in Fig. 1. The crack growth was monitored using a D.C. electric potential technique. The calibration equation (potential vs. crack length) was obtained from finite element analysis (25). The relationship between the crack length,  $c$ , and the electric potential across the notch,  $V_c$ , was found to be:

$$\frac{c}{W} = 1. - 1.17513 e^{-0.42289(\frac{V_c}{V_0})} \quad (1)$$

where  $V_0$  is the initial potential corresponding to the initial notch depth,  $c_0$ .

A four-point symmetric loading, with respect to the crack location, was chosen for the crack growth study in Mode I and transient single, and cyclic Mode I over-loads. For transient single and cyclic Mode II loadings, a nonsymmetrical four-point bending was designed, as shown in Fig. 2. The moment and shear diagrams show that by making  $S=0$ , the crack is subjected to pure Mode II. An elastic plastic finite element analysis confirms Mode II loading, for this configuration. A similar set up was used by Gao et al (26) for mixed mode crack growth study. The fatigue crack growth rate was related to the stress intensity factors in Modes I and II. For an applied moment  $M$  and shear force  $Q$ , these are defined as (26-27):

$$K_I = \frac{6M}{BW^2} \sqrt{\pi c} f\left(\frac{c}{W}\right) \quad (2)$$

$$K_{II} = \frac{Q}{BW^{\frac{3}{2}}} g\left(\frac{c}{W}\right) \quad (3)$$

where  $B$  and  $W$  are the thickness and width of the specimen, respectively. Fatigue Tests.

Fatigue Tests

Effects of transient single and cyclic Modes I and II loadings on subsequent Mode I crack growth rate at constant  $\Delta K_I = 10 \text{ MPa}\sqrt{\text{m}}$ ,  $\Delta K_I = 15 \text{ MPa}\sqrt{\text{m}}$ , and  $R$  ratio of 0.05 and 0.25, were obtained at room temperature using an MTS servo-hydraulic machine. After initiating

crack at  $\Delta K_I = 25 \text{ MPa}\sqrt{\text{m}}$ , the load was gradually reduced, until the desired  $\Delta K_I$  (10 or 15  $\text{MPa}\sqrt{\text{m}}$ ) was reached. The crack was grown at this constant  $\Delta K_I$  for about 3 mm before transient Modes I and II applied. For Mode II loading, the specimen was repositioned from symmetric four point bending to nonsymmetric four point bending, so there would be no Mode I loading, Fig. 2. At this configuration,  $S_0$ ,  $S_1$  and  $S_2$  were 0.0, 22.2, and 73.03 mm, respectively. The transient single and cyclic Modes I loadings constituted 100% and 200% over-load with respect to the steady state situation. For Mode II loading, the force P was calculated such that Mode II over-load would result in the same transient plastic zone size as for 100% or 200% Mode I over-loads. The plastic zones  $(r_p)_I$ , in Modes I and II, for small scale plasticity, and yield stress of  $\sigma_{ys}$  are given in [26].

$$(r_p)_I = \frac{1}{2\pi} \left( \frac{K_I}{\sigma_{ys}} \right)^2 \quad (4)$$

$$(r_p)_{II} = \frac{3}{2\pi} \left( \frac{K_{II}}{\sigma_{ys}} \right)^2 \quad (5)$$

The changes in compliance of the specimens before and after transient Modes I and II were measured by plotting load vs. crack opening displacement, using a COD clip gage.

#### RESULTS AND DISCUSSIONS

The effects of 100 and 200% single, and Cyclic Mode I and its equivalent Mode II over-load (same transient plastic zone size) on Mode I fatigue crack growth at  $\Delta K_I = 10$ , and 15  $\text{MPa}\sqrt{\text{m}}$ , and R-ratios of 0.05 and 0.25 are shown in Figs. 3-7. The results show single or cycle 100% or 200% Mode I over-load, causes crack growth retardation or the arrest of the crack. Single Mode II loading, on the other hand neither retards nor arrests the subsequent Mode I crack growth, and even may give rise to crack growth acceleration for a very short distance of much smaller than the transient plastic zone. In contrast, cyclic Mode II loading (specimens were subjected to 10,000 cycles in Mode II) give rise to a significant crack growth retardation (growth rate less than  $1 \times 10^{-7}$  mm/cycle) in Mode I. This results can be explained as follows:

##### Role of Residual Plastic Strain in Crack Front

Elber's plastic induced crack closure model attributes the closure in Mode I to the residual plastic stretch of the material in the crack front. In order to compare these residual plastic stretches after Mode I and Mode II loading, an elastic plastic finite element analysis was performed. For four point symmetric loading (Mode I) half of the specimen was analyzed, Fig. 8. For nonsymmetric four point bending (Mode II) the whole specimen was analyzed in order to

avoid inputting uncertain boundary condition in the crack plane, Fig. 9. The material was assumed as elastic/plastic with linear work hardening, Fig. 10. Triangular quadratic isoparametric elements, formed by collapsing one side and placing the mid-side node near the crack tip at the quarter point was employed for the analysis of stress/strain field around the crack, Fig. 11. Barsoum [28] has shown that triangular elements (2-D problems) formed by collapsing one side, lead to simulation of  $1/\sqrt{r}$  singularity at the crack tip. It is also shown that the triangular element produces far better results (stress intensity factor) than rectangular (2-D) elements with nodes closed to the crack tip placed at the quarter point. In this research, both types of elements were employed. Here the results of triangular elements are reported. These results were almost equal to the results of having rectangular elements. Finite Element program ADINA was used for these analyses. The load was corresponded to a 200% Mode I over-load and its equivalent Mode II over-load. The nominal plastic zone in this case was 4.38 mm. Since the finite element program ADINA does not provide plastic strains  $(\epsilon_x)^P$ ,  $(\epsilon_y)^P$ ,  $(\gamma_{xy})^P$ , a supplementary program was developed to find  $(\epsilon_x)^P$ ,  $(\epsilon_y)^P$ ,  $(\gamma_{xy})^P$ . Knowing displacement  $U_i$ ,  $V_i$  at nodal points in x and y direction, along with interpolation functions  $\psi_i$ , plastic strains were calculated as follow [29].

$$x = \sum_{i=1}^8 \psi_i(\xi, \eta) X_i \quad y = \sum_{i=1}^8 \psi_i(\xi, \eta) Y_i \quad (6)$$

$$u = \sum_{i=1}^8 \psi_i(\xi, \eta) U_i \quad v = \sum_{i=1}^8 \psi_i(\xi, \eta) V_i \quad (7)$$

$$J = \begin{bmatrix} \frac{\partial x}{\partial \xi} & \frac{\partial y}{\partial \xi} \\ \frac{\partial x}{\partial \eta} & \frac{\partial y}{\partial \eta} \end{bmatrix} \quad (8)$$

$$\begin{bmatrix} \frac{\partial u}{\partial x} \\ \frac{\partial u}{\partial y} \end{bmatrix} = (\epsilon_x)^P = J^{-1} \begin{bmatrix} \frac{\partial u}{\partial \xi} \\ \frac{\partial u}{\partial \eta} \end{bmatrix} \quad (9)$$

$$\begin{bmatrix} \frac{\partial v}{\partial x} \\ \frac{\partial v}{\partial y} \end{bmatrix} = (\epsilon_y)^P = J^{-1} \begin{bmatrix} \frac{\partial v}{\partial \xi} \\ \frac{\partial v}{\partial \eta} \end{bmatrix} \quad (10)$$

where  $X_i$ ,  $Y_i$  are the coordinate system of the nodes in x and y direction.

The results show that although the effective plastic strains,  $(\epsilon^P)_{\text{eff}}$ , are comparable for both Mode I and Mode II over-load, but

## FATIGUE 87

the plastic strain ( $\epsilon_p$ )<sup>P</sup> for Mode I is significantly higher, Figs. 12-13. From this analysis no Elber's plasticity crack closure after Mode II loading should be anticipated. Furthermore there was no noticeable change in load vs. crack opening displacement (COD) before and after Modes I and II loadings (single or cyclic), Fig. 14. This also proves the invalidity of Elber's model on the effect of Mode II loading on subsequent Mode I crack growth. Almost unnoticeable crack retardation after single Mode II loading, can be related to the residual shear stress, and subsequent crack deviation from the straight path in Mode I (crack is after the plane of maximum normal stress).

The observed retardation in Mode I crack growth after cyclic Mode II loading can be explained as follows:

### Effects of Branch Cracks on Mode I crack Growth:

For specimens subjected to 10,000 cycles in Mode II ( $r_{II}$  1.22-2.73 mm), a 45° branch crack, with the length of less than 0.05mm was formed off the main crack. Although this branch crack did not have any effect on the compliance of the specimen in Mode I, it had a significant effect on subsequent crack growth rate in Mode I, Fig. 15. The crack was retarded for a short distance, but never arrested. In contrast, the specimens subjected to 200% Mode I over-load, resulted in complete arrest of the crack. The compliance of the specimen was not also effected by Mode I over-load. Detailed metallographic examination of the crack front did not reveal any crack branching. This may suggest the crack tip blunting may have greater influence in crack closure phenomena than crack branching for a plain strain crack.

### Fractography

Upon completion of the tests, the fracture surface of the specimens were cleaned and gold plated. Using a scanning electron microscope, the micro-mechanism of crack growth before and after Mode II loading were studied. The results showed that, there was not any significant difference in micro-mechanism of the crack growth before and after single Mode II loading, and crack growth was a typical transgranular fatigue crack growth, Fig. 16. However the cyclic Mode II loading gave rise to formation of a significant amount of cavities, and micro cracks, Figs. 17- 18. These cavities may be responsible for not arresting the crack, even though crack bifurcated from the main crack as a result of cyclic Mode II loading. The fracture surface after Mode I over-load was not any different than that before over-load. This may further suggests that the dominant mechanism of crack growth retardation in plain strain, is crack tip blunting.

## FATIGUE 87

### CONCLUSIONS

Effect of single and cyclic Mode II loading on steady state crack growth at  $\Delta K_I = 10, 15 \text{ MPa}\sqrt{\text{m}}$ , and R-ratios of .05, and .25 were studied on AISI 4340 steels. The results showed in contrast to a single Mode II loading of plastic zones (.8-4.5 mm) which did not have any effect on Mode I crack growth, cyclic Mode II gave rise to a branch crack formation, and slowed the subsequent Mode I crack growth. In contrast Mode I over-load resulted in a significant crack growth retardation. The elastic/plastic finite element analysis, using triangular elements showed that the Elber's plasticity crack closure model is not an applicable model for crack closure due to transient Mode II loading. Furthermore the results suggest that the crack tip blunting may be more significant in crack retardation in Mode I, than crack branching.

### Acknowledgments

The authors are indebted to professor J. Rossetos, for valuable discussions and encouragements, to Dr. Sayyedi for analyzing the fracture surfaces. Financial support from the U.S. National Science Foundation, Army Material and Mechanics Research Center are thankfully acknowledged

TABLE 1 - Composition in Wt. % of AISI 4340 Steel studied

C	Mn	Ni	Cr	Mo	Si	P	S	Cu
0.04	0.78	1.77	0.81	0.25	0.26	0.007	0.013	0.14

TABLE 2 - Ambient Temperature Mechanical Properties of AISI 4340 Steel

	Yield Strength		Tensile Strength	
	MN/m <sup>2</sup>	(Ksi)	MN/m <sup>2</sup>	(Ksi)
Tempered				
200°C	761	(110)	967	(140)
400°C	640	(93)	688	(100)
600°C	361	(52)	426	(62)
Hot Rolled (as received)	424.4	(61.5)	470	(68.2)

## FATIGUE 87

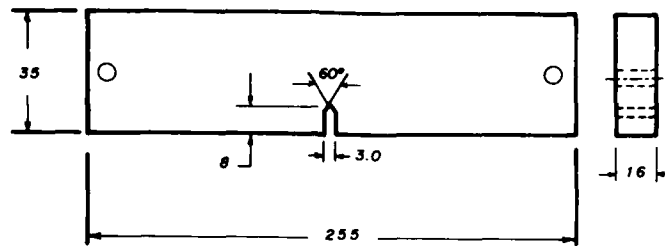
### REFERENCES

- (1) Paris P. C., and Erdogan F., J. Basic Eng., 1963 pp. 528
- (2) McMillan J.C., and Pelloux R. M. N., "Fatigue Crack Propagation Under Program and Random Loads," ASTM STP 415, 1967, pp. 505.
- (3) Grosskreutz J. C., "Fatigue Mechanisms in the Sub-Creep Range," ASTM STP 435, 1971, pp. 5-60.
- (4) Hudson C. M., and Hardrath H. F., "Effects of Changing Stress Amplitude on the Rate of Fatigue Crack Propagation of Two Aluminum Alloys," NASA TN D-360, 1961.
- (5) Elber W., "The Significance of Fatigue Crack Closure," ASTM STP 486, pp. 230-242, 1971.
- (6) Elber W., Eng. Fract. Mech., Vol. 2, 1970, pp. 37-45.
- (7) Budiansky B., and Hutchinson J. W., ASME J. Appl. Mech., Vol. 45, 1978, pp. 267-276.
- (8) Rice J. R., and Rosengren G. F., J. Mech. Phys. Solids, Vol. 16, 1968, pp. 1-12.
- (9) Hutchinson J. W., J. Mech. Phys. Solids, Vol. 16, 1968, pp. 13-31.
- (10) Parks D. M., "The Dominance of the Crack Tip Fields of Inelastic Continuum Mechanics," Sec. Int'l Conf. on Numerical Methods in Fract. Mech., Swansea, July 1980.
- (11) Hayeb-Hashemi H., Suresh S., and Ritchie R. O., Mater. Sci. and Engng., Vol. 59, pp. L1-L5, 1983.
- (12) Zaïken E. and Ritchie R. O., Engng. Fract. Mech., Vol. 22, No. 1, 1985, pp. 35-48.
- (13) Yu M. T., and Topper T. H., ASME J. Engng. Mater. Tech., Vol. 107, 1985, pp. 19-25.
- (14) Castro J. T. P. D., "Load History Effects on Plane Strain Fatigue Crack Growth," Ph.D. Thesis, M.I.T., 1982.
- (15) Erdogan F. and Sih G. C., ASME J. Bas. Engr., Vol. 85, 1963, pp. 519-527.
- (16) Williams J. G., and Ewing P. D., Int. J. Fract. Mech., Vol. 8, 1972, pp. 441-446.

## FATIGUE 87

- (17) Finnie I., and Saith A., Int. J. Fract. Mech., Vol. 9, 1973, pp. 484-486.
- (18) Iida S., and Kobayashi A. S., ASME J. Bas. Engng. Vol. 91, 1969, pp. 764-769.
- (19) Bilby B. A., and Cardew G. E., Int. J. Fract. Mech., Vol. 11, 1975, pp. 708-712.
- (20) Wu C. H., ASME J. Appl. Mech., Vol. 45, 1975, pp. 533-558.
- (21) Sih C. G., Int. J. Fract. Mech., Vol. 10, 1974, pp. 305-321.
- (22) Sih C. G., and MacDonald B., Engng. Fract. Mech., Vol. 6, 1974, pp. 361-386.
- (23) Sih C. G., and Barthelemy B. M., Engng. Fract. Mech., Vol. 7, 1974, pp. 439-451.
- (24) Otsuka A., Mori K., and Miyata T., Engng. Fract. Mech., Vol. 7, 1975, pp. 429-439.
- (25) Nayeb-Hashemi H., Taslim M. E., Zotos J., and Cohen M. D., "Effect of Mode II Overload on Subsequent Mode I Crack Growth," The Mechanism of Fracture, Conf. Proceeding, ASM, 1985 pp. 387-398.
- (26) Gao H., Brown M. W., and Miller K. J., Fatigue Engng. Mater. Struct. Vol. 5, 1982, pp. 1-17.
- (27) Tada H., Paris P. C., and Irwin G. R., "The Stress Intensity Handbook," Del Research Corp., Hellertown, PA, 1973.
- (28) Barsoum R. S., Int. J. for Numerical Methods in Engineering, Vol. 11, 1977, pp. 85-98.
- (29) Reddy J. N., "An Introduction to the Finite Element Method," McGraw-Hill, 1984.

# FATIGUE 87



All Dimensions in mm

Figure 1 Schematic diagram of the four-point bending specimen

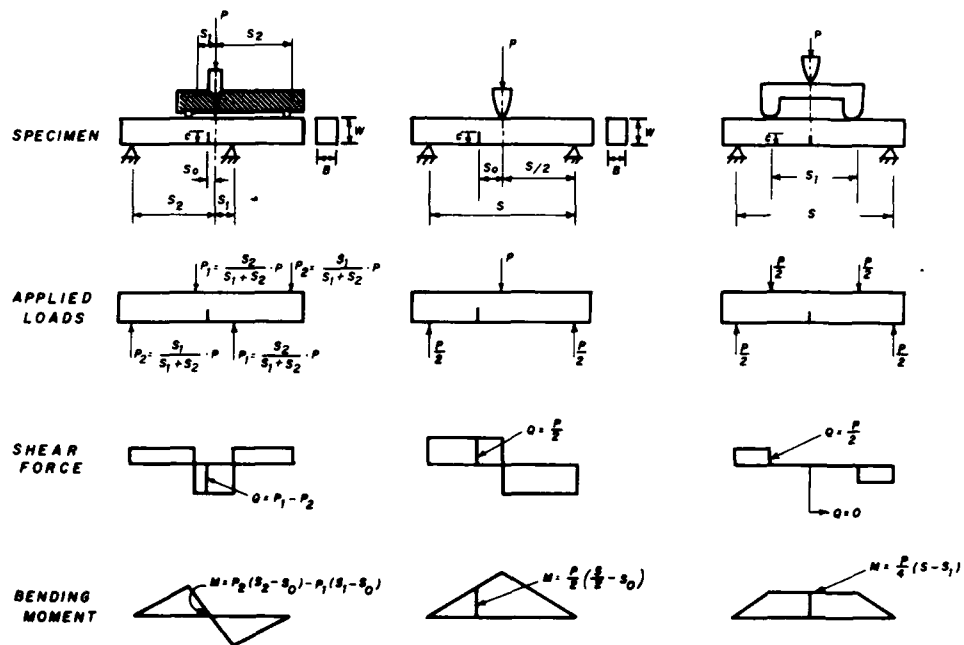


Figure 2 Moment and Shear diagram for three- and four points loadings, showing magnitude of shear and moment at a desired crack location

# FATIGUE 87

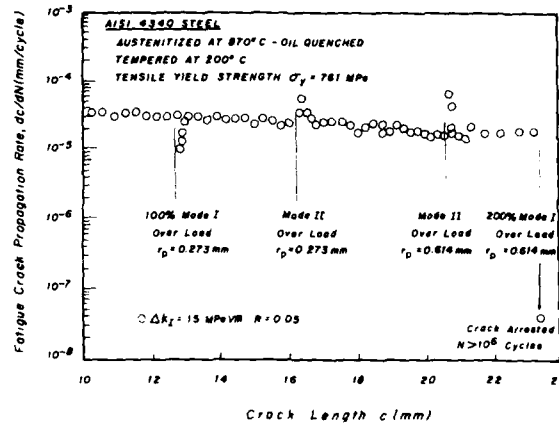


Figure 3 Effects of Single Modes I and II Overloads on Mode I crack Growth Rate at  $\Delta K_I = 15$  MPa√m, and R-ratio = .05, in AISI 4340 ( $\sigma_{ys} = 761$  MPa)

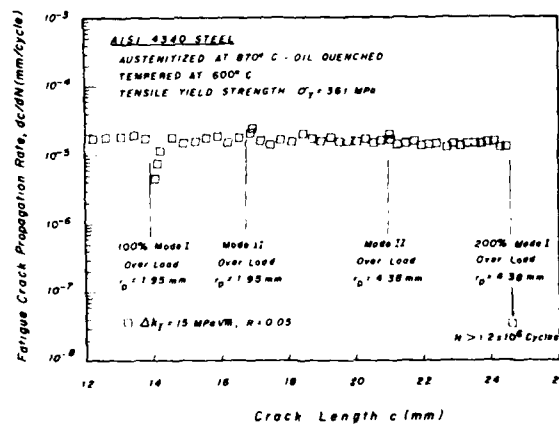


Figure 4 Effects of Single Modes I and II Overloads on Mode I Crack Growth Rate at  $\Delta K_I = 15$  MPa√m, and R-ratio = .05, in AISI 4340 Steel ( $\sigma_{ys} = 361$  MPa)

# FATIGUE 87

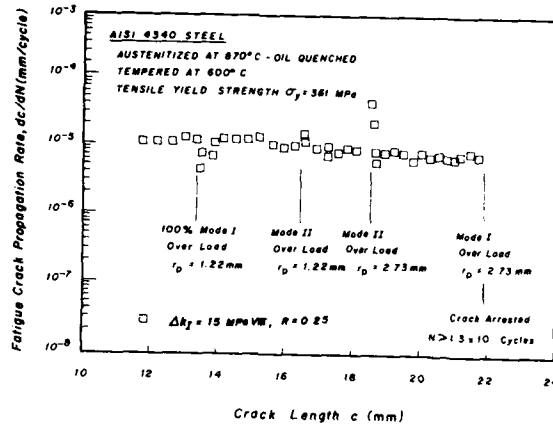


Figure 5 Effects of Single Modes I and II Overloads on Mode I Crack Growth Rate at  $\Delta K_I = 15 \text{ MPa}\sqrt{\text{m}}$ , and R-ratio=0.25, in AISI 4340 Steel ( $\sigma_{ys} = 361 \text{ MPa}$ )

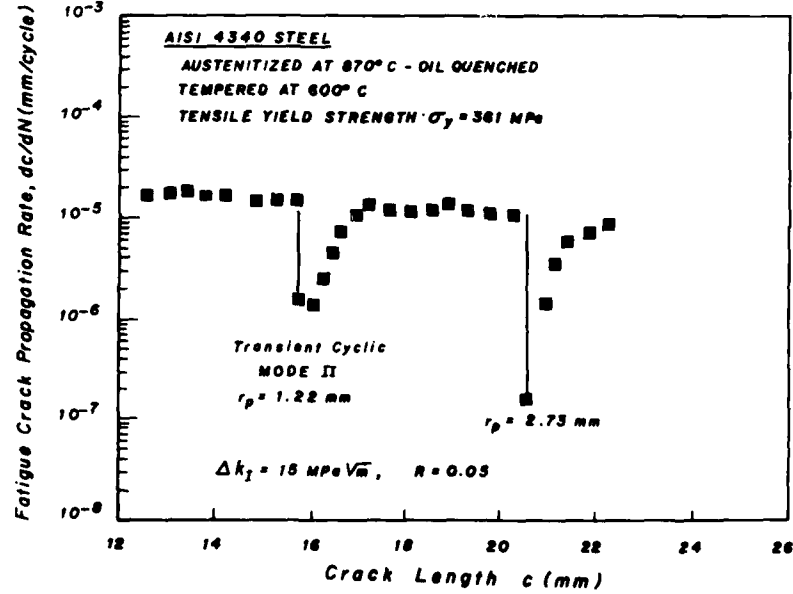


Figure 6 Effect of Cyclic Mode II on Mode I Crack Growth Rate at  $\Delta K_I = 15 \text{ MPa}\sqrt{\text{m}}$ , and R-ratio=0.05, in AISI 4340 Steel ( $\sigma_{ys} = 361 \text{ MPa}$ )

# FATIGUE 87

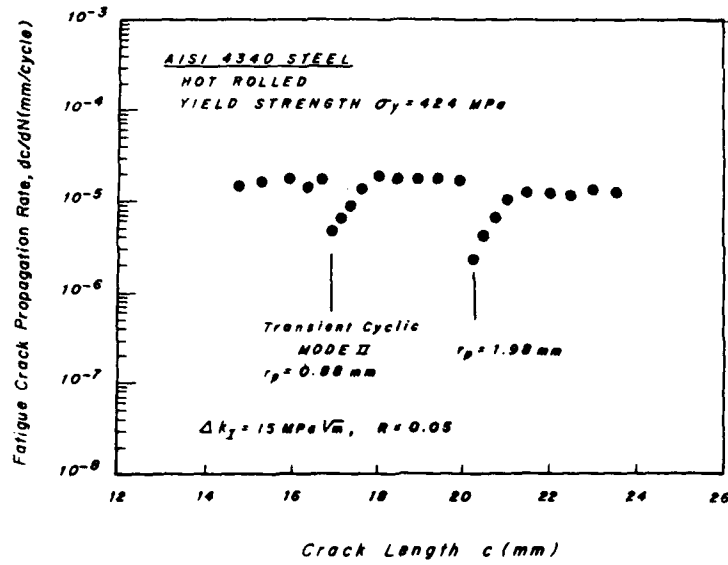


Figure 7 Effect of Cyclic Mode II on Mode I Crack Growth Rate at  $\Delta K_I = 15 \text{ MPa}\sqrt{\text{m}}$ , and R-ratio = .05, in AISI 4340 Steel ( $\sigma_{ys} = 424.4 \text{ MPa}$ )

FATIGUE 87

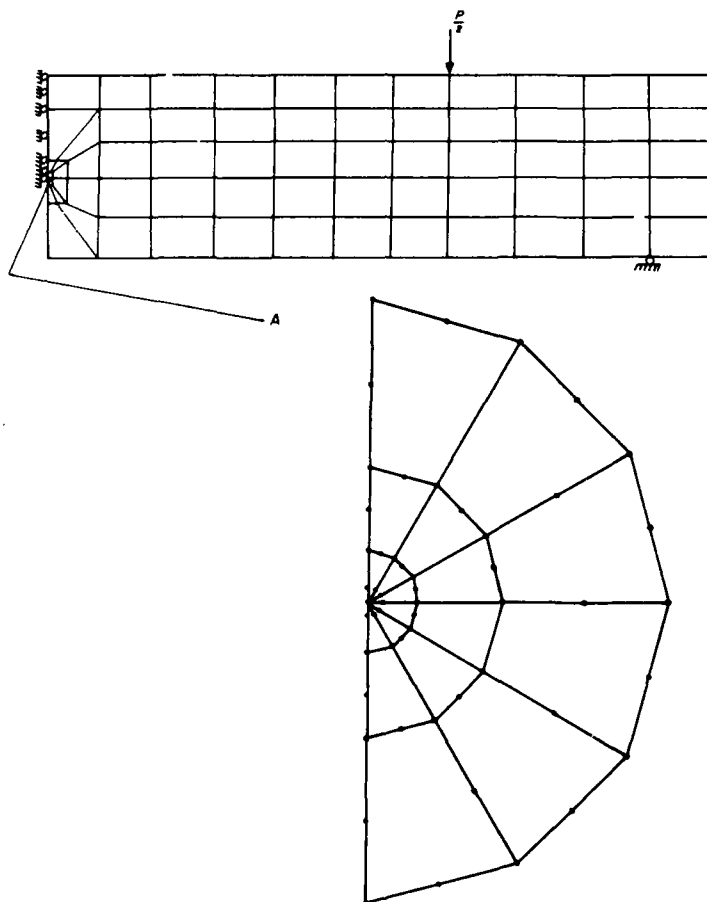


Figure 8 Finite Element Mesh for Elastic/Plastic Analysis of Strain Fields Around the Crack Tip in Mode I

# FATIGUE 87

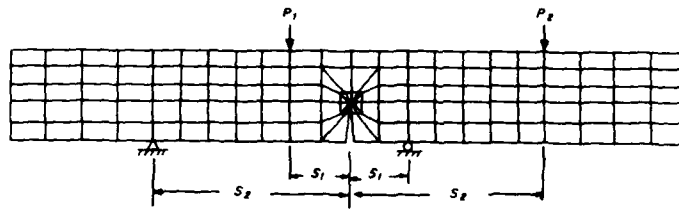


Figure 9 Finite Element Mesh for Elastic/Plastic Analysis of Strain Fields Around the Crack Tip in Mode II

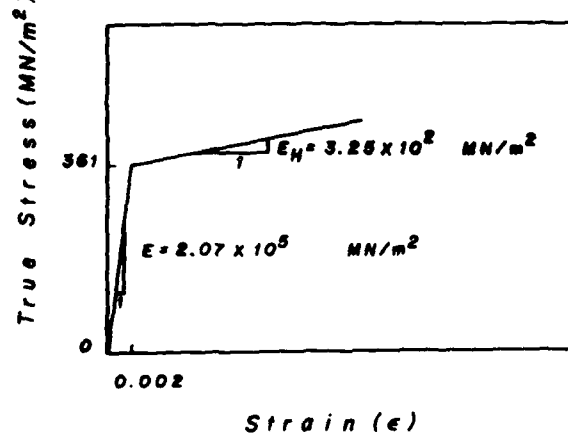


Figure 10 Idealized Model for Material Behavior in Elastic/Plastic Analysis

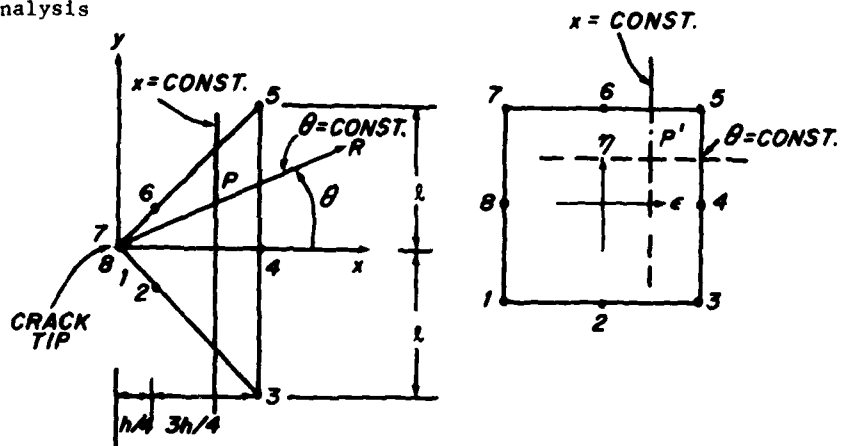


Figure 11 2-D Triangular Quarter Point Element in Global and Natural Coordinate Systems

# FATIGUE 87

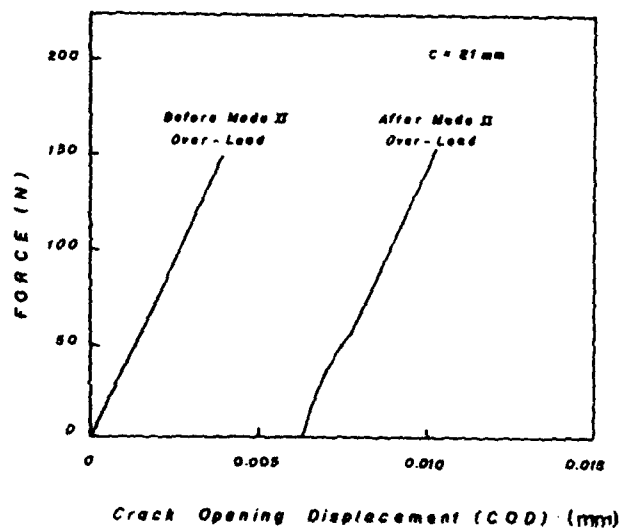


Figure 14 Load Vs. Crack Opening Displacement in Mode I after Mode II Loading (Transient Plastic Zones = 4.38 mm)

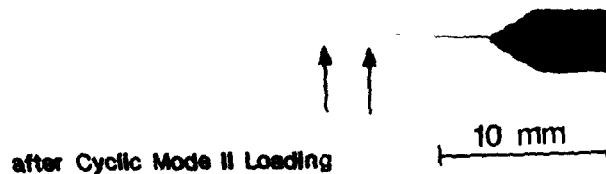


Figure 15 Photo Micrograph of the Crack Path after Cyclic Mode II Loading

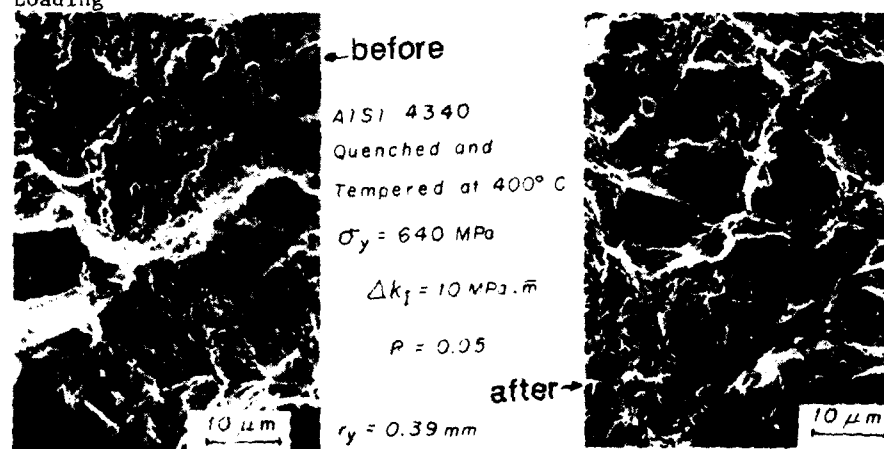


Figure 16 Photo Micrograph of Fracture Surface before and after Single Mode II Loading

# FATIGUE 87

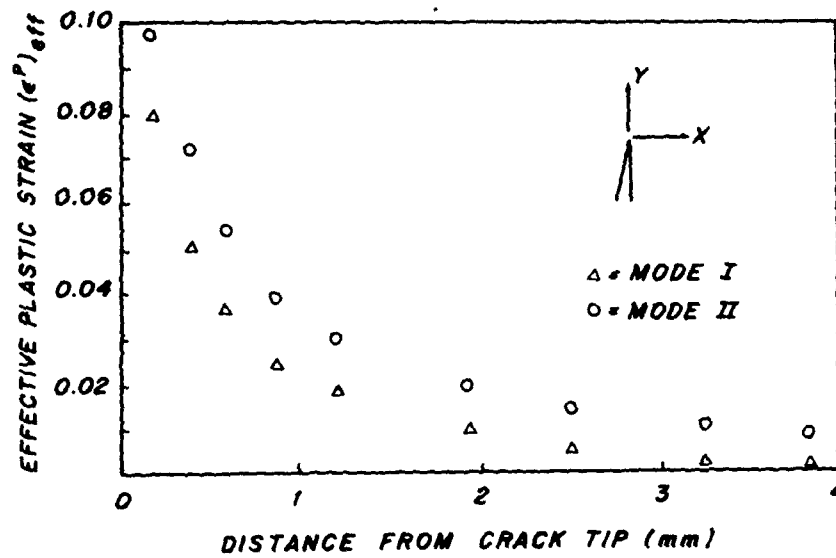


Figure 12 Comparison of the Effective Plastic Strain in Modes I and II in Plain Stress Analysis for Equal Nominal Plastic Zones.

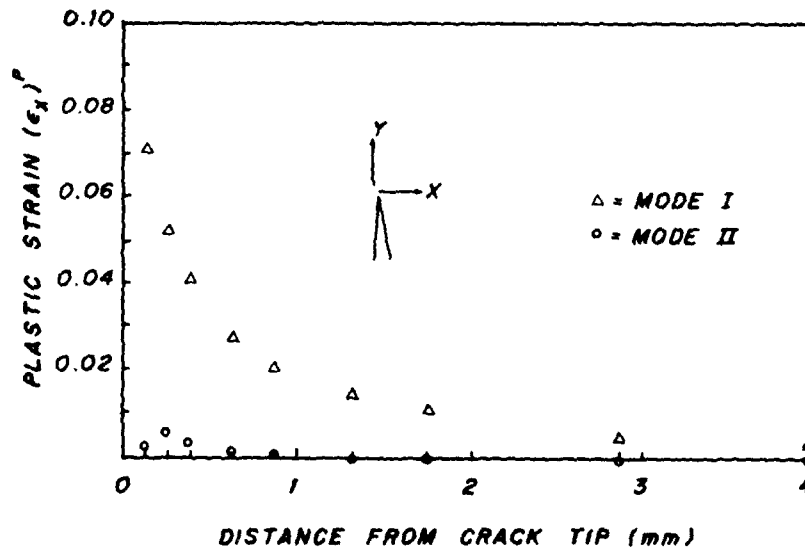


Figure 13 Comparison of Plastic Strain (Plastic Stretch in Crack Front in Mode I and II) for Equal Nominal Plastic Zones

# FATIGUE 87

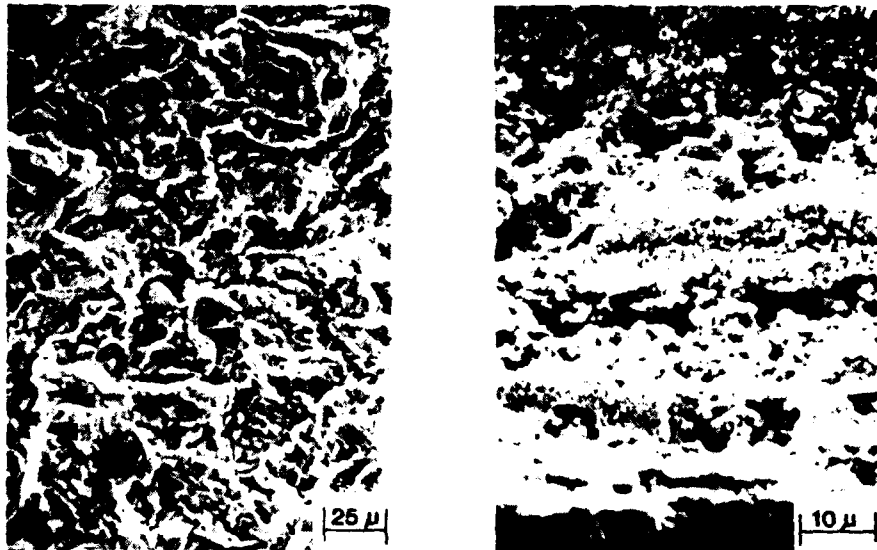


Figure 17 Photo Micrograph of the Fracture surface before and after Cyclic Mode II Loading (AISI 4340,  $\sigma_{vs} = 361$  MPa,  $(r_p)_{II} = 2.73$  mm)

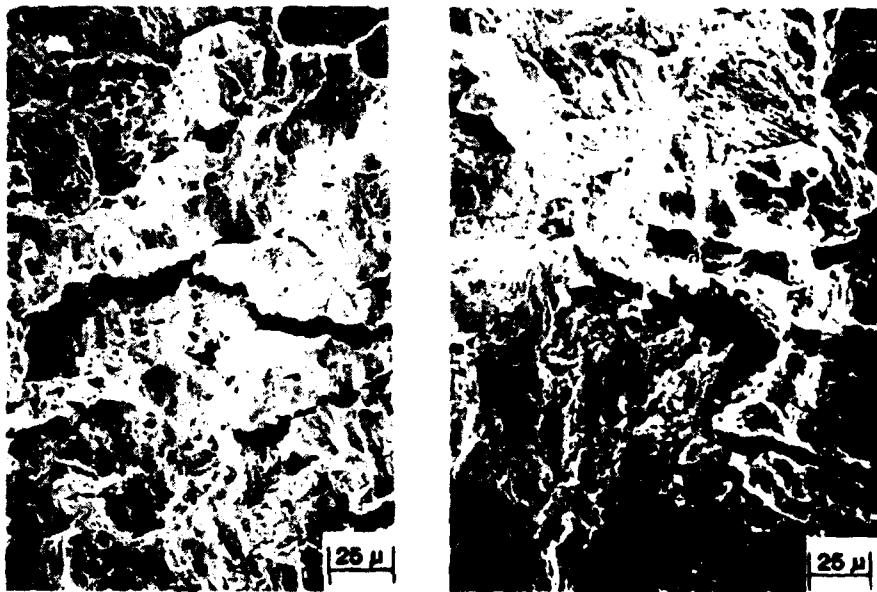


Figure 18 Photo Micrograph of the Fracture Surface after Cyclic Mode II Loading (AISI 4340  $\sigma_{ys} = 424.4$  MPa,  $(r_p)_{II} = 1.98$  mm)

MULTIAXIAL FATIGUE FAILURE CRITERION : A NEW APPROACH

K. Dang Van\* , Y.V. Papadopoulos\*

A new version of a fatigue failure criterion is presented. In this criterion local microscopic stresses associated to the stabilized microscopic stress cycle are used. This new theory is applied to Nishihara-Kawamoto tests of out-of-phase bending and torsion. Correlation of experimental results with theoretical predictions is quite good.

INTRODUCTION

Fatigue is one of the major considerations in the design of mechanical structures subjected to repeated loading. More often than not the loadings are complex, that is, they lead to two or three dimensional stress state that may be nonproportional. Such stress histories are very difficult to analyse. The fatigue behavior is usually treated by the mean of a stress or strain parameter that reduces the complex multiaxial loading to an "equivalent" uniaxial one. The fatigue design against failure consists on the definition of a fatigue failure criterion describing the endurance domain in the space of stresses. Then the "equivalent" stress obtained for a multiaxial stress state by the use of the fatigue failure criterion has to be compared with uniaxial fatigue data (fatigue limits). Many theories exist on this subject (1), (2), (3), (4), (5), (6). But these theories are usually limited in the case of proportional loading. Also as Y.S. Garud (7) underlined it, their formulation is often ambiguous and so they are difficult to handle with. The problem of fatigue failure criterion has not yet been satisfactorily resolved. The purpose of this paper is to present a different theory initially proposed by Dang Van (8). This theory is then applied to Nishihara-

---

\*Laboratoire de Mécanique des Solides, ECOLE POLYTECHNIQUE, Palaiseau, FRANCE

## FATIGUE 87

Kawamoto tests (8) of out-of-phase bending and torsion. The application of the theory in two industrial cases and in the Mc Diarmid test data of biaxial stresses of different frequencies (22) are also given in references.

### SHORT REVIEW OF COMMON

### FATIGUE FAILURE CRITERIA

The point of view adopted in all the classical fatigue theories is the decomposition of any component of the stress tensor  $\Sigma_{ij}(t)$  in static  $\Sigma_{ij}^s$  and cyclic  $\Sigma_{ij}^c$  parts. In the common case of proportional sinusoidal loading the cyclic part  $\Sigma_{ij}^c$  is the well defined amplitude of the stress  $\Sigma_{ij,a}$

$$\Sigma_{ij,a} = \frac{1}{2} (\Sigma_{ij,max} - \Sigma_{ij,min}) \quad (1)$$

and the static part is the mean value of the stress  $\Sigma_{ij,m}$

$$\Sigma_{ij,m} = \frac{1}{2} (\Sigma_{ij,max} + \Sigma_{ij,min}) \quad (2)$$

Two of the first fatigue failure criteria are the "ellipse quadrant",

$$\frac{\Sigma_a^2}{f^2} + \frac{T_a^2}{t^2} - 1 \leq 0 \quad (3)$$

and the "ellipse arc"

$$\frac{T_a^2}{t^2} + \left(\frac{f}{t} - 1\right) \frac{\Sigma_a^2}{f^2} + \left(2 - \frac{f}{t}\right) \frac{\Sigma_a}{f} - 1 \leq 0 \quad (4)$$

proposed by Gough and Pollard (1) for the case of alternating in phase bending and torsion. For the case of proportional loading around a non zero mean value the Sines criterion (2) is widely used:

$$\Sigma_{equ,a} + A P_m - B \leq 0 \quad (5)$$

where

$$\Sigma_{equ,a} = \frac{1}{3} \left[ (\Sigma_{1,a} - \Sigma_{2,a})^2 + (\Sigma_{2,a} - \Sigma_{3,a})^2 + (\Sigma_{3,a} - \Sigma_{1,a})^2 \right]^{1/2} \quad (6)$$

# FATIGUE 87

and  $P_m$  is the mean hydrostatic pressure :

$$P_m = \frac{1}{3} (\Sigma_{1,m} + \Sigma_{2,m} + \Sigma_{3,m}) \quad (7)$$

$\Sigma_{i,a}$ ,  $\Sigma_{i,m}$ ,  $i = 1, 2, 3$  are the amplitude and the mean value respectively of the principal stresses. A and B are material constants defined by :

$$A = \sqrt{2} \left( \frac{\sqrt{3}t}{f_0} - 1 \right), \quad B = \frac{\sqrt{6}t}{3} \quad (8)$$

where  $f_0$  is the endurance limit in zero tension fluctuating stress. If in the place of the mean hydrostatic pressure  $P_m$ , we use the maximum hydrostatic pressure in a stress cycle  $P_{max}$ , the Crossland fatigue failure criterion (5) is obtained,

$$\Sigma_{equ,a} + A' P_{max} - B \leq 0 \quad (9)$$

where now

$$A' = \sqrt{2} \left( \frac{\sqrt{3}t}{f} - 1 \right) \quad (10)$$

A linear combination of  $\Sigma_{equ,a}$ ,  $P_m$  and  $P_{max}$  is also proposed (4) as a possible fatigue criterion.

Another group of fatigue failure criteria is based on a linear combination of the maximum shear stress amplitude and the normal stress acting on the plane of maximum shear (5). Mc Diarmid's criterion (6) is the most elaborated one of that group. It can be written in the following form :

$$T_{n,a} - \left[ t - \frac{(t - f/2)}{(f/2)^{1.5}} \Sigma_{n,a}^{1.5} \right] \left[ 1 - \frac{\Sigma_{n,m}}{R_u/2} \right]^{0.5} \leq 0 \quad (11)$$

where  $T_{n,a}$  is the permissible maximum shear stress amplitude,  $\Sigma_{n,a}$  and  $\Sigma_{n,m}$  are the amplitude and the mean value respectively of the normal stress acting on the maximum shear stress plane and  $R_u$  is the ultimate tensile strength of the material. Mc Diarmid's criterion is also extended in the case of alternating out-of-phase bending and torsion (10).

From the preceding equations (5) to (11), we conclude that any one of the common fatigue failure criteria can be expressed as a

## FATIGUE 87

function of the amplitudes and the mean values of the stress tensor components :

$$F(\Sigma_{ij,a} , \Sigma_{ij,m}) \leq 0 \quad (12)$$

If now for instance we consider a sinusoidal loading defined as follows :

$$\Sigma_{ij}(t) = \Sigma_{ij,a} \sin(\omega t + \delta_{ij}) + \Sigma_{ij,m} \quad (13)$$

the fatigue failure criterion will be function not only of the stress components but also of their phase lags  $\delta_{ij}$  , (11). The failure condition is :

$$F(\Sigma_{ij,a} , \Sigma_{ij,m} , \delta_{ij}) \leq 0 \quad (14)$$

For the case of a sinusoidal loading with stresses of different frequencies,

$$\Sigma_{ij}(t) = \Sigma_{ij,a} \sin(\omega_{ij} t) + \Sigma_{ij,m} \quad (15)$$

the fatigue criterion takes the form :

$$F(\Sigma_{ij,a} , \Sigma_{ij,m} , \omega_{ij}) \leq 0 \quad (16)$$

Finally if we investigate a type of loading corresponding to,

$$\Sigma_{ij}(t) = \Sigma_{ij,a} \sin(\omega_{ij} t + \delta_{ij}) + \Sigma_{ij,m} \quad (17)$$

the fatigue failure criterion will be a function not only of the stress components but also of the six phase lags  $\delta_{ij}$  and the six different frequencies  $\omega_{ij}$  :

$$F(\Sigma_{ij,a} , \Sigma_{ij,m} , \delta_{ij} , \omega_{ij}) \leq 0 \quad (18)$$

It seems clear to the authors that this way to extend classical fatigue failure criteria in the general case of non-radial periodic

loading is unrealistic. In the next paragraph a different method will be given. This method is suitable for the fatigue analysis of any case of general periodic loading.

#### FATIGUE FAILURE CRITERION IN RELATION WITH THE MICROSTRUCTURE OF A POLYCRYSTALLIN MATERIAL

Principle of the proposed theory. First, let us remark that nucleation of fatigue cracks is a microscopic phenomenon which happens at the scale of one or some grains. At this scale the material is no longer homogeneous nor isotropic and local stresses  $\sigma_{ij}$  and strains  $\epsilon_{ij}$  could be very different from macroscopic ones (resp.  $\Sigma_{ij}$ ,  $E_{ij}$ ), used by engineers. What can be perceived in the macroscopic scale has already been somehow filtered by the macrovolume element (corresponding for instance to the dimension of the strain gage).

To work out rules for fatigue prevention Dang Van recommended to postulate a fatigue criterion by using microscopic stresses  $\sigma_{ij}$  (8). The main particularity of this criterion is the following: the usual characterization of the fatigue cycle (for example  $\Sigma_{equ,a}$ ,  $P_m$ ) is replaced by the local (microscopic) loading path at each time  $t$  of the cycle (current stress state). In this way damaging parts of the loading path can be distinguished.

As it is already stated fatigue crack nucleation phenomenon is microscopic. It occurs in some grains which necessarily had undergone plastic glide (12). Local parameters ( $\sigma_{ij}$ ,  $\epsilon_{ij}$ ) have to be evaluated in these plastified grains. Near the fatigue limit, the applied macroscopic stresses  $\Sigma_{ij}$  are rather low and it is reasonable to suppose that the material has a purely elastic response in the macroscopic scale. So it is easy to derive macroscopic parameters. The passage from macroscopic to microscopic parameters is a rather difficult problem. It will be solved here by the use of Lin-Taylor hypothesis (13). For this purpose two scales have to be distinguished:

- A macroscopic one characterised by an elementary representative volume  $V(M)$  surrounding the point  $M$ . This is the usual scale of the engineer. Macroscopic variables  $\Sigma_{ij}(M,t)$ ,  $E_{ij}(M,t)$  are homogeneous in  $V(M)$ . (Fig. 1).

- A second smaller one of the order of grain size which is a subdivision of  $V(M)$ . (Fig. 1). The microscopic quantities  $\sigma_{ij}(P,t)$ ,  $\epsilon_{ij}(P,t)$  are not homogeneous in  $V(M)$ . By Lin-Taylor hypothesis, one has:

$$E_{ij}(M,t) = \epsilon_{ij}(P,t) = \epsilon_{ij}^e(P,t) + \epsilon_{ij}^p(P,t), \quad \forall P \in V(M) \quad (19)$$

Also the mean in  $V(M)$  of  $\sigma_{ij}(P,t)$  equals the macroscopic stresses but locally the microscopic stress tensor fluctuates around  $\Sigma_{ij}(M,t)$ . In general one has: (14)

# FATIGUE 87

$$\sigma_{ij}(P,t) = A_{ijkl}(M,P) \Sigma_{kl}(M,t) + \rho_{ij}(P,t) \quad (20)$$

where  $A_{ijkl}$  is the elastic localisation tensor, which equals the fourth order unity tensor under Lin-Taylor hypothesis, and  $\rho_{ij}(P,t)$  is a local residual stress field. Assuming an isotropic hardening rule for the grains which undergone plastic deformations it can be proved by the use of Melan theorem (15) as extended by Mandel (16), that the microscopic stresses  $\sigma_{ij}(P,t)$  tend toward a shake down state under a macroscopic periodic loading. This means that for time  $t \geq t_1$ , a time independent residual stress field  $\rho_{ij}^*(P)$  exist, such as the corresponding microscopic stresses  $\hat{\sigma}_{ij}(P,t)$

$$\hat{\sigma}_{ij}(P,t) = \Sigma_{ij}(M,t) + \rho_{ij}^*(P) \quad (21)$$

never violate the locale plastic criterion. In the proposed fatigue failure criterion local variables  $\hat{\sigma}_{ij}$  associated to the shaked down cycle (equ. 21) are used. The fatigue criterion is stated as follows:

- crack initiation will happen in those grains, of the volume  $V(M)$ , which had undergone plastic strains, if, for at least one time  $t$  of the shaked down cycle, one has :

$$g(\hat{\sigma}_{ij}(P,t)) > 0, \quad P \in V(M) \quad (22)$$

The explicit form of the function  $g$  is given by Dang Van (8) as following :

$$g(\hat{\sigma}_{ij}(t)) = \tau(t) + ap(t) - b \quad (23)$$

By ordering the microscopic principal stresses  $\hat{\sigma}_1 > \hat{\sigma}_2 > \hat{\sigma}_3$ , the corresponding maximum shear stress  $\tau$  and hydrostatic pressure  $p$  are respectively

$$\tau(t) = \frac{\hat{\sigma}_1(t) - \hat{\sigma}_3(t)}{2}, \quad p(t) = \frac{\hat{\sigma}_1(t) + \hat{\sigma}_2(t) + \hat{\sigma}_3(t)}{3} \quad (24)$$

The endurance domain in the  $\tau - p$  plane is delimited by the  $p$  axis and the straight line  $D$ , corresponding to  $g(\hat{\sigma}_{ij}) = 0$  (Fig. 4)

Evaluating microscopic stresses of the shaked down cycle. To apply the fatigue criterion (equ. 23,22) local stresses  $\hat{\sigma}_{ij}(t)$  have to be evaluated. First, let us note that, under Lin-Taylor assumption, the local residual stress field  $\rho_{ij}$  is a deviatoric one. Thus

$$p(t) = \frac{1}{3} \Sigma_{kk}(t) \quad (25)$$

# FATIGUE 87

To derive  $\rho_{ij}^*$  and then  $\tau(t)$  (see equ. 21,24), one needs only the deviatoric part  $S_{ij}(t)$  of the macroscopic stress tensor  $\Sigma_{ij}(t)$ . Assuming a local plastic criterion of Von Mises type associated with an isotropic hardening rule an optimum choice of the time independent residual stress tensor  $\rho_{ij}^*$  can be done by the solution of the following min-max problem, (18),

$$\min_{Z_{ij}} \left\{ \max_t \sqrt{(S_{ij}(t) - Z_{ij}) (S_{ij}(t) - Z_{ij})} \right\} \quad (26)$$

where the variables transformation,  $\rho_{ij} = -Z_{ij}$ , is used.

For a better understanding of the min-max problem (equ. 26) the following geometrical interpretation can be given :

- for a periodic loading the macroscopic deviatoric stress tensor  $S_{ij}(t)$  describes a closed curve in the 5-dimensional deviatoric space. The solution of the min-max problem coincides with the construction of the minimum ball containing the closed curve described by  $S_{ij}(t)$ . The center, say  $Z_{ij}^*$  of this minimum ball is the solution of the min-max problem (equ. 26). The minimum ball can be obtained by the construction of the convex hull of the curve  $S_{ij}(t)$ .

The algorithm for this geometrical construction is based on Garathey's theorem (19) and is given elsewhere (20). Thus the time independent residual stress field  $\rho_{ij}^* = -Z_{ij}^*$  can be obtained for any kind of periodic loading. So Dang Van fatigue criterion is of generalised application in fatigue design against failure. The choice of  $\rho_{ij}^*$  as the solution of the min-max problem equ. 26, satisfies all the conditions of Melan shake down theorem as extended by Vandel (See (16)).

In the case of radial periodic loading or of sinusoidal out-of-phase loading, the closed curve described by  $S_{ij}(t)$  possesses a center of symmetry defined by the tensor  $S_{ij,m}$  corresponding to the mean values of the components of the macroscopic deviatoric stress tensor  $S_{ij}(t)$ , (20). In that case the solution of the min-max problem,  $Z_{ij}^*$ , coincides with  $S_{ij,m}$ . Thus one has :

$$\rho_{ij}^* = -Z_{ij}^* = -S_{ij,m} \quad (27)$$

For this kind of loading the microscopic maximum shear stress  $\tau(t)$  is given by :

$$\tau(t) = \frac{1}{2} \left[ (\Sigma_1(t) - \Sigma_{1,m}) - (\Sigma_3(t) - \Sigma_{3,m}) \right] \quad (28)$$

## FATIGUE 87

It is obvious that in the case of alternating radial or out-of-phase loading the microscopic stress tensor  $\hat{\sigma}_{ij}(t)$  of the shaked down cycle coincides with the macroscopic one,  $\Sigma_{ij}(t)$ .

By using this last result we can identify the constants  $a$  and  $b$  of the fatigue criterion (equ. 23,22). If for instance we know the fatigue limits in alternating torsion  $t$  and tension-compression  $f$ , the constants  $a$  and  $b$  are given by : (fig. 4)

$$a = \frac{t - f/2}{f/3}, \quad b = t \quad (29)$$

### ANALYSIS OF TEST DATA WITH THE PRESENT THEORY

The tests in alternating out-of-phase bending and torsion of Nishihara and Kawamoto (9) were analysed with the present theory. Two materials, a mild steel and a hard steel were tested. The constants  $a, b$  of the fatigue criterion are given in the next table I :

TABLE I

mild steel				hard steel			
t	f	a	b	t	f	a	b
(MPa)	(MPa)		(MPa)	(MPa)	(MPa)		(MPa)
137.3	235.4	0.25	137.3	196.2	314.0	0.37	196.2

Comparisons of theoretical predictions with experimental data were made in the basis of the security coefficient  $C$  defined as follows, (20) :

$$C = \max_t \tau_{\text{equ}}/b, \quad \tau_{\text{equ}} = \tau(t) + ap(t) \quad (30)$$

Obviously  $C = 1$  corresponds to a perfect agreement between theory and test data. Disagreement is expressed in %. As the tests were performed under an alternating loading, microscopic stresses  $\hat{\sigma}_{ij}(t)$  coincides with the macroscopic ones. So :

$$\hat{\sigma}_{11}(t) = \Sigma_a \sin \omega t, \quad \hat{\sigma}_{12}(t) = T_a \sin(\omega t - \varphi) \quad (31)$$

# FATIGUE 87

where  $\Sigma_a$  is the amplitude of normal stress due to bending and  $T_a$  in the amplitude of the shear stress due to torsion. The results of the analysis are given in the table II.

It is clear that the theoretical predictions are within 7 % of the experimental values in all cases, (Column 7 table II), except the special case of  $\lambda = 0,5$  ,  $\phi = 90^\circ$ . In these cases theoretical predictions are influenced by the fact that all surface planes of the tested sample are planes of maximum shear stress and therefore there is a greater statistical chance of crack initiation. As an example of the analysis done, the stress variation with time for  $\lambda = 0,21$  ,  $\phi = 90^\circ$  is given in fig. 2 , for the mild steel case. In fig. 3 the loading path in the stress space for the same case is given. It is an ellipse wich possesses the origin of axis as center of symmetry. Finally in the fig. 4 the path described by the microscopic stresses of the shaked down cycle  $\hat{\sigma}_{ij}(t)$  in the  $\tau - p$  plane of the fatigue failure criterion is given.

TABLE II - Nishihara and Kawamoto fatigue limit data analysed by the proposed criterion.

	$\Sigma_a$ MPa	$T_a$ MPa	$\lambda = T_a/\Sigma_a$	$\phi$	max $\tau_{equ}$ MPa	C	error(%)
	1	2	3	4	5	6	7
1	mild steel						
2	99.6	120.5	1.21	0°	138.7	1.01	1.0
3	103.4	125.1	1.21	60°	133.2	0.97	-3.0
4	108.6	131.4	1.21	90°	131.5	0.96	-4.2
5	180.3	90.2	0.50	0°	142.5	1.04	3.8
6	191.5	95.7	0.50	60°	131.4	0.96	-4.3
7	201.1	100.6	0.50	90°	117.3	0.85	-14.6
8	222.6	46.7	0.21	0°	139.3	1.01	1.4
9	229.8	48.3	0.21	90°	134.0	0.98	-2.4
10	hard steel						
11	137.9	166.8	1.21	0°	197.5	1.01	0.7
12	140.1	169.5	1.21	30°	195.8	1.00	-0.2
13	145.4	175.9	1.21	60°	190.6	0.97	-2.8
14	149.9	181.3	1.21	90°	182.4	0.93	-7.0
15	245.5	122.8	0.50	0°	203.9	1.04	3.9
16	249.8	124.9	0.50	30°	200.1	1.02	2.0
17	252.4	126.2	0.50	60°	182.2	0.93	-7.0
18	258.1	129.1	0.50	90°	160.9	0.82	-18.0
19	298.5	62.7	0.21	0°	198.7	1.01	1.3
20	303.9	63.9	0.21	90°	189.4	0.97	-3.5

CONCLUSIONS

The fatigue limit behavior of metals can be predicted by Dang Van fatigue failure criterion for any case of periodic loading. The criterion makes use of the microscopic shakedown stress cycle. The evaluation of microscopic stresses (20) is based on Melan theorem as extended by Mandel for hardening materials (16). Application of this new theory is given by the analysis of Nishihara and Kawamoto test results. Correlation of experimental results with predictions of the presented theory is good and it is slightly better than the correlation given by Mc Diarmid fatigue failure criterion which was applied in the same test results (10).

The Dang Van fatigue failure criterion is also used in the fatigue analysis of a crank shaft under simulated real stresses with good results (21). Another application of industrial interest concerning the fatigue design of ball bearings, is also given in reference (17). Finally, the predictions of the presented theory is also compared with the experimental results of the tests of biaxial stresses of different frequencies done by Mc Diarmid (22). The correlation was good (20). These encouraging results should allow in the future to conceive at the stage of designers, structures which have to resist against fatigue and so a lot of costly tests could be spared.

SYMBOLS USED

$\Sigma_{ij}$  ,  $E_{ij}$  : macroscopic stress (resp. strain) tensor

$\sigma_{ij}$  ,  $\varepsilon_{ij}$  : microscopic stress (resp. strain) tensor

REFERENCES

- (1) Gough, J.H., Pollard, H.V and Clenshaw, W.J., Aero. Research Council, Rand M 2522, HMSO, London 1951.
- (2) Sines, G., Metal Fatigue, ed. Sines and Waisman, New York 1959
- (3) Crossland, B., Proc. Int. Conf. on Fatigue of Metals, I. Mech. E. London 1956.
- (4) Kakuno, H. and Kawada, Y., Fatigue of Engng. Mat. and Structures Vol. 2, 1979.
- (5) Findley, W.N., Trans. ASME, Series B, Journal of Engineering for Industry, Vol. 81, n° 4, 1959.
- (6) Mc Diarmid, D.L., Proc. 2nd. Int. Conf. on Pressure vessel Techn., ASME, USA, 1973.

# FATIGUE 87

- (7) Garud, Y.S., Journal of Testing and Evaluation, JTEVA, Vol. 9, N° 3, 1981.
- (8) Dang Van, K., Mémorial de L'Artillerie française, 3ème fascicule, 1973.
- (9) Nishihara, T. and Kawamoto, M., Memoirs, College of Engineering, Kyoto, Imperial University, Vol XI, 1945.
- (10) Mc Diarmid, D.L., The Aeronautical Journal, March 1981.
- (11) Hashin, Z., Int. Journ. of Fracture, Vol. 17, 1981.
- (12) Klesnil, M. and Lukas, P., Materials Science Monographs, 7, Elsevier Scientific Publishing Company, 1980.
- (13) Lin, T.H. and Ito, M., J. Mech. Phys. Solides, Vol. 13, 1965.
- (14) Mandel, J., Cours CISM, Springer-Verlag, Udine 1971.
- (15) Melan, E., Z. Angew. Math. Mech., Vol. 12, 1932.
- (16) Mandel, J., Mech. Res. Comm., Vol. 3, 1976.
- (17) Dang Van, K., Griveau, B. and Message, O., ASTM, STP, Sheffield 1986.
- (18) Mandel, J., Zarka, J. and Halphen, B., Mech. Res. Comm., Vol. 4 (5), 1977.
- (19) Lay, S., Convex Sets and their applications, John Wiley and Sons, 1982.
- (20) Papadopoulos, Y.V., Rapport CEFI n° 4, L.M.S., Ecole Polytechnique, 1986.
- (21) Dang Van, K., Le Douaron, A. and Lieurade, H.P., Int. Conf. Fract. Mech., I.C.F. 6, New Delhi, 1984.
- (22) Mc Diarmid, D.L., ASTM STP 853, Philadelphia 1985.

# FATIGUE 87

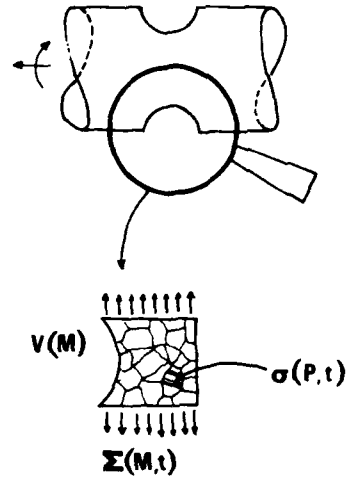
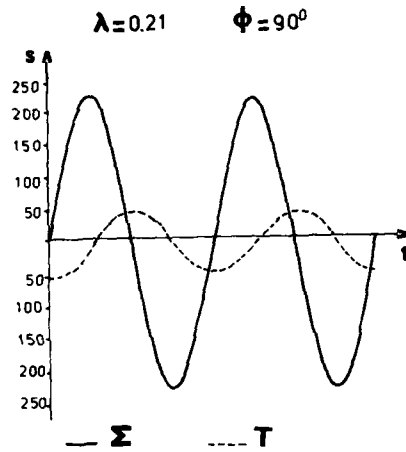


Fig. 2 : Out-of-phase bending and torsion stress variation with time      Fig. 1 : Macroscopic and microscopic scales

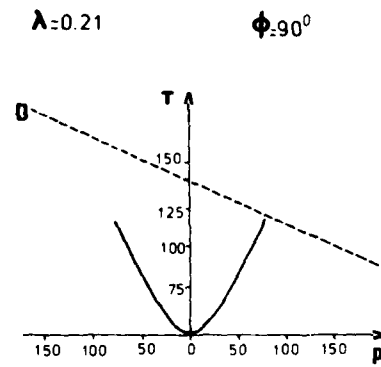
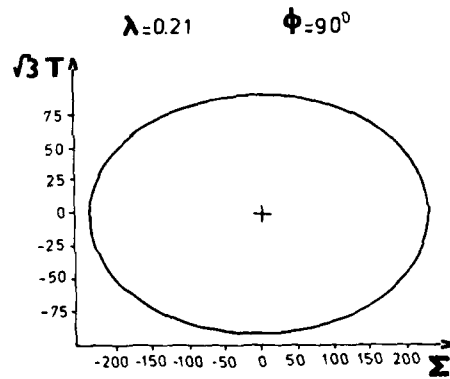


Fig. 3 : Loading path in the stress space

Fig. 4 : Microscopical loading path in the plane of the fatigue criterion

## FATIGUE 87

### PROFILES OF SELF STRESS AND OF LOAD STRESS AT NOTCHES

H.O. Fuchs<sup>\*</sup> and S.B. Lee<sup>\*\*</sup>

The reduction of fatigue strength by notches can be mitigated or cancelled by suitable surface treatments. Analysis of these effects requires consideration of the profiles of stresses below the surface of notches. An example of optimization by such analysis is shown. Approximations to stress profiles and sources of stress profiles are presented. Details are given in the appendix.

### INTRODUCTION

Fatigue cracks in structures and components usually start at notches. Materials data refer to smooth or precracked specimens. We are concerned with relating the fatigue behavior of notched parts to the available materials data.

The Fatigue Strength Reduction Factor. The theoretical stress concentration factor  $k_T$  can be obtained by various methods or from the literature (Peterson 1974). It can serve as a first approximation for calculating the fatigue strength of notched parts at fully reversed stresses and long life from the fatigue strength of smooth specimens. The fatigue notch factor (or fatigue strength reduction factor)  $k_F$  relates the observed behavior of the notched specimens to the data obtained from smooth specimens. Neuber (1946) and Peterson (1974) have correlated the difference between  $k_F$  and  $k_T$  with the stress gradient. Their formulas relate the stress gradient to the notch radius, regardless of the notch geometry. Siebel and

---

<sup>\*</sup> Dept. of Mechanical Engineering, Stanford University  
<sup>\*\*</sup> Korea Institute of Machinery and Metals

## FATIGUE 87

Stieler (1955) have published more detailed data on stress gradients which are shown in Figure 1 in terms of the length  $y$  which is defined in Figure 2. Schijve (1980) has discussed those formulas and the gradient problem.

The notch factor  $k_f$  depends not only on  $k_T$  and the stress gradient but very strongly on the mean stress. Tensile mean stress can raise the notch factor  $k_f$  far beyond the stress concentration factor  $k_T$ . Compressive mean stress can wipe out the notch effect. Figure 3 shows the long life notch factor for a bar with stress concentration factor  $k_T = 3.4$  plotted over the mean stress. The solid line is obtained from the data in MIL HDBK 5 (1976) the dotted line from tests by Katz (quoted by Fuchs 1972). The same trends can be calculated from formulas for mean stress effect like  $S_{eq} = k_b S_a^m S_{max}^{(1-m)}$  where  $k_b$  is  $k_f$  at zero mean stress and long life. Similar formulas have been shown by Walker (1970) and Smith & al. (1970) to represent the behavior of many materials. They indicate that fatigue cracks will not grow unless tensile stress is present during some part of the cycle.

Strength Enhancement. Practicing engineers have long known that they can prevent failure of notched parts by certain treatments such as nitriding, carburizing, surface rolling, or shot peening. Research has shown that the beneficial effect of such treatments depends mainly on the compressive stresses produced in a shallow surface layer (Almen 1963). These self stresses prevent fatigue cracks from growing beyond a small depth (Gerber & Fuchs 1970). To analyze the action of the beneficial surface treatments and to optimize their application it is necessary to know the profiles of these self stresses and of the load stresses.

### STRESS PROFILES

An Example. Figure 4 shows profiles of bending stress ( $L$ ), of the negative of shot peening self stress ( $P$ ), of the net stress ( $N = L - P$ ), and of the fatigue limit ( $F = 552 + 0.35P$  MPa). That set of profiles is one of many computed to find the optimum peening intensity. This intensity is high enough to arrest cracks started at the surface by a high bending load, but not so high that it would start cracks below the surface where the equilibrating tensile self stress decreases the fatigue strength. In Figure 4, cracks start at A but are stopped by the high compressive stress below the surface. Cracks also start at B and are not stopped from growing inwards. The optimum for a shaft with  $D = 25.4$ mm,  $d = 20$ mm,  $r = 0.9$ mm was computed to be four times as great as the usually specified intensity. The much greater fatigue resistance was verified by tests (Fuchs 1986).

## FATIGUE 87

Load Stress Profiles. The profiles of load stresses may be known, as for thick walled tubes, or they may be computed by finite element methods. For many applications it is sufficient to approximate the load stress profile by the formula

$$L = S[a + b(1 - x/R) + c(1 - x/R)^n] \quad (1)$$

in which the four parameters  $a$ ,  $b$ ,  $c$ , and  $n$  are chosen to match the stress concentration factor at the surface, the stress gradient, and equilibrium with the nominal stress distribution, as shown in the appendix. The load stress profile shown in Figure 4 was obtained in this manner.

Stress concentration factors for many notch geometries are available in the literature; stress gradients for a few notch geometries are listed in Figures 1 and 5. For quarter-circular fillets in plates we computed stress profiles and found that the ratio of the intercept  $y$  to the notch radius is no longer constant when the ratio of notch radius to width of plate becomes small. The same is true for semi-circular notches in plates, as shown in Figure 5. Details are shown in the appendix. Information on load stress profiles can thus be obtained.

Stresses From Overloads. Information on self stress profiles is more difficult to find. Only self stresses produced by overloading can be computed from the loads, the geometry, and the materials properties. (Heller & al. 1964; Gerber & Fuchs 1970; Underwood & Kendall 1984; Dietrich & Potter 1977).

Thermally Induced Stresses. The profiles of self stresses produced by thermal treatments are very important but difficult to compute and rarely published. (Horger 1950; Mattson & Robinson 1965; Sharma & al. 1979; Vasilakis 1986)

Mechanically Induced Stresses. Profiles of mechanically produced self stresses are not quite so rare. The Proceedings of the International Conferences on Shot Peening (Niku-Lari 1981; Fuchs 1984), the report by Brodrick (1955) and a collection of profiles available from a supplier of shot peening (Fuchs 1987) show a good selection.

In first approximation one may assume that these profiles are parabolic, with the peak of the parabola at  $1/4$  of the total depth to which the compressive stress extends; that this depth is equal to the width of the impression created by the peening balls or by rollers; and that the peak compressive stress equals half of the strain hardened yield strength. At notches these self stresses are also concentrated, but less than the load

## FATIGUE 87

stresses, as shown by Todd (1971). This is usually neglected. The peening stress profile shown in Figure 4 was obtained in this manner.

Multiaxiality. The stresses below the surface of notches are of course multi-axial. This was neglected for the purposes of this paper. If one wants to consider all three principal stresses one can calculate an equivalent stress for the early stages of crack formation, but for crack propagation the largest tensile stress range is still the most suitable criterion.

### CONCLUSION

To achieve high fatigue resistance one should consider the profiles of the load stresses and of the self stresses which may be used to enhance fatigue resistance. This was expressed as early as 1960 in the abstract of the Murray lecture (Peterson 1961) *"Lecturer explains why engineers and designers must be concerned with more than maximum stresses and stress concentration factors. Also, he considers the fatigue of notched members in terms of crack initiation and crack propagation."* With the computing machines available today the consideration of stress profiles is more readily feasible than it was in 1960. It can provide substantial benefits in fatigue strength improvement.

### ACKNOWLEDGEMENT

Support of this work by Metal Improvement Co., by the Korea Science and Engineering Foundation and by MacNeal-Schwendler Corp. is gratefully acknowledged.

### APPENDIX.

#### Finite Element Work

Finite element work to obtain the load stress profiles was done on a PC, with the program MSC/pal 2 developed by MacNeal-Schwendler. The MSC/pal 2 program allows only 100 nodes. Plane stress, two-dimensional analysis provided the stress distributions around quarter-circular fillets and semi-circular notches in plates. The stress gradient intercept point  $y$  between the gradient and the  $x$ -axis are obtained as  $y = -k_T S / (dL/dx)$ .

Factors in load stress profile in tension. The factors  $a$ ,  $b$ ,  $c$ , and exponent  $n$  in eq. (1) are calculated to satisfy the stress concentration at the surface, the stress gradient, and the equilibrium with nominal stress distribution. For the plates we

## FATIGUE 87

use  $w$  instead of  $R$  in equation (1).

$$\begin{aligned} a &= (k_T/y - k_T(k_T - 1))/(k_T/y - (k_T - 1)) \\ b &= 0 \\ c &= k_T - a \\ n &= (k_T - 1)/(1-a) \end{aligned} \quad (2)$$

These are good for plates with quarter-circular fillets or semi-circular notches under tension. Figure 5 shows the stress concentration  $k_T$ , the ratio  $y/r$ , the factors  $a$ ,  $c$ , and the exponent  $n$  for various ratios of radius  $r$  to half width  $w$ . Figure 5(B) compares the load stress profile by formula with finite element results for a quarter-circular fillet of  $r/w = 0.25$ .

Factors in load stress profile in bending. For the shaft loaded in bending, mentioned in the text, the equations used to find the coefficients were

$$\begin{aligned} a &= 0 \\ b &= k_T - c \\ c &= (R/y - 1)k_T/(n - 1) \\ n &= ((R/y - 3)k_T + 2)/(k_T - 1), \end{aligned} \quad (3)$$

which apply only to similar shafts.

### Nomenclature

$a, b, c$ :	Constants in the load stress profile.
$d$ :	Small diameter of filleted shaft (mm).
$D$ :	Large Diameter of filleted shaft (mm).
$k_b$ :	$k_F$ at zero mean stress and long life.
$k_F$ :	Fatigue notch factor.
$k_T$ :	Stress concentration factor.
$L$ :	Load stress at point $x$ (MPa)
$m$ :	Exponent in mean stress effect formula.
$n$ :	Exponent in the load stress profile.
$r$ :	Radius of fillet or semi-circular notch (mm).
$R$ :	Radius of shaft (mm).
$S$ :	Nominal stress (MPa).
$S_{eq}$ :	Equivalent stress (MPa).
$S_a$ :	Alternating stress (MPa).
$S_m$ :	Mean stress (MPa).
$S_{max}$ :	Maximum stress (MPa).
$x$ :	Distance from surface (mm).

## FATIGUE 87

- y:** Distance to the point where slope of load stress profile meets the x-axis (mm).  
**w:** Half width of fillet or notch in their narrow section (mm).

### REFERENCES

- Almen, J.O. & Black, P.H. (1963), "Residual Stresses and Fatigue in Metals," McGraw-Hill Co., New York.
- Brodrick, R.F. (1955), Protective Shot Peening of Propellers, WADC Tech. Report 55-56, U.S. Dept. of Defense.
- Dietrich, G. & Potter, J.M. (1977), "Stress measurements on cold worked fastener holes," Advances in X-Ray Analysis, Vol. 20, pp. 321-328.
- Fuchs, H.O. (1972), "Regional tensile stress as a measure of the fatigue strength of notched parts," Mechanical Behavior of Materials, Vol. 2, pp. 478-488, Soc. Materials Science Japan, Kyoto.
- Fuchs, H.O., ed. (1984), Shot Peening. Proc. 2nd Intl. Conf. SAE Warrendale, PA.
- Fuchs, H.O. (1986), "Approx. analysis for optimizing prestress treatments," in Symposium ....Residual Stress Effects in Fatigue, Phoenix, AZ, Am. Soc. of Testing and Materials, Philadelphia, PA.
- Fuchs, H.O., ed. (1987), Shot Peening Stress Profiles, Metal Improvement Co., Paramus, NJ.
- Gerber, T.L. & Fuchs, H.O. (1970), "Improvement of the fatigue strength of notched parts by ....self stresses," STP 467, pp. 276-295. Am. Soc. of Testing and Materials, Philadelphia, PA.
- Heller, R.A., Seki, M. & Freudenthal, A.M. (1964), "The effects of residual stress on random fatigue life," Proceedings ASTM, Vol. 64, pp. 516-535.
- Horger, O.J. (1950), "Residual stresses," Ch. 11 in Hetenyi, M., ed. Hdbk. Exp. Stress Analysis, pp. 459-578, John Wiley & Sons.
- Mattson, R.L. & Robinson, G.H. (1965), "Case carburizing" in Metals Engineering-Design, pp. 284-290, McGraw-Hill, New York.
- MIL-HDBK-5C (1976), "Metallic Materials and Elements of

## FATIGUE 87

Aerospace Structures," page 3-284, US Dept. of Defense.

Neuber, H. (1946), Theory of Notch Stresses, J.W. Edwards, Ann Arbor, MI.

Niku-Lari, A., ed. (1981), Shot Peening. Proceedings 1st International Conference, Pergamon Press.

Peterson, R.E. (1961), "The role of stress distribution in fatigue," Experimental Mechanics, Vol. 1, No. 4, pp. 105-115.

Peterson, R.E. (1974), Stress Concentration Factors, John Wiley, New York.

Schijve, J. (1980), "Stress gradients around notches," Fatigue of Eng. Mat. and Structures, Vol. 3, No. 4, pp. 325-338.

Sharma, V.K., Walter, G.H. & Breen, D.H. (1979), "Predicting case depth for gears," Product Engineering, June 1979, p. 49.

Siebel, E. & Stieler, M. (1955), "Non-uniform stress distribution in fatigue" (in German), VDI-Zeitschrift, Vol. 97, No. 5, pp. 121-126.

Smith, K.N., Watson, P. & Topper, T.H. (1970), "A stress-strain function ...," J. of Materials, Vol. 5, No. 4, pp. 767-778.

Todd, R.H. & Fuchs, H.O., (1971), "Self stress concentrations," Exp. Mechanics, Vol. 11, No. 12, pp. 548-553.

Underwood, J.H. & Kendall, D.P. (1984), "Fracture analysis of a ....pressure vessel," Theor. & Appl. Fract. Mech., 2, pp. 47-58.

Vasilakis, J.D. (1986), "Thermal and transformation stresses in ....tubes," First Army Conference on Applied Math., George Washington University.

Walker, K. (1970), "The effect of stress ratio during ....fatigue," STP 462, pp. 1-14, Am. Soc. of Testing and Materials, Philadelphia, PA.

# FATIGUE 87

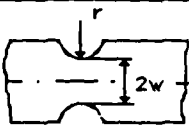
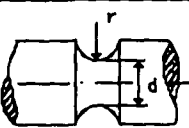
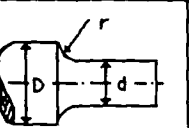
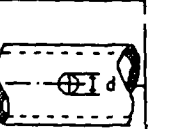
NOTCHES				
TENSION	$\frac{r}{2}$	$\frac{r}{2}$	$\frac{r}{2}$	—
BENDING	$\frac{r w}{2 w + r}$	$\frac{r d}{2 r + 2 d}$	$\frac{r (D + d)}{2 (D + d + 2 r)}$	—
TORSION	—	$\frac{r d}{2 r + d}$	—	$\frac{d}{6}$

Fig.1 Stress gradient intercept y for various notches.

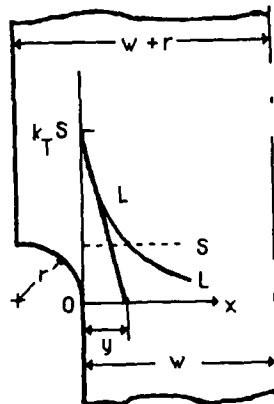


Fig.2 Definition of y in a fillet.

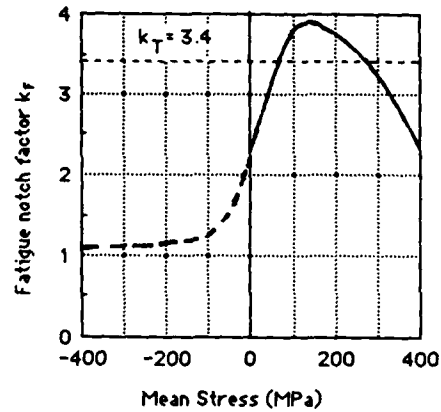
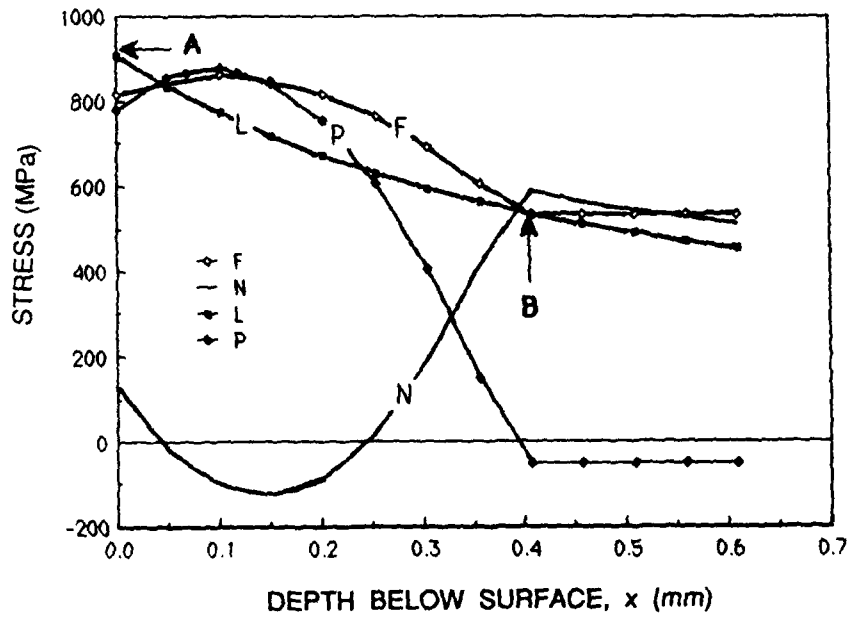


Fig.3 Fatigue notch factor as function of mean stress for 7075-T6 bar at 10 million cycles.

# FATIGUE 87



$$F \text{ (Fatigue Strength)} = 552 - 0.35 S_m = 552 + 0.35 P \text{ (MPa)}$$

$$N \text{ (Net Stress)} = L - P \text{ (MPa)}$$

$$L \text{ (Load Stress)} = S [ 0.9(1 - x/R) + 1.1 (1 - x/R)^{30.2} ] \text{ (MPa)}$$

$$P \text{ (Negative of Peening Stress)}$$

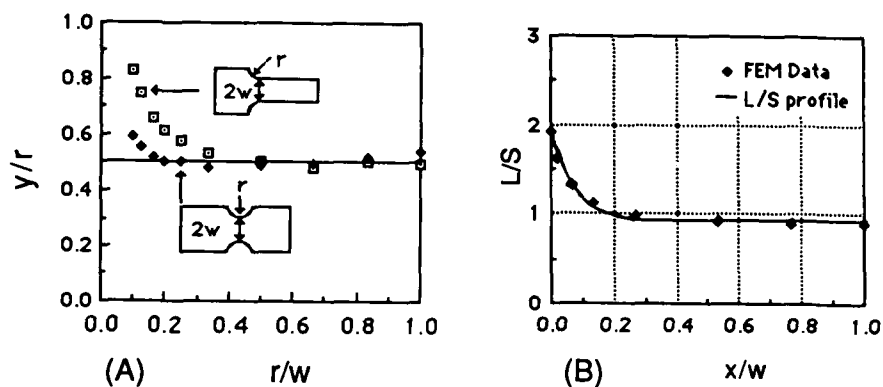
$$P = 876 [ 1 - \{(x/0.38 - 0.25)/0.75\}^2 ] \text{ (MPa)}$$

to  $x = 0.38$  mm, balanced by tension below 0.38 mm

Note: Cracks starting at A will be arrested by the compressive net stress near  $x=0.15$ . Cracks starting at B can propagate inwards.

Fig.4 Stress distribution near a shot peened fillet of a shaft in bending.

# FATIGUE 87



	$r/w$	$k_T$	$y/r$	$a$	$c$	$n$
NOTCH	0.100	2.766	0.591	0.931	1.835	25.50
	0.124	2.731	0.552	0.921	1.810	22.05
	0.166	2.672	0.518	0.905	1.767	17.58
	0.200	2.627	0.504	0.892	1.735	15.02
	0.250	2.560	0.500	0.871	1.689	12.13
	0.334	2.455	0.483	0.846	1.609	9.46
	0.500	2.254	0.477	0.808	1.446	6.54
	0.666	2.067	0.488	0.785	1.282	4.96
	0.834	1.899	0.517	0.769	1.130	3.90
	1.000	1.754	0.542	0.771	0.983	3.29
FILLET	0.100	1.918	0.833	0.962	0.956	24.08
	0.124	1.927	0.747	0.957	0.970	21.44
	0.166	1.931	0.660	0.948	0.983	17.93
	0.200	1.926	0.617	0.942	0.984	15.86
	0.250	1.916	0.575	0.932	0.984	13.55
	0.334	1.891	0.530	0.919	0.972	10.99
	0.500	1.826	0.488	0.898	0.928	8.06
	0.666	1.751	0.470	0.884	0.867	6.45
	0.834	1.671	0.503	0.864	0.807	4.94
	1.000	1.597	0.498	0.863	0.734	4.37

Fig.5 Load stress profiles for plates with notch or fillet in tension.

(A) Stress gradient intercept  $y$  for fillets and notches under tension.

(B) Comparison of FEM points and formula for fillet of  $r/w=0.25$ .

FATIGUE 87

**HIGH TEMPERATURE  
FATIGUE**

FATIGUE 87

FATIGUE OXIDATION INTERACTION IN LOW CYCLE FATIGUE

M.LEBIENVENU, Z.AZARI and G.PLUVINAGE\*

For the evaluation and the assurance of safety for equipment at elevated temperatures, it is indispensable to comprehend the influence of oxidation on the low cycle fatigue properties of materials. In the present study, fully reversed axial strain cycling tests were performed at 610°C by supplying smoothed specimens of 20CD10-05 steel, and the fatigue resistance and its temperature dependancy was discussed, based on the plastic strain range vs. fatigue life diagrams. The fatigue oxidation interaction was defined by quantifying the influence of mechanical cycling on the oxidation process in high temperature low cycle fatigue, with particular emphasis on the influence of the environment on the crack initiation stage of fatigue cracks in relation to the microstructure.

INTRODUCTION

A number of approaches have been proposed in recent years for treating the effects of oxidation and cycle frequency on low cycle fatigue at elevated temperatures. These have developed by correlating the results of smooth specimen, strain controlled, low cycle fatigue tests on various materials strain control simulates the local conditions of many design components which undergo cyclic plastic deformation and represent potential sources of low cycle fatigue failures. High temperature low cycle fatigue is one of the most important solicitation modes that appears in turbo machine parts and the environmental conditions are a key issue in the behaviour of materials against fatigue (1-8). Several authors (9-10), suggested that grain boundaries weakened by oxidation could generate the triggering sites. Under strong distortions, shape alterations appear inside the grain boundaries that cut the free-standing surface of the sample. This results in a natural notch effect. The amplitude of this effect is directly related to the size of the grains.

\*Faculté des Sciences. Ile du Saulcy, 57045 Metz Cedex .France

## FATIGUE 87

### EXPERIMENTAL TECHNIQUES

The composition of the 20CD10-05 steel is as follows: 2,4 % Cr, 0,4 % Mo and 0,21 % C. The conventional mechanical properties are given in table I

TABLE 1-Mechanical properties of 20CD10-05 steel.

T°C	Young Modulus(MPa)	Ultimate stress(MPa)
20	207000	780
610	159000	-

The strain controlled strain tests were carried out using servohydraulic machines, at strain rate  $\dot{\epsilon} = 0,003$  equipped with resistance furnaces.

### RESULTS AND DISCUSSION

The fatigue life results as a function of maximum stress amplitude  $\Delta\sigma/2$  is shown in figure 1. Using this representation an increase of temperature reduces the fatigue life drastically for a given stress amplitude, whatever the temperature range.

Most low cycle fatigue predictive techniques at elevated temperature have been outgrowth of the well known Coffin Manson equation:

$$(\Delta\epsilon_p \%) N_F^{\beta} = C \dots\dots\dots (1)$$

where  $\Delta\epsilon_p$  is the plastic strain range,  $N_F$  is cycles to specimen failure and  $\beta$  and  $C$  are material constants. The low strain fatigue lifetimes for a given  $\Delta\epsilon_p/2$  decrease by a factor 2 or 10 (Figure 2). This decrease can be attributed in part to the onset on high temperature intergranular cracking in relation with oxidation enhanced crack initiation. Let us consider first the life-plastic strain amplitude in the range of high plastic strain amplitudes the fatigue life is nearly insensitive to temperature. To clarify this behaviour isothermal oxidation specimen tests have been performed without external mechanical load to determine the kinetics law and the  $Q_0$  activation energy of the oxidation process at different temperatures. The penetration  $X$  of oxygen into the material follows a standard Arrhenius law:

$$X^2 = (1,89 \exp -167000/RT)t \dots\dots\dots (2)$$

with  $R = 8,32$  J/at.g/°K,  $T$  = temperature and  $t$  = time  
The study of the kinetics of oxidation under mechanical loading cannot be performed in situ. However, using the Erismann model (11), we can correlate the number of cycles performed at 610°C with the number of cycles performed at 20°C resulting in the same state of damage according to the equation:

# FATIGUE 87

$$\frac{\Delta n_i}{N_i} = \frac{\Delta n_j}{N_j} \dots\dots\dots(3)$$

with  $N_i, N_j$  numbers of cycles resulting in failure at 610 and 20°C being 660 and 7200 respectively;  $\Delta n_i$  is the number of cycles performed at 20°C and  $\Delta n_j$  is the equivalent number of cycles at 610°C resulting in equal damage. Table II lists the available results:

TABLE II Variation of activation energy of oxidation process under mechanical cycling.

Number of cycles at 20°C	Equivalent number of cycles at 610°C	Activation energy Q (kJ/mole)
12	1	167
591	50	161
1180	100	157
2360	200	146
4721	400	136
6492	550	128

Variation of the activation energy during the mechanical cycling can be described as follows:

$Q = Q_0 (1 - CN^a) \dots\dots\dots(4)$   
 where  $C = 1,8 \cdot 10^{-3}$  per cycle and  $a = 0,77$  are material constants and  $N$  the number of equivalent cycles performed at 610°C. The penetration of oxide into the material can be represented by:

$$X = \left[ 1,89 \exp. -167000(1-CN^a)/RT.t \right]^{\frac{1}{2}} \dots\dots\dots(5)$$

After application of a series of cycles at 610°C with 0,74% total strain amplitude, the length of the largest crack as well as the average thickness of oxide layers have been measured; the latter value can be compared with the value obtained using equation 5 with respect to the one hour preliminary heating time of the sample in the furnace. On figure 3 it is noticeable that cracks originate from the oxide layer and then progress into the material. Our hypothesis will be that the oxidation layer can be assimilated to microcracks of equal thickness that will be cracked during the mechanical cycling. The length  $a$  of the crack will be equal to the sum of  $a_i$ , the measured length of the crack and  $a_0$ , the initial oxide layer thickness.

This value will be compared with the penetration  $X$  of oxide into the material as calculated from equation 5 (Figure 4). Beyond 75 cycles, the length of the crack becomes greater than the oxide thickness. Remarkably enough many authors have defined the priming point as being a crack length equivalent to the average diameter of the grains.

## FATIGUE 87

### CONCLUSION

The number of crack initiation cycles in high temperature low cycle fatigue has been determined using a method based on the measurement of the penetration of oxide into the material, with the thickness of the initial oxide layer at the first cycle being assimilated to a microcrack of equal length. The number of cycles resulting in triggering corresponds to a microcrack equivalent to the average size of the grains.

### REFERENCES

- (1) Broom, T. and Nicholson, A. Jour. Inst. of Metals, 89, 1960, 183
- (2) Boettner, R. C., Laird, C. and McEvily, A. J., Trans. AIME, 223, 1965, 379
- (3) McMahon, C. J. and Coffin, L. F., Metall. Trans., 1, 1970, 3443
- (4) Coffin, L. F. ASTM STP, 520, 1973, 112
- (5) Skelton, R. P. and Bucklow, J. I., Metal Sci., 12, 1978, 64
- (6) Antolovich, S. D., Rosa, E. and Pineau, A., Mat. Sci. Eng., 47, 1981, 47
- (7) Bricknell, R. H. and Woodford, D. A., Metall. Trans., A12, 1981, 425
- (8) Reuchet, J. and Rémy, L., Mat. Sci. Eng., 58, 1983, 19
- (9) Swanson, J. W. and Marcus, H. L., Met. Trans. Vol. 1, 9A, 1978, 29
- (10) Rémy, J. L. and Reuchrt, J. Rev. Met., 8, 1982, 439
- (11) Erismann, T. H. Eng. Fract. Mech., 1976, 115

# FATIGUE 87

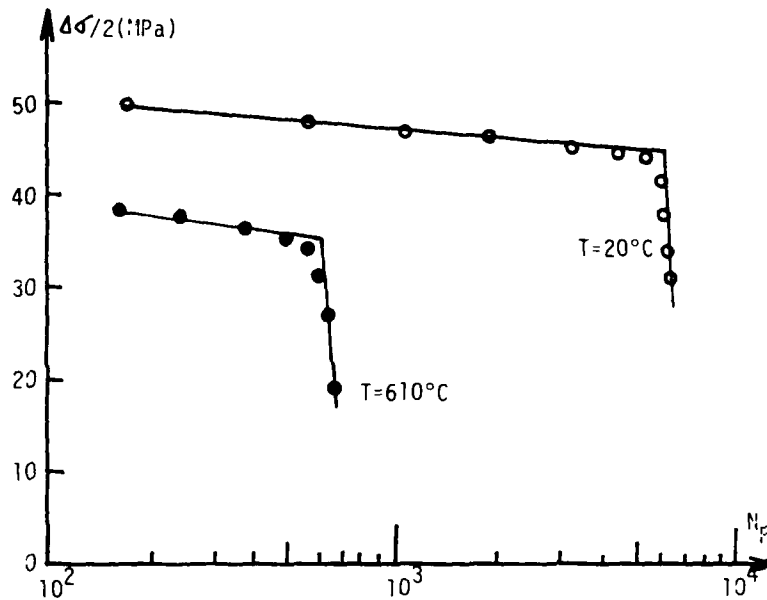


Figure 1 Fatigue life  $N_F$  as a function of the maximum stress amplitude ( $\Delta\epsilon_t = 0,74\%$ ).

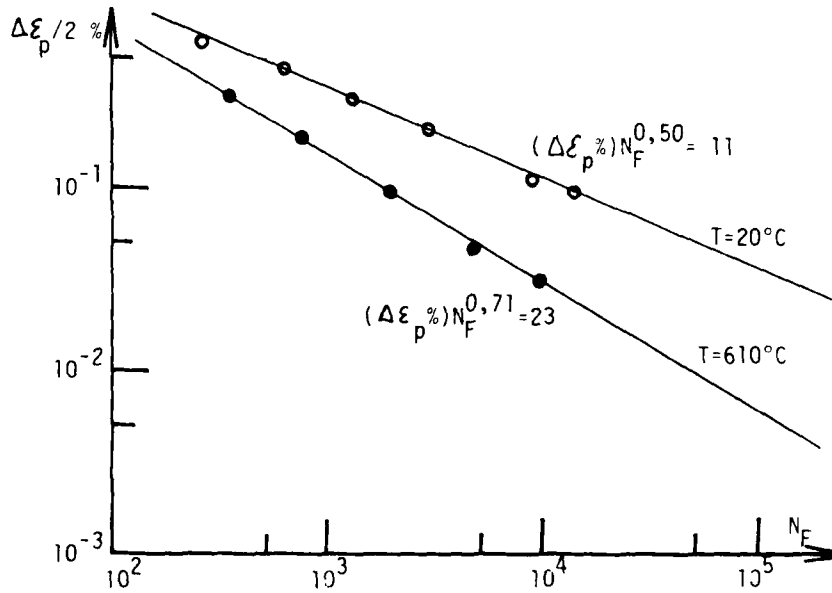
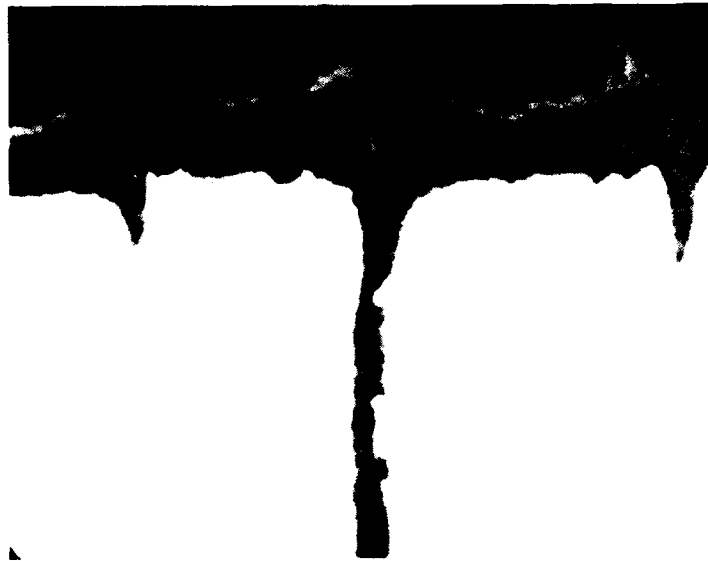


Figure 2 Fatigue life  $N_F$  as a function of the plastic strain amplitude.

# FATIGUE 87



N=550 cycles X 435

Figure 3 Cross section of oxidized specimen under mechanical cycling.

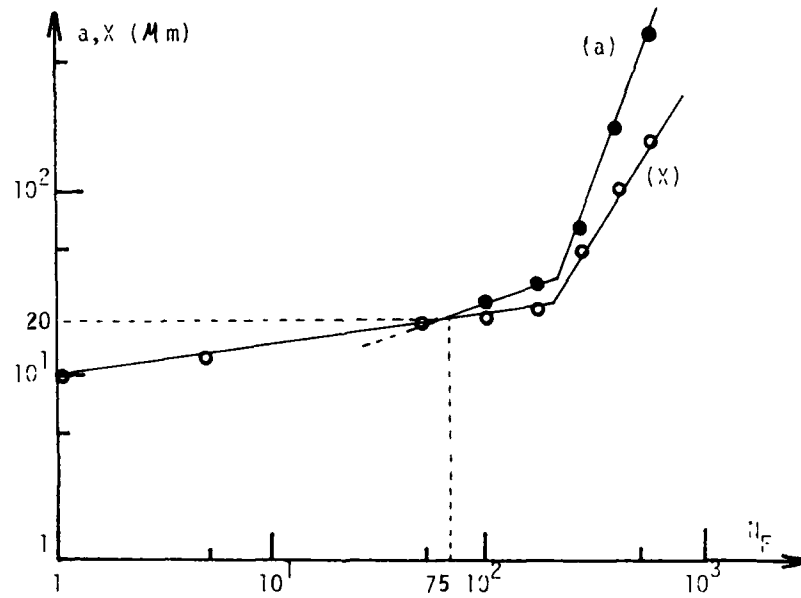


Figure 4 Comparison between depth of oxide (X) and crack length (a).

## FATIGUE 87

### EFFECT OF TEMPERATURE EXPOSURE ON FATIGUE CRACK PROPAGATION

K. K. Brahma\*, B. Dattaguru\* and R. Sunder\*\*

Experimental study of the effect of temperature exposure in between blocks of constant  $K_{max}$  loading on fatigue crack propagation (FCP) is carried out on Al-Cu-Mg alloy. The study attempts to explain these effects through crack closure phenomenon. The crack closure measurements are carried out through electron microscopy. The results indicate that the temperature exposure does significantly decrease the crack closure/opening stress and increase the FCP rate.

### INTRODUCTION

The load interaction effects on fatigue crack propagation (FCP) due to variable amplitude loading have been a subject matter of investigation for many years. The inability to adequately predict these interaction effects in arbitrarily varying loading cases, has prompted many workers to study the influence of relatively simple loading patterns on fatigue crack propagation. Some of the important contributions in these regard dealt with the decrease in the fatigue crack growth rate (delay or retardation) which is observed after a single or multiple overload cycles in between blocks of constant amplitude (CA) loading or a step reduction from high load cycles to lower load cycles (Hi-Lo). As pointed out by Schijve (1) and many others, this delay can have a significant influence on the fatigue life of a structure. In order to

\* Department of Aerospace Engineering, Indian Institute of Science, Bangalore 560 012, India

\*\* Materials Science Division, National Aeronautical Laboratory, Bangalore 560 017, India

## FATIGUE 87

understand these effects, many investigators studied the effect of overload ratio, the sign of overload, the number and sequence of overload cycles, mean stress levels, sheet thickness, exposure to elevated temperature after the overload as well as during the application of overload, rest period etc., on retardation. Newman (2) provided an excellent analytical model using Dugdale approach for understanding the effect of variable amplitude loading (but without temperature effect) on FCP through crack closure/opening phenomenon observed by Elber (3).

This paper concerns with the effect of temperature exposure in between blocks of constant  $K_{max}$  loading (as a significant aspect of exposure to environmental conditions) on fatigue crack propagation. The fact that temperature exposure effects the FCP rate has been observed before by Schijve and Arkema (4). But there was no systematic explanation of the effect of temperature exposure on various parameters affecting FCP rate. Most of the earlier observations on the effect of temperature are on the change in retardation produced by overload cycles in between blocks of CA loading. Some preliminary investigations have been carried out on the effect of temperature exposure after the application of a tensile overload cycle on the retardation in crack growth at room temperature in DTD 610 aluminum alloy by Raju et al (5). The temperatures involved in such studies are of the order of 80 °C to 180 °C and the exposure duration varying from 30 minutes to 24 hours. It was observed that retardation decreases with increasing duration of exposure at any given temperature and also the retardation significantly decreases at higher temperatures for any given exposure time. Shih (6) has found that in mill annealed Ti-6Al-4V, exposure to 293 °C following a room temperature tensile overload excursion, decreases the subsequent number of retardation cycles at room temperature when compared to the results without the temperature exposure. The same result has been observed by Chanani (7) when exposing 2024-T3 and 7075-T6 aluminum alloys to 1 hour soak period at 80 °C and 120 °C. Both Shih and Chanani have concluded that the decrease in retardation may be due to relaxation of residual stresses in the near crack tip region. Such a postulation is difficult to be checked experimentally and also they have no evidence to establish a definitive explanation to this effect.

This paper provides a systematic evidence for the effect of temperature exposure on FCP rate. The basic idea behind this work is that the temperature exposure effects the crack closure/opening stress. Experimental measurements on crack closure/opening stress

## FATIGUE 87

are carried out using electron fractography on specimens with and without temperature exposure. To facilitate the measurement, a special loading sequence (binary coded loading sequence) is applied to specimen and the crack closure/opening stress is measured from the striations on the fractured surface. The result of the present study shows that the temperature exposure effects the crack closure/opening stress and consequently FCP rate. The work is being extended to study the effect of temperature exposure on retardation after single or multiple overload cycles.

### EXPERIMENTAL PROGRAM

The experimental studies are carried out on specimens made from 5 mm aluminum alloy sheet. The program consists of fatigue crack growth tests in the case of a) without any temperature exposure and b) with temperature exposure at a prefixed crack length on all the specimens. The specially designed binary coded loading sequence is applied in the tests to create specific pattern of striations on the fracture surface for the measurement of crack closure/opening stress. Sunder and Dash (8) had earlier used the concept of specially designed loading block and subsequent TEM study of fractographs for estimating crack closure stress. The choice of D16AT (Al-Cu-Mg) alloy is particularly due to the fact that it is conducive to the formation of clear fatigue striations. The chemical composition and the mechanical properties of this alloy are given in Table 1. All the tests are carried out on 25 ton electro-hydraulic INSTRON testing machine at the National Aeronautical Laboratory, Bangalore.

TABLE 1 - Chemical Composition and Mechanical Properties of D16AT Aluminum Alloy

Chemical composition (weight %)					Mechanical properties		
Cu	Mg	Mn	Fe	Si	E (GPa)	$\sigma_y$ (MPa)	UTS (MPa)
4.4	1.5	0.6	0.5	0.5	73	323	460

**Specimen geometry.** Single-edge notched specimens of 75 mm width and 200 mm long are cut along the rolling direction from the 5 mm thick D16AT aluminum alloy sheet. 4 mm long and 0.5 mm wide saw cut is used as crack initiator. Figure 1 shows the specimen geometry used for the present study.

**Crack length measurements.** A single cantilever type crack opening displacement (COD) gage is used for automated measurement of crack length during fatigue crack propagation. This gage is fabricated at the National Aeronautical Laboratory, Bangalore and its principle of operation is described in detail elsewhere, Brahma, Sunder and Dattaguru (9). In brief, the gage measures the unloading compliance and the software estimates the crack length as a eighth order polynomial in terms of the unloading compliance. Software has been written to use this crack length and compute the current stress amplitude corresponding to the required stress intensity factor ( $K$ ) to carry out tests under any  $K$ -controlled mode.

**Fatigue tests.** a) precracking : The specimens are precracked from 4 mm to 5 mm crack length under constant amplitude loading at 30 Hz. b) specially designed loading : A specially designed load sequence is applied to leave striations on the fracture surface for crack closure/opening stress measurements. The specimens to be tested with and without temperature exposure are subjected to this special loading sequence. The base frequency for this test is 10 Hz. The test is carried out at constant  $K_{\text{mean}}$  of 7.0 MPa $\sqrt{\text{m}}$  at a minimum stress ratio of 0.1.

Computer software is developed to generate the required load sequence. A block of the above mentioned specially designed loading sequence is shown in Fig. 2. It consists of Marker Block (MB), Closure Block (CB), again Marker Block (MB) and finally Binary Block (BB). Marker Blocks (MB) and Binary Block (BB) consist of only two load levels marked '0' and '1'. The Marker Blocks of '1-0-1' and '1-0-0-1' indicate the beginning and the end of Closure Block respectively. The Closure Block (CB) consists of cycles with constant  $K_{\text{max}}$  and progressively decreasing  $K_{\text{min}}$ . The crack length does not change significantly during any one Closure Block and so each Closure Block corresponds to cycles with constant  $\sigma_{\text{max}}$  and progressively decreasing  $\sigma_{\text{min}}$ . Also, after the initial crack growth over few millimeters, the crack closure load under such a sequence would have stabilized and remain relatively constant throughout each Closure Block. This is supported by fractographic evidence by Pelloux, Faral and McGee (10), which

## FATIGUE 87

shows that striation spacing caused by the first cycle of a new load step is nearly equal to that caused by subsequent cycles of the same step.

**Temperature exposure.** Specimens to be tested without temperature exposure are subjected to binary coded closure block to grow the crack from 5 mm to 30 mm. Specimens to be tested with temperature exposure are subjected to binary coded closure block to grow the crack from 5 mm to 15 mm. Then the specimens are removed from the machine and are subjected to heat soak at a temperature of 150 °C for 4 hours. The specimen is then allowed to cool at room temperature. The test is continued thereafter till the crack length is 30 mm under the same loading. At 30 mm crack length, the specimens are subjected to tension load till failure and the fracture surfaces are replicated for TEM study.

**Crack closure/opening stress measurement.** Fatigue crack closure is mainly due to residual tensile strain in the wake of the crack. These strains will be lower at lower stress ratios, due to increased yield in compression in the wake during the unloading portion of the load cycle (after crack closure). Therefore, the crack closure load during a sequence of loads at constant maximum stress will correspond to that due to lowest preceding minimum load. At a particular stage, let  $K_{cl}$  be the stress intensity factor at the crack closure load for the lowest preceding minimum load. Under a sequence of loading with constant  $K_{max}$  and progressively decreasing  $K_{min}$ , load cycles with  $K_{min} > K_{cl}$  will leave behind striations which will be of progressively increasing width. For the case of  $K_{min} \leq K_{cl}$  the fracture surface would have equally spaced striations. Throughout this study, it is presumed that crack closure and opening stresses are the same.

Fatigue striations can be more clearly observed on Transmission than Scanning Electron Microscope (TEM and SEM) fractographs. It becomes tedious (nearly impossible) if a number of closely spaced striations have no discernible macro features which can be identified. Such situations make it extremely difficult to identify the precise macroscopic location associated with an observed fracture morphology. Therefore, it is essential to introduce coded patterns of fatigue striations on the fracture surface to register specific events during the test. The Binary Block (BB) consists of such "coded signature" which can be later identified as a loading block number during electron fractography of the fracture surface. In turn, it indicates the crack length (derived from the recording of crack length vs block numbers

## FATIGUE 87

obtained during the test) at which the fractography is being examined. The maximum and minimum stress for the two levels '0' and '1' in the binary coded block is kept well within the range of the overall test load history to avoid load interaction effects.

Typical electron fractograph at a crack length before temperature exposure of a specimen is shown in Fig. 3. Fig. 4 shows fractograph immediately after heat soak. Crack closure stress level is estimated from fractographs using the following procedure (8):

- 1) Count the number of equally spaced striations in one block of closure loading.
- 2) Determine the minimum stress level  $\sigma_{\min}^*$  corresponding to the last equally spaced striation.
- 3) Crack closure stress,  $\sigma_{cl}$ , will be equal to or less than the minimum stress  $\sigma_{\min}^*$  determined in the previous step, but will be greater than in the next step minimum stress. The increment,  $\Delta\sigma_{\min}$  between these two minimum stresses will control the accuracy of estimation of  $\sigma_{cl}$ . The relative crack closure stress  $\bar{\sigma}_{cl} = \sigma_{cl}/\sigma_{\max}$  is determined within the range,

$$\sigma_{\min}^*/\sigma_{\max} \geq \bar{\sigma}_{cl} > (\sigma_{\min}^* + \Delta\sigma_{\min})/\sigma_{\max}$$

Values of relative crack opening stress,  $\bar{\sigma}_{cl}$ , determined from a number of fractographs such as those in Figs. 3 and 4 are shown in Table 2.

TABLE 2 - Comparison of Relative Crack Closure Stress

Crack length (mm)	Condition	$\bar{\sigma}_{cl}$
19*	before heat soak	0.33
15	after heat soak	0.25

\* The same value of  $\bar{\sigma}_{cl}$  will be obtained at every crack length as the  $K_{\max}$  and minimum of  $K_{\min}$  of the load sequence are constant throughout the test.

## FATIGUE 87

### DISCUSSION OF RESULTS

Fatigue crack closure is clearly seen from the fractographic results. In closure block with constant  $K_{\max}$  and progressively decreasing  $K_{\min}$ , the varying striation spacing for  $K_{\min} > K_{cl}$  and equal striation spacing for  $K_{\min} \leq K_{cl}$  is a clear evidence of crack closure. Relative crack closure stress ( $\bar{\sigma}_{cl}$ ) determined from fractographic data, which is tabulated in Table 2, shows consistent values at different crack lengths before temperature exposure and is equal to 0.33. This also demonstrates the accuracy of the measurement technique. Relative crack closure stress ( $\bar{\sigma}_{cl}$ ) after temperature exposure is determined from Fig. 4 and this shows a value of 0.25. A significant reduction in  $\sigma_{cl}$  of the order of 24 percent, shows that the temperature exposure significantly alters the crack closure/opening stress.

The effect of temperature exposure can be explained by the relaxation of residual compressive stresses ahead and in the wake of the crack tip. This directly alters the crack closure stress and consequently affects the fatigue crack propagation. The temperature exposure, however, does not affect the extent of plastically stretched material. These results have an important bearing on the effect of temperature exposure observed on the retardation caused by overload cycle in between blocks of constant amplitude loading. Currently the present work is being extended for this situation. The present study indicates that the acceleration/retardation phenomenon is related to crack closure due to residual stress ahead and in the wake of crack tip and the wedging action of the stretched material on crack lips.

### CONCLUSIONS

The major conclusions of the present study could be summarised as follows :

- 1) The fatigue crack closure phenomenon can clearly be seen from the results of electron fractography.
- 2) Fractographic evidence shows a significant effect of temperature exposure (in between blocks of constant  $K_{\max}$  loading) on the crack closure stress, which, in turn, affects fatigue crack propagation.
- 3) The reduction due to heat soak in residual compressive

## FATIGUE 87

stresses and hence crack closure could explain its effect in decreasing the retardation produced by overload cycle in between blocks of constant amplitude loading.

### ACKNOWLEDGEMENTS

The authors would like to thank Dr. K. N. Raju, Deputy Director, Materials Science Division, National Aeronautical Laboratory for his intense discussions, useful suggestions and help. The authors also thank the National Aeronautical Laboratory for extending their INSTRON and TEM facilities for this work. The financial support of the Aeronautics Research and Development Board, Ministry of Defence, Govt. of India for research in fracture mechanics and acoustic emission is gratefully acknowledged.

### REFERENCES

- (1) Schijve, J., "The Prediction of Fatigue Crack Propagation under Service Load-time Histories", National Aerospace Laboratory NLR, The Netherlands, NLR MP 7301U, 1973.
- (2) Newman, J.C., Jr., "A Crack Closure Model for Predicting Crack Growth under Aircraft Spectrum Loading", ASTM STP 748, 1981, pp. 53-84.
- (3) Elber, W., "The Significance of Fatigue Crack Closure", ASTM STP 486, 1971, pp. 230-242.
- (4) Schijve, J. and Arkema, W. J., "Crack Closure and the Environmental Effect of Fatigue Crack Growth", Report VTH. 217, Delft Univ. of Technology, The Netherlands, April 1976.
- (5) Raju, K. N. and et al, Int. J. of Fracture Mechanics, Vol. 8, 1972, pp. 99-102.
- (6) Shih, T., "Fatigue Crack Growth under Variable Amplitude Loading", Ph. D Thesis, Lehigh University, 1974.
- (7) Chanani, G. R., "Fundamental Investigation of Fatigue Crack Growth Retardation in Aluminum Alloys", AFML-TR-76-156, 1976.
- (8) Sunder, R. and Dash, P.K., Int. J. of Fatigue, Vol. 4, No. 2, April 1982, pp. 97-105.
- (9) Brahma, K. K., Sunder, R. and Dattaguru, B., "Automated estimation of Fatigue Crack Length and Closure/Opening Stress", to appear in Int. J. of Fatigue, January 1987 issue.
- (10) Pelloux, R. M., Faral, M. and McGee, W. M., Fatigue Engg. Mater. and Structures, Vol.1, 1979, pp. 21-35.

# FATIGUE 87

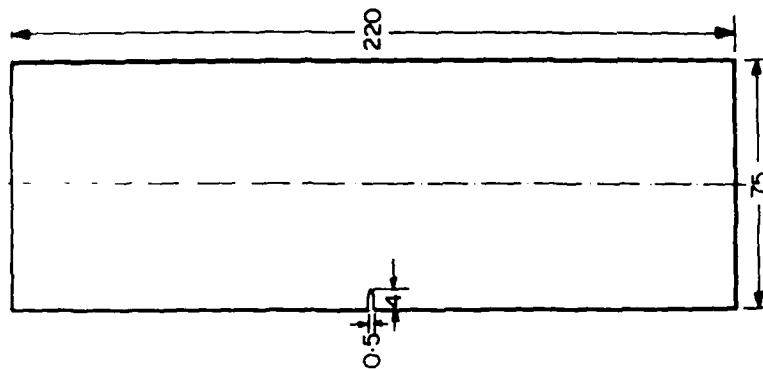


Figure 1 Specimen geometry (all dimensions are in mm)

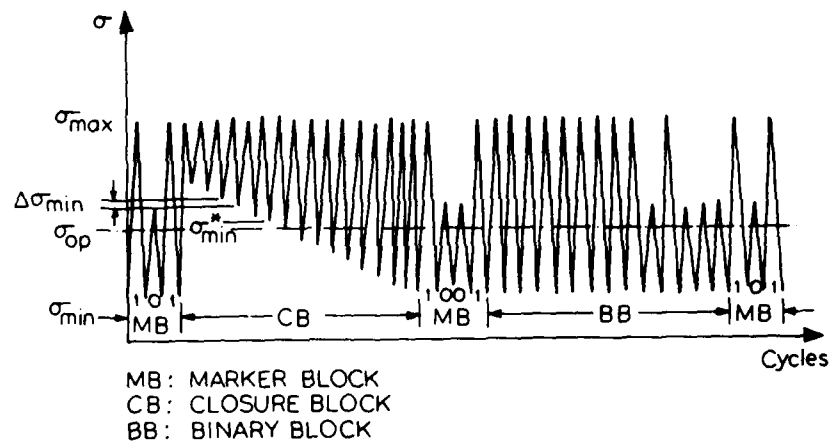


Figure 2 Schematic illustration of binary coded closure block

FATIGUE 87



Figure 3 Fatigue striations at mid-thickness (before heat soak, crack length = 19 mm)

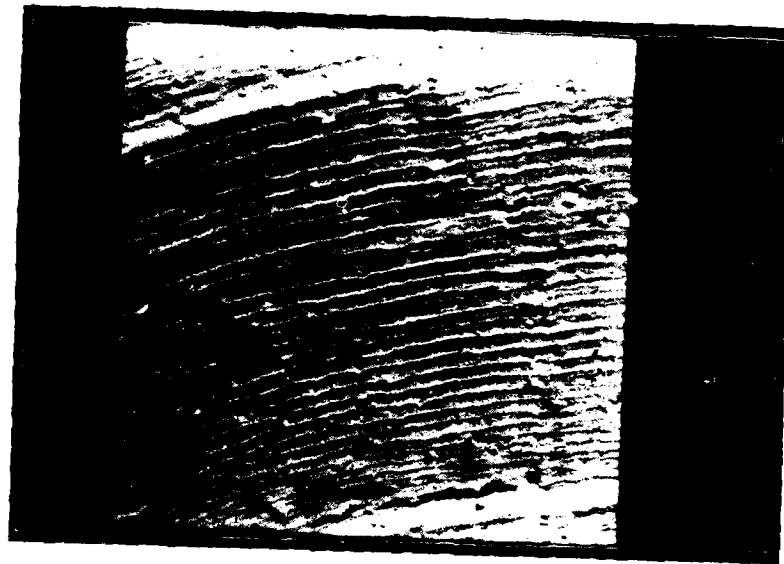


Figure 4 Fatigue striations at mid-thickness (after heat soak, crack length = 15 mm)

HIGH TEMPERATURE LOW CYCLE FATIGUE OF OXIDE DISPERSION  
STRENGTHENED AND SINGLE CRYSTAL NICKEL BASE SUPERALLOYS

M. Marchionni\*, V. Catena\*\*, D. Ranucci\*

In this paper the high temperature mechanical strength of an oxide dispersion strengthened alloy is compared with that of a single crystal alloy. The results show that the single crystal alloy exhibits a lower elasticity modulus and higher ductility in the temperature range 850°C-1050°C.

The cyclic curves of the ODS alloy are softening when strain is lower than 0.4-0.8 per cent and hardening at higher strains. The single crystal alloy shows a hardening behaviour at higher temperatures and a softening behaviour at 850°C.

The curves of fatigue life show that the single crystal alloy exhibits a higher fatigue endurance than that observed in the ODS alloy for all the test temperatures.

INTRODUCTION

The increase of service temperature in gas turbine components requires the use of new nickel base superalloys that exhibit high mechanical strength, good corrosion resistance and long creep and fatigue lives at elevated temperatures.

In the last ten years the oxide dispersion strengthened alloys have shown to be qualified for severe service conditions. Among different types of superalloys the Inconel MA6000 alloy is currently being evaluated for uncooled first stage turbine blade applications in advanced design of compact aeroengines (1). Analysis of the high temperature mechanical properties of oxide dispersion strengthened turbine blade alloys has shown that their benefits can be optimized by matching the blade mass distribution and temperature profile to the unique characteristic of this type of material (2).

\* ITM-CNR, Via Induno 10 - 20092 Cinisello B.(Milano)-Italy

\*\*FIAT AVIAZIONE, Via Nizza, 312 - 10100 Torino - Italy

## FATIGUE 87

Besides this type of superalloys stronger turbine blades for more fuel efficient aircraft engines were successfully developed using single-crystal (SC) casting technology and alloys specifically selected for SC applications (3,4). The absence of grain boundaries does not require grain boundaries strengthening elements in alloy composition.

Although the increasing service temperature determines a greater presence of creep phenomena in gas turbine components, however the low cycle fatigue effects can not be neglected.

The purpose of this work is to compare the low-cycle fatigue behaviour of an oxide dispersion strengthened nickel base superalloy and a single crystal superalloy.

### MATERIALS AND EXPERIMENTAL CONDITIONS

The nominal composition of Inconel alloy MA6000 is reported in Table 1. The alloy is powder metallurgy nickel base superalloy produced by the mechanical alloying process and containing a finely distributed dispersoid of yttrium oxide ( $Y_2O_3$ ) that allows to extend the operating temperature of conventional nickel base alloys to 1100°C (1).

TABLE 1 - Nominal chemical composition (Wt%) of MA6000 ODS nickel base alloy.

Cr	Al	Ti	W	Mo	Ta	C	B	Zr	$Y_2O_3$	Ni
15	4.5	2.5	4.0	2.0	2.0	0.05	0.01	0.15	1.1	balance

The material was supplied in bars after the following heat treatment: 1232°C x  $\frac{1}{2}$  hr, air cooled + 954°C x 2 hrs air cooled + 845°C x 24 hrs, air cooled.

The nominal composition of single crystal SRR99 alloy is reported in Table 2.

The material was supplied in bars after the following heat treatment: 1280°C x 1 hr + 1290°C x 2 hrs + 1300°C x  $\frac{1}{2}$  hr + 1305°C x  $\frac{1}{2}$  hr, quenched to 1000°C at a rate of 100 400°C/min, quenched to 800°C at a rate of 100 400°C/min and air cooled to room temperature.

## FATIGUE 87

TABLE 2 - Nominal chemical composition (Wt%) of SRR99 single crystal alloy.

Cr	Al	Ti	Co	W	Mo	Ta	C	Ni
8.0	5.5	2.25	5.0	10.0	0.25	2.75	0.015	balance

Fatigue tests have been performed by an electrohydraulic closed loop machine. Due to the directionally solidification process, both alloys exhibit a large anisotropy (5,6) and consequently it was not advisable to perform the fatigue tests in diametral strain controlled conditions. Therefore all tensile, cyclic and low cycle fatigue tests were carried out on cylindrical specimens with a diameter of 7 mm and a gauge length of 12.5 mm.

The samples were heated by induction coil in the temperature range 850÷1050°C. The tests were performed in longitudinal strain control with a triangular wave form and a zero mean value ( $R = -1$ ). The strain rate was  $10^{-2}.s^{-1}$ .

During the experiments the hysteresis loop and the stress response were recorded.

### TENSILE AND CYCLIC TESTS

Fig. 1 shows the tensile and cyclic curves of MA6000 alloy at different temperatures. We can observe that when temperature increases from 850°C to 1050°C, the stress response decreases sensibly both for tensile and cyclic curves. In correspondence of all the test temperatures the alloy exhibits a softening behavior at low strains (0.4:0.8% depending on test temperature) and a hardening behavior at higher strains. The primary softening effect is reduced when test temperature increases.

In Fig. 2 the single crystal SRR99 alloy shows firstly a lower elasticity modulus than that observed in MA6000 alloy at all the test temperatures and secondly a stress response sensibly higher than that exhibited by MA6000 alloy.

At the higher temperatures the alloy shows a hardening behaviour (more marked at 950°C) and a softening behaviour at 850°C. This effect could be ascribed to the change of deformation mechanisms when test temperature changes from 850°C to 950°C and from 950°C to 1050°C.

### LOW CYCLE FATIGUE RESULTS

In Fig. 3 the fatigue curves of ODS MA6000 alloy at different temperatures are reported. The diagram shows that the temperature increasing does not affect markedly fatigue life, mainly at higher total strains. At lower strains the reduction of fatigue life is of 2 or 3 times for each temperature change.

Fig. 4 shows the fatigue curves of SRR99 single crystal alloy at the same test temperatures of ODS MA6000 alloy. When test temperature increases the trend of fatigue curves is similar to that found in MA6000 alloy, save the value of number of cycles to failure that at the same temperature and strain is increased of a factor 10.

Figs. 5 and 6 present the stress response of the alloys determined at half life ( $1/2 N_f$ ) in function of total strains. For both alloys the temperature increasing gives a decrease of stress response according to the behaviour of the cyclic curves, but this trend is more marked in MA6000 alloy.

### DISCUSSION

The creep and fatigue results of MA6000 alloy in the temperature range  $760^{\circ}\text{C} \div 1050^{\circ}\text{C}$  (7  $\div$  10) and the creep results of SRR99 single crystal alloy (11) in the temperature range  $600^{\circ}\text{C} \div 1050^{\circ}\text{C}$  have shown that these new alloys are suitable to be used under severe service conditions.

A previous work on the low cycle fatigue of MA6000 alloy performed in our laboratory (12) has shown that in the temperature range  $850^{\circ}\text{C} \div 950^{\circ}\text{C}$  the use of an ODS alloy instead of an investment cast alloy is not convenient because the fatigue life is comparable and the cost of ODS alloy is very expensive. The employ of such alloy is recommended at temperatures over  $1000^{\circ}\text{C}$ .

However the fatigue results shown in Figs. 3 and 4 demonstrate that in all temperature range the single crystal alloy exhibits a higher fatigue life than ODS alloy of a factor between 6 and 10. This can be ascribed to the absence of grain boundaries and consequently of boundary precipitations that, in fatigue, can accelerate the crack initiation on the external surface of the specimens. The temperature increasing is supported better by single crystal alloy as shown in the plot of stress response at half life versus total strain. At  $850^{\circ}\text{C}$  the stress response is higher in MA6000 alloy than in SRR99 alloy, but at  $950^{\circ}\text{C}$  and  $1050^{\circ}\text{C}$  the

## FATIGUE 87

MA6000 alloy exhibits a lower stress response due to the higher reduction of strength and to the increasing of ductility with the temperature, as can be observed also in the tensile and cyclic curves.

The results previously discussed are not completed and a better understanding of these new alloys can be obtained by optical examinations of the structure evolution during fatigue processes and by scanning electron microscopy examinations of fracture surfaces for the study of damage mechanisms. However at this point of the investigation the SRR99 alloy seems to be more resistant to fatigue damage than MA6000 alloy in the temperature range studied.

### CONCLUSIONS

The analysis of the mechanical behaviour of MA6000 alloy and SRR99 single crystal alloy at elevated temperature can be summarized as follows:

- the single crystal alloy exhibits a lower elasticity modulus, a higher stress response and an Ultimate Tensile Strength less sensitive to temperature variations;
- the cyclic curves show that the ODS alloy is softening at lower strains and hardening at higher strains, while SRR99 alloy is completely hardening at higher temperatures and softening at 850°C;
- the fatigue curves show that the SRR99 alloy has a longer fatigue life than the ODS alloy of a factor from 6 to 10 depending on temperature and total strain;
- the slope of fatigue curves and the stress response at half life in function of total strain confirms that the ductility of both alloys increases with temperature increasing.

### ACKNOWLEDGEMENTS

The authors have gratefully appreciated the help of Mr. E. Picco in conducting experimental activity.

### SYMBOLS USED

$\sigma$	stress (MPa)
$\Delta\sigma$	stress range (MPa)
$\epsilon$	strain
$\Delta\epsilon_t$	total strain range
$N_f$	cycles to failure

## FATIGUE 87

### REFERENCES

- (1) Hack, G.A.J., "Inconel Alloy MA6000 - A New Material for High Temperature Turbine Blades". Metal Powder Report, Vol. 36, n. 9, September 1981.
- (2) Benjamin J.S., "Potential of ODS Superalloys for Advanced Gas Turbines". ASME, Gas Turbine Division, Pamphlet 76-GT-118, 1976.
- (3) VerSnyder F.L. and Gell M. Fundamental Aspects of Structural Alloy Design (ed. R.I. Jaffee and B.A. Wilcox, Plenum Press, New York) 1977, p. 209.
- (4) MacLean M. Directionally solidified materials for high temperature service, Book 296, The Metals Society of London, 1983.
- (5) Shah, D.M. and Duhi, D.N. Superalloys 1984, Conference Proceedings, 1984, p. 105-114.
- (6) Reppich, B., Listl, W. and Meyer, T. High Temperature Alloys for Gas Turbines and Other Applications 1986. Conference Proceedings, 1986, p. 1023-1035.
- (7) Benn, R.C. and Kang, S.K. Superalloys 1984, Conference Proceedings, 1984, p. 319-326.
- (8) Huis, A.J. in't Veld, Bronsweld, P.M., De Hosson, J.th.M. High Temperature Alloys for Gas Turbines and Other Applications 1986, Conference Proceedings, 1986, p. 1049-1056.
- (9) Bressers, J. and Arzt, E. Ibid, p. 1067-1080.
- (10) Hymia, A. et al., Ibid, p. 1091-1102.
- (11) Ford, D.A. and Arthey, R.P. Superalloy 1984, Conference Proceedings, 1984, p. 115-124.
- (12) Marchionni, M. and Ranucci, D. Fatigue at High Temperature, Conference Proceedings, Parigi, 1986, p. 232-238.

# FATIGUE 87

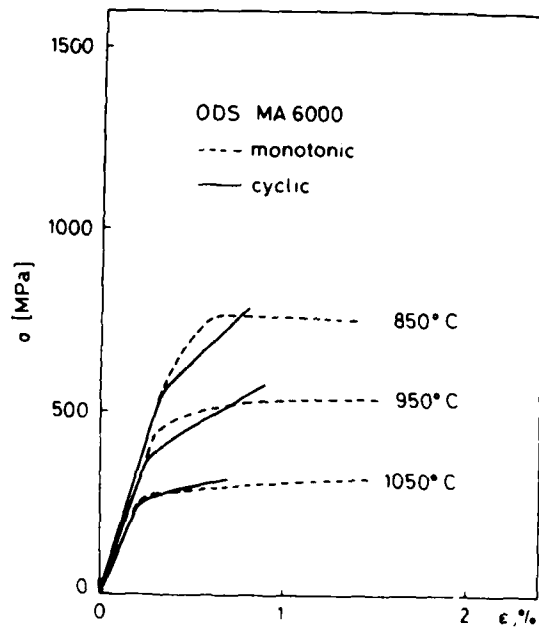


Figure 1 Tensile and cyclic curves of MA6000 alloy

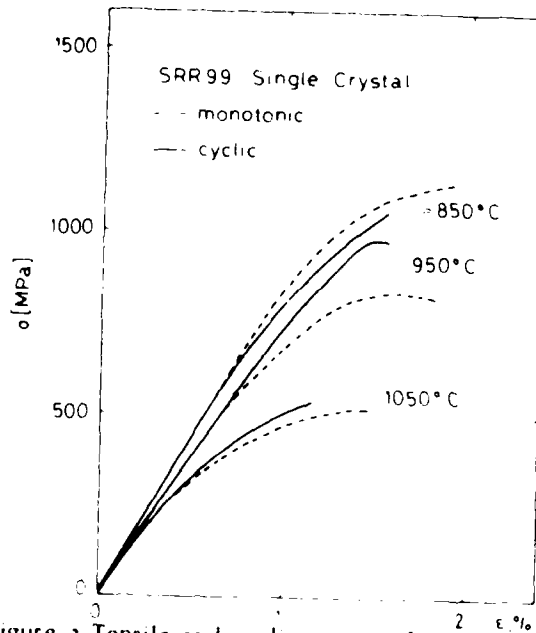


Figure 2 Tensile and cyclic curves of SRR99 alloy

# FATIGUE 87

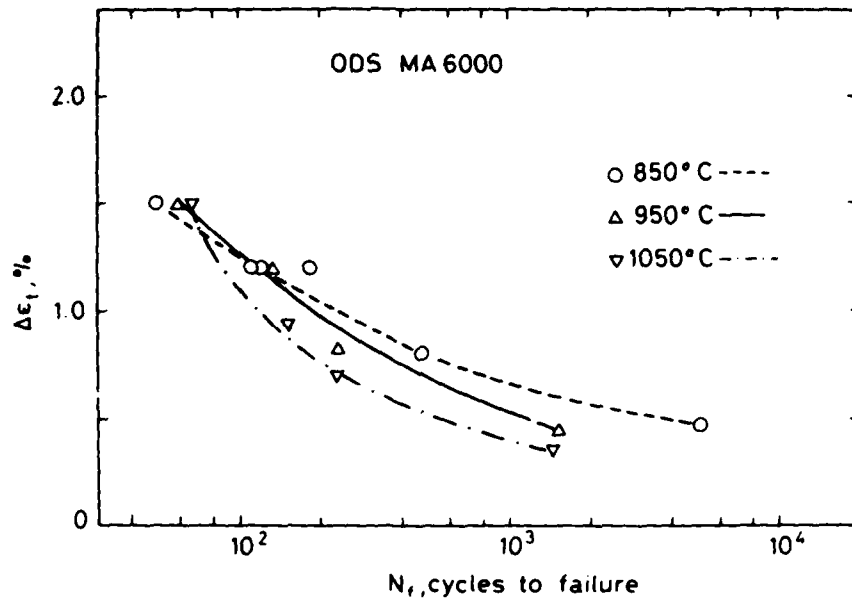


Figure 3 Fatigue life of MA6000 alloy

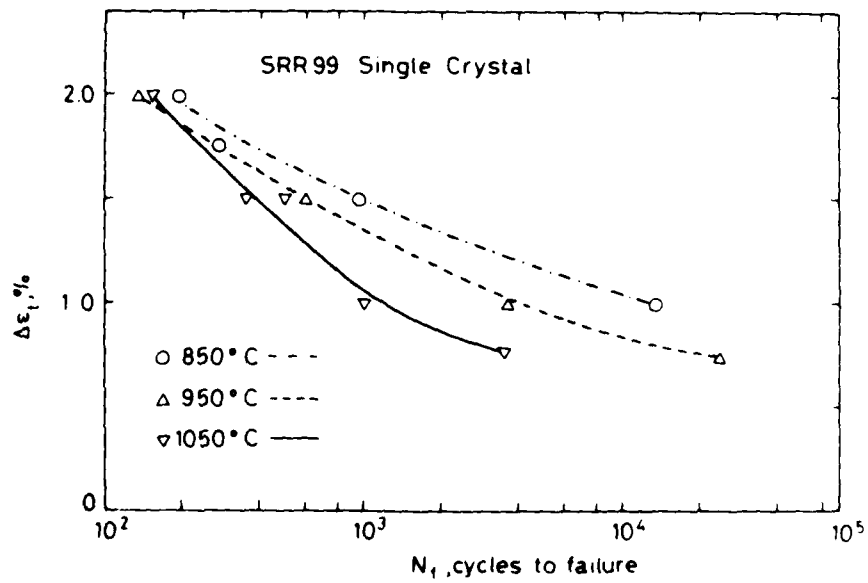


Figure 4 Fatigue life of SRR99 alloy

# FATIGUE 87

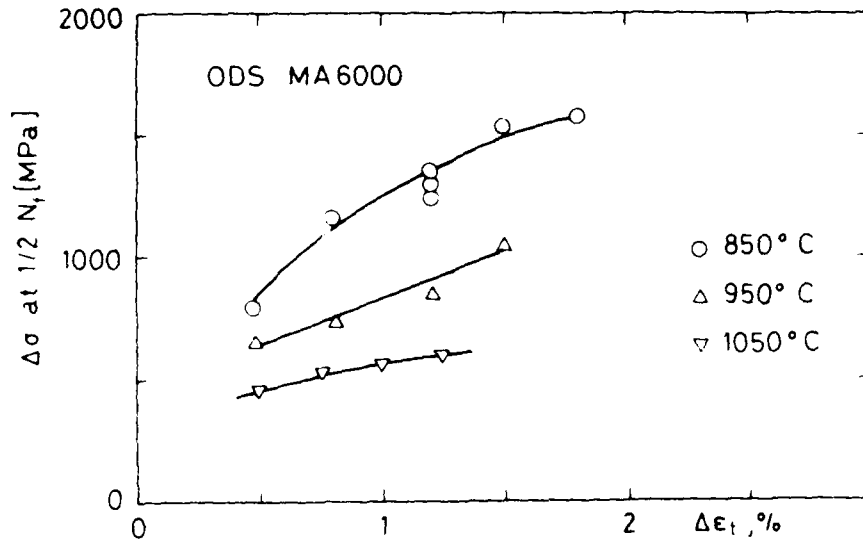


Figure 5  $\Delta \sigma$  at half life vs  $\Delta \epsilon_t$  for MA6000 alloy

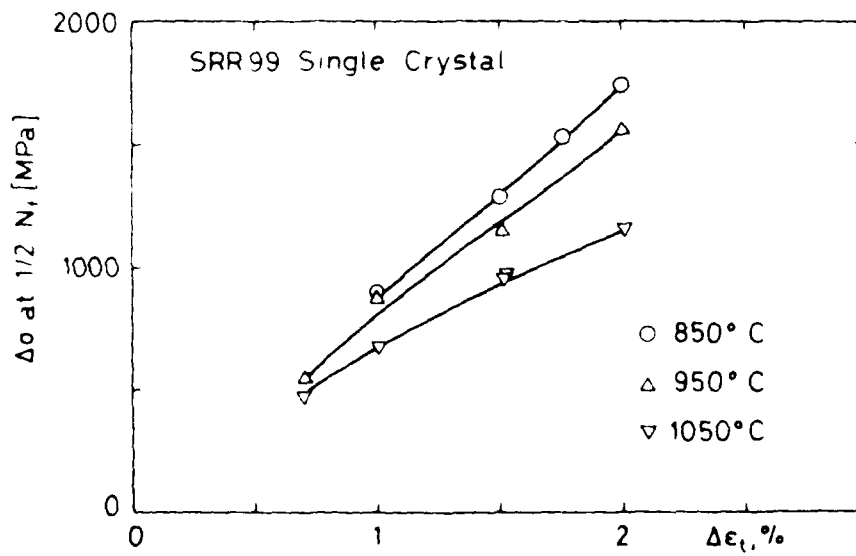


Figure 6  $\Delta \sigma$  at half life vs  $\Delta \epsilon_t$  for SRR99 alloy

FATIGUE 87

## FATIGUE 87

### ORIENTATION EFFECTS IN COPPER SINGLE CRYSTALS FATIGUED AT ELEVATED TEMPERATURES

L. L. Lisiecki\*\*, F. Boehme and J. R. Weertman\*

Copper single crystals oriented for one of 3 different double slip possibilities have been fatigued at 250°C or 405°C ( $1/2 T_m$ ). The dominant dislocation reactions expected in the 3 orientations lead to the production of sessile jogs, Lomer locks or cells formed by coplanar slip. After fatiguing at 250°C, PSBs, veins and cells are seen; at 405°C only cells. A plateau in the saturation stress is present at 250°C but not at 405°C. The various strengthening mechanisms (jogs, Lomer locks, cells) differ markedly in their response to increasing temperature.

### INTRODUCTION

In order to understand the processes involved in such a complicated subject as fatigue, it frequently is of value to study model systems which are simplified as much as possible. Accordingly a large number of investigations have been carried out on the fatigue behavior of single crystals of pure copper oriented for single slip [1-3]. Most of these tests were done at room temperature but a few were conducted at cryogenic temperatures (e.g., [4]). Recently Jin [5] and Jin and Winter [6,7] have examined room temperature fatigue in Cu single crystals oriented for double [6] and multiple [7] slip. For a fixed primary slip system the choice of the secondary system determines the dominant dislocation reaction which takes place upon fatigue. It was found from these tests that the dislocation structure which evolves during fatigue testing does indeed vary with the choice of secondary slip system. The saturation stress, for a given plastic strain amplitude, also

\* Department of Materials Science and Materials Research Center, Northwestern University, Evanston, IL 60201

\*\* Present address: Metallurgy Department, Risø National Laboratory, DK 4000 Roskilde, Denmark

differs among the orientations but the effect is not large: about 21% variation between the weakest and the strongest orientation in the case of double slip [6]. In the present research the mechanical behavior and dislocation structures in Cu single crystals oriented for each of the three possibilities for double slip again have been explored. Fatigue tests were carried out at 250°C (the highest temperature at which small dislocation loops in Cu are reasonably stable [8]) and 405°C (one half the absolute melting temperature). These experiments were designed to examine the effects of increasing temperature on the dislocation structure which evolves with fatiguing and, consequently, on the mechanical behavior. It is of interest to observe the response to temperature of each of the various strengthening mechanisms produced by double slip. Finally an effort was made to determine whether or not an observation made on fatigued polycrystalline Cu samples, namely, that persistent slip bands (PSBs) do not form at 405°C [9,10], carries over to the case of single crystals. A preliminary, partial account of this work is given in reference [11].

#### EXPERIMENTAL PROCEDURE

Seeded single crystals of 99.999% pure Cu were grown in a split graphite mold by a modified Bridgman technique. The gauge sections of the fatigue specimens were cut by an electric discharge machine (EDM) and the surfaces were chemically polished to eliminate surface damage. The crystals were seeded such that the stress axis was close to a [210], [211] or [221] direction (Fig. 1). In all cases (11 $\bar{1}$ ) [101] was the primary slip system. Specimens stressed near the [210] direction have the next highest Schmid factor on the (111) [10 $\bar{1}$ ] system. The interaction between the perpendicular screw dislocations on the two slip systems causes the formation of sessile jogs. In the case of samples oriented with the stress axis near [221] the primary and secondary slip systems share the same slip plane. When stress is directed parallel to [211] dislocations on the two most highly stressed slip systems interact to form Lomer or Lomer-Cottrell locks. The orientations, reactions, and Schmid factors for the three orientations are summarized in Table 1. Note that the ratio  $Q^*$  [12] of the Schmid factor on each of the three possible secondary slip systems to the Schmid factor on the primary is close to one for the favored secondary system but considerably lower for the other two cases.

The specimens were fatigued in plastic strain control mode in an MTS servohydraulic test machine which had been modified [13] to handle the small strains used in these experiments ( $10^{-5}$  to  $10^{-4}$ ). Testing was carried out at a total strain rate of  $10^{-4}$ /s at 250°C or 405°C in an atmosphere of Ti-gettered argon. Slices of specific crystal planes were cut by EDM for examination by transmission electron microscopy (TEM).

## RESULTS

Figure 2 shows cyclic hardening curves for specimens of orientation "a", near [210] (see Fig. 1). The shear stress amplitude  $\tau$  resolved on the primary slip plane is plotted as a function of the accumulated plastic strain  $\gamma_{pl,cum}$ . Here  $\gamma_{pl,cum} = 4N\gamma_{pl}$ , where  $N$  is the number of fatigue cycles and  $\gamma_{pl}$  is the plastic strain amplitude in the primary slip system. The value of  $\gamma_{pl}$  was increased after stress saturation was reached several times in the course of a test. A stress plateau of about 14 MPa is seen at 250°C. No plateau is evident at 405°C with the strain amplitudes chosen for the step test. The TEM micrographs of [210] specimens cycled at 250°C at low strain amplitudes to a cumulative plastic strain of about 12 show a vein structure and a few PSBs near the surface. Persistent slip bands are observed all the way through the specimen after cycling at the highest plastic strain amplitude ( $9.1 \times 10^{-4}$ ) to a  $\gamma_{pl,cum}$  of 65. Some regions of the specimen show that a transformation to a cell structure already is under way. Unfortunately no TEM examination was possible of the specimen tested at 405°C because it buckled shortly after the second increment in  $\gamma_{pl}$ .

Figure 3 shows cyclic hardening curves for specimens of orientation "b" (near [221], Fig. 1). Two crystals were cycled at 250°C and 405°C at similar values of  $\gamma_{pl}$  ( $\sim 9 \times 10^{-4}$ ) and a third was tested at  $\gamma_{pl} = 2 \times 10^{-4}$  at 405°C. Secondary cyclic hardening, defined by Wang and Maghrabi [14] as slow hardening at large cumulative glide strains, is seen in the two specimens cycled at the higher plastic strain amplitude. This hardening is associated with the formation of cells and their subsequent misorientation. The TEM micrographs of specimens fatigued at 250°C show short PSBs and extensive regions of cells. Little vein structure is found. Not much contrast is seen in the cell structure when viewed on the (11 $\bar{1}$ ) slip plane but, as seen in Fig. 4, considerable misorientation exists across cell boundaries viewed on the (1 $\bar{2}$  $\bar{1}$ ) plane in the [11 $\bar{1}$ ] direction. Only cells, usually equiaxed, were observed in the samples fatigued at 405°C (Fig. 5). Little misorientation is apparent. As expected, the cell size is considerably larger at 405°C than at 250°C.

The cyclic hardening curves of "c" orientation specimens (near [211], Fig. 1) are given in Fig. 6. The saturation stresses obtained in the step test conducted at 250°C remain reasonably constant over a range of  $\gamma_{pl}$  values. The plateau stress is about 14 MPa, the same value as found in fatigued [210] specimens. However the saturation stress appears to depend somewhat on strain history, as shown by the tests run at  $3.5\text{--}3.7 \times 10^{-4}$ . There was no indication of a stress plateau at 405°C. Dislocation structures were observed by TEM in foils cut parallel to the common cross slip plane, (11 $\bar{1}$ ). Persistent slip bands were seen on the two most highly stressed slip planes after fatigue at 250°C. In

## FATIGUE 87

specimens tested at 405°C, equiaxed cells are observed on the (111) plane.

### DISCUSSION

It can be seen from the cyclic hardening curves of Figs. 2 and 6 that a plateau exists in the saturation stress of crystals with orientations near [210] or [211] which are fatigued at 250°C. (There are insufficient data to draw any conclusions about [221] crystals.) The curves for Figs. 2 and 6 indicate that the plateau probably extends from  $10^{-4} < \gamma_{pl} < 10^{-3}$ . This range is somewhat shorter than that observed at room temperature. (Mughrabi [1], who used crystals with the same orientation (near [210]), found that the region of constant saturation stress in Cu fatigued at room temperature reaches from  $6 \times 10^{-5}$  to  $7.5 \times 10^{-3}$ .) There is no indication of any stress plateau at 405°C from the limited cyclic hardening measurements at that temperature.

The TEM observations of dislocation structures are consistent with the mechanical behavior of the various fatigued crystals. No PSBs were seen in specimens fatigued at  $0.5T_m$  and thus no saturation stress plateau is to be expected. (Unfortunately the number of 405°C samples which did not buckle in the course of testing and thus were suitable for TEM examination is small, so there still exists the possibility that PSBs can form at 405°C under some special conditions.) This seeming absence of PSBs at 405°C is in agreement with the results of a study of dislocation structure in polycrystalline Cu fatigued at 250°C and 405°C [9,10]. While PSBs are common at 250°C none was seen at the higher temperature. The disappearance of PSBs at high temperatures may be related to Wang and Mughrabi's observation [14] that PSBs eventually transform to cells in crystals fatigued at room temperature for a very long time. It appears that the cell structure may be more stable but the transformation from vein and PSBs to cells is slow. At high enough temperatures the change from vein to cell structure can be made directly. (One mechanism whereby the vein to cell transformation is accomplished was observed during a study of dislocation structure evolution in polycrystalline Cu fatigued at 405°C [15]. The interiors of veins gradually clear out, leaving the dense edges to serve as cell walls in the new structure.) Consistent with the argument that elevated temperature assists the transformation to cell structure is the observation that at 250°C the high  $\gamma_{pl}$  limit of the plateau is shortened considerably over the value at room temperature, down to  $10^{-3}$  from  $7.5 \times 10^{-3}$ . The change at the low  $\gamma_{pl}$  end is not so great.

The TEM micrographs show that the dislocation structures which evolve in the course of fatigue depend on orientation as well as on temperature,  $\gamma_{pl}$  and  $N$ . Fatigue at 250°C in the range  $10^{-4} < \gamma_{pl} < 10^{-3}$  of specimens oriented to produce sessile jogs results in veins and PSBs. If the orientation is such as to lead

to coplanar slip, cells and some short PSBs are seen. The Lomer lock orientation produces PSBs on both the highly stressed slip planes together with a few veins. By and large, these observations are similar to those of Jin [5] and Jin and Winter [6] on crystals of the same orientations fatigued at room temperature. At 405°C only cells, usually equiaxed, were observed.

Several types of hardening behavior were found. At 250°C, specimens with [210] or [211] orientation fatigued at  $\gamma_{pl} \sim 1.5 \times 10^{-4}$  underwent gradual hardening as the dislocation structure built up (Figs. 2 and 6). Note that this was the initial testing for each of these specimens. At higher amplitudes ( $3.5 \times 10^{-4}$  for [211], step tests after cycling at the initial  $\gamma_{pl}$  for both [211] and [210]) the hardening was extremely rapid and was followed by an extended period of softening. All specimens tested at 405°C experienced essentially immediate hardening, then softening which was completed in a shorter amount of cumulative plastic strain than at 250°C. In the case of [221] crystals at both temperatures, hardening (but not quite so rapid as at the other orientations) was followed by a slight softening (Fig. 3). A similarly shaped curve for [221] fatigue at room temperature was seen by Jin and Winter [6]. The [221] specimens tested at  $\gamma_{pl} \sim 9 \times 10^{-4}$  both experienced secondary hardening. Wang and Mughrabi [14] observed secondary hardening at room temperature, but only after a much greater cumulative plastic strain.

It is of interest to examine the influence of orientation on strength. At 250°C the saturation stresses corresponding to the three orientations, although considerably lower than at room temperature, are in the same order as that determined by Jin and Winter [6]. Specimens oriented near [221] are strongest, followed by [210] and [211]. However at 405°C the [210] crystals have a markedly lower saturation stress than those of the other two orientations. At elevated temperatures the sessile jogs which form in [210] specimens can move by climb. The enhanced vacancy mobility increases the ease of climb, thermally activated cross slip can occur, and thus the [210] orientation becomes progressively weaker relative to [221], the orientation which leads to rapid cell formation. On the other hand, specimens which produce Lomer locks [211] become harder relative to those near [221]. The influence of temperature on the various strengthening reactions is summarized in Fig. 7, which shows plots of the ratio of saturation stress of [210] and [211] crystals to that of [221] as a function of temperature. The three dislocation reactions become widely divergent in their effectiveness as strengthening mechanisms at high temperatures.

## FATIGUE 87

### CONCLUSIONS

1. At 250°C the dislocation structures corresponding to the three double slip orientations differ noticeably. A vein structure and PSBs were seen in samples oriented to produce sessile jogs. Persistent slip bands on both of the highly stressed slip planes and a few veins were found in the Lomer lock orientation, and cells and short PSBs occur in specimens oriented for coplanar slip. Only cells, usually equiaxed, were observed in crystals fatigued at 405°C.
2. A plateau in the saturation stress still is seen in 250°C but probably has disappeared by 405°C. This behavior is consistent with the fact that PSBs form at 250°C but not at 405°C.
3. The various strengthening mechanisms resulting from dislocation reactions in the three orientations vary significantly in their response to increasing temperature. Sessile jogs are weak at high temperatures while Lomer locks, the least effective at room temperature, become comparatively the strongest.

### ACKNOWLEDGMENTS

This research was supported under the NSF-MRL program through the Materials Research Center of Northwestern University (Grant DMR-8216972). Two of the authors wish to acknowledge fellowships: Owens-Corning Fiberglas (LLL) and the Guggenheim Foundation (JRW).

### REFERENCES

- (1) Mughrabi, H., Mater. Sci. Engng. 33, 207 (1978).
- (2) Mughrabi, H., Ackermann, F. and Herz, K. in Fatigue Mechanisms, Proc. of ASTM-NBS-NSF Symp. 1978, Kansas City, MO (edited by J. T. Fong), p. 69, ASTM-STP675 (1979).
- (3) Neumann, P., (1983), "Fatigue" in Physical Metallurgy, edited by R. W. Cahn and P. Haasen (Amsterdam, Elsevier), Chapter 24, pp. 1553-1594.
- (4) Basinski, Z.S., Korbel, A.S. and Basinski, S.J., Acta Metall. 28, p. 191 (1980).
- (5) Jin, N.Y., Phil Mag. 48A, L33 (1983).
- (6) Jin, N.Y. and Winter, A.T., Acta Metall. 32, p. 989 (1984).
- (7) Jin, N.Y. and Winter, A.T., Acta Metall. 32, p. 1173 (1984).
- (8) Segall, R.L., Partridge, P.G. and Hirsch, P.B., Phil. Mag. 6, p. 1493 (1961).

# FATIGUE 87

- (9) Shirai, H. and Weertman, J.R., Scripta Metall. 17, p. 1253 (1983).
- (10) Shirai, H., Ph.D. Thesis, Northwestern University, (June 1984).
- (11) Lisiecki, L.L. and Weertman, J.R., Scripta Metall. 20, p. 249 (1986).
- (12) Cheng, A.S. and Laird, C., Mater. Sci. Engng. 51, p. 55 (1981).
- (13) Baker, J.P., Lisiecki, L.L. and Weertman, J.R., Experimental Techniques 10, p. 26 (1986).
- (14) Wang, R. and Mughrabi, H., Mater. Sci. Engng. 63, p. 147 (1984).
- (15) Page, R.A. and Weertman, J.R., Scripta Metall. 15, p. 223 (1981).

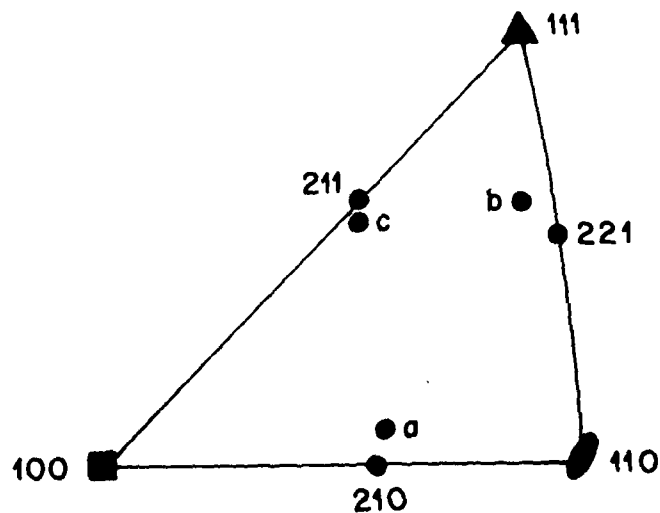


Figure 1 Orientations of specimen single crystals shown in a standard stereographic triangle.

Position in stereo- graphic triangle	Tensile axis near	Schmid factor	Q* (sessile jogs)	Q* (Lomer locks)	Q* (cells)	Most highly stressed slip systems	Product of dominant dislocation reaction
a	[210]	0.50	0.96	0.57	0.47	(111)-[101] (111)-[101]	Sessile jog
b	[221]	0.41	0.58	0.69	0.90	(111)-[101] (111)-[011]	[110] glissile in (111)
c	[211]	0.42	0.69	0.98	0.64	(111)-[101] (111)-[110]	Lomer or Lomer- Cottrell lock

Table 1. Schmid factors, Q\*'s, slip systems and dominant dislocation reactions for single crystal specimens used in this work.

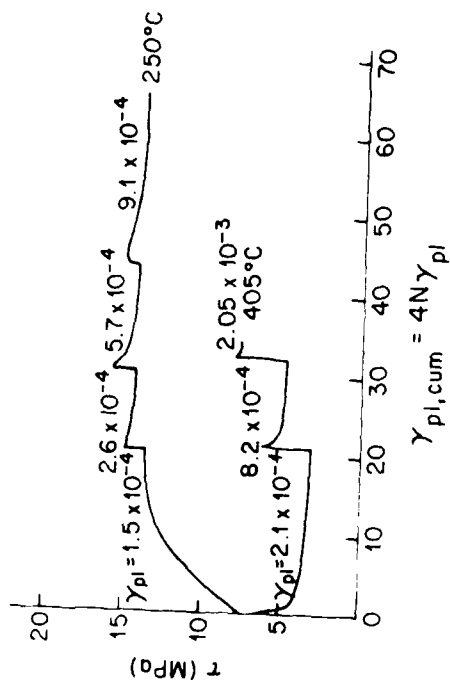


Figure 2 Cyclic hardening curves at 250 and 405°C for specimens oriented near [210].

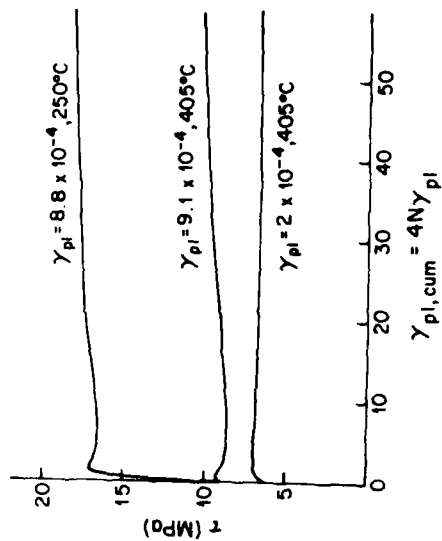


Figure 3 Cyclic hardening curves for specimens oriented near [221].



Figure 4 (121) plane of specimen oriented near [221] cycled at 250°C with a plastic strain amplitude of  $8.8 \times 10^{-4}$  to a cumulative plastic strain of 73.

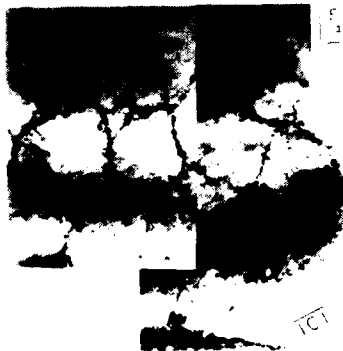


Figure 5 ( $\bar{1}\bar{2}\bar{1}$ ) plane of specimen oriented near [221] cycled at 405°C with a plastic strain amplitude of  $9.4 \times 10^{-4}$  to a cumulative plastic strain of about 3.3.

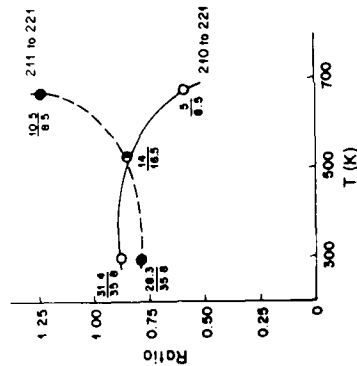


Figure 7 Approximate ratios of saturation stresses of specimens oriented near [210] (which form sessile jogs) and near [211] (which form Lomer or Lomer-Cottrell locks) to those of specimens oriented near [221] (which form cells) as a function of temperature. At 250°C: for [210],  $\tau \approx 14$  MPa at  $\gamma_{pl} = 9.1 \times 10^{-4}$ ; for [211],  $\tau \approx 14$  MPa at  $\gamma_{pl} = 6.8 \times 10^{-4}$ ; for [221],  $\tau \approx 16.5$  MPa at  $\gamma_{pl} = 8.8 \times 10^{-4}$ . At 405°C: for [210],  $\tau \approx 5$  MPa at  $\gamma_{pl} = 8.2 \times 10^{-4}$ ; for [211],  $\tau \approx 10.5$  MPa at  $\gamma_{pl} = 6.3 \times 10^{-4}$ ; for [221],  $\tau \approx 8.5$  MPa at  $\gamma_{pl} = 9.1 \times 10^{-4}$ .

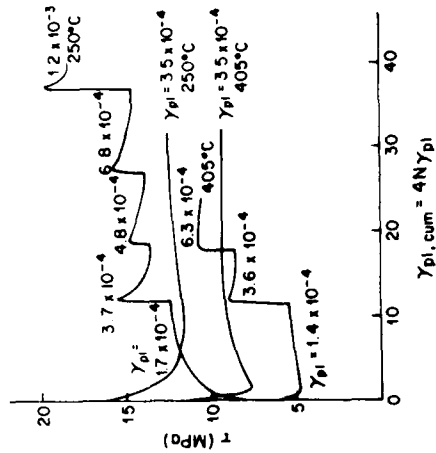


Figure 6 Cyclic hardening curves for specimens oriented near [211].

## FATIGUE 87

### ELEVATED TEMPERATURE FATIGUE CRACK PROPAGATION

D. J. Michel\* and A. W. Thompson\*\*

The effects of environment and hold time on the crack propagation behavior of austenitic stainless steel were examined as part of an effort to couple the available experimental fatigue and creep-fatigue results with the microstructural observations concerning the mode and character of crack propagation. The examination suggested that the primary contributions to the crack propagation process included the cyclic deformation, the thermally-activated, time-dependent tensile creep and the time-dependent environmental effects. A phenomenological approach incorporating these contributions was used to construct a model of the crack propagation behavior. The development of the model will be discussed and experimental and model results will be compared for 316 stainless steel.

### INTRODUCTION

A large body of evidence has been obtained concerning the processes responsible for fatigue and fracture at elevated temperatures. In particular, the processes of cavity nucleation and growth, grain boundary sliding and crack formation, and interactions with inter-granular precipitates have been studied both experimentally (1-4) and theoretically (5,6) for a variety of materials. The results in all cases show that the inter-relationships of the micro-and macro-mechanical parameters produce a primarily intergranular fracture character despite the wide variation both in possible microstructure and in the stress and strain levels experienced by the materials during the fatigue and fracture deformation (7-11). Although the overall aspects of the fatigue and fracture processes are complex, both fracture mechanism maps and deformation mechanism maps have provided important initial steps toward unifying the understanding of fracture (12).

\* Material Science and Technology Division  
Naval Research Laboratory, Washington, DC 20375-5000

\*\*Metallurgical Engineering and Materials Science Department  
Carnegie-Mellon University, Pittsburgh, PA 15213

## FATIGUE 87

The purpose of the present study has been to extend the understanding of fatigue and fracture processes through an attempt to couple the experimental fatigue and creep-fatigue crack propagation results at high temperatures (13,14) with the microstructural observations concerning the mode and character of the fracture (3,4,6). The model material for the purposes of this study was taken as 316 stainless steel for which numerous studies of fatigue and creep-fatigue crack propagation have been reported in the literature.

### FATIGUE CRACK PROPAGATION MODEL

An approach based on the energy expended at the crack tip during the process of crack propagation was adopted in the development of the model used in this study at high temperatures (15). A phenomenological approach which utilizes a limited number of parameters was considered to be most realistic (16) as compared with dislocation-based models which appear to be overly simplistic.

It is assumed that a crack is present in the material initially and that the damage produced at the tip of the crack consists of both strain energy and thermal contributions such that we may write the damage per cycle as

$$dD/dN = A \exp(-(Q - m' \log[\Delta W^*/W_0])/(kT)) \quad (1)$$

and the linear dimension of the volume where the deformation take place as

$$R_p = [E/\sigma_{ys}^2] \Delta J, \quad (2)$$

where  $Q$  is the activation energy,  $E$  is the elastic modulus,  $\sigma_{ys}$  is the yield strength,  $\Delta J$  is the applied J-integral range,  $\Delta W^*$  is the strain energy density,  $kT$  has the usual meaning and  $A$ ,  $m'$  and  $W_0$  are constants. If we now take the crack propagation rate as proportional to the total energy expended within the crack tip zone, we can write

$$\begin{aligned} da/dN &= R_p(dD/dN) = A(\Delta J)^{m'+1} [\exp(-Q/kT)] \\ &= A(\Delta W_t a)^{m'+1} [\exp(-Q/kT)], \end{aligned} \quad (3)$$

where  $a$  is the crack length,  $m=m'/kT$ ,  $\Delta W_t$  is the tensile energy input, and  $A$  is a constant.

We now focus our attention directly on the crack tip region. For the purposes of the development of the model, we will consider three primary contributions to the crack propagation process. These contributions are (1) the cyclic damage production, (2) the

## FATIGUE 87

thermally activated, time-dependent tensile creep and (3) the time-dependent environmental effects. Of these contributions, the fatigue component  $\Delta a_f$ , will be considered to result from the applied cyclic tensile loading.

The creep component,  $\Delta a_{cr}$ , will be considered to result from the tensile load being held constant for a time period during each loading cycle. We can write the creep contribution as a power law function of the tensile hold time such that

$$\Delta a_{cr} = A_{cr}(t/t_{hold})^q \Delta J, \quad (4)$$

where  $t$  is the total cycle and  $t_{hold}$  is the tensile hold time. The environmental component,  $\Delta a_{env}$ , will be considered to result from the interaction of the active species in the test environment with the crack tip region, especially for tests where the load is held constant for a time period during each loading cycle. The form of the environmental effect is taken as a log function of the time of exposure, or tensile hold time,  $t_{hold}$ , of the fresh crack surface such that we can write

$$\Delta a_{env} = A_{env} \log(t/t_{hold}) \Delta J. \quad (5)$$

Combining the contributions of these effects, we can write the crack propagation during each loading cycle as

$$\Delta a = \Delta a_f + \Delta a_{cr} + \Delta a_{env}. \quad (6)$$

It is recognized that, in certain cases, the individual terms of this expression may be exponential to indicate the extent of mutual interaction. For the initial formulation, however, we will retain the linearized form of the expression.

Equation 6 can be re-written as a more generalized relation of the form

$$\begin{aligned} da/dN = [ & A_f + A_{env} \log(t/t_{hold}) \\ & + A_{cr}(t/t_{hold})^q ] \times \Delta J^{m+1} \exp(-Q/kT), \end{aligned} \quad (7)$$

or as

$$\begin{aligned} da/dN = [ & 1 + \alpha \log(t/t_{hold}) \\ & + \beta (t/t_{hold})^q ] \times \Delta J^{m+1} \exp(-Q/kT), \end{aligned} \quad (8)$$

where  $\alpha = A_{env}/A_f$  and  $\beta = A_{cr}/A_f$ .

If we express the applied J-integral range in the form of the stress intensity factor range, we can write

$$\Delta J = \Delta K^2/E. \quad (9)$$

## FATIGUE 87

The crack propagation rate can then be written as

$$da/dN = A'_f [F_i] (\Delta K^2/E)^{m+1}, \quad (10)$$

where  $A'_f$  will be a constant for a given material and temperature and  $F_i$  is the parameter for the fatigue-creep-environmental interaction, given by the expression

$$F_i = 1 + \alpha \log(t/t_{hold}) + R(t/t_{hold})^q. \quad (11)$$

The form of this equation is similar to the familiar Paris equation for crack propagation usually written as

$$da/dN = C(\Delta K)^n. \quad (12)$$

### FATIGUE CRACK PROPAGATION EXPERIMENTAL DATA

A large body of experimental fatigue crack propagation data for type 316 stainless steel has been obtained, primarily in air, at temperatures from 21 to 700°C (3,4,6,13,14). This data includes results for a variety of tensile hold times applied during the individual tests. For the specific purposes of this study, test results at temperatures between 500 and 700°C were selected for detailed analysis since both creep and environmental components are believed to have contributed to the crack propagation process in this temperature range. For the individual test results, however, the  $a$  vs.  $N$  data necessary for the analysis are usually unavailable in the literature. This required that these data be obtained from the original investigators (4,13,14) where necessary.

### CALCULATION OF MODEL VS. EXPERIMENTAL RESULTS

The comparison of the fatigue crack propagation model of a previous section of this paper with the experimental data is conveniently handled by computer calculation. A program previously developed by Smith and Michel (2) was used to compute, store and graphically display the results of the model from the individual experimental data. The program was also used to determine the constants  $A'_f$ ,  $\alpha$ , and  $R$  for the model calculations. A separate program was used to calculate the  $da/dN$  vs.  $\Delta K$  values based on the model and experimental results.

The comparison between the model and experimental results for the crack propagation rate  $da/dN$  vs.  $\Delta K$  is shown in Figure 1. The model results are shown as solid lines and the experimental results as open circles. The model results are in good agreement with the experimental results.

AD-A184 046

FATIGUE '87 VOLUME 2(U) VIRGINIA UNIV CHARLOTTESVILLE  
SCHOOL OF ENGINEERING AND APPLIED SCIENCE  
R O RITCHIE ET AL JUN 87 N00014-87-G-0006

6/6

UNCLASSIFIED

F/G 20/11

NL

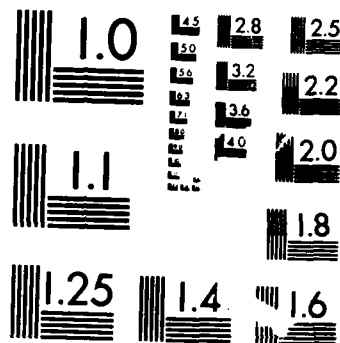
END

DATE

FILED

10-87

U.S.



## FATIGUE 87

the data considered and suggest that the model may provide a good representation of these experimental results in vacuum. This is not surprising, but reassuring due to the flexible functional form of the expressions, and suggests that the model is physically realistic.

Figure 3 provides a comparison between the calculated and the experimental results in air at 593°C. The comparison shows that the model provides a reasonable representation of the zero hold time experimental results and the one minute hold time results at all  $\Delta K$  levels considered.

Figure 4 compares the model and the experimental results for the case of extended hold times ( $>1$  min.) in air at 593°C. The comparison shows that the model follows the lower portion of the  $da/dN$  vs.  $\Delta K$  curve where the hold time at maximum cyclic load was 8 minutes or less. However, for the case of the extended hold times of 16 minutes or longer, the model underestimates the crack propagation rates of the experimental results. This is reasonable since the coefficients  $\alpha$ ,  $\beta$  and  $m$  in the model were determined based on the shorter hold time data ( $<8$  minutes) without regard for the extended hold times where cavity interactions became important. If the presence and linkage of intergranular cavities are considered, the  $da/dN$  values predicted by Equation 10 approximate those for the experimental results shown in Figure 4 for the transition to the accelerated crack propagation at hold times of 16 minutes or longer.

### SUMMARY

A phenomenological approach was used to model the effects of hold time and environment on crack propagation at elevated temperatures. The model provides a reasonable representation of the experimental results for austenitic stainless steels tested in air and in vacuum for hold times from 1 to 8 minutes. For longer hold time, the interaction and linkage of intergranular cavities must be included in the model calculations to represent the experimentally observed crack propagation performance.

### ACKNOWLEDGEMENTS

This work was supported by the Office of Naval Research and was conducted, in part, while one author (DJM) was a Visiting Scientist in the Department of Metallurgical Engineering and Materials Science at Carnegie-Mellon University.

### REFERENCES

- (1) K. Sadananda and P. Shahinian, Metal Science, 1981, vol. 15, p. 425.

# FATIGUE 87

- (2) K. Sadananda, Nucl. Engr. & Design, 1984, vol. 83, p. 303.
- (3) D. J. Michel and H. H. Smith, Res Mechanica, 1985, vol. 14, p. 271-285.
- (4) D. J. Michel and H. H. Smith, J. Nucl. Mater., 1981, vol. 103 & 104, p. 871.
- (5) K. Sadananda, in ADVANCES IN FRACTURE RESEARCH, S. R. Valluri et al., Eds., Pergamon Press, New York, 1984, p. 211.
- (6) D. J. Michel and H. H. Smith, Acta Metall., 1980, vol. 28, p. 999.
- (7) E. E. Underwood, in HANDBOOK OF APPLIED METALLOGRAPHY, G. F. Vander Voort, Ed., Van Nostrand Reinhold Co., Inc., 1985.
- (8) E. E. Underwood and E. A. Starke, Jr., in FATIGUE MECHANISMS, ASTM STP 675, J. T. Fong, Ed., American Society for Testing and Materials, 1979, p. 633.
- (9) A. W. Thompson, Acta Met., 1983, Vol. 31, p. 1517.
- (10) A. W. Thompson and M. F. Ashby, Scripta Met., 1984, vol. 18, p. 127.
- (11) R. O. Ritchie and W. W. Thompson, Metall. Trans. A, 1984, vol. 16A, p. 233.
- (12) H. J. Frost and M. F. Ashby, DEFORMATION MECHANISM MAPS, Pergamon Press, New York, 1982.
- (13) D. J. Michel and H. H. Smith, in ASME-MPC Symposium on Creep-Fatigue Interactions, R. M. Curran, Ed., MPC-3, American Society for Mechanical Engineers, 1976, p. 391.
- (14) D. J. Michel, H. H. Smith and H. E. Watson, in Structural Materials for Service at Elevated Temperatures in Nuclear Power Generation, A. O. Schaefer, Ed., MPC-1, American Society for Mechanical Engineers, 1975, p. 167.
- (15) V. M. Radhakrishnan, Trans. ASME, J. Engr. Matls. & Tech., 1983, vol. 105, p. 273.
- (16) J. P. Bailon and S. D. Antolovich, in FATIGUE MECHANISMS: ADVANCES IN QUANTATIVE MEASUREMENT OF PHYSICAL DAMAGE, ASTM STP 811, J. Lankford et al. Eds., American Society for Testing and Materials, 1983, p. 313.

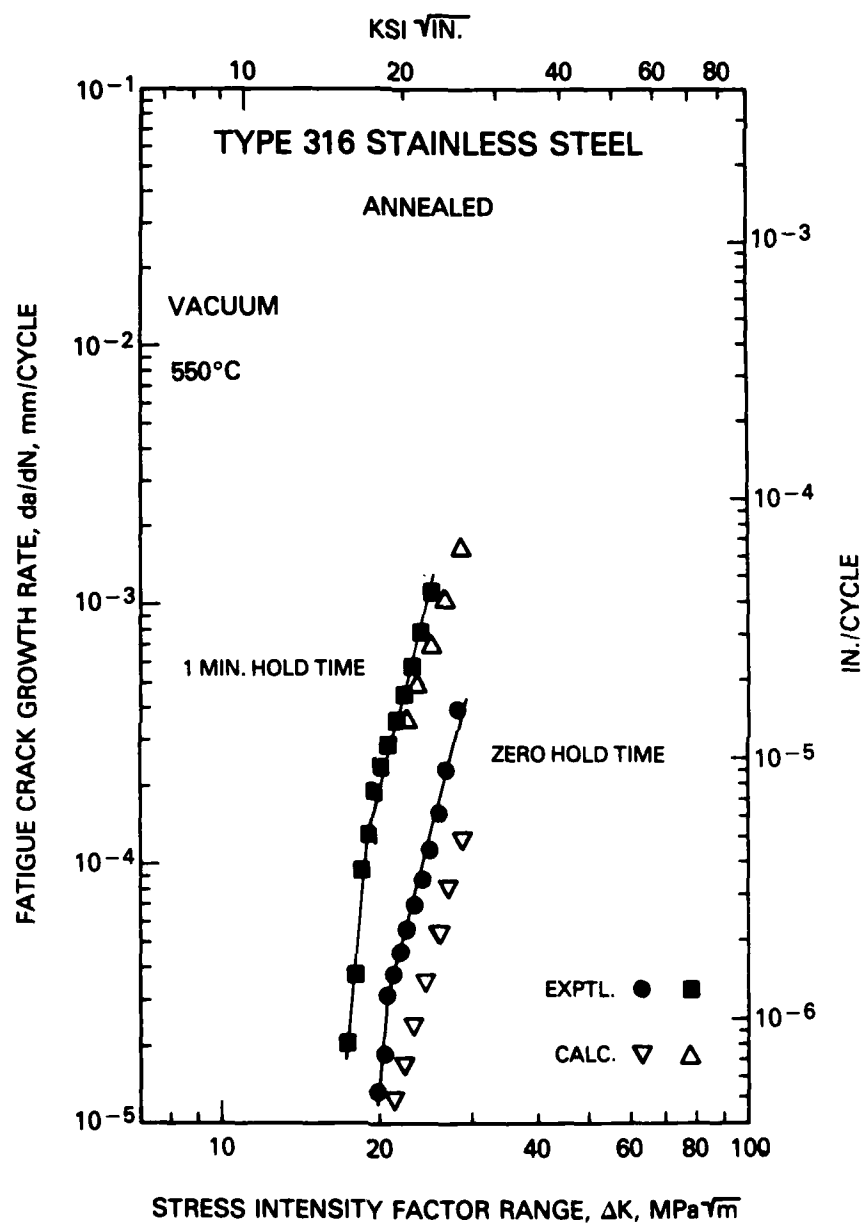


Figure 1 Comparison of experimental and calculated fatigue crack propagation rates in vacuum at 550°C.

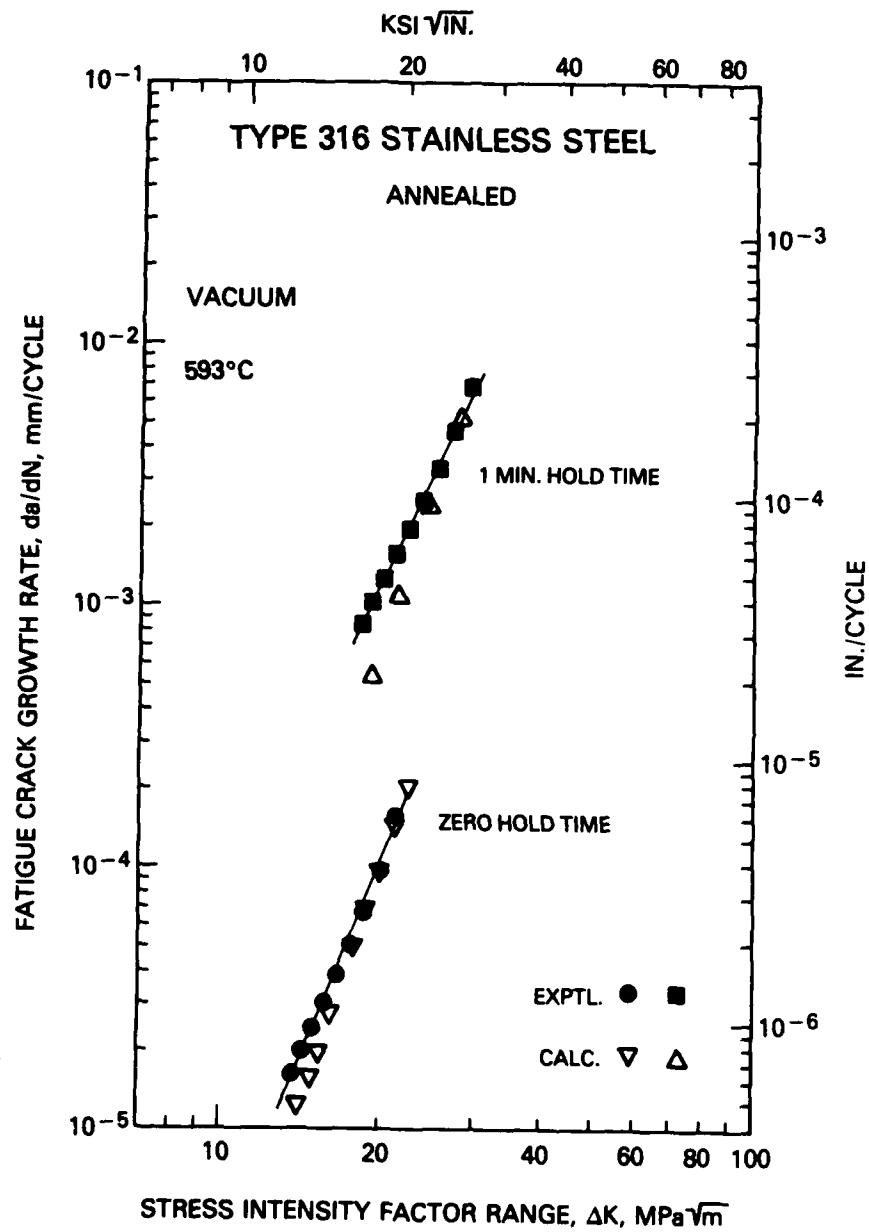


Figure 2 Comparison of experimental and calculated fatigue crack propagation rates in vacuum at 593°C.

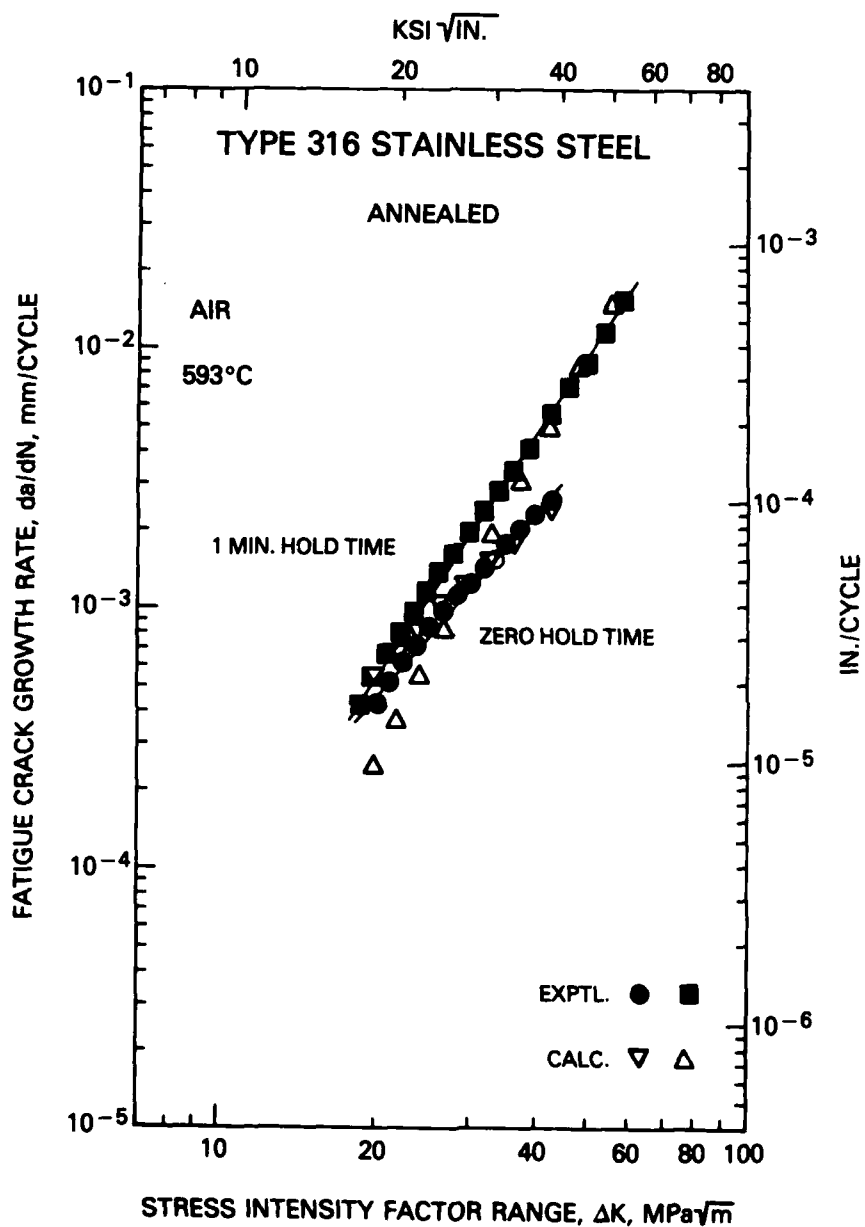


Figure 3 Comparison of experimental and calculated fatigue crack propagation rates in air at 593°C.

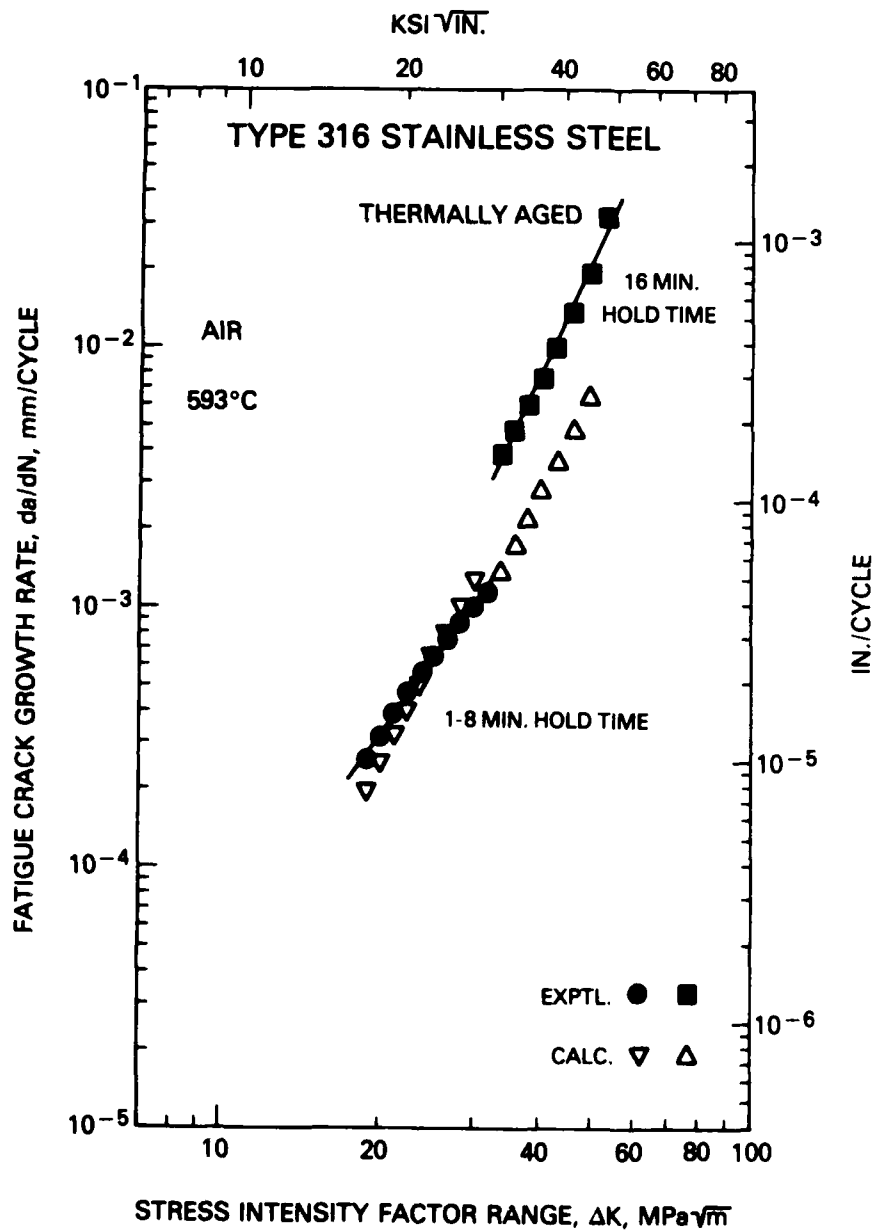


Figure 4 Comparison of experimental and calculated fatigue crack propagation rates in air at 593°C for extended hold times.

## FATIGUE 87

### HIGH TEMPERATURE LOW CYCLE FATIGUE BEHAVIOR AND CREEP-FATIGUE INTERACTION OF MA 6000 ODS ALLOY

M. Nazmy\*, W. Ebeling\* and M. Staubli\*

The high temperature low cycle fatigue (HTLCF) behavior, under different types of strain wave shapes, in the ODS alloy MA 6000 was investigated at 950°C. The cycles with tensile hold times were the most effective regarding the internal damage. Three models for HTLCF lifetime were evaluated for their ability to correlate the fatigue data on MA 6000. These models are strain range partitioning (SRP), the frequency separation (FS) and the frequency modified damage function (FMDf). In general, the three models correlated the HTLCF data relatively well.

### INTRODUCTION

The development of gas turbines requires the use of new materials with improved high temperature capabilities. These materials are needed mainly for blade and vane application as well as for other components. Thermal fatigue and hence HTLCF are important criteria that should be taken into consideration when selecting an alloy for a fluctuating temperature application. Directionally solidified and single crystal nickel-base superalloys were introduced for their improved creep rupture and thermal fatigue resistance, in the solidification direction, as compared to their polycrystalline counterparts.

\* Department of Metallurgical Lab.,  
Brown Boveri & Co. Baden - Switzerland

## FATIGUE 87

The mechanically alloyed oxide dispersion strengthened (ODS) class of alloys has shown attractive high temperature properties, e.g. the nickel-base ODS MA 754 alloy is used in advanced gas turbine engines (1). The MA 6000 ODS alloy has shown improved high temperature creep rupture properties as compared to many nickel base superalloys (2). Several investigations were carried out to characterize the creep and high cycle fatigue behavior of MA 6000 (3,4). Recently, a number of investigations were carried out to characterize the HTLCF behavior of MA 6000 at different temperatures (5-7). However, in all of these investigations, simple triangular strain waves were used.

The aim of the present study was to investigate the HTLCF behavior of the ODS alloy MA 6000 at 950°C using different types of strain waves, and to determine the correlative ability of three different lifetime prediction models as applied to this alloy.

### EXPERIMENTAL PROCEDURE

The material used in this investigation is hot rolled and fully heat treated Inconel alloy MA 6000 cast #CBB 0094. The specific composition (in weight percent) is: balance Ni, 14.96 Cr, 2.37 Ti, 4.37 Al, 1.98 Mo, 1.95 Ta, 3.99 W, 0.99 Fe, 0.15 Zr, 1.08 Y, 0.56 O, 0.058 C, and 97 ppm B. Thermomechanical processing results in elongated grains. The average grain aspect ratio was greater than 10:1. The  $Y_2O_3$  dispersoids are uniformly distributed throughout the matrix and range in size from 10 nm to 70 nm. The alloy exhibits a strong texture, with 110 crystallographic direction parallel to the rolling direction (8).

HTLCF specimens with the dimensions as given in reference (9) were machined in the longitudinal direction, i.e. rolling direction of the MA 6000 bar stock. Final machining was carried out by low stress grinding to remove surface defects due to prior machining.

The HTLCF behavior was investigated under fully reversed total axial strain conditions using a servo-hydraulic testing machine. Testing was done in air at 950°C. Four types of strain wave shapes were used to examine the effect of strain wave shape on the fatigue life: triangular wave with a strain rate of  $10^{-2}$  s<sup>-1</sup> and truncated waves with hold times in tension or in compression or in both tension and compression. The hold

## FATIGUE 87

times varied from 60 to 300 seconds. The stress and strain ranges were determined at half-life of the specimens.

### RESULTS AND DISCUSSION

The variation of the fatigue life of MA 6000 at 950°C with different types of strain waves is shown in Figure 1. In general, the fatigue lives of the specimens tested under tensile hold time conditions are longer than the fatigue lives of the specimens tested under the other three types of cycles. Metallographic investigation of the fractured specimens showed extensive damage and multiple surface crack formation in the specimens tested with strain cycles that included tensile hold times. These features are clearly shown in Figure 2. The modes of crack initiation and propagation in these specimens are intergranular. This behavior of multiple cracking and extended fatigue lives in MA 6000 specimens tested under tensile hold time conditions is similar to what has been reported on the cast nickel-base alloy IN 738 LC tested under the same type of strain cycles (9). The multiple cracking and crack branching cause some sort of load shedding and a decrease in the stress intensity factor ( $K_{max}$ ) as compared with a single crack (10). Artificially induced multiple surface cracks in HTLCF specimens of IN 738 LC, resulted in longer fatigue lives under cycles with tensile hold times (11).

In the case of specimens tested under triangular strain waves, the modes of crack initiation and propagation were transgranular. Specimens tested under compressive hold times showed transgranular stage I crack initiation and stage II transgranular crack propagation. No grain boundary damage was observed in the latter type of specimens. Specimens tested under equal hold times of tension and compression exhibited stage I multiple cracking. The crack initiation was transgranular and intergranular, and propagation was intergranular. In all specimens tested under different strain waves, specimen failure took place by surface crack initiation and propagation. This observation may indicate the significance of environmental effect on the HTLCF behavior of this alloy.

LIFETIME PREDICTION MODELS

The HTLCF results on MA 6000 were correlated using the SRP model and the interaction damage rule (12). The coefficients in this model were calculated using a least square fit computer program. In order to make a quantitative comparison of the data correlation capability of the various model, the standard deviation was defined as follows:

$$S = \sqrt{\frac{1}{n-1} \sum_{i=1}^n [\ln N_f^i - \ln N_p^i]^2} \quad (1)$$

Where  $N_f^i$ ,  $N_p^i$  are the observed and the predicted number of cycles to failure, and  $n$  is the number of data points. Figure 3, shows the HTLCF data correlation using the strain range partitioning model with  $S = 0.30$ .

The FS model postulates that the basic parameters necessary to predict the creep-fatigue life are the inelastic strain range, the tension-going frequency, and the hysteresis loop-time unbalance (13). The data of this investigation were correlated using this model and the result is shown in Figure 4, with  $S = 0.30$ .

In the FMDF model, the measure of deformation or damage is the tensile hysteretic energy absorbed by the specimen (14). This energy is approximated as the product of the width of the hysteresis loop, its height, and a shape factor. A frequency term is used in this model to account for time dependent effects. Figure 5, shows the correlation of the data of the present investigation using the FMDF model with  $S = 0.24$ .

The data correlation capability of the three models is similar, i.e. all the data were enclosed within the well accepted scatterband of a factor of two. The fact that the FMDF model correlated the data with the smallest  $S$  may indicate the significance to the HTLCF behavior of MA 6000 of including the stress as a parameter in the lifetime prediction model. It has been tried to predict the HTLCF lives of MA 6000 reported in the literature i.e. ref. (6) using the calculated constants of the three models used in this investigation. However, the literature HTLCF results exhibited an inherent scatter more than that usually expected in the HTLCF studies.

## FATIGUE 87

### CONCLUSIONS

- 1-Strain cycles with tensile hold times were the most severe regarding internal damage. Nevertheless, the fatigue lives were longer under these cycles than when tested under triangular strain waves, due to the development of multiple cracking and crack branching.
- 2-The correlation of the data from the present study having the smallest standard deviation was obtained with the FMDF model.
- 3-The SRP and the FS models correlated the data equally well.

### ACKNOWLEDGEMENTS

The skillful experimentation of W. Meixner, H. Baldinger and R. Häring is greatly appreciated.

### REFERENCES

- ( 1) Crawford, W., "Oxide Dispersion Strengthened Materials in Engines-INCONEL MA 754" in Proceedings of Conference "Frontiers of High Temperature Materials II", Benjamin, J. and Benn, R., eds., 22-25 May 1983.
- ( 2) Meetham, G.W., in "High Temperature Alloys for Gas Turbines and Other Applications 1986", Betz, W., Brunetand, R., Coutsouradis, D., Fischmeister, H., Gibbons, T.B., Kvernes, I., Lindblom, Y., Marriot, J.B. and Meadowcroft, D.B., eds., Riedel Publishing Company, 1986, pp. 1-50.
- ( 3) Singer, R.F. and Arzt, E. in "High Temperature Alloys for Gas Turbines and Other Applications 1986", Betz, W., Brunetand, R., Coutsouradis, D., Fischmeister, H., Gibbons, T.B., Kvernes, I., Lindblom, Y., Marriot, J.B. and Meadowcraft, D.B., eds., Riedel Publishing Company, 1986, pp. 97-126.
- ( 4) Höffelner, W. and Singer R.F., Metall, Trans. A, Vol. 16A, March 1985, pp. 393-399.

## FATIGUE 87

- ( 5) Dreshfield, R.L., Hoppin III, G.S. and Sheffler, K.D., "Progress Toward Determining The Potential of ODS Alloys For Gas Turbine Applications" in Proceedings of Conference "Frontiers of High Temperature Materials II" Benjamin, J., Benn, R., eds., 22-25 Mai 1983.
- ( 6) Bressers, J. and Arzt, E., in "High Temperature Alloys for Gas Turbines and Other Applications 1986", Betz, W., Brunetand, R., Coutsouradis, D., Fischmeister, H., Gibbons, T.B., Kvernes, I. Lindblom, Y., Marriot, J.B. and Meadowcraft, D.B., eds Riedel Publishing Company, 1986, pp. 1067-1080.
- ( 7) Hynnä, A., Kuokkala, V.T., Lepistö, T., Mäntylä, T. and Kettunen, P. in "High Temperature Alloys for Gas Turbines and Other Applications 1986", Betz, W., Brunetand, R., Coutsouradis, D., Fischmeister, H. Gibbons, T.B., Kvernes, I. Lindblom, Y., Marriot, J.B. and Meadowcraft, D.B., eds., Riedel Publishing Company, 1986, pp. 1091-1102.
- ( 8) Nazmy, M., Singer, R. and Török, E. in Proceedings of 7th Int. Conf. on Textures of Materials, Brakman, C.M., Jongenburger, P. and Mittemeijer, E.J. eds., Netherlands Society for Materials Science, 17-21 Sept. 1984, pp. 275-280.
- ( 9) Nazmy, M., Metall, Trans. A Vol. 14 A, March 1983, pp. 449-461
- (10) Underwood, J.H. and Throop, J.F., in "Part-Through Crack Fatigue Life Prediction, ASTM STP 687, 1977, p. 195.
- (11) Nazmy, M., Scripta Metall. Vol. 17, 1983, pp. 491-494.
- (12) Manson, S.S., in "Fatigue at Elevated Temperatures" ASTM STP 520, 1973, pp. 744-782.
- (13) Coffin, L.F. Jr., In ASME-MPC Symposium on Creep-Fatigue Interaction, MPC-3, 1976, pp. 349-364.
- (14) Ostergren, W.J., in ASME-MPC Symposium on Creep-Fatigue Interaction, MPC-3, 1976, pp. 179-202.

# FATIGUE 87

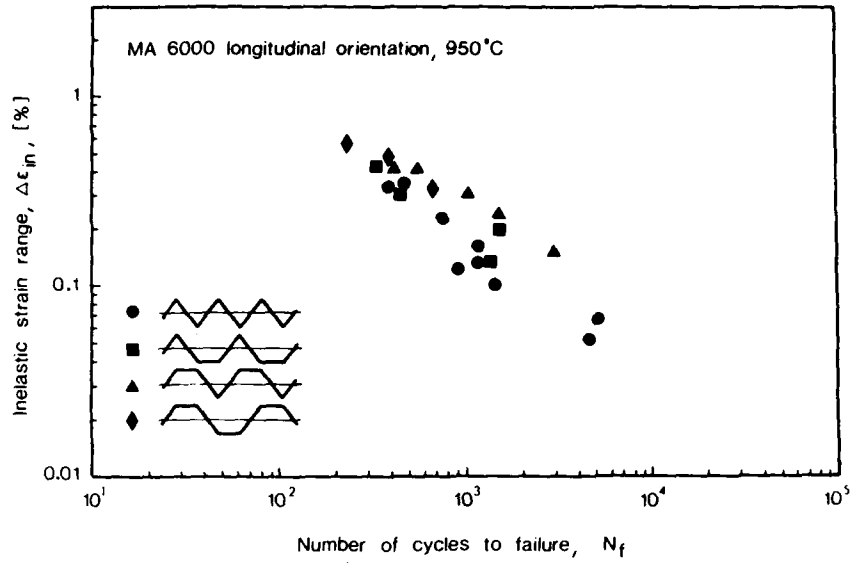


Figure 1 Inelastic strain range vs number of cycles to failure

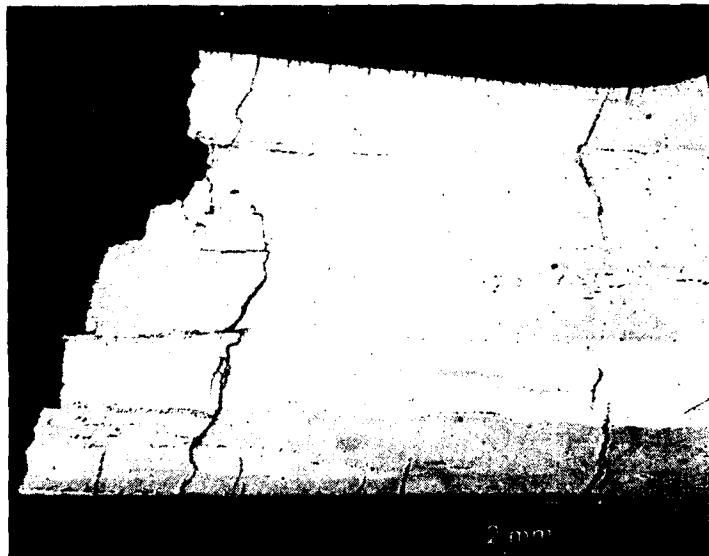


Figure 2 HTLCF specimen tested under strain wave with hold time in tension showing multiple cracking

# FATIGUE 87

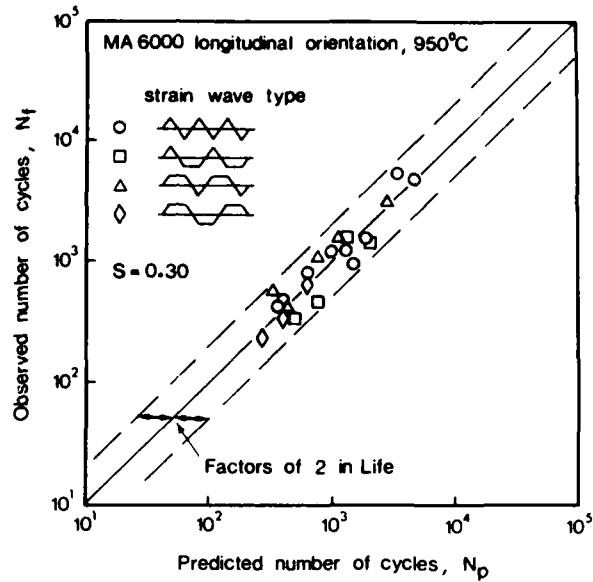


Figure 3 Observed vs predicted numbers of cycles to failure for the HTLCF data using the SRP model

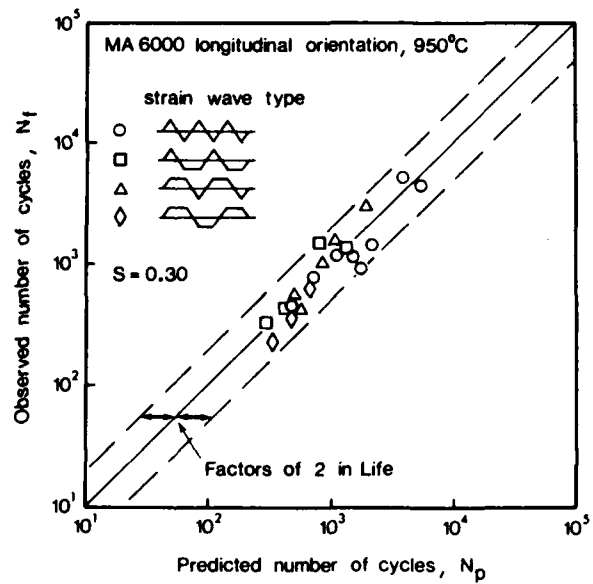


Figure 4 Observed vs predicted numbers of cycles to failure for the HTLCF data using the FMDF model

# FATIGUE 87

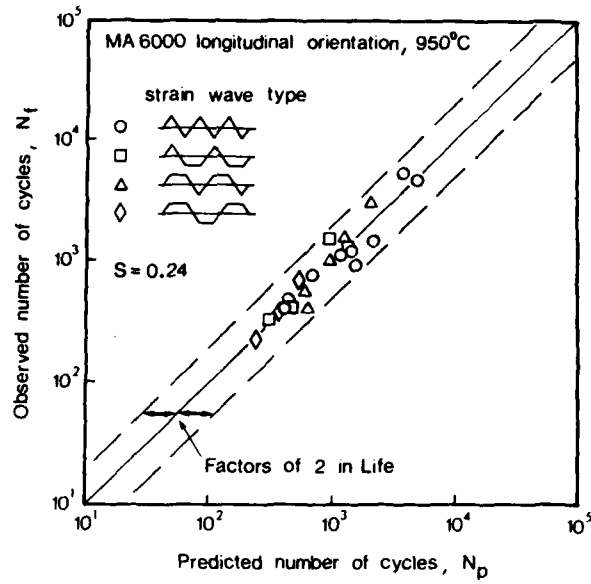


Figure 5 Observed vs predicted numbers of cycles to failure for the HTLCF data using the FMDF model

FATIGUE 87

## FATIGUE 87

### CREEP-FATIGUE CRACKING IN HIGH TEMPERATURE TURBINE ROTORS

A.T. Stewart, D.A. Miller, D.C. Martin and G. Wignore\*

The mechanisms by which creep-fatigue damage can arise in high temperature rotors in power plant are presented, and the different failure modes observed in practice are described. Life prediction methods based on life fraction and ductility exhaustion techniques of damage summation are described and applied to one particular instance of cracking. The importance of the creep ductility of high temperature materials is stressed.

#### INTRODUCTION

In high temperature power plant, steam turbine components, such as HP and IP chests, casings and rotors, are subject to cyclic stressing as a result of start-up and shut-down of the unit. During such operations, transient thermal gradients are set up, giving rise to thermal stresses which can be particularly severe at surfaces directly exposed to steam. Such stresses can result in plastic deformation at stress concentrating features such as grooves and other geometric discontinuities during start-up/shut-down cycles, leading to the development of thermal fatigue damage. In addition, creep damage can accrue during steady operating conditions.

In base load units, the number of such cycles over the design life is relatively small. However, flexible operation of power plant is becoming increasingly important, even on modern large (500 MW) turbogenerators, involving weekend or nightly shut-downs.

\*Scientific Services Department, CEGB (SW Region), Bedminster Down Bridgwater Road, Bristol, England.

## FATIGUE 87

Under these circumstances, there is a need to reappraise the expected lifetime of components subject to regular cyclic duty. There is also a major economic incentive to extend the life of power plant well beyond its original design; this, in turn, will further increase the number of cycles the plant is required to survive.

In this paper, some of the life prediction methods for components undergoing high temperature, cyclic loading are reviewed in the light of recent instances of thermal fatigue cracking in high temperature rotors within CEGB(UK). In particular, the importance of a clear understanding of the metallurgical processes occurring under combined creep and fatigue loading is highlighted, together with the need to obtain materials data under truly representative conditions. Finally, areas of further work are discussed which would enable improved predictive procedures to be produced and thermal fatigue cracking to be avoided during service.

### STRESSING DURING START-UP/SHUT-DOWN CYCLES

The stress and strain transients that occur during start-up and shut-down of a component such as an HP or IP rotor, depend on the presence of stress concentrating features and local temperature gradients. An example of a typical stress-strain cycle experienced at the surface of a large, high temperature rotor is shown in Figure 1. When steam enters the turbine, the surface is rapidly heated and attempts to expand. However, it is constrained by the underlying body of cooler material, and eventually surface yielding in compression occurs (OBC). On subsequent temperature equilibration, residual tensile stresses are generated (CD). During steady operation (dwell), these tensile stresses relax by creep (DE) and elastic strains are converted to creep strain giving rise to microstructural damage. During shut-downs, the temperature gradients are reversed, giving rise to further tensile straining of the surface (EAO).

Whilst the amount of fatigue damage accumulated is dictated by the number of start-up/shut-down cycles to which the plant is subjected, the magnitude of the tensile residual stress and the length of the dwell primarily control the amount of creep damage accrued. However, it should be recognised that the thermal cycle serves to re-establish the residual stress following its relaxation during the previous dwell period.

### THERMAL FATIGUE CRACKING MECHANISMS

As the "dwell" or creep component in the cycle is increased, the failure mode can change. The failure modes can be categorised into three different regimes, ie. fatigue dominated, creep-fatigue

## FATIGUE 87

interaction, and creep dominated, as shown schematically in Figure 2. In creep-fatigue interaction, creep cavitation damage is accumulated in the material and interacts with the fatigue cracking, resulting in accelerated crack growth and a reduction in endurance. Under some circumstances, eg. long dwells at high temperatures, the creep component can dominate, leading to failure by creep cavitation with little or no interaction with any fatigue damage present.

Examples of thermal fatigue cracking found in two different high temperature rotors within the CEBB are shown in Figure 3. In one case (Figure 3a), the cracking was fatigue dominated, being blunt and transgranular, and had initiated at a groove operating at a relatively low temperature (450°C). The thermal fatigue cracking shown in Figure 3b, however, is creep dominated, with extensive grain boundary cavitation, and had developed from a groove operating at a temperature well within the creep regime of the rotor material (525°C).

The creep ductility of a material is also an important parameter in determining the failure mechanism, with low ductilities (together with low strain ranges and long dwell periods) favouring creep dominated failures. Creep ductility is known to vary as a function of applied strain rate, temperature, stress state and material. In particular, the reduction in ductility from a high level at high strain rates to a low minimum value at low rates is important. The cracking shown in Figure 3b was in fact found to have occurred in a 1½ CrMoV rotor steel that exhibited good creep strength but very low creep ductility at long exposures. The results of creep testing miniature samples of the actual rotor material in argon are shown in Figure 4, where they are compared to data from a range of forgings of similar manufacture (Group A). It can be seen that the ductility of the rotor steel in which thermal fatigue cracking developed in service is at the lower bound of the Group A data.

### LIFE PREDICTION METHODS

Within the literature, several methods have been proposed to predict the life of components subject to combined cyclic and creep deformation. Various methods have been devised (1, 2) based on the familiar Manson-Coffin relationship, taking into account environmental and other time dependent effects through a frequency term in the equation:

$$\Delta \epsilon_p N^\alpha F^\beta = \text{const.} \quad (1)$$

However, the design procedure most widely used at present is ASME Section III, Code Case N47 (3), which is based on the superposition of fatigue and creep damage via a linear life

## FATIGUE 87

fraction rule:

$$\sum N/N_F + \sum t/t_R = 1 \quad (2)$$

Whilst this approach is simple to apply and involves knowledge of relatively simple fatigue and creep data, it has little or no mechanistic basis, and therefore its applicability is material dependent. Whilst some workers have found reasonable agreement between predicted and observed lifetimes for some materials (eg low alloy ferritic steels), others (eg. Priest and Ellison (4)) have found major discrepancies and effective damage summation factors varying between 0.2 and 10, instead of unity, have been reported (Jaske et al (5)).

Recent studies have shown that an approach based on ductility exhaustion can have significant advantages over life fraction methods, giving accurate predictions of endurance when compared with test data for a range of austenitic and ferritic materials (Miller et al (6)). This method is based on the early work of Edmunds and White (7), who suggested that creep ductility is exhausted each cycle by an amount equal to the strain accumulated during the dwell period in the cycle. Creep dominated endurances can then be predicted using the simple equation:

$$N_F = D_C / \Delta \epsilon_r \quad (3)$$

It is also possible to pessimistically cater for the interaction between creep and fatigue damage via an additive equation, as in N47 (6):

$$\text{ie: } \sum \frac{\Delta \epsilon_r}{D_C} + \sum \frac{N}{N_F} = 1 \quad (4)$$

although, under those circumstances where there is no interaction, a more appropriate approach would be to rewrite equation (4) as:

$$\sum \frac{\Delta \epsilon_r}{D_C} \text{ or } \sum \frac{N}{N_F} = 1 \quad (5)$$

It is becoming increasingly clear that interaction effects are not commonly encountered in many materials used within the power generation industry, with most failures being either fatigue or creep dominated. In fact, in most cases involving components operating at temperatures within the creep regime, the service conditions encountered involve small strain ranges and long dwell periods, favouring creep dominated failures. It is under these circumstances that the ductility exhaustion approach is particularly useful.

COMPARISON OF LIFETIME PREDICTIONS WITH THE ENDURANCE  
OF SOME HIGH TEMPERATURE ROTORS

It is instructive to compare the endurance of real structures subject to cyclic and creep loadings, such as high temperature rotors which have developed cracking in service, with the predictive models discussed earlier. Recently, within CEGB, shallow thermal fatigue cracking was found at several interstage grooves in a large IP rotor. The nature of this cracking has been described earlier in the paper (see Figure 3b). At the time the cracking was discovered, the rotor had seen about 65,000 hours service, and had experienced about 230 starts, of which 82 were from cold and therefore particularly severe. This rotor was one of a family of nine, but subsequent detailed examination of several of the other rotors failed to reveal any significant damage. An important question in the investigation then was, why was this rotor unique, despite very similar materials of construction, design and history of operation to the others? Examination of the forging certificates showed that this rotor had seen a different heat treatment to all the others, involving a higher austenitising treatment and a shorter subsequent tempering time. Both factors would be expected to produce a material with higher creep strength but lower creep ductility. The creep properties of the cracked rotor steel have already been shown in Figure 4; those typical of the other eight rotor materials are shown in this Figure as well (Group B).

Based on station records for the start-up and shut-down performance of the rotors, stress-strain hysteresis loops, like Figure 1, were constructed as a function of start-up rate and severity. This involved detailed elastic-plastic-creep finite element structural analysis of the actual rotor geometry and modelling the centrifugal, bending and torsional loading, in addition to thermal loads. Materials data were based on extensive tests of similar 1% CrMoV steel forgings, involving cyclic stress-strain, high temperature fatigue, stress relaxation and creep data such as that shown in Figure 4.

The results of the analyses using both the life fraction and ductility exhaustion approaches are summarised in Table 1. These calculations demonstrated that the cold (fast) starts are the predominantly damaging ones. The results are also based on an estimated average of 1000 hour dwell periods between start-up/shut-downs. When compared to the actual number of cold starts the cracked rotor had seen (ie. 82), the predictions of both the life fraction and the ductility exhaustion techniques are reasonable, especially when it is noted that they are based on lower bound materials data, and that the cracking will have initiated much earlier in life. Similar calculations for the undamaged rotors revealed large differences in the lifetime predictions by the

## FATIGUE 87

**TABLE 1 - Predicted Lives of IP Rotors Determined Using Life Fraction and Ductility Exhaustion Techniques.**

Rotor	Predicted Life (Cycles)	
	Life Fraction	Ductility Exhaustion
Cracked IP Rotor	24	43
Other (Group B) IP Rotors	18	134

two methods. As can be seen from Figure 4, these rotors (Group B) had lower creep strengths than the cracked rotor. Using the life fraction approach, this results in a larger creep damage term and hence a reduced endurance prediction. However, these materials also had better long term creep ductility, and therefore, using the ductility exhaustion approach, a much increased endurance is predicted, directly in line with the observations of no cracking in these (Group B) rotors. This example clearly confirms the advantages of the ductility exhaustion approach when assessing creep dominated, thermal fatigue cracking.

### CONCLUDING REMARKS

This paper has briefly reviewed some of the present life prediction techniques that can be applied to components undergoing combined creep and fatigue loadings. The importance of creep ductility and the length of the dwell period have been particularly highlighted in determining the cracking mechanism and the endurance of components. Further, where failures are creep dominated, the ductility exhaustion approach appears to have clear advantages over other methods such as life fraction techniques, and can give good predictions of the performance of both laboratory type samples and real structures such as high temperature rotors.

However, considerable further work is required before such techniques can be widely adopted. For example, creep-fatigue endurance data are required over a wider range of material ductility and at considerably longer dwells than is available at present. This is necessary to give added confidence in the extrapolation of the life prediction techniques to the typical service conditions seen by high temperature power plant. It is also important to investigate whether the creep and fatigue damage terms in the life equations are independent or additive.

## FATIGUE 87

Finally, methods of estimating the rate of development of thermal fatigue cracks and the conditions under which crack arrest can occur are of particular importance. Whilst fracture mechanics methods for assessing fatigue dominated cracking are well established, methods of incorporating creep cracking during dwells and the interaction between creep and fatigue damage require development, and the use of correlation parameters such as reference stress and  $C^*$  needs to be explored.

### SYMBOLS USED

- $\Delta\epsilon_p$  = inelastic strain range  
 $\alpha$  = a constant  
 $\beta$  = a constant  
 $t_R$  = creep rupture life (hours)  
 $D_c$  = creep rupture ductility  
 $\Delta\epsilon_r$  = component of creep strain accumulated during dwell giving rise to intergranular creep damage

### ACKNOWLEDGEMENT

This paper is published with the permission of the Executive Director, CEBG SW Region.

### REFERENCES

- (1) Coffin, L.N., "Fatigue at High Temperatures", ASTM STP 520, 1973, pp 5-34.
- (2) Leven, M.M., J. Exp. Mech., Sept. 1973, pp 353-372.
- (3) ASME Boiler and Pressure Vessel Code, Section III, Code Case N-47, 1974.
- (4) Priest, R.H. and Ellison, E.G., Res. Mech., Vol 4, 1982, pp 127-150.
- (5) Jaske, C.E., Mindlin, H. and Perrin, J.S., ASTM STP 520, 1973 p 365.
- (6) Miller, D.A., Priest, R.H., and Ellison, E.G., High Temp. Mats and Processes, Vol. 6, 1984, pp 155-194.
- (7) Edmunds, H.G. and White, D.J., J.Mech. Eng. Sci., Vol. 8, 1966, pp 310-321.

# FATIGUE 87

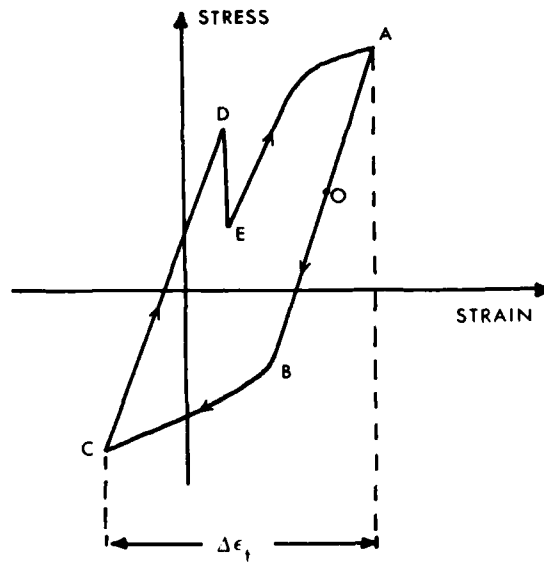


Figure 1. Start-up/Shut-down stress-strain cycle.

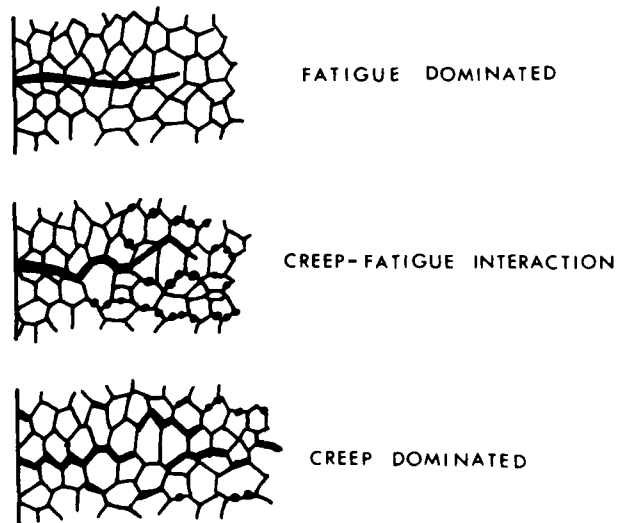


Figure 2. Thermal fatigue failure modes.

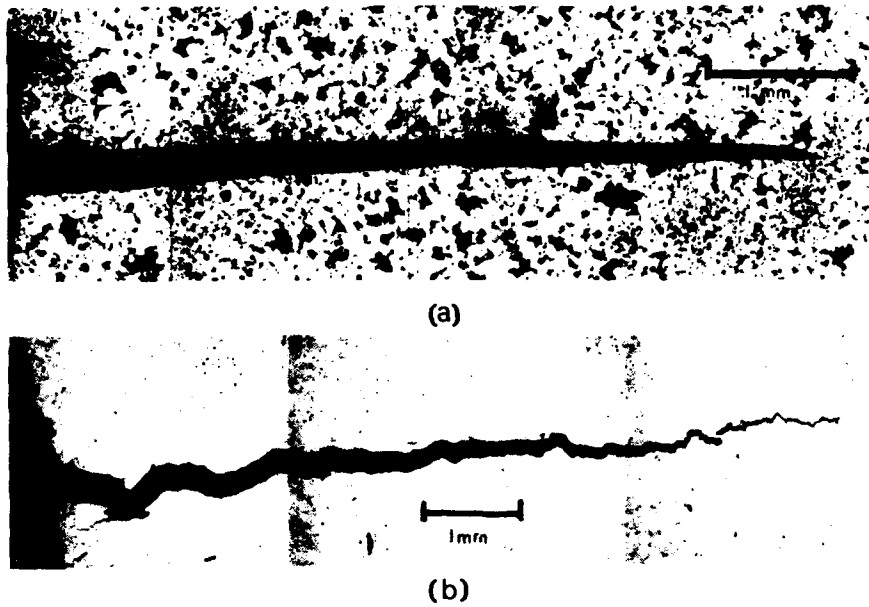


Figure 3. Examples of thermal fatigue cracking in rotors.

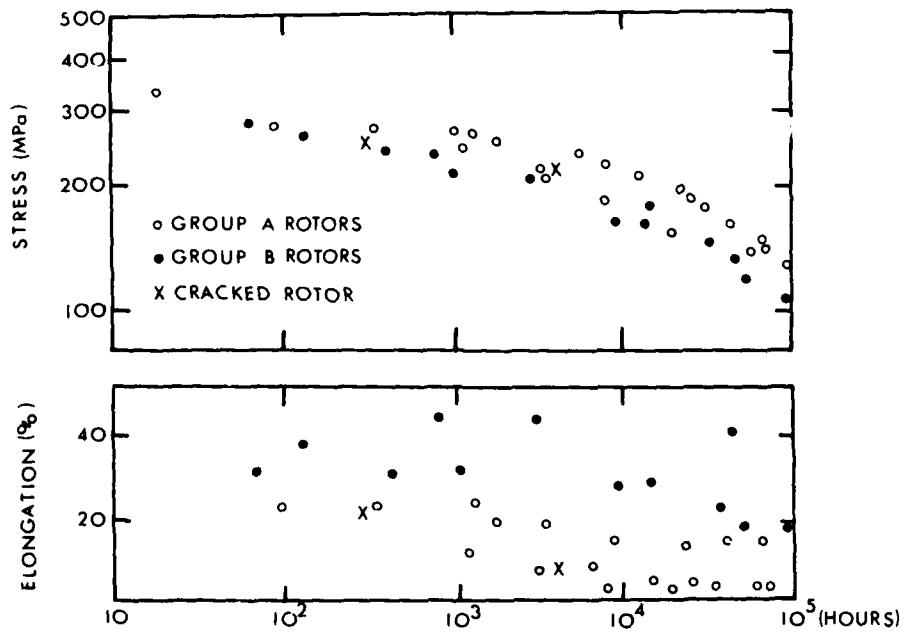


Figure 4. Creep rupture properties of 1% CrMoV rotors at 550°C.

FATIGUE 87

## FATIGUE 87

### THE EFFECT OF TEMPERATURE ON FATIGUE CRACK INITIATION FROM ALUMINOSILICATE INCLUSIONS

P. Woollin\* and J.F. Knott\*

Fatigue cracks have been observed to initiate and grow from aluminosilicate inclusions in powder formed alloy AP-1 at stress intensities below the long crack threshold, both in air and under vacuum. Measured crack growth rates lie below previously reported short crack growth rate data for Astroloy under similar conditions. This is consistent with the presence of residual, tessellated stress fields associated with the inclusions.

In vacuum, higher crack growth rates were observed at 600°C than at 20°C. Also the transition from stage I to stage II crack growth occurs at lower applied  $\Delta K$  levels at 600°C than 20°C. These effects are related to the reduction of the residual stresses with increasing temperature.

#### INTRODUCTION

Nimonic AP-1 is a powder-formed Nickel-based superalloy suitable for use as a gas turbine disc material. The life of a turbine disc is now recognised to be limited by the growth of fatigue cracks from small (< approximately 100  $\mu\text{m}$  diameter) pre-existing defects in the component, although conventional terminology refers to this as initiation-controlled fatigue. The main source of defects in a powder formed disc is the non-metallic particles in the alloy powder (Wildgoose et al (1)).

During cooling from the hiping or forging temperature strains develop in and around the inclusions due to the different thermal expansion coefficients of the metal matrix and the inclusion. At high temperatures (above perhaps 800°C) these strains may be relaxed by plastic flow or diffusion but at lower temperatures a residual, tessellated stress distribution develops. The magnitude of these stresses is proportional to  $\Delta T$ , the difference between

\* Department of Materials Science and Metallurgy, University of Cambridge, England

## FATIGUE 87

the final temperature of the specimen and the temperature at which the thermal strains begin to develop. The thermal expansion coefficient of a typical aluminosilicate refractory is less than those of the Nickel-based superalloys so that a residual compressive stress will develop in the particle. This will be balanced by a residual tensile stress field in the surrounding matrix.

Theoretical calculations for a pure Alumina particle in alloy IN718 or N901 show that these stresses could reach 730 MPa at the particle/matrix interface before tailing off to less than 200 MPa at a distance of one particle radius away from the particle (Tsubota et al (2)). As the temperature of the alloy is increased towards the original hiping or forging temperature the magnitudes of these stresses decrease in a linear fashion with temperature.

If the residual stresses associated with the non-metallic inclusions in powder formed components are of this magnitude it would be expected that they would have a significant influence on the growth of fatigue cracks away from the particles i.e. that the residual stress distribution would modify the local stress distribution associated with the particle as a simple geometrical stress raiser.

The work has investigated the growth of fatigue cracks from aluminosilicate particles at room temperature in air and in a vacuum. The effect of changing the temperature to 600°C on the magnitude of the residual stresses has been observed in vacuum so as to be independent of any environmental effects. Environmental effects have been studied at room temperature.

### MATERIALS

The work was carried out on Nimonic alloy AP-1 which had been doped with 0.188 g of crushed aluminosilicate refractory per Kg. of alloy powder. The aluminosilicate particles observed were all less than 300  $\mu\text{m}$  in any dimension. The alloy was hiped at 1160°C and forged at 1110°C before being heat treated. It had a fine uniform grain size of approximately 15  $\mu\text{m}$  and contained both large  $\gamma'$  particles which were undissolved during the solution treatment and finer  $\gamma'$  which formed during the heat treatment. The composition of the alloy is given in Table 1 and its properties over the range 0°C to 700°C are shown in Figure 1.

TABLE 1 - Composition of alloy AP-1(wt%) (3)

Co	Cr	Mo	Al	Ti	W	Zr	C	Ni
16.80	14.80	5.00	4.00	3.55	0.05	0.04	0.023	Balance

## FATIGUE 87

### EXPERIMENTAL TECHNIQUES

Testing was carried out on 10 mm square smooth bar specimens. These specimens all showed between 14 and 19 inclusions greater than 50  $\mu\text{m}$  in at least one dimension, in the uniformly stressed central region of the specimen. The testing was carried out in a vacuum furnace mounted on a servohydraulic testing machine of 30 KN capacity so that tests could be carried out in air or at a pressure of  $< 1 \times 10^{-6}$  mbar (later referred to as vacuum). Under vacuum testing was conducted both at room temperature ( $-20^{\circ}\text{C}$ ) and at  $600^{\circ}\text{C}$ . All specimens were loaded in four point bend and subjected to a sinusoidal loading cycle of frequency 40 Hz and R-ratio 0.1.

Surface crack growth rates were determined by removing a specimen from the furnace and examining it optically, first after  $5 \times 10^5$  cycles and then at similar successive intervals.

### EXPERIMENTAL RESULTS

All of the cracks which grew during the tests originated at the deliberately added aluminosilicate inclusions. Most of these grew from surface breaking particles but a number grew from particles just beneath the surface.

Some of the cracks initiated and grew in the early parts of the experiment but later retarded and showed little or no further growth (these are later referred to as non-propagating cracks) whilst others continued to grow throughout the cyclic loading. Table 2 shows the number of non-propagating and propagating cracks found in each experiment. Figures 2, 3 and 4 show the crack growth rates measured under the various conditions.

TABLE 2 - The number of cracks initiated in each test

Temperature ( $^{\circ}\text{C}$ )	Environment	$\Delta\sigma$ (MPa)	No. of Propagating Cracks	No. of Non- Propagating Cracks	Total No. of surface Particles
$-20^{\circ}\text{C}$	AIR	405	3	—	17
$-20^{\circ}\text{C}$	VACUUM	405	1	2	15
$-20^{\circ}\text{C}$	VACUUM	525	9	6	16
$600^{\circ}\text{C}$	VACUUM	405	3	2	14
$600^{\circ}\text{C}$	VACUUM	525	9	3	19

## FATIGUE 87

In all the tests conducted under vacuum a number of cracks were observed to become non-propagating but none were seen to become non-propagating during testing in air, although only one such test was carried out and only three cracks were formed in this test.

The growth rates were generally observed to increase with increasing applied stress and increasing temperature but the most significant increase in growth rates was seen when the fatigue was carried out at room temperature in air rather than under vacuum.

### DISCUSSION

#### The effect of the residual stress field on fatigue crack growth

All of the cracks observed were less than 200  $\mu\text{m}$  in length after the first  $5 \times 10^7$  cycles and most had not exceeded 500  $\mu\text{m}$  after  $2 \times 10^8$  cycles. Assuming the cracks to be semi-circular in shape (presumably they follow the particle shape initially) then for the lower stress levels these crack lengths correspond to applied  $\Delta K$  levels of 5.3 to 8.5  $\text{MPa m}^{1/2}$ . For the higher stress levels the corresponding  $\Delta K$  values are 6.9 and 11.0  $\text{MPa m}^{1/2}$  (4). The measured growth rates in this range are shown in figure 2 together with previously published long and short crack data for alloy AP-1 under similar conditions. The cracks in these tests grew well below the long crack threshold measured in air or vacuum (King (5) and Hicks and King (6)). Clearly, the cracks in the present experiments are not showing standard long crack behaviour.

Alloy AP-1 is a powder formed derivative of Astroloy which is a cast superalloy and corresponding short crack growth rates in fine grained Astroloy in air at room temperature and an R-ratio of 0.1 lie in the range  $5 \times 10^{-10}$  to  $2 \times 10^{-9}$  m/cycle (Brown, King and Hicks (7)). The growth rates measured here under the same conditions lie in the range  $2.4 \times 10^{-11}$  to  $3.8 \times 10^{-10}$  m/cycle. These are well below those previously reported for short cracks growing from smooth surfaces so it seems that the residual stresses associated with the particles are influencing crack propagation from the particles.

For an ideally "penny-shaped" crack growing out radially from the centre of an isolated spherical inclusion in an infinite body there are two components of the stress intensity at the crack tip due to the tessellated stresses associated with the particle. One is due to the compressive stress within the particle and the second is due to the tensile stresses present in the metal matrix. By integration of appropriate weight functions, the following expressions for the stress intensity are obtained.

$$K^I \text{ (compressive)} = 2p(\pi a)^{-1/2} \{a - (a^2 - r_i^2)^{1/2}\} \quad (1)$$

## FATIGUE 87

$$K^{II} \text{ (tensile)} = -p(\pi a)^{-\frac{1}{2}} (r_i^2/a^2) (a^2 - r_i^2)^{\frac{1}{2}} \quad (2)$$

where

$$p = \beta / \{ \{ (1 + \nu_m) / 2E_m \} + \{ (1 - 2\nu_i) / E_i \} \} \quad (3)$$

$$\beta = (\alpha_m - \alpha_i) \Delta T \quad (4)$$

The suffix i refers to the inclusion and m to the metal matrix. The net stress intensity at the tip of a crack which extends through the particle and into the matrix is given by the sum of these two components (James and Knott (8)). The variation of the net stress intensity due to the tessellated stresses with crack length is shown in figure 5. This shows that the overall compressive effect of the residual stresses decreases as the crack grows away from the particle.

Whilst a crack that runs through a particle is growing through the residual stress field, then its net effect upon the crack is always compressive and will act so as to reduce the effective R-ratio of the fatigue cycle. This will allow any closure effects to have more influence on the fatigue process. In particular, roughness induced closure is likely to occur during the faceted, structure sensitive crack growth which occurs in the early stages of growth away from the particle.

If the effective R-ratio ever becomes negative then during the compressive part of the fatigue cycle the crack will be completely closed and the effective  $\Delta K$  will be equal to  $K_{max}$ .

This explains why the short crack data reported here differ from those reported elsewhere. The residual stress field in and around the aluminosilicate inclusions can act so as to reduce the effective R-ratio of the applied fatigue cycle and so allow closure contributions to become more important and reduce the rates of crack growth as observed.

### Propagating and non-propagating cracks

The initial growth rates of those cracks which later ceased growing and those which continued growing were of similar magnitude. Also both types of crack grew in similar orientations roughly perpendicular to the applied stress (except for one crack which grew almost parallel to the applied stress). However, thirteen of the sixteen cracks which showed pronounced retardation only grew on one side of the particle and did not manage to grow right across the particle during the test.

If a crack initiates at the particle/matrix interface then it will experience a residual tensile stress as it grows into the matrix. This will increase the effective R-ratio of the fatigue cycle and

## FATIGUE 87

tend to reduce any closure effects which may be acting on the crack. If the crack extends further into the matrix then it will grow into a region of lower residual tensile stress so that the average residual tensile stress acting along the crack length will be reduced. Similarly, if it grows into the particle itself then it is growing into a region of compressive residual stress and again the average residual stress acting on the crack will decrease and it may become compressive.

Overall, these will both act so as to reduce the effective R-ratio of the loading cycle. Although the early stages of such crack growth may be quite rapid due to the residual tensile stress acting, as the crack propagates the average residual stress acting along the crack will decrease. It is quite possible that this could lead to decreasing growth rates as the cracks propagate.

This may explain the existence of a significant number of cracks which showed substantially reduced growth rates after propagating quite normally early on. In some cases these stopped growing to any measurable extent at the surface of the specimen. Many of these cracks were between 10 and 50  $\mu\text{m}$  in length and so it may be argued that in fact they were impeded by grain boundaries or small particles but there was no firm evidence to support or disprove this from the crack paths. However, one crack was seen to retard by a factor of ten when it was 230  $\mu\text{m}$  in length and showed only very slow growth afterwards. This crack had extended right through the particle and grown to a short distance on either side of it before retarding (figure 6).

Note should also be made of one crack which grew away from a sharp, pointed particle in a direction almost parallel to the applied stress. This ceased growing when about 50  $\mu\text{m}$  in length. Whilst it seems odd that a crack should grow in this direction, it does perhaps reflect the presence of a large residual tensile stress field around that particular inclusion.

### The effect of temperature on rates of crack growth

At 600°C the residual stress field around the inclusions should be reduced by at least 50% as the magnitude of the residual stresses is proportional to the difference between the ambient temperature and the maximum temperature at which strains can be relaxed by plastic flow or diffusion during cooling from the forging temperature. This should be reflected by a corresponding reduction at the higher temperatures in those effects which are caused by the residual stress field.

The effect of the residual stress field upon the rate of crack growth away from the particle is difficult to observe at 600°C as it is masked by other effects of temperature upon the fatigue crack growth process (any environmental effect is eliminated by testing

## FATIGUE 87

under vacuum). It has been reported (6) that increasing temperature decreases the roughness of the crack faces produced by structure sensitive fatigue crack growth and can therefore reduce surface roughness induced closure contributions. However, during the earliest stages of crack growth surface roughness induced closure should be largely absent as there is little opportunity for mismatch of the crack faces to develop and examination of the cracks after  $5 \times 10^5$  cycles showed no sign of this. Later some mismatch between crack faces did develop and the cracks became wedged open even when unloaded (figure 7). Finally, the yield strength of the alloy falls with temperature, although the reduction is only ~6% between  $20^\circ\text{C}$  and  $600^\circ\text{C}$  (figure 1). Structure sensitive crack growth is thought to occur when slip is confined to a single slip plane within each grain. Crack extension then occurs because of partial irreversibility of the slip process. Hence, the rate of such crack growth will be related to the yield strength of the alloy, so we might expect growth rates to increase by ~6% as the temperature increases due to the decrease in yield strength.

The data show an average increase in initial crack growth rates of ~60% at both stress levels. Some of this increase may be attributable to the effects mentioned above but it seems that part of it is due to the reduction of the residual stresses around the inclusions. This will lead to the effective R-ratio of the fatigue cycle being higher at  $600^\circ\text{C}$  than at  $20^\circ\text{C}$ . At  $20^\circ\text{C}$  the R-ratio is likely to be negative in the earlier stages of crack growth due to the large compressive stress present in the particle itself. When the temperature is increased and the effective R-ratio increased then the net tensile portion of the fatigue cycle will also be increased. Therefore, the effective  $\Delta K$  acting on the crack will be larger and this would be expected to lead to corresponding increases in crack growth rates. Short crack growth rates are typically not as sensitive to increases in the effective  $\Delta K$  as are long crack data (7) so this helps to explain why this effect is not very large even though the reduction of the residual stresses over this temperature range is considerable.

### The transition from faceted to striated crack growth

Further evidence of the reduction of residual stresses by increasing temperature from  $20^\circ\text{C}$  to  $600^\circ\text{C}$  was found in the appearance of the final fracture surfaces of those specimens tested at the higher stress levels (these were chosen simply because the specimens failed after a reasonable length of time).

At both temperatures an area of faceted, structure-sensitive crack growth was present around the initiating particle although this had a more angular appearance in the room temperature specimen. Farther away from the particle, the fracture morphology became typical of a striated mode of crack growth which is normal for a

## FATIGUE 87

small crack under constant load due to the steady increase of  $\Delta K$ . It has been suggested that this transition coincides with that  $\Delta K$  value at which the crack tip reversed plastic zone is approximately equal in size to some microstructural unit, often the grain size (5).

At 20°C the transition occurred at approximately 1.5 mm away from the centre of the initiating particle whereas at 600°C the transition occurred at about 550  $\mu\text{m}$  away from the centre of its initiating inclusion. These positions correspond to approximate applied  $\Delta K$  values of 26.4 and 16.0  $\text{MPa m}^{1/2}$  respectively. The reversed plastic zone size in plane stress given by:

$$r_{\text{rpz}} = \frac{1}{\pi} \left( \frac{\Delta K}{2\sigma_y} \right)^2 \quad (4)$$

is approximately equal to the grain size (15  $\mu\text{m}$ ) at a  $\Delta K$  value of 13.7  $\text{MPa m}^{1/2}$  at 20°C and 13.5  $\text{MPa m}^{1/2}$  at 600°C. At 600°C the two values for the position of the transition are reasonably close but the room temperature values are much farther apart.

This may be explained, at least partially, by the residual stress fields associated with the particles. The net compressive effect of the residual stresses reduces the effective R-ratio and will also reduce the effective  $\Delta K$  and the crack tip opening displacements if the R-ratio becomes negative or if closure contributions develop. In some cases surface roughness induced crack closure clearly developed (figure 7) leading to wedging open of the crack flanks even when off load, so the reduction of the effective R-ratio is of importance.

These reductions in the effective  $\Delta K$  will correspondingly decrease the size of the reversed plastic zone at the crack tip and hence delay the transition from stage I to stage II crack growth. Although this seems to be a plausible explanation for the delayed stage I to stage II crack growth transition, calculations suggest that beyond a distance of one particle diameter from the initiating particle the net effect of the residual stress on the crack tip is negligible whereas this transition occurred at more than four particle diameters from the initiating inclusion in both cases. This delay may therefore be due to some other effect of temperature e.g. on the slip characteristics of the alloy. Effects of this type leading to modified crack morphology at high temperatures have been observed in alloy AP-1 (6).

It is difficult to say what the exact cause of this delay is but if it is due to the residual stresses then it does suggest the presence of a strong residual stress field at 20°C. At 600°C the delay is considerably reduced which indicates that the residual stresses have fallen with increasing temperature as expected. The effect is small at 600°C which suggests that at this temperature

## FATIGUE 87

the residual stresses have largely disappeared. This suggests that during cooling from the forging temperature the thermal strains developed can be removed by plastic flow or diffusion down to a temperature of around 700 to 800°C as has been proposed earlier (Brooksbank and Andrews (9)).

### The effect of environment

The growth rates observed in air were approximately an order of magnitude greater than those recorded under vacuum. This is typical of faceted crack growth which has been observed in many alloys to be sensitive to the environment in which the crack is growing (e.g. (5), Yuen et al (10)). In air there is a plentiful supply of gas molecules which can be adsorbed onto new surfaces created at the crack tip and lead to reduced slip reversibility and enhanced fatigue crack growth rates. At the lower pressure of  $< 1 \times 10^{-6}$  mbar there are many fewer molecules available and so crack growth rates are correspondingly lower.

The environment does not seem to have had a significant effect on the process of crack initiation from an inclusion at room temperature as tests in both environments at the lower stress level showed the same number of cracks growing from inclusions although they then grew more quickly in air than under vacuum. None of those cracks formed in air ceased growing but some did show reduced growth rates after initiation before accelerating later, as a result of the residual stress distribution discussed earlier.

### CONCLUSIONS

1. Cracks initiated and grew both in air and vacuum from aluminosilicate inclusions at stress intensity levels below the published long crack threshold. These cracks grew away from the inclusions at rates substantially below those reported for short cracks initiated at slip bands. This reflects the overall compressive effect which the residual stresses associated with the aluminosilicate inclusions, in alloy AP-1 have on a crack which extends through a particle and into the matrix.
2. A number of cracks were observed to initiate and grow away from the aluminosilicate particles before later retarding and in some cases becoming non-propagating. This is again consistent with the residual stresses in and around the refractory inclusions.
3. Early crack growth away from the inclusions was observed to occur more rapidly at 600°C than at 20°C. This may be due to the reduction of the residual stresses associated with the inclusions when the temperature of the alloy is increased from 20°C to 600°C.

## FATIGUE 87

4. The transition from stage I, faceted crack growth to stage II, striated crack growth occurred at lower values of applied  $\Delta K$  at 600°C than at 20°C. This may be due to the reduction of the residual stresses caused by increasing the temperature. This may alternatively be due to some other effect of temperature e.g. on the slip characteristics of alloy AP-1.

### ACKNOWLEDGEMENTS

Thanks are due to Professor D. Hull for provision of research facilities at the University of Cambridge. The authors also thank Rolls-Royce PLC, Derby for the financial support of one of them (P.W.) and INCO Alloy Products Ltd for provision of materials. The assistance of T.G. Whitworth during testing is gratefully acknowledged.

### SYMBOLS USED

- $p$  = residual compressive stress within an inclusion (Pa)
- $K^I$  = stress intensity due to residual stresses in the particle ( $\text{MPa m}^{1/2}$ )
- $K^{II}$  = stress intensity due to residual stresses in the metal matrix ( $\text{MPa m}^{1/2}$ )
- $r_i$  = inclusion radius (m)
- $\Delta T$  = difference between alloy temperature and temperature at which thermal strains begin to develop (°C).
- $\alpha$  = thermal expansion coefficient

### REFERENCES

- (1) Wildgoose, P., Turner, N.G., Davies, H.F., Helliwell, B.J., Ubank, R. and Harrison, H., Powder Met. No. 2, 1981 pp 75-86
- (2) Tsubota, M., King, J.E. and Knott, J.F., 1st, Parsons Institute Turbine conference, Trinity College, Dublin. Parsons Press, 1984, pp 189-196
- (3) Bridges, P.J. and Eggar, J.W., "Conference on Powder Metallurgy Aerospace Materials", Berne, 1984
- (4) Holdbrook, S.J. and Dover, W.D., Engineering Fract. Mech. Vol.12, 1979 pp347-364
- (5) King, J.E., Fatigue Engng Mater. Struct. 5, No.2, 1982 pp 177-188

## FATIGUE 87

- (6) Hicks, M.A. and King, J.E., Int. J. Fatigue, Vol.5, No.2, 1983 pp 67-74
- (7) Brown, C.W., King, J.E. and Hicks, M.A., Met. Sci., Vol.18, 1984 pp 374-380
- (8) James, M.N. and Knott, J.F., AGARD Conf. Proc. No.393, 1985, pp 10-1 to 10-12
- (9) Brooksbank, D. and Andrews, K.M., J. Iron and Steel Inst., Vol.210, 1972 pp 246-255
- (10) Yuen, J.L., Schmidt, C.G. and Roy, P., Fatigue Fract. Engng Mater. Struct., Vol.8, No.1, 1985 pp 65-76
- (11) Henry Wiggin and Co. Ltd., "Nimonic Alloys". Publication 25048E, 1973

# FATIGUE 87

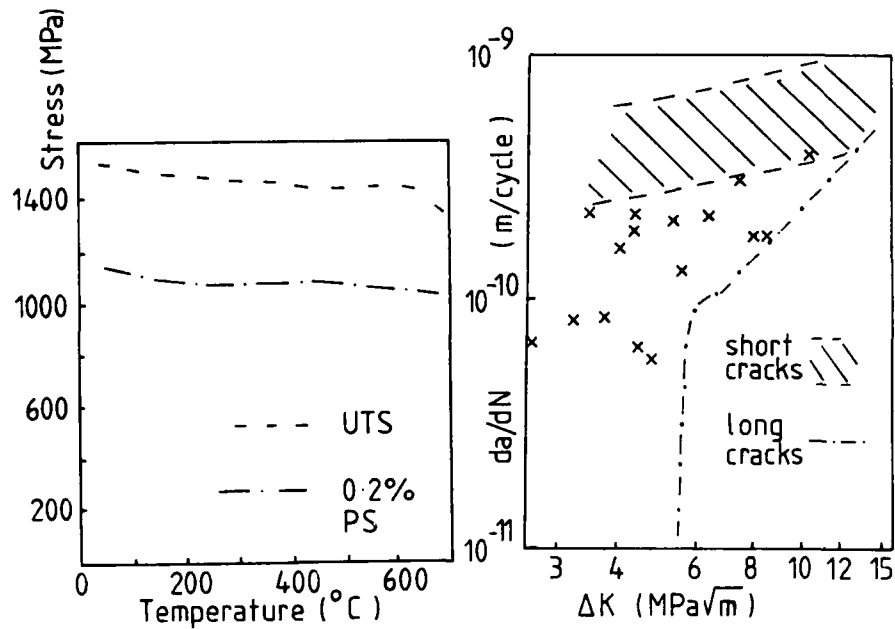


Figure 1. Proof Stress and UTS of AP-1 (3). Figure 2. Growth rates from inclusions, with long & short crack data (7). 20°C, air.

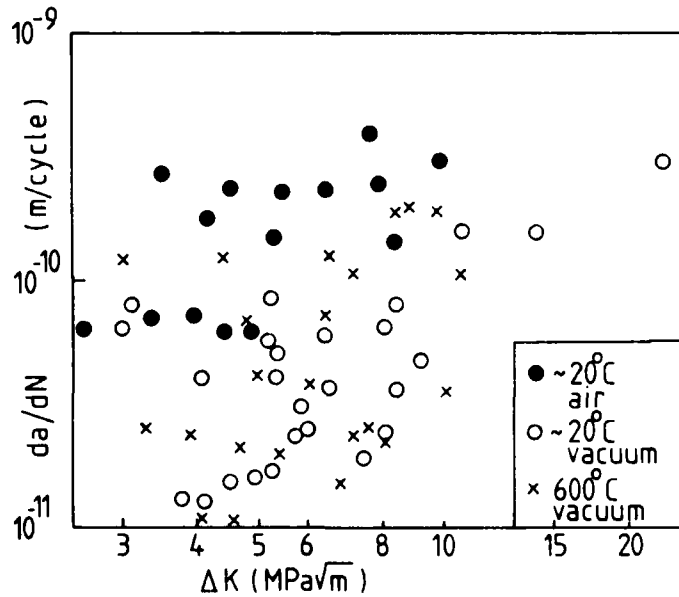


Figure 3. Crack growth rates from aluminosilicate inclusions, 40 Hz R = 0.1.

# FATIGUE 87

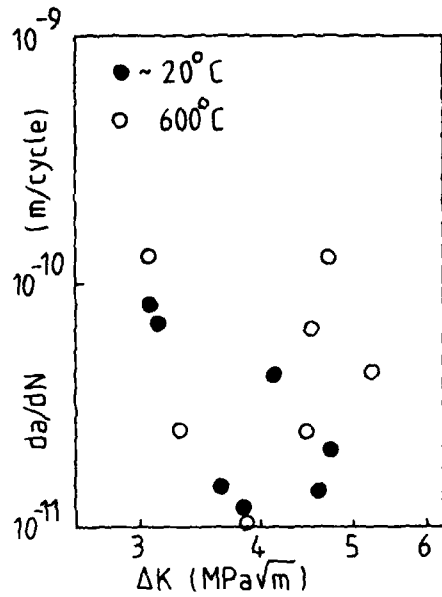


Figure 4 Initial crack growth rates in vacuum

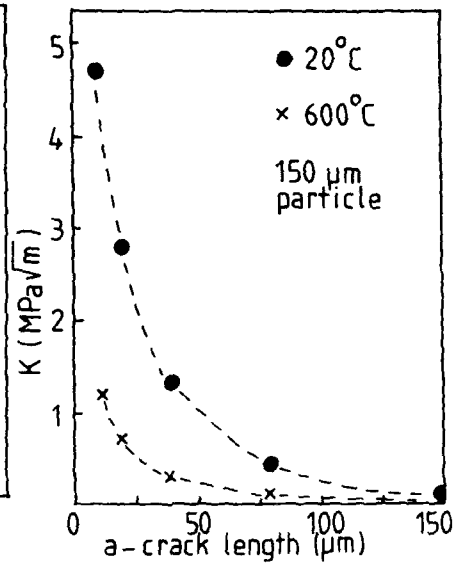


Figure 5 Calculated stress intensity due to residual stresses (8,11)



Figure 6 A non-propagating, through particle crack

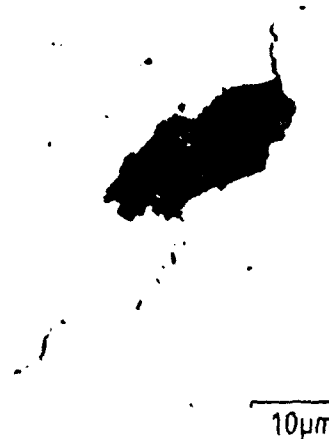


Figure 7 Closure in a crack from an inclusion

FATIGUE 87

1100

## FATIGUE 87

### DEPENDENCE OF STRAINRANGE PARTITIONED FATIGUE LIFE AT ELEVATED TEMPERATURE ON MONOTONIC STRESS-STRAIN PROPERTIES

A. Berkovits\* and S. Nadiv\*\*

On the basis of mechanical tests and metallographic studies SRP lives were predicted by introducing stress-strain materials parameters into the Universal Slopes Equation. This was the result of correlation between fatigue damage mechanisms and deformation mechanisms operating at elevated temperatures. The parameters which must be evaluated for PP- and CC-life are the maximum stress achievable under entirely plastic and creep conditions respectively and corresponding inelastic strains, and the elastic modulus. For plasticity/creep interaction conditions (PC and CP) two more pairs of stress-strain parameters must be ascertained. The correlation between high-temp. fatigue and stress-strain properties was satisfactory for nickel-base superalloys and stainless steel.

### INTRODUCTION

Estimating fatigue life based on the strongly rate-dependent deformation processes which control material response at elevated temperature is a major problem in the design of turbomachinery. Such deformation processes include time-dependent creep and time-independent plasticity while strain is increasing in tension or compression during the fatigue cycle. Success in estimating low-cycle fatigue life under such conditions has varied considerably (Fong (1), Burke and Weiss (2), Amzallag et al. (3), Brunetaud et al. (4)).

One of the more successful phenomenological methods for predicting high-temperature, low-cycle fatigue life is the strainrange partitioning approach, which was developed at NASA by Manson, Halford, and Hirschberg (5) and has become a viable engineering design tool (Saltsman and Halford (6)). The procedure involves the experimental determination of the four basic life relationships, resulting from the four possible combinations of plastic or creep strainrange in the tensile or

\* Dept. of Aero. Engg. and \*\*Dept. of Materials Engg., Technion - Israel Inst. of Technology.

## FATIGUE 87

compressive halves of the fatigue cycle\* for a given material, and their use in conjunction with an interaction damage rule to predict cyclic lives.

The present work was undertaken in order to achieve an understanding of the basic mechanisms which are responsible for observed material response, and thereby achieve a prediction model. Specific objectives were:

1. Analysis of strain-cyclic mechanical response in the light of monotonic creep and plasticity response.
2. Metallographic determination of the plasticity and creep damage mechanisms operating during SRP fatigue loading.
3. Development of a method for the estimation of the strain-life relations, based on the mechanical and microstructural response.

In the present program (Refs. 7 through 9) both cyclic and supporting monotonic tests were conducted on MAR-M200+2%Hf under strain control at constant strainrates. Cyclic data on the other materials studied were found in the literature, so that only monotonic tests were required. The emphasis in this paper is on observed mechanical behavior. A more extensive discussion of microstructural response is found in Nadiv et al. (10).

### CYCLIC AND MONOTONIC DAMAGE MECHANISMS IN MAR-M200+Hf

The initial position of this research included an extensive mechanical and metallographic study of directionally solidified MAR-M200+2%Hf, tested at 975C. Strain-controlled cyclic and monotonic tests, conducted over a range of strainrates, yielded strainrange-partitioned life data and stress-strain data in both the plasticity and creep regimes. Subsequent microscopic examination of test specimens revealed the damage mechanisms operating under the various strain conditions imposed.

#### Monotonic Behavior

The tensile stress-strain response of MAR-M200+Hf material at

---

\*Throughout the discussion strainrange partitioning notation is used, namely:

Not.	Tensile Loading	Compressive Loading
PP	Plasticity	Plasticity
CC	Creep	Creep
PC	Plasticity	Creep
CP	Creep	Plasticity

## FATIGUE 87

975C is represented by the curves in Fig. 1. Examination of the failed test specimens revealed three distinct damage mechanisms, depending on the region of strain and strainrate.

Beyond the points of maximum true stress the stress-strain curves form a set of more or less parallel, gradually decreasing lines. This region is governed by dynamic recovery of the material. It is bounded on the left by the maximum stress developed under a given strainrate. On the right the region is bounded by the fracture strain, which is constant at the lower strainrates which characterize creep, and decreases somewhat in the high-strainrate, plasticity-affected regime.

Plasticity is the dominant process at strainrates above  $0.001 \text{ sec}^{-1}$  in the region before the maximum stress is attained for the given strainrate. Here the stress-strain relationship is independent of the strainrate at low inelastic strain. At these relatively high strainrates, dislocation locking akin to strain-aging does not begin to be felt until considerable strain has taken place under strain-hardening conditions. In fact, by the time strain-aging-like effects can take place in this range they are over-shadowed by the recovery process which eventually leads to failure. The lower bound of the plasticity region is defined by a time-constant controlled by the material diffusion rates.

Dislocation generation, pile-ups and interactions, causing a hardening effect, dominate the low strainrate, low strain region of the stress-strain curves. At low strainrates, low to moderate stresses develop due to dislocation climb and diffusion processes in the material. Recovery rates at the low energy levels involved here are over-shadowed until substantial strain is achieved. The diffusion processes are increasingly inhibited by continuing locking, with the result that as strainrate decreases the strain to achieve a given stress increases, until sufficient strain is accumulated so that recovery becomes the dominant cause of straining.

Thus an area where time-independent strain occurs at high-strainrates prior to initiation of the recovery process, and a region of time-dependent deformation at more moderate strainrates, are defined. Time-dependent deformation is caused by dynamic recovery in the material, evidenced as straining initiated at moderate strainrate and again when failure is approached. Between these extremes dislocation locking mechanisms retard deformation and lead to transitory hardening of the material. These characteristics of monotonic straining have been emphasized because of their significance relative to cyclic response.

### Cyclic Behavior

The cyclic response curves obtained under symmetrical strain-control ( $R_\epsilon = -1$ ) were unique functions of loading frequency, which was constant throughout each cyclic test. For a given frequency a single family of hysteresis loops resulted, bounded by common tensile and compressive inelastic stress-strain curves, regardless of strain amplitude, for both PP and CC tests (Fig. 2). Furthermore, the plasticity half of CP and PC hysteresis loops coincided with PP results, while the creep half matched results obtained from CC tests. The fact that the cyclic stress-strain relationships did not change as a result of altering the strain amplitude (and accordingly the strainrate) at a given test frequency, indicates that little or no hardening occurred under cyclic loading, the material remaining almost fully recovered and soft. This suggests that radically different characteristics were active in the microstructure under cyclic and monotonic conditions, before the onset of the cracking and failure phase. Similar response under cyclic conditions was noticed previously by Berkovits (11) for Udimet-700, as well as for 316 stainless steel.

The phenomenon of preserved "softness" of the material under cyclic conditions has also been noted by others (Kear and Oblak (12)). It is apparently the result of relaxation of dislocation back stress and pile-up during reverse loading, so that the material responds as if it were virgin material following each load reversal. In this respect the cyclic response is quite different from monotonic behavior, which will be important when fatigue life prediction is discussed in the next section.

### STRAINRANGE PARTITIONED LIFE PREDICTION

The crux of the study of constitutive behavior of materials is its use in predicting failure. This objective has seldom been achieved (cf. Ross (13)). Fatigue-life data obtained from MAR-M200+Hf material at 975C will now be presented and discussed. A method of predicting fatigue life, based on the monotonic stress-strain behavior, will be proposed.

The key to cyclic-creep life prediction is to be found by interpretation of the cyclic and monotonic stress-strain response in terms of the controlling deformation process. It was stated previously that recovery-controlled deformation is defined by the negative slope of the stress-strain curves in the high-strain region, and by a line which separates the plasticity and dynamic recovery regimes at low strains. (These curves can be related to the diffusion energy relation.) The hardening process which occurs at low strains can be described as a family of curves emanating from the recovery initiation line and intersecting the recovery family at strains corresponding to the maximum stress at

## FATIGUE 87

each strainrate. The line of intersection of the two families of curves which represent the controlling processes, is significant when attention is turned to the cyclic loading case.

Under cyclic CC loading, stress ranges above 600 MPa indicated some cyclic hardening, while lower stress amplitudes exhibited slight cyclic softening. Very low frequency tests underwent hardening similar to monotonic tests at commensurate strainrates. It is significant that the observed hardening and softening rates were such that the cyclic response converged in all cases on a state-point defined by a stress-range equal to 600 MPa and a corresponding creep strain amplitude of 0.007. The fact that this point falls on the line of maximum stresses for given strainrates, and on the recovery curve for a stress of 600 MPa, may not be coincidental. Failure of MAR-M200+Hf at 975C is due to the dynamic recovery processes and occurs in the creep region at an upper stress limit of approximately 600 MPa. The recovery mechanism appears to be coarsening of  $\gamma'$  precipitate particles (10). Although at higher stresses failure comes after plastic deformation, it is still due to recovery. However, here the recovery mechanism is dissolution of  $\gamma'$ , and ductility is reduced as a result of the earlier plastic deformation. (An extensive discussion of the microstructural developments is given in Ref. 10.)

Thus the monotonic stress and inelastic strain coordinates, 600 MPa and 0.007 respectively, indicated in Fig. 1, are sufficient to define conditions leading to failure under the completely relaxed creep cycling, which controls CC, CP and PC failure in the directionally solidified MAR-M200+Hf material under discussion. (In most materials CP and PC damage mechanism are not identical to CC mechanisms, as will be discussed presently.) On this basis a relation of the Universal-Slopes type can be suggested as

$$\frac{\Delta \epsilon}{2} = \frac{\sigma_{UCC}}{E} N^{-0.12} + \epsilon_{UCC} N^{-0.6} \quad (1)$$

where  $\sigma_{UCC}$  is the ultimate time-dependent stress (equal to 600 MPa in MAR-M200+Hf at 975C), and  $\epsilon_{UCC}$  is the corresponding time-dependent strain (equal to 0.007 in MAR-M200+Hf at 975C).

The present contention, that fatigue life is determined by the material response at its maximum monotonic strength, before the onset of dynamic recovery leading to failure, can be applied to PP data as well. Maximum stress under plasticity conditions occurred in the material investigation at  $\sigma_{upp}$  equal to 900 MPa. The corresponding plastic strain  $\epsilon_{upp}$  was approximately 0.007, coincidentally the same value as for  $\epsilon_{UCC}$ . These values of the constitutive parameters were substituted in a PP relation

## FATIGUE 87

of the form:

$$\frac{\Delta \epsilon}{2} = \frac{\sigma_{UPP}}{E} N^{-0.12} + \epsilon_{UPP} N^{-0.6} \quad (2)$$

Lifetime of strainrange partitioned tests conducted under constant strainrates are shown as symbols in Fig. 3. The PP-life results show significantly longer lives than CC, PC or CP results. The latter all have similar fatigue lives, because there are almost no transverse grain boundary segments to act as crack initiation sites under tensile creep conditions in the directionally solidified material (Manson and Halford (14)). In all cases detectable fatigue cracks developed only during the last 20% of the cyclic tests. Somewhat more oxidation occurred on the crack face in tests during which the tensile phase was at low strainrate (CC and CP) than in those with high tensile strainrate (PP and PC).

Correlation of calculated results obtained from Eqs. (1) and (2), and shown as curves in the figure, with CC, CP, PC as well as PP data is excellent.

### CP AND PC LIFE PREDICTION FOR OTHER MATERIALS

In directionally solidified MAR-M200+Hf material CP and PC fatigue life was dominated by the creep loading. More importantly the plasticity half of the strain cycle did not significantly affect the response of the creep half of the hysteresis loop. As a result, the creep parameters remained the controlling factors in CP and PC life. However, in other materials the effect of compressive plasticity on the subsequent tensile creep half-cycle, in a CP test, and that of compressive creep on subsequent tensile plasticity in a PC test, must be quantified in order to predict CP and PC lifetimes from the Universal-Slopes Equation. The appropriate values of  $\sigma_U$  and  $\epsilon_U$  may be determined from the tensile side of one-cycle-to-failure tests, in which compressive stress and strain equivalent to the negative of the maximum (P or C) stress and strain are applied prior to tensile (C or P respectively) loading to failure. The life-prediction relations for CP and PC conditions then become:

$$\frac{\Delta \epsilon}{2} = \frac{\sigma_{UCP}}{E} N^{-0.12} + \epsilon_{UCP} N^{-0.6} \quad (3)$$

and

$$\frac{\Delta \epsilon}{2} = \frac{\sigma_{UPC}}{E} N^{-0.12} + \epsilon_{UPC} N^{-0.6} \quad (4)$$

## FATIGUE 87

respectively. The validity of this approach was investigated for a number of other elevated temperature materials.

### COMPARISON BETWEEN PREDICTED AND EXPERIMENTAL SRP LIFE

The key to cyclic life prediction for MAR-M200+Hf at elevated temperature was perceived by interpretation of the cyclic and monotonic mechanical response in terms of the controlling microstructural processes. When the interaction of dynamic recovery and strain-hardening processes was understood in terms of the microstructure, a method of life prediction evolved.

Clearly, in other materials different chemico-mechanical processes may be responsible for strain hardening. The significant point is that cyclic strength persists as long as the hardening process, whatever its cause, dominates the deformation. When the hardening mechanism is superseded by recovery processes, both monotonic and cyclic resistance are essentially exhausted. Thus the stress and strain parameters obtaining at the point of mechanism-change in the monotonic test are also the controlling parameters for estimating cyclic life. These parameters are the true stress and the corresponding true strain in the plasticity and creep-range strength tests.

Evaluating these parameters in the plasticity stress-strain curve is straight-forward. However, they must also be ascertained for the (unknown) strainrate at which the full creep capability of the material is realized. In principle the required stress-strain curve is that for which the ultimate stress corresponds to the proportional limit stress of the plasticity curve. In practice the correct curve may be better determined by taking some small plastic strain such as the 0.1% offset, as the limit, instead of the proportional limit (Fig. 1).

In order to test the validity of the relationship between the perceived critical damage point on the stress-strain curve and strainrange partitioned life, a comparison was performed for four nickel-base superalloys and a stainless steel. Fatigue life data were taken from the literature for the following materials:

René 80	at 1000C	Kortovich and Sheinker (15)
AF2-10A	at 760C	Saltsman and Halford (6)
Udimet-700	at 760C	Berkovits (16)
S.S. 316	at 705C	Hirschberg and Halford (17)

For each material a series of six stress-strain tests were conducted under strain control at the appropriate temperature. The six tests consisted of:

1. high-strainrate test to define plasticity parameters;

# FATIGUE 87

2. one-cycle-to-failure tests (one CP, one PC) at strainrates and compressive strain limit defined by the previous tests;
3. moderate-strainrate tests to define the creep region upper limit.

Values of stress and strain parameters obtained from these tests for use in the life-prediction Eqs. (1) to (4) are tabulated in Table 1. Values for MAR-M200+Ht are also included for completeness. Total strainrange against lifetime curves for the five materials calculated with the aid of Table 1 are compared with experimental data in Figs. 3 to 7. In general the correlation supports the proposed method. Results of the comparison indicate that parameters required for Universal-Slopes prediction of SRP lifetimes can be evaluated from critical damage points of monotonic stress-strain data.

TABLE 1 - Stress-Strain Parameters for Prediction of SRP Life from Universal-Slopes Equation.

Parameter	Material				
	MAR-M200	René 80	AF2-10A	U-700	S.S. 316
Temp., C	975	1000	760	760	705
E, GPa	81.7	124.0	161.6	162.7	111.0
$\sigma_{UPP}$ , MPa	900	448	1041	1320	300
$\epsilon_{UPP}$	.007	.02	.006	.122	.08
$\sigma_{UCC}$ , MPa	600	300	965	1060	300
$\epsilon_{UCC}$	.007	0.18	.005	.135	.08
$\sigma_{UCP}$ , MPa	600	317	834	950	300
$\epsilon_{UCP}$	.007	.014	.0115	.036	.02
$\sigma_{UPC}$ , MPa	600	276	1062	1320	300
$\epsilon_{UPC}$	.007	.0136	.02	.122	.02

## FATIGUE 87

### CONCLUSION

A metallographic study of the correlation between SKP fatigue damage mechanisms, and deformation mechanisms operating in the early stages of monotonic plastic and creep ductility at elevated temperatures, evolved a method of evaluating material parameters for Universal-Slopes prediction of fatigue life. Besides the elastic modulus of the material, the required parameters are the maximum true stress and corresponding inelastic strain under the four strainrange partitioning conditions. These conditions include the strainrates which produce entirely plastic and creep deformations, and two one-cycle-to-failure cases which define plasticity/creep interactions. The parameters can be evaluated at a given temperature by as few as six stress-strain tests.

Comparison of predicted lifetimes with experimentally determined fatigue lives for five elevated temperature materials demonstrated that the principles on which the prediction method is based are sound.

### REFERENCES

- (1) Fong, J.T. (ed.), "Fatigue Mechanisms", ASTM-STP 657, Philadelphia, PA, 1979.
- (2) Burke, J.J. and Weiss, V. (eds.), "Fatigue Environment and Temperature Effects", Plenum, NY, 1983.
- (3) Amzallag, C., Leis, b.N. and Rabbe, P. (eds.), "Low-Cycle Fatigue and Life Prediction", ASTM-STP 770, Philadelphia, PA, 1982.
- (4) Brunetaud, R., et al. (eds.), "High Temperature Alloys for Gas Turbines 1982", D. Reidel, Dordrecht, Holland, 1982.
- (5) Manson, S.S., Halford, G.R. and Hirschberg, M.H., 1st Symp. on Design for Elevated Temperature Environment, ASME, San Francisco, 1971, pp. 12-28.
- (6) Saltsman, J.F. and Halford, G.k., "An Update of the Total-Strain Version of SRP", NASA TP2499, 1985.
- (7) Berkovits, A. and Nadiv, S., Proc. Mechanical Behavior of Materials-IV, 1, 1983, pp. 149-156.
- (8) Berkovits, A. and Nadiv, S., Proc. V. Internat. Cong. on Experimental Mechanics, SESA, Brookfield Center, CT, 1984.
- (9) Berkovits, A., "Estimation of High Temperature Low Cycle Fatigue on the Basis of Inelastic Strain and Strainrate", NASA TM88841, Oct. 1986.

## FATIGUE 87

- (10) Nadiv, S., Berkovits, A. and Shalev, G., Internat. Conf. on Fatigue, - Corrosion Cracking, Fracture Mechanics, Failure Analysis", ASM, Metals Park, OH, 1986.
- (11) Berkovits, A., AIAA J. of Aircraft, 11, 1974, pp. 10-14.
- (12) Kear, B.H. and Oblak, J.M., J. de Physique, 35, 1974, pp. 7-35 to 7-45.
- (13) Koss, D.A., Chang, T.Y. and Thompson, R.L. (eds.), "Nonlinear Constitutive Relations for High Temperature Applications", NASA Conf. Pub. 2271, Washington, DC, 1983.
- (14) Manson, S.S. and Halford, G.R., Israel J. of Technology, 21, 1983, pp. 29-53.
- (15) Kortovich, C.S. and Sheinker, A.A., "A Strainrange Partitioning Analysis of Low Cycle Fatigue of Coated and Uncoated René 80", AGARD-CP-243, 1978, pp. 1-1 to 1-23.
- (16) Berkovits, A., ASME J. of Engineering Materials and Technology, 96B, 1974, pp. 106-108.
- (17) Hirschberg, M.H. and Halford, G.R., "Use of Strainrange Partitioning to Predict High-Temperature Low-Cycle Fatigue Life", NASA TN D-8072, 1976.

# FATIGUE 87

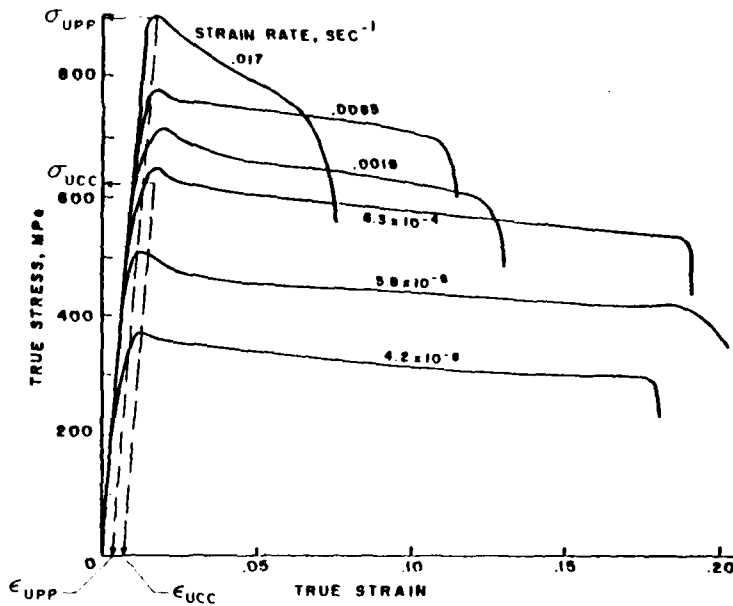


Figure 1 Tensile properties of MAR-M200+Hf at 975C

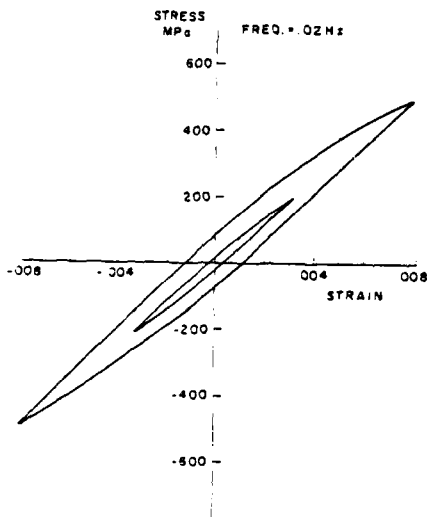


Figure 2 Hysteresis loops for MAR-M200+Hf at 975C

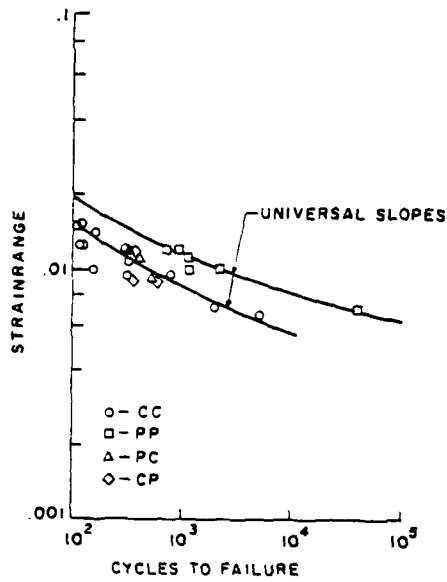


Figure 3 SRP lifetime of MAR-M200+Hf at 975C

# FATIGUE 87

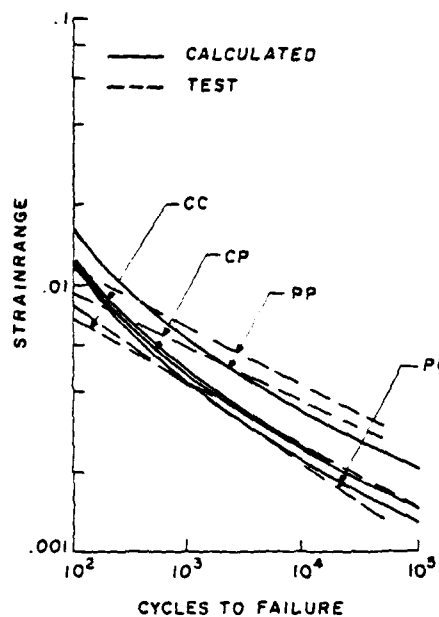


Figure 4 SRP lifetime of Rene 80 at 1000C

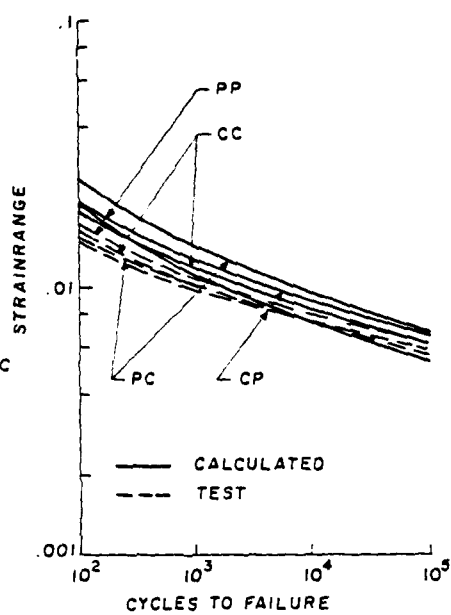


Figure 5 SRP lifetime of AF2-1DA at 760C

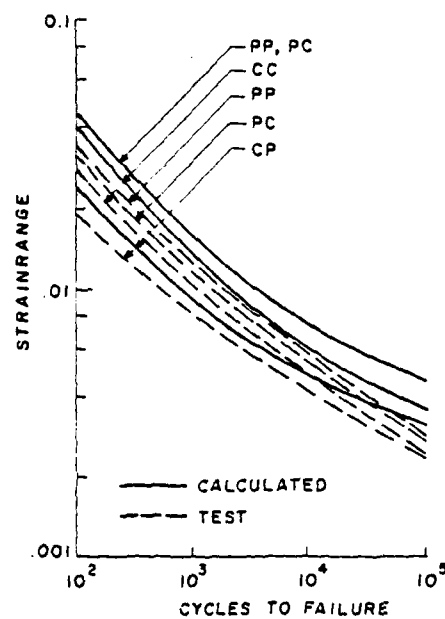


Figure 6 SRP lifetime of Udimet-700 at 760C

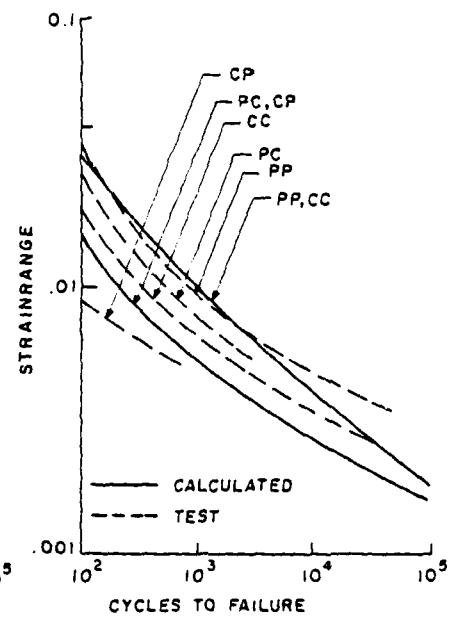


Figure 7 SRP lifetime of 316 stainless steel at 705C

## FATIGUE 87

### THERMAL MECHANICAL LOW CYCLE FATIGUE OF 25CDV4-10 STEEL

J.GILGERT, M.LEBIENVENU and G.PLUVINAGE\*

Thermal mechanical fatigue behaviour was investigated for constant amplitude, fully reversed, strain cycling of uniaxially loaded specimens at two ranges of temperature: 100-500 and 300-500°C with strain in phase with temperature. A model based on a relationship between thermal mechanical fatigue strain and low cycle fatigue strain is proposed and discussed. The material used in this program is a 25CDV4-10 steel that was representative of rotor materials used by present-day large steam turbine-generator manufacturers.

### INTRODUCTION

Many industrial problems arise because of damage and failure of metallic components arising from cyclic plastic strains introduced by restraint of thermal expansion under conditions of repeated temperature change. The effect is generally referred to as thermal fatigue although there has been some confusion in nomenclature and a plea for more terminology has been made by Spera (1). Thermal fatigue has been defined by Carden (2) as that process by which cracks originate and are propagated in materials that both cyclic temperature and cyclic mechanical strain at a critical location. There are essentially two experimental techniques used to obtain such material data. The conventional thermal fatigue technique entails cycling the test between a hot source and a cold source. The other experimental technique, known as thermal mechanical fatigue cycles both the mechanical strain and the temperature independently.

\* Faculté des Sciences. Ile du Saulcy. 57045 Metz Cedex.  
FRANCE

## FATIGUE 87

Thermal fatigue life prediction is generally determined on stabilized hysteresis loops, stress-strain or strain-temperature by a cumulative damage rule in isothermal fatigue. This method may be based on a linear (3, 4, 5) or no linear (6) interaction or an equivalent temperature concept (7, 8). This implies that, for a given value of the plastic strain  $\Delta \epsilon_p$ , an isothermal fatigue test leads to the same fatigue life as the thermal testing. However, only few studies dealt with the description of isothermal low cycle fatigue at various temperatures, then applicable to thermal fatigue.

This paper described the results of a study where the low cycle fatigue of 25CDV4-10 steel was investigated for conditions of thermal and mechanical strain cycling.

### EXPERIMENTAL PROCEDURE

The thermal mechanical fatigue experiments are conducted using a servocontrolled electrohydraulic machine. The axial mechanical strain and temperature were controlled to follow one of the both basic constant amplitude waveforms ( $\epsilon_{\max}$  is in phase with  $T_{\max}$ ). The control program waveform was provided by a function generator. Heating rate was constant and determined by the thermal response of the specimens and the heating equipment with the length of the thermal cycle maintained at about 2,5 min ( $T_{\max}=300^\circ\text{C}$ ,  $T_{\min}=100^\circ\text{C}$ ) or 5 min ( $T_{\max}=500^\circ\text{C}$ ,  $T_{\min}=100^\circ\text{C}$ ). The total strain amplitude  $\Delta \epsilon_t$  varies from 0,2 to 2,4%. A strain rate of  $3,2 \cdot 10^{-3}/\text{s}$  is used in isothermal low cycle fatigue tests. The material was a chromium-molybdenum steel with nominal composition in weight percent of 1Cr, 1Mo, 0.3V, 0.25C and the remainder iron.

### RESULTS AND DISCUSSION

#### Isothermal low cycle fatigue.

A common way to fit the data is with a universal slopes (9) equation of the form:

$$\Delta \epsilon_t = A(2N_R)^a + B(2N_R)^b \dots \dots \dots (1)$$

where the constants A, a, B, b (Table 1) are determined from regression analysis of the elastic and the plastic components of strain.

Numerical values of reversals to failure ( $2N_R$ ) against total strain amplitude are given in Table 2.

# FATIGUE 87

TABLE 1-Cyclic material constants.

T°C	A%	b	B%	c
100	0,90	-0,074	104	-0,65
300	0,92	-0,076	100	-0,66
500	0,84	-0,085	88	-0,70

TABLE 2-Axial fatigue data:number of reversals ( $2N_R$ ) to failure.

$\Delta\epsilon_t\%$	0,6	1	1,4	2	2,4
500°C	6600	2230	1400	660	440
300°C	-	4970	2400	1350	1010
100°C	-	7460	3100	1410	1030

## Thermal mechanical fatigue.

Results of experiments are summarized in Table 3.

TABLE 3-Thermal mechanical data:number of reversals ( $2N_R$ ) to failure.

$\Delta\epsilon_t\%$	T: 300 to 500°C	T: 100 to 500°C
2,4	366	460
2	420	794
1,4	1076	2370
1,1	5380	-
1	6010	-
0,2	860	1230
0,028	5000	1872

Typical hysteresis loop generated in 25CDV4-10 steel is shown in figure 1. Results of thermal mechanical fatigue experiments are compared with isothermal fatigue data in terms of  $\Delta\epsilon_t$  in figure 2.

Taira (7) has suggested the use of the concept of an equivalent temperature for correlating thermal fatigue behaviour with isothermal behaviour. This concept states that, regarding thermal fatigue cycling between two temperatures, the same fatigue life will be developed by isothermal cycling at an equivalent temperature  $T_e$ . So we can write according to Taira:

$$T_e = (T_{\max} + T_{\min})/2 \text{ or } T_e = T_{\max} \dots\dots\dots(2)$$

In Table 4 experimental results are compared with the life prediction given by Taira's concept.

# FATIGUE 87

TABLE 4- Results of tests temperatures for thermal fatigue and their equivalent temperatures.

T: 300 to 500°C t %	Reversals to failure (2N <sub>R</sub> )		
	Experimental	T <sub>e</sub> =500°C	T <sub>e</sub> =400°C
2,4	366	440	644
2	420	660	784
1,4	1076	1400	1746
1,1	5380	-	-
1	6010	2230	3820
0,2	860	-	4430
0,028	5000	-	6480
T: 100 to 500°C			
2,4	460	440	796
2	794	660	1110
1,4	2370	1400	2120
0,2	1230	-	4480
0,028	1872	-	6800

The details of the Taira's model are described in reference 7. Degallaix and al (8) fit the damage with the expression:

$$\Delta\Phi = 1/N_R = A_1 (\Delta\epsilon_p)^{B_1} \exp(-Q/RT) + A_2 (\Delta\epsilon_p)^{B_2} \dots (3)$$

where  $A_1, B_1, A_2, B_2$  are material constants and  $Q$  is an apparent activation energy. In order to evaluate the damage progress in a thermal fatigue test, they will argue with Taira's assumptions, in particular the linear damage rule. Then the increment of damage  $d(\Delta\Phi)$ , connected with the increments of plastic strain  $d(\Delta\epsilon_p)$  and of temperature is given by the expression:

$$d(\Delta\Phi) = \left[ (A_1 B_1) / 2 \Delta\epsilon_p^{B_1 - 1} \exp(-Q/RT) + (A_2 B_2) / 2 \Delta\epsilon_p^{B_2 - 1} \right] d(\Delta\epsilon_p) + \left[ (A_1 / 2) \Delta\epsilon_p^{B_1} Q / RT^2 \exp(-Q/RT) \right] dT \dots (4)$$

With numerical values  $\Delta\epsilon_p$  and  $T$  taken on the stabilized hysteresis loop, the integration of relation 4 allows the damage evaluation during the heating ( $T_1 \rightarrow T_2$ ) and cooling ( $T_2 \rightarrow T_1$ ) paths. Then the thermal fatigue damage per cycle is given by

$$\Delta\Phi_{T_1 \rightleftharpoons T_2} = \Delta\Phi_{T_1 \rightarrow T_2} + \Delta\Phi_{T_2 \rightarrow T_1} \dots (5)$$

By using equation 3, parameters  $\Delta\epsilon_p$  and  $T$  of equivalent isothermal test can be determined. Making up evolution of plastic strain  $\Delta\epsilon_p$  as a function temperature, results are shown in Table 5.

# FATIGUE 87

TABLE 5-

$\Delta T : 300 \text{ to } 500^\circ\text{C}$			$\Delta T : 100 \text{ to } 500^\circ\text{C}$		
$\Delta \epsilon_t$ % Reversals to failure			$\Delta \epsilon_t$ % Reversals to failure		
Experimental Degallaix			Experimental Degallaix		
2,4	366	664	2,4	460	790
2	420	878	2	794	1094
1,4	1076	1812	1,4	2370	2080
1,1	5380	3800	0,2	1230	4980
1	6000	3960	0,028	1872	3910
0,2	860	5580			
0,028	5000	8640			

The thermal mechanical fatigue live values obtained from experiments were much lower than life predicted from Taira or Degaillaix' model. It appears that in thermal mechanical fatigue it is necessary to take into account the evolution of thermal strain. The mechanical strain  $\Delta \epsilon_m$  can be written by the equations:

$$\Delta \epsilon_m = \Delta \epsilon_t - \Delta \epsilon_{th} \text{ if } \Delta \epsilon_t > \Delta \epsilon_{th} \dots\dots\dots(6)$$

$$\Delta \epsilon_m = \Delta \epsilon_t + \Delta \epsilon_{th} \text{ if } \Delta \epsilon_t < \Delta \epsilon_{th} \dots\dots\dots(7)$$

where  $\Delta \epsilon_{th}$  represents thermal strain between  $T_{min}$  and  $T_{max}$ . Table 6 gives the values of  $\Delta \epsilon_m$  for all tests.

TABLE 6-Values of mechanical strain.

$\Delta \epsilon_{th} = 0,79 \text{ (100-500}^\circ\text{C)}$	$\Delta \epsilon_t$ %	$\Delta T (^\circ\text{C})$	$\Delta \epsilon_m$ %	$2N_R$
$\Delta \epsilon_{th} = 0,56 \text{ (300-500}^\circ\text{C)}$				
$\Delta \epsilon_m = \Delta \epsilon_t - \Delta \epsilon_{th}$	2,4	300-500	1,87	366
	2,4	100-500	1,62	460
	2	300-500	1,46	420
	2	100-500	1,23	794
	1,4	300-500	0,85	1076
	1,4	100-500	0,62	2370
	1,1	300-500	0,45	5380
$\Delta \epsilon_m = \Delta \epsilon_t + \Delta \epsilon_{th}$	1	300-500	0,44	6010
	0,2	300-500	0,38	860
	0,2	100-500	0,99	1230
	0,028	300-500	0,59	5000
	0,028	100-500	0,81	1872

Life as a function of mechanical strain  $\Delta \epsilon_m$  is shown in figure 3 and can be predicted by the equation:

$$\Delta \epsilon_m = 17,2 (2N_R)^{-0,50} \dots\dots\dots(8)$$

## FATIGUE 87

We can see in figure 4 that the mechanical strain curve breaks through the plastic strain lines in isothermal fatigue for three points A,B,C corresponding with the thermal strain between 20°C and the considered temperature as it is seen in Table 7-

TABLE 7-

T°C	Point position	value of	$\Delta\epsilon_{th}$ (20 to T°C)
100	A	0,14	0,12
300	B	0,24	0,38
500	C	0,86	0,80

So we can write that thermal mechanical fatigue experiments with mechanical strain are equivalent to isothermal fatigue experiments with plastic strain. For each temperature, the number of cycles to failure can be expressed as

$$2N_R = (\Delta\epsilon_p/B_T)^{1/b_T} = g(\Delta\epsilon_m)^s \dots\dots\dots (9)$$

where  $B_T$  and  $b_T$  are the coefficients of the equation 1 at the considered temperature T in isothermal experiments g and s are material constants no function of temperature Mechanical strain can be written:

$$\Delta\epsilon_m = \alpha(T_i + 20^\circ\text{C}) \dots\dots\dots (10)$$

but neglecting thermal strain between 0 and 20°C, we obtain for each temperature  $T_i$ :

$$\Delta\epsilon_m = \alpha T_i \dots\dots\dots (11)$$

So equation 9 can be written:

$$g(\alpha T_i)^s = (\alpha T_i/B_T)^{1/b_T} \dots\dots\dots (12)$$

$$\text{with } 2N_R = g(\Delta\epsilon_m)^s \dots\dots\dots (13)$$

Material constants g and s are determined from the results in isothermal experiments. For our material, the values of g and s are:  $g=0,012$  and  $s=-2$

### CONCLUSION

Many criteria for thermal fatigue failure have been proposed but almost all of them seem to be little authorized Both of the combined effects of temperature and strain as well as the wide variations of test methods make it dif-

## FATIGUE 87

ficult to find a general rule.

The experimental results in thermal mechanical fatigue were compared with the predicted life of the material obtained from isothermal fatigue. A relationship between mechanical strain and number of cycles to failure can be written by  $\Delta \epsilon_m = 17,2(2N_f)^{-0,5}$ . A model based on a relationship between thermal fatigue and isothermal fatigue is proposed.

### REFERENCES

- (1) Spera, D.N. ASTM STP 612, 1976, p.3
- (2) Carden, A.E., ASTM STP 465, 1970, p.163
- (3) Spera, D.A., ASTM STP 520, 1973, P.648
- (4) Chaboche, J.L. and Stoltz, C., Rev.Fr.Meca., 52, 1974, p.37
- (5) Halford, G.R. and Manson, S.S., ASTM STP, 612, 1976, 239
- (6) Lemaitre, J. and Chaboche, J.L., Symp.AUTAM, ONERA, T.P. 1394
- (7) Taira, S., ASTM STP 520, 1973, P.80
- (8) Degallaix, G. and FOCT J., Mat.Sci.Eng., 58, 1983, 55
- (9) Morrow, J., ASTM STP 378, 1965, p.45

# FATIGUE 87

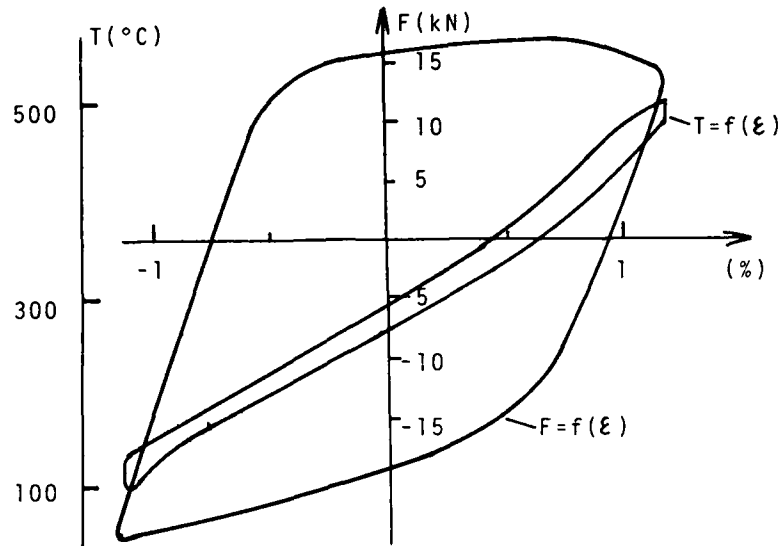


Figure 1 Experimental stress strain hysteresis loop

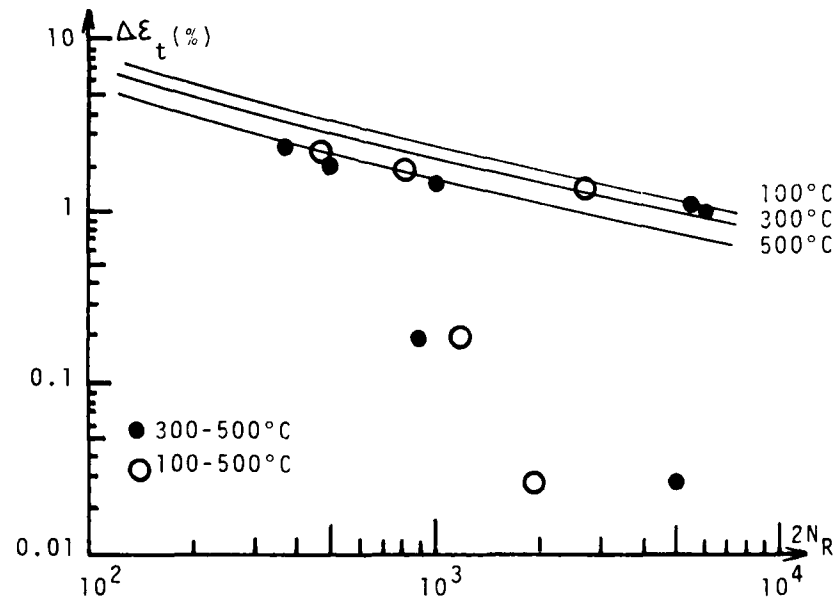


Figure 2 Isothermal and thermal cycle fatigue tests

# FATIGUE 87

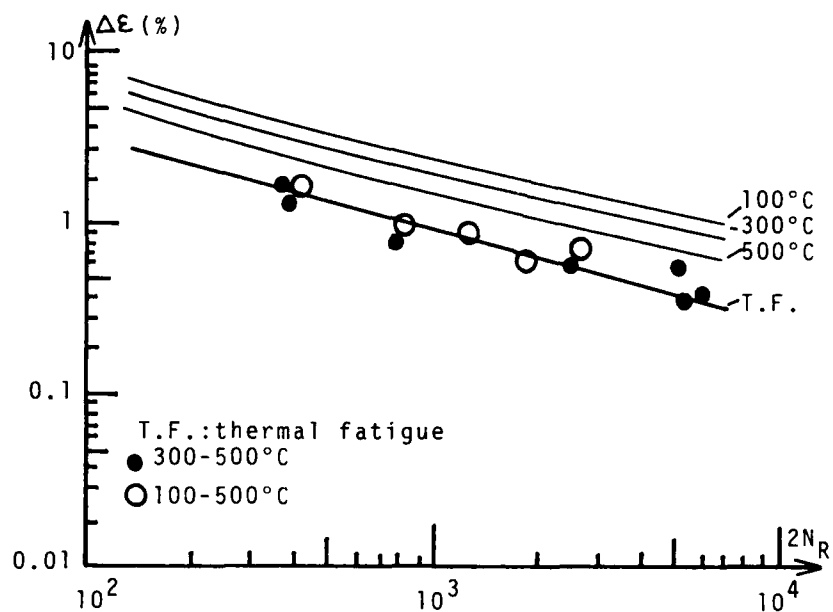


Figure 3 Comparison of mechanical strain in thermal fatigue with total strain in low cycle fatigue

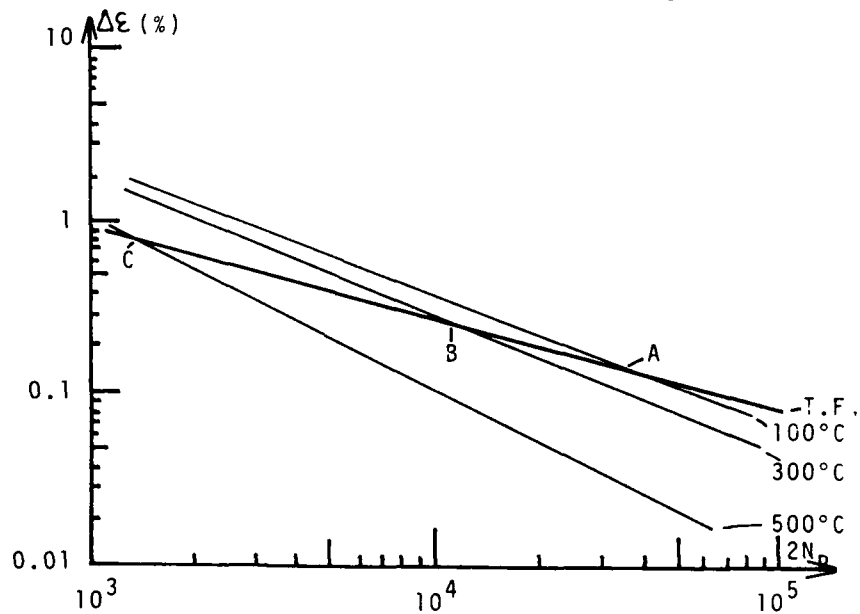


Figure 4 Comparison of mechanical strain in thermal fatigue with plastic strain in low cycle fatigue

FATIGUE 87

## FATIGUE 87

### AXIAL CREEP-FATIGUE DAMAGE ASSESSMENT IN TYPE 316 SS MATERIAL

S. Y. Zamrik and D. C. Davis \*

Failure resulting from the interaction of creep-fatigue under a 30 minute hold-time and in LCF at 620°C (1150°F) was assessed in terms of mechanical and microstructural response. Damage was analyzed by applying two strain ranges whereby the effect of plastic strain and creep strain was characterized. A strain rate concept is introduced in this paper for predicting creep-fatigue cumulative damage. The microstructural response to the interaction process was evaluated through fractographs.

### INTRODUCTION

Creep-fatigue interaction is a major research area and of concern to design engineers of structural components such as in power plants, gas and steam turbine engines and pressure vessels and piping systems which operate in an elevated temperature environment; therefore, the cycle of operation is not only mechanical but also thermal. Life assessment approaches of these components are normally based on results obtained from simple loading where, in actuality, the loading is complex; hence, these approaches must consider the effect of multiaxial stresses and strains. The damage due to creep-fatigue interaction, then becomes a function of multiaxiality. The first step in multiaxial damage analysis is the understanding of basic fatigue and creep damage mechanisms that occur as a result of simple uniaxial loading. Therefore, the authors are presenting the case of uniaxial creep-fatigue

\*Department of Engineering Science and Mechanics,  
The Pennsylvania State University

## FATIGUE 87

interaction as a first step in their research work on micro-macro multiaxial creep-fatigue damage. The material in this study is type 316 stainless steel of known heat. It is not the authors intention to review the literature since a great number of papers have been appearing each year discussing this subject; however, very few investigators have studied the micro-macro response of the material to creep-fatigue damage.

### SPECIMEN AND TEST PROCEDURE

Type 316 material of known heat was donated by Oak Ridge National Laboratory. The material had a coarse grain structure (ASTM #3) and was supplied in the form of a 2.5 cm x 305 cm (1"x120") bar. Specimens, as shown in Figure 1, were fabricated in the tubular form and were specifically designed for axial as well as torsional loading. Specimens were machined by a low stress grind process and then annealed prior to testing.

Low cycle fatigue tests were carried out under two strain range amplitudes, 1.0% and 0.5%, covering both high and low plastic strains. The LCF tests were run with a fully reversed triangular wave form at 10 cycles per minute, producing a constant strain rate with minimum creep effect. Hysteresis loops, and stress-strain data output was recorded and transmitted to a computerized storage data system. The creep effect was introduced through a 30 minute hold-time applied at the tension side of the LCF cycle, as shown schematically in Figure 2. In addition, the relaxed stress during the hold-time period, was recorded and stored for analysis. Strain measurements were taken by a high temperature extensometer mounted on the gage section. Temperature of 620°C (1150°F) was applied through an induction heating system and all specimens were held at zero load to obtain thermal equilibrium prior to cycling. Failure was determined by a 5% drop in the load from the half-life amplitude. Post fracture analysis of the failed specimens was conducted, using scanning electron microscopy techniques. Details of experimental procedure and test equipment can be found in reference (1).

### EXPERIMENTAL RESULTS

Stress range vs. number of cycles for the LCF and hold-time tests are shown in Figure 3 for two strain range levels. In both

types of tests, the material showed hardening up to 100 cycles followed by softening when the total strain range was held constant at 1%; however, at the lower strain range of 0.5%, there was a saturation stage followed by a quick drop in the softening stage. The stress relaxation data recorded during the hold-time tests is shown in Figure 4 as stress range vs. 30 minute hold-time at approximately 30%, 50% and 90% of life.

## DISCUSSION

### Macrostructural Evaluation

Analysis of the data, presented in Figure 3, shows that the fatigue life ( $N_f=4000$ ) of the 0.5% total strain range LCF test was greater than the fatigue life ( $N_f=863$ ) of the 1% total strain range by 63%. Examination of LCF strain range components at mid-life showed that  $\Delta\epsilon_{pp}(=0.64\%)$  was 64% of the total 1% strain range; whereas, in the 0.5% LCF test,  $\Delta\epsilon_{pp}(=0.22\%)$  was only 44%. These results indicate that more plastic (inelastic) strain interacted with the fatigue process during the 1% total strain range LCF test, and hence caused a greater reduction in fatigue life. Returning to Figure 3, the 30 minute hold-time effect is shown to be detrimental to fatigue life. The mid-life hold-time data show that the 1% total strain range test has a total inelastic strain range  $\Delta\epsilon_{in}(=0.687\%)$ , which contains a  $\Delta\epsilon_{pp}(=0.648\%)$  and a  $\Delta\epsilon_{cp}(=0.0392\%)$ , is 68.7% of the total strain range. On the other hand, the hold-time mid-life data for the 0.5% total strain range test show the  $\Delta\epsilon_{in}$  to be 0.281%, consisting of a  $\Delta\epsilon_{pp}(=0.258\%)$  and a  $\Delta\epsilon_{cp}(=0.023\%)$ , is 56% of the total strain range. At the 1.0% strain range level, both the LCF and hold-time tests, had an inelastic strain range component greater than at the 0.5% range. However, this observation does not mean that the 1.0% hold-time test has more creep than the 0.5% test. For the 1.0% hold-time test, the creep strain accumulation ( $\Delta\epsilon_{cp} \times N_{fh}$ ) is 13.25%, whereas the total creep strain accumulation for the 0.5% test is 22.66%. These results suggest that the fatigue life at 0.5% total strain range is more creep dominant than at 1.0%.

The stress relaxation data obtained from the 30 minute hold-time test, Figure 4, is shown in Figure 5 in terms of stress relaxation rate vs. hold-time. Normalizing the stress rate data

## FATIGUE 87

by Young's modulus yields a power law creep model that can be expressed as:

$$\epsilon_{cp} = A t^m \quad (1)$$

where A and m are material constants evaluated from Figure 5. Creep strain as expressed in equation (1) is plotted for the two strain ranges as shown in Figure 6. Comparison of the two curves indicates that the 0.5% is more representative of low-stress long-term creep.

### Cumulative Damage Rule

The linear cumulative damage rule for creep-fatigue interaction is normally expressed as:

$$\emptyset_f + \emptyset_c = 1 \quad (2)$$

where  $\emptyset_f$  and  $\emptyset_c$  are respectively the fatigue damage fraction and the creep damage fraction. The fatigue damage fraction  $\emptyset_f$  is defined as:

$$\emptyset_f = N_{fh} / N_f \quad (3)$$

where  $N_{fh}$  and  $N_f$  are the number of cycles to failure in fatigue with hold-time and number of cycles to failure in LCF at the same total strain range.

From the data shown in Figure (5), a creep damage fraction model based on ductility exhaustion is given in the form of:

$$\emptyset_c = N_{fh} \int [\dot{\epsilon}_{cp} / D(\dot{\epsilon}_{cp})] dt \quad (4)$$

where  $\dot{\epsilon}_{cp}$  is obtained from Figure 5 and  $D(\dot{\epsilon}_{cp})$  is the material ductility function. Equation (4) can be integrated numerically as:

$$\emptyset_c = N_{fh} \sum_{i=1}^n (\dot{\epsilon}_{cp} / D(\dot{\epsilon}_{cp}))_i \Delta t_i \quad (5)$$

where  $n$  is the number of steps in the integration over the hold-time period. This proposed integration method is in agreement with Wareing et al. (3) model since it takes into account the instantaneous magnitude of creep strain rate and the ductility dependency on strain rate. However, data on ductility at low strain rates is not well documented.

#### Microstructural Evaluation

The LCF cyclic stress strain response at 1.0% strain range showed the material to harden and gradually soften. The hardening was mainly associated with edge dislocation multiplication mechanism which was uniformly distributed in all grains with no dislocation pile-up observed at the grain boundaries. The gradual softening was associated with grain boundary migration due to dislocation free zones at these boundaries and the formation of high dislocation density in subgrains. Secondary cracks were not observed on the fracture surface, indicating a high rate of crack propagation. Therefore, damage was a result of high dislocation density regions. For the 30 minute hold-time test, the cyclic stress strain response showed strain hardening and softening similar to the LCF test but with a drastic loss in life. The effect of hold-time facilitated dislocation subgrain formation and extensive grain boundary migration. A decrease in dislocation density occurred by dislocation interaction such as dislocation annihilation and grain boundary migration. The extensive migration of grain boundaries was the result of dislocation free zones, and absence of carbides or cavities along the migrated grain boundaries. Zahiri (4) showed grain ejection by the migration of three adjacent grain boundaries as in Figure 7. A large number of intergranular secondary cracks were observed on the gage surface and few on the fracture surface, indicating a slower crack propagation rate. The fracture surface showed cracks initiated and propagated by an intergranular mode.

The LCF stress strain response at the 0.5% strain range showed hardening, saturation and softening stages. The saturation stage was a balance between the hardening mechanism, dislocation accumulation, the softening process, grain boundary migration, and grain ejection. Secondary cracks were concentrated along grain boundaries with dislocation pile-up at the boundaries. The fracture surface showed crack initiation to be intergranular rather than transgranular as

## FATIGUE 87

found for the 1.0% strain range test. The propagation was relatively transgranular with fatigue striations. Damage was identified to be both the formation of high density dislocation debris and grain boundary migration. With the inclusion of the 30 minute hold-time at 0.5% strain range, grain boundary migration was not observed but extensive cavities along grain boundaries and carbides precipitation were observed as shown in Figure 8. The fracture surface exhibited intergranular initiation and propagation modes. Striations were not detected on the fracture surface, indicating an embrittlement of the grain's interior either by oxygen atom penetration or carbides precipitation. Damage was attributed to cavity formation which caused deterioration in the material resistance to intergranular fracture and to loss of ductility as a result of carbides precipitation.

### CONCLUSIONS

Creep-fatigue interaction of type 316 stainless steel at 620°C (1150°F) showed a plasticity dominated deformation mechanism when the 1.0% strain level was applied, and a creep dominated mechanism at the 0.5% strain range level. The difference in the two mechanisms is attributed to the microstructural response of the material to plasticity and to creep. High dislocation density with grain boundary migration and cavity formation with carbides precipitation were the two main microscopic deformation mechanisms affecting the interaction process. A creep-fatigue cumulative damage rule approach based on strain rate is proposed when creep is the dominant component.

SYMBOLS USED

$D$  = creep ductility  
 $D(\dot{\epsilon})$  = material ductility function  
 $\Delta\epsilon_{cp}$  = creep strain range followed by plastic strain range  
 $\dot{\epsilon}_{cp}$  = creep strain rate ( / min)  
 $\epsilon_{cp}$  = creep strain  
 $\Delta\epsilon_{in}$  = inelastic strain range  
 $\Delta\epsilon_{pp}$  = plastic strain range  
 $\Delta\epsilon_t$  = total strain range  
 $\Delta\sigma$  = stress range (MPa)  
 $\sigma_{max}$  = maximum stress range (MPa)  
 $\sigma_r$  = relaxed stress (MPa)  
 $E$  = Young's modulus of elasticity  
 $f$  = frequency ( / sec)  
 $LCF$  = low cycle fatigue  
 $A, m$  = material constants  
 $N$  = number of cycles  
 $N_f$  = number of cycles at failure in LCF  
 $N_{fh}$  = number of cycles at failure with hold-time  
 $t$  = time (min)  
 $t_h$  = hold-time period (min)  
 $\phi_c$  = creep fraction damage  
 $\phi_f$  = fatigue fraction damage

REFERENCES

- (1) Antolovich, S.D. and Zamrik, S. Y. , "Fatigue Damage Under A Complex Loading System," NASA-CR-174787, Oct. 1984
- (2) Mirdamadi, M., "Ph.D. Thesis Research In Progress," The Pennsylvania State University.
- (3) Wareing J., Bretherton, I and Hales, R. , "Failure Criteria During Elevated Temperature Creep-Fatigue Cycling of Austenitic Stainless Steel," Proceedings 8th International Conference on Structural Mech. in Reactor Tech., pg. 31-54, Aug. 26-27, 1985.
- (4) Zahiri, F., "M.S. Thesis Research In Progress," The Pennsylvania State University.

- (5) Majumdar, S. and Maiya, P., "Creep-Fatigue Interaction in Austenitic Stainless Steel," Canada. Metal. Quart. 18, 57, 1979.
- (6) Hales R., "A Method of Creep Damage Summation based on Accumulated Strain for Assessment of Creep-Fatigue Endurance," Fatigue and Fracture of Eng. Mater. and Structures, 6, 121, 1983.
- (7) J. J. Blass and S. Y. Zamrik, 1976 ASME-MPC Symposium on Creep-Fatigue Interactions, ASME, 1976, pp. 129-159.

#### ACKNOWLEDGEMENT

Research results presented in this paper are part of a program supported by Pressure Vessel Research Council (PVRC), of the Welding Research Council under the guidance of "Cyclic and Creep Behavior of Components S/C" of the Fabrication Division and "Elevated Temperature Design S/C" of the Design Division.

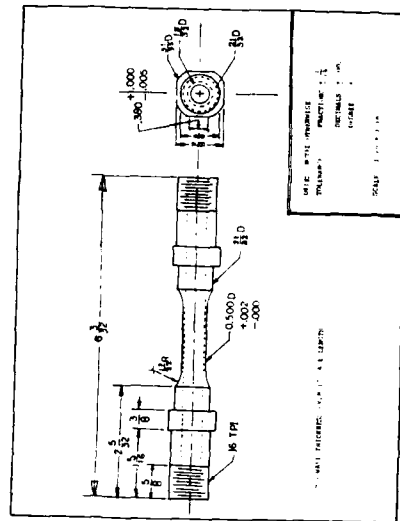


Figure 1. Test Specimen

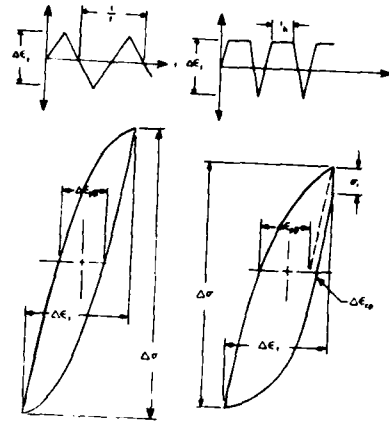


Figure 2. Test Cycles - Hysteresis Loops

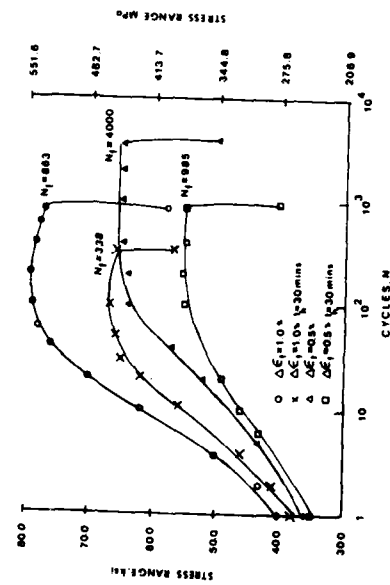
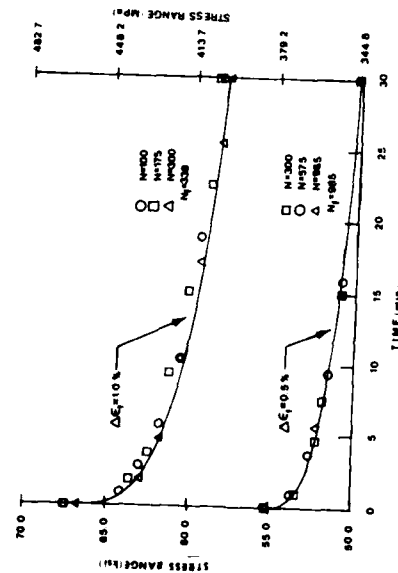


Figure 3. Stress Range vs. N



#### Figure 4. Stress Relaxation

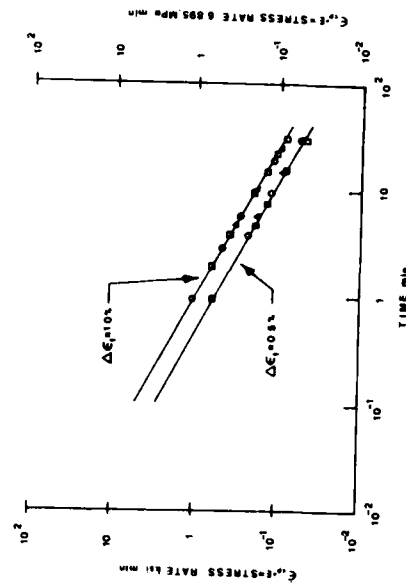


Figure 5. Stress Relaxation Rate, (2)

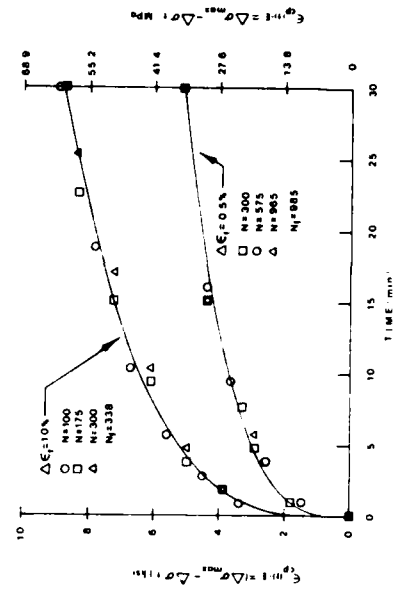


Figure 6. Creep Strain



Figure 7. Grain Ejection



Figure 8. Grain Boundary Cavitation

AN ANALYSIS OF TEMPERATURE EFFECT ON LCF CRACK GROWTH RATES IN  
SUPERALLOY GH36

Xie Jizhou and Liu Shaolun\*

The low-cycle fatigue (LCF) crack growth rates of a superalloy GH36 have been determined by D. C. potential drop method in the temperature range from 160°C to 600°C. The experimental results have been analysed by LEFM parameter  $\Delta K$  and EPFM parameter  $\Delta J$ , respectively. It was found that the high temperature LCF crack growth rates of alloy GH36 can be characterized by stress intensity factor range  $\Delta K$ , and the coefficient and exponent in Paris' formula are functions of temperature. An expression for Paris' formula of alloy GH36 over a wide range of temperature has been proposed.

INTRODUCTION

Experience shows that fatigue cracks appear easily at slot bottom in the I-st stage turbine disk of some aero-engines. However, after the crack initiation, the crack growth is very slow. Therefore, the turbine disks with fatigue cracks still have enough residual strength and can safely operate for a long time(1). In order to make a damage tolerance design and determine the allowable crack length, it is necessary to measure and analyse the fatigue crack growth rates at various temperature.

Generally speaking, the fatigue crack growth rates of components operating at high temperature, such as turbine disks and blades, are mainly affected by temperature. At present, studies about the effect of temperature on LCF crack growth are still in such a stage that fatigue crack growth rates can only be quantitatively analysed through measurements at various temperature. In this way, it's very difficult to satisfy the requirement of quantitative analysis over a wide temperature range in engineering practice. Not long ago, McGowan and Lin(2) proposed a so-called kinetic model which correlates

\* Institute of Aeronautical Materials,  
Beijing, China

fatigue crack growth rates with frequency. This model assumes that both temperature and frequency only effect the coefficient in Paris' formula, and the exponent is a constant. However, some experiments have shown that the coefficient and exponent in Paris' formula change with temperature.

In this paper, LCF crack growth rates for alloy GH36 have been determined by D.C. potential drop method in temperature range from 160°C to 600°C and the expression for Paris' formula of alloy GH36 over a wide range temperature has been constructed.

#### MATERIAL AND EXPERIMENTAL PROCEDURE

The chemical compositions and mechanical properties of the material are listed in Table 1 and 2, respectively. The specimens were cut from the turbine disk and were heat-treated at 1000°C/45 min. rise to 1140°C/90 min. water cool; 650°C/15 min. rise to 783°C/17 hr. air cool prior to machining.

TABLE 1. Chemical compositions of alloy GH36 (wt%)

C	Si	Mn	Ni	Cr	Mo	Nb	Ti	Fe
0.37	0.56	8.4	8.11	12.5	1.24	0.34	0.012	bal.

TABLE 2. Mechanical properties of alloy GH36 at R. T.

Ultimated Tensile Strength (MPa)	Yield Strength (MPa)	Elongation (%)	Area Reduction (%)
1044.7	686.7	21.5	4.3

The specimens used were WOL-type with 10 mm thick, as shown in Fig. 1. The expression of stress intensity factor(3) is

$$K = \frac{P}{B\sqrt{W}} F\left(\frac{a}{W}\right) \dots\dots\dots (1)$$

$$\text{where } F\left(\frac{a}{W}\right) = 30.96\left(\frac{a}{W}\right)^{1/2} - 195.8\left(\frac{a}{W}\right)^{3/2} + 730.6\left(\frac{a}{W}\right)^{5/2} \\ - 1186.3\left(\frac{a}{W}\right)^{7/2} + 754.6\left(\frac{a}{W}\right)^{9/2}$$

p - load (KN)  
a - crack length (mm)  
B - specimen thickness (mm)  
w - specimen width (mm)

The fatigue tests were performed in a hydraulic LCF testing

## FATIGUE 87

machine with a high temperature furnace, and were run at 160, 350, 500 and 600°C with stress ratio,  $R=0.1$  and a frequency 0.5 Hz using a triangular wave form.

The fatigue crack length was measured by D.C. potential drop method. For the J-integral tests, a special extensometer with a linear variable differential transducer (LVDT) measuring the displacement between load points was employed.

### EXPERIMENTAL RESULTS AND DISCUSSION

da/dN- $\Delta K$  curves. The curves da/dN- $\Delta K$  of alloy GH36 at 160, 350, 500 and 600°C are shown in Fig. 2. Their expressions for Paris' formula are as follows:

$$da/dN = 0.7019 \times 10^{-7} (\Delta K)^{2.0402} \quad (600^\circ\text{C}) \quad \dots\dots\dots (2)$$

$$da/dN = 0.3657 \times 10^{-9} (\Delta K)^{3.0269} \quad (500^\circ\text{C}) \quad \dots\dots\dots (3)$$

$$da/dN = 0.5875 \times 10^{-10} (\Delta K)^{3.3429} \quad (350^\circ\text{C}) \quad \dots\dots\dots (4)$$

$$da/dN = 0.1639 \times 10^{-12} (\Delta K)^{4.4082} \quad (160^\circ\text{C}) \quad \dots\dots\dots (5)$$

where  $\Delta K = K_{\max}(1-R)$ ,  $K_{\max}$  is the maximum stress intensity factor,  $R$  is stress ratio. From Fig. 2 it can be seen that the fatigue crack growth rates constantly increase with the increase of temperature. The curves slope are different from each other and increase with the decrease of temperature.

Experimental Results of cyclic J-integral. In order to verify the validity of  $\Delta K$  in the high temperature LCF crack growth rates of alloy GH36, we have carried out some experiments with EPFM parameter  $\Delta J$ . The tests were conducted with load-control technique and method determining J-integral is shown schematically in Fig. 3. The total and elastic deformation work of each measured point is calculated through loading-displacement hysteresis loops recorded by X-Y recorder. The cyclic J-integral is calculated by the following equation(4)

$$\Delta J = \frac{2}{Bb} (\alpha_1 \cdot U + \alpha_2 \cdot \Delta P \cdot \Delta \delta) + \frac{2U_e}{Bb} \cdot \begin{cases} -1.2025 \frac{a}{w} + 0.6233 & 0.3 \leq \frac{a}{w} \leq 0.5 \\ -0.02 \sin \left[ \frac{\pi}{0.23} \left( \frac{a}{w} - 0.53 \right) \right] & 0.5 \leq \frac{a}{w} \leq 0.95 \end{cases} \quad \dots\dots\dots (6)$$

where  $U$ ,  $U_e$  total and elastic deformation work, respectively.  
 $\Delta P$ ,  $\Delta \delta$  load and displacement increment, respectively.  
 $b=w-a$  specimen ligament size.  
 $\alpha$ ,  $\alpha_1$ ,  $\alpha_2$  constants.

$$\alpha_1 = 2 \left[ \left( \frac{a}{b} \right)^2 + \left( \frac{a}{b} \right) + \frac{1}{2} \right]^{1/2} - 2 \left( \frac{a}{b} + \frac{1}{2} \right)$$

# FATIGUE 87

$$\alpha_1 = \frac{1+a}{1+a^2} - a \frac{1-2a-a^2}{(1+a^2)^2}$$

$$\alpha_2 = a \frac{1-2a-a^2}{(1+a^2)^2}$$

The curves  $da/dN-\Delta J$  were fitted by following formula

$$\frac{da}{dN} = D(\Delta J)^\gamma \quad \dots\dots\dots (7)$$

where D,  $\gamma$  material constants.

The results obtained, i.e. curves  $da/dN-\Delta J$  are shown in Fig. 4. Their expressions are as follows

$$da/dN = 0.2739 \times 10^{-3} (\Delta J)^{2.6710} \quad (600^\circ\text{C}) \quad \dots\dots\dots (8)$$

$$da/dN = 0.7448 \times 10^{-4} (\Delta J)^{3.2854} \quad (500^\circ\text{C}) \quad \dots\dots\dots (9)$$

$$da/dN = 0.7416 \times 10^{-4} (\Delta J)^{2.7548} \quad (350^\circ\text{C}) \quad \dots\dots\dots (10)$$

In order to verify the validity of  $\Delta K$  in the high temperature LCF crack growth rates of alloy GH36, we have compared to the results with  $\Delta K$  and  $\Delta J$ , as shown in Fig. 5. The max. error is listed in Table 3. From the point of view of engineering, it may be considered that at 600, 500 and 350°C, the LCF crack growth rates of alloy GH36 expressed by  $\Delta K$  or  $\Delta J$  are all effective and the  $da/dN$  of alloy GH36 until 600°C belongs to linear elastic behaviour under given specimen size and load level requirements in this paper.

TABLE 3 Max. error of  $da/dN$  with  $\Delta K$  and  $\Delta J$

Temperature °C	350	500	600
$\left\{ \frac{(da/dN)_{\Delta K} - (da/dN)_{\Delta J}}{(da/dN)_{\Delta K}} \right\}_{\max.}$	27.04	-15.98	14.62

Application of McGowan-Liu' Kinetic Model and Its Modification. Not long ago McGowan and Liu(2) proposed a so-called kinetic model which contains effects of temperature, frequency, hold time and stress ratio on fatigue crack growth rates. For cyclic dependent condition, this model can be written

$$da/dN = C_1 \left( \frac{1}{v} \right)^m e^{-C_2/T} (\Delta K)^{n_3} \quad \dots\dots\dots (11)$$

where  $v$  frequency  
 $T$  temperature  
 $C_1, C_2, n_3, m$  constants

# FATIGUE 87

As mentioned above, the fatigue crack growth rates of alloy GH36 expressed by  $\Delta K$  or  $\Delta J$  are all effective. Thus the equation (11) can be applied to this case, as shown in Fig. 6. By means of least square method of binary function, the fit result is

$$\frac{da}{dN} = 0.1576556 \times 10^{-9} \exp\left[-24.744\left(\frac{1}{T} - \frac{1}{160}\right)\right] \Delta K^{2.9872} \dots\dots\dots (12)$$

But the equ. (12) assumes  $n_i$  to be unchangeable with temperature. This may be suitable for some structure steels (5), but it is not suitable for superalloys, such as alloy K5 (6), In-718 (7) (see Table 4) and alloy GH36 (see Fig.7).

TABLE 4 Dependence of C and n in Paris' formula with temperature

Alloy	Temp., °C	Material Conditions	C	m
K5	700	Conventional casting	$0.183 \times 10^{-18}$	8.52
		Directional solidification	$0.238 \times 10^{-13}$	5.54
	950	Conventional casting	$0.792 \times 10^{-11}$	4.04
		Directional solidification	$0.132 \times 10^{-10}$	3.81
IN718	24	Normal heat-treatment	$0.106 \times 10^{-48}$	10.26
	316	"	$0.609 \times 10^{-20}$	3.37
	427	"	$0.553 \times 10^{-19}$	3.17
	538	"	$0.857 \times 10^{-18}$	2.98

Therefore, the expression of fatigue crack growth rate with  $\Delta K$  and temperature T has been proposed in present paper.

$$da/dN = C(T) (\Delta K)^{n(T)} \dots\dots\dots (13)$$

where  $C(T)$ ,  $n(T)$  are 3 order polynomial of temperature. The expressions of  $C(T)$  and  $n(T)$  for alloy GH36 are as follows:

$$C(T) = (63174.3384T^3 - 63754.9645 \times 10^3 T^2 + 1962.2329 \times 10^6 T - 17665.1062 \times 10^8) \times 10^{-19}$$

$$n(T) = -9 \times 10^{-8} T^3 + 1.028 \times 10^{-4} T^2 - 4.037 \times 10^{-2} T + 8.744$$

$$(160^\circ\text{C} \leq T \leq 600^\circ\text{C})$$

To compare the equ. (13) with the equ. (11), the experimental results as well as calculated  $da/dN$  vs.  $\Delta K$  curves according to the

## FATIGUE 87

equs. (13) and (11) are plotted in Fig. 8.

It can be seen that calculated  $da/dN$  vs.  $\Delta K$  curves by the equa. (13) are in better agreement with experimentally determined values than that from equa. (11). The present method has been applied successfully to estimate residual life of the 1-st stage turbine disks of some aero-engine.

### CONCLUSIONS

Through a large number of LCF crack growth rate measurements for alloy GH36 and analysing its elastic-plastic behaviour with cyclic J-integral tests, the following conclusions have been obtained:

1. Under present test condition, LCF crack growth rates of alloy GH36 can be expressed by  $\Delta K$  using WOL specimen up to 600°C and increase with the increase of temperature.
2. The coefficients and exponents in Paris' formula are function of temperature. The equa. (13) can be applied into estimating the LCF crack rates at any temperature up to 600°C for GH36.

### REFERENCES

- (1) Nie Jingxu and Nie Cong, An analysis on J-integral of fatigue crack growth behaviour at slot bottom in turbine disk, proceeding of Chinese Aviation Society Symposium on Structural Strength and Vibration of Air Engine, pp. 175-185, 1981 (in Chinese).
- (2) McGowan, J. J. and Liu, H. W., J. of Eng. Mat. & Tech., Vol.103, pp. 246-251, 1981.
- (3) Zhu Wuyang et al., Measurement of Fracture toughness, Science Press, p. 78, 1979 (in Chinese).
- (4) Liu Shaolun and Xie Jizhou, J. of Engng for Gas Turbine and Power, Vol.108, pp. 521-524, 1986.
- (5) Fatigue at Evalated Temperature, ASTM STP520, p. 530, 1973.
- (6) Xie Jizhou and Liu Shaolun, An Investigation of High Temperature LCF Crack Growth Rates for D. S. Ni-Base Superalloy K5, The Proceeding of 2-ed International Conference on Fatigue and Fatigue Thresholds, Vol. III, Sept. 3-7, 1983.
- (7) James, L. A., J. of Eng. Mat. & Tech., Vol.103, pp. 234-239, 1981.

# FATIGUE 87

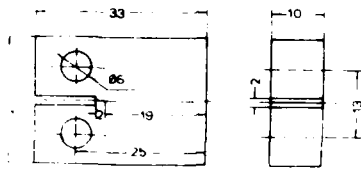


Fig. 1. WOL specimen

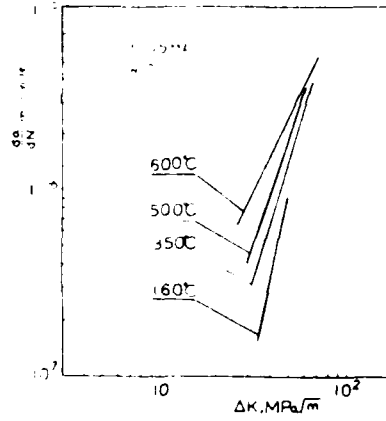


Fig. 2. Effect of temperature on fatigue crack growth rates

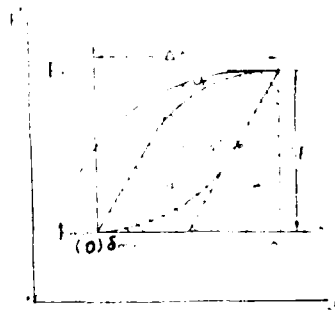


Fig. 3. Load-displacement hysteresis loop

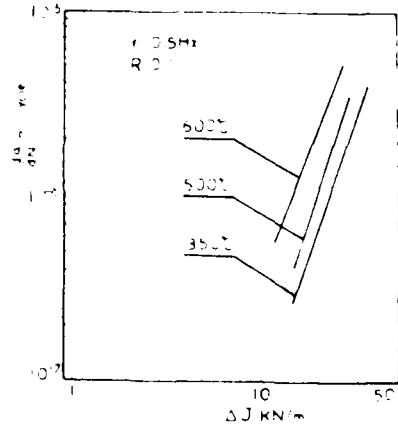


Fig. 4.  $da/dN$ - $\Delta J$  curves

# FATIGUE 87

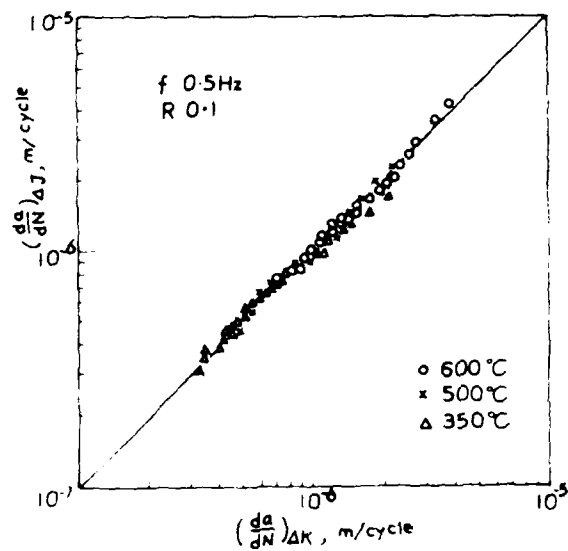


Fig. 5. Comparison of fatigue crack growth rate expressed by  $\Delta K$  with one by  $\Delta J$ .

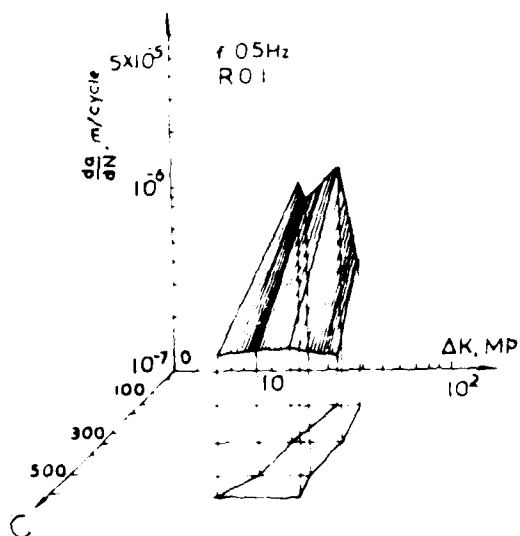


Fig. 6. Dependence of  $da/dN$  on  $\Delta K$  and temperature  $T$

# FATIGUE 87

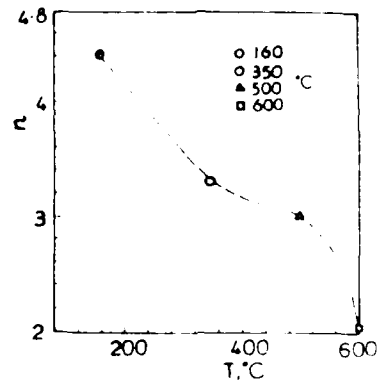


Fig. 7. Correlation between exponents and temperature

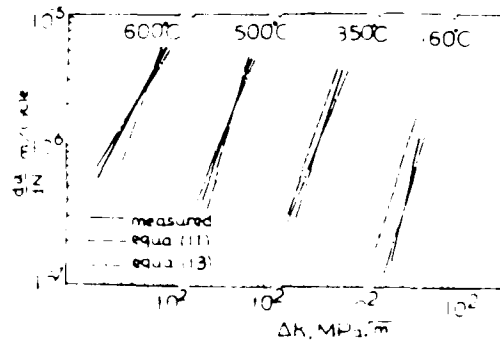


Fig. 8. Comparison of results calculated by equ. (11) with equ. (13)

FATIGUE 87

## FATIGUE 87

### THERMOMECHANICAL FATIGUE OF LEAD-BASE LOW TIN SOLDER

L. R. Lawson\*, M. E. Fine\* and D. A. Jeannotte†

Preliminary results are described of thermomechanical testing of a lead-base, low tin solder alloy. The effects of combined temperature and strain cycling are discussed. The effects of varying the relative timing of the temperature and strain cycles are presented. Data are also reported for the effects of varying the strain range and hold time at maximum strain. Changes with yield stress during cycling are discussed and the effect of the relative phasing of the strain and temperature cycles is correlated with a phenomenological model.

### INTRODUCTION

Life is often shorter in thermomechanical fatigue than in isothermal fatigue at the maximum temperature of the TMF cycle. Marchand and Pelloux give a list of 15 articles to illustrate this (1). Often such effects have been observed in the high temperature regime, where the homologous temperature is near 0.5. Consequently, two areas of economic importance have emerged, aircraft engine alloys and soft solders used in electronics. In this paper we present information about the character of thermomechanical fatigue in a soft solder, 3.5Sn-97.5Pb, having an homologous temperature of 0.5 near room temperature. In solders, considerable attention has been given to thermal and mechanical fatigue separately (2,3,4,5). However, little previous information appears to be available on the combined thermomechanical testing of solder.

In these tests two separate temperature regions have been explored. The first was 15 to 60°C. The second was 25 to 80°C.

\* Department of Materials Science and Engineering and Materials Research Center, Northwestern University, Evanston, IL.

† IBM Corporation, East Fishkill Facility, Hopewell Junction, NY.

## FATIGUE 87

The phase diagram for the system is given by Hansen and shows a solvus near 70°C. Isothermal tests were run at 80°C for comparison. The results of these tests indicate, first, that there is a strong effect relating life to the timing relationship between the thermal and mechanical cycles. Second, fatigue life in an in-phase test can be materially shorter than that predicted from the isothermal test. Third, the character of the peak stresses as a function of the number of cycles is different for the isothermal case than for the thermally-cycled material. Scanning electron micrographs taken of the samples before and after fatigue show that in the case of TMF the fracture mode was essentially intergranular.

The failure criterion used was one that has been adopted for the "initiation of an engineering crack": failure occurs at the point at which the peak stress begins to drop due to cracking (7). Intrusion and extrusion microcracking are commonly seen in solder after only a dozen or so cycles. So, this criterion includes initiation plus small crack propagation. Failure thus defined occurs at a critical point in the stress curve. In order to facilitate locating this point, data were smoothed by a fifth-degree least squares polynomial fit.

### MATERIAL

The experiments were conducted using a commercial grade solder alloy having a composition by analysis of 96.4% Pb, 3.5% Sn and 0.1% impurities. The material was cast into molds at 375°C. The reduced section of the sample measured 0.5 x 0.25 inch in cross-section and was 0.5 inch in length. Samples were homogenized for 4 days at 175°C and aged for a minimum of 7 days at room temperature to allow precipitation of the tin-rich phase. The average grain size as determined by the linear intercept method was 0.50 mm. The precipitates appeared to be Widmanstaetten plates oriented in  $\langle 110 \rangle$  directions. Samples were polished by electropolishing prior to testing.

### TEST APPARATUS AND PROCEDURE

Tests were conducted in air at 55%  $\pm$  3% relative humidity (23°C) using an MTS servohydraulic fatigue testing system. This system was outfitted with thermal cycling grips illustrated in Figure 1. These grips incorporate heaters and coolers operated under computer control. Strain and temperature were cycled using linear ramps in a nominally tension-tension test. The recoverable elastic strain was always a very small fraction of the total strain. Heating and cooling were accomplished through the ends of the sample in order to facilitate microscopy and eliminate surface temperature gradient effects. The ramp times were therefore set by the sample geometry and thermal constants. A ramp time of 1.5

## FATIGUE 87

minutes was used in the low temperature cycle and two minutes in the high temperature cycle in order to limit the maximum temperature gradient in the sample to near 6 degrees per cm. and the maximum departure from linearity within the cycle to near 3 degrees. Endpoints were held to a 0.5 degree tolerance. The details of the thermal cycling apparatus are described elsewhere (8).

One group of samples was fatigued with a total strain range of 0.73% and a 15 to 60°C temperature cycle consisting of 1.5 minute ramps. The phase of the mechanical cycle was delayed with respect to that of the temperature cycle by varying amounts ranging from 0 to 270 angular degrees. Total strain is defined here by:

$$\epsilon_{\text{total}} = \epsilon_{\text{mechanical}} + \epsilon_{\text{thermal}}$$

Another group of samples was fatigued using a 25 to 80°C temperature cycle. Cycles were composed of 2-minute linear ramps and hold times. Strain ranges were varied from 0.47% to 0.60% net mechanical strain. A third group was isothermally fatigued at 80°C. Strain ranges of 0.44%, 0.55% and 0.65% were used in conjunction with 2-minute linear ramps.

### RESULTS AND DISCUSSION

The tests over the 15 to 60°C range showed that fatigue life is definitely a function of the phase angle between the thermal and mechanical cycles. The table below shows some values of fatigue life obtained.

TABLE 1 - Effects of Lag on Thermomechanical Fatigue.

Lag	N <sub>f</sub> (cycles)	Net Mechanical Strain Range
0°	375 (averaged)	0.63%
90°	404	0.73%
180°	1174	0.83%
270°	1472	0.73%

Fatigue life correlated with the integral of the product of the instantaneous tensile stress and an Arrhenius function of the instantaneous temperature. Vaynman found an equivalent effective activation energy for isothermal fatigue of this material (5). Fatigue life did not correlate with mean stress, area under the hysteresis curves, peak stress nor peak strain.

A simple model to compare the effect of phase in a TMF cycle where all other variables are fixed is:

# FATIGUE 87

$$(N_f)^{-1} \propto \int_{\text{cycle}} \sigma^p \exp(-Q/kT) dt$$

The fatigue damage rate is proportional to the tensile stress times a reaction or diffusion rate. Conceptually, this damage rate may be thought of as a small crack growth rate or as an induction parameter for a large "engineering crack" since the details of the process have not been experimentally determined. The fatigue life as previously defined is thus inversely proportional to this damage rate. Table 2 compares the reciprocal of the observed relative fatigue lives to numerical evaluation of the above integral using different values for p and Q.

TABLE 2 - Relative  $(N_f)^{-1}$  for Various Lag Angles

	0°	90°	180°	270°
Observed	1	0.92	0.32	0.25
Q=45 (KJ/M)				
p=1	1	1.07	0.56	0.37
Q=45				
p=2	1	0.98	0.58	0.41
Q=50				
p=2	1	0.98	0.53	0.35
Q=65				
p=2	1	0.99	0.40	0.23

The model is suggestive but more information is needed before p and Q can be assigned values. A previous fit using different stress data gave p=1 as a better approximation than p=2 (8). For comparison, Vaynman obtained values up to 45 KJoules/Mole for the effective activation energy for isothermal fatigue of this alloy (5). In lead, the activation energy for vacancy formation is 51 KJoules/M (9). The activation energy for self diffusion is 107 KJoules/M (10). Consequently, the activation energy for vacancy motion is 56 KJoules/M. The activation energy for the diffusion of oxygen through PbO, which might be rate controlling in a corrosion fatigue scenario, is 93.7 KJoules/M (11).

In the 0-degree lag test (in-phase cycling) and in the 90-degree test, the peak stress vs. N curves seemed to indicate a period of latency followed by the rapid growth of a single large crack. SEM examinations showed a single large crack, initially transgranular, which became partially intergranular as it grew. In addition to this single crack, a few other apparently intergranular cracks were seen. In the 180-degree and 270-degree tests, the peak stress vs. N curves showed a more gradual change similar

## FATIGUE 87

to that seen in the isothermal tests to be discussed. SEM examination showed apparently intergranular cracking. These short cracks were numerous but did not link to form any large cracks.

A second group of tests was conducted using a 25 to 80°C temperature cycle. These tests compared the effects of strain range and hold time. Comparisons are also made with isothermal tests. Figures 2 through 4 show the curves of peak tensile stress (MPa) vs. N and related curves for a TMF test at 0.6% strain range and isothermal tests at 80°C of 0.55% and 0.65%. The differences are striking. The TMF sample failed rapidly near 150 cycles. The isothermal sample at the lower strain range lasted approximately 930 cycles and that at the higher strain range lasted about 535 cycles. SEM examinations showed that in TMF a single crack was responsible for failure. In the isothermal test, multiple unlinked short cracks were seen. Clearly, isothermal testing at the highest temperature of the cycle is not a good estimator of fatigue life in TMF in the case of solder.

Figure 5 shows a Coffin-Manson plot of the isothermal test data over a limited range along with related TMF data points. The fit has been obtained by weighting the data with confidence factors hence the allowed error is greatest for the 0.44% strain point since this appeared to represent an early failure. In any case, the life in TMF is materially shorter than that in isothermal fatigue. The fitted line represents the expression:

$$N_f = 1.70E-7 \Delta\epsilon^{-4.29}$$

Besides the relatively short life of solder in TMF, there are other differences between isothermal and thermomechanical fatigue. These may be seen in Figures 3 and 4. In these, the isothermal data resembles that for out-of-phase testing. During the first 20% of life there is a stabilization period after either cyclic hardening or softening followed by gradual hardening until significant cracking begins. This pattern is consistent in most all tests. The compressive stresses are increased in in-phase TMF over those seen isothermally. Consequently, the absolute stress ratio is smaller while the stress range is larger. Most of this effect can be explained by the effect of temperature on yield stress since the compression portion of the cycle is at low temperature relative to the tension portion of the cycle.

Figure 6 illustrates the effect of strain range on thermomechanical fatigue of the solder. An increase in mechanical strain range from 0.47% to 0.60% causes a reduction in life from 315 cycles to 155 cycles. As expected, the increase in strain brought about an increase in peak tensile stress from typical values of 6.6 MPa to 7.3 MPa. Thus a 27.6% fractional increase in strain caused a 10.6% increase in the tensile stresses and a 51% decrease in life. The curves for peak compressive stress are

## FATIGUE 87

similar to those for tensile stress and show a similar fractional increase with strain. The one difference is that during the stabilization period the compressive stress is increasing as the tensile stress is decreasing. The changes in stabilization are changes mostly in stress ratio and affect the stress range to a lesser extent. The stress range chart is often helpful in deciding whether a given fluctuation represents a crack or a stabilization-like fluctuation.

Figure 7 illustrates the effect of hold time on thermomechanical fatigue life. Hold times are zero, 60 and 120 seconds at 80°C. At the mechanical strain range of 0.47% the addition of 60 seconds hold time decreases fatigue life from 315 cycles to about 90 cycles. Increasing the hold time further to 120 seconds did not appear to affect the fatigue life assuming the inflection at 45 cycles does not represent failure. SEM examination of the sample at the end of the test showed only several cracks about 1 to 3 mm in length. Vaynman (5) found saturation of the hold time effect near 120 seconds in isothermal tests near 80°C.

The results indicate that in-phase TMF is the worst case for this solder. It is also seen that the fatigue life in a TMF test may be as little as 1/5 that of the same alloy experiencing the same cyclic strain at the highest temperature of the TMF cycle. During TMF and to a lesser extent during isothermal testing, fluctuations are seen in the tensile and compressive yield stresses during the first 20% of life. These fluctuations do not appear to be related to macroscopic crack formation but do lead to higher compressive than tensile yield stresses. The effects of hold time and strain range are similar to those seen by Vaynman (5) in isothermal testing.

### SYMBOLS USED

- $N_f$  = number of cycles to failure
- $\epsilon$  = tensile strain
- $\Delta\epsilon$  = tensile strain range
- $\sigma$  = instantaneous stress (MPa)
- $P$  = stress exponent
- $Q$  = effective activation energy (KJ/M)

## FATIGUE 87

### REFERENCES

- (1) Marchand, N. and Pelloux, R., Eleventh Canadian Fracture Conference on Time Dependent Fracture, 1984.
- (2) Bendix Corporation, "Thermal Fatigue of Solder Alloys", Report BDX-613-2341, 1980.
- (3) Burgess, J., IEEE Trans. on Components, Hybrids and Mfg. Tech., Vol. CHMT-4, 1984, p. 405.
- (4) Lau, J. and Rice, D., Solid State Technology, Vol. 28, 1985, p. 91.
- (5) Vaynman, S., "Isothermal Fatigue of 96.5Pb-3.5Sn Solder", Ph.D. dissertation, Northwestern University, Evanston, IL, 1986.
- (6) Hansen, M., "Constitution of Binary Alloys", McGraw-Hill, New York, 1958.
- (7) Thielen, P. N., Fine, M. E. and Fournelle, R. A., Acta Metall., Vol. 34, 1976, p. 1.
- (8) Lawson, L., "Thermomechanical Fatigue Testing of 97Pb-3Sn", M.S. dissertation, Northwestern University, Evanston, IL, 1986.
- (9) D'Heurle, F., J. Phys. Soc. Japan, Vol. 18, Supp. 2, 1963, p. 184.
- (10) Okkerse, B., Acta Metall., Vol. 2, 1954, p. 551.
- (11) Kofstad, P., "Nonstoichiometry, Diffusion and Electrical Conductivity in Binary Metal Oxides", Wiley, New York, 1972, p. 358.

### ACKNOWLEDGEMENT

This work was supported by a grant from the IBM Corporation.

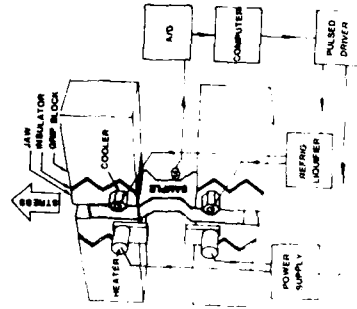


Figure 1 Thermal cycling grips

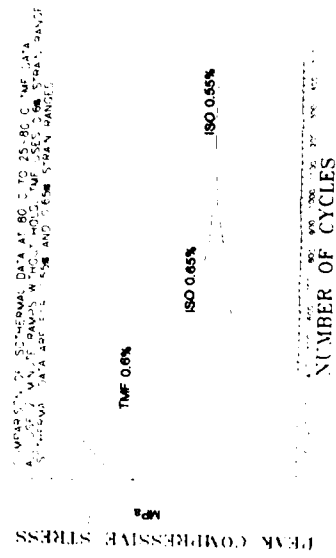


Figure 3 Peak compressive stress

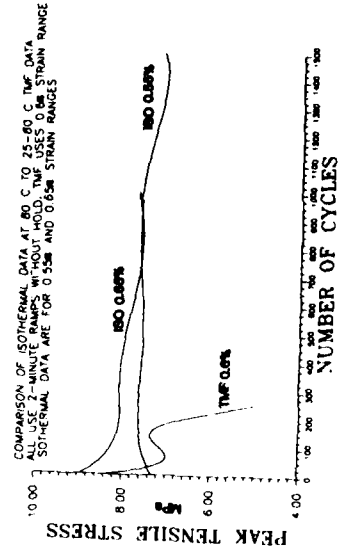


Figure 2 Peak tensile stress

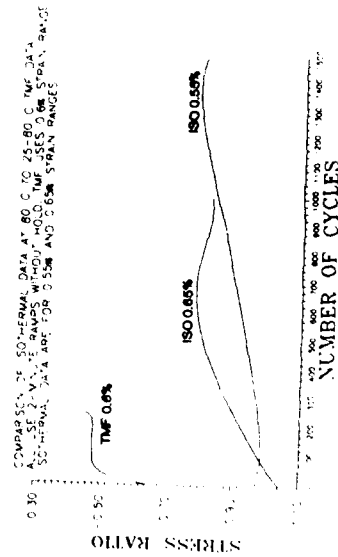


Figure 4 Stress ratio

# FATIGUE 87

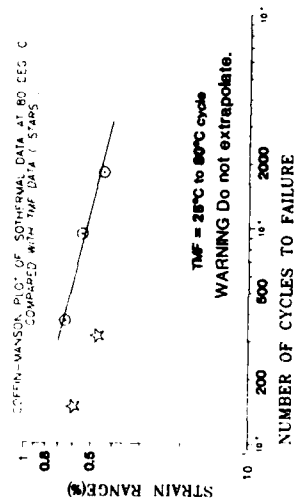


Figure 5 Coffin-Manson plot

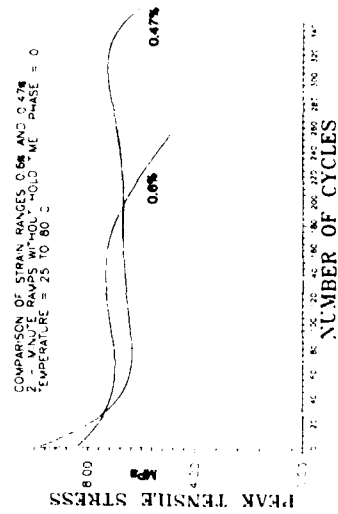


Figure 6 Strain range effect (TMF)

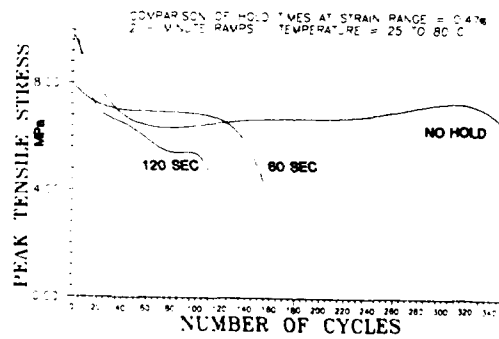


Figure 7 Hold time effect (TMF)

FATIGUE 87

LED  
8